Numerical Investigation of Cryogenic Cavitation in Liquefied Natural Gas (LNG) Flows Using a Homogeneous Flow Model

by

Saeed Rahbarimanesh

A THESIS SUBMITTED IN PARTIAL FULFILLMENT OF
THE REQUIREMENTS FOR THE DEGREE OF

Doctor of Philosophy

in

THE COLLEGE OF GRADUATE STUDIES
(Mechanical Engineering)

THE UNIVERSITY OF BRITISH COLUMBIA
(Okanagan)

July 2020

The following individuals certify that they have read, and recommend to the College of Graduate Studies for acceptance, a thesis/dissertation entitled:

Numerical Investigation of Cryogenic Cavitation in Liquefied Natural Gas (LNG) Flows Using a Homogeneous Flow Model

submitted by **Saeed Rahbarimanesh** in partial fulfillment of the requirements of the degree of **Doctor of Philosophy in Mechanical Engineering**.

Examining Committee:

Dr. Joshua Brinkerhoff, School of Engineering, UBC

Supervisor

Dr. Sunny Li, School of Engineering, UBC

Supervisory Committee Member

Dr. Rudolf Seethaler, School of Engineering, UBC

Supervisory Committee Member

Dr. Morad Abdelaziz, School of Engineering, UBC

University Examiner

Dr. Peter Oshkai, Department of Mechanical Engineering, University of Victoria

External Examiner

Abstract

Fluid machinery used for pumping cryogenic liquid fuels are severely impacted by the onset and development of cavitation. Cavitation in non-cryogenic fluids is commonly assumed to be isothermal, but cavitation in cryogenic fluids is substantially influenced by thermal effects. The present research investigates the cavitation in liquefied natural gas (LNG) flows by developing a computational fluid dynamics solver for modeling cryogenic cavitation. The solver employs a homogenous equilibrium mixture approach to compute the multiphase solution in a density-based Eulerian framework. Thermal effects are captured via a coupled solution of a cryogenic form of the density, momentum, and energy equations. Thermophysical properties of the cryogenic fluid are corrected using the computed pressure and temperature fields to account for the baroclinic nature of the density field and temperature dependence of the fluid's saturation properties, specific heat, and dynamic viscosity. The developed cryogenic solver is validated against experimental measurements of cavitating flow of liquid nitrogen in a circular orifice and a Laval nozzle, achieving good agreement for the considered range of operating conditions. The resulting fluid properties of a simulated LNG cavitation flow inside the Laval nozzle are also verified with a good accuracy against the reference property database. Detailed physics of the LNG phase-change phenomena is investigated by employing the developed solver for simulating two fundamental case studies in a variety range of operating conditions: 1) cavitating flow of LNG inside the Laval nozzle; and 2) cavitating mixing layer of LNG behind a flat plate splitter, with the aim of characterizing the interaction mechanisms between LNG vaporization-condensation processes and shear-layer instabilities, and their correlations with thermodynamic effects. The conducted investigations exemplify the dynamics of LNG cavitation in basic wall-bounded and free shear layers of LNG, so providing a refined database for understanding cavity-vortex interactions in complex LNG-based turbomachinery.

Lay Summary

With the rise of climate change, there is a recent interest in liquefied natural gas (LNG) as an alternative green fuel for commercial, marine, and mining vehicles. Because of the low-boiling cryogenic temperature of LNG, most of the LNG-based fuel systems operate near the saturation point to deliver the highest efficiency. Nevertheless, this may improve the likelihood of LNG phase change from the liquid to vapor -- termed cavitation -- which undesirably degrades the system performance significantly. In addition to degrading the efficiency, cavitation may cause damaging cyclic stresses and erosion of the system components. Because of the high-cost experimental facilities and the complexity of measuring cavitation in cryogenic conditions, the popular computation fluid dynamics (CFD) is employed in this research for developing a cost-effective numerical solver to simulate LNG cavitating flows in a range of practical machinery, aimed at facilitating more reliable future designs of LNG-based fuel systems.

Preface

The present PhD research work was supervised by Dr. Joshua Brinkerhoff at the UBC Advanced Computational Modeling Laboratory (ACML), with the cooperation of Westport Fuel Systems©, Compute Canada©, and International Institute for Cavitation Research (ICR).

During this research, several publications and conference proceedings have been contributed to scientific communities. The list of highlighted contributions pertaining to this thesis, including the "current" and "ongoing" publications, is as follows:

- **Current Contributions:**

1) S. Rahbarimanesh, J. Brinkerhoff, J. Huang, *Development and Validation of a Homogeneous Flow Model for Simulating Cavitation in Cryogenic Fluids*, Applied Mathematical Modeling 56, 2018, pp. 584-611.

My contribution to this paper was development, implementation, and validation of the numerical model. I also performed the numerical simulations including grid generation, test set-up, and post-processing, and prepared the manuscript. Dr. Brinkerhoff and Dr. Huang proposed the preliminary motivation, reviewed the methodology and results, and provided resources.

Parts of the texts, figures, and tables of Chapters 2-5 have been used in this paper.

2) S. Rahbarimanesh, J. Brinkerhoff, *A Numerical Study on the Effects of Cavitation Number on Cavitating Mixing Layer of Liquefied Natural Gas (LNG) behind a Flat Plate Splitter*, ASME series: Proceedings of the 10th International Cavitation Symposium (CAV2018), 2018, ASME Press.

My contribution to this paper was conducting the numerical simulations including grid generation, test set-up, and post-processing, along with preparing the manuscript. Dr. Brinkerhoff supervised the work, reviewed the results and manuscript, and provided resources.

Parts of the texts, figures, and tables of Chapters 2-4, and 8-9 have been used in this paper.

3) S. Rahbarimanesh, J. Brinkerhoff, *Effects of Interfacial Tension Forces on Cavitating Flow of Liquefied Natural Gas (LNG) in a Laval Nozzle*, 26th Annual Conference of the CFD Society of Canada (CFDSC2018), 2018, Winnipeg, Canada.

My contribution to this paper was development and implementation of the numerical model. I also performed the numerical simulations including grid generation, test set-up, and post-processing, and prepared the manuscript. Dr. Brinkerhoff proposed the preliminary motivation, reviewed the methodology and results, and provided resources.

Parts of the texts, figures, and tables of Chapters 2-6 have been used in this paper.

4) S. Rahbarimanesh, J. Brinkerhoff, *Numerical Investigation of a Cavitating Mixing Layer of Liquefied Natural Gas (LNG) behind a Flat Plate Splitter*, Proceedings of the 70th Annual Meeting of the APS Division of Fluid Dynamics (APS-DFD), 2017, Denver, United States.

My contribution to this paper was conducting the numerical simulations including grid generation, test set-up, and post-processing, along with preparing the manuscript. Dr. Brinkerhoff supervised the work, reviewed the results and manuscript, and provided resources.

Parts of the texts, figures, and tables of Chapters 2-4, and 8 have been used in this paper.

5) S. Rahbarimanesh, J. Brinkerhoff, *A Numerical Study on Cavitating Flow of LNG inside a Laval Nozzle: Effects of Cavitation Number and Nozzle Expansion Angle*, Proceedings of the 16th European Turbulence Conference (ETC16), 2017, Stockholm, Sweden.

My contribution to this paper was conducting the numerical simulations including grid generation, test set-up, and post-processing, along with preparing the manuscript. Dr. Brinkerhoff supervised the work, reviewed the results and manuscript, and provided resources.

Parts of the texts, figures, and tables of Chapters 2-6 have been used in this paper.

6) S. Rahbarimanesh, J. Brinkerhoff, *Diffusion Angle Effects on Cavitating Flow of Liquefied Natural Gas (LNG) Inside a Laval Nozzle*, Proceedings of the 26th Canadian Congress of Applied Mechanics (CANCAM 2017), 2017, Victoria, Canada.

My contribution to this paper was conducting the numerical simulations including grid generation, test set-up, and post-processing, along with preparing the manuscript. Dr. Brinkerhoff supervised the work, reviewed the results and manuscript, and provided resources.

Parts of the texts, figures, and tables of Chapters 2-6 have been used in this paper.

- **Ongoing Contributions:**

1) S. Rahbarimanesh, J. Brinkerhoff, *A Parametric Numerical Investigation on the Effects of Cavitation Number on Cavitating Mixing Layer of Liquefied Natural Gas (LNG) behind a Flat Splitter Plate*, International Journal of Heat and Fluid Flow, 2020. (to be submitted)

2) S. Rahbarimanesh, J. Brinkerhoff, *A Parametric Numerical Study on the Effects of Operating Conditions on Cavitating Flow of Liquefied Natural Gas (LNG) inside a Converging-Diverging Nozzle*, Computers and Fluids, 2020. (to be submitted)

3) S. Rahbarimanesh, J. Brinkerhoff, *Three-Dimensionality in Cavitating Flows of Liquefied Natural Gas (LNG): A Qualitative Assessment*, Proceedings of the 6th International Conference on Multiphase Flow and Heat Transfer (ICMFHT 21), London, UK, 2021. (to be submitted)

Table of Contents

List of Tables

List of Figures

List of Notations

Roman Characters

a	Acoustic velocity
A	Throat cross-section area of nozzle
A_i	Enclosed domain area filled with cell i
b	Nozzle throat diameter
c	Splitter plate length
c_p	Specific heat at constant pressure
Ca	Cavitation number
d	Orifice diameter
$\boldsymbol{g}$	Gravity
h	Enthalpy
K	Kinetic energy
L	Latent heat of vaporization
p	Pressure
Pr	Prandtl number
Q	Second invariant of velocity gradient tensor
$\boldsymbol{q}$	Heat flux
Re	Reynolds number
S	Cross section area
T	Temperature
u, v, w	Cartesian velocity components in streamwise, transverse, and spanwise directions
$\overline{u'u'}, \overline{v'v'}, \overline{u'v'}$	Velocity fluctuations (mean-square): normal streamwise, normal transverse, primary shear stress (covariance)
$\boldsymbol{u}$	Velocity vector
y^+, z^+	Inner layer coordinate in y and z directions

Symbols

α	Vapor volume fraction
α_V	Equivalent pure vapor thickness
γ	Surface tension coefficient
δ_w	Vorticity thickness
θ	Momentum thickness
κ	Thermal diffusivity coefficient
κ_s	Curvature of liquid-vapor interface
μ	Molecular viscosity
ν	Kinematic viscosity
ρ	Density

$\boldsymbol{\tau}$	Shear stress tensor
ψ	Compressibility function
$\boldsymbol{\omega}$	Vorticity vector

Math Operators

D/D_t	Substantial derivative
$\nabla, \nabla\cdot$	Gradient, divergence
$\boldsymbol{e} \times \boldsymbol{e}$	Cross product ($\boldsymbol{e}$ vector)

Subscripts and Superscripts

$(\ )^*$	Isothermal condition
$(\ )'$	Fluctuating part of the quantity
$(\ )^T$	Transpose of matrix
$(\ )^0$	Quantity at initial condition
$\overline{(\ )}$	Mean part of the quantity
$(\ )_\infty$	Free stream quantity
$(\ )_c$	Thermodynamic critical condition
$(\ )_{HTR}$	High temperature range
$(\ )_{i,j\ ,k}$	Quantity in the x, y, z direction
$(\ )_l$	Liquid phase
$(\ )_{LTR}$	Low temperature range
$(\ )_m$	Cryogenic mixture of vapor and liquid
$(\ )_{mean}$	Spatially-averaged quantity
$(\ )_n$	Normalized parameter
$(\ )_r$	Reduced parameter
$(\ )_{sat}$	Saturation condition
$(\ )_t$	Temporally-averaged quantity
$(\ )_v$	Vapor phase
$(\ )_w$	Quantity at wall
$(\ )_{x,y,z}$	Quantity in the x, y, z direction

Acknowledgements

First and foremost, I would like to express my deepest gratitude to my supervisor Dr. Brinkerhoff for his kind patience, motivation, professionalism, and valuable technical guidance throughout the entire period of my research. By promoting creative scientific thinking space in the research group, I was given the chance to approach distinct areas related to my research over the years, while knowing he would always have my back, anytime needed. I am very thankful and simply cannot appreciate all his help.

I would also like to extend my gratitude to Dr. Huang at Westport Fuel Systems for providing expertise and support in better understanding the numerical and experimental techniques applicable to the project, as well as getting to know the real-life sides of the problem.

I gratefully acknowledge and appreciate the contributions of my research supervisor Dr. Gavaises and his team especially Dr. Karathanassis and Dr. Koukouvinis in the UK for lending their expert advice and support for advancing my research quality and pursuing the work towards a wider range of industrial applications.

I would also like to very much appreciate my advisory committee members Dr. Li and Dr. Seethaler for their encouraging words and constructive feedbacks during my research, and for their insightful suggestions in reviewing my proposal and dissertation.

My special thanks goes to the lab members especially Nima, Mohammad, Ehsan, Evan, Frank, Dylan, Sid, Ian, Aaron, Andrew, and Umair for their continued assistance and friendship; without my office mates, the five years of my doctorate would have probably sounded like much longer time!

Finally and most of all, I owe my deepest appreciation to my family for their endless support, care, encouragement, and advice over my challenging years of study and work. This accomplishment could not be achieved without them.

1. Introduction

1.1. Motivation

Sustainable cryogenic liquefied natural gas (LNG) is widely known as "green" fuel in the internal combustion engines (ICE), due to providing high efficiency and decreasing pollutant emissions (e.g. around 37% in CO_2) compared to conventional fossil fuels, i.e. petrol and diesel [1]. LNG is produced mainly from the simplest hydrocarbon, methane CH_4, which has almost the highest octane rating and combustion heat in comparison with other complex hydrocarbons. Furthermore, it occupies much less volume than that in the gaseous state (about $1/600^{th}$). This feature leads LNG to deliver higher energy density compared to compressed natural gas (CNG) and diesel fuels [2]. Thus, in a commercial scale, given that almost 50% of transportation costs for conventional vehicles attributes to fuel consumption, using the promising LNG as an alternative fuel for IC engines benefits both customer economy and environmental costs [3].

Recent regulations for toxic emissions of the IC engines in North America restrict particulate matter (PM) and nitrogen oxides (NO_x) emissions of engines to be lower than 0.001g/bhp-hr and 0.05g/bhp-hr, respectively [4,5]. Due to compatibility of LNG with internal combustion engines, particularly with high pressure direct injection (HPDI) engines, the concept of bi-fuel internal combustion engines (namely direct-injection (DI) engines) with the use of LNG-based turbomachines has been recently developed in a vast number of applications including automobile and aeronautics industries [2-5]. An example of this includes the modern LNG-based engines in heavy duty trucks, which have become more popular due to their abilities in releasing the least amount of un-burnt greenhouse gases into the atmosphere [4-6]. Achieving the highest efficiency in these types of engines in terms of their operating conditions, i.e. high injection pressure in moderately short combustion (mixing) time, is majorly dependent on the characteristics of LNG flow, i.e. instability, phase-change, and laminar/turbulent behaviors, which have been a matter of challenge over the past decade.

Although several experimental and numerical works have been conducted regarding natural gas performance in industrial applications (see for example [7-16]), the unsteady phase-change (termed cavitation) behavior of LNG, as a decisive parameter in design of modern LNG-based turbomachinery such as LNG pumps, has not been studied sufficiently. This is mainly due to the complicated physics of the cavitating flow of LNG, as it involves compressibility, phase-change from liquid to vapor, heat transfer, and turbulence, which makes conducting experimental tests and numerical modeling rather difficult and expensive. Cavitation becomes even more important to address knowing that the fluid machinery used for storage and pumping of cryogenic LNG fuels may undergo severe damages, e.g. loss of volumetric efficiency, cyclic stresses, and erosion, through the onset and development of non-isothermal cavitating fields [17-20]. The low temperature behavior of the LNG phase change phenomena makes the control and handling of these damages extremely challenging compared to the conventional machinery working under isothermal cavitation conditions [15-20], as it may cause unpredictable evolutions of the shear layers in the machinery depending on the employed operating condition [18,19].

The present research work aims to fill the gap in physical understanding of the LNG cavitation. Since experimental measurements for LNG cavitation flows are inconvenient and extravagant, due to the need for low-temperature storage and test facilities, and that there is a high demand for numerical modeling in industry, the computational fluid dynamics (CFD) is employed to this end. A cost-effective accurate CFD solver is developed to predict the complex 2D and 3D cavitating behaviors of LNG flow within selected geometries including Laval nozzle, and behind a flat plate splitter. By examining the LNG cavitation behavior under different operating conditions using highly refined temporal and spatial grids, a broad range of findings are obtained that can be utilized in design of a wider extent of LNG-based turbomachinery.

1.2. Objectives

The main objective of the conducted research project is to develop and validate a numerical model that can precisely predict the cavitating behavior of LNG flow, including cavitation onset and progression through laminar-to-turbulent transition, in fluid machinery to optimize their performance. The research sub-objectives are:

1) Investigate the thermodynamic effects of cryogenic conditions on development behavior of LNG cavitation and shear layers.
2) Characterize the interaction mechanisms between shear layer growth, flow separation, interfacial/surface tension forces, and cavitating structures in unsteady LNG flows.
3) Study the effects of operating conditions as well as geometrical parameters on the global behavior of the LNG cavitation in different flow regimes.

1.3. Methodological Approach

The proposed cryogenic cavitation solver, called `cryogenicCavitatingFoam` [21], is developed in the open-source CFD package, OpenFOAM® (an object-oriented C++ code based on the finite volume method (FVM) [22]), by using the available open-source CFD resources, i.e. multiphysics libraries and utilities. These utilities enable the user to functionally modify the source codes in terms of the problem complexity to generate new numerical frameworks, transport models, boundary conditions, etc. The developed model employs homogeneous equilibrium mixture (HEM) approach with a barotropic equation of state in a density-based framework. Non-isothermal effects pertinent to cryogenic fluids are captured through an enthalpy-based energy equation with a thermophysical model that are sequentially solved along with the mass, pressure, and momentum equations. The governing equations are solved on highly refined temporal and spatial grids without any turbulence modeling assumptions. The full description of the development and validation of the developed solver is given in Chapter 3 and 4, respectively.

One of the main features of OpenFOAM is its compatibility with parallel computation such that, depending on the availability of computational resources as well as the scale of computation complexity, a large number of core processors could be used. In the view of the complex physics behind the cavitating flows of LNG, numerical tests of the present study (described in Table I) are carried out in parallel using on average 36 and 448 core processors, respectively, for each 2D and 3D simulation. Visualization and post-processing of the results are performed through the open-source visualization tool, Paraview®.

1.4. Research Plan

To achieve the research objectives, the developed CFD model is used to explore the cavitating behavior of LNG flow through the following investigations:

1.4.1. Study 1: Investigation of Cavitating Flow of LNG inside a Laval Nozzle

There is a lack of in-depth understanding of the cavitation behavior of LNG flow in turbomachinery applications. The available CFD models for non-cryogenic fluids cannot be relied upon for predicting the behavior of cavitating flows of cryogenic substances i.e. LNG, which is due to the presence of several complex phenomena in LNG cavitation including strong influence of temperature on saturation pressure, large compressibility/density variations, and small density ratio between the gas and liquid phases [23]. As a result, a focused numerical study is required to accurately identify the cavitation mechanisms in LNG flows and compare it with cavitation in isothermal conditions.

Following the experimental work of Nagashima and Tani [24], Study (1) performs a series of 2D and 3D simulations by employing the developed CFD model to characterize thermal effects in cavitation of LNG flow inside a converging-diverging Laval nozzle. The characterization is achieved through an accurate analysis of the resulting flow statistics, by using available post-processing tools e.g. data sampling/probing, which uncovers the phase-change properties of LNG and its correlations with other flow fields including velocity, density, temperature, etc. In doing so, the role of surface/interfacial forces in the evolution of the cavitating LNG flow is also identified to further illustrate the trade-off between pressure and viscous forces with interfacial properties of LNG phase-change.

Study (1) also investigates the combined effects of cavitation number ($Ca = \frac{p - p_v}{0.5\rho u^2}$) and diffusion angle of the nozzle on the cavitating behavior of LNG. Numerical simulations are performed to explore how the operating conditions influence the interactions of shear-layer instabilities and cloud/sheet cavitation patterns. This is accomplished by analyzing the frequency spectrums, as well as vorticity budgets in the flow, including vorticity production, baroclinicity, and dilatation terms. Chapters 5-7 of this thesis investigate the evolutions of the described 2D and 3D in-nozzle cavitation flows of LNG.

1.4.2. Study 2: Investigation of Cavitating Mixing Layer of LNG behind a Splitter Plate

The complex physics in cavitating cryogenic flows are heavily influenced by interactions between shear layer instabilities leading to coherent vortical structures, phase-change, and thermodynamic effects. As a result of these interactions, the cavity structures exhibit complicated behaviors especially in their closure regions where a distinct interface may not exist and thus the flow is very unsteady [25-27]. Due to lack of knowledge concerning these interactions, especially in the case of temperature-dependent cavitation, the objective of Study (2) is to explore the nature of these interactions via fundamental investigation of a cavitating mixing layer of LNG. Based on the experimental work of Aeschlimann et al. [25], the developed cavitation solver is used for simulating a 2D cavitating mixing layer of LNG generated behind a flat plate splitter, for a selected range of high- to low-speed side pressure ratios. The 2D simulations are then extended to explore the three-dimensionality effects on the growth of disturbances within the mixing layer and their subsequent influence on the phase-change of LNG in downstream regions. The growth patterns of LNG cavitating spots and their interaction mechanisms with viscous instability characteristics are also identified through a detailed analysis of the resulting flow statistics and investigations of vorticity transport mechanisms in the flow. Chapter 8-10 discuss the behaviors of 2D and 3D cavitating mixing layers of LNG behind the splitter plate at a selected range of working conditions, and further characterize the detailed cavity-vortex interaction mechanisms with thermal parameters.

1.4.3. Study 3: Identification of Transition Process and Turbulence Production Mechanisms in Turbulent Cavitating Flows of LNG

The cavitating flow of LNG in Studies (1)-(2) works within laminar to transitional regimes with moderate range of unsteadiness. Depending on operating conditions, cavitating flow in LNG-based turbomachinery could also operate in fully-turbulent flow regimes. The presence of turbulence is mainly due to high levels of unsteadiness from the unstable cavitating spots which is accompanied by strong shear layer instabilities, making the dynamics of the liquid-vapor interface even more complex. Such interaction mechanisms correlating turbulent flow characteristics to cavitating structures, especially in LNG-based applications, are not well understood; this highlights the need for more fundamental studies focused on elucidating the physical processes responsible for the formation of the complex structures in transitional to turbulent cavitating flows of LNG.

As a contribution to future investigations, Study (3) investigates the cavitation-turbulence interacting mechanisms in transitional to turbulent cavitating flows of LNG passing through the geometries considered in Studies (1)-(2). Following the Laval nozzle case study (Study (1)), Study (3) will identify the effects of a transverse upward jet, introduced upstream of the diverging part of the nozzle, on instability behavior of the 2D/3D cavitating flows of LNG.

Study	Phase	Simulation Description	Outcome
1	1-a	2D laminar to transitional cavitating flow of LNG inside a Laval nozzle	Evolution of cavitation patterns and transient behavior of shear layers of LNG in the nozzle are characterized.
	1-b	Vortex-cavity interactions in 2D laminar to transitional cavitating flow of LNG inside the Laval nozzle	Vorticity budgets and interaction mechanisms between shear vortex structures and cavitating vapor spots in the LNG in-nozzle flow are identified.
	1-c	Effects of cavitation number and nozzle diffusion angle on 2D laminar to transitional cavitating flow of LNG inside the Laval nozzle	Effects of operating condition and geometrical parameters i.e. nozzle diffusion angle on global and instability behaviors of the cavitating LNG in-nozzle flow are evaluated.
	1-d	Effects of interfacial tension forces on cavitating behavior of 2D LNG flow inside the Laval nozzle	Effects of interfacial tension forces on global and instability behavior of the cavitating LNG in-nozzle flow are examined.
	1-e	3D laminar to transitional cavitating flow of LNG inside the Laval nozzle	Effects of three-dimensionality on evolution of cavitating spots and vortex-cavity interactions in the LNG in-nozzle flow are characterized.
2	2-a	2D laminar to transitional cavitating mixing layer of LNG behind a flat plate splitter	Evolution of phase-change patterns and shear layer instability mechanisms in the LNG mixing layer are evaluated.
	2-b	Vortex-cavity interactions in 2D laminar to transitional cavitating mixing layer of LNG behind the flat plate splitter	Vorticity budgets and interaction behavior of vortex structures with cavitating spots in the LNG mixing layer are characterized.
	2-c	Effects of operating conditions on 2D laminar to transitional cavitating mixing layer of LNG behind the flat plate splitter	Effects of operating conditions on global and instability behaviors of the LNG cavitating mixing layer are examined.
	2-d	3D laminar to transitional cavitating mixing layer of LNG behind the flat plate splitter	Three-dimensionality effects on growth patterns of cavitation spots and their correlations with shear layer vortex structures in the LNG mixing layer are evaluated.
3	3-a	2D and 3D transitional to turbulent cavitating flows of LNG inside the Laval nozzle with a transverse upward jet	Effects of upstream perturbation on transient behavior of LNG cavitating structures in the nozzle, and their interactions with shear layer instabilities are characterized.
	3-b	2D and 3D transitional to turbulent cavitating mixing layers of LNG behind the flat plate splitter with a turbulent inflow generator	Effects of inflow perturbation on shedding mechanisms in cavitating mixing layer of LNG behind the splitter, and their subsequent influences on evolution of turbulent cavitating structures are identified.

Table I: Description of the simulations in Studies (1)-(3)

In the case of cavitating mixing layer of LNG (Study (2)), a time-dependent fluctuating velocity boundary condition is proposed, based on the vortex method of Sergent [28] and Mathey et al. [29], and used as the turbulent inflow boundary condition for both the high- and low-speed sides of the mixing layer. The implemented boundary condition imposes time-variant tangential fluctuations to a prescribed velocity profile at the inlet to generate a synthetic turbulent inflow [29]. Study (3) will then perform 3D simulations of transitional to turbulent cavitating mixing layer of LNG generated behind the flat plate splitter. By employing the post-processing methods described in Studies (1)-(2), characteristics of the transitional to turbulent cavitating structures of LNG in the given geometries will be identified. Chapter 11 briefly discusses these investigations as a part of future studies.

Studies (1)-(3) are accomplished through performing a series of CFD simulations by using the developed solver through the phases described in Table I. By conducting the described simulations in Table I the complicated physical aspects of the cavitating flow of LNG in different flow regimes are investigated, from which a fundamental understanding of the phase-change dynamics in LNG flows can be established and used in simulation-driven design optimization of LNG-based turbomachinery.

The present thesis is organized in the following chapters: a review of the existing literature focused on the experimental and numerical studies of temperature-dependent cavitation flows is provided in Chapter 2. The governing equations and computation procedure of the developed numerical solver are illustrated in the Chapter 3. Validation of the developed model, with discussions on proper setup of the numerical schemes and appropriate boundary conditions, are discussed in Chapter 4 for cavitating flows of liquid nitrogen (LN_2) inside a converging-diverging Laval nozzle and a circular orifice with well-refined grid configurations. Chapter 5-7 address the investigations of Study 1: Chapter 5 focuses on the 2D cavitating flows of LNG inside the Laval nozzle at a selected operating condition, and further examines the detailed behavior of the flow in terms of temperature-dependent cavitation patterns and vortex interactions (Phase 1(a)-(b)). In Chapter 6, the 2D LNG cavitation flow of Chapter 5 undergoes a parametric study to investigate the influence of operating conditions on the interaction behavior of LNG cavitating patterns and vortex structures in the nozzle (Phase 1(c)). Chapter 6 also studies of the effects of interfacial tension forces on the evolution of LNG cavitation flow inside the nozzle, and compares the resulting cavity-vortex interactions with the findings of Chapter 5 (Phase 1(d)). The 3D cavitating flow of LNG in the nozzle is explored in Chapter 7 to particularly evaluate the influence of three-dimensionality on the interactions of LNG vortex and cavity structures with thermal parameters found in Chapter 5 (Phase 1(e)). Chapter 8-10 address the investigations of Study 2: in Chapter 8, the 2D LNG cavitating mixing layer behind the splitter plate is investigated for a selected operating condition, through characterizing the thermally-affected cavitation patterns and their interactions with vortex development mechanisms (Phase 2(a)-(b)). Chapter 9 performs a parametric study on the 2D mixing layer of

Chapter 8 to evaluate the effects of operating conditions on the evolution of LNG cavitation patterns and vortex-cavity instability mechanisms (Phase 2(c)). The 3D cavitating mixing layer of LNG behind the splitter is studied in Chapter 10, to disclose the effects of three-dimensionality on the development behaviors of cavitating spots and vortex structures obtained in Chapter 8 (Phase 2(d)). Concluding remarks of the present research work and a review of the future recommendations are given in Chapter 11 (Phase 3(a)-(b)).

2. Literature Survey

2.1. Cryogenic Cavitation

Because of the low boiling temperature of cryogenic fluids including LNG, most of the cryogenic turbomachinery, such as the positive-displacement pumps frequently used in LNG fuel systems, operate near the saturation conditions [18-21]. In this situation, phase change from liquid to vapor may occur if the local temperature exceeds the fluid's saturation temperature (termed boiling) or if the local pressure drops below the fluid's saturation pressure (termed cavitation) [23]. In cryogenic conditions, both cavitation and boiling may occur simultaneously and interactively due to the temperature dependency of saturation pressure. The vapor forms sheets or bubble clusters that, if not controlled, may cause undesirable effects by generating high-amplitude and high-frequency oscillations that lead to localized stresses on components, material erosion, and significant efficiency drop [30]. Traditional isothermal cavitation scenarios in water pumps or marine propellers are typically considered to occur at constant temperature [29,31]. In contrast, cryogenic fluids are characterized by large compressibility variations, a smaller density ratio between the liquid and gas phases, and lower latent heats of vaporization that significantly distinguish their cavitation behavior from the isothermal cases [29].

2.1.1. Experimental Investigations

Experiments of cavitating flows under cryogenic conditions have been conducted with the aim of developing cavitation models tailored to fluids at cryogenic conditions [32-41]. However, due to the complexity and expense of test facilities and the challenging data measurement and visualization requirements in cryogenic flows, there is limited research available compared to typical cavitation studies of water. Among the early experimental works, Hord [32,33] and Simoneau and Hendricks [34] conducted a series of experiments to investigate the cavitation behavior of liquid nitrogen and hydrogen (LN_2 and LH_2, respectively) in nozzle, hydrofoil, and ogive geometries under a range of inlet velocities and temperatures. Also, Franc et al. [35] studied the impacts of temperature variations on cavitating flow of Freon R-114 generated around an inducer blade. In the comparative study of Yuka et al. [36], it was shown that the intensity of the generated cavitation field for water was larger than that in liquid nitrogen. Later on, Nagashima and Tani [24] conducted experimental and numerical observations of cavitating water and liquid nitrogen in a converging-diverging Laval nozzle. In addition, Niiyama et al. [37] carried out experimental and numerical tests to clarify the effects of temperature and turbulence intensity on cavitating behavior of LN_2 in a circular orifice. The B-factor parameter of Stepanoff [38] was used to estimate the degree of thermal sensitivity of the cavitation process via a dimensionless temperature drop accompanying the vaporization process, defined in terms of the vapor volume fraction α as $B = \frac{\alpha}{1\text{-}\alpha} = \frac{\Delta T}{T^*}$, where the normalizing temperature parameter is $T^* = \frac{\rho_v L}{\rho_l C_{Pl}}$ and L is the latent heat of vaporization, ρ_v and ρ_l are the vapor and liquid densities, and C_{Pl} is the liquid specific heat [38,42]. They then demonstrated that the B-factor increases as the cavitation number and turbulence intensity decreases. The same analysis of cavitation using the B-factor was also implemented by Yoshida et al. [39], who estimated the temperature variations in cavitating flows of LN_2 and water in an inducer. More recently, Jiakai et al. [43] studied the unsteady cavitating structures of LN_2 and water in a venturi by using high-speed camera observations for different values of inlet/outlet pressure ratio and flow rates. By developing a one-dimensional theoretical equation in consideration of thermal effects to estimate the speed of the shock-wave induced condensation front, they reported benchmark observations on dynamic cavitation characteristics of LN_2 and water including that the wave generated from the collapse of the cavitation cloud is considered to be the dominant mechanism in cavitation shedding.

2.1.2. Numerical Investigations

Computational models of cryogenic cavitation have been explored via various approaches primarily developed for isothermal cavitating flows i.e. water which have been studied for several decades [31]. Numerical calculations of isothermal cavitation models the phases using two common approaches: two-fluid models in which separate sets of conservation equations are solved for the liquid and vapor phase [29,31,42]; and mixture models where the slip velocity between phases is omitted and the flow is modeled in a single-fluid framework [44]. Lately, semi-empirical cavitation models have been used extensively to predict cavitation occurrence [44,45]. These models, in general, are divided into three main categories [44]: interfacial dynamics models (IDM), density-based cavitation methods (DCM), and transport equation-based models (TEM). In the IDM models, such as those of Senocak and Shyy [45-47], surface tension forces at the liquid/vapor interface are taken into account and added to the momentum equation. Using the assumption of a biphasic zone separating the vapor from liquid region in these models, source terms in the governing equations are found by balancing the momentum and mass across the cavity interface. In this method, the continuum surface force (CSF) model is used to address surface tension forces and to produce an interface [48]. Although the IDM models can precisely capture the baroclinic vorticity generation, $(\nabla p \times \nabla \rho)/\rho^2$, in the closure region of attached cavity structures [42,45], unreliability of this approach is reported in cases of cavity detachment and growth [48,49]. Also, the highly-resolved spatial and temporal grids needed to capture the interface increase the computational costs of these models [49].

Within the DCM approach, density field variations are formulated in terms of the pressure using the well-known homogeneous equilibrium mixture (HEM) model [50]. In this approach, a single-fluid mixture is defined for both vapor and liquid regions and the corresponding density fields are obtained by solving an additional equation for the vapor volume fraction. This equation is coupled to pressure through a pressure correction procedure using a specific closure equation such as a barotropic equation of state (EoS) [51]. Related to this method, Bicer et al. [52] investigated turbulent spray cavitation of water in an injector using the homogeneous equilibrium model coupled with a barotropic equation for the density field. Good agreement between the simulated cavitation region thickness and length with their experimental data was reported. Moreover, Coutier-Delgosha et al. [53] simulated the shedding behavior of vapor cavities in two venturi-shaped geometries using a homogeneous flow model with variable density and a barotropic equation of state to capture the vaporization and condensation processes.

The popular TEM models such as those of Kunz [54], Zwart [55], and Schnerr-Sauer [56] are developed based on the bubble two-phase flow (BTF) approach [57] and Rayleigh-Plesset equation [23], which work in conjunction with a Lagrangian tracking framework for the multiphase flow. These models solve separate transport equations for the liquid and vapor phases with source terms to account for the condensation and vaporization of the two phases. For example, Hidalgo et al. [58] used two different cavitation models of Schnerr-Sauer [56] and Zwart [55] to compare unsteady turbulent cavitating behavior of water around the NACA 66 airfoil. Among the TEM approaches, the full cavitation model (FCM) of Singhal [59] has been more widely used. Example of this includes Zhang et al. [60] work that proposed a dynamic cavitation model by adding a pressure-dependent bubble radius equation to FCM to simulate quasi-steady cavitation of water around submerged cylindrical geometries.

Earlier numerical research on the thermal effects of cavitation includes the study of Cooper [61] who used a dimensionless vaporization parameter and incorporated it into a barotropic EoS to implicitly calculate pressure changes due to thermodynamic effects. However, property variations within the liquid phase were neglected in Cooper's work and by definition was limited to an incompressible framework. Prosperetti [62] employed a similar framework to investigate the damping effects of thermal variables on dynamic behavior of individual oscillating bubbles such as the impact of the heat transfer and liquid-vapor interface temperature on the growth rate of bubbles. Deshpande et al. [49] addressed the cryogenic vapor flow inside a cavity by utilizing a pre-conditioned density-based approach with a temperature equation in the liquid domain by applying Neumann boundary conditions and assuming the equality of the bulk velocity inside the cavity and the free stream velocity. An explicit tracking strategy was used to capture the liquid-vapor interface region, and temperature gradients across the cavity surface were found by deriving a local conductive heat balance equation. Brennen [63] probed the air diffusion across the interface of a cavity generated behind a spherical headform and discovered a turbulent boundary layer around the cavity surface formed as a result of the flow separation on the sphere surface. Based on this observation, he proposed that the vapor flux at the cavity interface could be modeled as a function of temperature difference between the cavity and the upstream flow. Hosangadi and Ahuja [64] proposed a pressure-based cavitation model using a semi-barotropic approach to derive a compressible, multiphase formulation for the energy conservation equation with variable thermodynamic parameters of the fluid to highlight the essential accurate treatment of "real" fluid properties in cryogenic cavitaiting flows. They used this model for simulating attached sheet cavity flow of LN_2 around a hydrofoil. By comparing against the B-factor study of Stepanoff [38], they concluded that the attached LN_2 cavity on the hydrofoil is sustained primarily by direct convection of mass into the cavity such that the viscous/thermal diffusion at the vapor-liquid interface are secondary factors in cavity formation.

More recently, the TEM-based cavitation modeling has become more popular in cryogenic cavitation studies. For instance, Sun et al. [44] investigated the quasi-steady evolution of cavitating LN_2 around a hydrofoil under isothermal and cryogenic conditions. By employing a modified Zwart cavitation model [55], which considers thermodynamic effects, they concluded that dynamic behavior of LN_2 cavities are distinct for these two cases such that cryogenic condition causes shorter cavitation regions around the hydrofoil. Zhang et al. [65] introduced a modified version of FCM where an equation for condensation/vaporization rate of vapor bubbles was derived in terms of the bubble radius and the local pressure and temperature fields; this was achieved by employing the Young-Laplace equation for capillary pressure and an integral form of the Gibbs-Duhem theory [66]. Cao et al. [67] used a full cavitation model in ANSYS Fluent® and coupled it with an energy equation to investigate the effects of temperature and pressure on cavitation mechanisms of LN_2 and LH_2 around hydrofoil and ogive geometries. Utturkar [68] developed a so-called "mushy" IDM and addressed the frothy behavior of cryogenic cavitation by redefining the production and destruction terms of the cavitation model of Senocak and Shyy [45,46] in terms of iterative thermodynamic variables, and employing the speed of sound model of Senocak and Shyy [46] and Wu [69].

Tseng and Shyy [70] addressed the uncertainty of the inflow variables on turbulent cryogenic cavitation patterns by assessing the local numerical resolution of the flow structures with the computed turbulence characteristic length. They proposed a filter-based, ensemble-averaged version of the Navier-Stokes equations with a two-equation turbulence closure model coupled to a transport-based cavitation model with refined modeling parameters. Employing the model for calculating cryogenic cavitation fields of liquid nitrogen around a hemi-spherical projectile and a NACA66MOD hydrofoil, they found that the thermodynamic parameters affect the interplay between the saturation vapor pressure variations and the liquid-vapor density by modifying the local cavitation numbers and liquid-to-vapor density ratios. Their proposed filter-based approach - with computational grid resolution as the filtering criterion - along with the turbulent viscosity correction procedure comparing the computed turbulence length scale and the assigned filter size, yields a significant reduction in the influence of the eddy viscosity on viscous damping, hence making the proposed model somewhat a combined RANS-DNS approach.

The above-noted experimental and numerical approaches have been extensively used to address the physics of liquid-vapor phase-change phenomena in different practical applications. A review of the major contributions on the physics of cryogenic cavitation is provided in Sections 2.2-2.7.

2.2. Cavitating Flows under Different Operating/Geometrical Conditions

Effects of dynamic factors such as operating velocity and cavitation number as well as the geometrical parameters on cavitation characteristics have been reported in a number of numerical and experimental investigations majorly focused on observations of in-nozzle cavitation behavior of different fluids [71-73]. Among the benchmark studies, Sun et al. [74] numerically investigated a 3D cavitating diesel flow inside an injector nozzle, based on a high-pressure common-rail direct injection (DI) diesel engine, by using the cavitation model of Schnerr-Sauer [56] and k-ε turbulence modeling [75]. They addressed the influences of nozzle geometrical parameters such as the circular bead of nozzle inlet, the ratio of the nozzle length to orifice diameter, and the roughness of the orifice inner wall, on distributions of turbulent kinetic energy and vapor volume fraction fields. Using the same approach, Som et al. [76,77] performed numerical simulations to observe cavitation dynamics of diesel within a nozzle working under distinct inlet-outlet pressure differences and geometric configurations. They concluded that the use of a cone-shaped orifice can improve the cavitation performance via suppressing the cavity production. Payri et al. [78,79] studied the influence of nozzle orifice diameter and the fuel type on cavitation and near-nozzle spray performance into a pressurized chamber by using a "test rig pressurized with fuel" experimental laser technique. They found that the cavitation performance is largely determined by both the upstream and downstream pressure conditions in the nozzle as well as the jet injection angle.

Ito et al. [80] experimentally studied the periodic shedding behavior of the cloud cavitations of hot water and liquid nitrogen around a “plano-convex” hydrofoil by use of a blowdown cryogenic cavitation tunnel. By investigating the effects of cavitation number, inlet velocity, and the flow incidence angle, as well as the airfoil chord length and the tunnel width, they reported benchmark observations on cavitation behavior of water and LN_2. For instance, they noted that the shedding of cloud cavitation occurs only in the cases where both the adverse pressure gradient and the slow flow region on the hydrofoil coexist.

Yan et al. [81] proposed a two-phase flow model, derived in terms of the single-bubble dynamics formulation of Wang and Su [82], and coupled it with the WAVE droplet breakup model of Reitz [83] and the droplet collision-coalescence model of O’Rourke [84] to simulate the cavitation and atomization performance in a large-scale high-power marine diesel engine with high chamber air density and long injection time under a range of injection pressures. By comparing the results with high speed photography experimental data of Zhao et al. [85], they reported that by increasing the injection pressure, the pressure fluctuations inside the nozzle and the spray angle become more intense. This conclusion was also observed by numerical study of Zhang et al. [86], Eulerian-Lagrangian model of Hohmann and Renz [87], and planar laser-induced fluorescence experiment of Huang et al [88] who, respectively, reported that the diesel cavitation, spray droplet evaporation rate, and spray penetration are intensified by increasing the injection pressure, chamber temperature, and reducing the discharge pressure.

2.3. Cavitating Shear Layers

The cavitating shear flow associated with attached cavitation - referred as vortex cavitation since the cavity forms in low-pressure cores of streamwise and spanwise liquid vortices [89] - plays an important role in the formation of cloud cavitation in turbomachinery. This type of cavity flow, which normally occurs within regions of flow separation and in the turbulent wakes of bluff objects, is the main cause for formation of strong vortices downstream of partial cavities [90,91] causing the overall flow to change by decreasing the mean flow density, increasing the overall flow volume, or locally modifying the pressure and vorticity fields [89,92]. The study of shear layers (also referred to as mixing layers) under the influence of cavitation conditions has been limited to experimental investigations mainly focused on isothermal fluids i.e. water [92-94]. Among the earlier studies, Katz and O'Hern [95] examined cavitation inception and development in a plane shear layer of water downstream of a sharp-edged plate for a range of Reynolds numbers. By employing observations made under stroboscopic light and flash photography, it was reported in their work that cavitation inception occurs within the streamwise vortices of the shear layer through stretching streamwise vortical structures in between large-scale spanwise vortices leading to a reduction in the vortex diameter and core pressure.

Iyer and Ceccio [89] performed an experimental study to determine the effects of growth and collapse of cavity structures on dynamic behavior of downstream flow in cavitating and non-cavitating shear layers of water. By conducting PIV measurements of velocity, vorticity, and turbulent stresses in downstream regions, they showed that the growth rate and mean flow characteristics of the shear layer are significantly affected by cavity structures such that crosswise velocity fluctuations are reduced in downstream of the cavitating case compared with the non-cavitating flow. This significant influence of the developed cavitation on dynamics of turbulent vortices was also detected by Belahadji et al. [92] who employed high-speed photography to reveal cavitation effects in rotational structures of a turbulent wake flow behind a 2D obstacle.

More recently, Aeschlimann et al. [96] used experimental high-speed visualization laser doppler velocimetry (LDV) technique with a specific method of image processing of time series, to investigate the dynamics and topology of vorticity regions of a 2D cavitating mixing layer of water at high Reynolds numbers to resemble and characterize the patterns of cavitation and turbulence in the mixing layers generated in rocket engine turbopump inducers. By employing statistical analysis with visualizations on the convective velocity and the shedding frequency of cavitating vortices, they estimated a quasi-linear increase rate of vapor thickness as the instability develops. They also concluded that the presence of vapor structures only slightly affects the spatial development of mixing area through changing vortex development behaviors.

Among computational research, Okabayashi et al. [97] performed direct numerical simulation (DNS) and large eddy simulation (LES) tests to model the modulation of kinetic energy and dissipation rate of elementary vortices of a spatially-developing turbulent cavitating mixing layer of isothermal water. Their modeling was conducted through a quasi-compressible framework, developed based on a fractional step computation method of Okita and Kajishima [98] - and a modified Chen's cavitation model [99] based on the analytical solution of Rayleigh-Plesset equation. By comparing the behavior of vortical structures and turbulence intensities for single-phase and cavitation conditions, they concluded that turbulence intensity in the braid region of the cavitating mixing layer tends to decrease compared with that in the non-cavitating single-phase case.

2.4. Cavitation under Interfacial Tension Force

Investigation of surface tension effects on cavitation has been reported in a number of numerical works mostly focused on isothermal cavitation. For instance, Franc and Michel [100] used a force equilibrium equation for resonance frequency analysis of cavity bubble nucleus in water and reported that the influence of surface tension force on the bubble growth significantly decreases with increasing the nucleus diameter. Yu et al. [101] presented a compressible, multiphase volume of fluid large eddy simulation (VOF-LES) approach by reformulating the Schnerr [56] and Kunz [54] cavitation models to eliminate non-physical mass transfer rates within phase-change processes. The surface tension force between liquid and vapor was treated by employing De Villiers et al.'s [102] method. By applying the model for calculating in-nozzle cavitation phenomena in a diesel injector, they reported that the modified Kunz model predicts a larger air inflow at the nozzle outlet than the modified Schnerr model. Michael et al. [103] proposed a one-field formulation for the vapor-liquid two-phase flow with VOF interface tracking method to model cavitation through using a simplified Rayleigh-Plesset equation with a built-in surface tension force term. They used a level set method coupled with a ghost fluid approach to treat sharp jump conditions in velocity and pressure fields due to surface tension effects. A marching cube method was also used to compute the interface area velocity components at the interface grid cells. A good comparison between their numerical results and experimental data was reported for a cavitating NACA66 hydrofoil.

Among thermo-sensitive cavitation modeling approaches, De Giorgi et al. [104] developed a mixture model combined with a VOF-based interface capturing approach and validated it for cavitation flows of LN_2 and LH_2 around an ogive. They employed an extended version of the Schnerr model [56] and coupled it with a temperature equation to account for thermodynamic effects in terms of latent heat release/absorption and convective heat transfer in liquid-vapor interface regions. Liu et al. [105] studied the effect of liquid pressure on growth process of homogeneous and heterogeneous bubble nuclei by proposing an analytical thermodynamic model based on a phase-change energy equation coupled with a quadratic temperature distribution of thermal boundary layer around the bubble. By using the model for simulating cavitation flow of diesel in an injector nozzle, they concluded that the evolution of the bubble growth in the nozzle can be divided into three stages i.e. surface tension controlled stage, transitory stage, and heat transfer controlled stage. Riznic et al. [106] proposed a model based on the Scriven's [107] approach, by assuming the presence of a thermal boundary layer around the bubble, to study the influence of interface curvature on temperature gradients within liquid-vapor interface. His model was later improved by Chang and Lee [108] who used exponential and polynomial temperature profiles to predict the boundary layer thickness and spatial temperature derivatives near the liquid-vapor interface regions of flash boiling sprays in a DI spark ignition engine.

Lü et al. [109] coupled a mathematical stability analysis method to the bubble-droplet breakup model of Zeng and Lee [110] to investigate the influence of viscous, inertia, and surface tension forces on the stability and breakup behavior of a cavitation bubble in a diesel droplet surrounded by ambient air. By using a set of linearized disturbance governing equations to describe the disturbance growth rate of the bubble instability and setting up a breakup criterion in terms of initial disturbance of the diesel droplet, it was found in their work that the surface tension and viscous forces tend to stabilize the cavitation bubble, unlike the inertial forces which ease the bubble breakup.

2.5. Turbulent Cavitating Flows

In the case of turbulent cryogenic cavitation, investigations have been limited due to the lack of measurement techniques in experimental studies, and to the expensive modeling of thermally-affected multi-scale turbulent structures generated within unsteady cavitation processes. Nevertheless, most of these studies have employed Reynolds-averaged Navier-Stokes (RANS) and, more recently, large eddy simulation (LES) methods to accommodate turbulence effects in cavitation modeling, mainly because of the challenges in direct numerical simulations (DNS) i.e. costly capture of transient to turbulent dynamics of real-scale cavity structures formed in a very short spatial-temporal scales, and difficult dynamic tracking of vapor-liquid interface region [111,112].

Among the experimental works, Gustavsson et al. [113] investigated the cavitating flow of fluoreketone around a NACA0015 hydrofoil by using flash-exposure high-speed imaging method in a wide range of cavitation numbers, temperatures, and angles of attack. Kelly and Segal [114] used high-speed photography and planar laser scattering imagery to identify the flow characteristics of different cryogenic fluids operating near the thermodynamic critical point in a turbopump inducer. On the numerical side, in a comparative study, Mani et al. [115] examined the uncertainty associated with the choice of RANS turbulence models on cavitation prediction around a 3D cryogenic turbopump inducer. By breaking the flow around the inducer into simple well-known canonical flow problems to isolate the influence of the turbulence closure models in RANS models and to eliminate the uncertain behavior of coupling effects between turbulence and cavitation models, they studied LH_2, Freon R-114, and water cavitation behavior in four distinct flow regimes around a hemispherical headfoam, an axisymmetric hydrofoil, a rotating ship propeller, and inside a 2D venturi. It was found that the sensitivity of the vapor phase distribution to the turbulence model is strongly dependent on the cavitation model such that, for example, the barotropic equation of state cavitation models are more sensitive to the turbulence closure model compared with the transport-based models (TEM). This sensitivity, however, was reported to be dependent on the flow type i.e. bounded and unbounded cavitation flows.

Jiakai et al. [116] investigated the unsteady cavitation of LH_2 and water around a 3D NACA0015 hydrofoil with angle of attack of AoA = 6º by using LES with the Sauer-Schnerr cavitation model [56] and a filtered bubble number density formulation in a compressible framework. With the main focus on the frequency analysis of cavitation clouds and the effects of re-entrant flow as well as pressure waves on the cavity dynamics, they found that the *St* number ($St = \frac{fc}{U}$ where f and c are shedding frequency and airfoil chord, respectively) for LH_2 cavitation is much smaller compared with the water case in a specific range of *Ca*/2AoA numbers: when *Ca*/2AoA is reduced to a critical value, the relative effects of thermal parameters on the cavitation shedding is substantially weakened compared with the vortex-related effects. Falcucci et al. [111] performed a benchmark direct numerical simulation of a flow-induced incipient cavitation inside an orifice utilizing statistical discrete lattice Boltzmann modeling of multiphase flow with a non-ideal thermodynamic equation of state. By using a corrected Joseph's minimum tension criteria [117], an accurate capture of the cavitation onset, as a result of interface emergence by non-ideal intermolecular interactions between vapor and liquid phases, and strong dependence of the bubble morphology on the interfacial tensions were reported in this work.

Because of the expensive computation of LES, and steady behavior of the flow in RANS simulations, some recent approaches have been developed which combine the advantages of LES and RANS to optimize the turbulence modeling accuracy with respect to computational cost. The validity of these models, however, for highly unsteady compressible cavitation flows under thermal conditions has not been adequately addressed [118,119]. An example of this includes Sun et al. [120] who used the so-called partially averaged Navier-Stokes (PANS) hybrid method of Girimaji [121] with a modified k-ε model to numerically investigate the unsteady behavior of thermo-sensitive cavitating flows of fluoreketone and liquid nitrogen around a NACA0015 hydrofoil with the particular emphasis on thermal effects and dynamic evolution of cavity structures. By comparing the results against the experimental data of Kelly and Segal [114,122], they reported a significant influence of the thermal effects on cavitation transition and suggested that a small *Ca*/2AoA is required in thermo-sensitive fluids to achieve the similar cavitation behavior as in isothermal fluids.

2.6. Cavitating Flows under Imposed Upstream Perturbation

Studies of transitional to turbulent cavitation flows under the effects of upstream perturbations are now reviewed. While a limited number of experimental and numerical investigations have been reported, these studies are mainly conducted for isothermal cavitating flows of water without taking the thermal parameters into consideration. Billard et al. [123] conducted experimental tests of transitional to turbulent cavitation of water in a venturi by imposing a pre-turbulence field through an upstream turbulence generator. By comparing the results against the corresponding laminar cavitating flow, they observed a delay in cavity inception and a reduction of noise in the turbulent case, which was attributed to the formation of high-frequency, small-amplitude turbulent pressure fluctuations affecting the morphology of the cavity structures. Using the same methodology, Baur and Ngeter [124] studied the evolution 3D turbulent horseshoe-shaped cavity structures in downstream regions of a turbulent channel flow by mounting a rectangular sill on the lower wall upstream of the channel. Xing et al. [125] performed direct numerical simulation of vortex cavitation in a 3D submerged transitional round jet by using a locally homogeneous cavitation model of Kubota [50], which accounts for non-linear bubble-bubble interactions within spherical bubble clusters, along with a quasi Poisson equation for pressure accounting for density variations in cavitating regions. A top-hat streamwise inlet velocity profile with small amplitude sinusoidal disturbances was used in their work to assure adequate perturbation of the flow. By comparing the cavitation and non-cavitation flow fields, they concluded that the cavitation occurs in the cores of the primary vortical structures and causes substantial distortion and eventual breakup of the vortex rings, thus suppressing the jet growth rate by damping the velocity fluctuations. Seo et al. [126] introduced a density-based homogenous equilibrium model in a compressible two-phase flow framework and coupled it to a linearized EoS to perform direct numerical simulations for predicting noise in cavitating flows of water in a semi-infinite region bounded by a flat moving wall with sinusoidal oscillations, and around a circular cylinder operating under a range of Reynolds and cavitation numbers. They employed a sixth-order compact central scheme with a spatial filtering technique to resolve the non-linear interactions in cavitating regions. By deriving an acoustic analogy, they reported that the noise characteristics of cavitating flows are significantly altered compared to the non-cavitating flows, which is due to the shock waves emitted upon coherent collapse of cloud cavity structures in wake regions.

2.7. Instability and Investigation of Interaction Mechanisms in Cavitating Flows

In the past decade there have been a limited number of investigations on the cavity/shear-layer interaction mechanisms and instability behaviors in cryogenic cavitating flows. Among the recent benchmark studies, Ito et al. [80] conducted cavitation experiments on a “plano-convex" -shaped hydrofoil with hot water at T = 363 K and LN_2 at T = 83 K and found that the shedding frequency of the LN_2 cavitation cloud (90 Hz) is smaller than the hot water (110 Hz) under the same experimental conditions. Zhu et al. [17] numerically analyzed the cavitating flow of LH_2 over an ogive geometry using a compressible framework for both gas and liquid phases, based on a homogeneous mixture model coupled with the Schnerr-Sauer cavitation model and a large eddy simulation approach. By evaluating the interactions of vortical structures with the calculated unsteady flow parameters, they introduced a special cavitation mechanism, named "partially shedding mode", in which the primarily generated cavity stays in a quasi-steady state, while much smaller vortex-induced cavity clouds intermittently form near the leading edge inside the primary cavity. They further concluded that the generation of vorticity in the ogive LH_2 cavitation flow mainly occurs near the solid surface inside the cavity, and not only at the interface and/or closure regions of the cavity frequently seen in isothermal cavitation flows. Also, Long et al. [127] numerically explored the unsteady characteristics of a cavitating turbulent flow of LH_2 around an ogive by using a mass transfer homogenous cavitation model based on the Rayleigh-Plesset equation [100], coupled with an energy equation and a modified renormalization-group (RNG) k-ε turbulence model with local density correction. By investigating the cavitation-vortex interactions through assessing the dilatation and baroclinic terms of a reference compressible vorticity transport equation, they reported the predominance of vorticity dilatation in modulating vorticity inside the large-scale cavity structures. Moreover, by introducing an integrated 1D-2D method to study the cavity-excited pressures, they demonstrated that the cavity volume acceleration is primarily responsible for cavitation-induced pressure fluctuations in the flow.

More than the limited vortex-cavity interaction studies in cryogenic cavitation flows are the experimental and numerical investigations focused on transient features of 3D cavitating flows in isothermal fluids [128-130], addressing in-detail behavior of cavitating structures around different geometries such as axisymmetric projectile [131] and hemispherical head-form body [132]. Among these studies, Ji et al. [119] used LES coupled with the cavitation model of

Schnerr and Sauer [56] to address the turbulent cavitating flow of water around a Clark-Y hydrofoil through accurate capture of the main unsteady features of cavitation processes including attached cavity growth, sheet/cloud cavitation transition, and cloud cavity collapse. By using Q-criterion and vorticty budget calculations, they reported a quasi-periodic cloud cavitation shedding around the hydrofoil with the slide and roll-down of the shed large-scale vortex structures on the hydrofoil suction side. They further concluded that the flow turbulence level is significantly influenced by the cavity shedding. The same authors [133] also numerically investigated the interactions between vortex formation procedures and cavitation structures of water around the 3D hydrofoil of Delft University of Technology [134] by employing the mass transfer cavitation model of Zwart et al. [55] and a modified RNG k-ε model with a local density correction for turbulent eddy viscosity. By comparing the numerical results against the experimental data of Foeth et al. [134], and evaluating the vorticity contributions from the vortex stretching, dilatation and baroclinic terms, they concluded that the cavitation triggers vortex production and escalates the boundary layer thickness by promoting the likelihood of local separation and unsteadiness. Wang et al. [135] investigated the unsteady pressure fluctuations of breakup and shedding of unsteady sheet and cloud cavitating structures of water in a convergent-divergent geometry using experiment and CFD. For the experimental tests, they employed a simultaneous sampling technique to synchronize the transient cavitation behaviors and wall-pressure signals, whereas the compressible transport equation-based cavitation model of Zwart in a compressible RNG k-ε turbulence modeling approach was used for their numerical tests. Using a 1D bubbly shock wave relationship analysis, they concluded that the re-entrant jet and the vapor fraction discontinuity propagation mechanisms are the two main reasons causing cavity breakup and shedding in the unsteady sheet and cloud cavity structures.

3. Numerical Model

3.1. Justification

Although reasonable accuracy of the available numerical cavitation models has been achieved in prior studies (detailed in Chapter 2), some of the primary assumptions in the derivation of these models may incur considerable uncertainty especially in unsteady solutions of cryogenic cavitating flows containing large-scale vapor cloud structures [136]. This uncertainty is confirmed by Wang et al. [26], who pointed out that the vapor phase density variation found from the mass-transfer TEM models is usually higher than that in pure vapor cavities. The assumptions used for deriving these cavitation models can be summarized as follows [26,42,64]:

- Vapor regions are assumed to be clusters of bubbles of various scales.
- During the cavitation process, bubbles are at their maximum possible radius found from balancing drag and surface tension forces.
- Effects of local pressure and temperature variations on bubble size are neglected. This methodology provides accurate results for mean cavity solutions i.e. sheet cavity structures where high level of unsteadiness is not present, but is poorer for transient cavitation behavior.
- The initial bubble distribution and diameter are needed as initial conditions.
- Empirical constants implemented in the derivation of governing equations cause varying levels of uncertainty when used for different fluids.
- Due to lack of a dependable EoS, sound propagation and compressibility effects in the mixture regions and cloud cavity structures cannot be captured properly in pressure-based solvers.

Some of the above-noted assumptions have been, however, relaxed by recently developed models. For instance, Zhang et al. [65] proposed a dynamic cavitation method based on the Singhal model [59] where the bubble size solution is found in terms of the resulting pressure and temperature fields. Notwithstanding, the impact of thermodynamic effects on cryogenic cavitation instabilities has not yet been addressed adequately. Moreover, most of the cryogenic studies are limited to investigating the attached sheet cavity behavior where large scale unsteadiness, frequently seen in unsteady cloud structures, is not present in the closure region of the cavity and thus the growth, detachment, and shedding of the vapor clouds is not captured.

The need to predict the phase-change behavior of cryogenic fluids such as LNG, especially in LNG-based turbomachinery equipment with high level of flow unsteadiness, points to a need for further investigation of highly transient cavitation patterns in cryogenic flows. The present numerical model develops an efficient numerical approach to predict the effects of thermophysical property variations on time-dependent phase-change behavior of cryogenic fluids in complex geometries where unsteady cavitation patterns generate large pressure, temperature, and density fluctuations in the flow. In Section 3.2, a description of the developed model [21] is presented, which will be used for simulating the LNG cavitating flows introduced in Table I.

3.2. Model Development

The present cryogenic cavitation model is developed in the open-source OpenFOAM libraries [137,138] and is a transient cavitation solver that employs the HEM approach to capture phase-change in thermo-sensitive, compressible cavitating flows. The isothermal cavitation modeling via HEM is based on the following assumptions [16,63,64]:

1. The fluid is treated as a homogeneous mixture; flow properties are weighted by a vapor phase fraction field that takes values between 0.0 (fully liquid) and 1.0 (fully vapor).
2. A barotropic equation of state is used to couple density and pressure variations, and to close the system of governing equations. Coupling between density and pressure is done by means of the generic compressibility models of Wallis [139] and Chung [52,66].
3. Liquid and vapor phases are in kinematic and thermodynamic equilibrium: velocity and temperature differences between phases are neglected, and the energy conservation equation is not solved.

However, since cavitation in cryogenic fluids does not occur at thermodynamic equilibrium conditions, the latter two assumptions are invalid. Therefore, to model cryogenic cavitation within the HEM approach, the energy equation must couple with cryogenic forms of the mass and momentum conservation equations to ensure that non-equilibrium processes, including latent heat transfer, are captured. In addition, thermophysical models of the simulated cryogenic fluid must account for the non-equilibrium behavior in its thermal properties, such as saturation pressure changes with temperature. The governing equations and thermophysical property models employed in the developed cryogenic cavitation model are presented in the Sections 3.2.1-3.2.5; detailed derivation of the governing equations is given in Appendix A.

3.2.1. Governing Equations

The model is developed based on a barotropic closure equation of state correlating cryogenic mixture density ρ_m to pressure p by employing a compressibility function ψ:

$$\frac{D\rho_m}{Dt} = \psi_m \frac{Dp}{Dt} \tag{1}$$

where,

$$\psi_m = \alpha\psi_v + (1-\alpha)\psi_l \tag{2}$$

represents the mixture compressibility. The linear model of Wallis [138,139] is used in which the compressibility of the mixture ψ_m is correlated to the compressibility of the vapor and liquid phases (ψ_v and ψ_l , respectively) by using the volume fraction of vapor α in the mixture. The vapor volume fraction is defined as

$$\alpha = \frac{\rho_m - \rho_{l,sat}}{\rho_{v,sat} - \rho_{l,sat}} \tag{3}$$

where the 'sat' subscript stands for saturation conditions and v and l denote vapor and liquid phases, respectively. The vapor phase density at saturation condition $\rho_{v,sat}$ is given as

$$\rho_{v,sat} = \psi_v \, p_{sat} \tag{4}$$

in which p_{sat} indicates the saturation pressure of cryogenic fluid. One of the main features of the barotropic equation of state is its compatibility with both liquid and vapor phases, which makes the solver suitable for mixtures and also for cases of pure vapor or liquid [42,52]. The corresponding equations of state for vapor and liquid phases, respectively, are

$$\rho_v = \psi_v \, p \tag{5}$$

$$\rho_l = \rho_l^0 + \psi_l \, p \tag{6}$$

where ρ_l^0 is the density of liquid at a specified operating temperature as follows

$$\rho_l^0 = \rho_{l,sat} - \psi_l \, p_{sat} \, . \tag{7}$$

In cryogenic fluids, the saturation pressure (p_{sat}) is highly dependent on the flow temperature [26,100]. To account for this in the equation of state, we derive an explicit relation between temperature and saturation pressure. Consider energy balance for a unit volume of liquid mass

dm undergoing phase change into vapor. As given in [100], the latent heat transfer L and the temperature change dT are related by

$$(dm + \alpha\rho_v)\, L = (1 - \alpha)\rho_l\, c_p\, dT \tag{8}$$

where $dm + \alpha\rho_v$ is the vapor mass after the phase change of the liquid dm, $(1 - \alpha)\rho_l$ is the liquid mass, and c_p is the specific heat found from a generic thermophysical model described in Section 3.2.3. Since the contribution of vapor in the heat balance Equation (8) is negligible as compared to the liquid phase, (8) can be simplified as [100]

$$dm\, L = (1 - \alpha)\rho_l\, c_p\, dT\,. \tag{9}$$

Differentiating Equation (9) with respect to dp_{sat} gives

$$\frac{dm}{dp_{sat}} = \left(\frac{(1 - \alpha)\rho_l\, c_p}{L}\right)\frac{dT}{dp_{sat}} \tag{10}$$

where the term $\frac{dT}{dp_{sat}}$ is the inverse of the slope of the phase change curve expressed by the Clausius-Clapeyron relation [100],

$$\frac{\rho_v L}{T_\infty} = \frac{dp_{sat}}{dT} \tag{11}$$

for a liquid with free stream temperature of T_∞. We take the integral of Equation (11) with respect to temperature T to yield

$$p_{sat} = \frac{\rho_v L}{T_\infty}\Delta T + p_{sat}^* \tag{12}$$

where $\Delta T = T - T_\infty$, representing a correction for temperature variation corresponding to the latent heat exchange due to the occurrence of cryogenic cavitation when the flow departs from an assumed initial isothermal state to a subsequent cryogenic state. In Equation (12), p_{sat}^* is the initialization saturation pressure at the assumed initial isothermal state with operating temperature T_∞, and temperature T is found from the energy equation discussed in the following. Equation (12) explicitly describes the saturation pressure p_{sat} variation in a cryogenic state with specific temperature, vapor density, and latent heat relative to the constant saturation pressure in the assumed initial isothermal state (p_{sat}^*). The assumption of initialization flow being in an isothermal state with p_{sat}^* is reasonable since $T = T_\infty$ initially, so giving the constant $p_{sat} = p_{sat}^*$ in (12), which is the case in isothermal cavitation flows. Nevertheless, this assumption needs to be corrected and resolved in the present numerical solution, so that the variations of p_{sat} and L in cryogenic cavitation flows can be captured properly. As discussed in Section 3.2.2 and 3.2.5, this is made by updating Equation (12) in an iterative procedure during simulation, which resolves the primary isothermal state assumption, thus yielding accurate calculations of flow properties at the subsequent cryogenic states. Substituting Equation (12) in (5) and (7) gives

$$\rho_{v,sat} = \psi_v \left(\frac{\rho_v L}{T_\infty}\Delta T + p_{sat}^*\right) \tag{13}$$

and

$$\rho_l^0 = \rho_{l,sat} - \psi_l \left(\frac{\rho_v L}{T_\infty}\Delta T + p_{sat}^*\right). \tag{14}$$

Using this explicit description of saturation pressure variation with temperature, the mass conservation equation for the cryogenic mixture is (see Appendix A for detailed derivation)

$$\frac{\partial \rho_m}{\partial t} + \nabla\cdot(\rho_m \boldsymbol{u}) = \frac{\partial}{\partial t}\left(\frac{(1-\alpha)\,\psi_l\,\Delta T \rho_v L}{T_\infty}\right) + \nabla\cdot\left(\frac{(1-\alpha)\,\psi_l\,\Delta T \rho_v L}{T_\infty}\boldsymbol{u}\right) \tag{15}$$

where $\boldsymbol{u} = (u, v, w)$ is the velocity vector. The right-hand-side terms are effectively source terms to account for mass transfer between phases during phase change. In order to calculate the mixture density variations in terms of phase properties, Kärrholm’s theory is used [140] which introduces an iterative mixture’s equilibrium equation of state for the mixture density by using equations (5)-(7), the vapor volume fraction field, and a pressure-density correction term:

$$\rho_m = (1-\alpha)\rho_l^0 + (\alpha\psi_v + (1-\alpha)\psi_l)\,p_{sat} + \psi_m(p - p_{sat}) \tag{16}$$

where the saturation pressure is found from Equation (12). By integrating (15) using Equation (16) for the mixture density, a pressure equation for the mixture is formulated in terms of the mixture density [141]. Thus, the mixture pressure equation becomes

$$\begin{aligned}\frac{\partial(\psi_m\,p)}{\partial t} - (\rho_l^0 + (\psi_l - \psi_v)\,p_{sat}^*)\,\frac{\partial \alpha}{\partial t} - p_{sat}^*\,\frac{\partial \psi_m}{\partial t} + \nabla\cdot(\rho_m \boldsymbol{u})\\ = -\,\psi_v\,(\frac{\Delta T \rho_v L}{T_\infty})\,\frac{\partial \alpha}{\partial t} + (\frac{\Delta T \rho_v L}{T_\infty})\,\frac{\partial \psi_m}{\partial t} + \nabla\cdot\left((1-\alpha)\frac{\psi_l\,\Delta T \rho_v L}{T_\infty}\boldsymbol{u}\right)\end{aligned} \tag{17}$$

in which the velocity field is determined from the momentum equation,

$$\begin{aligned}\frac{\partial(\rho_m\,\boldsymbol{u})}{\partial t} + \nabla\cdot(\rho_m\,\boldsymbol{u}\boldsymbol{u}) = -\,\nabla p + \nabla\cdot[\,\mu_m(\nabla\boldsymbol{u} + (\nabla\boldsymbol{u})^T)]\\ + \frac{\partial}{\partial t}\left((1-\alpha)\,\frac{\psi_l\,\Delta T \rho_v L}{T_\infty}\,\boldsymbol{u}\right) + \nabla\cdot\left((1-\alpha)\,\frac{\psi_l\,\Delta T \rho_v L}{T_\infty}\,\boldsymbol{u}\boldsymbol{u}\right)\end{aligned} \tag{18}$$

with mixture molecular viscosity μ_m,

$$\mu_m = \alpha\mu_v + (1-\alpha)\,\mu_l \tag{19}$$

which is found from a generic Sutherland model described in Section 3.2.3. The last two terms on the right-hand-side of (18) account for momentum transfer between phases during phase change, as detailed in Appendix A.

In order to address thermodynamic effects on cavitation patterns in cryogenic fluids, an enthalpy-based energy equation for the mixture is employed as follows [142]:

$$
\begin{aligned}
&\frac{\partial \rho_m h}{\partial t} + \nabla \cdot (\rho_m \boldsymbol{u} h) + \frac{\partial \rho_m K}{\partial t} + \nabla \cdot (\rho_m \boldsymbol{u} K) - \frac{\partial p}{\partial t} = -\nabla \cdot \boldsymbol{q} + \nabla \cdot (\boldsymbol{\tau} \cdot \boldsymbol{u}) \\
&+ \frac{\partial}{\partial t}\left((1-\alpha)\frac{\psi_l\, \Delta T \rho_v L}{T_\infty}(K+h)\right) + \nabla \cdot \left((1-\alpha)\, \frac{\psi_l\, \Delta T \rho_v L}{T_\infty}(K+h)\, \boldsymbol{u}\right)
\end{aligned}
\tag{20}
$$

where the LHS terms represent the transport of total energy (enthalpy plus kinetic energy K) and the RHS terms are, respectively, thermodynamic power ($\nabla \cdot \boldsymbol{q}$) where conductive heat flux is $\boldsymbol{q} = -\kappa\, \nabla h$ with thermal diffusivity $\kappa = \nu/Pr$, viscous work $\nabla \cdot (\boldsymbol{\tau} \cdot \boldsymbol{u})$ with shear stress tensor $\boldsymbol{\tau}$, plus two additional source terms accounting for latent heat transfer during phase change (detailed in Appendix A). Note that the mechanical power due to gravity forces is neglected.

The energy Equation (20) needs to be linked to the rest of the governing equations to establish a coupled system of equations. In coupling the energy equation, the deviatoric part of the stress term is unknown (because of the unknown shear stress tensor $\boldsymbol{\tau}$) and needs a separate closure equation. The Stokes' theorem for compressible Newtonian fluids is used to resolve the unknown term, and therefore, to close the system of equations [75]. Thus, the deviatoric stress tensor in terms of the covariant derivative of velocity is

$$
\boldsymbol{\tau} = \mu_m (\nabla \boldsymbol{u} + (\nabla \boldsymbol{u})^T) - \frac{2}{3} \mu_m\, \nabla \cdot \boldsymbol{u}\,. \tag{21}
$$

By substituting (21) into (20), the system of governing equations is closed.

3.2.2. Calculation of Latent Heat

Equation (12) in Section 3.2.1 is used for initialization of the iterative procedure in the developed solver by making an explicit correlation between the saturation pressure (p_{sat}) variation in a primary cryogenic state relative to the constant saturation pressure in an assumed initial isothermal state (p_{sat}^*). Nevertheless, this equation needs to be updated during simulation so that the assumed initial isothermal state with p_{sat}^* is resolved, and thus the variations of latent heat and saturation pressure are accurately calculated at the resulting cryogenic states. This is made by rewriting the Clausius-Clapeyron Equation (11) as

$$\frac{\rho_v^r L^r}{T_\infty} = \frac{p_{sat}^r - p_{sat}^{r-1}}{[T - T_\infty]^r - [T - T_\infty]^{r-1}}, \tag{22}$$

which is used as a closure to find the latent heat in the iterative calculation of the discretized governing equations during simulation. In Equation (22), the superscripts 'r' and 'r – 1' indicate the properties at iterations r and r – 1; p_{sat}^{r-1} is the stored vapor pressure found from iteration r – 1, and p_{sat}^r is given by the updated saturation pressure equation

$$p_{sat}^r = \frac{\rho_v^{new} L^{old} [T - T_\infty]^{new}}{T_\infty} - \frac{\rho_v^{old} L^{old} [T - T_\infty]^{old}}{T_\infty} + p_{sat}^{old} \tag{23}$$

in the PIMPLE loop described in Section 3.2.5 [147,149,150]. In Equation (23), the superscripts 'old' and 'new' respectively represent the properties, at iteration *r,* before and after the energy equation is solved in the loop [138,147,148].

3.2.3. Thermophysical Properties

A modified thermophysical model is used to specify the thermophysical properties of the cryogenic fluid being modeled in conjunction with the governing equations. This model is updated iteratively based on the updated pressure and temperature values obtained from the solution. Particular attention is paid to selecting the appropriate thermophysical models for describing the cryogenic specific heat and dynamic viscosity of LNG. A series of numerical simulations were thus performed to examine the accuracy of different thermophysical models in OpenFOAM. Reasonable agreement with property data from NIST [143-145] were obtained by adapting the Sutherland and JANAF thermodynamic models for viscosity μ_m and specific heat c_p, respectively. The Sutherland model calculates the viscosity of LNG for two selected high (HTR) and low (LTR) –temperature ranges for the vapor and liquid phases, respectively:

$$\mu_v(T) = \mu_{HTR}(T) = \frac{\mathrm{A}\sqrt{T}}{1+\frac{\mathrm{B}}{T}} \tag{24}$$

$$\mu_l(T) = \mu_{LTR}(T) = \frac{\mathrm{C}\sqrt{T}}{1+\frac{\mathrm{D}}{T}} \tag{25}$$

where the coefficients A, B, C, and D are given in Table II for selected operating pressure values and temperature ranges in this work. Within the pressure range considered in this study (approximately 4-8 bar), the pressure effect on dynamic viscosity occurs only indirectly by modifying the saturation temperature; within a given phase, the pressure effect is less than 0.50%. Therefore, this work assumes that the dynamic viscosity only varies with temperature.

Fluid	Pressure	HTR	LTR	A	B	C	D
LNG	4.13 bar	132.3 K < T < 180.0 K	100.0 K < T < 132.3 K	7.59×10^{-7}	80.28	2.61×10^{-6}	-83.49
	6.89 bar	141.4 K < T < 180.0 K	100.0 K < T < 141.4 K	8.10×10^{-7}	90.04	2.49×10^{-6}	-84.87

Table II: Sutherland dynamic viscosity model coefficients for LNG

The JANAF thermophysical model calculates specific heat as a fourth-order polynomial of temperature by specifying two sets of coefficients taken from the JANAF lookup tables [143]. These coefficients are used for two low- and high-temperature ranges connected by a common temperature i.e. the saturation temperature. In the present work, equations (26)-(27) are used to approximate c_p for the selected high (HTR) and low (LTR) temperature ranges:

$$c_{p,v}(T) = c_{p,HTR}(T) = \mathrm{H}_1\, T^4 + \mathrm{H}_2\, T^3 + \mathrm{H}_3\, T^2 + \mathrm{H}_4\, T + \mathrm{H}_5 \tag{26}$$

$$c_{p,l}(T) = c_{p,LTR}(T) = \mathrm{L}_1\, T^4 + \mathrm{L}_2\, T^3 + \mathrm{L}_3\, T^2 + \mathrm{L}_4\, T + \mathrm{L}_5 \tag{27}$$

where the polynomial coefficients for LNG for the appropriate temperature ranges are given in Table III. Note that these polynomial coefficients are found from a fitting function correlating specific heat at a given pressure to NIST data [143] across the selected temperature range.

Fluid	Pressure (bar)	HTR LTR	H_1 L_1	H_2 L_2	H_3 L_3	H_4 L_4	H_5 L_5
LNG	6.89	141.4 K < T < 180.0 K 100.0 K < T < 141.4 K	2.15×10^{-7} 5.13×10^{-8}	-1.44×10^{-4} -2.18×10^{-5}	3.65×10^{-3} 3.58×10^{-3}	-4.12 -0.26	177.5 10.4
	4.13	132.3 K < T < 180.0 K 100.0 K < T < 132.3 K	6.96×10^{-8} 3.75×10^{-8}	-4.60×10^{-5} -1.54×10^{-5}	1.14×10^{-3} 2.45×10^{-3}	-1.27 -0.17	55.7 7.86

Table III: Primary coefficients of the JANAF specific heat capacity model for LNG

The main drawback of the JANAF model is its temperature-based derivation. Therefore, in the present study, $c_{p,HTR}(T)$, and $c_{p,LTR}(T)$ are extended such that they are able to account for both temperature and pressure effects on cryogenic cavitation. This generic JANAF model $c_p(p,T)$ is developed by using the available interpolation/extrapolation libraries in OpenFOAM. Fig. 1

shows the variation of c_p obtained by using the extended model of JANAF $c_p(p,T)$, which works for a broad range of pressure and temperature via linear interpolation/extrapolation.

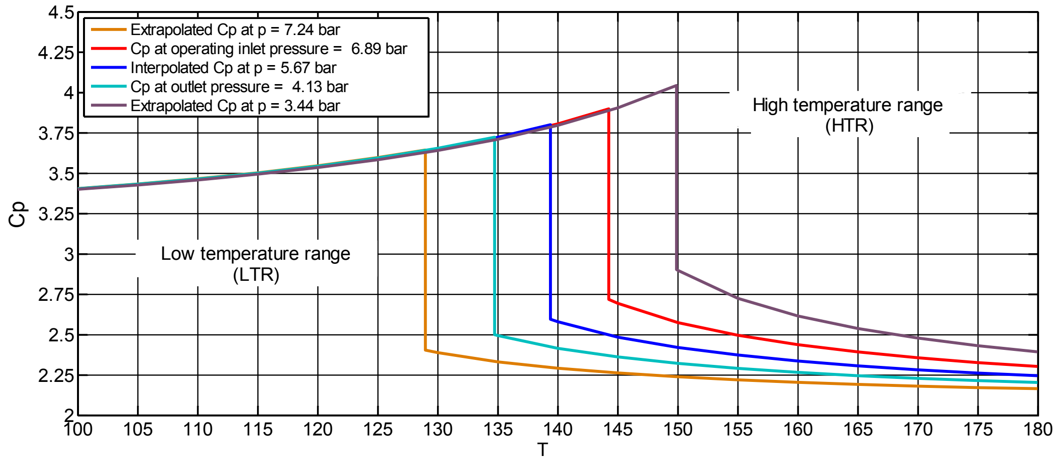

Fig. 1: Variation of c_p (kJ/kg K) with temperature and pressure for LNG from the extended JANAF model used in the cryogenic cavitation solver. The plotted pressure and temperature ranges are 3.44 bar < p < 7.24 bar and 100 K < T < 180 K, respectively.

3.2.4. Coupling of Energy Equation and Thermophysical Properties

In order to couple the fluid properties obtained from the thermophysical model to those employed in the conservation equations, the thermophysical properties are rewritten in terms of OpenFOAM thermophysical classes to link them to the solved enthalpy field. By doing so, the α and ρ_m fields are corrected to incorporate the effects of cryogenic conditions on cavitation. It also allows the boundary and initial conditions for the enthalpy equation to be imposed in terms of temperature, which simplifies comparison to experiments. The temperature field in this procedure is calculated from the solved sensible enthalpy h by using the Newton-Raphson method [146], as follows

$$\int_{T_{est}}^{T_j} \Big(\sum_{i=0}^{i=4} b_i\, T^i\Big)\, dT = h_j \tag{28}$$

where T_j and h_j are the temperature and the solved sensible enthalpy at the selected cell j and T_{est} is an estimated initial temperature [146].

3.2.5. Coupling Loop of Governing Equations

In the present cryogenic cavitation model, the merged PISO-SIMPLE algorithm (PIMPLE) is used to couple the momentum and pressure equations through an iterative multi-step prediction-correction procedure [147,148]. The semi-implicit method for pressure-linked equations (SIMPLE) [149] is used for steady problems where subsequent iterations under-relax the solution properties to improve convergence. By contrast, the pressure-implicit splitting operator (PISO) [150] is used for transient problems to accurately resolve the pressure-velocity coupling (and for non-isothermal flows, pressure-temperature coupling) at each time step. The merged PIMPLE algorithm solves the governing equations in a PISO loop to accurately capture non-linear coupling effects in an overall SIMPLE algorithm to under-relax the flow properties and improve convergence, with the overall result that the solution remains stable for larger time steps.

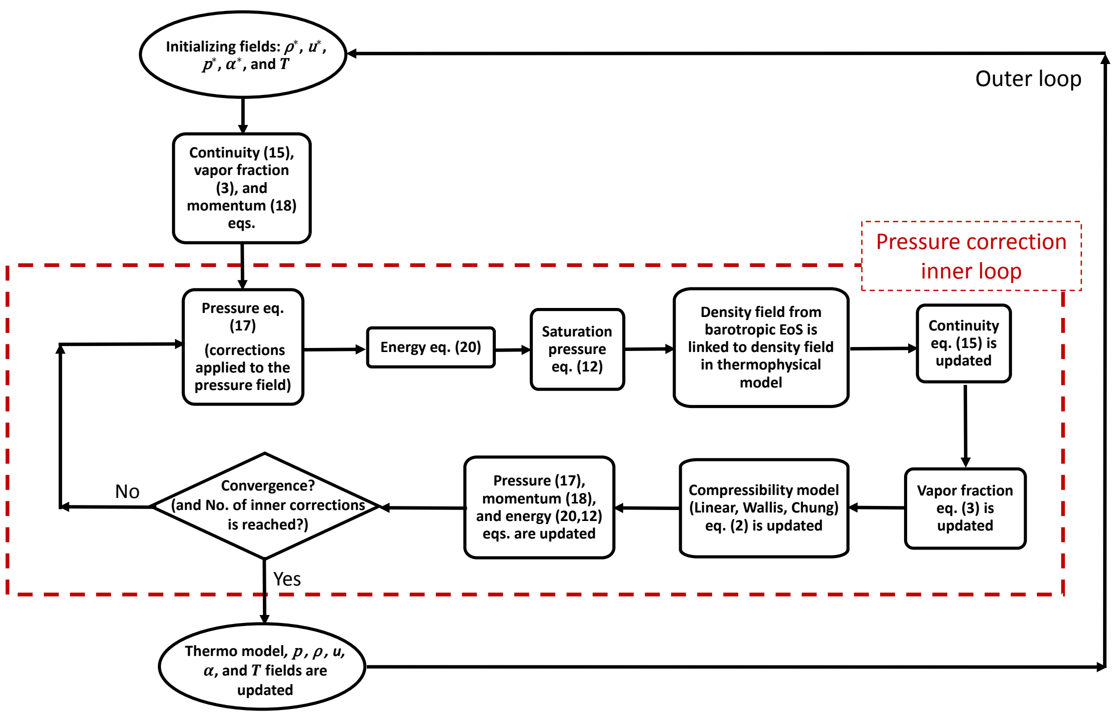

Fig. 2: Flowchart of the modified PIMPLE algorithm used in the cryogenic cavitation solver

The temperature field obtained from the specific heat and the enthalpy field resulting from the solution of Equation (20) are outside the predictor-corrector loops of the PIMPLE algorithm. As a result, the solved vapor volume fraction field is decoupled from the solution of the energy equation. In order for the vapor phase fraction field to be updated and coupled to the computed temperature field and also to capture large density variations in cloud cavitating regions [68], the following modifications are implemented in the PIMPLE loop:

1. Energy Equation (20) is added to the inner (PISO) loop.
2. Saturation pressure Equation (12) is added to the inner loop.
3. The mixture density field computed from the barotropic equation of state (1) is updated with the density field found from the thermophysical model and the enthalpy equation.
4. Mixture continuity Equation (15) is updated for the computed mixture density (16).
5. Compressibility model (2) is updated.
6. Barotropic equation of state (1) is updated.
7. Pressure (17), momentum (18), and enthalpy equations (20) are updated.
8. Thermophysical model, velocity, pressure, vapor volume fraction, density, viscosity, and temperature fields are updated for the next outer loop.

The modified PIMPLE loop is depicted in Fig. 2, noting that it works in an outer time loop that is not shown here. Also, the vapor phase fraction Equation (3) in the developed solver is written in terms of the density, so no further step is required to separately update the phase fraction equation.

4. Validation of the Developed Model

The developed cryogenic cavitation solver is validated for cavitating flow of liquid nitrogen (LN_2) inside a 2D Laval nozzle, based on the experimental studies of Simoneau and Hendricks [34] and Nagashima and Tani [24], as well as for cavitating flow of LN_2 through a 2D circular orifice following the experiment of Niiyama et al. [37]. In the nozzle case, a series of numerical tests for cavitating LN_2 flow is conducted for a range of operating pressures at a constant temperature to compare the behavior of the nozzle throat pressure and mass flow rate against the Nagashima and Tani's data. In the orifice case, the streamwise behavior of the Stepanoff's dimensionless parameter B-factor (which is often used to estimate the thermodynamic effects on cavitation patterns [38,42] by demonstrating a direct correlation between vapor phase production (α) and temperature depression (ΔT)) for the cavitating LN_2 flow operating under a range of Ca numbers are numerically explored and compared against the experimental findings of Niiyama et al. [37]. The developed solver is also verified for a cavitating flow of LNG inside the Laval nozzle, to examine the capability of the numerical model in accurately capturing LNG phase change properties against the actual saturation properties of LNG obtained from the NIST property tables. More details on the validation procedure are provided in the following sections.

4.1. Validation Study 1: Cavitating Flow of LN_2 inside a 2D Laval Nozzle

4.1.1. Numerical Setup

Compressible cavitating flow of LN_2 inside a 2D Laval nozzle geometry is studied using the developed cryogenic cavitation solver. Following the experimental study of Nagashima and Tani [24], a computational domain of $32A\times12A$ (A: throat cross-section area) with throat length of 1.053 cm is developed for the nozzle and meshed using 721,600 non-uniform structured elements, as illustrated in Fig. 3(a). A 20×12 cm^2 buffer zone is attached to the end of the domain so that any disturbances generated near the outlet do not affect the region of interest in the converging-diverging sections. To resolve the high-gradient regions near the walls, near-wall clustering of grid nodes is used with 12 prismatic layers, a smallest element thickness of 0.41 mm, and wall-normal grading rate of 1.176 (Fig. 3(b)-(c)); the grid independence is discussed in Appendix B. For the working fluid of LN_2, the initial fluid is only liquid nitrogen with an inlet density of 732.78 kg/m^3, kinematic viscosity of 1.28×10^{-7} m^2/s, and fixed inlet temperature of T_0

= 94.72 K. The inlet total pressure is 33.97 bar and the outlet pressure is 5.27 bar, yielding a pressure ratio of 6.45.

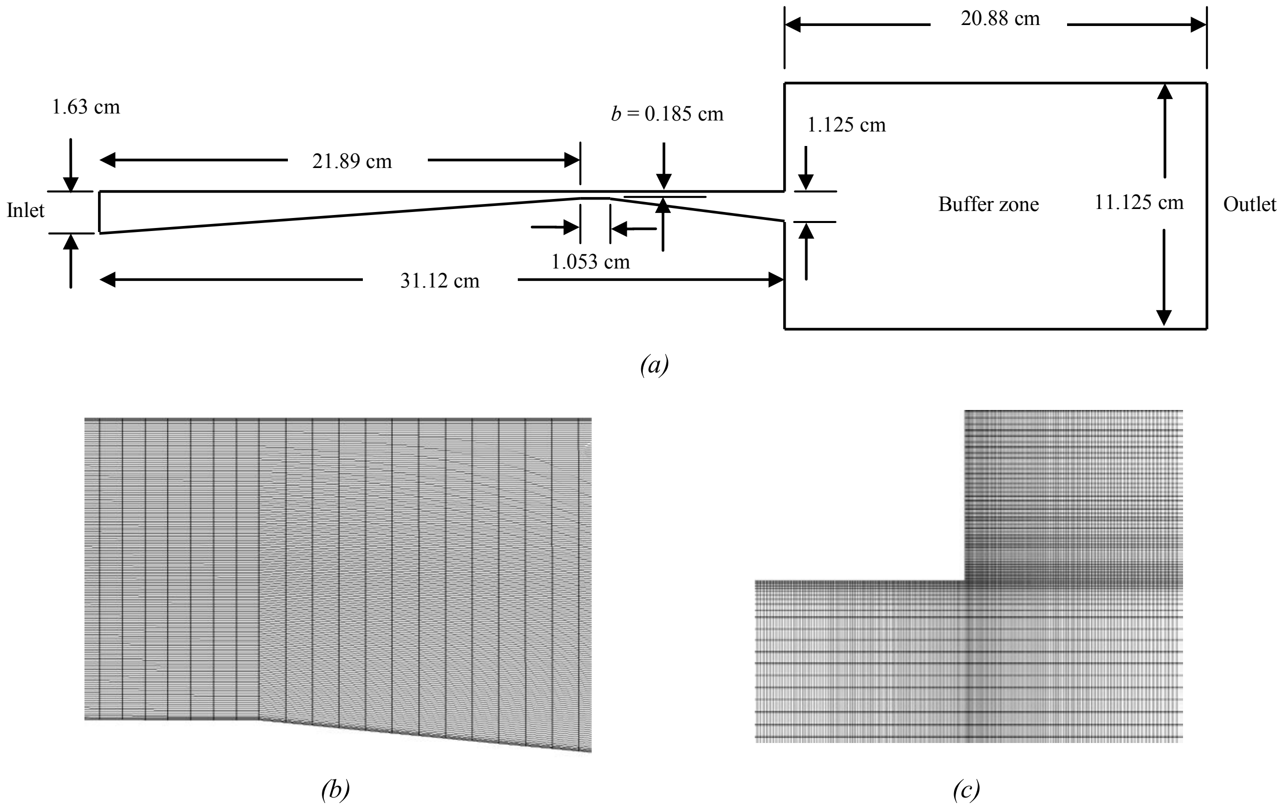

Fig. 3: (a) Computational domain for the 2D Laval nozzle simulation; zoomed view of the mesh at the throat (b) and at the entrance to the buffer region (c).

4.2. Validation Study 2: Cavitating Flow of LN_2 inside a 2D Circular Orifice

4.2.1. Numerical Setup

The experimental study of Niiyama et al. [37] is also selected to evaluate the accuracy of the developed solver in capturing thermodynamic behavior of cavitating cryogenic fluids. As indicated in Fig. 4, a 2D computational domain of $16.57d \times 2.36d$ (d is the orifice diameter) is meshed with 580,500 non-uniform structured elements by employing the same grid generation method as used in the nozzle case, with comparable resolution of the near-wall shear layers; the grid independence is discussed in Appendix B. Transient cryogenic cavitation of LN_2 through the circular orifice is simulated at an inlet temperature of 81.0 K, density of 790.28 kg/m^3, total inlet pressure of 5.0 bar, and outlet static pressure of 1.55 bar.

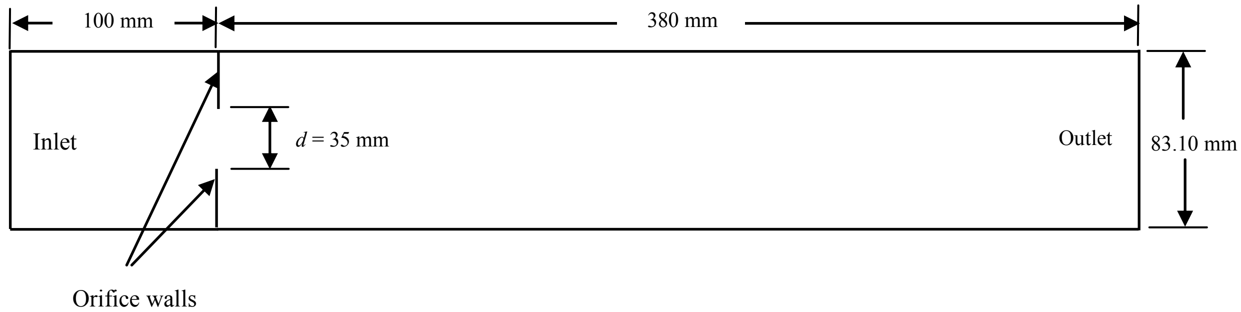

(a)

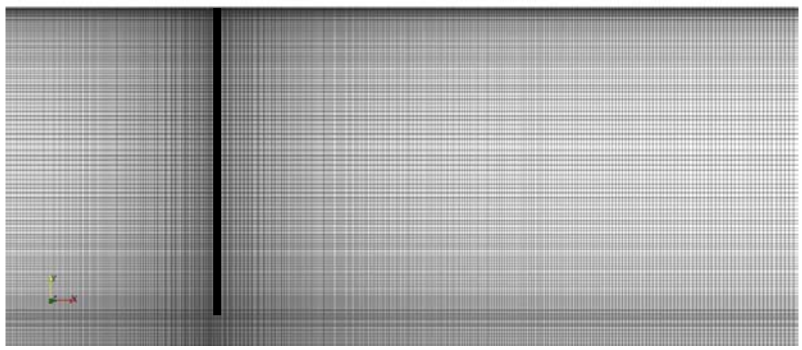

(b)

Fig. 4: (a) Computational domain for the 2D circular orifice simulation; (b) zoomed view of the mesh around the upper wall of the orifice.

4.3. Solution Procedure and Numerical Schemes

The flow governing equations in OpenFOAM are discretized by employing standard Gaussian finite volume integration to form a set of matrix equations [137,151]. In order to ensure the accuracy of the numerical solutions in this work, third-order cubic interpolation is used to interpolate between nodal and facial values. Interfacial fluxes are limited via a van Leer flux limiter to ensure total-variation-diminishing (TVD) behavior of the spatial discretization. One additional explicit corrector loop is performed to correct for the non-orthogonality of the spatial grids. Temporal derivatives employ a second-order backwards Euler discretization method. An iterative Gauss-Seidel solver with an incomplete-LU (lower-upper) pre-smoother is used to solve the matrix system of equations for density, momentum, enthalpy, and phase fraction, and an algebraic multi-grid method with an incomplete-Cholesky smoother is used for pressure. The stability of the iterative solution is governed by the Courant number estimated by

$$CFL = \frac{u\,\Delta t}{\Delta x} + \frac{v\,\Delta t}{\Delta y} \le 1.0 \tag{29}$$

where u and v are the streamwise and transverse velocities, and Δx and Δy are the smallest cell sizes in the x and y directions, respectively. The acoustic Courant number is also relevant in the compressible framework, for which the velocities given in Equation (29) are replaced with $u + a$ and $v + a$ where a is the speed of sound. A robust solution for the present simulations is achieved for the CFL range of 0.30-0.40 giving time step size of the order of $\Delta t \approx O(10^{-6})$ s, varying based on the operating conditions and mesh size. The maximum acoustic Courant number is set to 5.0 to stabilize high-speed pressure waves in the flow and to reduce artificial diffusion between phases. The simulations are run using a message passing interface (MPI) parallel computing method on a 3.0 GHz Intel-Xeon machine with 36 processors.

4.4. Results and Discussion

4.4.1. Cavitating Flow of LN_2 inside the Laval Nozzle

In order to validate the developed numerical model and to examine the reliability of the results for different inflow conditions, a series of validating simulations are here compared against the experimental study of Simoneau and Hendricks [34]. Numerical tests of cavitating cryogenic LN_2 inside the Laval nozzle is conducted for five different reduced pressures of P_r = 0.4, 0.8, 1.2, 1.6, and 2.0 at a reduced temperature of T_r = 0.75; reduced pressure/temperature is defined as the ratio of inlet to critical pressure/temperature. Results are compared on the basis of dimensionless pressure and mass flow rate ratios, $P_n = \frac{\text{throat pressure}}{\text{stagnation pressure}}$ and $G_r = \frac{\text{throat mass flow rate}}{\text{critical mass flow rate}}$, respectively. Note that the critical mass flow rate equals $(\rho_c\, p_c/z_c)^{0.5}$, where z_c is the critical compressibility factor.

Fig. 4 compares the simulated values of G_r and P_n against the experimental data of Simoneau and Hendricks [34]. To account for spatial and temporal non-uniformities in the simulated flow, the results are averaged spatially and temporally at 100 vertically-spaced data points at the throat over 25 time instances within an interval of two flow-through times for each reduced pressure. As expected, the mass flow rate of LN_2 at the throat (Fig. 5(a)) increases with increasing stagnation pressure while an opposite behavior is observed for the throat pressure (Fig. 5(b)). The numerical results agree reasonably well with the experiment results; discrepancies are likely due to three-dimensional or turbulence effects in the experiment that cannot be captured in the 2D laminar simulations.

(a)

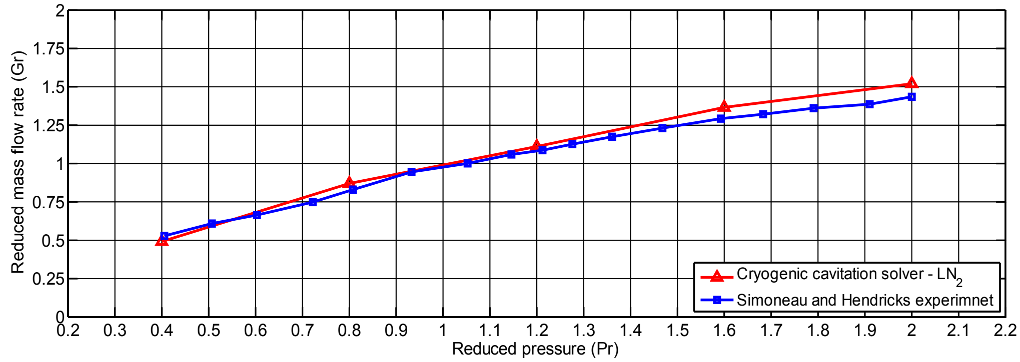

(b)

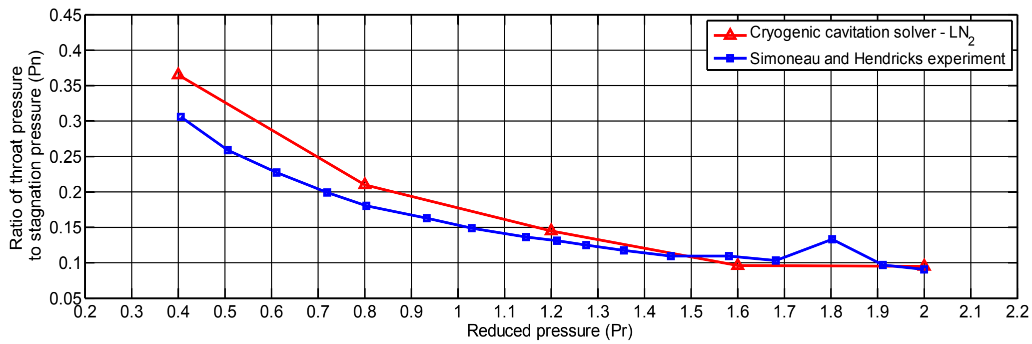

Fig. 5: Computed and measured throat flow rate ratio (a) and pressure ratio (b) of LN_2 flow in the Laval nozzle. Experimental measurements are from Simoneau and Hendricks [34].

4.4.2. Cavitating Flow of LN_2 inside the Circular Orifice

Visualization of the orifice simulation results is presented in Fig. 6. The instantaneous vapor fraction field, plotted in Fig. 6(a), shows that vapor cavities start growing immediately downstream of the orifice edges. These cavities are coincident with vortices shed from the orifice walls. With further progress of the cavity structures, they develop into large-scale vapor clouds. The latent heat of the phase change process is plotted in Fig. 6(b) to illustrate the spatial non-uniformity of the latent heat caused by the strong temperature dependence of the saturation pressure, which further highlights the importance of thermal effects in cryogenic cavitation. To validate these results against Niiyama et al. [37], Stepanoff's dimensionless parameter B-factor defined in Section 2.1.1 is plotted in Fig. 6(c) at four streamwise stations downstream of the orifice. The *x/b* locations of these stations are indicated in Fig. 6(a). It is notable that the B-factor, which is often used to estimate the thermodynamic effects on cavitation patterns [5,38], demonstrates a direct correlation between vapor phase production (α) and temperature depression (ΔT), illustrating that the latent heat required for the formation of a vapor spot is obtained from its surrounding liquid [37,38]. Fig. 6(c) compares the results from the developed cryogenic cavitation solver and an isothermal cavitation solver presently available in OpenFOAM for LN_2 at cavitation numbers equal to 0.31 and 0.83.

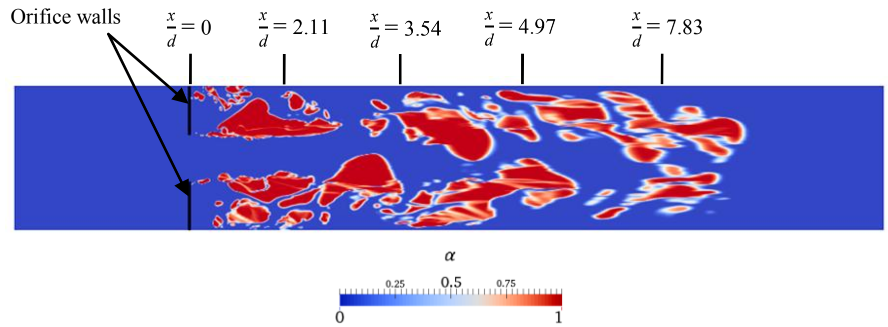

(a)

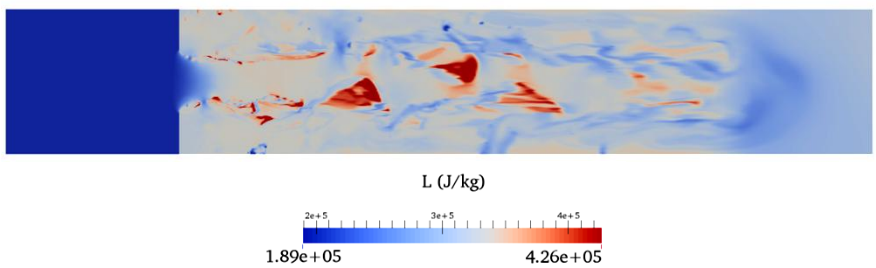

(b)

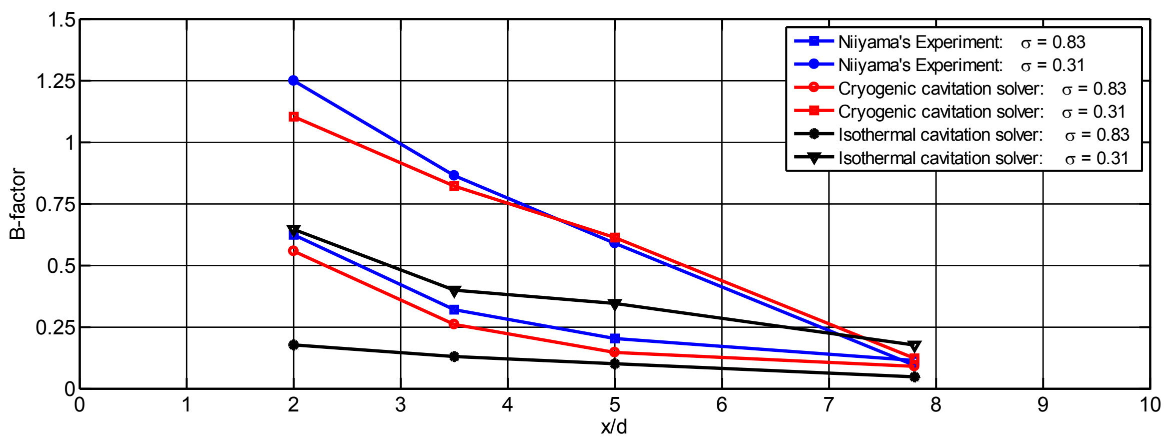

(c)

Fig. 6: Distribution of the dimensionless B-factor at four streamwise stations in the cavitating flow of liquid nitrogen (LN_2) inside the 2D circular orifice: (a) vapor phase fraction field at t = 0.213 s; (b) latent heat of vaporization field (J/kg) at t = 0.213 s; (c) comparison of B-factor from the numerical simulation and experimental data of Niiyama et al. [37]. σ is Niiyama's cavitation number.

Average B-factors at each streamwise station in Fig. 5(c) are obtained by spatially averaging 100 vertically-spaced data points at each streamwise location, which are then averaged temporally for 50 equally-spaced time instances over two flow-through times. Although general trends are captured between the isothermal case results and the experimental data, a much better and reasonable collapse of the results is achieved for the cryogenic solver. The discrepancies for the cryogenic case are estimated to be due to the presence of three-dimensionality and turbulence effects (turbulence intensity ≅ 2.75% in the experimental tests), which are not resolved in the present 2D laminar simulations.

From Fig. 5(c) it is also observed that the B-factor decreases with increasing streamwise distance from the orifice, indicative of decreasing vapor production with downstream distance. The further collapse of cavity structures in downstream regions that accompanies condensation causes more latent heat of condensation to be released, leading to smaller temperature depressions further downstream [37,59]. Moreover, isothermal results yield lower B-factor values, indicating lower vaporization of cavitating LN_2 and highlighting the thermal sensitivity of the cavitation process.

Another important observation in Fig. 5(c) is the increase of the B-factor with decreasing cavitation number. Both solvers predict an increasing trend for B-factor, with the larger numbers found in the cryogenic case corroborated by the experiment. The increase of the B-factor at lower cavitation numbers is attributed to higher production of cavity spots in upstream regions, as higher production of vapor leads to further temperature depression in these regions where more latent heat of vaporization is transferred into the developing vapor cavities [35,37]. This increase with cavitation number, however, is observed to be smaller for downstream stations.

4.5. Validation Study 3: Cavitating Flow of LNG inside the Laval Nozzle

A lack of LNG experimental data makes validation of the developed solver for LNG flows challenging. Therefore, to verify that the output of the cryogenic cavitation solver accurately predicts the liquid-vapor phase change of LNG, a numerical simulation of compressible LNG cavitaton flow inside the described nozzle of the validation Study 1 (see Section 4.1) is performed, and results of which are compared against the actual saturation properties of LNG obtained from the NIST property tables for the computed flow conditions [143]. The numerical setup and mesh configuration are similar to the LN_2 cavitation case (Section 4.1-4.3) with the difference being here that the operating conditions are set for LNG; the boundary conditions consist of a total inlet pressure of 6.89 bar and outlet pressure of 4.13 bar, resulting in a pressure ratio of 1.67 between the inlet and outlet zones. The operating cavitation number *Ca* is 1.41. The

Reynolds number in terms of the throat length and the initial liquid kinematic viscosity of 1.98×10^{-7} m^2/s is 8720.0. The initial flow field contains only liquid methane ($\alpha_0 = 0$) with an inlet density of 390.93 kg/m^3 and a fixed inlet and initial temperature of T_0 = 132.0 K, giving the Mach number of 0.57. Also, identical discretization schemes and solution methodologies to the LN_2 orifice case are used for the LNG tests, except the maximum acoustic Courant number is 4.0 and the maximum Courant number is 0.40, yielding a time step size of $\Delta t = 1.18\times10^{-5}$ s.

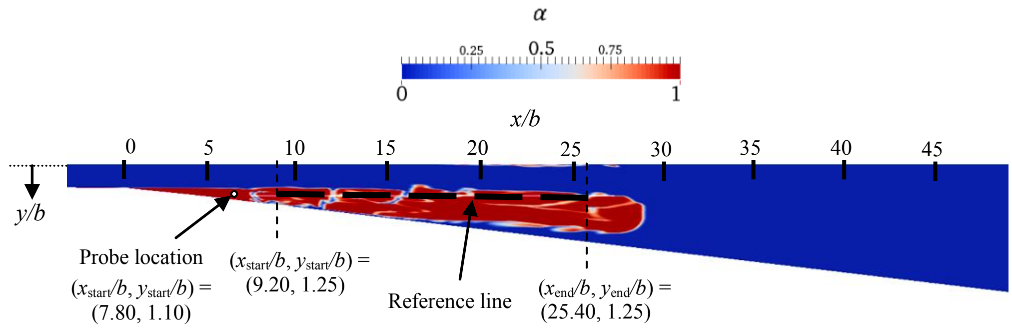

Fig. 7: Phase fraction contour for cavitating LNG in the diverging part of the Laval nozzle at t = 0.636 s. Locations of the reference line and probe are indicated.

Verification process is conducted using a reference line with dimensionless length of 16.2*b* placed in the computational domain at a selected time of t = 0.636 s, as shown in Fig. 7. At this time instance, the line is located near the edge of the vapor cavity such that it crosses multiple vapor/liquid interfaces. By comparing the computed temperatures and pressures along the reference line to the saturation temperatures and pressures obtained from NIST [143], the likelihood of phase-change can be identified and compared against the computed phase fraction. This is illustrated in Fig. 8, which plots the simulated flow property distributions along the reference line in terms of the computed vapor fraction, static pressure, and temperature; the horizontal axis indicates the dimensionless streamwise distance from the throat. The corresponding saturation pressure and temperatures along the reference line, obtained from the NIST property tables [143], are also plotted. The vapor fraction distribution in Fig. 8(a) indicates that mostly vapor phase exists along the reference line, although there are localized regions where the vapor condenses to liquid e.g. near the *x/b* = 21.35 location. The pressure distribution in Fig. 8(b) shows that the computed pressure is below the saturation pressure in regions where the phase fraction is close to unity, which is consistent with the LNG changing phase to vapor. At locations where the computed pressure exceeds the saturation pressure, such as near *x/b* = 20.25, the phase fraction reverts to liquid phase over a finite distance, which corresponds to the "frothy" zones noted in literature [68,100]. If the computed pressure only briefly exceeds the saturation pressure, such as near x/b = 10.55, the phase-change process cannot respond quickly enough such that only a small dip occurs in vapor phase fraction.

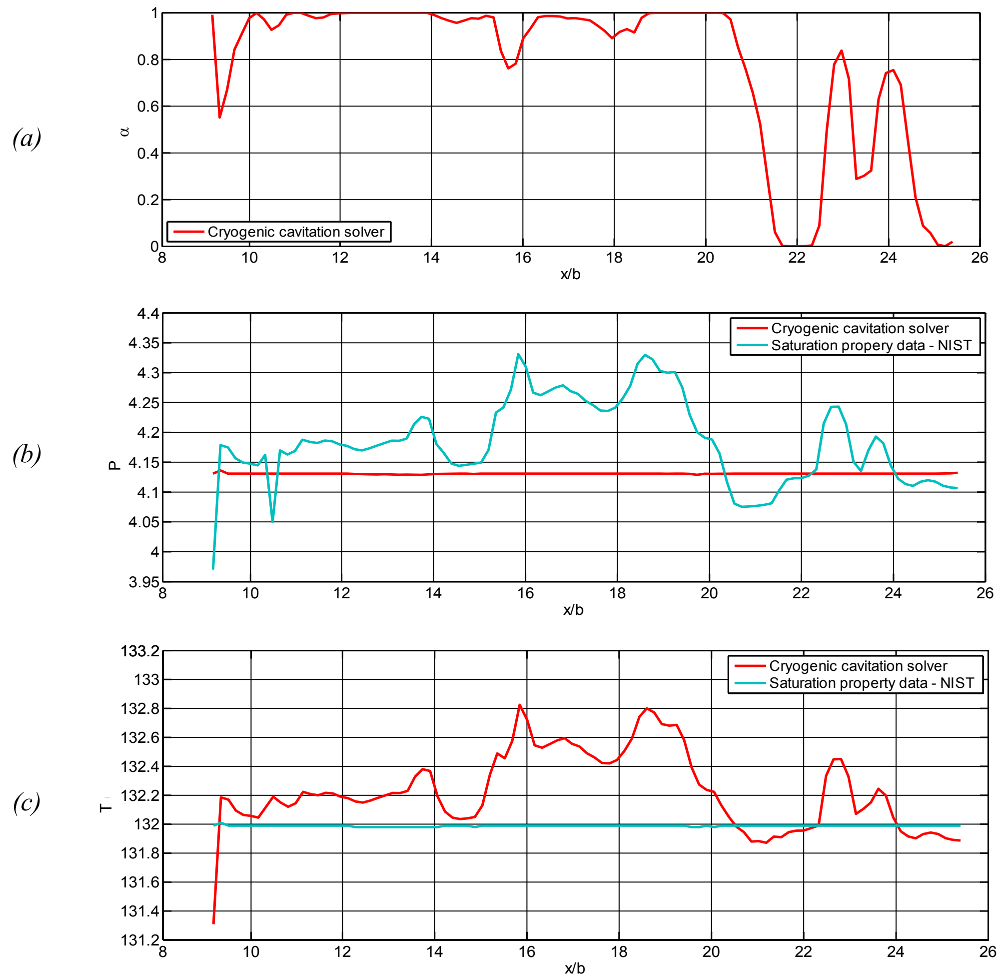

Fig. 8: Streamwise variation of the flow properties of cavitating LNG along the reference line in the diverging part of the nozzle at t = 0.636 s: (a) computed vapor fraction; (b) computed static pressure vs. reference saturation pressure (bar); (c) computed temperature vs. reference saturation temperature (K).

A similar comparison can be made in Fig. 8(c) between the computed temperature, saturation temperature, and vapor phase fraction; when the computed temperature exceeds the saturation temperature, vapor phase predominates, and when it drops below the saturation temperature (such as near x/b = 20.25), condensation to liquid phase occurs. This correspondence between the computed phase fraction, the computed temperatures and pressures, and the tabulated saturation properties was verified at several other locations and time instances, suggesting that the vaporization and condensation processes are captured with reasonable accuracy in the simulation.

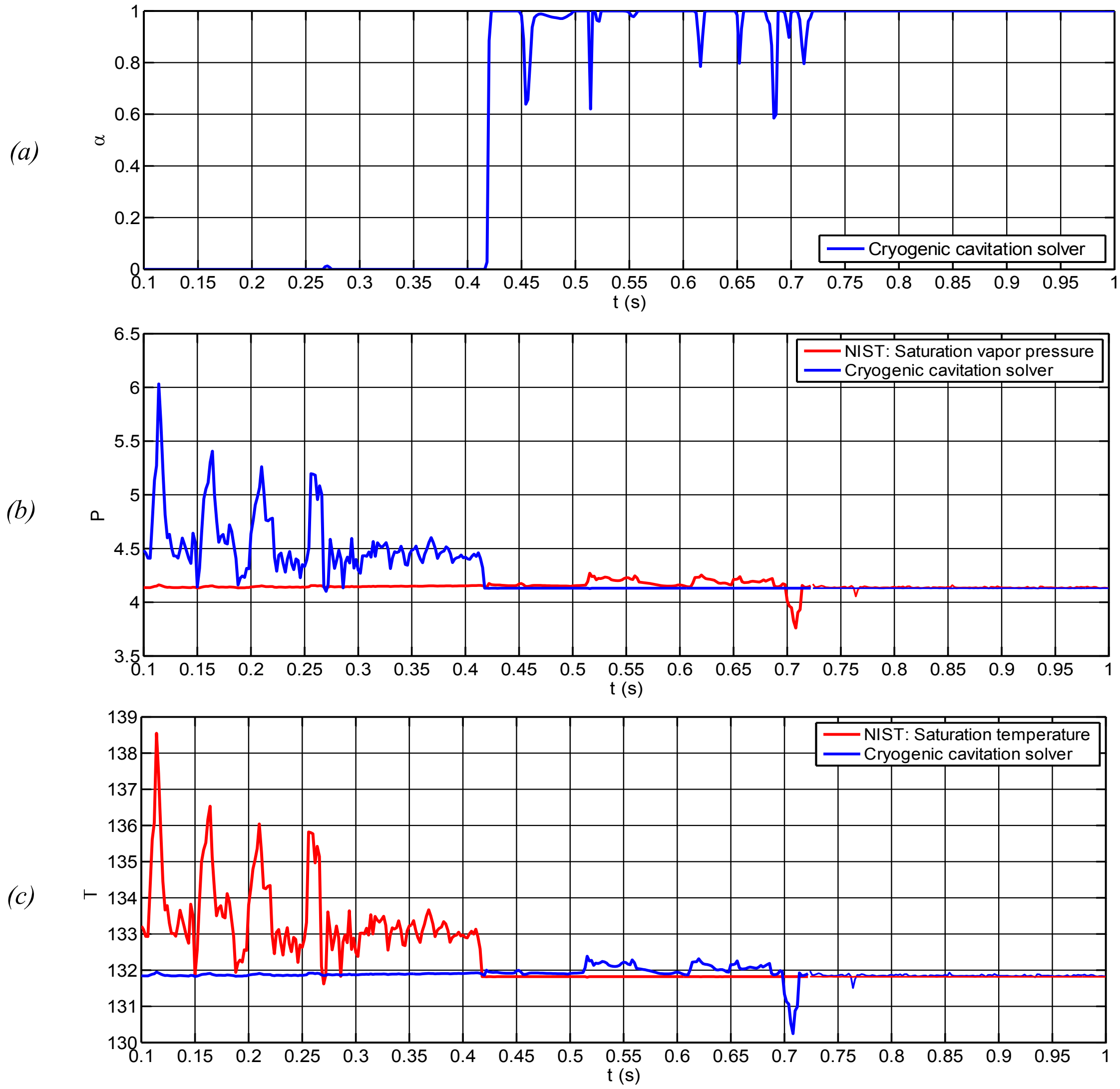

Fig. 9: Time history of the flow properties of cavitating LNG at the probe placed at x/b = 7.80 and y/b = 1.10 in the diverging part of the nozzle: (a) computed vapor fraction; (b) computed static pressure vs. reference saturation pressure (bar); (c) computed temperature vs. reference saturation temperature (K).

To verify that the temporal variations associated with the condensation and vaporization processes are captured accurately, the simulation results are also sampled at a probe point placed at the beginning of the diverging section of the nozzle at *x/b* = 7.80 and *y/b* = 1.10 (see Fig. 7). Time histories of the vapor fraction, pressure, and temperature at the considered probe location over one flow-through time are plotted in Fig. 9. Again, the onset of non-zero vapor phase fraction coincides with when the computed static pressure decreases below the saturation pressure (Fig. 9(b)) or the computed temperature rises above the saturation temperature (Fig. 9(c)). This correspondence is a further verification that the temporal condensation and vaporization processes are captured accurately. From the pressure record in Fig. 9(b), it is also noted that large pressure fluctuations, including rapid and slow components, occur prior to t = 0.42 s when cavitation is initialized. With further development of the cavitating regime in the flow, these large pressure fluctuations are reduced [82]. By about t = 0.75 s, the local flow reaches a statistically steady state indicative of a stable, wall-attached vapor cavity [83,100].

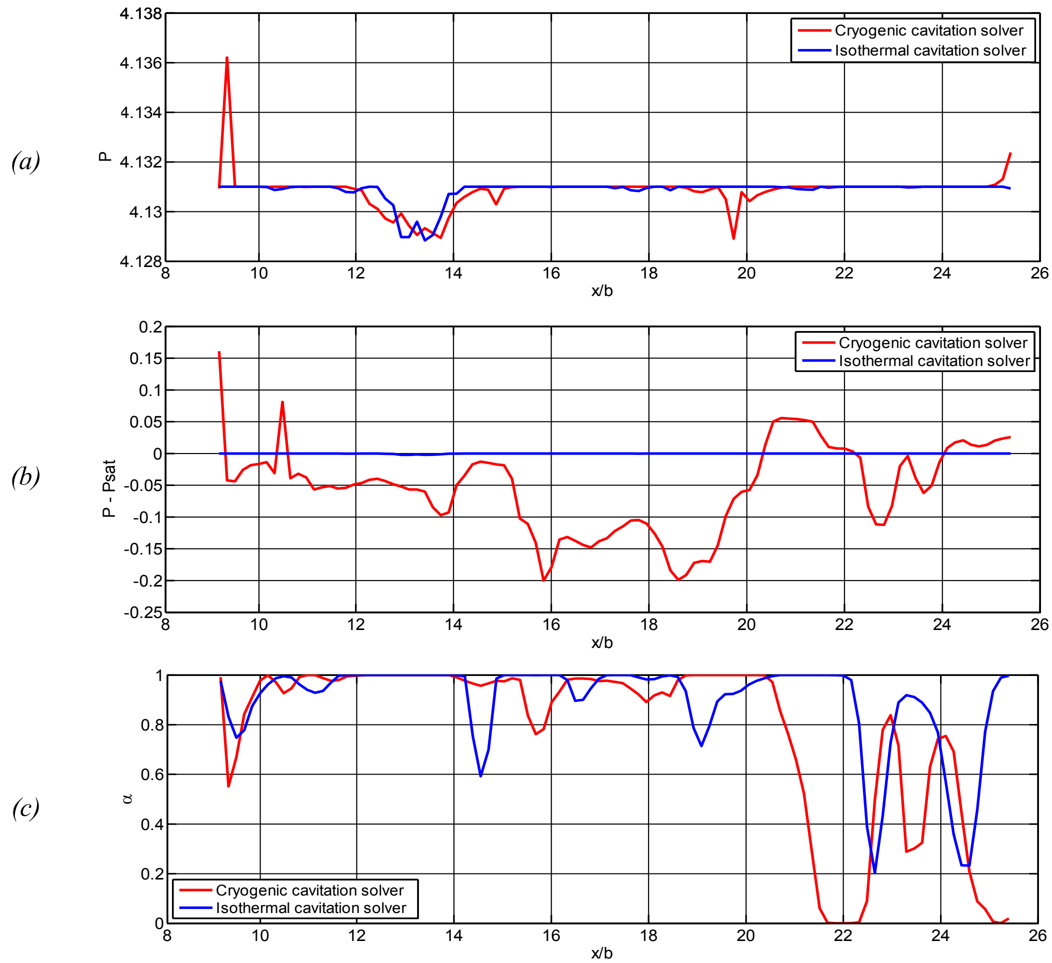

Fig. 10: Comparison of the streamwise variation of flow properties along the reference line in the diverging part of the nozzle at t = 0.636 s for the cryogenic and isothermal cavitation solvers: (a) static pressure (bar); (b) difference between static pressure and saturation pressure (bar); (c) vapor fraction.

The improved accuracy of the present cryogenic cavitation solver compared to the isothermal cavitation solver is considered in Fig. 10 by plotting results along the reference line from Fig. 7 using both solvers. The static pressure distribution in Fig. 10(a) shows that similar pressure fields are obtained from both solvers. However, the isothermal solver does not account for temperature variations or temperature-dependence of the saturation pressure. The significance of this is shown in Fig. 10(b) by plotting the difference between the computed static pressure and the saturation pressure; for the isothermal case, the saturation pressure is constant and the difference is less than 0.02 bar, while for the cryogenic case, differences of about 0.2 bar are recorded. The temperature dependence of the saturation pressure triggers phase changes in the cryogenic case that are not captured in the isothermal case [152,153], producing the differences in the vapor fraction between the two cases plotted in Fig. 10(c).

To assess the influence of the above-noted discrepancies between the cryogenic and isothermal solvers on the total vapor production in the nozzle, Fig. 11 compares the temporal variation of the spatially-averaged vapor fraction (i.e. $\alpha_{mean} = \frac{\iint_{x,y_1}^{x,y_2} \alpha_i dA_i}{\iint_{x,y_1}^{x,y_2} dA_i}$ where A is the domain area filled with cells with index i) in the nozzle over approximately two flow-through times. The spatial average is conducted only over the diverging section of the nozzle and the resulting average corresponds to the percentage of the nozzle volume that contains vapor.

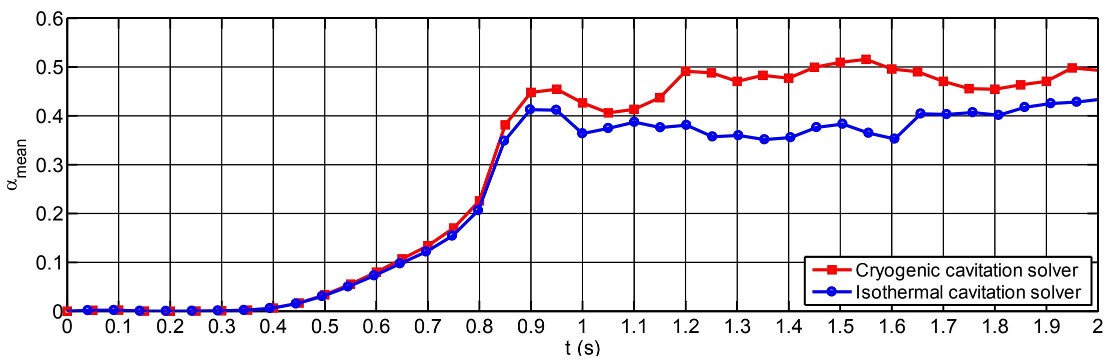

Fig. 11: Temporal variation of the spatially-averaged vapor volume fraction of LNG in the diverging part of the nozzle: comparison between the cryogenic and isothermal cavitation solvers.

Fig. 11 shows that early in the simulation, the isothermal and cryogenic solvers predict similar vapor production rates. After t = 0.85 s or about one flow-through time, vapor production in the cryogenic case begins to exceed that in the isothermal case such that the average vapor volume fraction is about 6.0% higher at steady state. The main reason for this behavior is estimated to be the increasing importance of thermal effects as cavitation progresses, which alter the saturation pressure of LNG such that the condensation of vapor cavities is delayed [36,37,49]. More details on the observed cavitation behavior of the in-nozzle LNG flow are discussed in Chapter 5.

5. Numerical Simulation of 2D In-nozzle Cavitating Flow of LNG

This chapter further addresses the baseline compressible cavitating flow of LNG inside the 2D nozzle introduced in Section 4.1. The global behavior of the LNG cavitating structures in the nozzle at selected time instants is first investigated to reveal the unsteady behavior of cavitating patterns from the instance of cavity inception up to the later cavitation development stages including formation of cavity clouds. Cavity-vortex interactions of the in-nozzle LNG flow are then investigated by employing a vorticity transport equation, to find correlative mechanisms governing the evolution and interaction of LNG vapor structures and shear layers. Further assessment of the instability mechanisms, including the shedding behavior of cavitating structures of LNG in the nozzle, are explored in the comparative studies of Chapter 6.

5.1. Nucleation and Growth of LNG Cavitation

To investigate the nucleation mechanism of LNG vapor cavities and their transient growth in the Laval nozzle, the distribution of flow properties along the lower wall of the nozzle near the interface of the throat and the diverging section are plotted in Fig. 12. Time instances at t = 0.25, 0.26, 0.27 and 0.28 s are plotted, which correspond to times immediately proximal to the initial nucleation of vapor cavities in the simulation. This is evident in the phase fraction distributions plotted in Fig. 12(a); pure liquid occurs for t = 0.25 s, and nucleation of a small vapor cavity develops thereafter. The wall shear stress distribution in Fig. 12(b) shows a peak at x/b = 0.0 for all times. This location corresponds to the surface discontinuity between the throat and diverging section of the nozzle. The wall vorticity distribution in Fig. 12(c) shows that the peak in the wall shear is associated with an accumulation of transverse vorticity component from the wall boundary layer at the surface discontinuity. Because the flow is in development, the average shear stress and vorticity levels increase with time, but the peak in the transverse vorticity is maintained for all times. The circulation associated with the elevated local vorticity produces a local decrease in the static pressure [153,154]. As the vorticity peak grows steadily stronger at t = 0.26 and 0.27 s, the static pressure continues to drop until it dips below the saturation pressure, which leads to the cavity nucleation between t = 0.25 and 0.26 s. The continued increase in the local transverse vorticity and wall shear stress at the surface discontinuity enlarges the static pressure depression yielding a growing vapor cavity [154].

(a)

(b)

(c)

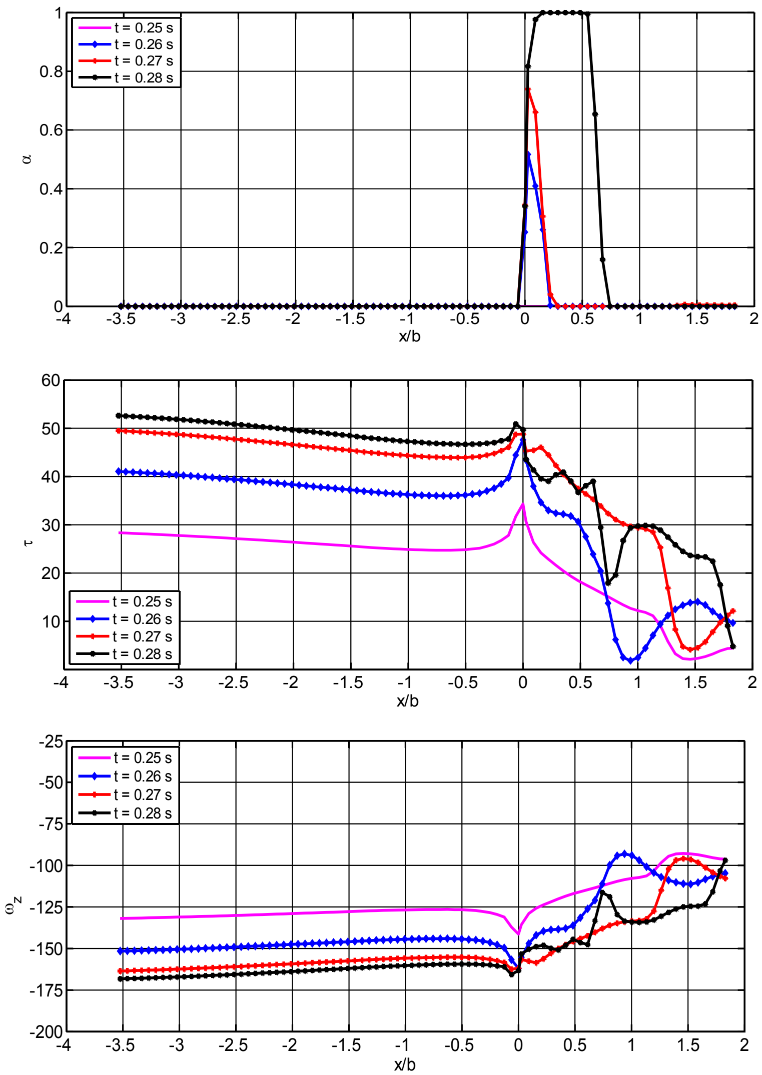

Fig. 12: Streamwise variation of the LNG cavitation flow properties along the lower wall of the nozzle at different time instances: (a) vapor fraction; (b) shear stress (Pa); (c) transverse vorticity (1/s).

The correspondence between the vapor cavity nucleation and the accumulation of boundary-layer vorticity in the nozzle is further illustrated in Fig. 13 through contour plots of the vapor phase fraction and vorticity fields at the same time instances as Fig. 12. As indicated in Fig. 13, the onset of vapor nucleation corresponds to the accumulation of transverse vorticity component at the surface discontinuity. This interaction between the developing wall boundary layer and vorticity in the near-wall regions is noted in literature to be a dominant factor in triggering the low-pressure vapor nuclei to expand into an attached vapor cavity [35,130].

The growth of the vapor cavity following the initial nucleation is plotted in Fig. 14 through contours of the vapor phase fraction and temperature fields at times t = 0.363-0.818 s. From the initial formation of the vapor cavity at about t = 0.27 s (visible in Fig. 13) to about t = 0.467 s, the vapor cavity remains attached to the wall. By t = 0.545 s, Fig. 14(a) shows that the cavity detaches from the wall and a vapor cloud with an oscillating vapor/liquid interface is shed through the nozzle. Detachment of the vapor cavity is mainly due to the presence of re-entrant liquid jets that impinge on the nozzle lower wall and generate unsteady regions of reversed flow [65,155], suggesting that the cloud shedding is actually driven by the re-entrant jet whose instability is substantially influenced by the sheet cavity thickness and length as well as by the intensity of the local adverse pressure gradients [156,157]. Prominent examples of the re-entrant jets are labeled at t = 0.636 s; they appear to "dissect" the attached vapor cavity into discrete detached vapor clouds.

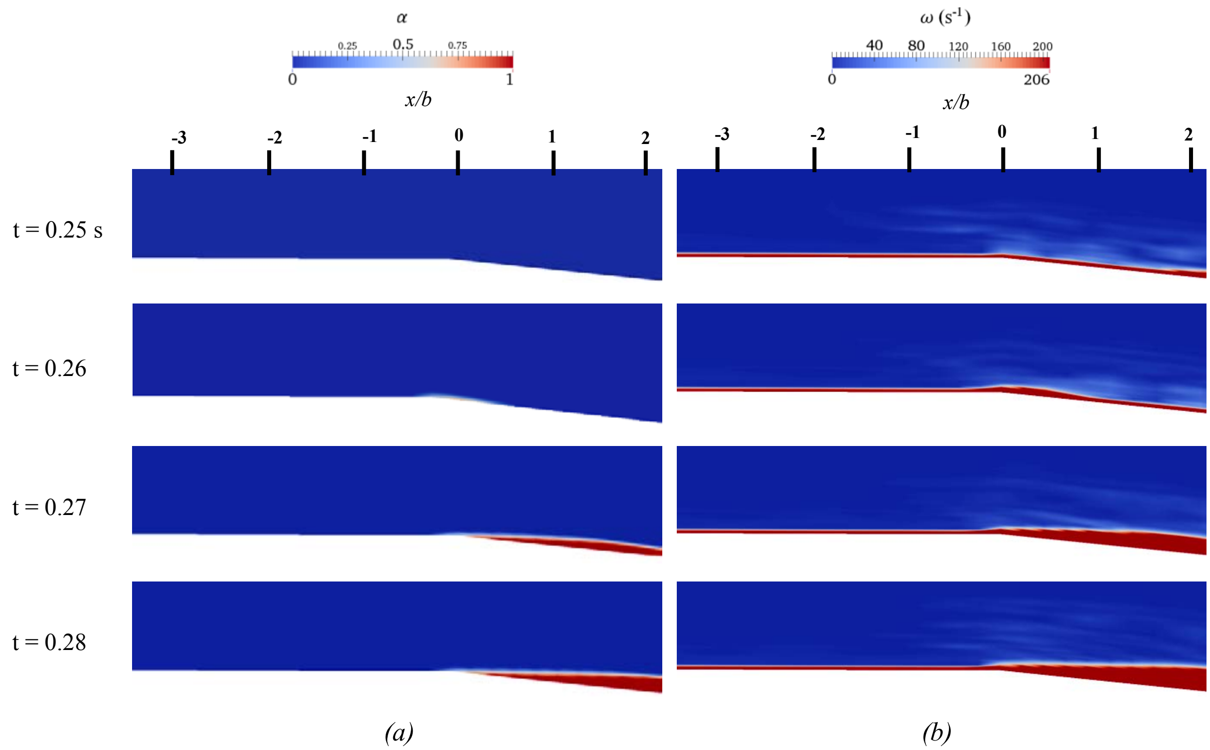

Fig. 13: Temporal evolution of the LNG cavity nucleation at the intersection of the throat and diverging part of the nozzle: (a) vapor fraction and (b) vorticity magnitude (1/s) fields.

The oscillating wall shear stress from the re-entrant jets triggers transient separation of the attached sheet cavity from the lower wall [158,159]. This can be further illustrated in Fig. 15 showing a zoomed view of the rear portion of the attached sheet cavity at t = 0.56 s interacting with the re-entrant jet progressing upstream. In Fig. 15(a)-(b), vapor fraction contour is respectively superimposed by the velocity vectors and streamlines. Corresponding velocity vectors in Fig. 15(a) show significant reduction of the overall mixture velocity (and momentum) in the vapor regions compared with the bulk liquid zones [126,127,160].

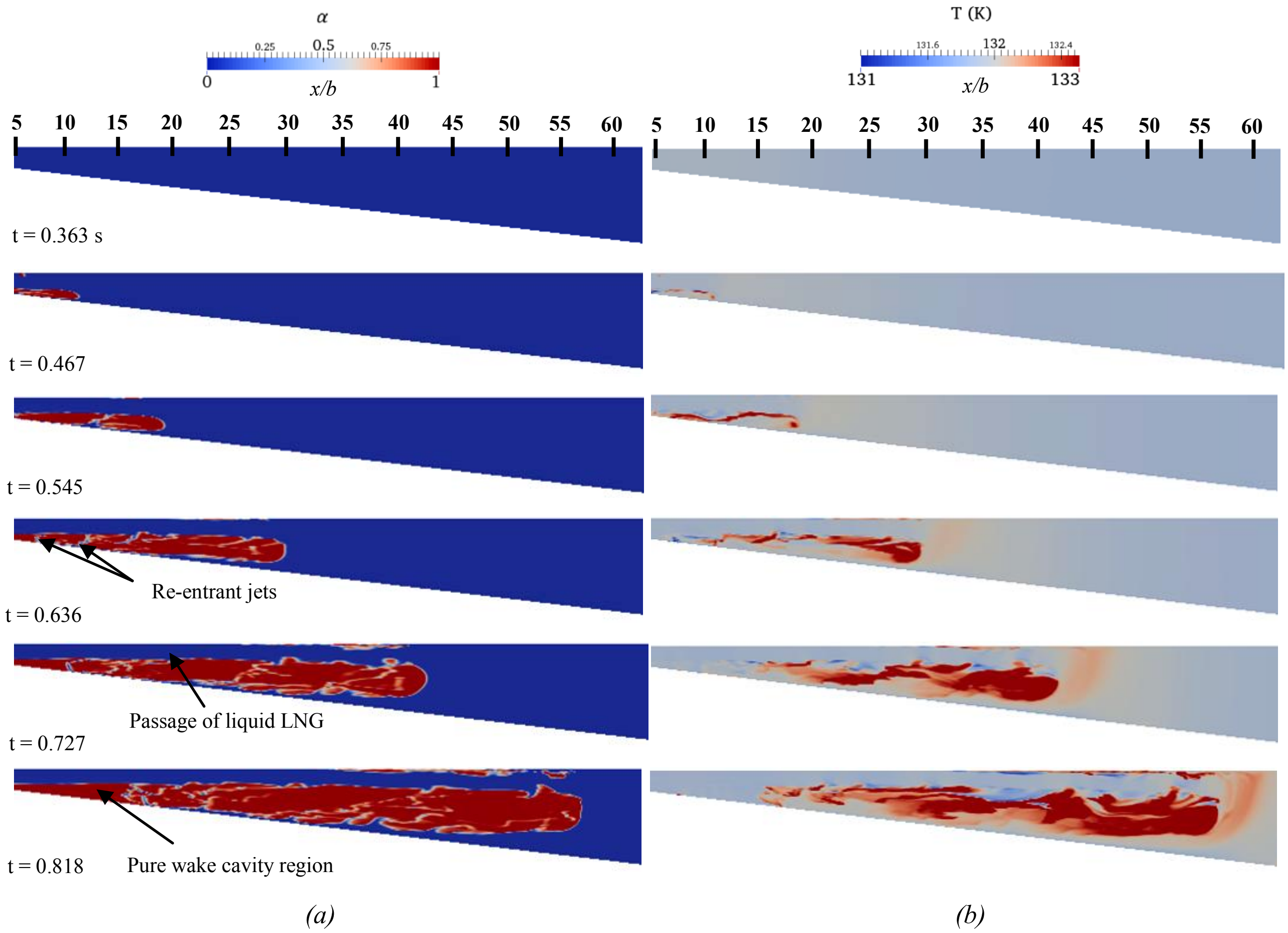

Fig. 14: Unsteady evolution of the LNG cavitation flow inside the diverging part of the Laval nozzle: (a) vapor fraction and (b) temperature (K) fields.

As for the re-entrant jet velocity magnitude, it is observed that it flows almost in the same order as of the main non-cavitating flow velocity. The deceleration of the jet however is mainly due to the interaction of the re-entrant jet with the unstable vapor cavity interface as well as the boundary layer on the lower wall hampering the smooth motion of the re-entrant jet [70,126,161]. The present observations imply that the cavitation zones in the present cavitating flow is overall maintained by 1) the balance of heat and mass transfer during vaporization and condensation processes at vapor-liquid interfaces; and 2) simultaneous convection of the liquid entering the cavity spots at locations where the vapor fraction is comparatively small and/or recirculating regions formed through the progress of re-entrant jets (Fig. 15(b)) [100,162,163].

Continued development of the vapor field in Fig. 14 after t = 0.727 s reveals two prominent features of the multiphase flow. First, the attached cavity region becomes longer in its streamwise extent. With time, a stable cavity behaving like a wake cavity is formed from the attached cavity (visible at t = 0.818 s). Second, the separated vapor cavities convecting from the attached cavity grow progressively unsteady as they develop through the nozzle. The growing unsteadiness of the cavities is likely due to instabilities of the strong shear layers formed along the liquid and vapor interface [57,164]. During this process, the cavity clouds collapsing in large wake regions further downstream produce large-intensity pressure waves (not shown in Fig. 15) that propagate upstream and destabilize the re-entrant flow through contraction and expansion of the rear part of the attached sheet cavity. Simultaneously, the upcoming high velocity liquid phase damps the intensity of the pressure waves, preventing them from destabilizing the whole sheet cavity [116,160,166].

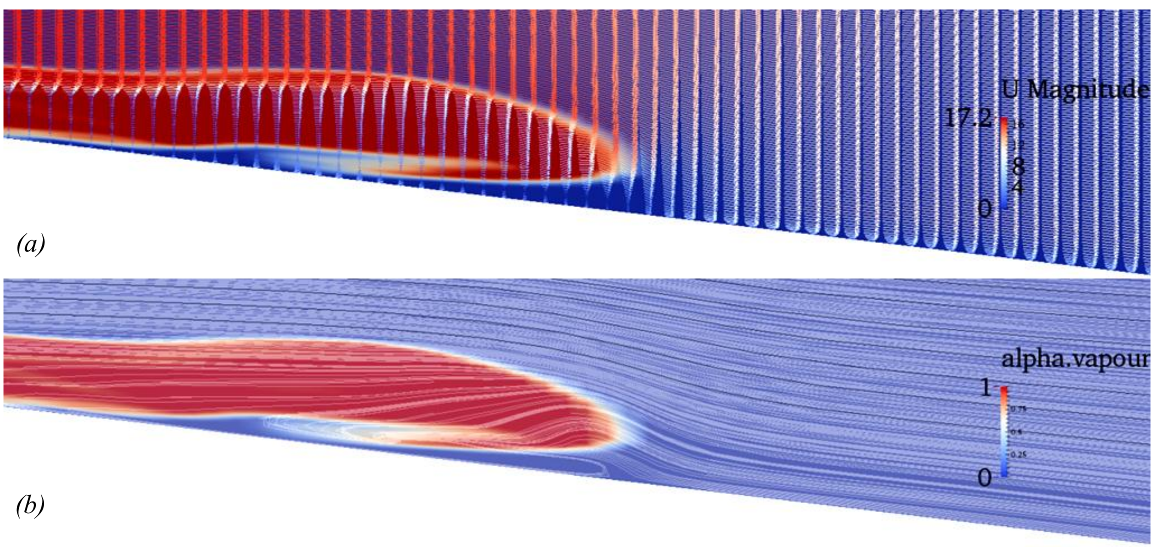

Fig. 15: Zoomed-in view (15.0 < x/b < 25.0) of the rear portion of the attached sheet cavity interacting with the re-entrant jet progressing upstream in the cavitating LNG flow inside the nozzle at t = 0.56 s: vapor fraction contour superimposed by (a) velocity vectors (cm/s) and (b) streamlines.

The unsteady temperature field associated with the developing multiphase flow is visualized in Fig. 14(b), showing a temperature variation of about ± 1.7 K throughout the whole domain. As the vapor spots nucleate and grow, latent heat of vaporization is absorbed from the surrounding liquid by the expanding cavities; thus, the liquid temperature surrounding the vapor cavity is reduced [164]. Since there is a direct connection between temperature and saturation pressure, the local reduction in temperature lowers the saturation pressure. Opposite behavior occurs for condensation of vapor cavities; an increase in liquid temperature around the cavity occurs due to the latent heat of condensation and corresponds to an increase in the local saturation pressure around the cavity, slowing the contraction of the vapor spots [36]. The preponderance of high-temperature vapor regions in Fig. 14(b) suggests that the temperature variation is mainly associated with heat transfer into vapor, which delays condensation of the vapor to liquid. The delay of the vapor condensation may also explain the noted increase in average overall vapor phase fraction in Fig. 11. This finding highlights the importance of thermodynamic parameters on the efficiency of LNG-based turbomachinery [100].

5.2. Global Behavior of Vortex-Cavity Interactions

As reported in [167-171], the interplay between cavity and vortex structures in a cavitating flow can be analyzed by using the vorticity transport equation. In the current study, a compressible form of the vorticity transport equation, shown in Equation (30), is employed to reveal the influence of vapor formation on the vorticity budgets, and thus on the instability behavior of the cavitating flow of LNG in the nozzle.

$$\frac{D\boldsymbol{\omega}}{Dt} = (\boldsymbol{\omega} \cdot \nabla)\boldsymbol{u} - \boldsymbol{\omega}(\nabla \cdot \boldsymbol{u}) + \frac{\nabla \rho_m \times \nabla p}{\rho_m^2} + \nu_m \nabla^2 \boldsymbol{\omega} \tag{30}$$

In Equation (30), the left-hand side (LHS) term is the rate of vorticity change. The vorticity budgets on the RHS - are respectively, a vorticity strain production term $\left((\boldsymbol{\omega} \cdot \nabla)\boldsymbol{u}\right)$ representing the stretching and tilting of vortex due to local strain rates; a vortex dilatation term $\left(\boldsymbol{\omega}(\nabla \cdot \boldsymbol{u})\right)$ denoting the vorticity change due to volumetric expansion/compression; a baroclinic torque $\left(\frac{\nabla \rho_m \times \nabla p}{\rho_m^2}\right)$ indicating the vorticity change due to misalignment of density and pressure gradients; and a vortcity diffusion term $(\nu_m \nabla^2 \boldsymbol{\omega})$ describing the vorticity change due to viscous diffusion.

Equation (30) is employed to analyze vortex-cavity interactions for the in-nozzle cavitating flow of LNG discussed in Section 5.1. Fig. 16 depicts the instantaneous vorticity strain-rate production components (i.e. vortex stretching and tilting in streamwise and transverse directions) at selected time t = 0.636 s. As indicated, within the initial stages of cavity cloud development at the selected time, the presence of high velocity gradients improves the vortex stretching in particular in the transverse direction (Fig. 16(a) and (c)). This is concurrent to a significant decrease in the streamwise vortex tilting (Fig. 16(b)), which seems to balance the improved transverse stretching to a certain degree. The overall dominance of vortex stretching due to velocity gradients is mainly observed at the rear part of the stable sheet cavity as well as in the interfacial and closure regions of the vapor clouds. This excess vortex stretching causes the fluid particles to increase their angular speed to conserve angular momentum, thus improving the vorticity production [169,171].

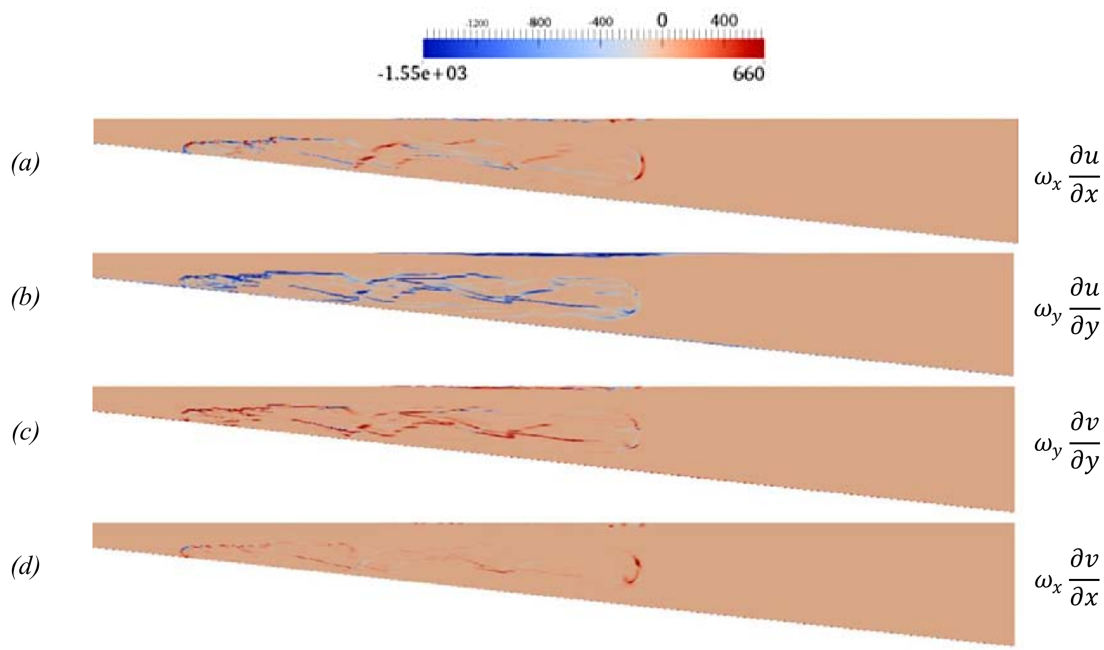

Fig. 16: Distribution of vorticity strain-rate production budget $((\boldsymbol{\omega} \cdot \nabla)\boldsymbol{u})$ components in the cavitating LNG flow inside the nozzle at t = 0.636 s: vorticity stretching (a) and tilting (b) in streamwise direction; vorticity stretching (c) and tilting (d) in transverse direction. Units are in $1/s^2$.

Fig. 17 shows the corresponding distributions of the vorticity dilatation, baroclinic torque, and vorticity diffusion terms in the cavitating flow of LNG inside the nozzle at the time instant of t = 0.636 s. Overall, effects of vortex diffusion (Fig. 17(c)) on the vorticity production is seen to be small compared to the other terms [168,170]. On the contrary, the dilatation term (Fig. 17(a)) and baroclinic torque (Fig. 17(b)) are found to have the largest impact on the overall vorticity distribution. This is mainly attributed to the strengthened pressure and density gradients owing to the large temperature and vapor volume fraction variations as cavitation develops, thereby generating vorticity in the shear layers and interfacial regions [132].

From Fig. 17 it can be also deduced that the main contributor for the vorticity production at the given time is the dilatation term, as it shows a larger magnitude compared to the other terms [168,172]. This however does not shade the large influence of baroclinicity on the observed cavitation evolution [127]. The vortex dilatation is increased at specific regions, e.g. the closure region of the cavity clouds and within the vapor-cavity interfaces, mainly due to the increased interfacial mass flux between liquid and vapor [119,168]. Such conclusion can be further illustrated by the compressibility criterion given by [168,173]

$$\nabla \cdot \boldsymbol{u} = \left({}^{1}/_{\rho_v} - {}^{1}/_{\rho_l} \right) \dot{m}\,. \tag{31}$$

Since the pressure waves inside a cavity structure increase the condensation rate $\dot{m}$ within the cavity [116,132], the velocity divergence and thus vorticity dilatation term correspondingly tend to increase (note that the pressure waves are mainly the result of neighboring cavities collapse processes [70,116]). Such a mechanism especially leads to further development of the re-entrant jet which strongly interacts with the vortex shear flow, causing the breakdown of the cavity and sustaining the cavity shedding process [116]. The vortex formation in this process however absorbs the energy of the pressure waves thus limiting the vapor condensation [116,168].

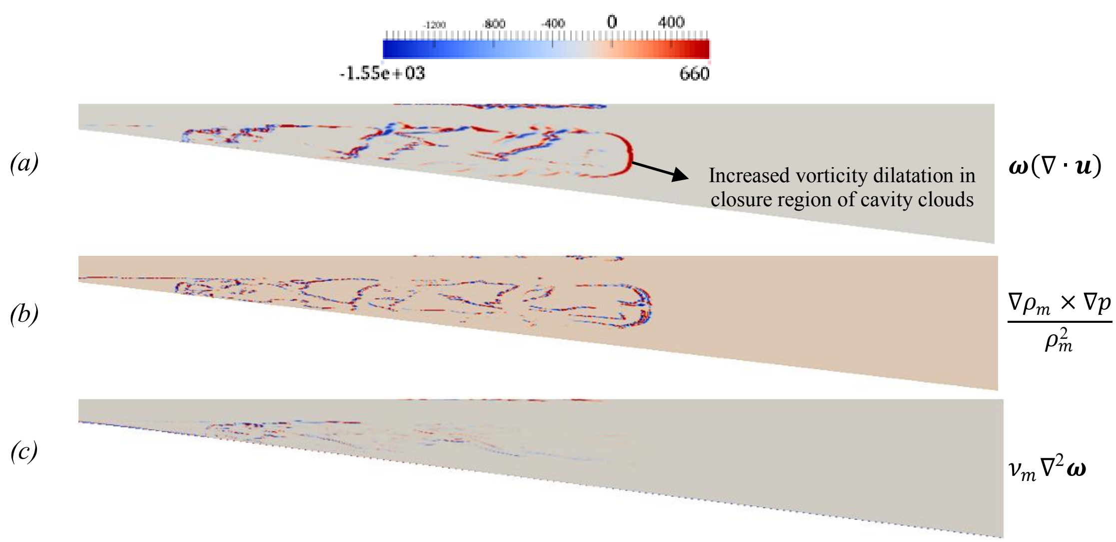

Fig. 17: Distribution of vorticity budgets in the cavitating LNG flow inside the nozzle at t = 0.636 s: (a) vorticity dilatation; (b) baroclinic torque; and (c) vorticity diffusion. Units are in 1/s^2.

In the contour of baroclinic torque term (Fig. 17(b)), it can be further observed that the baroclinicity has its largest variation within liquid-vapor interfaces [168,170], while acting more interactively compared to the dilatation term (Fig. 17(a)) [133]. The baroclinic torque alters the vorticity production in the interfacial regions with coalescence/collapse processes [116,172]. This is due to large compressibility effects and significant misalignment of the thermally-induced density and pressure gradients in these regions, triggering reproduction of cavitation through intensifying the overall vorticity variation [133,168]. It is notable that although the baroclinic term has a lower magnitude than the dilatation term, it still causes major changes in the vorticity field and, as reported by Ji et al. [119], could be even considered as the main mechanism for vorticity production. More details on the unsteady interactions of cavity and vortical structures with thermal parameters are discussed in the comparative studies of Chapter 6 in Sections 6.1.2-6.1.5.

The presented investigation in this chapter described the evolution of the baseline case of the in-nozzle LNG cavitating flow. In the next chapter, the baseline case study is extended to examine how different operating conditions can change the growth patterns of LNG cavitating structures in the nozzle and their detailed interaction mechanisms with instability characteristics under thermodynamic effects.

6. Numerical Simulations of 2D In-nozzle Cavitating Flow of LNG at Different Operating Conditions

This chapter is devoted to investigating the effects of operating conditions on the behavior of the baseline LNG cavitating flow inside the nozzle of Section 4.1. Specifically, evolution of the cavitating patterns of LNG at distinct diffusion angles of the nozzle, in a range of cavitation numbers, and under the effects of liquid-vapor interfacial tension forces are explored. Particular attention is paid to characterizing the phase-change and shedding mechanisms of the cavitating flow at the given operating environments. Cavity-vortex instability characteristics are evaluated to describe the shedding behavior of sheet/cloud cavitating spots under thermodynamic effects as well as their interactions with vortical structures.

6.1. Effects of Cavitation Number

To evaluate the influence of operating cavitation conditions on the evolution of LNG cavitating flow inside the nozzle, the baseline test case of Section 5.1 is further simulated here for selected cavitation numbers of Ca = 0.82 and 2.05, using the same numerical setup procedure as in Section 4.3 with the difference of using maximum acoustic Courant number of 2.5. Global behavior of the in-nozzle LNG cavitation flow at the given Ca numbers is addressed first in Section 6.1.1. Cavity-vortex interactions and instability mechanisms are then discussed in Sections 6.1.2-6.1.5.

6.1.1. Global Behavior of the Cavitation Flow

Fig. 18 compares the time evolution of vapor fraction and temperature fields of the in-nozzle LNG cavitating flow at operating cavitation numbers of Ca = 0.82 and 1.41. The flow evolutions are depicted at time instants of t = 0.40, 0.55, 0.65, and 0.85 s, in the span of $4.0 < x/b < 65.0$ in the diverging part of the nozzle. Note that at the larger cavitation number of Ca = 2.05 (not shown here) cavitation does not occur in the nozzle because static pressure does not drop below the vapor pressure. With the reduction of Ca to 1.41, as shown in Fig. 18(a)-(b), nucleation commences as the static pressure goes below the saturation vapor pressure (t = 0.40 s). Cavitating structures are then triggered as the flow experiences vortex shedding due to the formation of recirculating zones, especially in further downstream regions (t = 0.65-0.85 s). This is seen in both the Ca = 1.41 and 0.82 tests with the difference being on the level of cavitation;

larger cavity regions with improved vaporization processes within stronger recirculating zones are formed earlier in the *Ca* = 0.82 test (Fig. 18(c)-(d)).

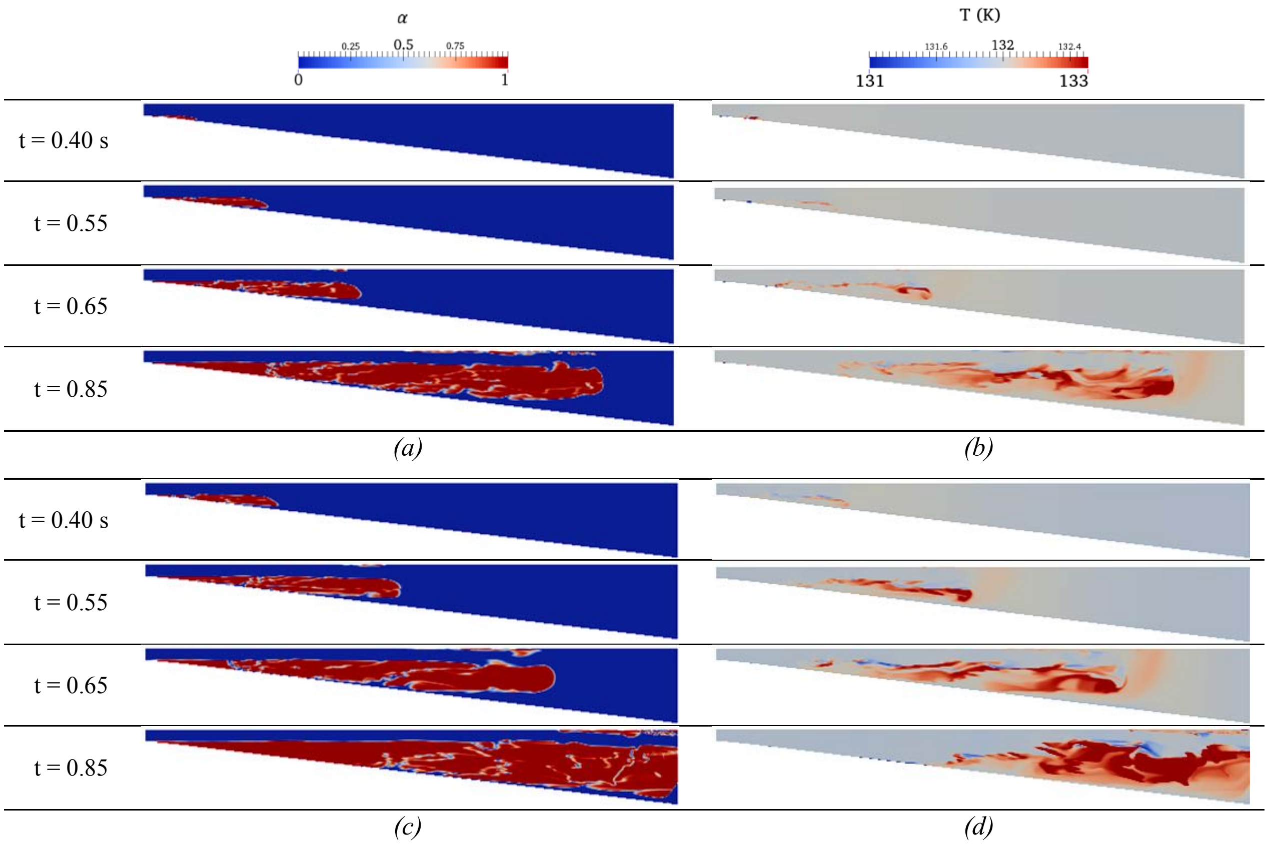

Fig. 18: Time evolution of the in-nozzle LNG cavitating flow at cavitation numbers of Ca = 0.82 and 1.41: instantaneous contours of vapor fraction and temperature (K) at Ca = 1.41 (a,b) and Ca = 0.82 (c,d) at time instants of t = 0.40, 0.55, 0.65, and 0.85 s.

At *Ca* = 0.82, in the early stages of flow development close to the throat, the sheet cavitation formed on the lower wall ($t < 0.4$ s) breaks off by the separated vortex shedding imposed by the re-entrant jet ($t \geq 0.55$ s), and is followed by the formation of cavitating clouds with larger temperature gradients as time goes on (t = 0.65-0.85 s). Within this later stage of flow development, the upstream portion of the cavity remains attached to the wall, while the downstream cavity clouds convect downstream with the shedding vortices. The shape of the attached sheet cavity remains quasi-stable within this process, while the cavity clouds are continuously formed and flow out from the primary sheet cavity [127]. At *Ca* = 1.41, the cavity flow follows approximately the same pattern as the *Ca* = 0.82 case except that the formation of cavity structures is slower. The delay highlights the effect of inertia on the progression of LNG cavity flow inside the nozzle; at larger *Ca* a smaller and more stable sheet cavity is formed on the lower wall due to weaker adverse pressure gradients. With a decrease in *Ca* and corresponding strengthening of the thermally-influenced adverse pressure gradients, the initial sheet cavity is larger and more quickly becomes unstable such that longer and stronger cavity clouds are shed from the rear of the cavity [116,154]. This observation is in agreement with Yan et al. [81], who investigated the effects of injection pressure on cavitation performance inside a marine diesel engine. They note that decreasing the operating cavitation number by increasing the injection pressure improves the vapor penetration into the liquid diesel.

To help identify the effect of *Ca* on the interactions of cavities and vortical structures in the flow, the evolution of the vorticity magnitude at different *Ca* is displayed in Fig. 19. As seen, instability of the cloud structures originates from the impingement of re-entrant jet(s) on the lower wall of the nozzle, which occurs at close to t = 0.40 s for *Ca* = 0.82 and t = 0.55 for *Ca* = 1.41. High adverse pressure regions at the rear of the sheet cavity, generated due to the presence of re-circulation zones following the flow separation from the wall, destabilize the flow and promote the re-entrant jet [75,168]. This is relevant to the Ji et al. [119] report stating that the re-entrant jet behavior is the main cause for development and shedding of the attached cavity structures. Further development of the re-entrant jet triggers the cavitating flow instability such that unsteady shedding cloud structures are formed downstream (t = 0.65-0.85 s) [120]. At *Ca* = 0.82, the unsteadiness in the upstream portion of the nozzle is reduced due to the dominance of inertia, such that a somewhat quasi-steady fully vapor region forms at t = 0.85 s (see also Fig. 18(c)-(d)). The steady fully vaporized region tends to cover the diverging part of the nozzle, and is developed because the re-entrant jet on the wall does not have enough time to penetrate into the cavity (i.e. large main stream inertia). These observations confirm that *Ca* reduction causes a faster breakup and penetration of vapor spots into the liquid phase which consequently results in an enhancement of the vaporization process [74,81]. The concurrent local reduction of unsteadiness in fully vaporized regions at the smallest *Ca* is in line with Niiyama's experiment [37] on a LN_2 cavitation flow in an orifice where the cavity length of LN_2 is reported to increase with weak oscillatory behavior as the cavitation number is reduced.

Further at *Ca* = 0.82, downstream of the diverging part of the nozzle close to the buffer zone, at the time instant of t = 0.85 s in Fig. 18(d), the vapor pockets seem to condense faster as the mean pressure increases with increasing effective area. Due to the interaction of these condensing vapor spots with the residual cavities convected from upstream, a highly transient zone is formed close to the nozzle outlet (Fig. 19(a) at t = 0.85 s) which prevents the formation of pure vapor region downstream [101]. The liquid flow from the buffer zone interacting with the re-entrant jets on the nozzle lower wall also induces large pressure and temperature gradients which promotes the collapse/coalescence of vapor spots, thus making the cavity flow to be strongly disturbed in the outlet region [90,95,132].

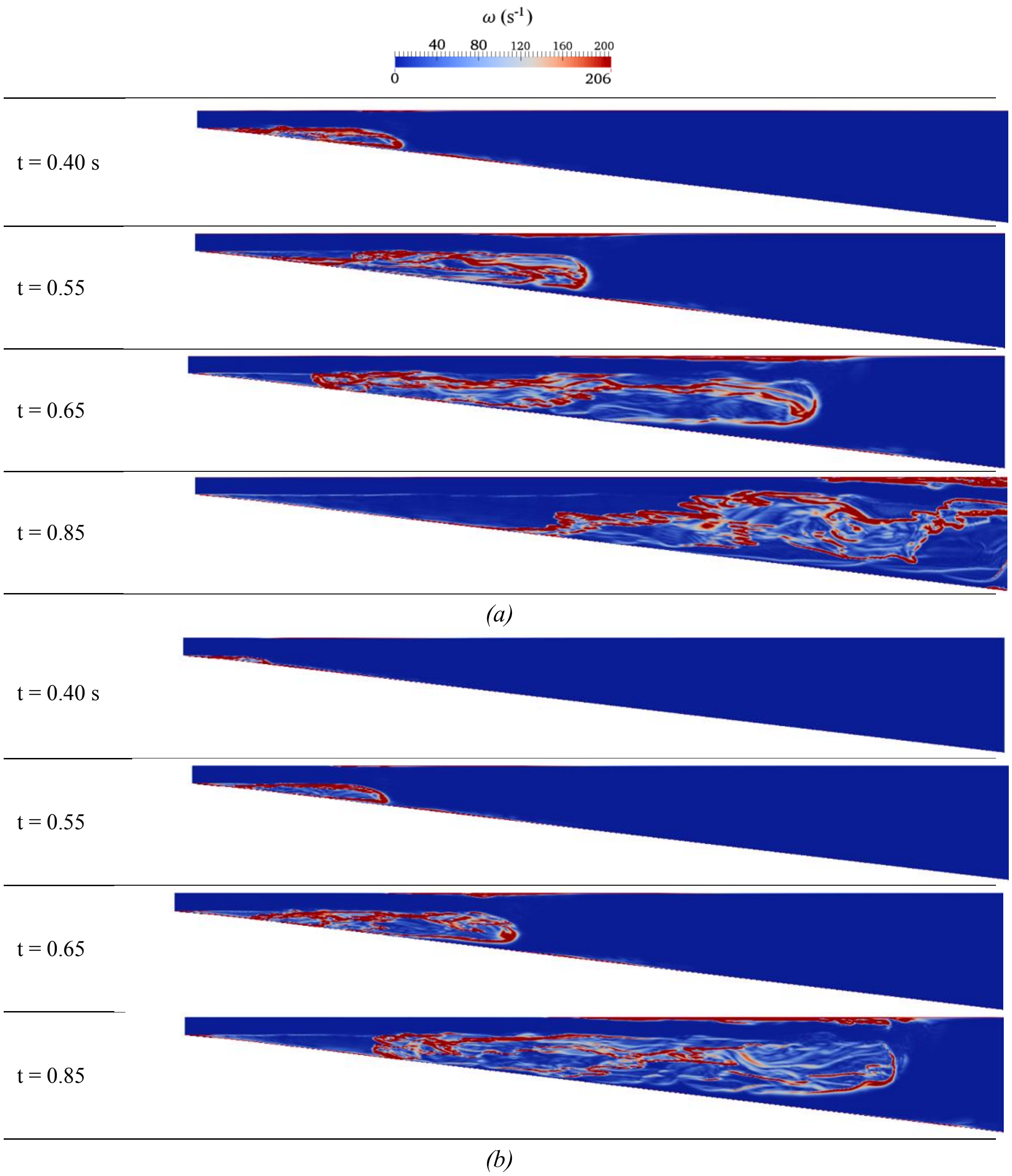

Fig. 19: Time evolution of the vorticity magnitude (1/s) in the in-nozzle LNG cavitating flow at cavitation numbers of Ca = 0.82 (a) and 1.41 (b) at time instants of t = 0.40, 0.55, 0.65, and 0.85 s.

With the increase of cavitation number to *Ca* = 1.41, the above-noted processes occur with a time lag compared to the *Ca* = 0.82 case (see for example Fig. 18(a)-(b) and 19(b) at *t* = 0.65 s where the cloud structures are still developing in the *Ca* = 1.41 test, whereas a quasi-steady vapor flow close to throat is already formed in the *Ca* = 0.82 case). It is notable that the cloud instability in the present cavity flows is also affected by the collapse of cavity spots, as a secondary factor, especially in further downstream regions. As a result of the collapse process pressure waves propagate within the cavity structures and cause sudden changes in the local pressure, temperature, and volume fractions [70,81]. More details on these behaviors are discussed in Sections 6.1.3-6.1.5.

6.1.2. Flow Properties along the Nozzle Lower Wall

Since the cavity behavior in near-wall regions can be significantly influenced by the presence of viscous effects, which is confined to a very thin region at low *Ca* [70,100], this section investigates the cavitation flow properties along the nozzle lower wall and its correlation with the vaporization/condensation mechanisms at the studied cavitation numbers. Fig. 20 compares the time-averaged vapor fraction and wall shear stress distributions on the lower wall of the nozzle for cavitation numbers of *Ca* = 0.82, 1.41, and 2.05. Fig. 21 compares the time-averaged streamwise and transverse pressure gradients, pressure gradients magnitude, and vorticity magnitude distributions on the lower wall of the nozzle. In both figures, time averaging is performed over 100 equally-spaced time steps within two flow-through times of progress after reaching statistically steady state. Fig. 20(a)-(b) show that the vapor fraction and the wall shear stress increase as *Ca* decreases. This is mainly because of the formation of weaker adverse pressure gradients on the wall at larger *Ca* (see Fig. 21(a)-(c)) which make the flow close to the wall experience smaller levels of unsteadiness [115]. The level of unsteadiness seems to be minimal in the case of *Ca* = 2.05 where the presence of favorable pressure gradients resists the formation of a re-entrant jet, thus preventing the formation of cavity clouds [157]. The reason for this is a weak separation of the flow close to the wall in the entire flow development period, which disallows the formation of re-circulating zones.

Conversely, as the cavitation number increases to 1.41, increase of the velocity gradients, due to accelerated flow separation process close to the wall [100,115,127], results in larger vorticity magnitudes (Fig. 21(d)) near the wall as compared to the *Ca* = 2.05 case [119,156]. This increase is even more substantial, especially in upper regions of the wall, for the *Ca* = 0.82 case. This observation is relevant to the fact that the phase change phenomena in the nozzle originates from the local exchange of thermally-affected static and dynamic pressure fields which causes the cavity behavior near the wall will be significantly influenced by viscous effects [77,100]. The present observations then suggest that the formation of vapor structures along the wall enhances the wall shear stress magnitudes through strengthening the flow gradients, e.g. thermally-affected gradients of pressure, as well as the vorticity field (Fig. 21(a)-(d)).

(a)

(b)

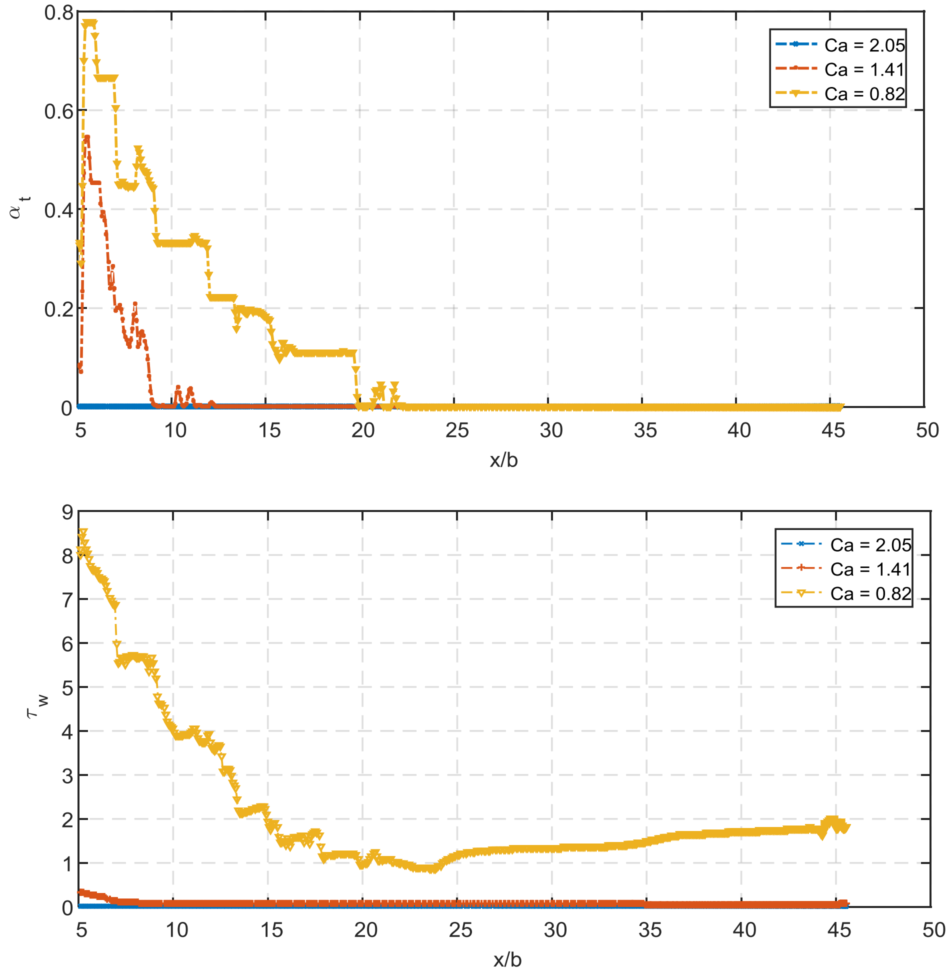

Fig. 20: Distributions of temporally-averaged (a) vapor fraction and (b) shear stress magnitude (Pa) along the nozzle lower wall for the in-nozzle LNG cavitating flow at cavitation numbers of Ca = 0.82, 1.41, and 2.05.

From Fig. 20-21, it can be also pointed out that the increase of wall shear stress causes the cavity regions to become elongated. The increase of near-wall stress is in connection with the velocity increase in the liquid phase caused by the restriction imposed from the vapor spots, eventually leading the vapor regions to stretch further in the streamwise direction [115]. Such behavior is due to the increased acceleration of the bulk liquid, especially within interfacial regions, imposed by the vapor structures in the domain. It is noted that the local flow accelerations are mainly caused by the formation of vapor spots in the center of vortex structures which make the local densities to reduce, thus giving a rise in spatial derivatives of velocity (conservation of mass). Spatial derivatives of velocity can even become more pronounced at smaller cavitation numbers because of the formation of bigger and stronger cavity spots generating larger derivatives of density [70,125 ,172]. It can be thus concluded from Fig. 20-21 that cavitation promotes vorticity production at the wall by promoting the likelihood of local flow separations by increasing the flow unsteadiness.

(a)

(b)

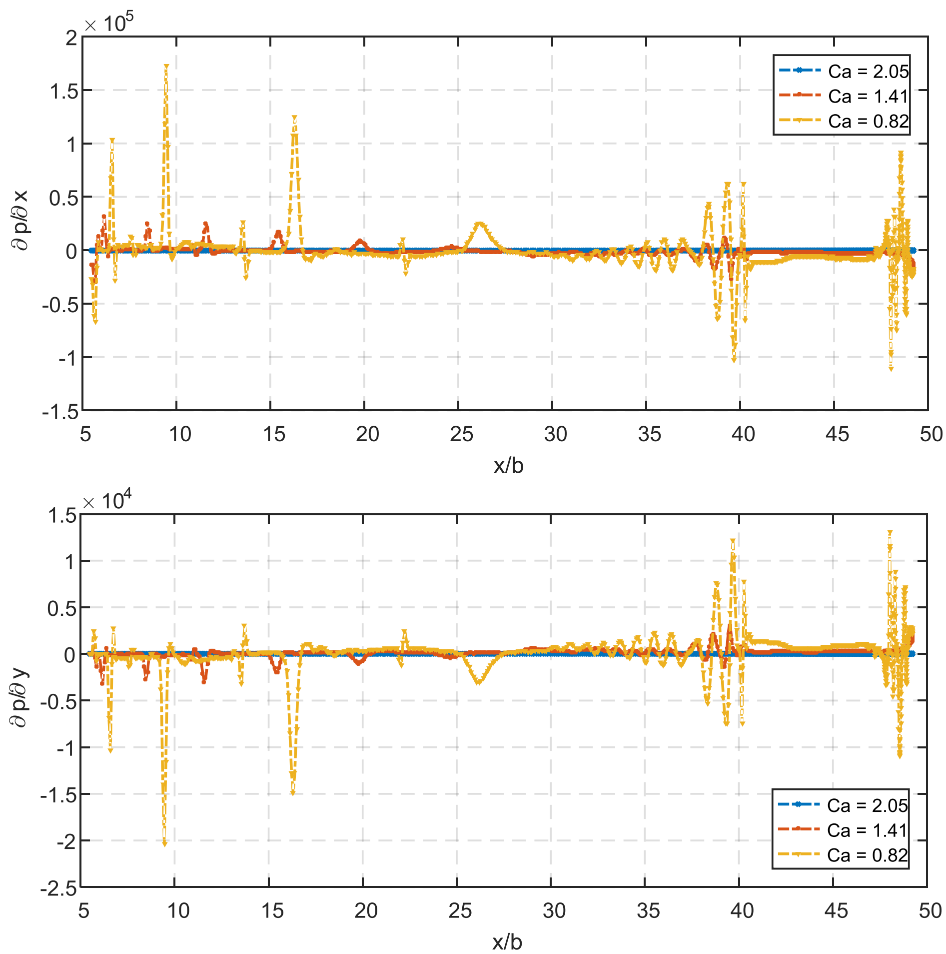

(c)

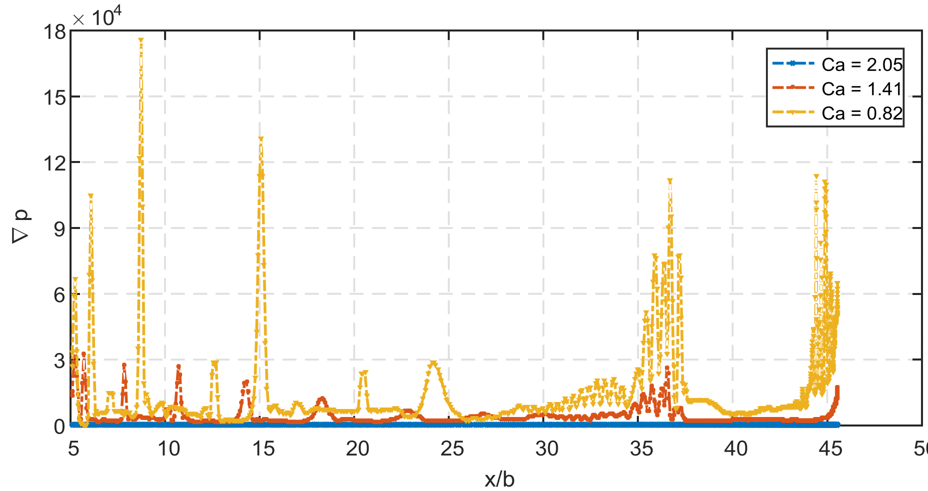

(d)

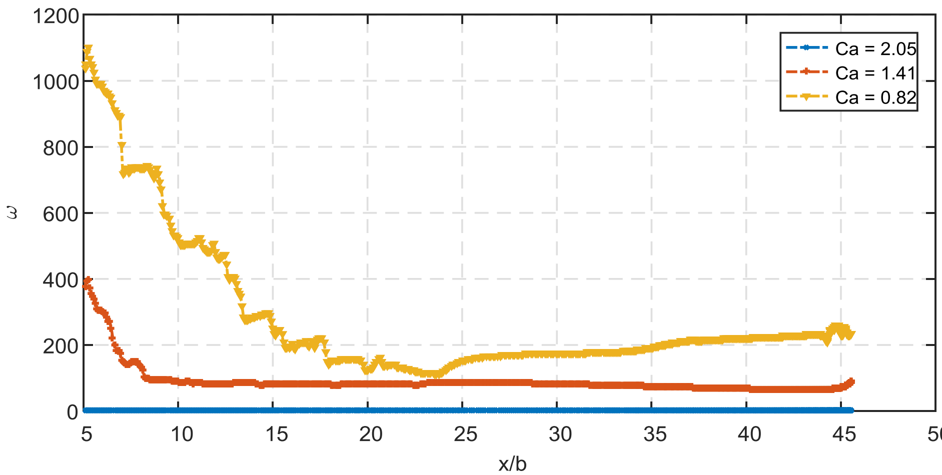

Fig. 21: Distributions of temporally-averaged pressure gradients in (a) streamwise and (b) transverse directions (Pa/m); (c) pressure gradient magnitude (Pa/m); and (d) vorticity magnitude (1/s) along the nozzle lower wall for the in-nozzle LNG cavitating flow at cavitation numbers of Ca = 0.82, 1.41, and 2.05.

6.1.3. Vortex-Cavity Interaction Mechanisms

To further illustrate the effect of cavitation number on the cavity dynamics, Fig. 22 displays the instantaneous distributions of the vorticity budgets of Equation (30) at the time instant of t = 0.93 s along the reference line introduced in Section 4.5 (see Fig. 7) for cavitation numbers of Ca = 0.82, 1.41, and 2.05. Fig. 22(a) shows that with the decrease of Ca, larger values of vapor fractions, i.e. larger vaporization in the flow, occur. This leads to more frequent baroclinic torques with larger magnitudes at smaller Ca numbers owing to the greater misalignment of pressure and density gradients. The contribution of baroclinic torque to the production of vorticity is illustrated in Fig. 22(c) (see for example the $x/b > 16.0$ region), which shows that the presence of larger temperature gradients at smaller Ca further triggers the misalignment

[169,170]. As for the dilatation term (Fig. 22(b)), based on the compressibility criterion of Equation (31), the velocity divergence is increased with the decrease of *Ca* (as interfacial mass transfer increases), causing the dilatation term of the vorticity transport equation to rise. The vorticity production associated with the dilatation term enhances the vaporization rate and promotes the production of vapor spots, as it increases the mass transfer from liquid to vapor (see for example $x/b > 16.0$ region of Fig. 22(a)-(b)) [70]. The presence of more fluctuating behavior in the $Ca = 1.41$ case (see for example $9.0 < x/b < 15.0$ region of Fig. 22) is attributed to the unsteadiness in the flow at the selected time of $t = 0.93$ s due to the development of re-entrant jets; at this time instant, the case with smaller $Ca = 0.82$ shows a quasi-steady fully vapor region (see Fig. 18) covering most of the reference line. The highly fluctuating zones are located at the rear portion of the sheet cavity which is subject to large interactions by the re-entrant jets. As a result of such strong interactions, the cavity flow is accompanied by larger gradients of velocity and density, and thus by stronger mass and latent heat transfer processes [127,132,157].

(a)

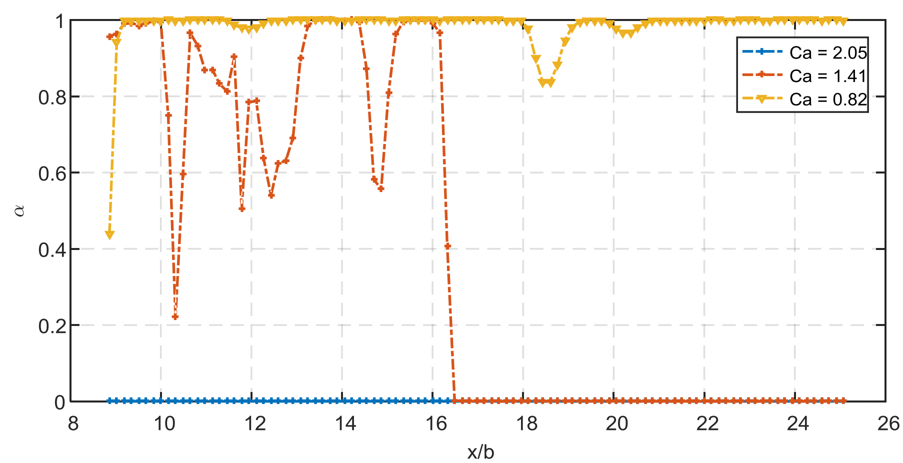

(b)

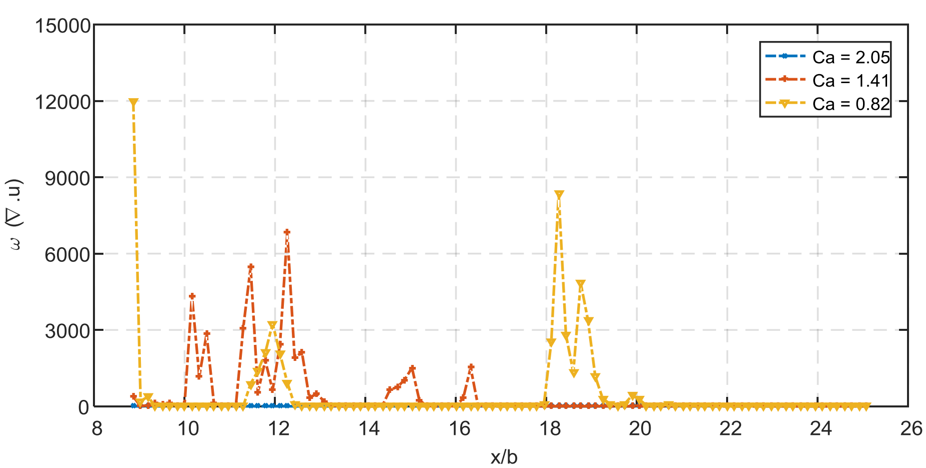

(c)

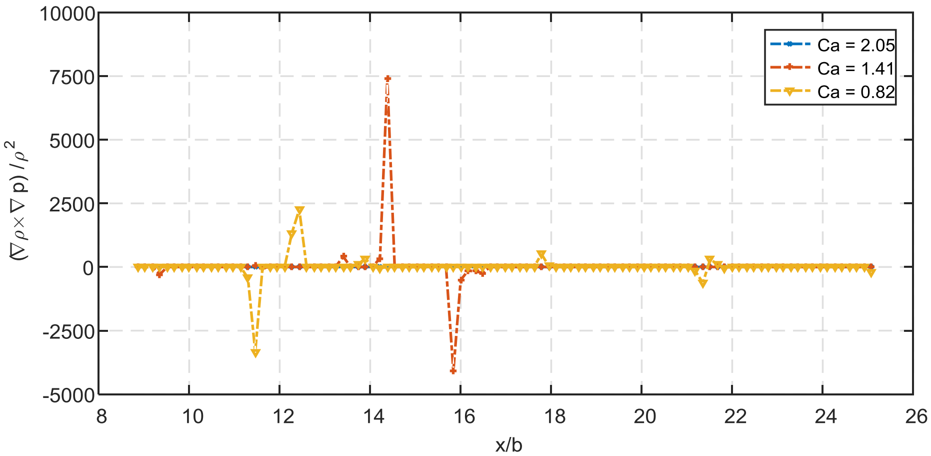
Ca = 2.05
Ca = 1.41
Ca = 0.82
$(\nabla\rho\times\nabla p)/\rho^2$
x/b

(d)

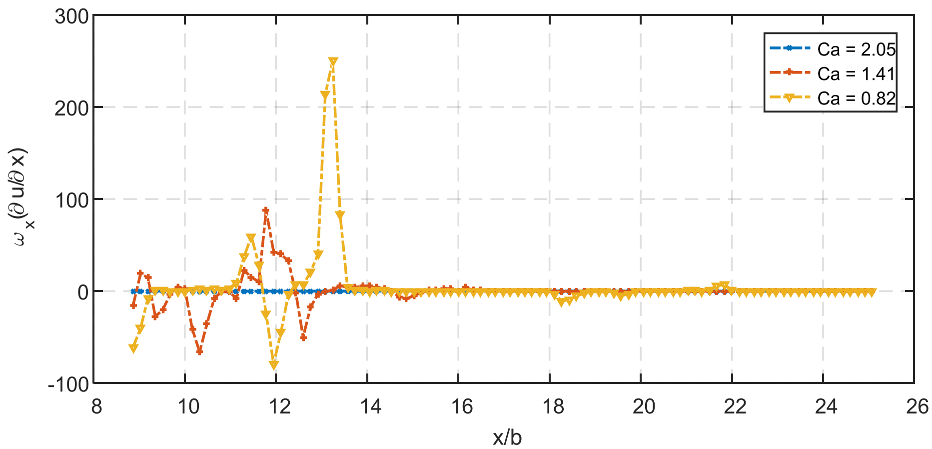
Ca = 2.05
Ca = 1.41
Ca = 0.82
$\omega_x(\partial u/\partial x)$
x/b

(e)

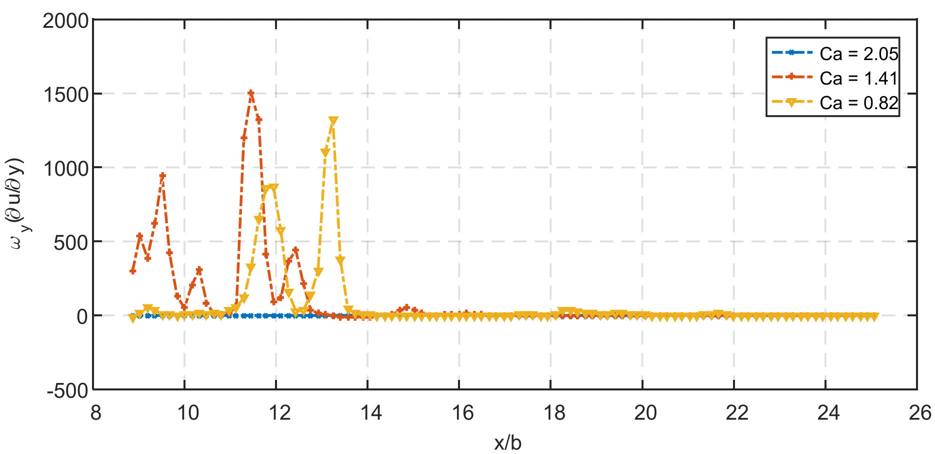
Ca = 2.05
Ca = 1.41
Ca = 0.82
$\omega_y(\partial u/\partial y)$
x/b

(f)

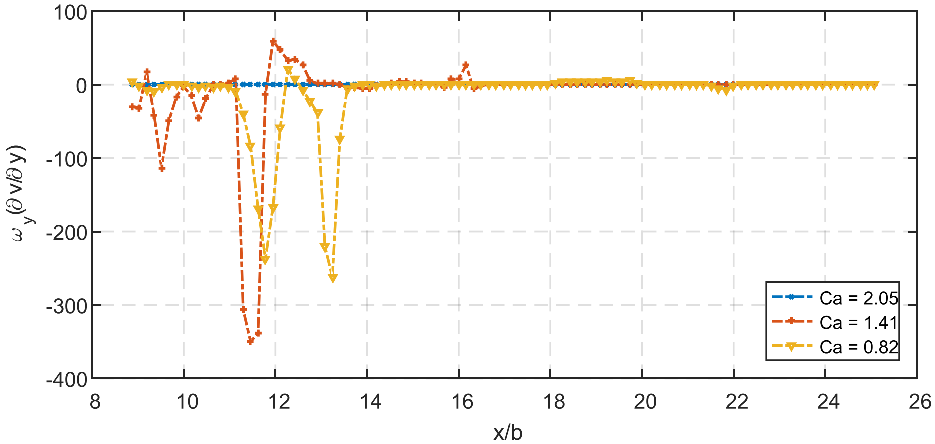

(g)

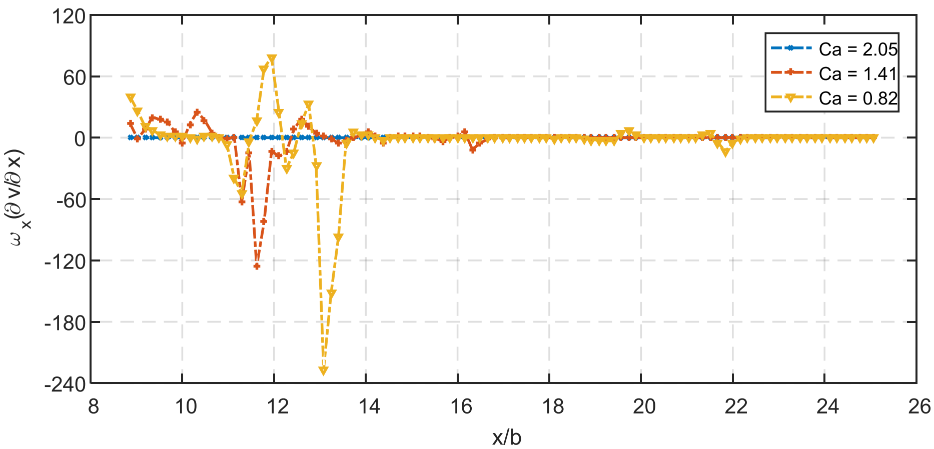

(h)

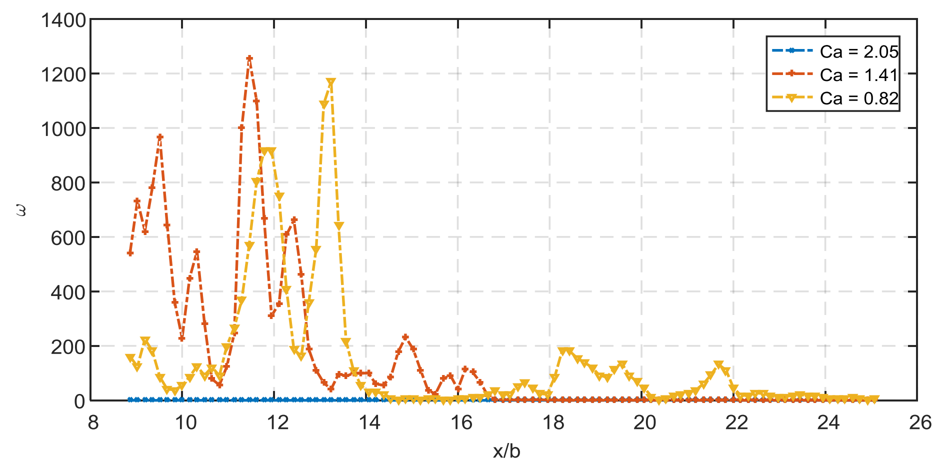

Fig. 22: Distributions of vorticity budgets along the reference line of Fig. 7 in the in-nozzle LNG cavitating flow at cavitation numbers of Ca = 0.82, 1.41, and 2.05 at t = 0.93 s: (a) vapor fraction; (b) vorticity dilatation magnitude (1/s^2); (c) baroclinic torque (1/s^2); streamwise vorticity (d) stretching and (e) tilting (1/s^2); transverse vorticity (f) stretching and (g) tilting (1/s^2); and (h) vorticity magnitude (1/s).

The vorticity stretching and tilting terms plotted in Fig. 22(d)-(g) show that with the reduction in *Ca*, the streamwise stretching and transverse tilting terms (Fig. 22(d) and 22(g), respectively) increase whereas the streamwise tilting and transverse stretching terms (Fig. 22(e) and 22(f), respectively) showing a reduction. This implies that vortex structures are preferentially elongated in the streamwise direction as cavitation progresses hence increasing vorticity production (see for example $x/b > 16.0$ region of Fig. 22(h)) [133,168]. Note that the vorticity diffusion term is not shown here as it was observed to be negligible compared to the other vorticity budgets (see also Fig. 16-17), which is consistent with the finding of a number of studies addressing vortex-cavity interaction mechanisms in cavitation flows; see for example [119,133,168].

Based on the literature survey of Sections 2.2 and 2.7and the vorticity budget contours of Fig. 16-17, it can be further observed from the distributions of Fig. 22 that all the vorticity budgets of Equation (30) contribute to enhancing vorticity production in the present cavitation flows. The baroclinic term particularly alters the vorticity production within the interfacial regions in the shedding cloud cavities with collapse processes [133]. The dilatation term mainly contributes in the regions with significant mass transfer between the liquid and vapor phases [127,172]. In the non-cavitating zones with the absence of cavity contraction/expansions and local interface mass and heat transfers, the vorticity generation mechanisms are mainly dependent on the vorticity stretching and tilting processes.

6.1.4. Transition Characteristics of Shear Layer Instabilities

6.1.4.1. Time History of the Probed Flow Fields

The vortex-cavity interaction mechanisms of the LNG cavitating flow in the nozzle can be further investigated by evaluating the temporal distributions of flow fields at selected probing station(s) in the domain. The time histories of the vapor fraction, relative pressure ($= p - p_{sat}$), and temperature fields within the first flow-through time at probe location ($x/b, y/b$) = (27.02,1.10) are shown in Fig. 23 for cavitation numbers of Ca = 0.82, 1.41, and 2.05. The probe is placed in the midway point of the upstream throat region and the downstream outlet area, so that the unsteady characteristics of the cavitation flow can be captured effectively without being influenced by the instabilities imposed from the main liquid stream and the buffer zone. Spectral analysis of the probed data is given in Section 6.1.4.2. The time signal of relative pressure in Fig. 23(b) shows that at lower Ca, higher frequency pressure fluctuations are captured by the solver.

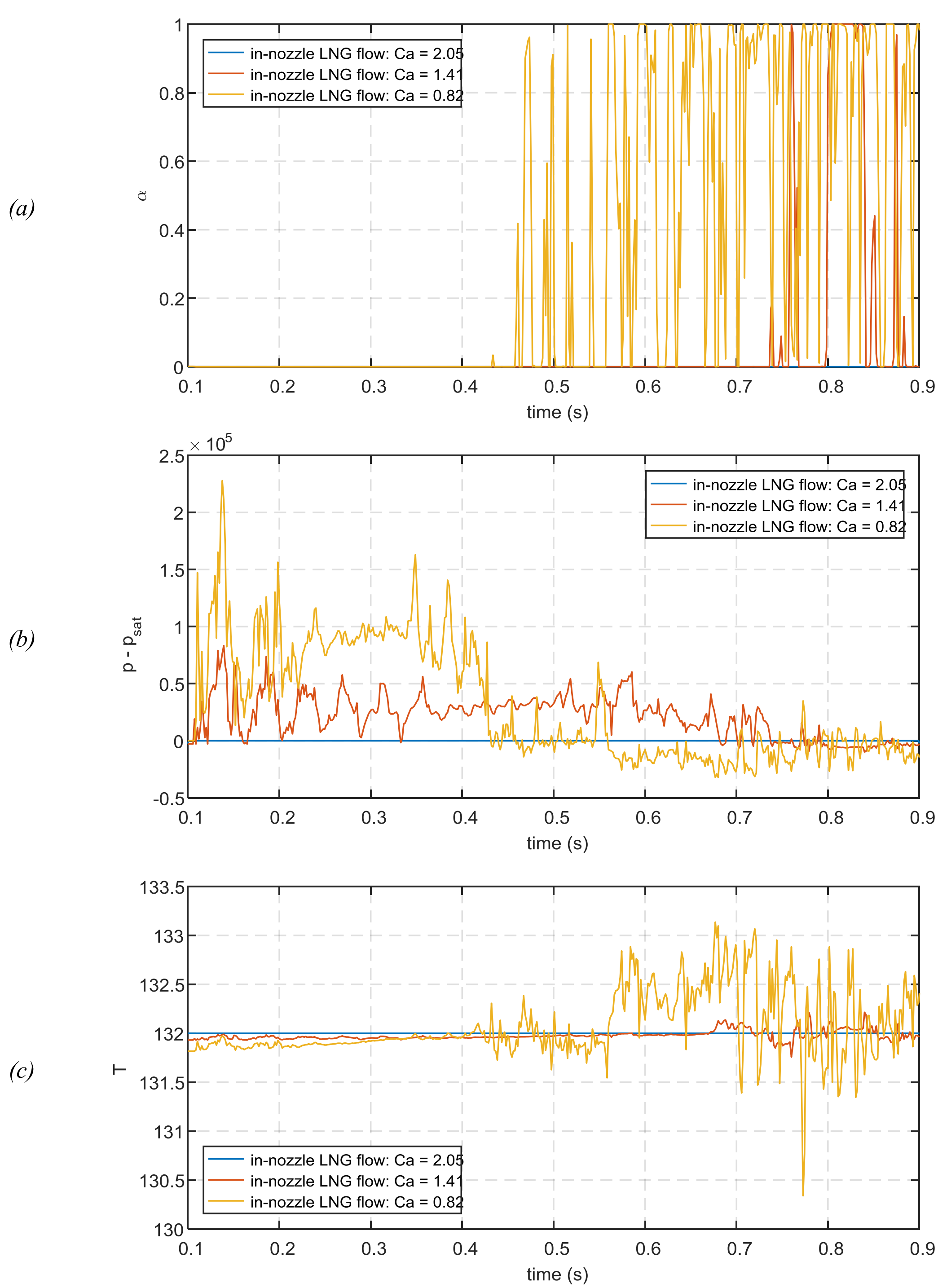

Fig. 23: Time histories of flow parameters at the probe location (x/b,y/b) = (27.02,1.10) in the in-nozzle LNG cavitating flow at cavitation numbers of Ca = 0.82, 1.41, and 2.05: (a) vapor fraction; (b) relative pressure (Pa); and (c) temperature (K).

At the smallest *Ca* = 0.82, the pressure fluctuations have larger magnitudes with larger pressure spikes due to stronger vapor collapse and inceptions happening in more frequent successive events, as similarly detected in Fig. 23(a) and (c) [81]. Such fluctuations are not observed in the non-cavitating case. It also appears that the cavitating flow behaves quasi-periodically, which pertains to the combined formation of large quasi-steady vapor regions in later stages of flow development and highly unsteady cavitating flow in early stages of flow development, as discussed in Sections 5.1 and 6.1.1 [119].

In Fig. 23(b), highly frequent pressure fluctuations with smaller magnitudes are noted for Ca = 0.82 at time instants between t = 0.42 and 0.90 s. These are due to the improved shedding behavior of cavity clouds involving vapor collapse and coalescence processes with larger saturation vapor pressure variations. These processes are linked to the presence of positive and negative values of pressure gradient in the streamwise and transverse directions promoting the cavitation development and transition [120]. It is further notable that the observed pressure spikes occur due to the collapse of cavitation clouds [100,120,172], which are typically detected inside and further downstream of the cavitation region especially when Ca is small. As a result of large cavitation cloud collapses in downstream regions, the pressure spikes propagate pressure waves upstream within cavities. This further leads the cavities to break down such that the downstream part of the cavity condenses to a relatively lower vapor content compared with the upstream part of the cavity. The upstream motion of the wave is continued until the whole cavity is divided into shedding smaller segments with larger levels of instability [116]. Moreover, the vapor fraction and relative pressure distributions in Fig. 23(a)-(b) show that with the reduction of cavitation number, cavity inception occurs faster (at $t \cong 0.46$ s in the Ca = 0.82 case compared to $t \cong 0.71$ s in the Ca = 1.41 case), and formation and collapse of cavity spots become more periodic. Since the vapor pressure is strongly dependent on temperature, the behavior of the relative pressure, and thus the local cavitation number, is strongly affected by local values of pressure and temperature fluctuations; it is reduced in the vapor regions with temperatures above the free-stream temperature i.e. T = 132 K and vice versa (see for example Fig. 23(b)-(c) at t = 0.60-0.90 s). The temperature drop reduces the vapor pressure causing a delay/resistance in the expansion of cavity structures, while making the vaporization to become more intensified locally inside the cavity central regions [116,120,127]. This is consistent with high-temperature vapor regions in the contours of Fig. 18(b) and (d) suggesting that the temperature variation is mainly associated with heat transfer into vapor, resulting in delayed condensation of the vapor to liquid. The relative pressure in Fig. 23(b) becomes smaller with increase in the cavitation number, which accords with the decreased vapor fraction variations at larger Ca plotted in Fig. 23(a).

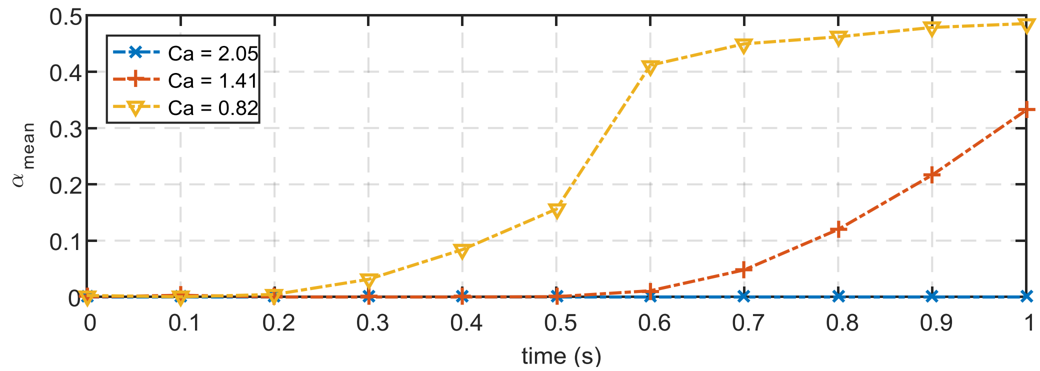

Fig. 24: Temporal distribution of spatially-averaged vapor fraction field (α_{mean}) for the in-nozzle LNG cavitating flow at cavitation numbers of Ca = 0.82, 1.41, and 2.05.

The significance of such temporal variations in the test cases can be summarized by evaluating the net vapor production in the nozzle during cavitation development. Temporal evolution of the spatially-averaged vapor fraction field (i.e. $\alpha_{mean} = \frac{\iint_{x,y_1}^{x,y_2} \alpha_i dA_i}{\iint_{x,y_1}^{x,y_2} dA_i}$ where A is the domain area filled with cells with index i) in the diverging part of the nozzle for a single flow-through time is depicted in Fig. 24 for cavitation numbers of Ca = 0.82, 1.41, and 2.05. As seen, the mean vapor volume decreases with increase in the cavitation number, in particular in later stages of the flow development. At Ca = 0.82, faster growth of the cavity spots make the net vapor production in the domain to quickly reach the saturated value of approximately 0.50 after which not a significant change occurs with time. As Ca increases to 1.41, the rate of vapor growth is reduced such that the net vapor production reaches its saturated value at a later time (not visible in the plot) compared to the Ca = 0.82 case. The case with Ca = 2.05 shows zero mean vapor production in the entire flow development time, indicating a single liquid phase behavior. The current observations further confirm the significance of thermally-dependent inertia effects in the cavitation flow of LNG which become more pronounced at lower operating Ca with larger temperature fluctuations (see Fig. 23) [43,120,168].

6.1.4.2. Spectral Analysis of the Probed Flow Fields

To better illustrate the instability of the in-nozzle LNG cavitation flow at different cavitation numbers, frequency characteristics are analyzed by performing spectral analysis of the pressure traces at the probed location described in Section 6.1.4.1. To do so, the fast Fourier transform (FFT) is performed of the probed pressure time histories, and then the dominant frequency corresponding to the maximum amplification rate is used to calculate the most-amplified Strouhal number i.e. $St = fb/U_\infty$ where f, b and U_∞ are the frequency of experiencing the largest amplification rate, the nozzle throat thickness, and the free stream velocity at each cavitation number, respectively.

Plots of the FFT of the pressure for three flow-through times at the probe location of $(x/b,y/b) = (27.02,1.10)$ are shown in Fig. 25 for Ca = 0.82, 1.41, and 2.05. At the lowest Ca (Fig. 25(c)), pressure spectra show larger peaks at lower frequencies as compared with the larger Ca numbers (Fig. 25(b) and (a)), suggesting the overall conclusion that the reduction of Ca improves the pressure-based acoustic noise.

(a)

(b)

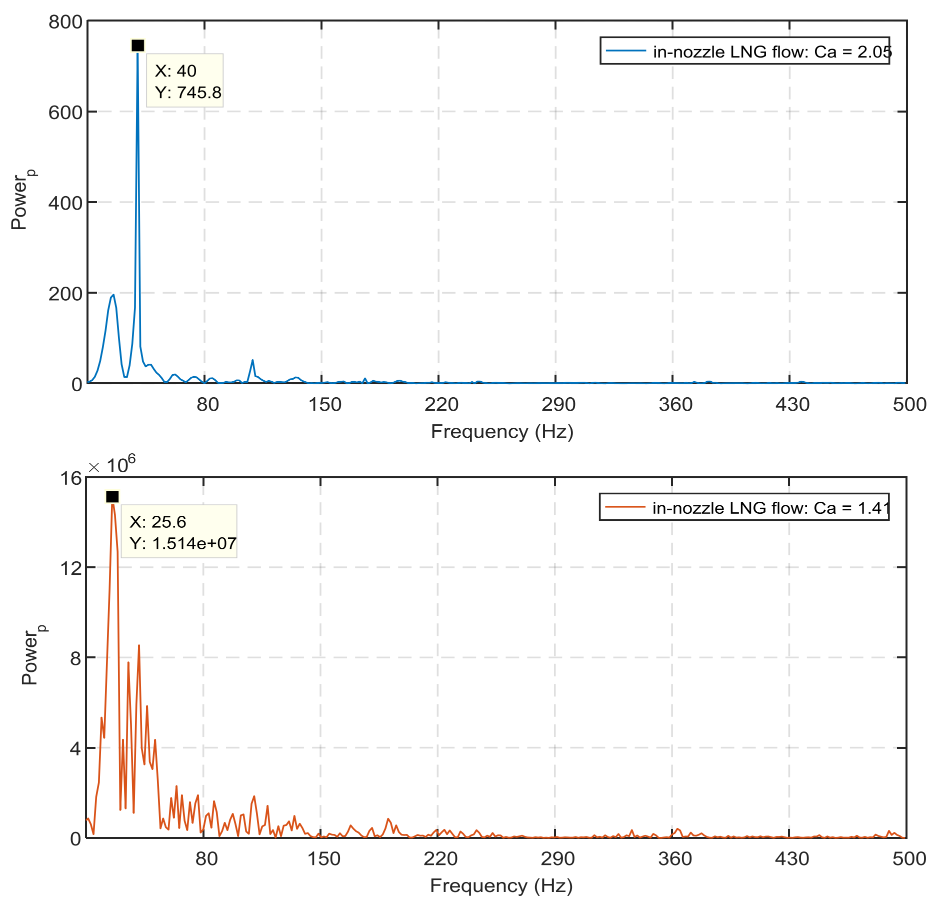

(c)

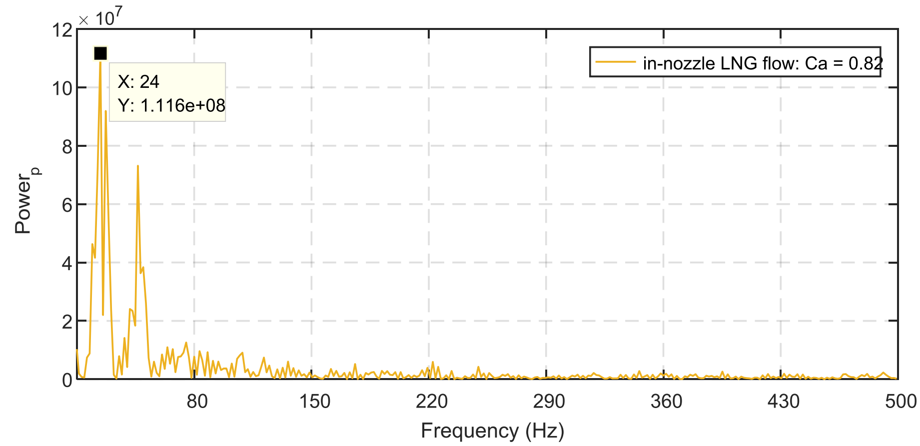
× 10^7
X: 24
Y: 1.116e+08
in-nozzle LNG flow: Ca = 0.82
Power_p
Frequency (Hz)

(d)

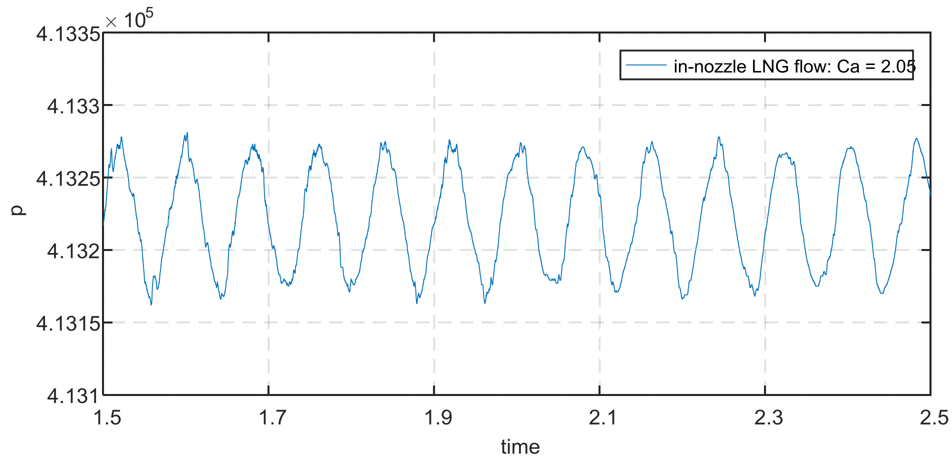
× 10^5
in-nozzle LNG flow: Ca = 2.05
p
time

(e)

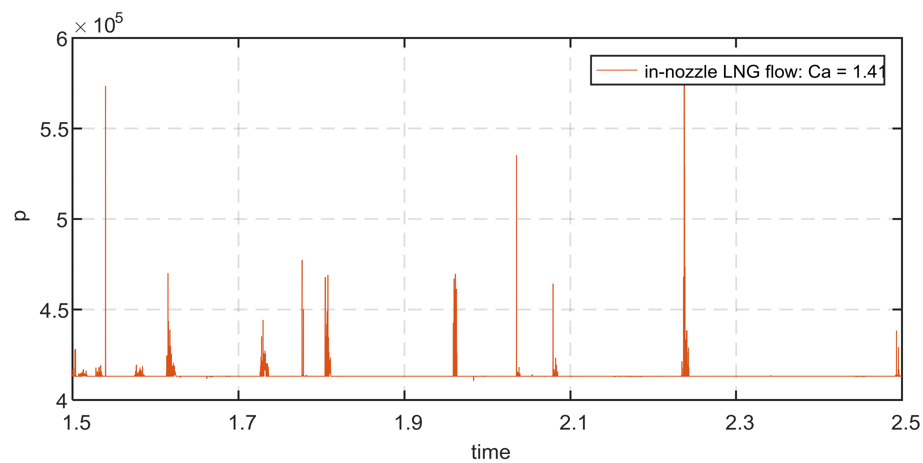
× 10^5
in-nozzle LNG flow: Ca = 1.41
p
time

(f)

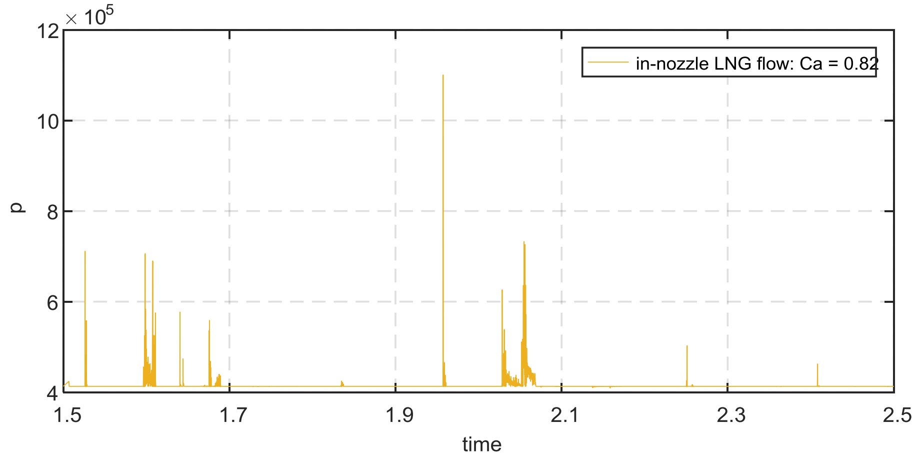

Fig. 25: Spectrogram and time history of pressure at the probe location (x/b,y/b) = (27.02,1.10) in the in-nozzle LNG cavitating flow at cavitation numbers of Ca = 2.05 (a,d); 1.41 (b,e); and 0.82 (c,f).

The characteristic frequencies in Fig. 25 are detected at small frequency range, regardless of the cavitation content. In the non-cavitating case (Fig. 25(a)), noise is due to the pulsation of the shear layer without vortex shedding and has a spectral peak at the frequency of f = 40.0 Hz which represents the shear layer instability. The lower level peaks are typically the sub-harmonics of the main oscillation due to the adverse pressure gradients [135,164]. In the cavitating cases, unlike the non-cavitating case, the characteristic frequencies are found to be due the alternate collapse/inception process of the cavity structures and/or the "low-frequency behavior of the elongated vortex cavities", as discussed in [126]. These are identified beside the characteristic vortex shedding frequency that exists in each case spectrum. At Ca = 1.41 (Fig. 25(b)), the maximum amplification rate frequency corresponds to the low-frequency behavior of the elongated cavities and the peak occurs at f = 25.60 Hz which is slightly smaller than the vortex shedding frequency at $f \cong 31.0$ Hz. The observed frequency peak at $f \cong 38.0$ Hz is due to the cavities collapse and breakdown processes. The same spectral evolution is detected at the smaller Ca = 0.82 (Fig. 25(c)), with the difference that the dominant frequencies at f = 24.0 and 26 Hz respectively pertain to the cavities collapse and breakdown processes and the low-frequency behavior of the elongated cavities. The frequency peak at $f \cong 40.0$ Hz is because of the vortex shedding. The smaller secondary peaks following these dominant peaks in the cavitating tests are likely attributed to the smaller cavity spots shed at higher frequencies [206]. The corresponding pressure time histories in Fig. 25(d)-(f) also indicate the predicted characteristic frequencies for the simulated cavitation numbers.

Cavitation Number (Ca)	Dominant Shedding Frequency (Hz)	Strouhal Number (St)
0.82	24	0.1121
1.41	25.6	0.1962
2.05	40	1.8301

Table IV: Comparison of St numbers for the in-nozzle LNG cavitating flow at cavitation numbers of Ca = 0.82, 1.41, and 2.05. Data correspond to the pressure time history probed at (x/b,y/b) = (27.02,1.10).

Table IV shows the *St* numbers corresponding to the maximum amplification rate frequencies from Fig. 25. As indicated, with the decrease in cavitation number, *St* number is also reduced due to the formation of larger vapor structures delaying the shedding of vortex structures [126]. The delay pertains to the reduction of mixture velocity as a result of vapor production -- it increases as *Ca* is reduced and larger cavities are generated more successively at smaller time intervals. The resulting spectra further suggest that with the increase of thermal effects at smaller *Ca*, there is more depression in the *St* number. The stronger thermal effects imply the presence of larger local temperature gradients, which is consistent with the results of Sections 6.1.2-6.1.4.1. The current results are relevant to the experimental work of Jiakai et al. [43] on LN_2 cavitation in a venturi, concluded that the propagation of shock wave-induced condensation fronts (pressure waves) from the collapse of cavitation clouds within the upstream attached cavities can be considered as the predominate mechanism of cavitation shedding. At smaller *Ca* the shock waves become stronger, due to stronger cavity collapse processes, so improving the instability [116].

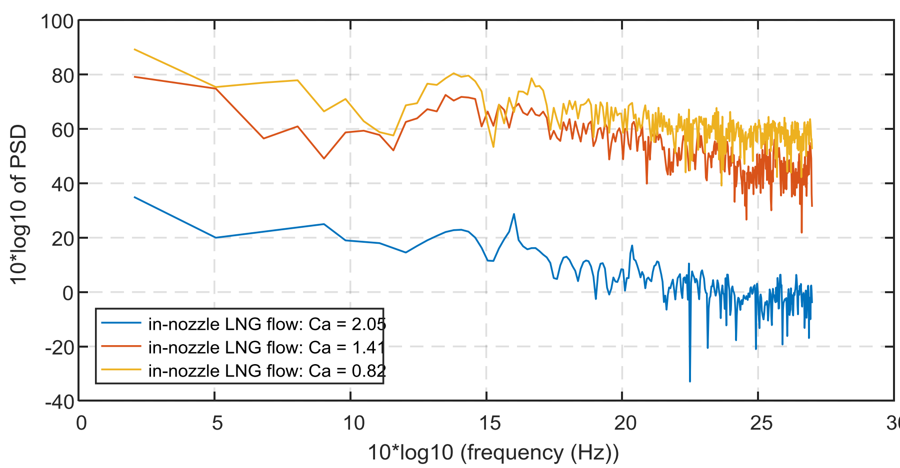

Fig. 26: Log-scale plot of pressure spectra at the probe location (x/b,y/b) = (27.02,1.10) for the in-nozzle LNG cavitating flow at cavitation numbers of Ca = 2.05, 1.41, and 0.82.

From Table IV it can be also deduced that with the increase of thermal effects (smaller cavitation numbers) there is more depression in the *St* number due to local temperature gradient increases, as observed in Fig. 23(c). In other words, the presence of strong thermal effects triggers the shedding process of cavity structures through improving the high-frequency oscillations [120]. This can be illustrated in Fig. 26 by plotting the power spectra in log scale, which more clearly highlights the increase in acoustic fluctuations at the higher frequencies in the *Ca* = 0.82 and 1.41 cases.

6.1.5. Velocity Fluctuation Profiles

Dynamic characteristics of the LNG cavitation in the nozzle can be further investigated by evaluating the evolutions of mean-square velocity fluctuations, i.e. streamwise normal ($\overline{u'u'}$), transverse normal ($\overline{v'v'}$), and shear fluctuations ($\overline{u'v'}$). Fig. 28 depicts the dimensionless velocity fluctuations along two transverse stations of *x/b* = 16.21 and 32.43, as indicated in Fig. 27, for the cavitation numbers of *Ca* = 0.82, 1.41, and 2.05. The profiles are non-dimensionalized with the local mean velocity at each station. The computed fluctuations express the interaction behavior of the bulk liquid with generated vapor structures for about two flow-through times of progress after reaching statistically steady state.

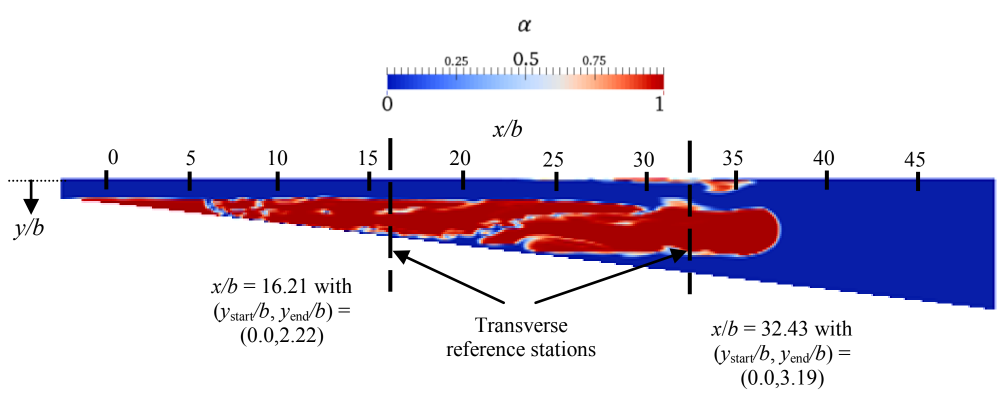

Fig. 27: Vapor fraction field of the cavitating LNG flow at Ca = 0.82 in the diverging part of the nozzle at time instant of t = 0.65 s. Locations of the transverse reference lines are indicated.

As indicated in Fig. 28, with the increase of the cavitation number, velocity fluctuations decrease at both of the reference stations. At *Ca* = 2.05 where cavitation is not formed, velocity fluctuations are quite small compared to the cavitating conditions of *Ca* = 0.82 and 1.41 due to the lower levels of adverse pressure gradients, which promote cavity inception. For the *Ca* = 0.82

and 1.41 cases, streamwise fluctuations show their maximum values in the liquid core (Fig. 28(a) and (d)), whereas the transverse (Fig. 28(b) and (e)) and shear fluctuations (Fig. 28(c) and (f)) having their peak values in the vapor and/or interfacial regions away from the walls. The streamwise fluctuations dominating in the liquid core is likely caused by: 1) deceleration of the liquid flow as it approaches the vapor region, and 2) momentum, mass, and heat transfers predominantly occur in the favorable gradient direction i.e. from liquid to vapor. The streamwise fluctuations seem to be strengthened as *Ca* is reduced, causing more entrainment of the liquid (stronger re-entrant jets) into the vapor zones. The intermittent behavior in the transverse and shear fluctuations (see $y/b > 1.0$ region of Fig. 28(b)-(c) and (e)-(f)), pertain to the vaporization and condensation processes imposing large density and pressure gradients. The intermittency is enlarged as *Ca* decreases. The present observations are consistent with the common conclusion in literature [81,88,125] that the reduction of cavitation number leads to larger production of vapor regions, and further indicate that the velocity fluctuations are improved at smaller *Ca*. This also highlights the fact that the *Ca* reduction leads to faster breakup and penetration of the vapor structures into the liquid phase by improving thermally-affected gradients, which consequently enhances the overall vaporization and mixing in the flow [74].

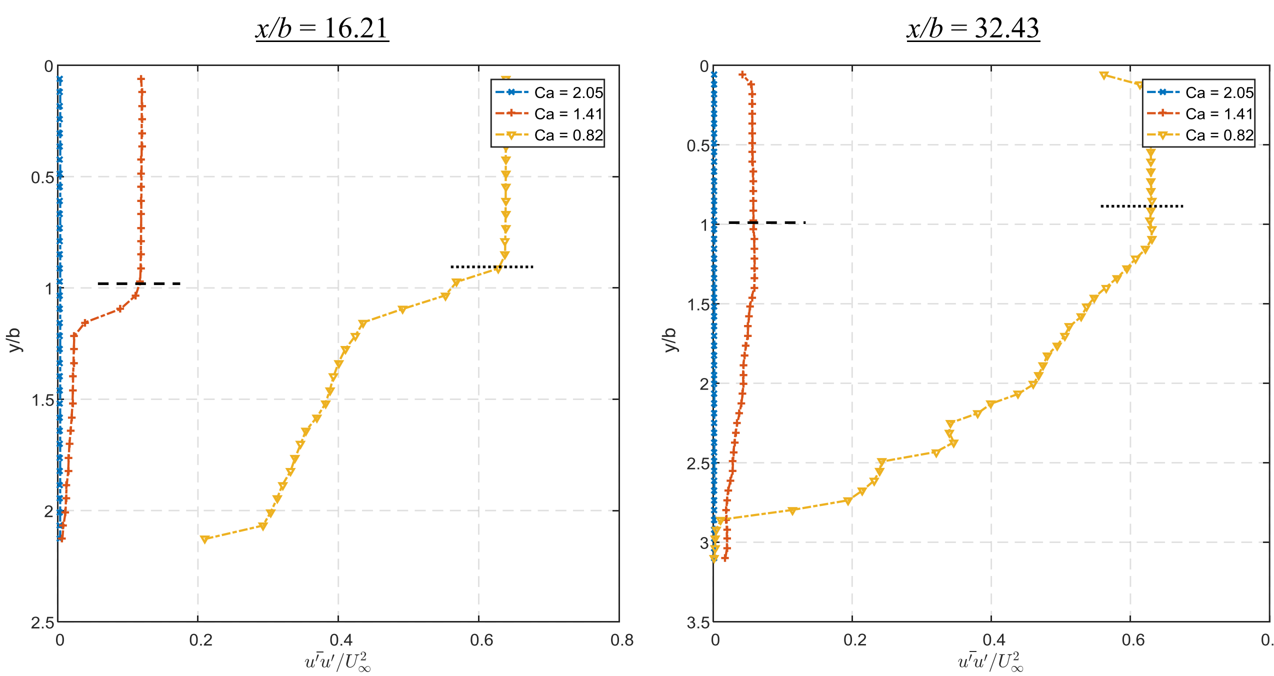

(a) *(d)*

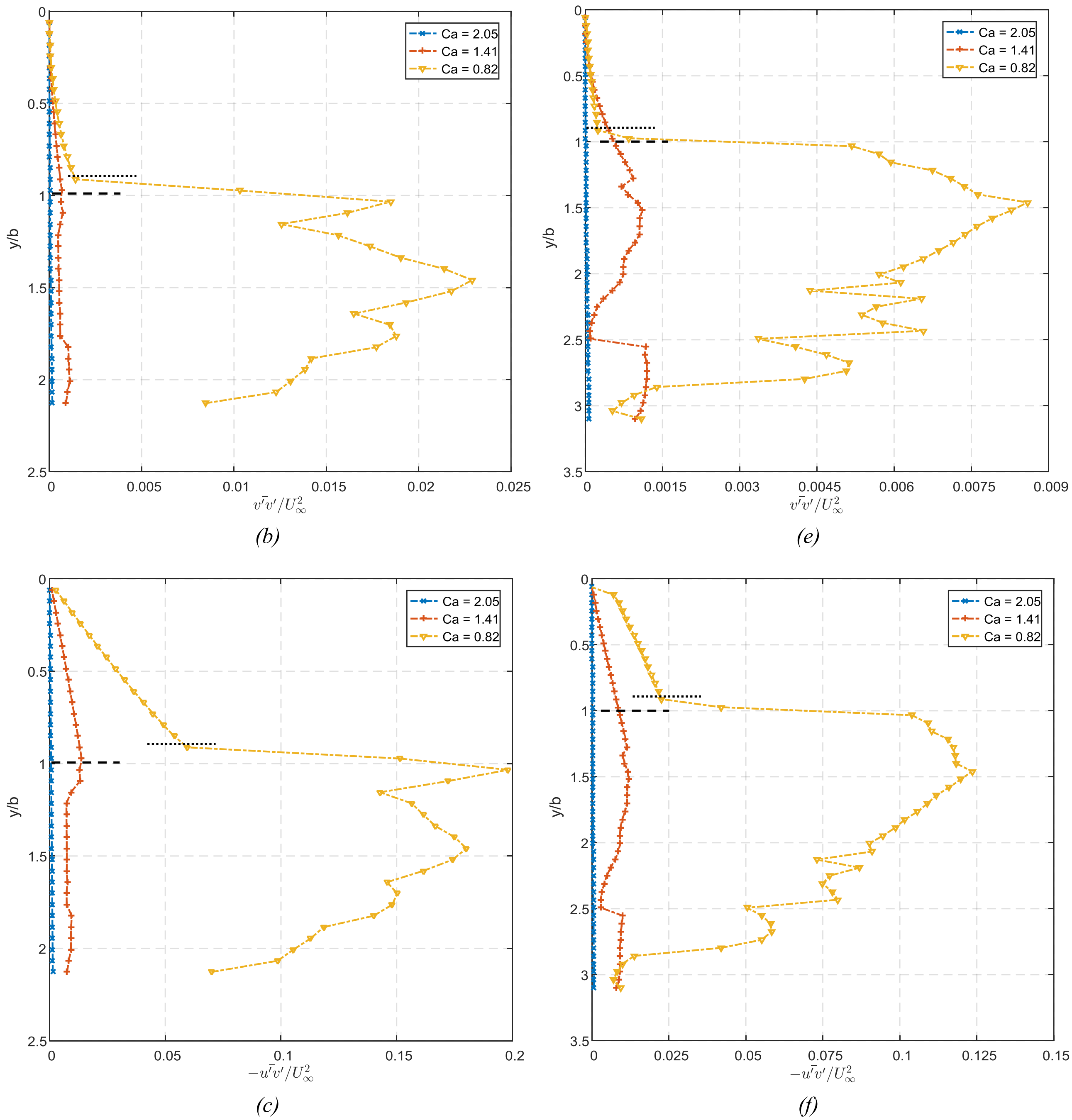

Fig. 28: Profiles of dimensionless mean-square velocity fluctuations along the transverse reference line stations of x/b = 16.21 and 32.43 in the in-nozzle LNG cavitating flow at cavitation numbers of Ca = 0.82, 1.41, and 2.05: (a,d) streamwise normal; (b,e) transverse normal; and (c,f) lateral shear components. The dotted and dashed lines separate the upper main liquid stream.

It is also notable in Fig. 28 that the presence of larger streamwise fluctuations at smaller *Ca* is in accordance with the behavior of velocity magnitude variations: larger values are observed in the shear layer core regions as *Ca* decreases. This is mainly due to 1) larger mean vapor production in the domain (see Fig. 29) modifying the shear stress (and vorticity magnitude, as indicated in Section 6.1.2) evolution on the wall and inside the flow by increasing the liquid-vapor interfacial friction; and 2) more contraction of the liquid mainstream by stronger vapor structures, causing larger momentum exchanges in the streamwise direction [100,117]. This behavior is not seen in the non-cavitating case where small velocity fluctuations are not affected by the strong interfacial gradients of pressure, density, and temperature [74]. Increase of the shear fluctuations with reduction of *Ca* might be also attributed to the stronger presence of cavity spots within the cores of large streamwise vortical structures which affects the process of vortex stretching by decoupling the vortex strain and rotation rate, weakening the relationship between streamwise and transverse velocity fluctuations, as reported in [27,174].

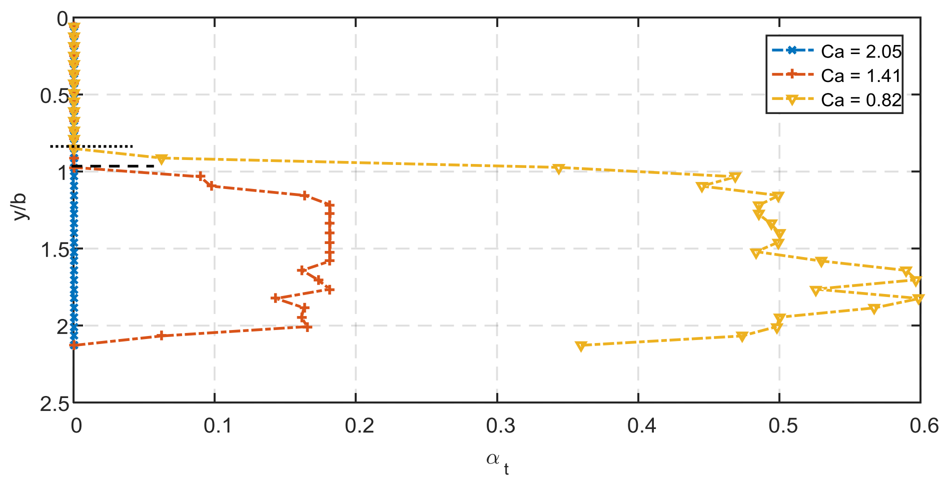

Fig. 29: Profiles of temporally-averaged vapor fraction field along the transverse reference line station of x/b = 16.21 for the in-nozzle LNG cavitating flow at Ca = 0.82, 1.41, and 2.05. Time averaging is performed over 100 equally-spaced time steps within two flow-through times of progress after reaching statistically steady state. Vapor production is increased as Ca decreases.

In Fig. 28 it can be further observed that the velocity fluctuations tend to gradually decrease in the streamwise direction as the flow is exposed to larger passage area [74,160]. This reduction seems to be improved in the case of transverse and shear components. Note that the non-zero fluctuations in near-wall regions of the figure (see for example the *y/b* > 2.0 region of Fig. 28(a)) are attributed to the inclined angle of the reference transverse line(s) with respect to the nozzle lower wall which makes two non-zero velocity components at the wall. Also, despite the fact that walls are generally resistant and impose damping effects on the flow their resistance becomes limited in the case of cavitating mixture flows with reduced densities [115,125]. The wall velocity fluctuations are more improved in the cavitating cases due to the presence of sheet cavity residuals evolving unsteady along the wall [120,127].

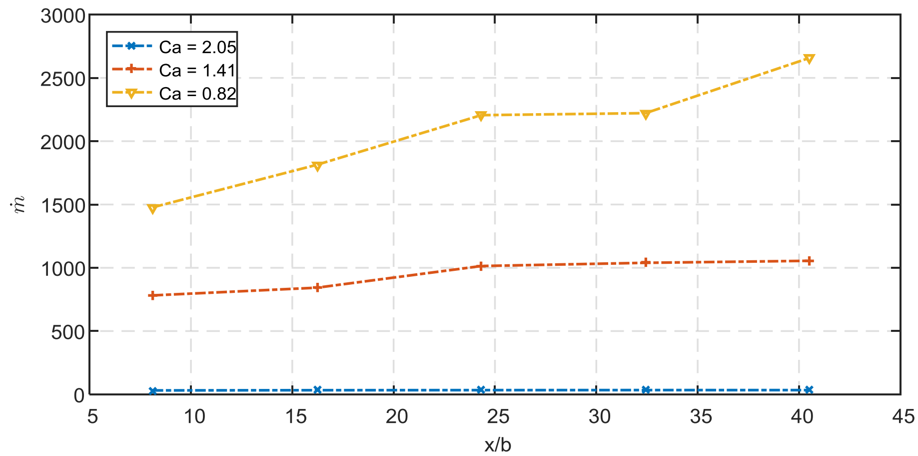

Fig. 30: Distributions of time-averaged mass flow rates (g/s) at the transverse line stations of x/b = 8.10, 16.21, 24.32, 32.43, and 40.54 in the in-nozzle LNG cavitating flow at Ca = 0.82, 1.41, and 2.05.

Another important observation in Fig. 28 is that in the cavitating portion of the resulting profiles (see for example y/b > 0.90 region in Fig. 28(a)) velocity fluctuations experience a gradual drop, in all the simulated *Ca* tests, due to the mass flow collapse. This drop seems to correspond to the cavitation inception and/or liquid-vapor interface regions, and illustrates the fact that the mean flow velocity in two-phase mixture regions significantly lowers as cavitation improves [90,100,170]. Related to this, Fig. 30 shows the evolution of the time-averaged mass flow rate in the streamwise direction for the present LNG cavitating flow at the given operating cavitation numbers. The mass flow rate is found by using $\dot{m} = \int \rho(\boldsymbol{u} \cdot \boldsymbol{n})\, dS$ relation (in which $\boldsymbol{u}$ is velocity vector and $\boldsymbol{n}$ is normal vector to the surface $dS = dydz$), applied to the data collected from five streamwise line stations x/b = 8.10, 16.21, 24.32, 32.43, and 40.54 for the flow progress from t = 0.0 s to t = 0.98 s. As indicated, $\dot{m}$ increases as *Ca* decreases, which illustrates the larger effects of inertia in governing the mixture cavity-vortex interactions at smaller *Ca*, despite the presence of larger cavities and more local velocity reductions. Note that the linear increase of $\dot{m}$ in the streamwise direction is because the flow is still in development stage.

6.2. Effects of Nozzle Diffusion Angle

To investigate the effects of geometrical parameters on the evolution of LNG cavitation inside the nozzle, the baseline simulation of Section 5.1 is extended for nozzle diffusion angles (*DA*) of *DA* = 1º, 2.5º, 7.5º and 15º operating at the cavitation number of *Ca* = 1.41. The simulations are set up similar to the description of Section 4.3. The following sections first address the global behavior of the in-nozzle LNG cavitation flow at *DA* = 1º and 15º. Further details on the cavity-vortex interactions and instability behaviors at the given diffusion angles are provided in Sections 6.2.2-6.2.5.

6.2.1. Global Behavior of the Cavitation Flow

Temporal evolution of the vapor fraction, temperature, and vorticity magnitude fields for the LNG cavitating flow in the nozzle with two different diffusion angles of DA = 1º and 15º operating at Ca = 1.41 are provided in Fig. 31-32 for time instants of t = 0.40, 0.60, 0.70, 0.90, and 1.0 s. Note that the cavitation process at the other diffusion angles of DA = 2.5º and 7.5º follows a similar evolution so they are not shown here. The flow fields of Fig. 31 are depicted for the streamwise section of x/b = 4.0-65.0 in the diverging part of the nozzle. It is seen that the cavitation evolution is directly controlled by the diffusion angle of the nozzle, mainly through manipulating vaporization and condensation processes as well as the cavity-vortex shedding behaviors. At DA = 1º, the attached sheet cavitation formed on the lower wall of the nozzle does not show a periodic behavior, such that an almost pure vapor region with a slightly wavy behavior in the interfacial regions is visible towards the nozzle outlet. The thin, continuous, stable cavity forms at around t = 0.60 s on the nozzle lower wall and remains steady within almost the entire given time period without generating any of the classical cloud cavitation structures with large instabilities (Fig. 31(a)).

The formation of a stable vapor cavity for DA = 1º is mainly attributed to the small cavity thickness and proximity of the cavity interface to the upper boundary which prevent the formation and progress of an unsteady re-entrant jet. The lack of strong temperature-based density and adverse pressure gradients in the flow due to the absence of separation/recirculation zones to trigger cavity inception are further causes for such evolution (Fig. 31(a)-(b)). At the time instants t = 0.90 and 1.0 s, though, the flow does show a weak development of a re-entrant jet with small scale frequencies in far downstream region close to the outlet. This is because of the formation of a small flow separation region on the lower wall, as well as the exposure of the flow to the buffer zone with larger flow area slightly triggering unsteady vaporization and condensation of the cavitating regions [100]. However, instability of the re-entrant structure is largely damped through the domination of inertia of the bulk liquid above the vapor region and the lack of a strong instability mechanism, disallowing the formation of large re-entrant flows to promote unsteady larger cavity clouds.

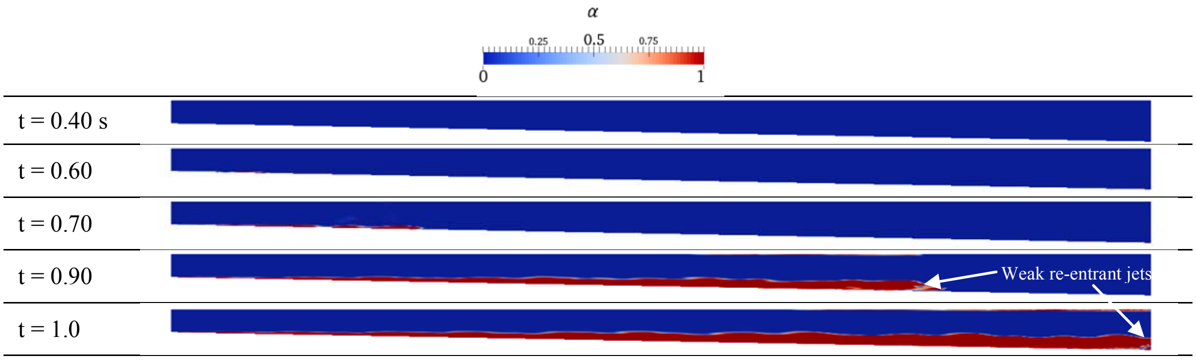
α
0.25
0.5
0.75
0
1
t = 0.40 s
t = 0.60
t = 0.70
t = 0.90
Weak re-entrant jets
t = 1.0

(a)

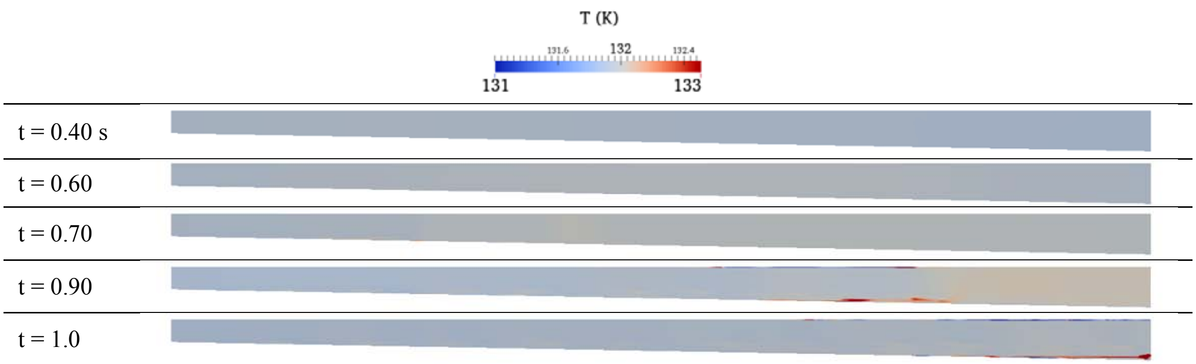
T (K)
131.6
132
132.4
131
133
t = 0.40 s
t = 0.60
t = 0.70
t = 0.90
t = 1.0

(b)

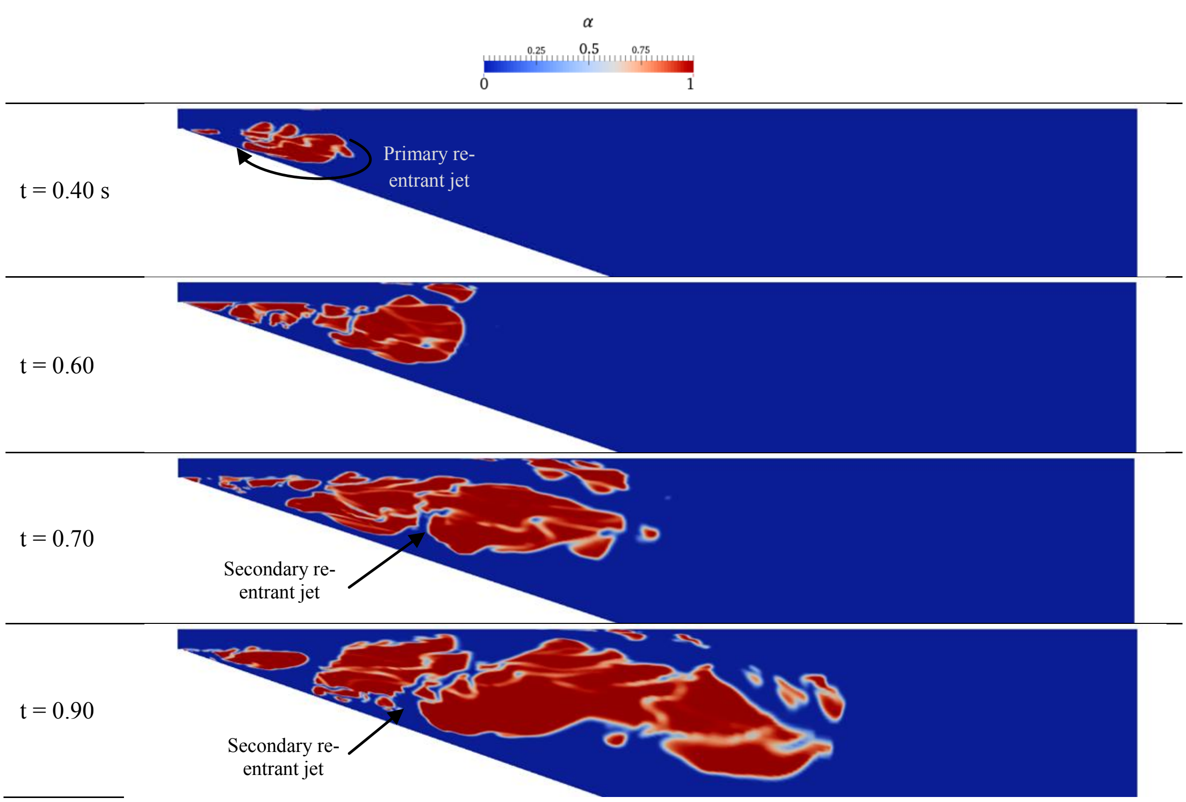
α
0.25
0.5
0.75
0
1
t = 0.40 s
Primary re-entrant jet
t = 0.60
t = 0.70
Secondary re-entrant jet
t = 0.90
Secondary re-entrant jet

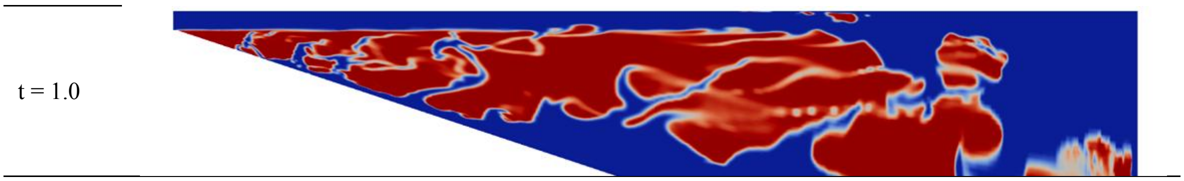

(c)

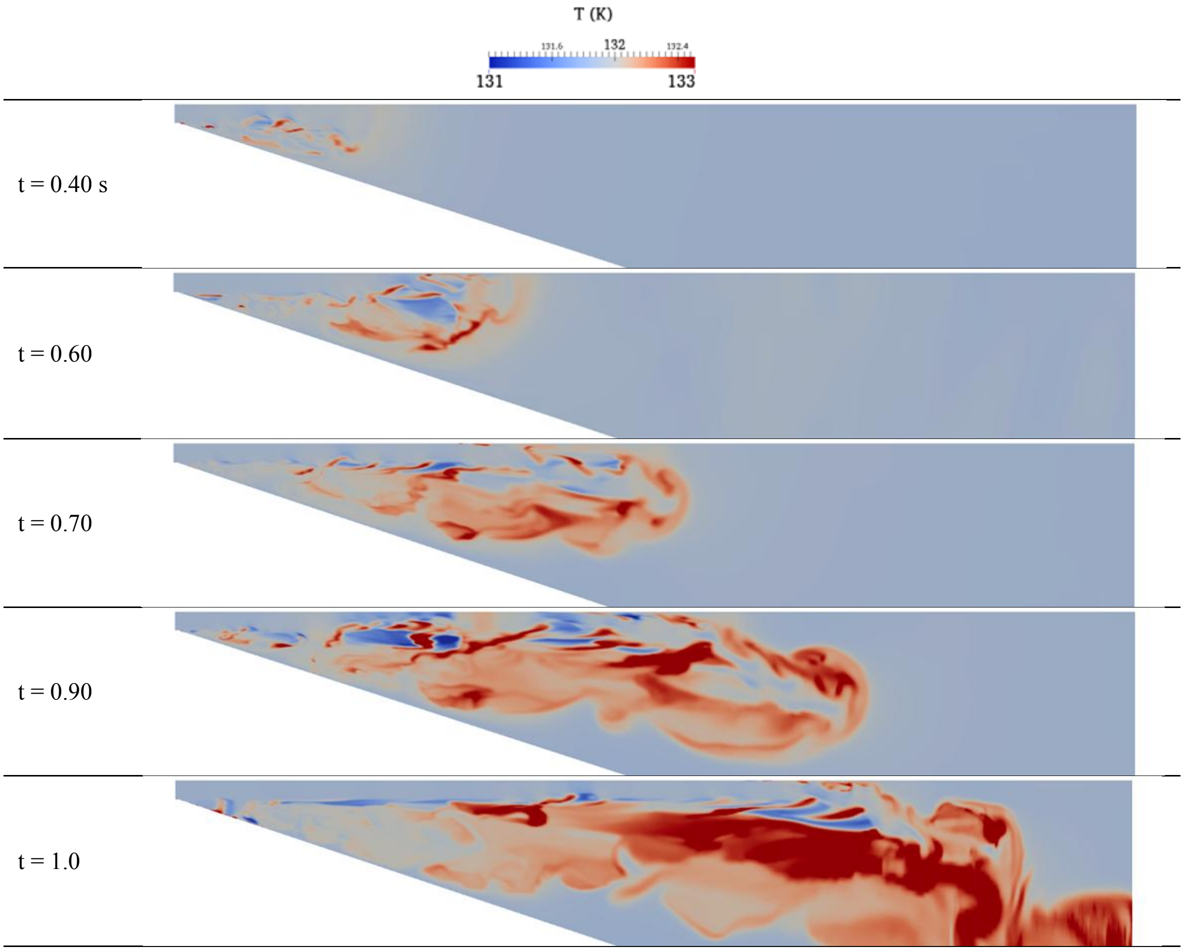

(d)

Fig. 31: Time evolution of the LNG cavitating flow in the nozzles with diffusion angles of DA = 1ºand 15º at the cavitation number of Ca = 1.41: instantaneous contours of vapor fraction and temperature (K) at DA = 1º (a,b) and DA = 15º (c,d) at time instants of t = 0.40, 0.60, 0.70, 0.90, and 1.0 s. Note the cut-off contours (sliced at y/b = 6.0) in the DA = 15ºcase.

As *DA* increases to 15º, the given contours of Fig. 31(c) and (d) indicate early breakdown of the sheet cavity, at $t < 0.40$ s, through faster progression of the unstable re-entrant jet compared to the *DA* = 1º case. This is due to the separation of the flow from the lower wall and immediate formation of recirculating zones which destabilize the sheet cavities that form from the intersection of the throat and diverging part of the nozzle [93,153]. As a result, the cloud cavitation tends to begin earlier (t = 0.40 s) while showing large levels of shedding associated with highly unsteady cloud structures in the entire development period ($t \geq 0.60$ s). Because of the periodic fluctuations of the relative pressure (p - p_{sat}) and density in the wake, the formation of vapor spots occurs at successive instants of time, leading to cyclic cavity development especially in the recirculating zones [126,160]. This behavior is downgraded as *DA* is reduced, as seen in Fig. 31(a) and (b), due to the absence of strong flow gradients. Such unsteady evolution that includes the formation of shorter cavity spots with highly frequent shedding incidents at cryogenic operating temperatures is also reported by Gustavsson et al. [113] and Kelly et al. [114] who studied the cryogenic cavitating flow of fluoreketone over a NACA0015 airfoil.

From the temperature contours (Fig. 31(b) and (d)), it can be also detected that a slight temperature variation of ±2 K is observed in both cases, similar to the temperature field reported in Section 5.1; the local temperature drops around the vapor areas because of the latent heat absorbed from the surrounding liquid, which delays the inception and growth rate of the vapor regions, and vice versa. Larger temperature gradients are observed at the larger diffusion angle of 15º, due to the presence of stronger phase change mechanisms within the larger recirculating zones. The preponderance of local high-temperature vapor regions implies that the temperature variation is mainly associated with heat transfer into vapor, leading to delayed condensation of the vapor to liquid in those regions [21]. The present results suggest that increasing the nozzle diffusion angle alters the thermal behavior of the cavities by influencing the shear-layer instability process, such that larger cavities in the larger angles are more strongly affected by temperature variations, through enhancing the local temperature depressions in liquid regions around the cavities. This is further investigated in the Sections 6.2.3-6.2.5.

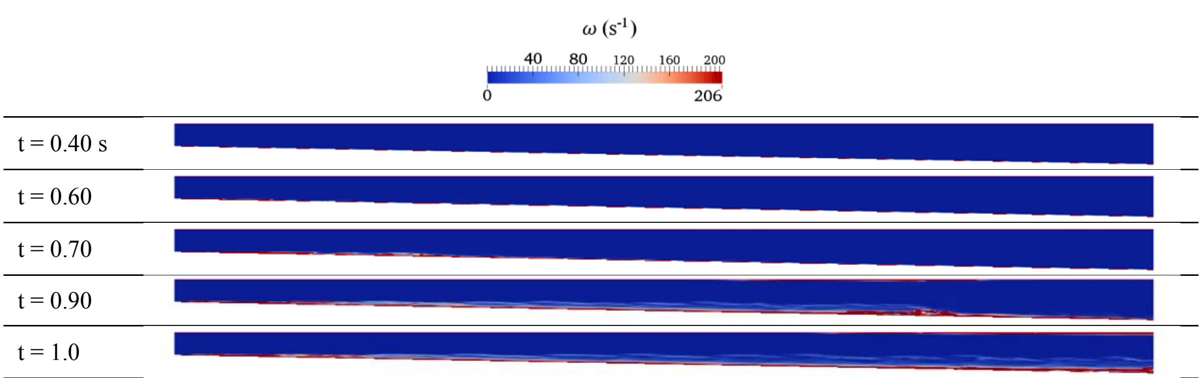

(a)

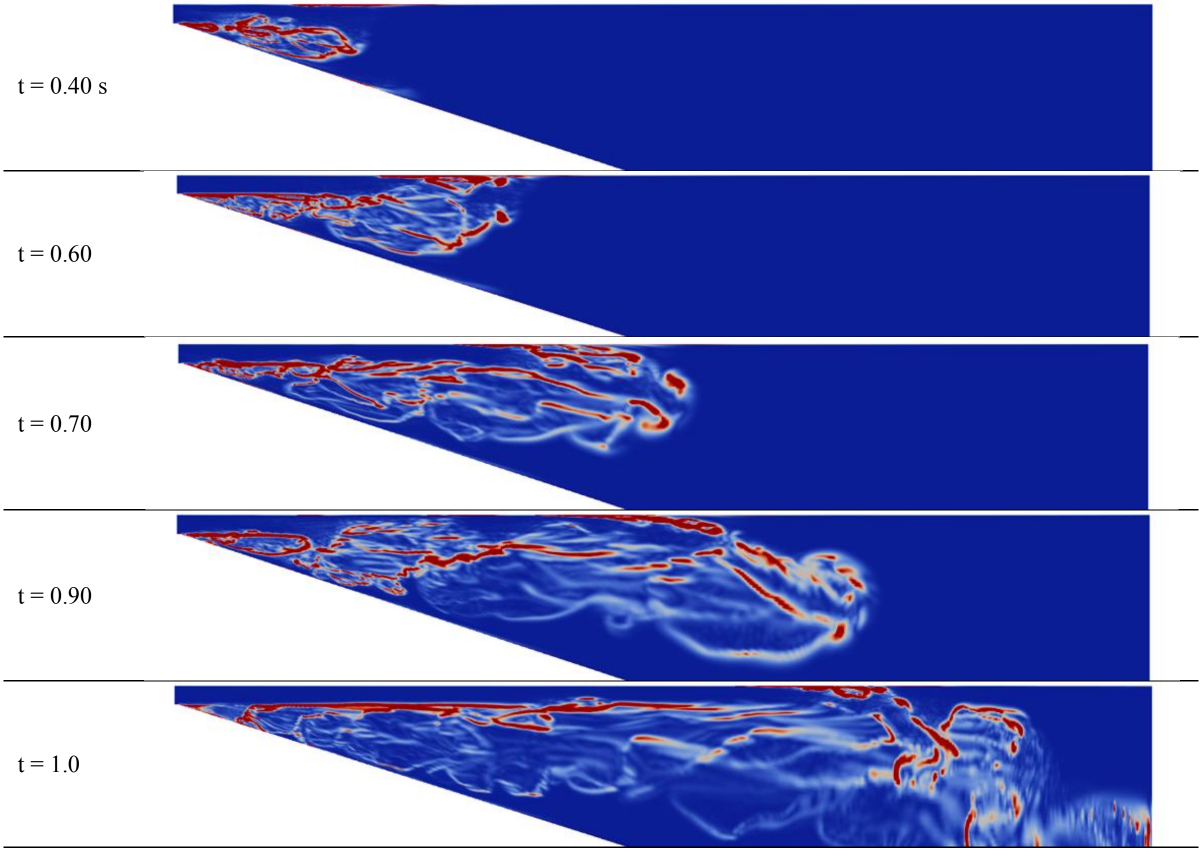

(b)

Fig. 32: Time evolution of vorticity magnitude (1/s) for the LNG cavitating flow in the nozzles with diffusion angles of DA = 1º (a) and 15º (b) at the cavitation number of Ca = 1.41 at time instants of t = 0.40, 0.60, 0.70, 0.90, and 1.0 s. Note the cut-off contours (sliced at y/b = 6.0) in the DA = 15ºcase.

The evolution of the cavity structures at the nozzle diffusion angles shown in Fig. 31 is further investigated through evaluating the behavior of the vorticity magnitude field and its correlation with the cavity development in the flow. Fig. 32 depicts the evolution of the vorticity magnitude field at the time instants of Fig. 31, for the nozzle diffusion angles of *DA* = 1º and 15º. As indicated in Fig. 31(c), upstream motion of the large unstable re-entrant jets towards the leading edge of the sheet cavity at *DA* = 15º is the primary reason for the development of highly shedding cavity pockets and cloud structures in the domain [81,100,173]. As a result of such motions, large scale instabilities, which mainly develop through the jet local interfacial zones, lead the primary cavity vapors near the throat to break at a number of points in an irregular fashion, thus causing shedding of the small vapor pockets from the rear of the sheet (Fig. 31(c) and 32(b) at *t* = 0.40-0.60 s). The vapor pockets turn into large cavity structures further downstream as time proceeds (*t* = 0.70-1.0 s). This process seems to be substantially triggered at the diffusion angle of 15º where the presence of larger flow gradients, e.g. larger adverse gradients of pressure, in stronger recirculating zones cause earlier formation of the clouds with more instability in the shedding processes. In contrast, at *DA* = 1º (Fig. 31(a) and 32(a)), weak interactions of the downstream re-entrant jets with the attached cavity interface prevents the formation of cloud cavities, so the cavity flow mostly appears in the form of a quasi-stable full vapor region. The present observations suggest that the transition of the sheet cavity into a periodically oscillating cloud cavity structures at larger diffusion angles, which is due to faster boundary layer separation and larger adverse pressure gradients, causes larger localized instability regions which induce significant shedding into the flow with increased vorticity in the interfacial regions and shear layers [119,133].

It is also notable from Fig. 31-32 that at *DA* = 15º, the primary re-entrant jet does not seem to interact continuously with the sheet cavity interface as it moves upstream in the given time period; the interaction is limited to the time instant(s) when the jet reaches the cavity leading edge and cuts through the cavity interface [100,154,157]. This is because of the stronger unsteadiness in the attached cavity as *DA* increases. More specifically, at *DA* = 15º, because the vortex flow becomes completely separated from the wall, the vortices become highly unsteady and more prone to shed from the wall (larger levels of disturbance as indicated in Fig. 32(b)), constraining the progress of the primary re-entrant jet by creating secondary re-entrant jets (see for example Fig. 31(c) at t = 0.70-0.90 s). This makes the pressure distribution more non-uniform compared with that in the smaller *DA*, thus causing further entrainment of the cavities to the lower pressure zones. Such behavior also explains the reason why cavitating clouds at the large *DA* are barely able to touch the lower wall of the divergent segment of the nozzle [43,116].

The above observations are relevant to the Franc and Michele [100] remarks stating that thicker sheet cavities generally shed larger-scale cavity clouds, whereas the smaller-scale cavitating pockets are produced from thinner sheet cavities. It can be thus concluded that the onset of instability and the formation of cloud cavity structures are more likely for rather short cavity spots which are significantly affected by large flow gradients, e.g. especially the adverse pressure gradients; long thin cavities, observed at the smaller diffusion angles (e.g. *DA* = 1º) do not show significant instability due to the weaker adverse pressure gradients. This is in agreement with Callenaere et al. [154] that proved a direct correlation between the region of cloud cavitation instability and the region of large adverse pressure gradients. It is noted that the presence of growing unsteadiness within the observed cavitating clouds in Fig. 31-32 is also associated with the vortex core instabilities and effects of micro-bubble accumulations at the vortex core causing the vortical structures to be elongated and distorted [154]. The strength of vortical structures seems to be enhanced by the improved collapse/coalescence of surrounding cavities at larger diffusion angles [158]. More details on the instability behavior of the in-nozzle LNG cavitating flow at the given diffusion angles are discussed in Sections 6.2.4-6.2.5.

6.2.2. Flow Properties along the Nozzle Lower Wall

The impacts of the nozzle diffusion angle on the dynamics of in-nozzle cavitating LNG flow is also investigated through evaluating the flow properties along the nozzle lower wall where the complex interactions of re-entrant jets with shear layers substantially govern the overall cavitation patterns. Fig. 33(a)-(c) compares the time-averaged distributions of vapor fraction, shear stress, and vorticity magnitude fields on the lower wall of the nozzle at the tested diffusion angles of *DA* = 1º, 2.5º, 7.5º and 15º. Time averaging is performed over 100 equally-spaced time steps within about two flow-through times of progress after reaching statistically steady state.

(a)

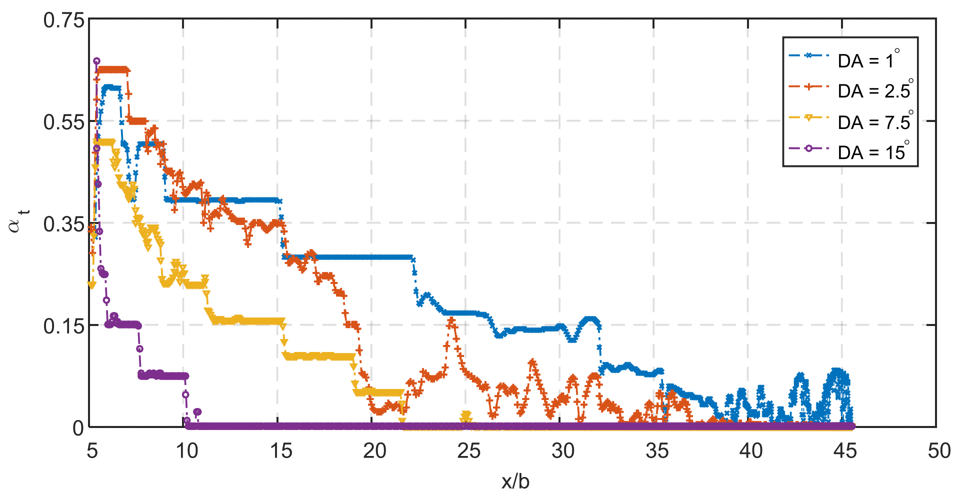

(b)

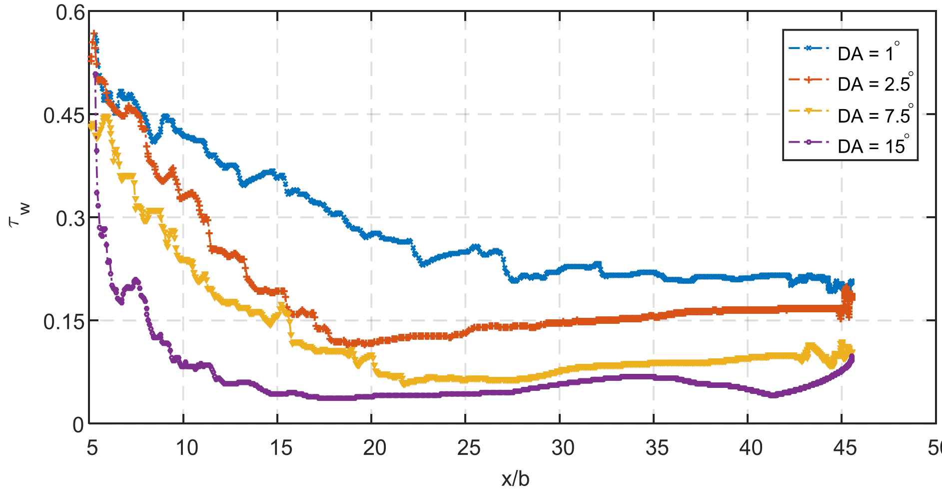

(c)

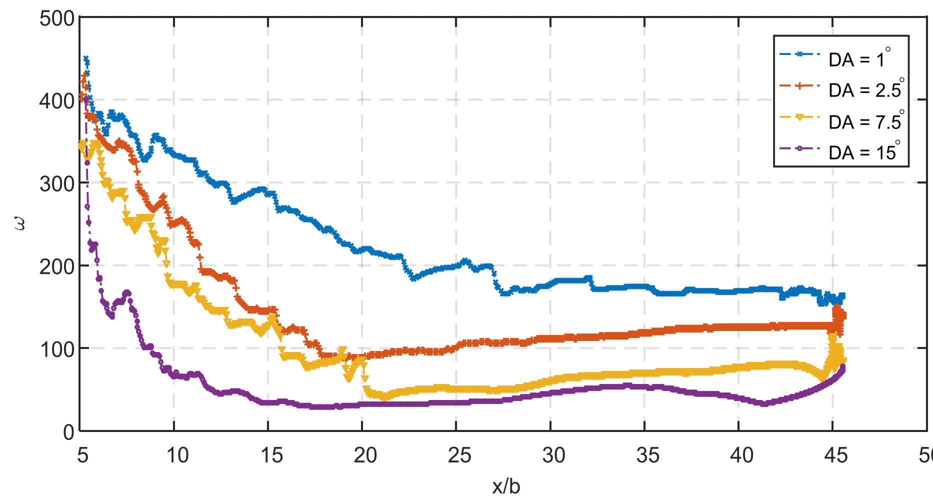

Fig. 33: Distributions of temporally-averaged (a) vapor fraction; (b) shear stress magnitude (Pa); and (c) vorticity magnitude (1/s) for the LNG cavitating flow in the nozzles with diffusion angles of DA = 1º, 2.5º, 7.5º and 15º. Data along the lower wall of the nozzle are plotted.

In Fig. 33(a)-(b), it is seen that the vapor fraction and shear stress magnitude decrease as *DA* increases. The reason for this is estimated to be due to the stronger detachment of unsteady cavitating structures from the lower wall as *DA* increases. Although separation occurs earlier for larger *DA*, which causes stronger shedding processes, earlier detachment of the cavities from the wall suppresses the wall shear stress and produces lower levels of unsteadiness in near-wall regions. On the contrary, away from the wall, larger diffusion angle leads the liquid flow to accelerate locally inside the recirculating zones and provide larger low-pressure areas, causing the formation of stronger unsteady vapor structures. The unsteady behavior of vapor cloud structures inside the wake regions yields larger density, pressure, and temperature gradients in the domain especially at cavity collapse and/or inception incidents [92,125,154], as reported in

Sections 6.2.3-6.2.5. This process however seems to be suppressed at the wall as *DA* increases such that smaller vorticity is generated at larger angles (Fig. 33(c)). This is consistent with the results of Section 6.1.2 stating that the frequent presence of vapor structures on the wall enhances the wall shear stress and vorticity. The increase of wall shear stress is further in relation to the increased local accelerations in the bulk liquid, imposed by the restricting vapor structures in the domain [115]. These local flow accelerations contribute to the local formation of vapor spots in the core of vortex structures. Such behavior seems to be enhanced at smaller diffusion angles where quasi-stable longer vapor cavities with smaller levels of exposure to temperature-based flow gradients are continuously generated on the lower wall [125,172].

Moreover from Fig. 33, it can be deduced that the presence of larger wall shear stresses at lower *DA* indicate more vaporization along the wall as well as more resistance of the attached sheet cavity past the throat to promote re-entrant jet unsteadiness. At larger *DA* faster breakdown of the attached sheet cavities on the lower wall (see contours of Fig. 31-32) degrades the wall shear stress, contrary to the smaller *DA* where the shear stress is improved due to delayed formation, or absence, of re-entrant jet. Faster formation of the re-entrant jet(s) at larger angles promotes the development of vapor structures away from the wall particularly inside the large recirculation zones. Note that the formation of large stable vaporizing regions at smaller *DA* is mainly associated with continuous reduction of mixture density in those regions causing the overall mass flow loss to become larger, thus resulting in a stronger cavity production [70]. This is more evident in the cases with *DA* = 1º and 2.5º where the lack of unsteady re-entrant jet makes the elongated sheet cavity evolve more smoothly, along most of the lower wall, with approximately no local breakdown incident.

6.2.3. Vortex-Cavity Interaction Mechanisms

To further demonstrate the effects of nozzle diffusion angle on the behavior of in-nozzle cavitating LNG flow, Fig. 34-35 show the instantaneous evolution of vorticity budgets of Equation (30) along the reference line of Fig. 7 (Section 4.5), at the time instant of t = 0.93 s. Note that the vorticity diffusion term is not shown in the figures since it is negligible compared to the other vorticity terms, as previously discussed in Sections 5.2 and 6.1.3. The figures compare the vorticity budgets for the nozzle diffusion angles of *DA* = 1º, 2.5º, 7.5º, and 15º. As indicated in Fig. 34(a)-(b), the vorticity dilatation and baroclinic terms increase as the diffusion angle increases up to DA = 7.5º. At DA = 15º, it is seen that the vortex baroclinicity and dilatation are decreased while showing more of a fluctuating behavior especially in the baroclinic term compared to the smaller angles. This is due to the presence of more frequent cavity collapse and/or inception events at DA = 15º causing stronger variations in the flow properties (see for example Fig. 34(d)), which are due to more instability in the flow, as further discussed in Section 6.2.4. The figures also indicate that the dilatation and baroclinic effects become more significant once the re-entrant jet is developed on the lower wall and initiates/progresses the cavity shedding process (see for example the $9.0 < x/b < 11.0$ region in the DA = 15º case), which is attributed to drastic changes in the local pressure and density fields. Note also that the baroclinic torque has a smaller magnitude compared to the dilatation term, and acts with more sensitivity to the vapor collapse/inception incidents [127], illustrating more effective influence on the global vapor fraction distribution (Fig. 34(c)). This significance is not observed in the non-cavitating regions of Fig. 34 where there is no volumetric contraction/expansion [119,170].

(a)

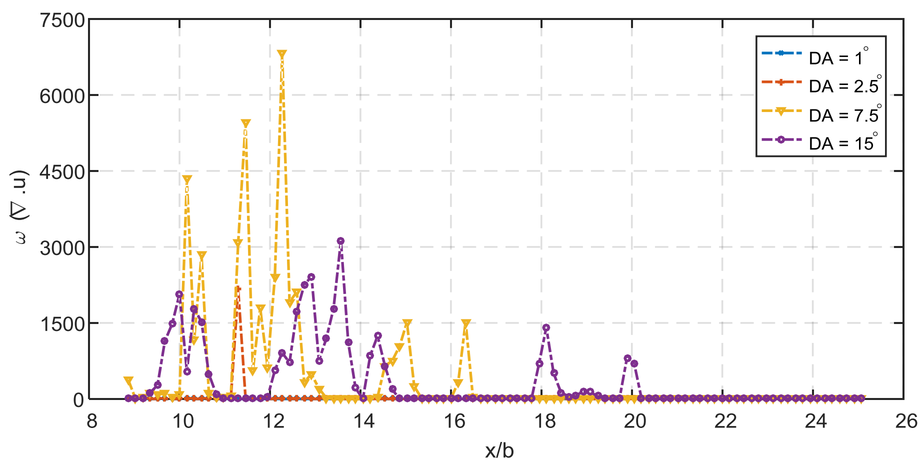

(b)

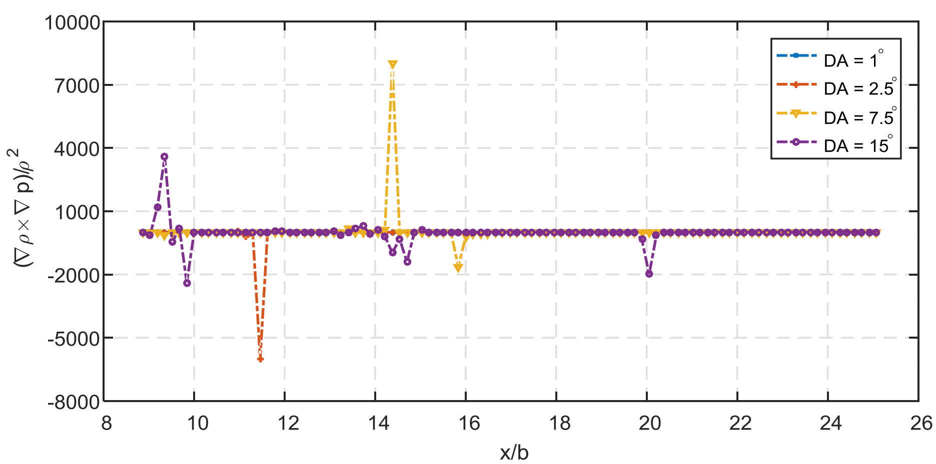

(c)

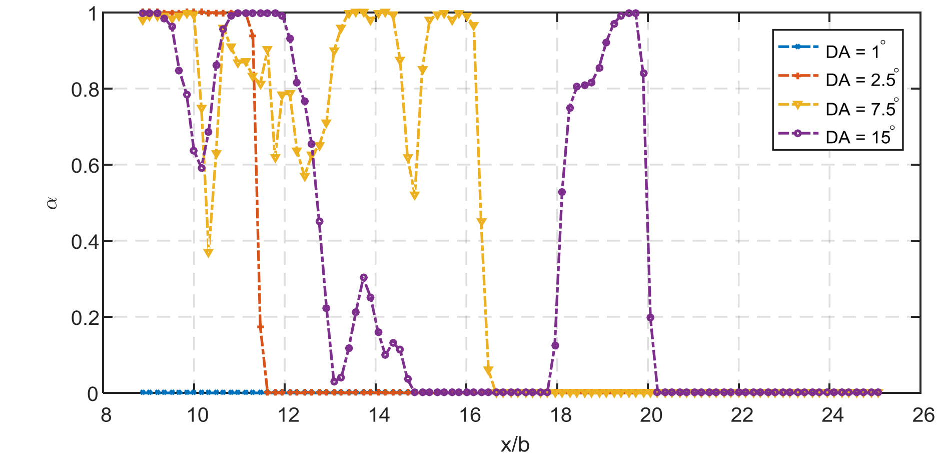

(d)

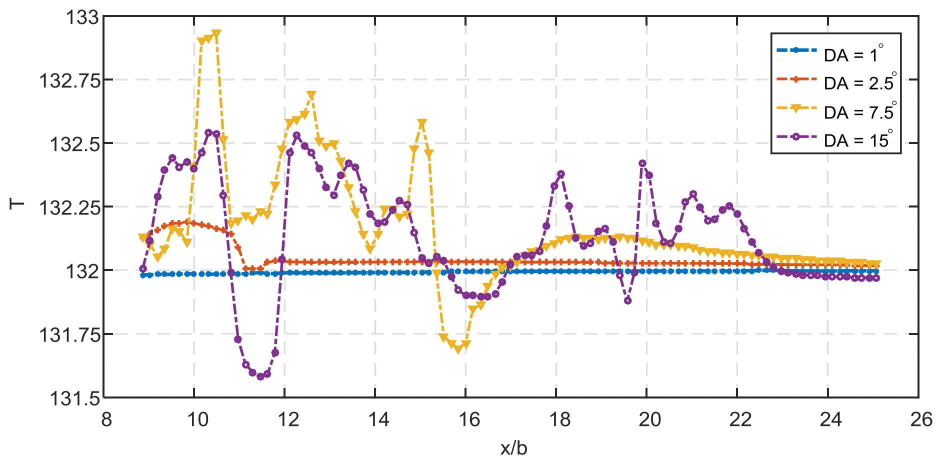

Fig. 34: Distributions of vorticity budgets along the reference line of Fig. 7 for the in-nozzle LNG cavitating flow with DA = 1º, 2.5º, 7.5º and 15º at t = 0.93 s: (a) vorticity dilatation magnitude ($1/s^2$); (b) baroclinic torque ($1/s^2$); (c) vapor fraction; and (d) temperature (K).

Corresponding evolutions of the vorticity stretch and tilt terms at the given diffusion angles are displayed in Fig. 35(a)-(d) and follow the trends observed in Fig. 34. Vortex stretch and tilt increase as *DA* increases up to 7.5º and decreases at *DA* = 15º, with the fluctuating behaviors being more evident in the streamwise stretch and transverse tilt terms, e.g. in the $16.0 < x/b < 22.0$ region at *DA* = 15º. The increasing behaviors with the diffusion angle up to 7.5º seem to pertain to the increase of liquid-vapor interfacial mass transfers at larger *DA* and improved cavity formation that trigger stronger thermal effects and flow gradients [115,127,168]. Lager *DA* is also suggested to cause more misalignment between the pressure and density gradients in the flow which leads to further production of baroclinicity. At *DA* = 15º however it is seen that despite the presence of more frequent vaporization and condensation processes with larger levels of unsteadiness – which causes more frequent vorticity oscillations along the reference line – the magnitude of vorticity budgets, and thus the overall vorticity (Fig. 35(e)) are decreased compared to the *DA* = 7.5º test. Such observations highlight the significance of geometrical parameters in altering the LNG cavity-vortex interaction mechanisms through modifying vorticity budgets at specific geometrical constraints.

(a)

(b)

(c)

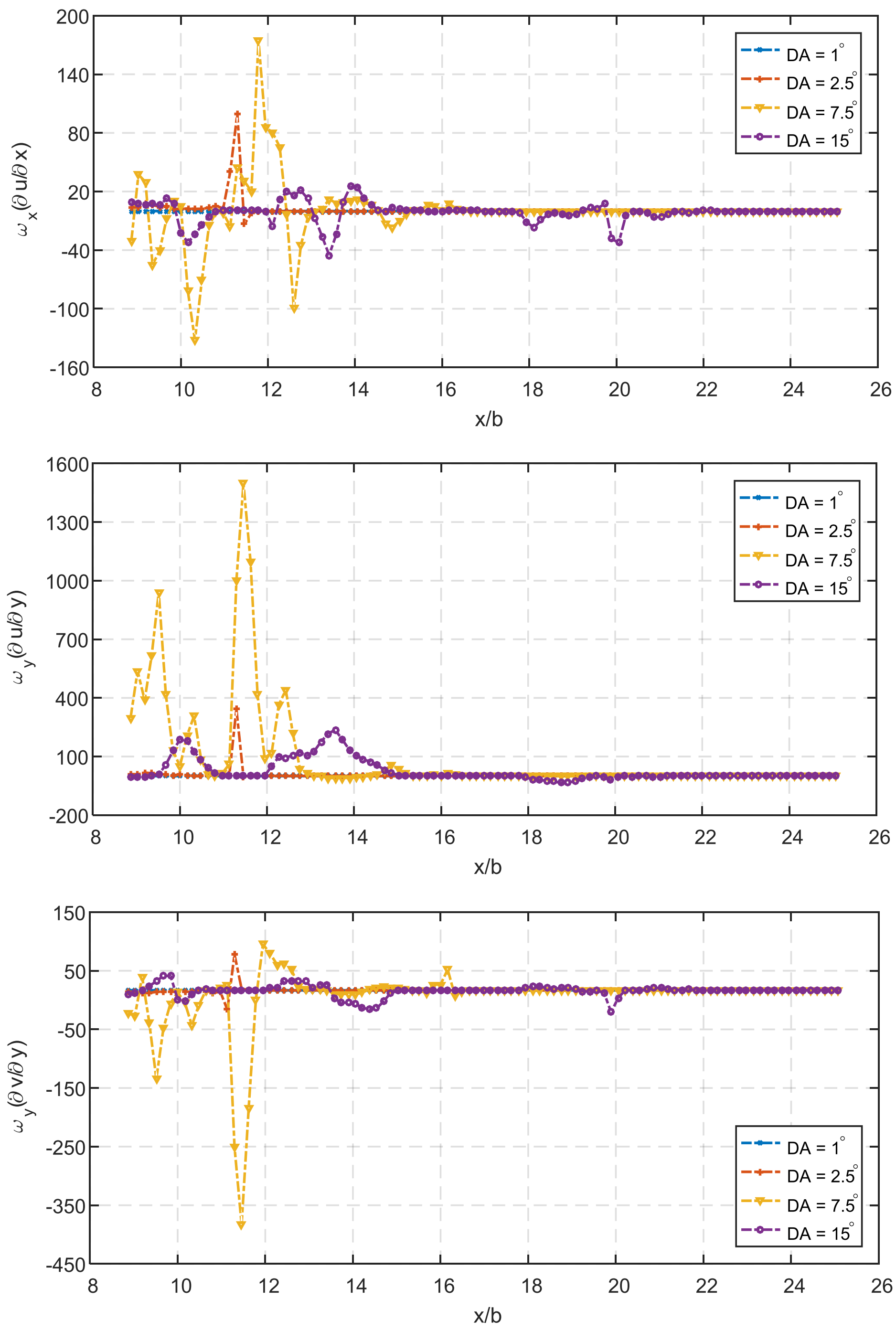

(d)

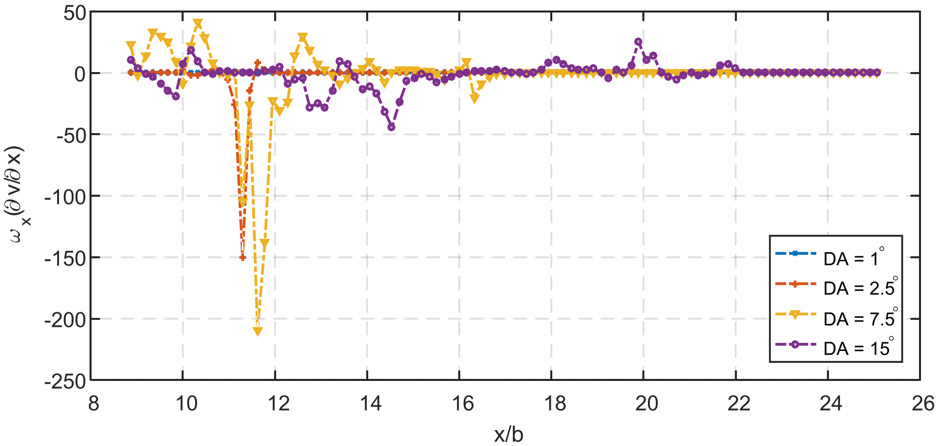

(e)

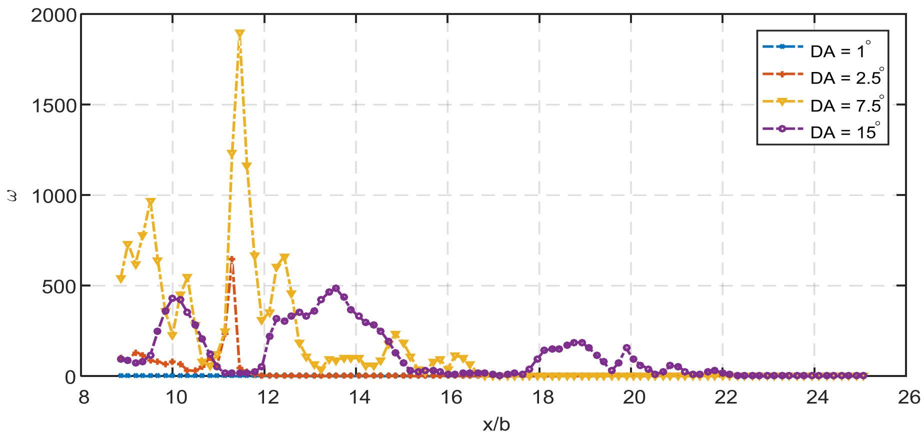

Fig. 35: Distributions of vorticity budgets along the reference line of Fig. 7 for the in-nozzle LNG cavitating flow with DA = 1º, 2.5º, 7.5º and 15º at t = 0.93 s: streamwise vorticity (a) stretching and (b) tilting (1/s^2); transverse vorticity (c) stretching and (d) tilting (1/s^2); and (e) vorticity magnitude (1/s).

The overall assessment of the vorticity budgets in Fig. 34-35 further indicates the significance of all the vorticity budgets in altering the cavity-vortex interactions in the present flows. This observation is not inconsistent with the general conclusions on vortex-cavity interactions in literature [119,125,168,170] stating the predominance of dilatation and baroclinic terms as the primary factors in modulating vorticity inside the large-scale cavity structures; in the current tests however the vorticity convection terms, i.e. vortex stretch and tilt, also play a major role in changing the cavitation behavior. The vorticity convection terms vary directly as functions of velocity gradients, and not the density and pressure gradients reflected in the dilatation and baroclinic terms.

6.2.4. Transition Characteristics of Shear Layer Instabilities

6.2.4.1. Time History of the Probed Flow Fields

To further evaluate the local effects of varying diffusion angle on the cavitation behavior of LNG flow inside the nozzle, Fig. 36 compares the temporal distributions of vapor fraction and relative pressure (p - p_{sat}) fields at the previously-noted probe location ($x/b,y/b$) = (27.02,1.10) of Section 6.1.4.1 for the diffusion angles of DA = 1º, 2.5º, 7.5º, and 15º, under the cavitation condition of Ca = 1.41. The collected time histories pertain to the first flow-through time. Overall, it is seen that the frequency of fluctuations becomes more pronounced as DA increases.

(a)

(b)

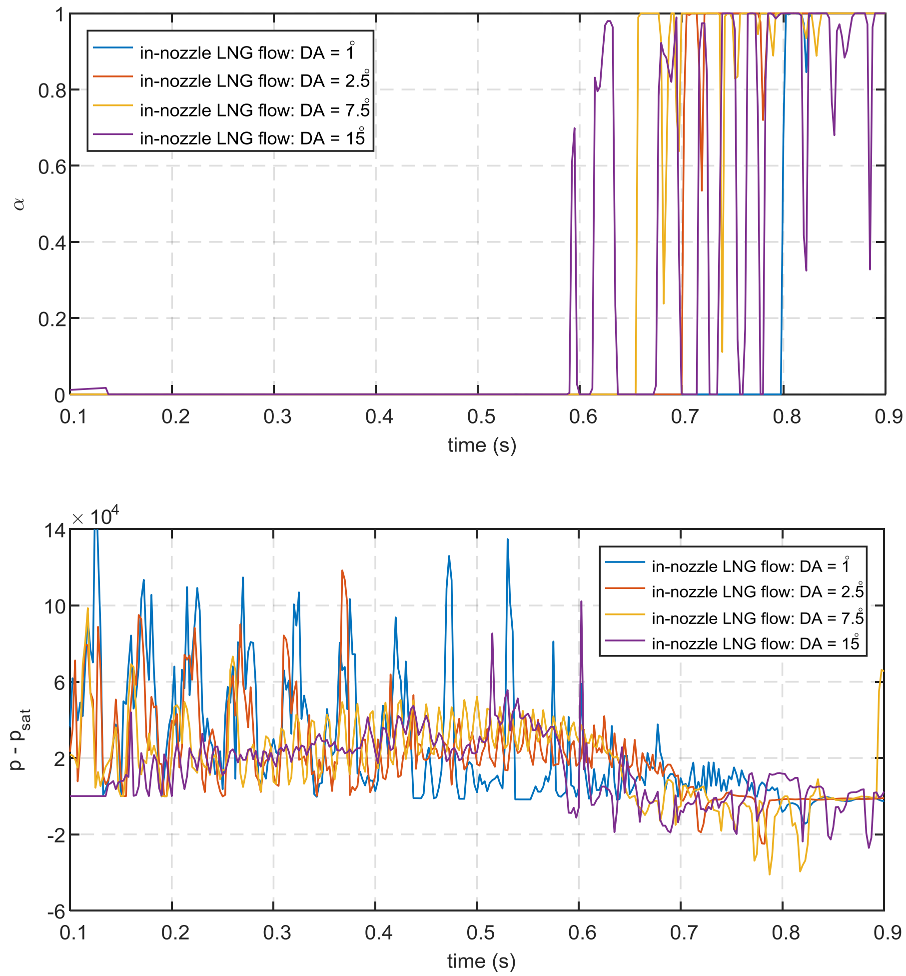

Fig. 36: Time histories of flow parameters over a single flow-through time at the probe location (x/b,y/b) = (27.02,1.10) for the LNG cavitating flow in the nozzles with diffusion angles of DA = 1º, 2.5º, 7.5º, and 15º: (a) vapor fraction and (b) relative pressure (Pa).

At smaller diffusion angles, the behavior of fluctuations shows less periodicity, i.e. more moderate oscillations with larger magnitudes indicating the tendency of the cavity flow to behave in a quasi-periodic wavy manner with relaxed shedding events (see Fig. 36(b)). This is mainly due to the presence of weaker alternating growth and decay of vapor structures in the cavitating regions occurring in longer periods of time compared with those at larger diffusion angles (see also Fig. 36(a)). For instance, at the smallest diffusion angle DA = 1º, the flow periodicity in $t < 0.70$ s is completely degraded as the generated large stable vapor in the domain damps out the flow oscillations. Conversely, at larger angles, it is observed that the stronger oscillations of flow parameters occur with reduced magnitudes and within smaller time periods. Emergence of this behavior at larger DA is significantly influenced by more periodic shedding of vortical structures at such angles, further causing the in-nozzle cavity flow to largely behave in alternating cavitating and non-cavitating modes [125]. More successive formation and collapse of cavity spots at larger DA triggers this process. The current observation confirms the presence of stronger local vaporization and condensation, including inception and collapse, processes with larger temperature, density, and pressure gradients at larger diffusion angles. The prevalence of stronger oscillations at larger DA are in accordance with the observations of flow contours in Fig. 31-32 showing that the widely-spread large recirculating zones create more instability through escalating local vortex shedding events [120,173,174]. These instabilities are more amplified by the collapse of downstream cavity clouds, which cause pressure waves to propagate upstream [116,172].

From the relative pressure distributions in Fig. 36(b), it can be also deduced that the stronger temperature fluctuations, which yield stronger variations in the saturation pressure, significantly alter the overall behavior of cavitation especially at larger DA such that the cavity cloud formation is delayed [89,100,127]. This implies somewhat a change in the balance between the vaporization and condensation processes as DA increases, at least in the initial stages of flow development; at smaller DA, vaporization rate seems to be improved by producing more vapor in the given time period, since the cavities are less prone to breakup due to local instabilities (see also the contours of Fig. 31-32). This can be better illustrated in Fig. 37 by comparing the temporal evolution of spatially-averaged vapor fraction field inside the diverging part of the nozzle over the flow progress of one flow-through time. Comparison is made for the nozzle diffusion angles of DA = 1º, 2.5º, 7.5º, and 15º. Similar to Section 6.1.4.1, spatial averaging is found using $\alpha_{mean} = \frac{\iint_{x,y_1}^{x,y_2} \alpha_i dA_i}{\iint_{x,y_1}^{x,y_2} dA_i}$ relation, taken over the diverging part of the nozzle to find the net vapor production. Note that to make the net vapor productions consistent, the resulting α_{mean} values from the α_{mean} integration are divided by the overall area of the diverging part at each diffusion angle, thus giving $\beta_{mean} = \alpha_{mean}(\iint_{x,y_1}^{x,y_2} dA_i)/(\iint_{x,y_1}^{x,y_2} dA_i)_{DA}$.

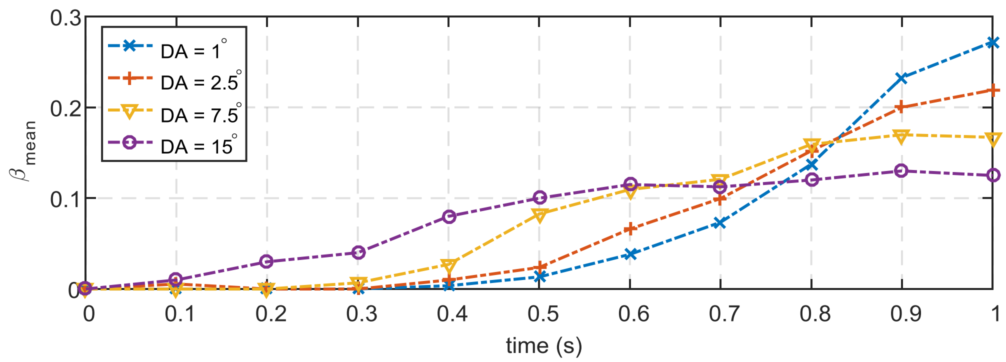

Fig. 37: Temporal distribution of β_{mean} in a single flow-through time for the LNG cavitating flow in the nozzles with diffusion angles of DA = 1º, 2.5º, 7.5º, and 15º.

It is observed in the figure that with the increase of *DA* up to 7.5º larger mean vapor values are initially generated in the domain up to the time instance of $t \cong 0.82$ s. After $t = 0.82$ s, this trend is reversed (inflection point) such that smaller mean values are produced at larger *DA*. In the *DA* = 15º case, the inflection point seems to occur earlier around $t = 0.65$ s. Such behavior indicates stronger vaporization before the occurrence of inflection point. After $t = 0.65$ s, the vaporization rate diminishes and stronger condensation processes occur in the *DA* = 15º case compared to the smaller diffusion angles. At the instance of inflection, larger thermally-influenced flow gradients within larger recirculating zones improve the instability of the flow at larger *DA* through promoting collapse (and condensation) processes which prevent the formation of quasi-stable fully vapor regions typically seen at smaller angles [115,165]. Particularly, this process seems to be accelerated at *DA* = 15º where stronger shedding mechanisms induce stronger instabilities with larger flow gradients. At smaller diffusion angles, e.g. *DA* = 1º, absence of such strong gradients causes the vaporization to be dominant compared with the condensation [100].

6.2.4.2. Spectral Analysis of the Probed Flow Fields

Effects of the nozzle diffusion angle on the instability behavior of in-nozzle LNG cavitation flow can be further illustrated through fast Fourier transform (FFT) analysis. Fig. 38 shows the distributions of the FFT of the of the time history of pressure at the probe location ($x/b,y/b$) = (27.02,1.10) for the simulated diffusion angles of DA = 1º, 2.5º, 7.5º, and 15º, under the cavitation condition of Ca = 1.41. FFT calculation follows the same procedure as described in Section 6.1.4.2 and is performed over about three flow-through times of progress. At the largest DA (Fig. 38(d)), pressure spectra show larger peaks at smaller frequencies as compared with the smaller DA (Fig. 38(a)-(c)), suggesting that the increase of diffusion angle enhances the pressure-based acoustic noise. The characteristic frequencies in Fig. 38 are detected at small frequency range, regardless of the diffusion angle. These frequencies are found to be mainly correlated to the alternate collapse/inception process of the cavity structures and/or the low-frequency behavior of the elongated vortex cavities, in addition to the typical characteristic vortex shedding frequencies. At DA = 1º (Fig. 38(a)), the maximum amplification rate frequencies at f = 42.50 and 40.0 Hz represent the shear layer vortex shedding instability, while the $f \cong$ 180.0 Hz peak pertains to the low-frequency behavior of the elongated cavities. At DA = 2.5º (Fig. 38(b)), the maximum amplification rate frequency occurs at f = 40.0 Hz and is due to the vortex shedding. The second- and third-largest peaks at $f \cong$ 10.0 and 80.0 Hz are respectively caused by the cavity collapse/breakdown processes and the low-frequency behavior of the elongated cavities. A similar spectral evolution is predicted at DA = 7.5º (Fig. 38(c)) and 15º (Fig. 38(d)), with the difference that the maximum amplification rate frequency at DA = 7.5º, i.e. f = 25 Hz, is due to the low frequency behavior of the elongated vortex cavities, whereas at DA = 15º (i.e. f = 17.5 Hz) is because of the alternating cavity collapse/inception processes with over-pressures. The dominant vortex shedding frequencies at DA = 7.5º and 15º are respectively found at $f \cong$ 50.0 and 41.0 Hz. The secondary peaks appearing with smaller magnitudes of power after these characteristic peaks are likely attributed to the smaller vapor structures shed at higher frequencies and/or the harmonics of the main vortex shedding [100,206]. The pressure time histories shown in Fig. 38(e)-(h) further indicate the predicted characteristic frequencies.

(a)

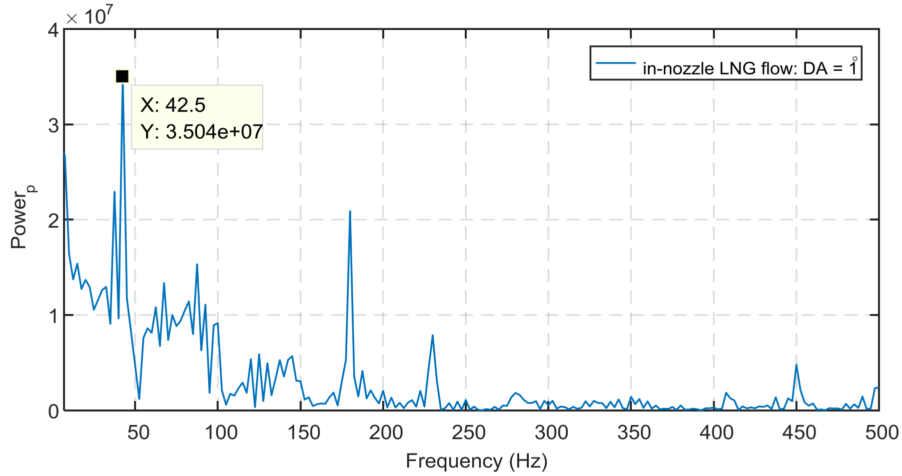

× 10^7
in-nozzle LNG flow: DA = 1°
X: 42.5
Y: 3.504e+07
Power_p
Frequency (Hz)

(b)

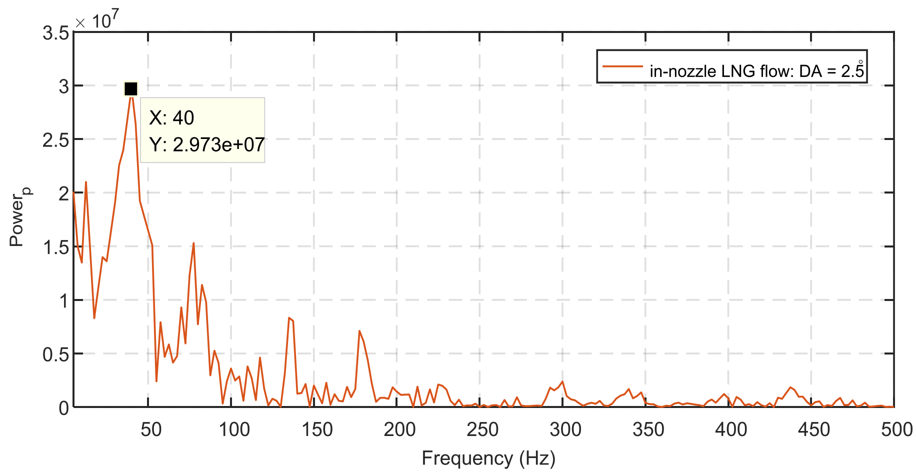

× 10^7
in-nozzle LNG flow: DA = 2.5°
X: 40
Y: 2.973e+07
Power_p
Frequency (Hz)

(c)

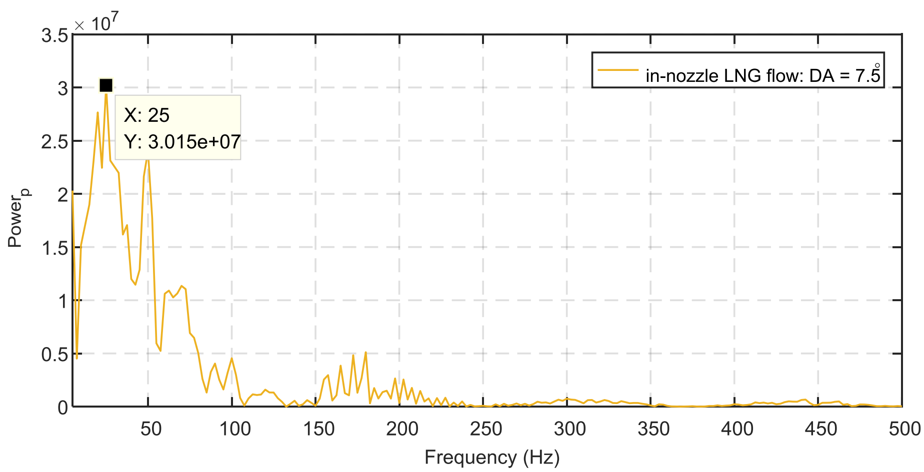

× 10^7
in-nozzle LNG flow: DA = 7.5°
X: 25
Y: 3.015e+07
Power_p
Frequency (Hz)

(d)

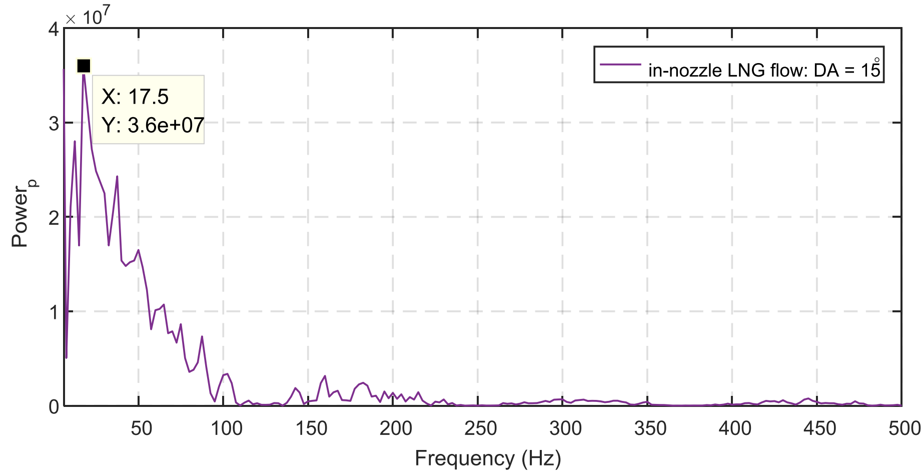

× 10^7
X: 17.5
Y: 3.6e+07
in-nozzle LNG flow: DA = 15°
Power_p
Frequency (Hz)
0
1
2
3
4
50
100
150
200
250
300
350
400
450
500

(e)

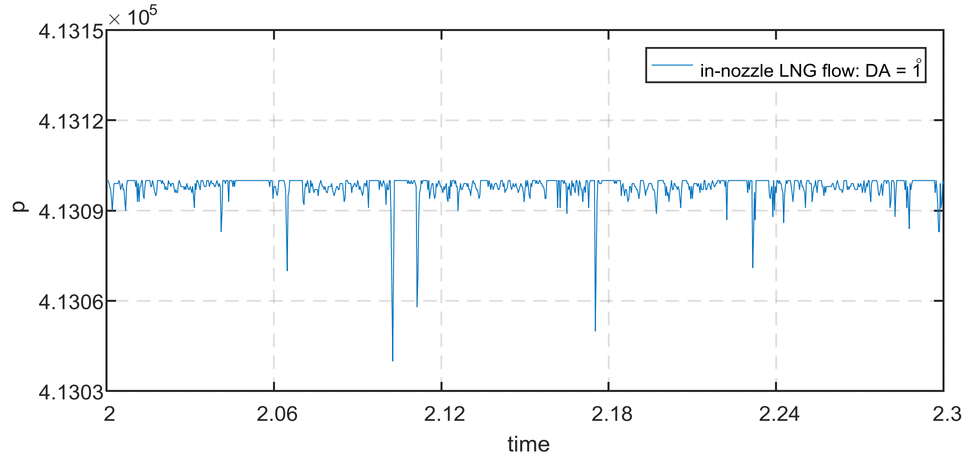

× 10^5
in-nozzle LNG flow: DA = 1°
p
time
4.1315
4.1312
4.1309
4.1306
4.1303
2
2.06
2.12
2.18
2.24
2.3

(f)

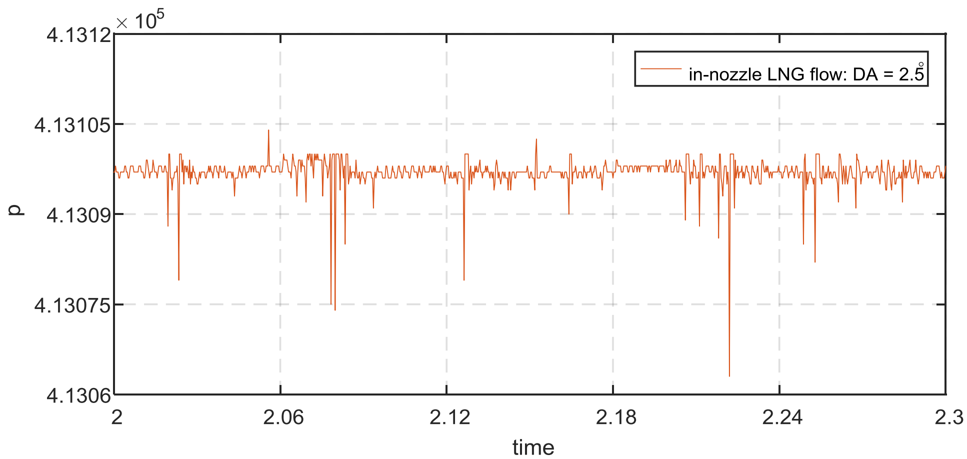

× 10^5
in-nozzle LNG flow: DA = 2.5°
p
time
4.1312
4.13105
4.1309
4.13075
4.1306
2
2.06
2.12
2.18
2.24
2.3

(g)

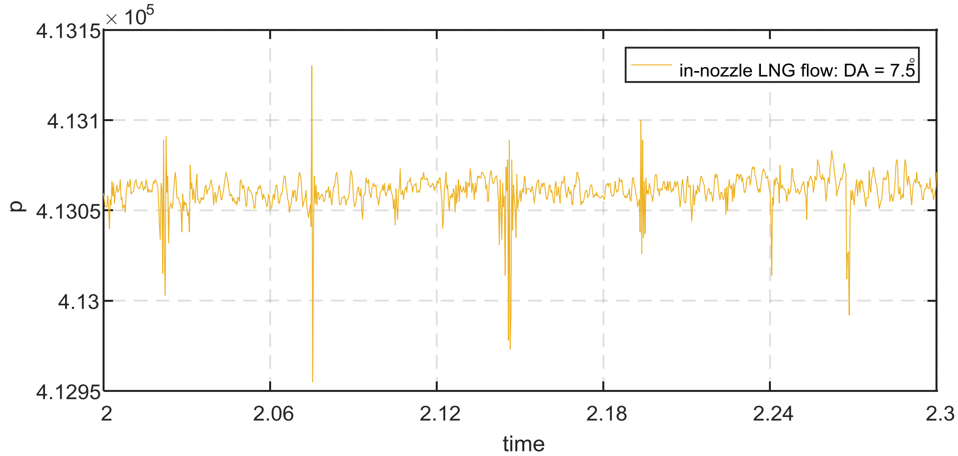

(h)

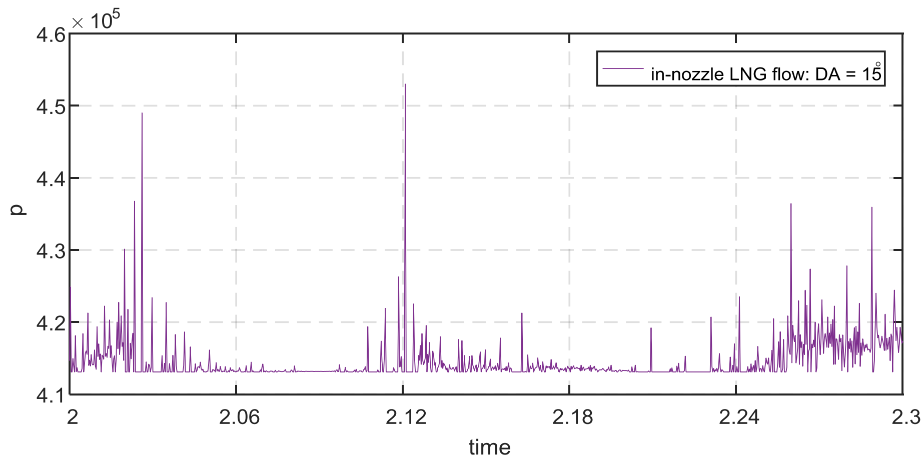

Fig. 38: Spectrogram and time history of pressure at the probe location (x/b,y/b) = (27.02,1.10) for the in-nozzle LNG cavitating flow with nozzle diffusion angles of DA = 1º (a,e); 2.5º (b,f); 7.5º (c,g); and 15º (d,h).

Nozzle Diffusion Angle (DA)	Dominant Shedding Frequency (Hz)	Strouhal Number (St)
1º	42.5	0.237
2.5º	40	0.217
7.5º	25	0.213
15º	17.5	0.214

Table V: Comparison of St numbers for the in-nozzle LNG cavitating flow with nozzle diffusion angles of DA = 1º, 2.5º, 7.5º, and 15º. Data correspond to the pressure time history probed at (x/b,y/b) = (27.02,1.10).

Corresponding Strouhal numbers *St* associated with the calculated dominant frequencies in Fig. 38 is given in Table V. Smaller shedding frequencies and *St* numbers are detected at larger diffusion angles, indicating the earlier occurrence of shedding process and instability, especially at smaller frequencies, as *DA* increases. *St* number at *DA* = 15º experiences a little increase, opposed to the decreasing trend seen in the smaller *DA* tests. Such behavior illustrates the dominance of unsteady vortex structures and inertia effects in governing the flow instability mechanisms as compared to the thermal parameters at higher *DA* values. This dominance seems to relax as *DA* decreases resulting in the observed increasing of *St*. The current observations are relevant to the experiments of Kelly et al. [114,122] on the cavitation of fluoroketone, concluding that the increase of thermal effects leads to an effective increase in shedding frequency. In the present tests, thermal effects seem to reduce their influence on the flow instability behavior (based on the pressure time history) at the largest *DA* = 15º. Nevertheless, the presence of temperature-based gradients is suggested to trigger the instability of cavitating structures at larger frequencies mainly through altering the density and vapor fraction evolutions [43,90,127]. This can be better shown in Fig. 39 comparing the power spectrum density (PSD) of the probed vapor fraction field at (*x/b*,*y/b*) = (27.02,1.10) for the given diffusion angles; for example at *DA* = 15º, PSD rises up for most part of the higher frequency domain.

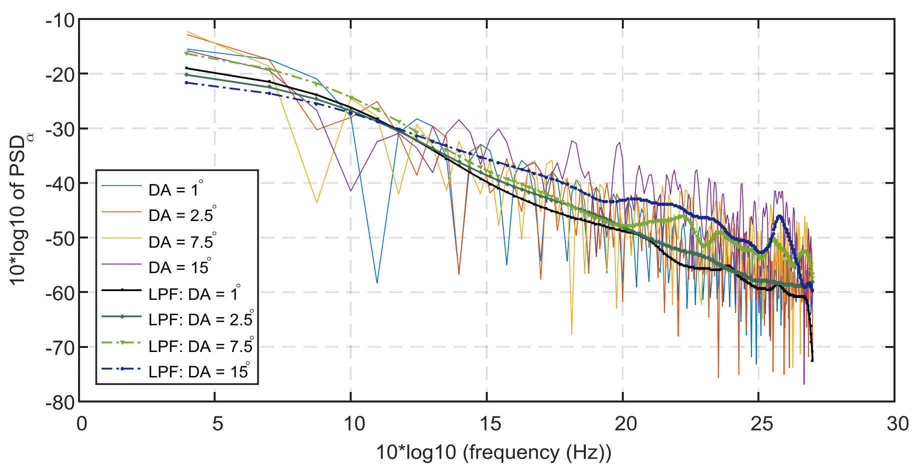

Fig. 39: Log-scale plot of vapor fraction spectra at the probe location (x/b,y/b) = (27.02,1.10) for the in-nozzle LNG cavitating flow with nozzle diffusion angles of DA = 1º, 2.5º, 7.5º, and 15º. LPF stands for low-pass filtered data calculated through a zero-phase digital filtering approach that uses a finite impulse response (FIR) section filter [181].

Fig. 38 and Table V also indicate that the presence of stronger vapor generation/collapses at larger *DA* strengthens the flow disturbance, especially in smaller frequency domain, resulting in faster cavity breakup/inception incidents compared to the smaller diffusion angles. This is mainly due to the faster separation of the flow past the nozzle throat which strengthens the re-entrant jet and vortical structures and promotes stronger spatial gradients. Decreasing *DA* seems to damp out the large-scale disturbances in the flow, resulting in the formation of smaller-scale vortex structures shedding at larger frequencies [81]. In particular at the smallest *DA* = 1º, the generated long thin cavity on the lower wall of the nozzle is not able to promote an unstable cloud cavitation, although its closure region coincides with moderate adverse pressure gradients on the lower wall (see flow contours in Fig. 31(a)-(b) and 32(a)). Such a behavior is attributed to the cavity size being small and thin which causes an uninterrupted interaction between the weak re-entrant jet and the cavity interface upstream of the jet, thus disallowing the formation of vapor structures in the form of large vortex cavity clouds [157]. The present observations further confirm the conclusions of Ji et al. [118,119] and Kawanami et al. [175] studies pointing out that the cloud cavity unsteadiness is intimately associated with shear cavity thickness and re-entrant jet characteristics.

It is noted that the distributions of Fig. 38-39 are consistent with the previous observations of the vorticity contours in Fig. 32 stating that under the geometrical constraint of nozzle diffusion angle, significant changes in the vortex-cavity interaction mechanisms are resulted. The vortex shedding patterns alter such that the larger stable cavities at smaller diffusion angles delay shedding of the vortex structures, hence making the shedding period smaller (larger shedding frequency) [43,57,126]. The low frequency behavior of the stronger vortex cavities at larger *DA*, which is caused by the instability of larger recirculating zones, affects the subsequent formation and collapse of vapor clouds by accelerating vortex shedding processes [70,126].

6.2.5. Velocity Fluctuation Profiles

To further illustrate the effects of diffusion angle on the in-nozzle LNG cavitating flow characteristics, Fig. 40 compares the evolutions of dimensionless mean-square velocity fluctuations along the transverse line stations of x/b = 16.21 and 32.43 in the x-wise direction (see Fig. 27) for the nozzle diffusion angles of DA = 1º, 2.5º, 7.5º and 15º. Streamwise normal ($\overline{u'u'}$), transverse normal ($\overline{v'v'}$), and shear ($\overline{u'v'}$) velocity fluctuations are evaluated in the figure for two flow-through times after reaching statistically steady state. The profiles are non-dimensionalized using the local mean velocity at each station. The velocity fluctuations at the first station at x/b = 16.21 (Fig. 40(a)-(c)) are increased with the increase of DA. This behavior can be also detected at the second station x/b = 32.43 (Fig. 40(d)-(f)) except in the DA = 15º case where the streamwise and shear fluctuations are largely decreased compared to that at the smaller angles. The reduction in these components highlights the interactions of vortex and cavity structures. As indicated in Sections 6.2.3-6.2.4, the increased cavitation instability within the cores of strong streamwise vortices at larger *DA* is the main reason to suppress the coupling between streamwise and transverse velocity fluctuations [91,100,127].

In the streamwise direction from the first to the second station, where the flow is exposed to larger domain area, velocity fluctuations are observed to decrease in the *DA* = 1º, 2.5º, and 7.5º tests. This is likewise shown in the *DA* = 15º case with the difference that the transverse component tends to increase in the *x* direction. The increase does not however seem to be large enough to alter the overall decreasing trend of $\overline{u'v'}$ that is similarly seen at the smaller angles. Improvement of the transverse component illustrates the presence of larger roll-up of vortical structures and recirculation zones at the angle of 15º, as a result of which stronger shedding mechanisms are generated within strong vortex-cavity interactions, as observed in Fig. 39. The strengthened vortex structures are specifically expected to appear with significant vorticity tilting and stretching in the transverse direction, which is mainly due to the improved mean transverse velocity gradients. This conclusion is consistent with the results of Section 6.2.3 (see the $x/b >$ 16.0 region in Fig. 35) declaring that at *DA* = 15º vorticity in the streamwise direction shows an overall improvement compared to the smaller diffusion angles. Note that the non-zero velocity fluctuations in near-wall regions (see for example the $y/b >$ 7.0 region of Fig. 40(a)) are due to the inclined angle of the reference transverse line(s) with respect to the nozzle lower wall which makes two non-zero components of velocity at the wall. The presence of sheet cavity residuals evolving unsteady on the wall can even further enhance the wall velocity fluctuations, as reported in [120,127].

The observed increase in the velocity fluctuations at larger *DA*, at the first station x/b = 16.21 (Fig. 40(a)-(c)), can be further explained by the presence of highly unsteady re-entrant jets promoting stronger vapor-liquid interactions through thermally-affected density, pressure, and viscosity gradients [158]. This process is accompanied by improved growth and collapse of cavity spots which trigger the production of small-scale instabilities and shedding processes in recirculating and separated flow regions [92,165,172]. These observations confirm that more shedding of the cavity spots magnify the level of velocity fluctuations particularly in the large-scale vortex structures of wake regions with highly-unsteady cavitating clouds [70,119]. This behavior changes at the downstream station x/b = 32.43 (Fig. 40(d)-(f)), e.g. transverse and shear fluctuations do not increase noticeably as diffusion angle increases from 1º to 2.5º, contrary to the behavior at the upstream station. Also in the *DA* = 15º test, significant reductions are observed in the streamwise normal and shear stress fluctuations compared to the DA = 7.5º case. This is estimated to be due to the presence of stronger vapor collapse (and condensation) processes at DA = 15º (see Fig. 41), altering the pre-dominance of inertia in phase change mechanisms through strengthening the instability of coherent vortical structures [125,129].

<u>*x/b* = 16.21</u>

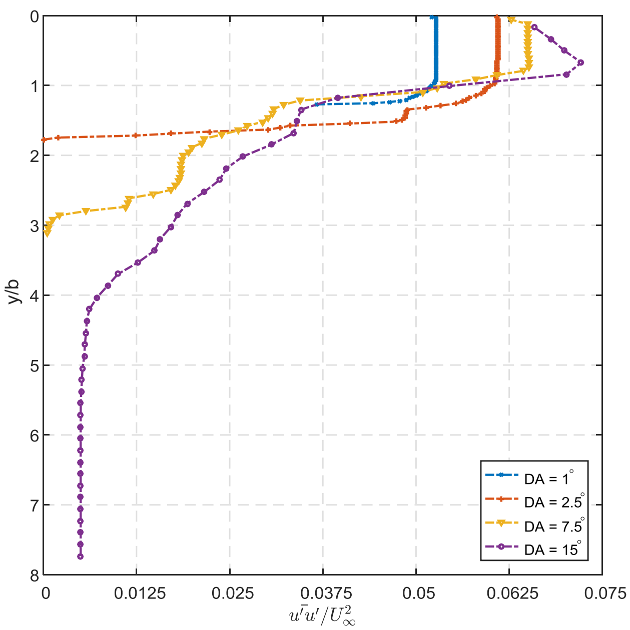

(a)

<u>*x/b* = 32.43</u>

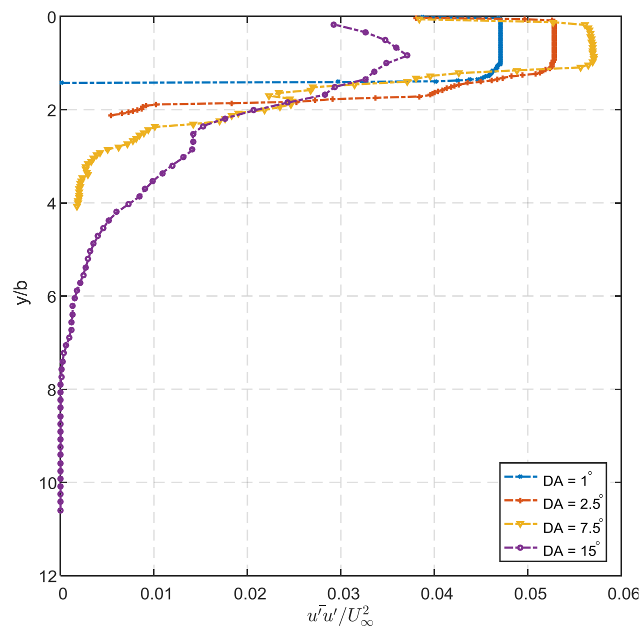

(d)

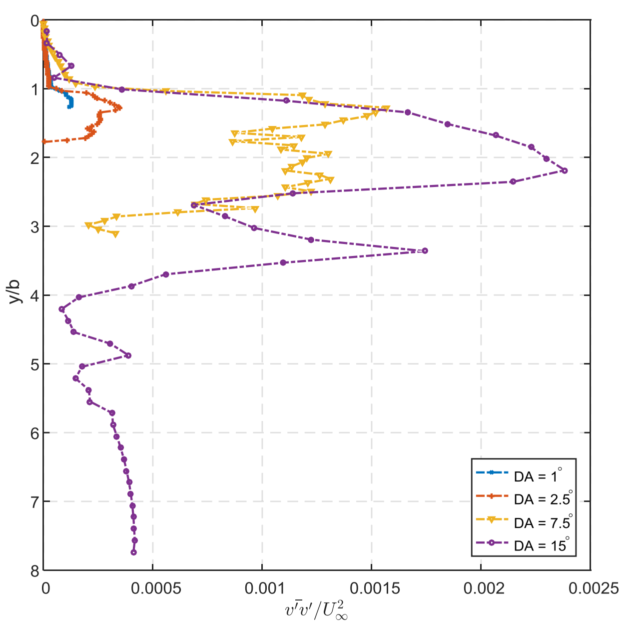

(b)

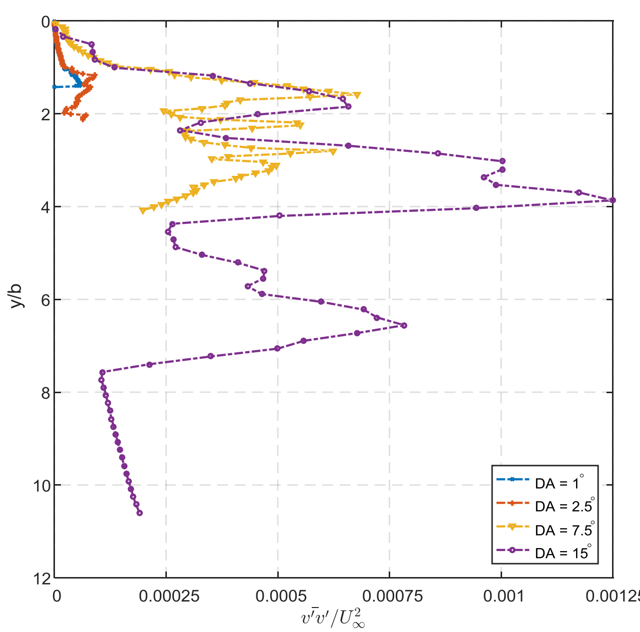

(e)

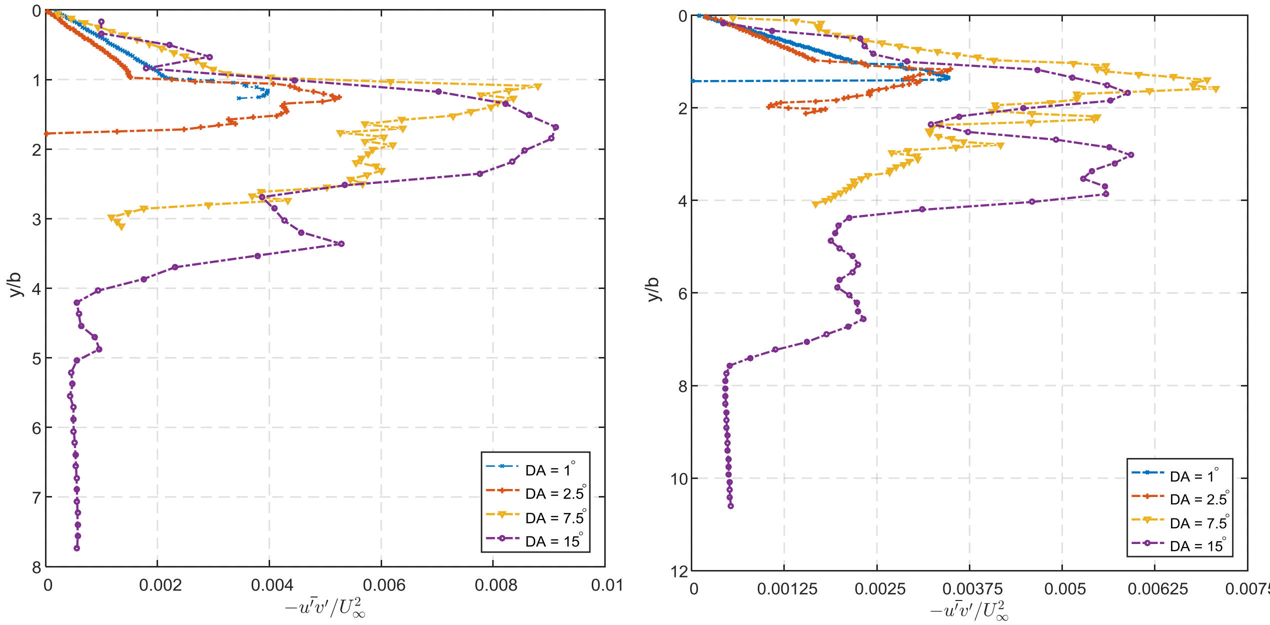

(c) *(f)*

Fig. 40: Profiles of dimensionless mean-square velocity fluctuations along the transverse reference line stations of x/b = 16.21 and 32.43 for the in-nozzle LNG cavitating flow with nozzle diffusion angles of DA = 1º, 2.5º, 7.5ºand 15º: (a,d) streamwise normal; (b,e) transverse normal; and (c,f) lateral shear components.

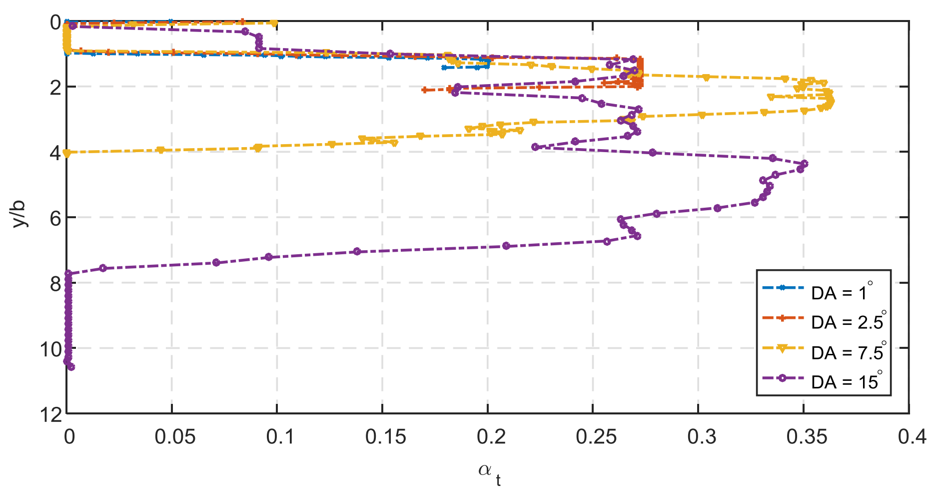

Fig. 41: Profiles of temporally-averaged vapor fraction field along the transverse reference line station of x/b = 32.43 for the in-nozzle LNG cavitating flow with DA = 1º, 2.5º, 7.5º and 15º. Time averaging is performed over 100 equally-spaced time steps within two flow-through times after reaching statistically steady state. Vapor evolution at DA = 15º experiences stronger condensation processes as against the smaller DA.

Further in Fig. 40, it is notable that the overall decrease of the fluctuations in the transverse direction after the peak -- visible in all the plots of Fig. 40 -- pertains to the local reductions of mixture velocity and density due to the presence of vapor spots. The local drops of mean velocity and density in the cavitating zones can be considered as a primary factor in suppressing the velocity/shear fluctuations, which occurs likely by modifying the local mass transfer patterns between liquid and vapor phases [91,165,170]. Related to this, Fig. 42 depicts the streamwise distribution of time-averaged mass flow rates along five transverse line stations of *x/b* = 8.10, 16.21, 24.32, 32.43, and 40.54 for the simulated diffusion angles. The flow rates are calculated using the formula given in Section 6.1.5, for the flow progress from *t* = 0.0 s to *t* = 0.95 s. It is indicated that the nozzle with the smallest diffusion angle has the lowest mass flow rate, i.e. due to larger reductions of mixture density in a smaller area, whereas the case with the largest *DA* delivers the highest rate. In the streamwise direction, similar linearly-increasing flow rates are seen in all the tests with larger slopes at larger *DA*. These observations suggest an improvement in the occurrence of local pressure drops, and thus in the formation of low-pressure regions, at larger *DA* as the flow develops inside the nozzle. This happens despite the fact that the flow at larger *DA* experiences larger inertia. This is consistent with the previous observations stating that larger diffusion angles cause stronger mass transfer variations between the liquid and vapor, i.e. due to the presence of larger cavitating regions with strengthened instabilities. These regions are generated mainly by stronger local pressure drops in the recirculating zones [135,174].

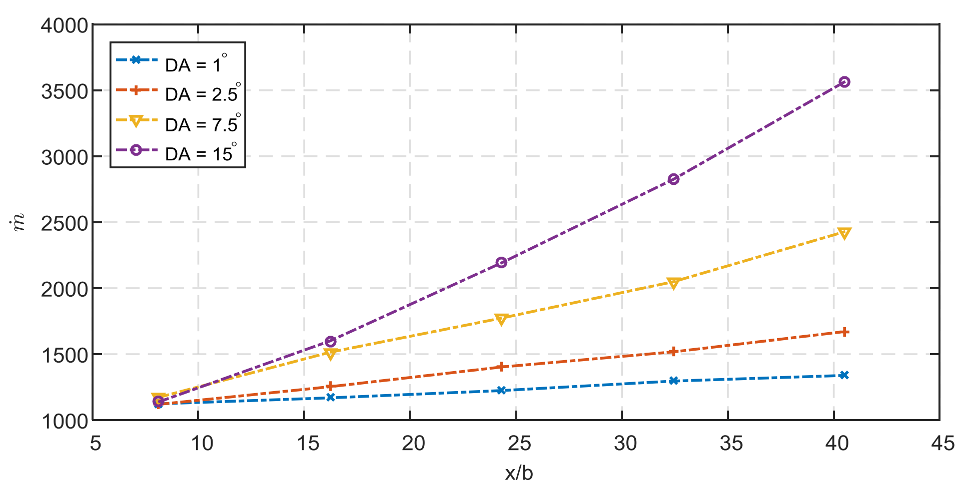

Fig. 42: Distributions of time-averaged mass flow rates (g/s) at transverse line stations of x/b = 8.10, 16.21, 24.32, 32.43, and 40.54 for the in-nozzle LNG cavitating flow with DA = 1º, 2.5º, 7.5º and 15º.

6.3. Effects of Interfacial Tension Forces

This section addresses the effects of interfacial tension forces on the behavior of LNG cavitation flow inside the nozzle geometry of Section 4.1. The numerical model of Section 3.2 is first modified to incorporate the interfacial tension force in the cavitation solver. The modified solver is then used to simulate the baseline test case of 2D in-nozzle cavitating flow of LNG described in Sections 4.5 and 5.1. Instability characteristics and phase-change mechanisms of the in-nozzle LNG cavitating flow with and without the influence of interfacial tension forces are particularly evaluated.

6.3.1. Methodology

The effects of interfacial tension forces on cavitation patterns in cryogenic fluids including LNG are not addressed sufficiently in literature especially on the unsteady compressible large-scale cavity structures. Therefore, the focus of the present section is to fill this gap by using a simulation model that is able to effectively describe the influence of such forces on LNG phase-change mechanisms. Since the interfacial tension force is usually neglected in most practical applications, such a model can potentially improve the understanding of detailed dynamics of LNG cavitating shear flows by characterizing the time-dependent interactions of vapor cavity structures and shear layer instabilities in LNG-based turbomachinery.

The present model is an extended version of the cryogenic cavitation model presented in Section 3.2 with the main difference being here that a surface tension force term is added to the governing equations. To do so, the De Villiers et al. [102] approach through the continuum surface force (CSF) model of Brackbill et al. [48] is employed by which a surface tension source term in volumetric form is incorporated into the momentum Equation (18), as follows:

$$\begin{gathered}\frac{\partial(\rho_m\,\boldsymbol{u})}{\partial t}+\nabla\cdot(\rho_m\,\boldsymbol{u}\boldsymbol{u})\;=-\nabla p+\nabla\cdot[\,\mu_m(\nabla\boldsymbol{u}+(\nabla\boldsymbol{u})^T)]\\+\frac{\partial}{\partial t}\left((1-\alpha)\,\frac{\psi_l\,\Delta T\rho_v L}{T_\infty}\,\boldsymbol{u}\right)+\nabla\cdot\left((1-\alpha)\,\frac{\psi_l\,\Delta T\rho_v L}{T_\infty}\,\boldsymbol{u}\boldsymbol{u}\right)+\boldsymbol{F_s}\end{gathered} \tag{32}$$

where $\boldsymbol{F_s}$ is the surface tension force found by

$$\boldsymbol{F_s}=\gamma\kappa_s(\nabla\alpha) \tag{33}$$

in which κ_s is the curvature of the vapor-liquid interface given by

$$\kappa_s=\nabla\cdot\left(\frac{\nabla\alpha}{|\nabla\alpha|}\right), \tag{34}$$

and γ is the surface tension coefficient. A generic interface property library which enables the solver to capture the LNG vapor-liquid interface properties, including the surface tension coefficient, for a broad range of temperature and pressures is also coupled to the surface tension term. The library is implemented in a similar manner to the generic thermophysical model discussed in Section 3.2.3.

6.3.2. Effects of Interfacial Tension Forces on the In-nozzle LNG Cavitation Flow

The extended model of Section 6.3.1 is applied to the baseline simulation of Section 5.1 to examine the interfacial tension effects on the behavior of 2D in-nozzle LNG cavitation flow. The simulation setup is similar to the given description of Sections 4.3 and 5.1 except for the maximum acoustic Courant number is set to 1.0 to improve numerical stability. Fig. 43 compares the evolutions of LNG cavitation in the diverging part of the nozzle ($0.0 < x/b < 35.0$) with and without the presence of interfacial tension forces (ITF), at the time instant of t = 0.98 s. The influence of ITF can be overall illustrated by visual inspection of the behavior of re-entrant jets: as indicated in Fig. 43(a), the presence of interfacial tension forces -- acting within vapor-liquid interfacial regions -- reshapes the cavitating patterns such that a delay in the breakup of cavity spots is observable compared to the case without ITF [176]. This delay seems to occur through decaying the progress of re-entrant jets. In other words, the presence of interfacial force causes more local stability in the flow by resisting the progress of re-entrant jets through enhancing the local vaporization processes inside the vapor regions (Fig. 43(b)), thus relaxing the local growth of large-scale disturbances (Fig. 43(c)).

The influence of interfacial tension forces on suppressing the instability in the in-nozzle LNG cavitation flow can be further indicated in Fig. 44(a)-(b) respectively showing the time histories of relative pressure and vorticity magnitude fields at probing station ($x/b,y/b$) = (43.24,1.10) over the flow progress of a single flow-through time. The figure evaluates the LNG cavitation field with and without the presence of ITF. Corresponding PSD of the pressure time histories are also displayed in Fig. 44(c) for the time period of about three flow-through times. As seen, smaller vorticity magnitudes with reduced fluctuations of relative pressures, particularly in the cavitation period ($t > 0.55$ s), are detected in the ITF case (Fig. 44(a)-(b)). This is also reflected in the PSD distributions (Fig. 44(c)): smaller PSD variation (especially in larger frequencies) is seen in the ITF test, indicative of relaxing effects of ITF on cavitation instability. These observations are in agreement with Lü et al. [177] and Shah et al. [178] works stating that interfacial tension force has a marked stabilizing effect on cavitation. Hence, it can be demonstrated that the exclusion of interfacial tension force can lead to an additional diffusion in the interfacial regions of the LNG cavitation flow particularly in the areas with stronger vapor condensation, e.g. re-entrant jets piercing through the vapor cavities [179].

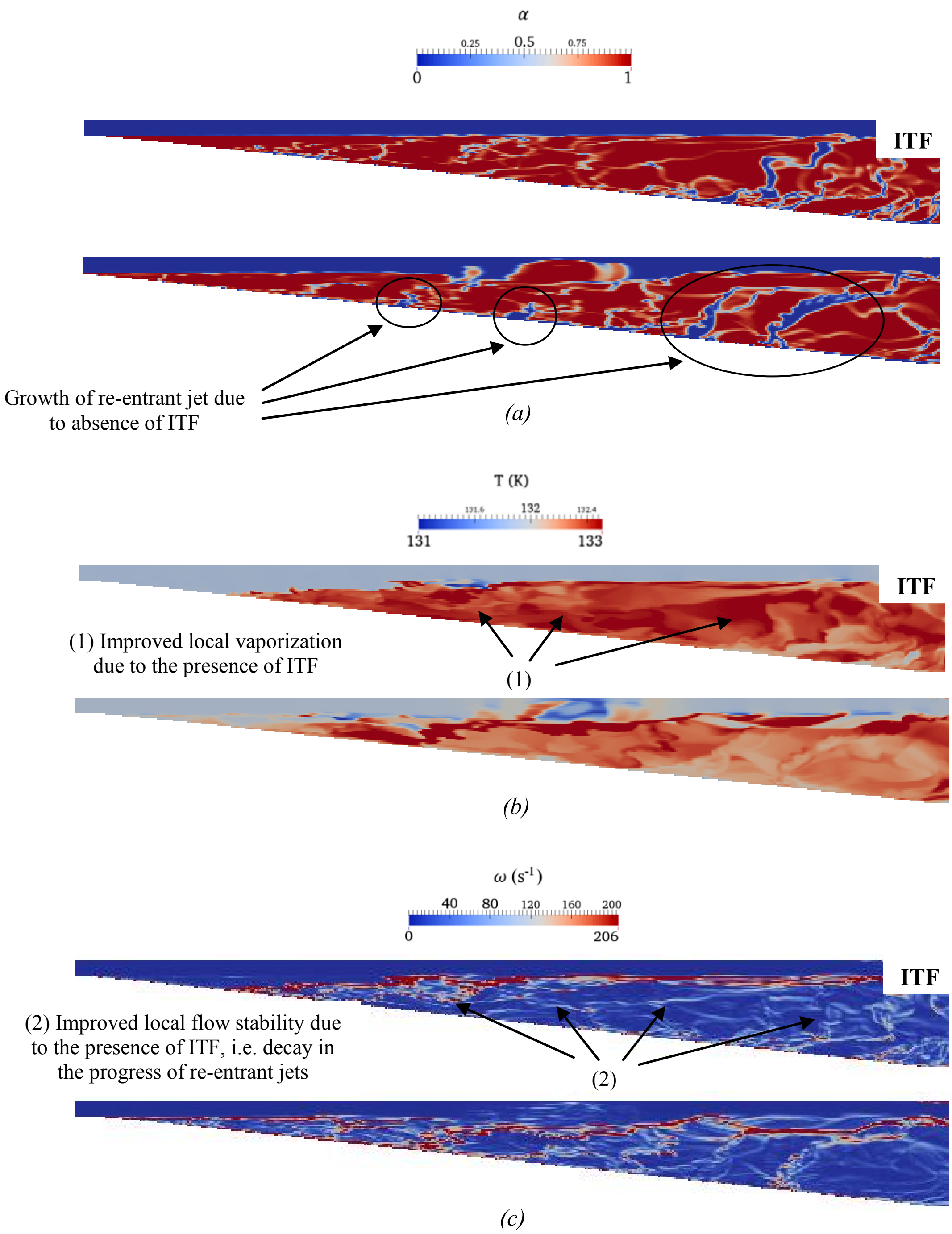

Fig. 43: Instantaneous contours of (a) vapor fraction; (b) temperature (K); and (c) vorticity magnitude (1/s) at t = 0.98 s for the baseline in-nozzle LNG cavitating flow with and without the presence of interfacial tension force. ITF-labeled contours present the case with interfacial tension force.

(a)

(b)

(c)

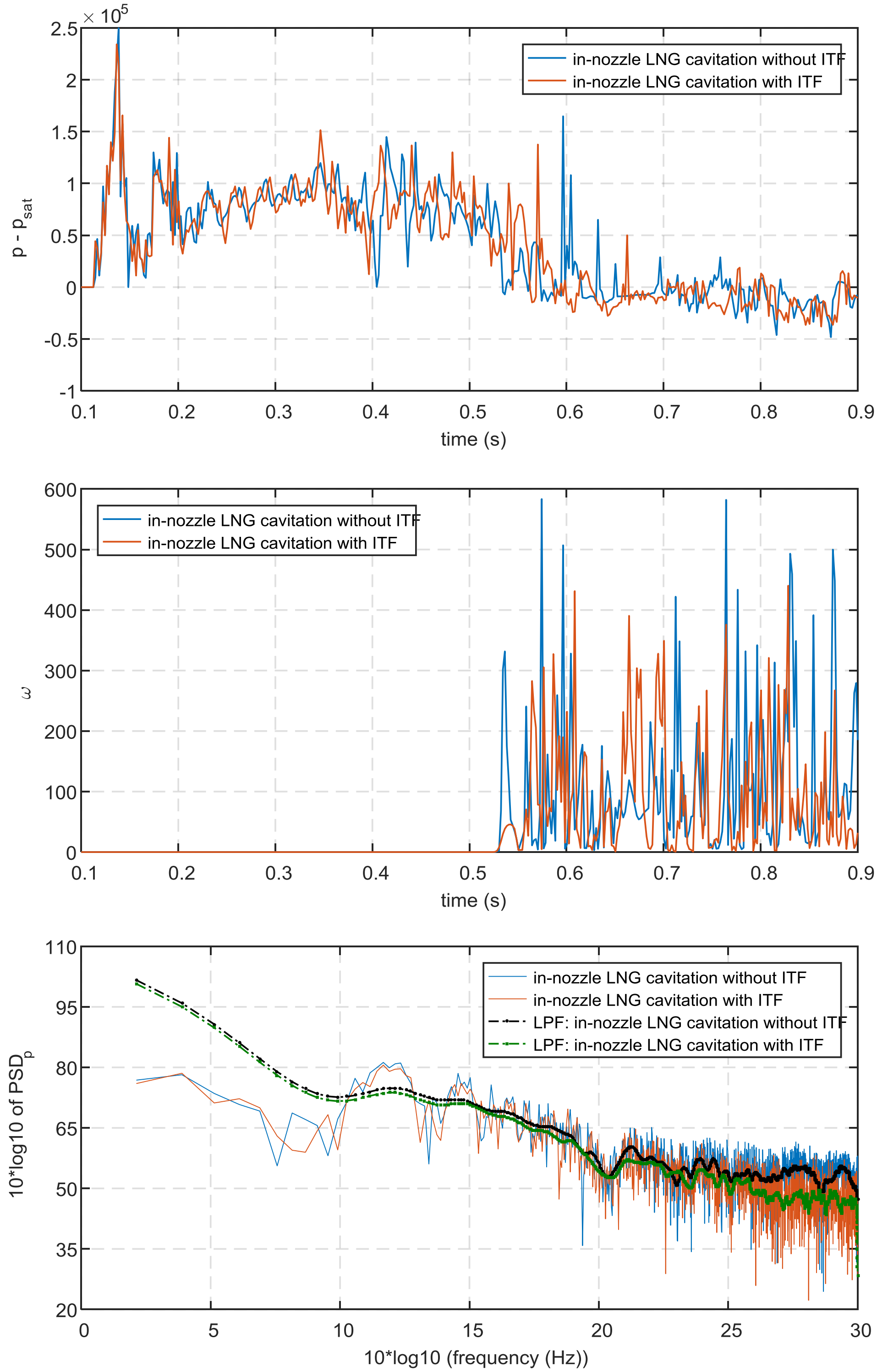

Fig. 44: Time histories of (a) relative pressure (Pa) and (b) vorticity magnitude (1/s); and (c) log-scale plot of pressure spectra (W/Hz) at the probe location (x/b,y/b) = (43.24,1.10) for the baseline in-nozzle LNG cavitating flow with and without the presence of interfacial tension force (ITF). LPF stands for low-pass filtered data.

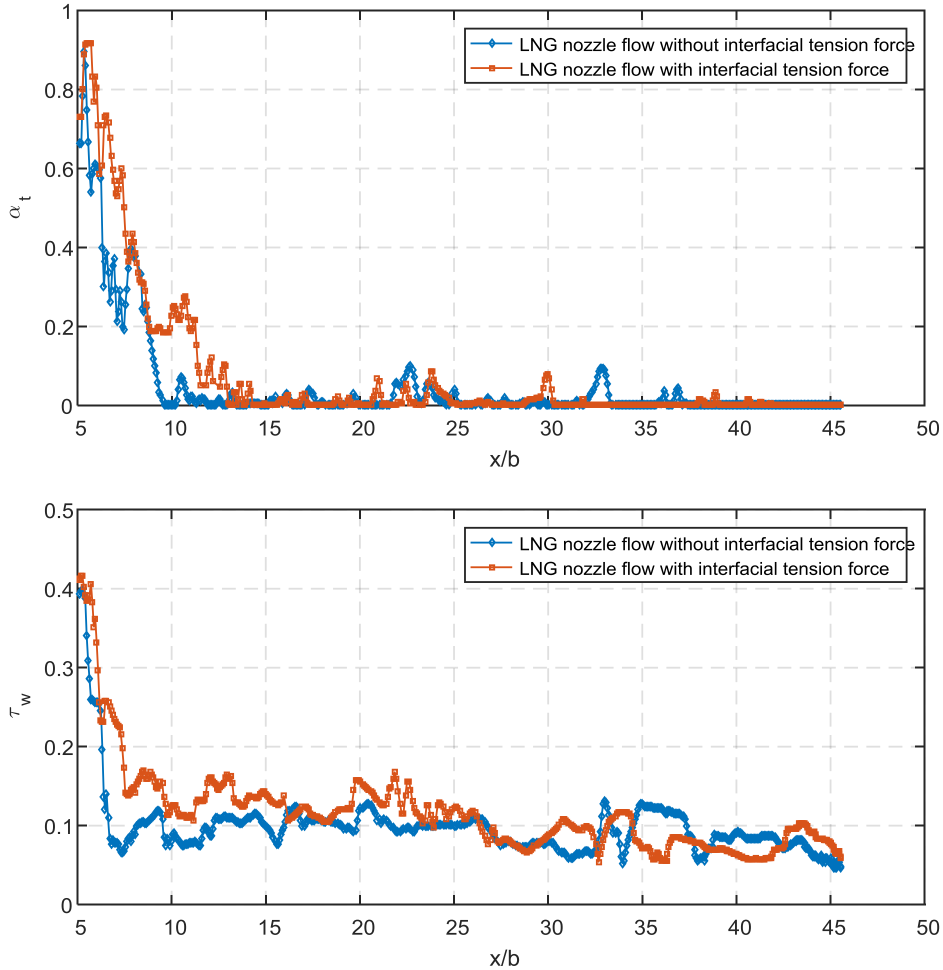

(a)

(b)

Fig. 45: Distributions of temporally-averaged (a) vapor fraction and (b) shear stress magnitude (Pa) along the lower wall of the nozzle for the baseline in-nozzle LNG cavitating flow with and without the presence of interfacial tension force. Time averaging is conducted over 100 equally-spaced time steps within two flow-through times after reaching statistically steady state.

In the distributions of Fig. 43-44, it is also notable that the vapor fraction field is largely influenced by the surface tension effects imposed from the bounding walls. These effects tend to decrease in the streamwise direction of the nozzle especially around the frontal side of the cloud cavity where the cavity elongation reaches a maximum value. As a result of elongation, the pressure due to surface tension force decreases in the cavity frontal region, so yielding a smaller influence on the cavity deformation [100,180]. In near-wall regions, however, addition of the interfacial tension forces to the wall shear stress enhances the vapor production especially close to the throat. This can be better illustrated in Fig. 45(a)-(b) that evaluate, respectively, the distributions of time-averaged shear stress and vapor fraction fields along the lower wall of the nozzle in the simulated tests. The improved wall shear stress and vapor production in the ITF case can be more clearly detected in the upstream $5.0 < x/b < 15.0$ region of the plots.

To further examine the impact of interfacial tension forces on the present in-nozzle LNG cavitation flow, Fig. 46 compares the temporal variation of spatially-averaged vapor fraction field in the aforementioned tests over approximately two flow-through times of progress. Note that the spatially-averaged mean vapor fractions are found using the given formula in Section 6.1.4.1 ($\alpha_{mean} = \frac{\iint_{x,y_1}^{x,y_2} \alpha_i dA_i}{\iint_{x,y_1}^{x,y_2} dA_i}$). As shown, the presence of interfacial forces only slightly improves the net vapor production in the domain, as observed after the time instant t = 1.12 s. Evaluation of this conclusion against the observations of Fig. 43-44 signifies the pre-dominance of temperature-dependent inertia and convective forces in the in-nozzle LNG vaporization processes, while interfacial forces emerge as secondary importance; their major influence is through decaying the local progress of re-entrant jets and/or relaxing the local instabilities.

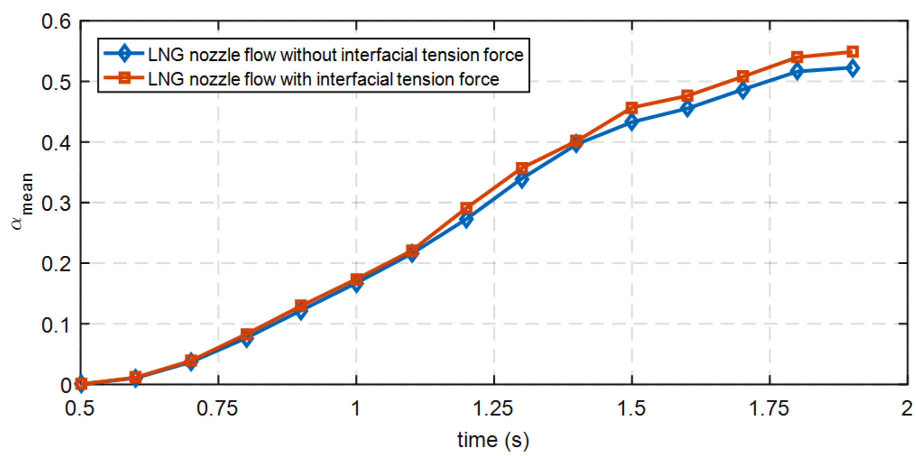

Fig. 46: Temporal distributions of spatially-averaged vapor fraction field over about two flow-through times for the baseline in-nozzle LNG cavitating flow with and without the presence of interfacial tension force.

7. Numerical Simulation of 3D In-nozzle Cavitating Flow of LNG

This chapter explores the compressible laminar to transitional cavitating flow of LNG inside a 3D planar configuration of the Laval nozzle geometry of Section 4.1. Global behavior of the 3D LNG cavitating structures in the planar nozzle at selected time instants is investigated to disclose the time-dependent evolution of LNG cavitating patterns within the first cavitation cycle starting from cavity inception up to cloud cavitation. Instability and cavity-vortex interaction mechanisms are also assessed with the aim of characterizing the three-dimensionality effects in modulating the 3D vapor and vortex structures.

7.1. Numerical Setup

The 3D laminar to transitional cavitating flow of LNG inside the nozzle is built by extruding the 2D domain of Section 4.1 in the spanwise direction for a span length of Δz = 0.22 cm. The 3D simulation is then conducted using the same operating conditions as in Section 4.3 except with reduced maximum acoustic Courant number of 1.0 to improve numerical stability, and use of 448 numbers of processors to speed up computation. Periodic boundary condition is used on the side patches of the extruded geometry. To properly resolve the 3D flow structures, the generated grid along the spanwise direction is carefully evaluated for a thermo-insensitive LNG cavitation test case with three spanwise node numbers of 25, 50, and 75. Corresponding numerical tests to the given three mesh configurations are then performed for a single flow-through time to find the maximum values of pressure in the domain during the simulation time. The spatially-averaged vapor fractions (α_{mean} from Section 6.1.4.1) is also compared at the last recorded time step t = 0.95 s to examine the net vapor productions in the domain.

Number of Nodes in Spanwise Direction	Maximum Pressure (Pa)	Spatially-Averaged Vapor Fraction
25	973326	0.3365
50	993983	0.3223
75	993972	0.3221

Table VI: 3D nozzle mesh convergence study: comparison of flow parameters, i.e. maximum pressure and mean vapor fraction (α_{mean}), for the 3D in-nozzle cavitating LNG flow with different spanwise grid resolutions. Data correspond to approximately one flow-through time of progress.

As noticed in Table VI, the differences are negligible between the medium (50) and fine (75) resolution grids, so the medium mesh resolution with 36,080,000 cells is selected to reduce the computational costs. It is noted that the selection of 50 nodes in z direction for the spanwise length of 0.22 cm in the 3D nozzle test ensures the proper capture of Kolmogorov length scale [75,181,182], given the operating Reynolds number Re = 8720.0, as indicated by Dittakavi et al. [174]. The selected spanwise length of 0.22 cm with uniformly distributed grid number of 50 also results in $\Delta z^{+} \cong 1.36$, satisfying the 3D grid spacing criterion to a good extent [75,174].

7.2. 3D Evolution of Cavity-Vortex Structures in the Cavitation Flow

Fig. 47 shows the time evolution of 3D iso-surface contours of LNG vapor fraction field for vapor structures with α = 0.65 at time instants of t = 0.32, 0.44, 0.57, 0.68, 0.79, and 0.89 s in the diverging part of the nozzle in $4.0 < x/b < 36.0$. To address the cavity-vortex interactions, Fig. 48 further displays the corresponding temporal evolution of iso-surface contours of Q-criterion field with Q = 1000.0 s^{-2} superimposed with the iso-surface contours of vapor fractions with α = 0.95. It is noted that the Q-criterion, which is defined as the second invariant of velocity gradient tensor and commonly used for presenting the 3D vortex structures [167-169], is found by:

$$\boldsymbol{Q} = \frac{1}{2}\left(|\boldsymbol{\Omega}|^2 - |\boldsymbol{Sr}|^2\right) \tag{35}$$

where Ω is the vorticity tensor and Sr is the strain rate tensor. Overall, it is seen that the cavitating flow is made of two parts: first is the attached sheet cavity near the throat region, and the second part is the vapor pockets and/or cloud structures frequently shed off at the rear of the sheet cavity while convecting downstream through non-uniformly covering the domain in mainstream and spanwise directions [164]. A major observation in the given contours is the presence of three-dimensionality that significantly alters the cavitation development behavior compared to the 2D results, such that the sheet and cloud structures emerge with curved closure surfaces, in particular with tightly interacting U-shaped vapor cavities as indicated in Fig. 47. The three-dimensionality specifically causes the entrant jets in the flow to have two components: one in streamwise (re-entrant); and the other in spanwise (side-entrant) direction, e.g. Fig. 47(a) at t = 0.44-0.57 s. These entrant jets which are mainly generated through spanwise pressure and temperature-dependent density gradients hinder the cavity flow from developing in its favorable direction, thus leading the overall shedding behavior to be more complex than the 2D case [165,168].

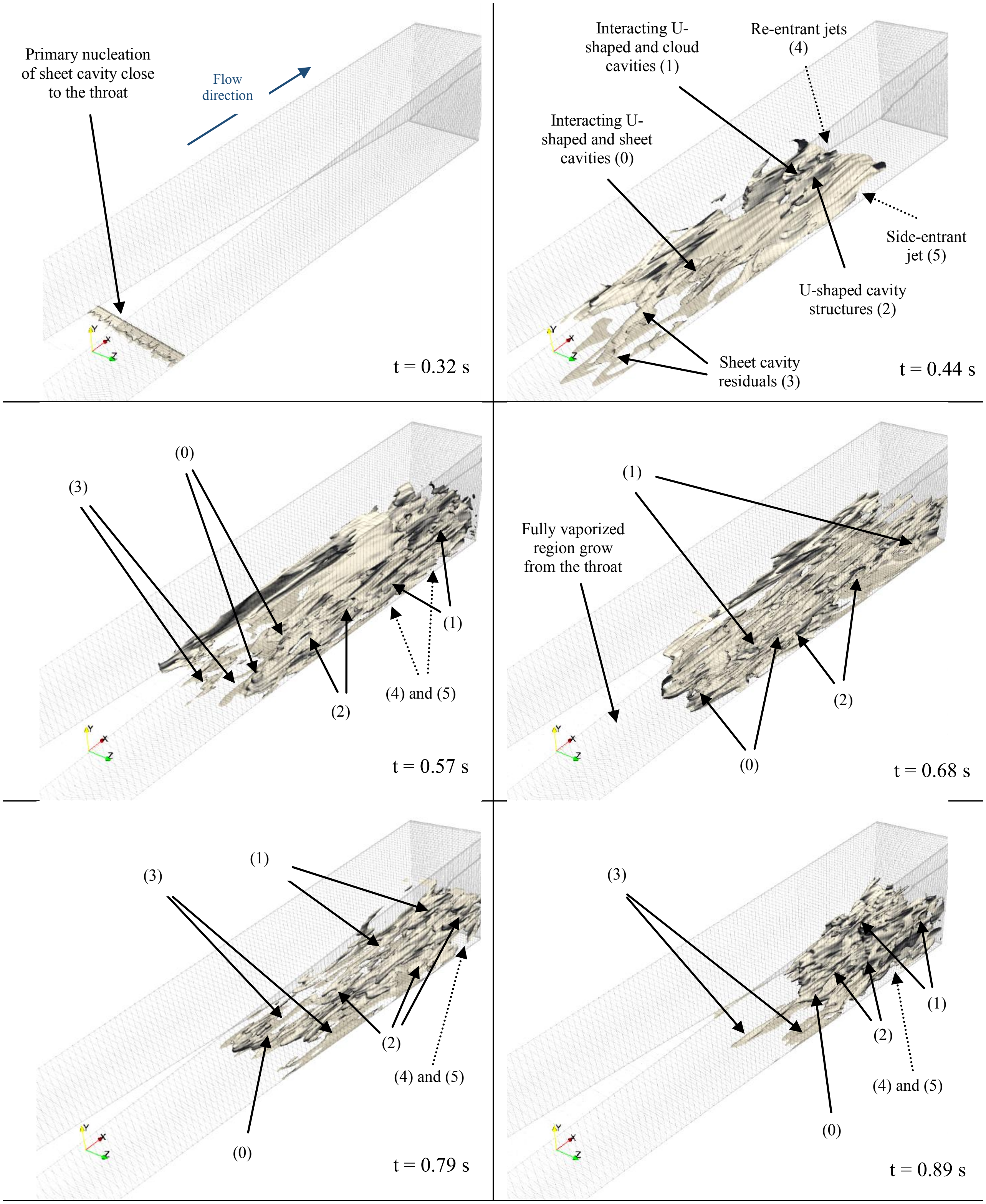
Primary nucleation of sheet cavity close to the throat
Flow direction
t = 0.32 s
Interacting U-shaped and cloud cavities (1)
Re-entrant jets (4)
Interacting U-shaped and sheet cavities (0)
Side-entrant jet (5)
U-shaped cavity structures (2)
Sheet cavity residuals (3)
t = 0.44 s
(0)
(3)
(1)
(4) and (5)
(2)
t = 0.57 s
(1)
Fully vaporized region grow from the throat
(2)
(0)
t = 0.68 s
(3)
(1)
(2)
(4) and (5)
(0)
t = 0.79 s
(3)
(1)
(2)
(4) and (5)
(0)
t = 0.89 s

(a)

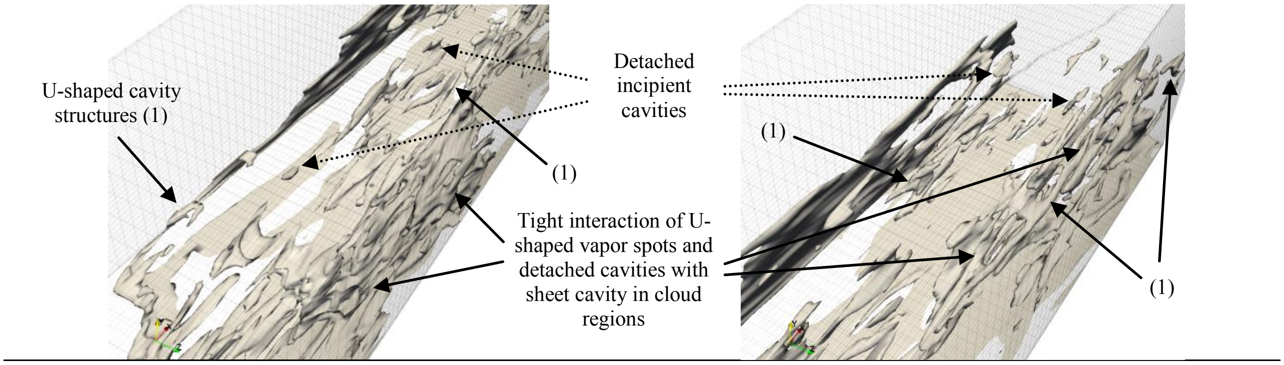

(b) *(c)*

Fig. 47: Time evolution of the 3D in-nozzle cavitating flow of LNG in the diverging part of the nozzle in 4.0 < x/b < 36.0: instantaneous iso-surface contours of vapor fraction with α = 0.65 at time instants of t = 0.32, 0.44, 0.57, 0.68, 0.79 and 0.89 s (a). U-shaped cavities tightly interacting with each other are observed widely in the entire flow development process. Note the zoomed-in contours in the cavitation regions of 11.80 < x/b < 16.25 (b) and 31.25 < x/b < 36.0 (c) at t = 0.61 s, to better show the U-shaped cavity interactions with detached/sheet cavities in vapor clouds.

The cavity generation mechanism can be further described from the contours of Fig. 47-48, noting that the overall procedure has similarities to the cavitation development in the 2D test described in Section 5.1: in Fig. 48(a), due to separation of the flow at t = 0.32 s in the diverging part of the nozzle, a shear layer starts growing on the lower wall. As time proceeds ($t \geq 0.44$ s), the shear layer develops and eventually turns into elongated and inclined vortical structures further downstream, e.g. at t = 0.57-0.68 s. This process is initialized mainly through the roll-up of primary unsteady vortex sheets around the throat region, and then improved by the progress of re- and side -entrant jets with variable flow gradients in large recirculating zones [115,173]. Local static pressure drop below the local saturation pressure in the core of the generated vortex structures results in nucleation and growth of cavitation spots appearing as complex cavity sheet, cavity pockets, and large cavitating clouds, as seen in Fig. 47.

The cavitation development process from the partially-attached sheet cavity region near the throat (Fig. 47(a) at t = 0.32-0.44 s) is significantly influenced by the presence of three-dimensionality, which leads the cavity to develop unevenly in the spanwise direction in addition to the x-wise evolution seen in the 2D test (Section 5.1). The direction and momentum of re- and side-entrant jets impinging through the sheet cavities are the predominant reasons promoting the 3D cloud cavity structures at $t > 0.57$ [43,127,174], as further explained in Section 7.3. It is also interesting to note in Fig. 48(a) that with further flow progress up to t = 0.68 s, the attached sheet cavity development on the wall shows a somewhat quasi-periodic shedding behavior (further discussion in Section 7.3), while accompanying compact distribution of incipient vapor pockets detach from its closure in an irregular fashion [154,157]. The formation of these temporally-varying vapor spots causes significant vortex distortions and leads the neighboring cavities to stretch and/or tilt (see Fig. 47(a) and 48(a) at t = 0.44-0.89 s) [125,170].

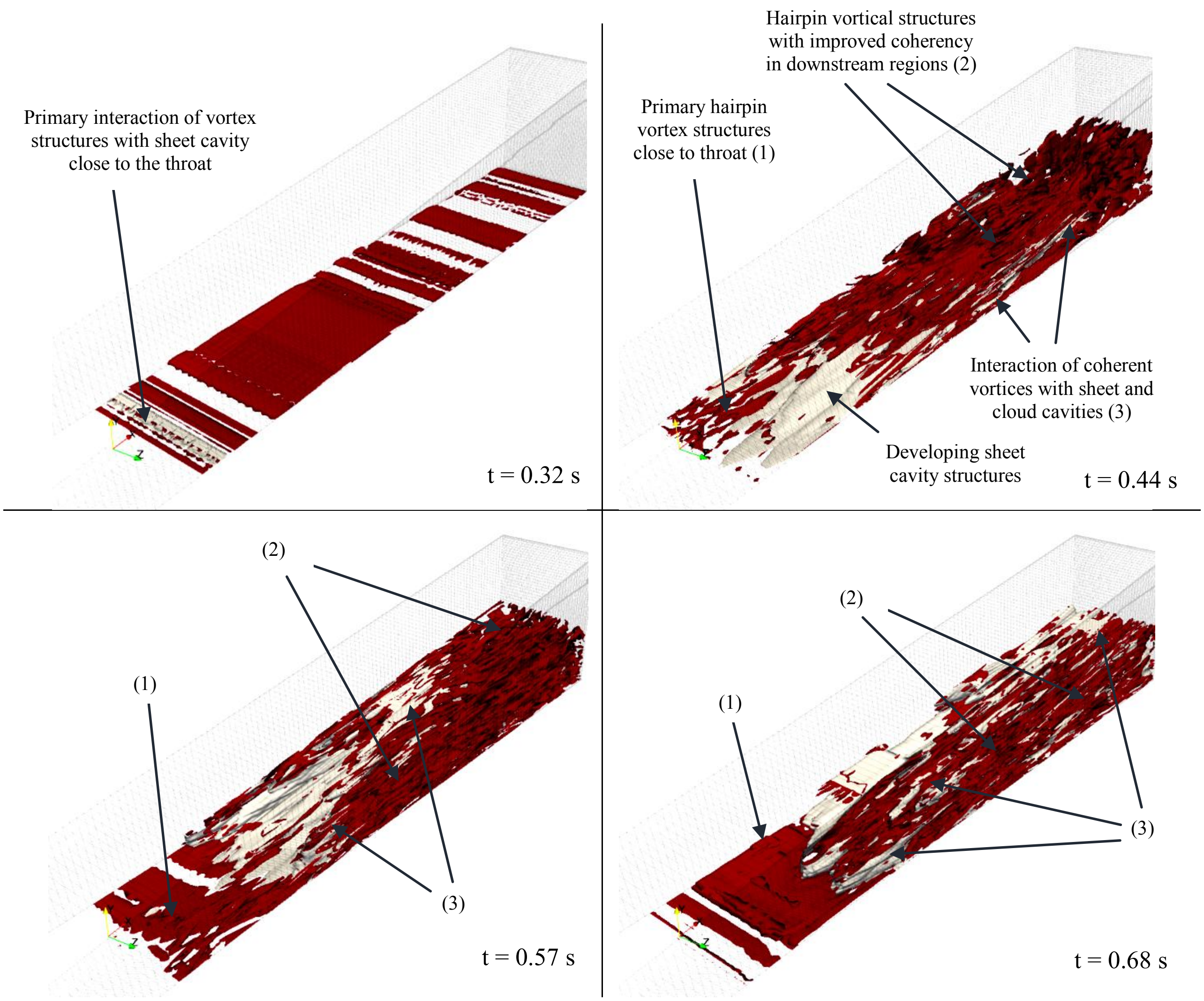

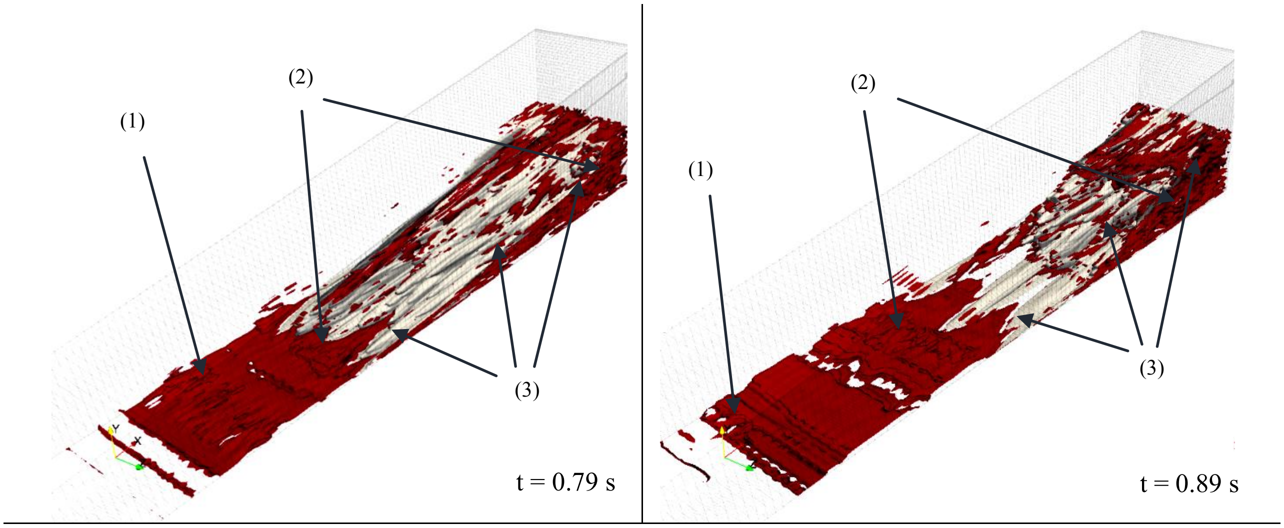

(a)

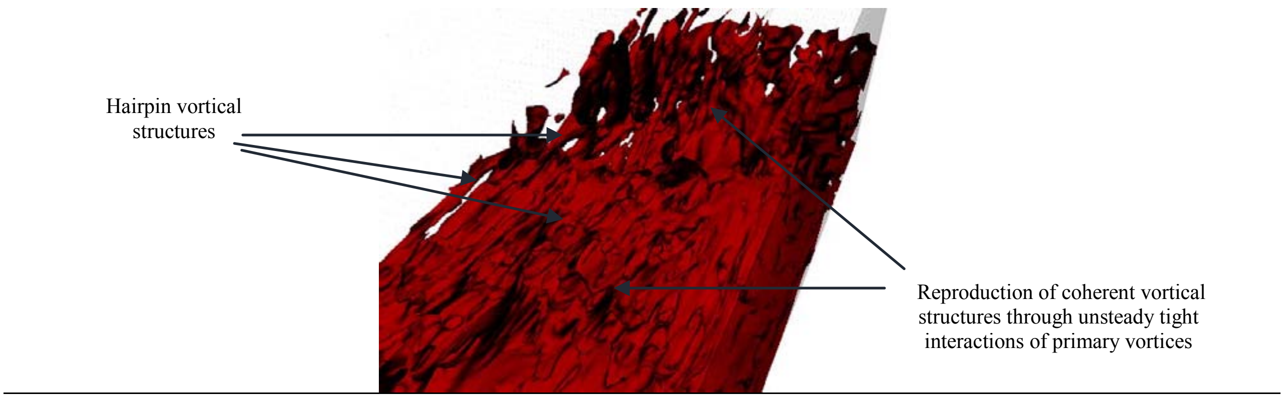

(b)

Fig. 48: Time evolution of the 3D in-nozzle cavitating flow of LNG in the diverging part of the nozzle in 4.0 < x/b < 36.0: instantaneous iso-surface contours of Q-criterion with Q = 1000.0 s^{-2} superimposed with iso-surface contours of vapor fraction with α = 0.95 at time instants of t = 0.32, 0.44, 0.57, 0.68, 0.79 and 0.89 s (a). Iso-surfaces of Q-criterion are colored in black red. Tight cavity-vortex interactions occur widely in the entire flow development process. Note the zoomed-in contour of Q in the region of 29.15 < x/b < 36.0 at t = 0.65 s (b), to better show the coherent vortical structures.

With further breakdown of the attached sheet cavity at t = 0.57-0.68 s, in Fig. 47(a), large cavity cloud structures tightly interacting with the earlier small incipient vapor pockets and/or the U-shaped vapor structures are detected downstream (see also Fig. 47(b)-(c)). As pointed out, this complex behavior of cavitating structures is likely due to the development of re- and side - entrant jets, respectively, on the lower wall and from the periodic side boundaries (see Fig. 49). These jets impose strong adverse pressure gradients along the wall that push the liquid flow against its favorable direction. These combined with the local relative pressure (p - p_{sat}) improvements promotes shrinking of the vapor area [164,173]. As time goes on, in further downstream regions periodicity becomes more involved with more progression of the entrant jets, such that long, slender, and highly-twisted cavities shed more periodically ($t > 0.68$ s). These structures are however contracted concurrently, if they become exposed to the surrounding high-pressure liquid zones and/or interact with vortices in wake regions [126]. The high-velocity vortex cavity structures can be detected within interfacial regions and through the liquid passages squeezed by cavities (orifice behavior), as indicated in Fig. 49.

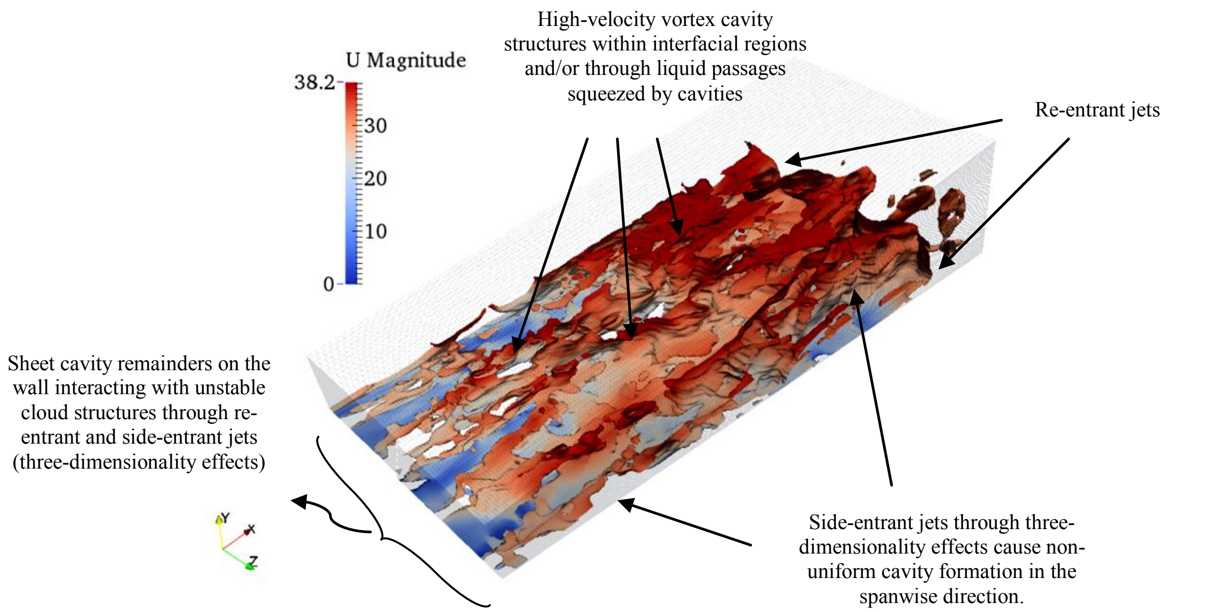

Fig. 49: 3D cavitating flow of LNG inside the nozzle at time instant of t = 0.60 s: zoomed-in view of the iso-surface contour of vapor fraction field for vapor structures with $\alpha = 0.65$ colored by velocity magnitude (cm/s). Contour field corresponds to the 9.0 < x/b < 21.0 region in the diverging part of the nozzle.

Beyond $t \geq 0.68$ s, a somewhat quasi-stable fully-vaporized region forms upstream of the throat that seems to progressively grow with time -- as illustrated later in the contours of Fig. 51, 53, and 54 in Section 7.3 -- until follow-on cavitation cycle(s) are developed. The observed evolutions are in agreement with Ji et al. [168] who concluded that the cavitating cloud structures mainly originate from either the cavity center and/or the cavity sides, due to the interaction of re-entrant jets with attached sheet cavity surface, as well as to the collision of side-entrant jets and radially diverging re-entrant jets.

The cavity-vortex evolution in Fig. 47-48 is also accompanied by the collapse of downstream cloud cavities, as they are exposed to high and low pressure zones, which eventually result in the formation of smaller-scale vapor structures (see for example Fig. 47(a) at t = 0.79-89 s). This further leads the coherent vortex structures to become irregularly enlarged and distorted as they convect into downstream regions (see for example Fig. 48(a) at t = 0.44-68 s, and Fig. 48(b))

[119]. The collapse of cavity structures is a major source of vorticity production and instability, triggering the regeneration of hairpin (horseshoe) type vortical structures, as pointed out in Fig. 48 [183,184]. The shed horseshoe vortices seem to coincide with the vapor clouds involving U-shaped vapor spots and/or the sheet cavity structures on the wall [119,127,183]. Strong horseshoe vortical structures occur with vorticity production along the nozzle wall and/or within the vapor-liquid interfacial regions, in particular at cavity breakup and collapse areas due to significant increase of baroclinic torque, as reported by Dittakavi et al. [174]. The re- and side - entrant jets piercing through the cavity also promote the hairpin structures [119,133,168]. For example, collision of the side-entrant jets with radially diverging re-entrant jets are reported to advance the hairpin vortices growth [127,168]. The observed behaviors are relevant to Gopalan and Katz [183] remarks stating that the flow downstream of cavity closure regions contains hairpin-like structures containing vapor bubbles in different scales. For example in Fig. 48(a) at t = 0.57 and 0.89 s, the coherent hairpin vortices are clearly seen to tightly interact with downstream cloud cavities. These interactions vary with time during each cavitation cycle.

It is further noted in Fig. 48 that the hairpin vortical structures also tend to be frequently formed close to the throat within the entire cavitation development stages. This is estimated to be due to: 1) the interactions of re-entrant jets with the thin attached sheet cavity; and 2) the presence of spanwise gradients from side-entrant jets, in near throat regions which jointly promote the elongation of vortices in the z direction [174]. These initially thick horseshoe vortical structures, which are located at an oblique angle relative to the nozzle lower wall, become weaker and reduce in size as time proceeds. The horseshoe vortex head which has larger momentum than the two legs travels more quickly downstream and eventually collapses due to local high pressure regions [119,168].

Another important observation from Fig. 47-48 is that the remainder of the sheet cavity structures on the lower wall (sheet cavity residuals) tend to trigger the formation of horseshoe vortical structures through asymmetrically breaking the primarily-formed vortices on the wall (these residuals can be better seen in Fig. 47(a) at t = 0.44, 0.57, 0.79, and 0.89 s). This leads the vortical structures to be alternately accumulated in either side of the domain in the spanwise direction, due to large values of velocity gradients entraining the flow within the cross-wise direction (for instance see the accumulation of vortical structures in Fig. 48(a) at t = 0.44-0.57 s) [70,127]. The asymmetry seems to occur at specific time incidents and is recovered as time goes on. The concurrent regional dominance of vapor structures in this process is attributed to the increased relative pressure gradients inducing temporary vaporization events. Such behavior is also attributed to the instability of vapor spots interacting with vortex structures. This is relevant to the observations of Laberteaux and Ceccio [165] showing that the cavity instability is strongly influenced by the spanwise pressure gradients such that the re-entrant jets may be directed away from the cavity interface, allowing sheet cavitation to form cloud cavities far downstream.

7.3. Cross-Sectional Evolution of Cavitating Structures

To better understand the physical mechanisms governing the dynamics of unsteady sheet/cloud structures in the 3D in-nozzle LNG cavitation flow, Fig. 51-54 display the temporal evolution of vapor fraction, temperature, and velocity magnitude fields at time instants of t = 0.35, 0.45, 0.55, 0.65, 0.75, 0.85, 0.95, and 1.05 s respectively on the selected cross-sectional streamwise reference planes of x/b = 14.86 (Fig. 51) and 31.08 (Fig. 52); transverse reference plane of y/b = 1.35 (Fig. 53); and spanwise reference plane of z/b = 0.0 (Fig. 54), as shown schematically in Fig. 50.

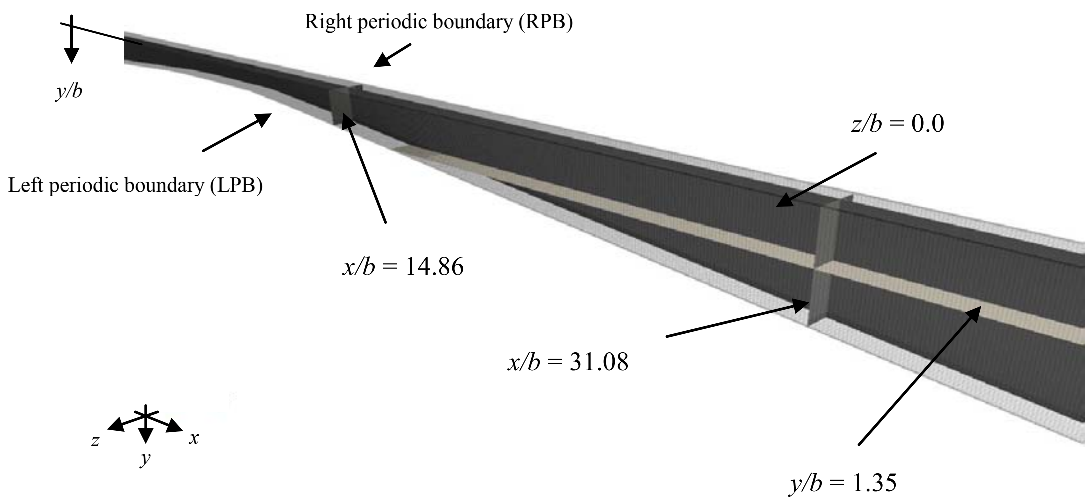

Fig. 50: Schematic of the selected 2D cross-sectional reference planes in the 3D in-nozzle LNG cavitating flow domain: streamwise x/b = 14.86 and 31.08; transverse y/b = 1.35; and spanwise z/b = 0.0 planes are shown in the diverging part of the nozzle. Corresponding flow contours are respectively depicted in Fig. 51-54. Note the right (RPB) and left (LPB) periodic side boundaries in the domain.

The resulting flow contours indicate the presence of a quasi-periodic shedding process of cavitation in the 3D in-nozzle LNG flow with some notable differences compared to the 2D evolution of Section 5.1, though showing similar cavitation development procedure in terms of latent heat transfer between the liquid and vapor phase during phase change (see temperature contours of Fig. 51(b), 52(b), 53(b), and 54(b)). The periodic process pertaining to the formation of cloud cavitation spots seems to involve two stages; in stage one, continuous collision of the primary re-entrant jet with the cavity interface causes the attached sheet cavity on the lower wall to shed frequently and dispatch incipient vapor pockets (see for example Fig. 51(a)-(c) and 54(a)-(c) at t = 0.35-0.55 s); in stage two, the remainder of the attached cavities on the wall from stage one develops a secondary shedding mechanism through the three-dimensionality effects.

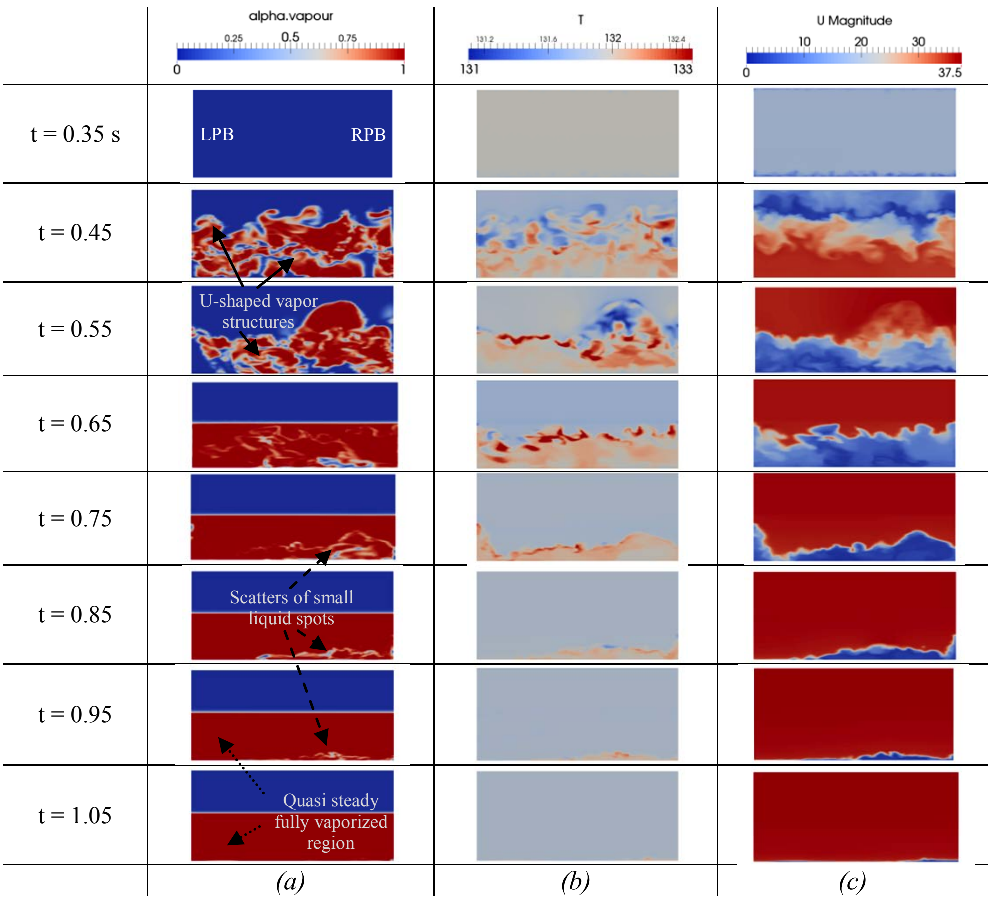

Fig. 51: Time evolution of the 3D in-nozzle LNG cavitating flow on the streamwise reference plane of x/b = 14.86: distributions of (a) vapor fraction; (b) temperature (K); and (c) velocity magnitude (cm/s) at time instants of t = 0.35, 0.45, 0.55, 0.65, 0.75, 0.85, 0.95, and 1.05 s. The mainstream liquid region of 0.0 < y/b < 0.40 is not shown for better resolution.

The cavity shedding process in stage one continues to grow quickly as time proceeds -- due to thermally-affected flow gradients within recirculating zones -- such that the small upstream vapor spots turn into highly-unsteady vapor clouds advecting downstream by the main liquid flow (t = 0.65-0.85 s). Simultaneously, the tail of the attached sheet cavities curl into a convex, U-shaped horseshoe vapor structures having one head and two legs, as similarly noted in the iso-contours of Fig. 47, and regrow with time, e.g. as indicated in the contours of Fig. 51(a), 52(a), and 53(a). The U-shaped vapor spots appear with increased temperature as they tend to grow (see for example Fig. 52(b) and 53(b) at t = 0.75-0.95 s).

The re-growth process of the upstream attached cavities is concurrent to alternate breakdown of downstream clouds (see for example Fig. 53(a) and 54(a) at t = 0.95-1.05 s) through the side- and re -entrant jet structures (see for example Fig. 52(a) at t = 0.75-0.95 s and 54(a) at t = 0.55-0.95 s) shrinking the overall vapor production in the domain. This process causes the liquid passages through vapor regions to be squeezed and expanded with time. For instance, large velocity regions downstream of Fig. 53(c) at t = 0.85-1.05 s are indicative of the liquid contraction behavior where the liquid passage accelerates through the vapor spots, thus resembling a jet flow. It is notable that as the detached cavity clouds expand through the low pressure wake regions downstream they also start collapsing due to the presence of high-pressure flow passages, hence improving the local flow gradients. The collapse process particularly causes a large propagation of pressure waves constraining the development of upstream attached sheet cavity, thus suppressing the production of cloud structures from its rear part [116,134,172]. The observed evolution of the LNG cavitation continues until condensation and vaporization of the cavity spots in the wake regions reach an equilibrium state (end of the cavitation cycle) [70] (see Fig. 51(a)-(c), 53(a)-(c), and 54(a)-(c) at t = 0.95-1.05 s). This equilibrium state can be clearly observed to form in the upstream regions close to throat where the flow slowly starts to behave in a somewhat quasi-steady state comprised of a fully vaporized region with small scatters of liquid inside the vapor zone and/or left over on the lower wall (Fig. 51(a)-(c), 53(a)-(c), and 54(a)-(c) at t = 0.75-0.95 s). The equilibrium quasi-steady vapor region is not formed further downstream in the given time period (see for example Fig. 52(a)-(c)) due to improved unsteadiness. Once the first cavitation cycle ends, unsteady nature of the flow leads the continuation of cavitation process through follow-on cavitation cycles which mainly occur due to reprogression of the re- and side -entrant jets along with imposed spanwise flow gradients.

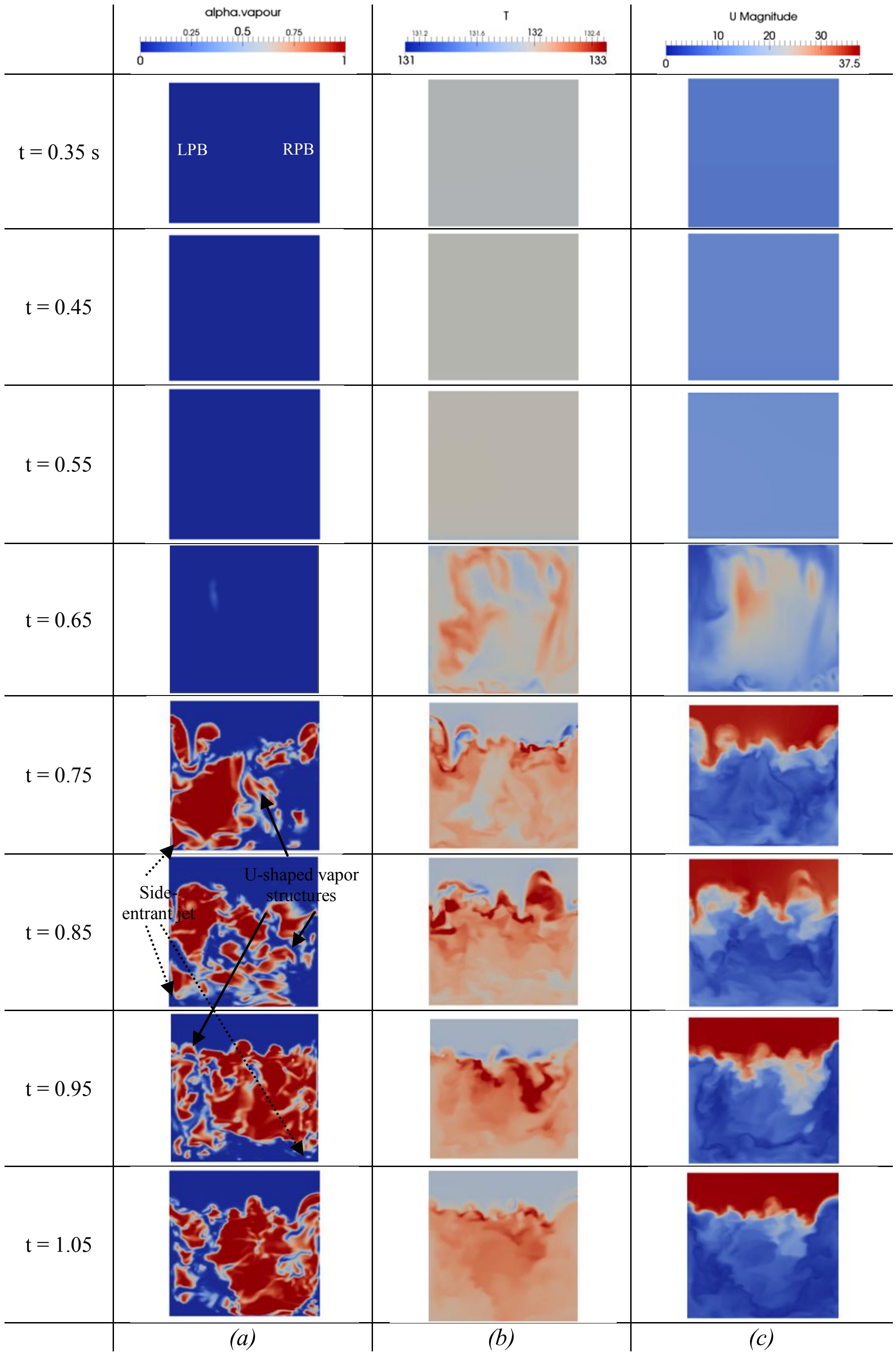

Fig. 52: Time evolution of the 3D in-nozzle LNG cavitating flow on the streamwise reference plane of x/b = 31.08: distributions of (a) vapor fraction; (b) temperature (K); and (c) velocity magnitude (cm/s) at time instants of t = 0.35, 0.45, 0.55, 0.65, 0.75, 0.85, 0.95, and 1.05 s. The mainstream liquid region of 0.0 < y/b < 0.40 is not shown for better resolution.

Further on the temperature variations in Fig. 51(b), 52(b), 53(b), and 54(b), it is observed that as the attached cavity breaks down through the development of entrant jets on the wall, and the shedding process begins via three-dimensionality effects, the temperature of the generated cloud structures varies through a combination of condensation and vaporization processes. Higher temperature gradients due to latent heat transfer processes can be spotted in the detached cavity structures downstream compared to the upstream (see for example Fig. 53(b) and 54(b) at t = 0.75-0.95 s). High temperature regions of the growing cloud cavities pertain to larger latent heat of vaporization absorbed from their surrounding liquid and vice versa. Relatively small temperature gradients are observed in the residuals of the attached sheet cavities on the wall (Fig. 51(b), 52(b), and 54(b) at t = 0.85-1.05 s) [120].

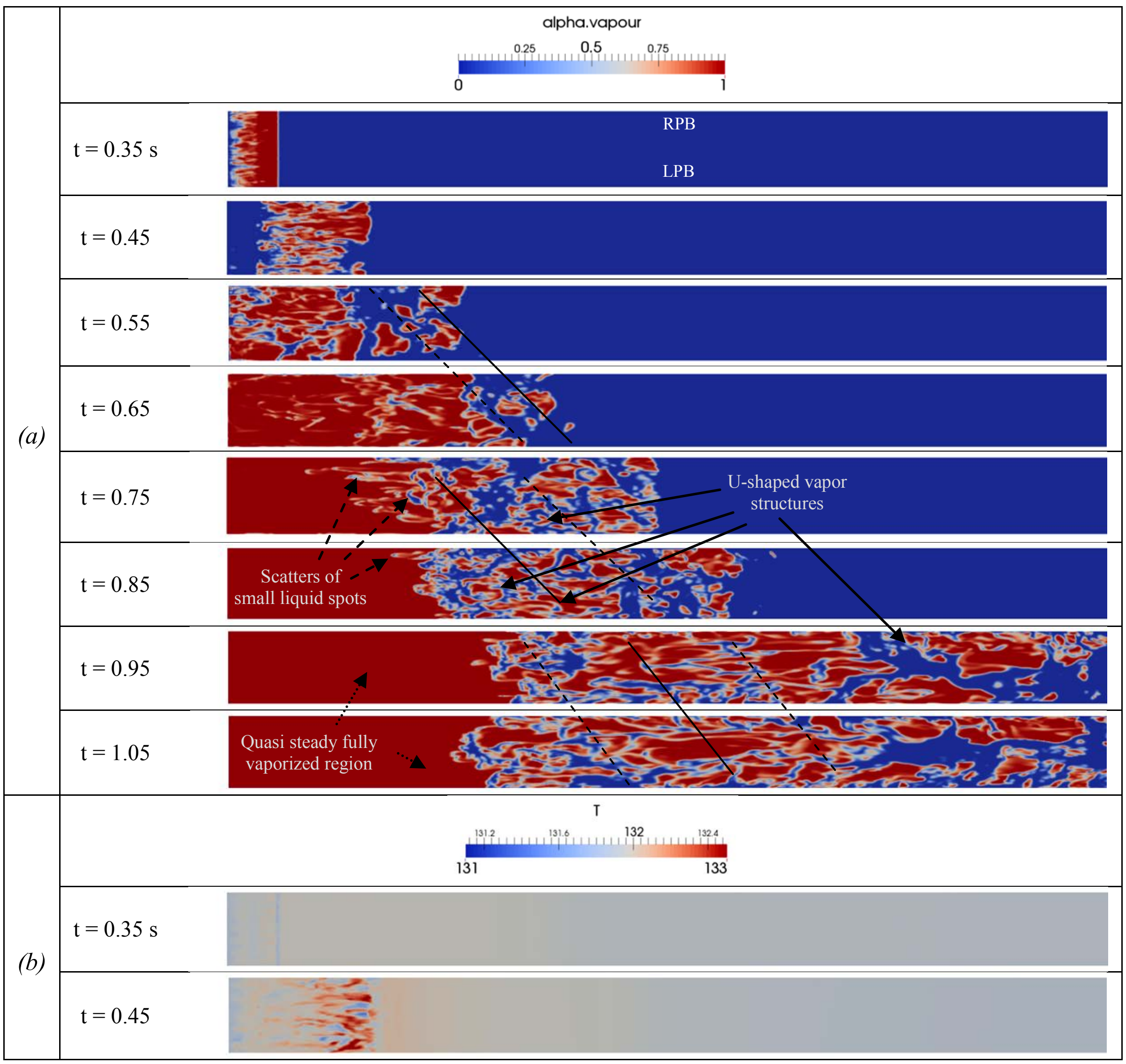

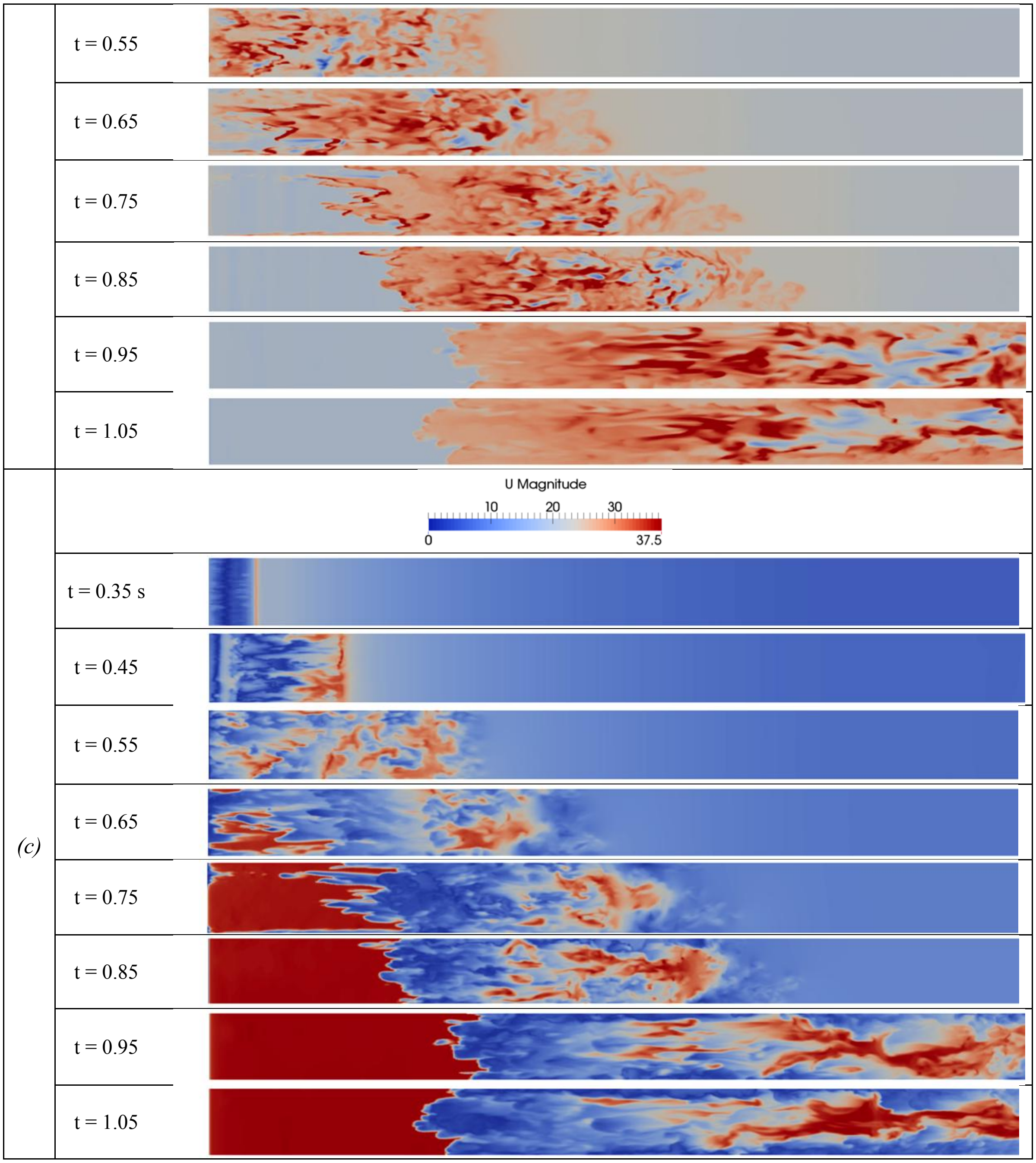

Fig. 53: Time evolution of the 3D in-nozzle LNG cavitating flow on the transverse reference plane of y/b = 1.35: distributions of (a) vapor fraction; (b) temperature (K); and (c) velocity magnitude (cm/s) at time instants of t = 0.35, 0.45, 0.55, 0.65, 0.75, 0.85, 0.95, and 1.05 s.

In the cavitation evolution of Fig. 51-54 it can be further seen that the side- and re -entrant jets influence the progress of sheet cavities from the primary stages of cavitation cycle, as indicated in Fig. 51(a)-(c) and 54(a)-(c) at t = 0.45 and 0.55 s. This is when the second stage of the periodic cavitation development process is initiated and the attached cavity residuals from stage one with the left-over liquid spots, e.g. on the wall, promote the secondary shedding mechanism (Fig. 52(a)-(c), 53(a)-(c), and 54(a)-(c) at $t > 0.75$ s) [135,174]. The secondary mechanism particularly seems to strengthen the entrant jets in the flow through the three-dimensionality effects, so improving the flow resistance to form a completely vaporized region in the divergent part. Larger formation of vapor spots in further downstream regions is however detected despite this mechanism (Fig. 53(a)-(c) and 54(a)-(c) at t = 0.95-1.05 s). Note that the presence of three-dimensionality within the secondary shedding mechanism can be more specifically observed in Fig. 52(a)-(c) and 53(a)-(c) at time instants t = 0.75-1.05 s depicting the frequent formation of downstream coherent horseshoe cavity structures in the shedding process of clouds (this is better indicated in the 3D iso-contours of Fig. 47-48 showing strong interactions of the coherent U-shaped cavity and vortex structures). As noted in Section 7.2, the main reason for such evolution is attributed to the progression of radially-diverging re- and side -entrant jets that impose large flow gradients in the streamwise and crosswise directions, thus strengthening the recirculating regions interactions with the shedding cavity clouds [134,168].

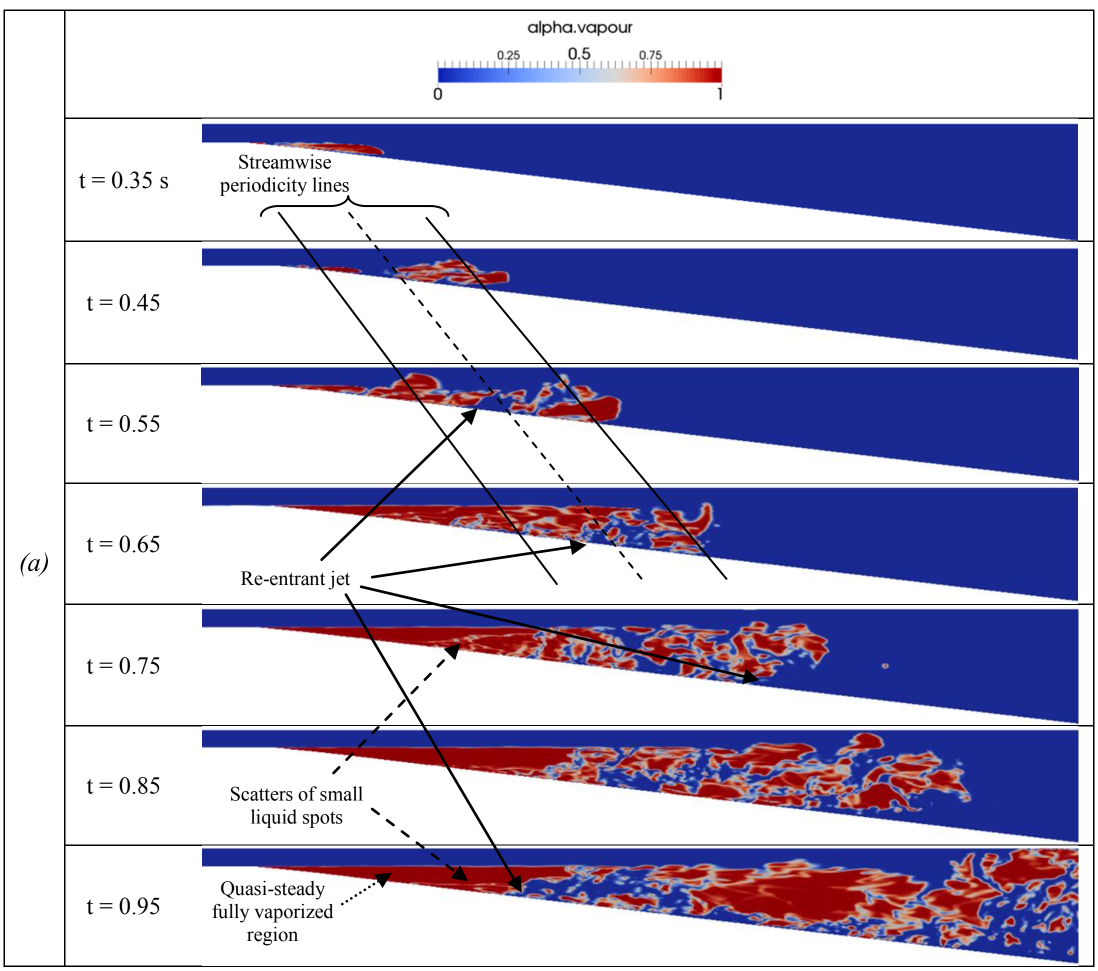

	t = 1.05	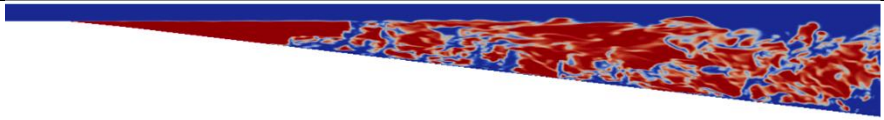
(b)		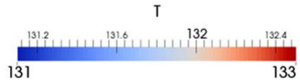
	t = 0.35 s	
	t = 0.45	
	t = 0.55	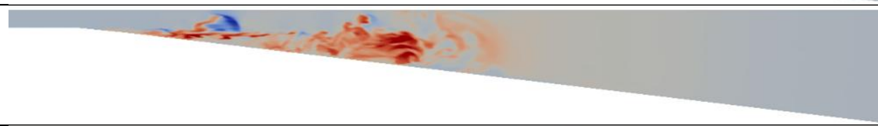
	t = 0.65	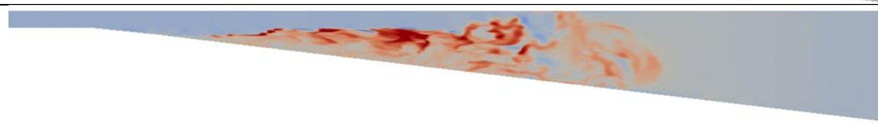
	t = 0.75	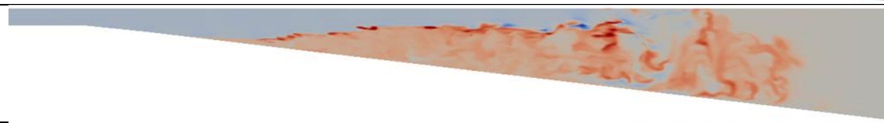
	t = 0.85	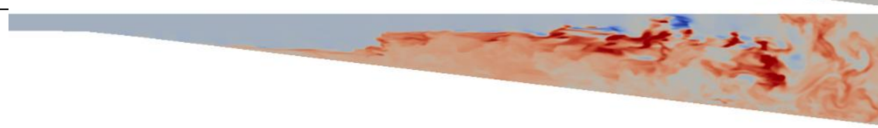
	t = 0.95	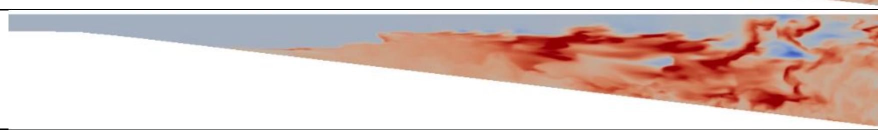
	t = 1.05	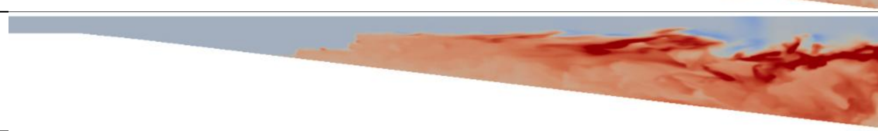
(c)		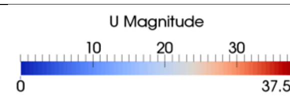
	t = 0.35 s	
	t = 0.45	
	t = 0.55	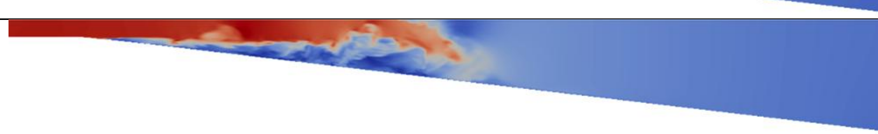
	t = 0.65	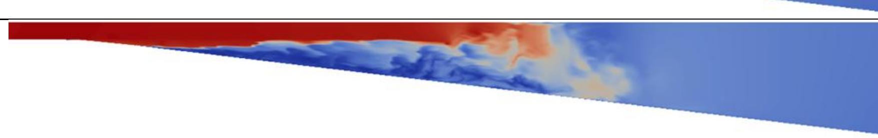

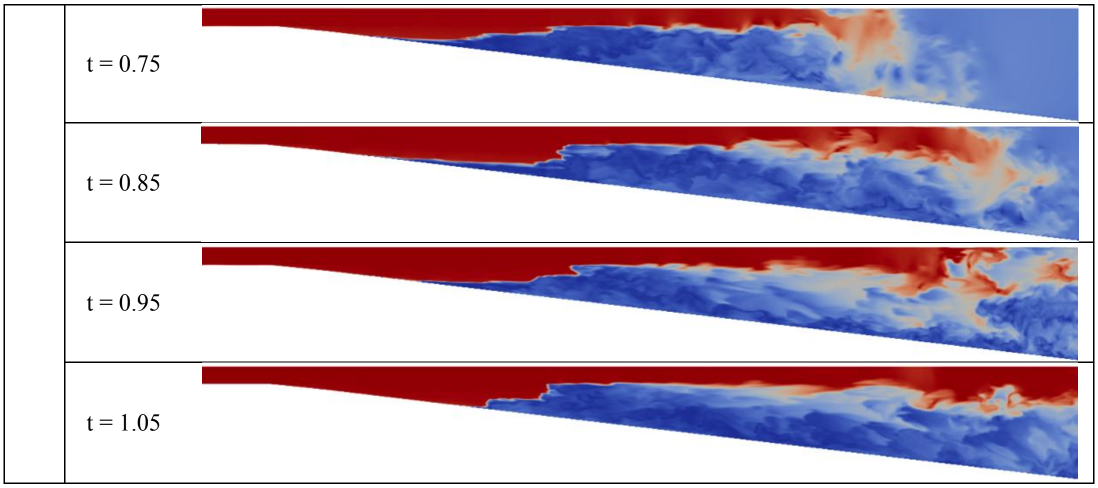

Fig. 54: Time evolution of the 3D in-nozzle LNG cavitating flow on the crosswise reference plane of z/b = 0.0: distributions of (a) vapor fraction; (b) temperature (K); and (c) velocity magnitude (cm/s) at time instants of t = 0.35, 0.45, 0.55, 0.65, 0.75, 0.85, 0.95, and 1.05 s.

The present evolution of the 3D LNG cavitating flow in the nozzle can be further evaluated against the corresponding 2D flow behavior. Compared to the 2D results, it is deduced from the visual inspection that the instabilities in the 3D case are extended in the spanwise direction (see for example Fig. 52(a) at t = 0.75-0.95 s, Fig. 53(a) at t = 0.75-1.05 s, and Fig. 54(a) at t = 0.45-0.65 s) such that a somewhat spatial periodicity can be found clarifying further shedding of the vapor structures along the nozzle span [100,157,175]. The spanwise periodicity can be detected when a large cavity passes across the side boundaries of the domain (this was similarly observed in the 3D visualizations of Fig. 48): for example in Fig. 52(a), the large cavity cluster on the left boundary LPB (at t = 0.75 s) breaks down into smaller vapor spots while moving to the right (at t = 0.85 s) to generate another large cavity cluster on the right boundary RPB (t = 0.95 s). This periodicity can be also detected in the streamwise direction; it appears when a large accumulated region of vapor spots is generated and collapsed at specific wavelengths within successive time steps (see for example Fig. 54(a) at t = 0.45-0.65 s). The streamwise periodicity seems to occur at larger wavelengths as the flow reaches downstream and larger cloud structures are formed (see for example Fig. 53(a) at t = 0.55-1.05 s). The inhomogeneous spanwise behavior is caused by spanwise temperature-dependent density, viscosity, and pressure gradients, which leads the formation of multiple realizable cloud regions shedding in the spanwise direction [116,118]. More specifically, from the top-view contours of Fig. 53(a)-(c) it is seen that the cloud structures initially appear in an irregular shape (up to t = 0.45 s), from an irregular break-off of the primary attached sheet cavity on the lower wall, and then turn into a sort of detectable spanwise two (to four) -pieced clouds at the rear of the primary sheet cavity at t = 0.55-0.75 s [100,175]. Note that the overall evolution of the clouds seems to be quite complicated, i.e. due to the complex compressible nature of the flow involving highly-unsteady vortex-cavity interactions with thermal effects.

(a)

(b)

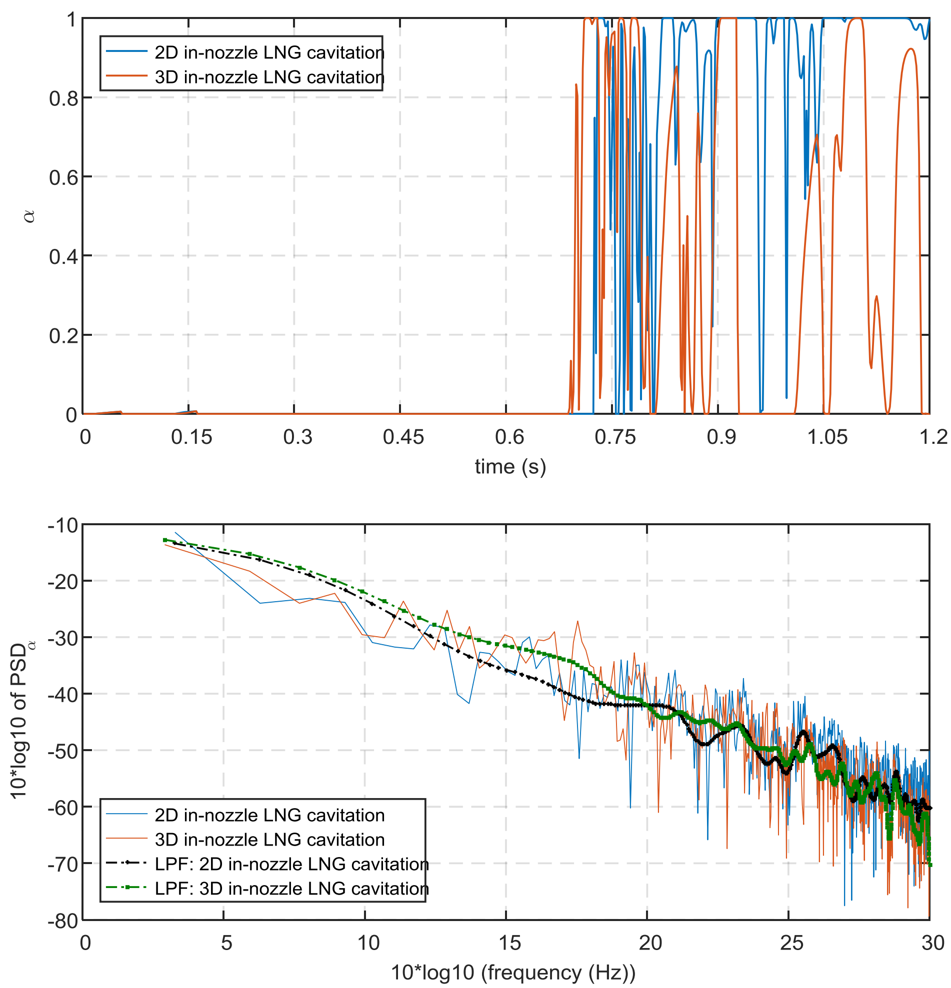

Fig. 55: Time histories (a) and log-scale spectra (b) of vapor fraction field at the probe location (x/b,y/b) = (32.91,1.10) for the 2D and 3D in-nozzle cavitating flows of LNG. LPF stands for low-pass filtered data.

The observed behaviors of the 3D in-nozzle LNG cavitation flow are not present in the evolutions of the 2D test in Section 5.1. As previously stated, such difference is mainly related to the presence of side-entrant jets acting in the spanwise direction within the closure of the cavities, strengthening the overall flow gradients [100,115,127]. This also explains the reason for the improved unsteadiness in the 3D case; frequent collisions of the re- and side-entrant jets lead the cavity structures to pinch-off multiple times over a cavitation cycle, hence triggering the secondary shedding mechanism [135]. This conclusion can be further confirmed in Fig. 55

comparing the time history and PSD distributions of vapor fraction field at a downstream probing station of ($x/b,y/b$) = (32.91,1.10) over more than a single flow-through time. The figure particularly illustrates the effects of three-dimensionality on the unsteady behavior of the in-nozzle cavitating flow of LNG; improved disturbance amplification is seen in the 3D test against the 2D test especially in the lower frequency range. The improved unsteadiness also causes the cavity inception to start earlier in the 3D flow at $t \cong 0.68$ s compared to $t \cong 0.72$ s in the 2D case.

8. Numerical Simulation of 2D Cavitating Mixing Layer of LNG

This chapter investigates the baseline simulation of a 2D compressible cavitating mixing layer of LNG behind a flat splitter plate in a laminar to transitional flow regime. The global behavior of LNG cavitating structures in the mixing layer at selected time instants is first examined to disclose the time-dependent behavior of cavitating patterns from the very beginning onset of cavitation up to later development stages including the formation of shedding cavitating clouds. The cavity-vortex interactions are then explored by utilizing a vorticity transport equation, to discover correlative mechanisms governing the evolution and interaction of LNG vapor cavity structures. Further assessment of the mixing layer instability mechanisms, including the shedding behavior of cavitating spots and vortical structures, are investigated in the comparative studies of Chapter 9.

8.1. Numerical Setup

The proposed baseline reference simulation is based on the experimental study of Aeschlimann et al. [25], and simulates a 2D cavitating mixing layer of LNG behind a flat splitter plate using the developed cryogenic cavitation solver in Chapter 3. The splitter plate has a thickness of 6 mm with a rounded edge of 0.2 mm radius, and is placed in a 250×80 mm^2 rectangular domain (Fig. 56(a)) meshed with 525,700 non-uniform structured 2D elements, as schematically shown in Fig. 56(b)-(c). The mesh is generated using the same method as for the nozzle case in Section 4.1; the grid independence is discussed in Appendix B.

(a)

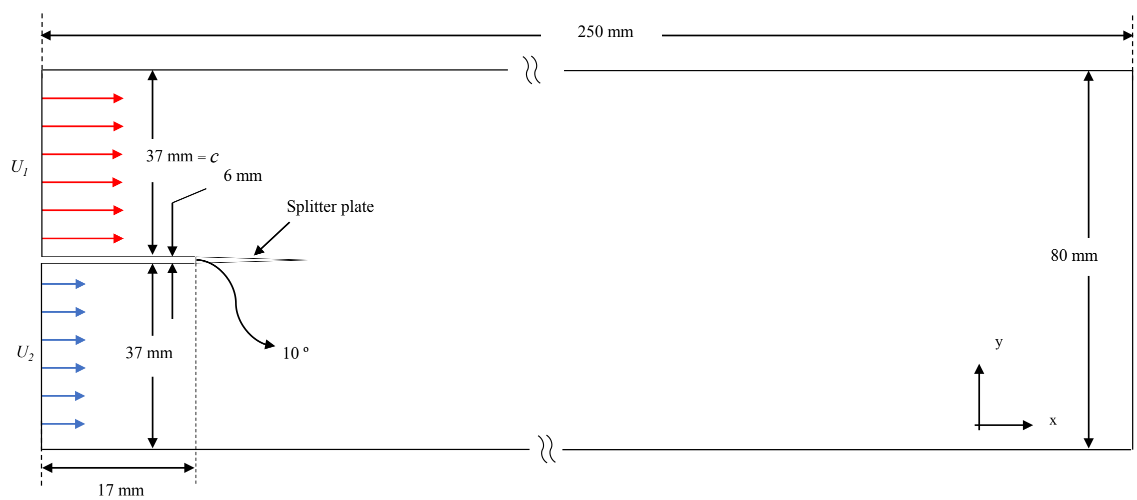

(b)

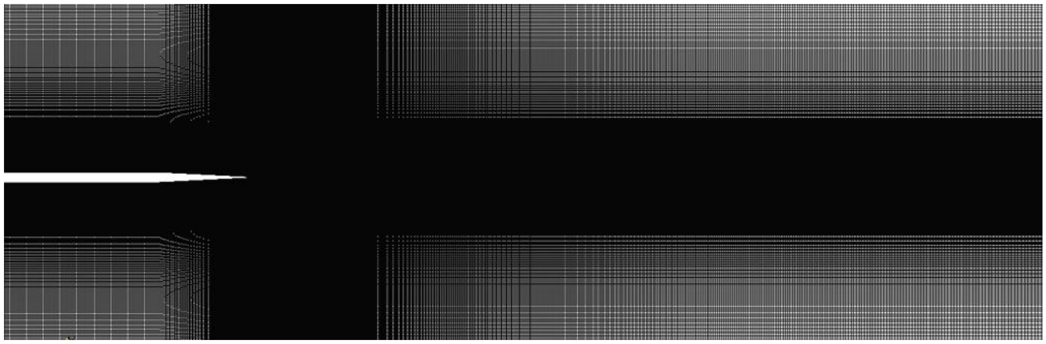

(c)

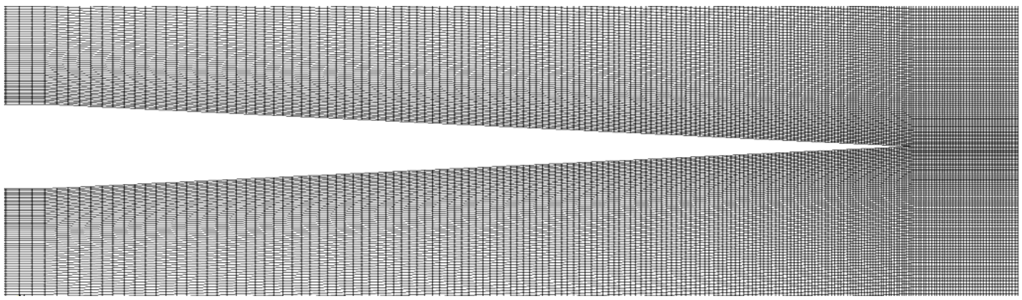

Fig. 56: Computational domain for the 2D cavitation mixing layer simulations of LNG (a); overall (b) and zoomed-in (c) views of the mesh resolution around the splitter trailing edge.

The baseline test is simulated for a selected cavitation number of Ca = 0.21, with the splitter upper to lower stream velocity ratio of U_1/U_2 = 4.52. Noting that the cavitation number is defined in terms of the low-speed side pressure at the inlet, corresponding total pressure ratio between the high- and low -speed sides is 1.064 with the outlet static pressure fixed at 4.13 bar. The Reynolds number in terms of the primary mixing layer minimum vorticity thickness (see Section 9.4 for more discussion) and the initial liquid kinematic viscosity of 1.96×10^{-7} m^2/s is Re = 60,981.41. Initial flow field contains only liquid methane with an inlet density of 391.79 kg/m^3 at initial temperature of T_0 = 132 K, giving the Mach number of 0.39. The simulation is performed by use of the same numerical setup as in Section 4.3 with the difference here that the maximum acoustic Courant number is set to 1.5, giving average time step size of $\Delta t = 3.41\times10^{-6}$ s.

8.2. Nucleation and Growth of LNG Cavitation

To investigate the cavity nucleation and growth mechanisms in the development process of the LNG mixing layer, Fig. 57-58 respectively show the temporal evolution of vapor fraction and vorticity magnitude fields at time instants of t = 6.08, 19.79, 36.40, 52.89, 69.82, 87.54, 106.76, 124.38 and 142.12 s during the first cavitation cycle. The resulting contours pertain to the span of $0.0 < x/c < 3.0$ and $-0.65 < y/c < 0.65$ inside the mixing region after the splitter trailing edge

(T.E.). Here, c is the wall-normal height of the streams upstream of the splitter plate, which is analogous to the nozzle height dimension in Chapters 5-7. As indicated, the cavity development in Fig. 57 is mainly driven by the mixing layer instability mechanisms deduced from Fig. 58. The high-speed flow on the upper side of the splitter plate causes an earlier separation of the flow against the low-speed side as a result of larger adverse pressure gradients. This brings the upper stream near-wall vorticity to coincide with the high-vorticity region at the splitter trailing edge, thus leading the fluid sheet behind the splitter to roll up into discrete small vortical structures, i.e. the trailing edge vortices, through a development of wavy-shaped Kelvin-Helmholtz (K-H) instability (see for example Fig. 58 at t = 6.08-36.40 s) [75,185,186]. The resulting primary infinitesimal disturbances then start growing to promote the expanding vortical structures downstream, while the initiated mixing layer at the T.E. breaks down with time (see for example Fig. 58 at t = 52.89-106.76 s).

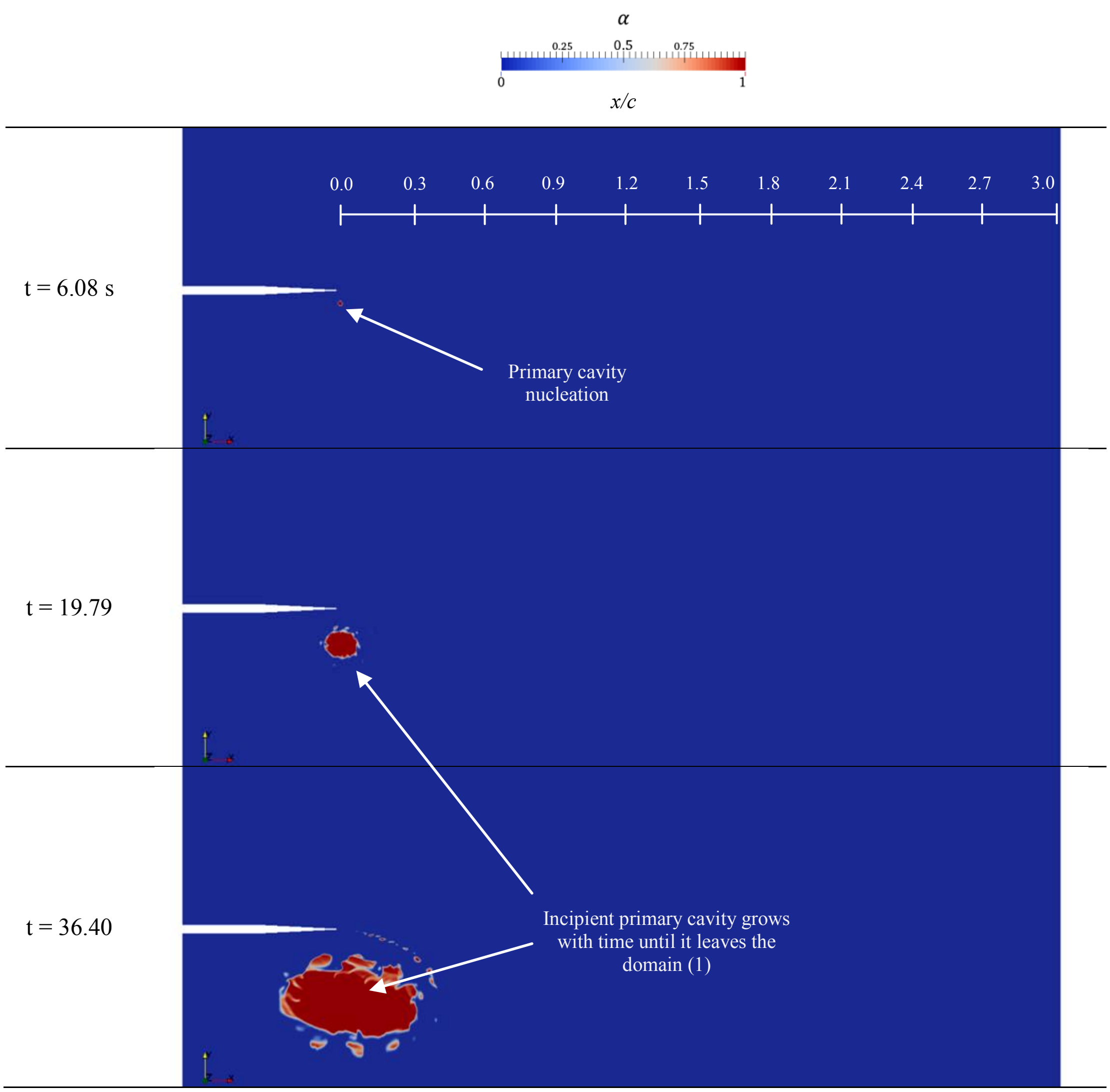

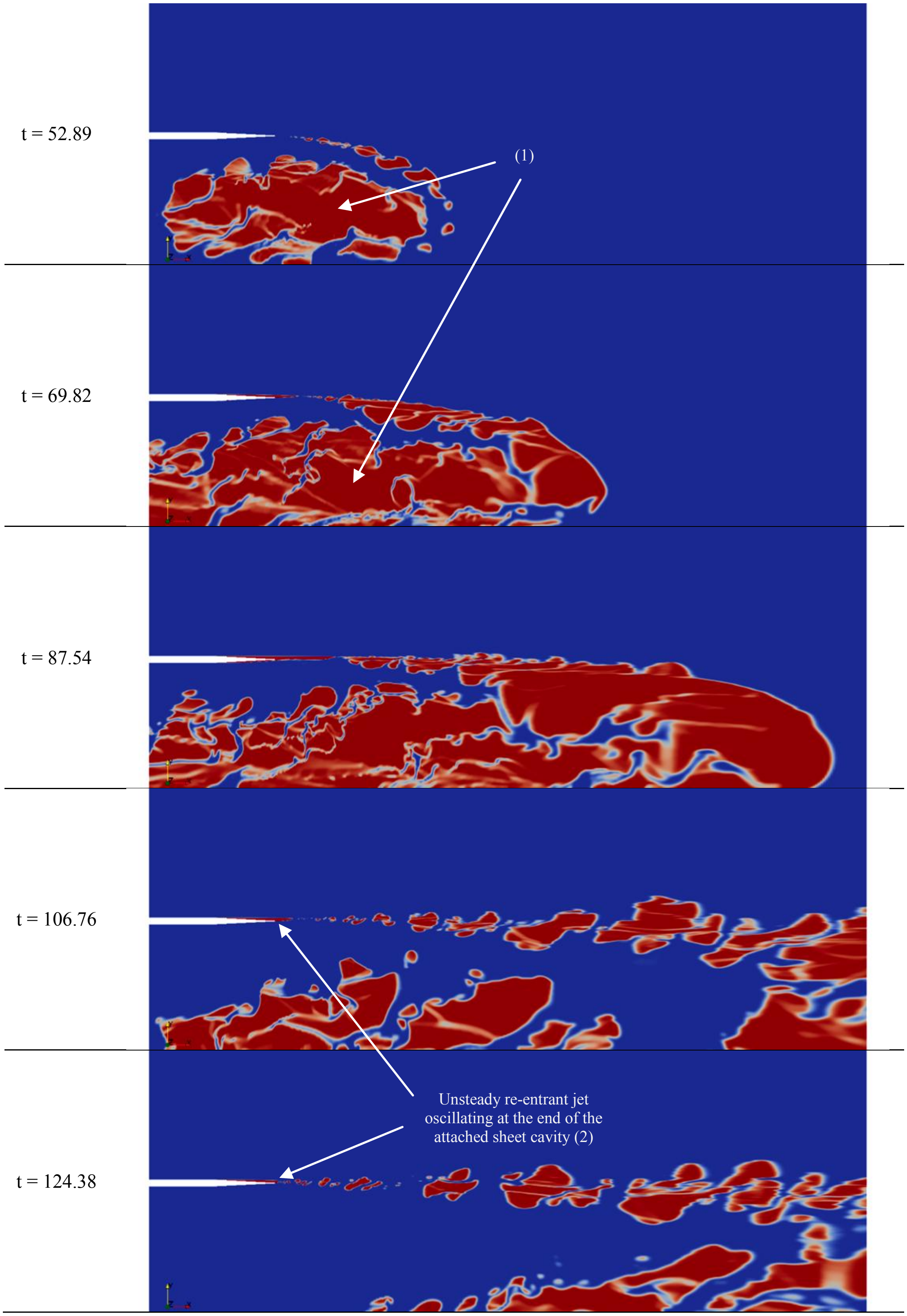
t = 52.89
(1)
t = 69.82
t = 87.54
t = 106.76
Unsteady re-entrant jet oscillating at the end of the attached sheet cavity (2)
t = 124.38

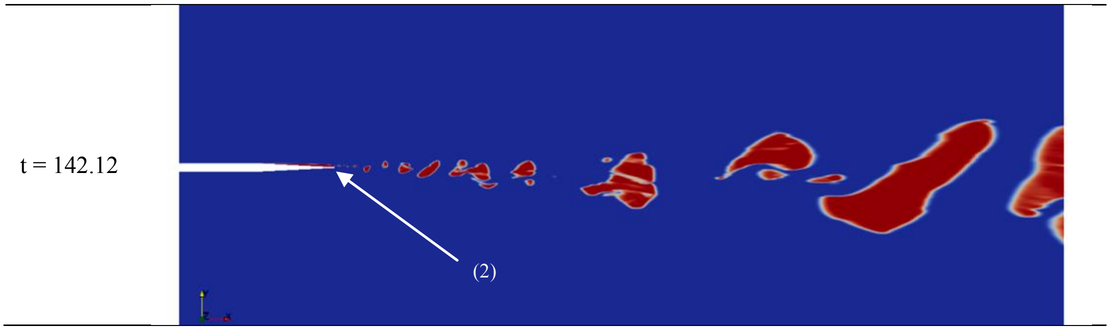

Fig. 57: Unsteady evolution of the cavitating mixing layer of LNG behind the splitter plate at Ca = 0.21: instantaneous contours of vapor volume fraction at time instants of t = 6.08, 19.79, 36.40, 52.89, 69.82, 87.54, 106.76, 124.38, and 142.12 s.

In the earliest stages of the mixing layer development around the T.E., when streamwise vortical structures are stretched and expanded through interactions with neighboring vortices their angular velocity is increased, so causing the pressure to drop in their core. A primary example of this is the rolled up fluid sheet in Fig. 58 at t = 6.08-19.79 s forming a large vortex at its tail in the lower stream. This creates a site for vapor cavity nucleation once the local pressure drops below the corresponding saturation vapor pressure, as in the primary cavity nucleation seen at $x/c \cong 0.02$ in Fig. 57 at t = 6.08-19.79 s [89,185,187]. The deflection of the primary nucleation site(s) within the primary wavy disturbances to the lower stream (Fig. 57-58 at $t <$ 87.54 s) is due to the initial deceleration of the mixing layer high-speed side towards the low-speed side, which is eliminated as time proceeds; follow-on cavities nucleation occur around the mixing layer centerline, as indicated in Fig. 57 at, for example, $t >$ 106.76 s. Note that the primarily-nucleated cavity, which is of an incipient type, grows substantially with time (see for example Fig. 57 at t = 52.89-106.76 s), and eventually leaves the domain within the first flow-through time (Fig. 57 at $t >$ 142.12 s).

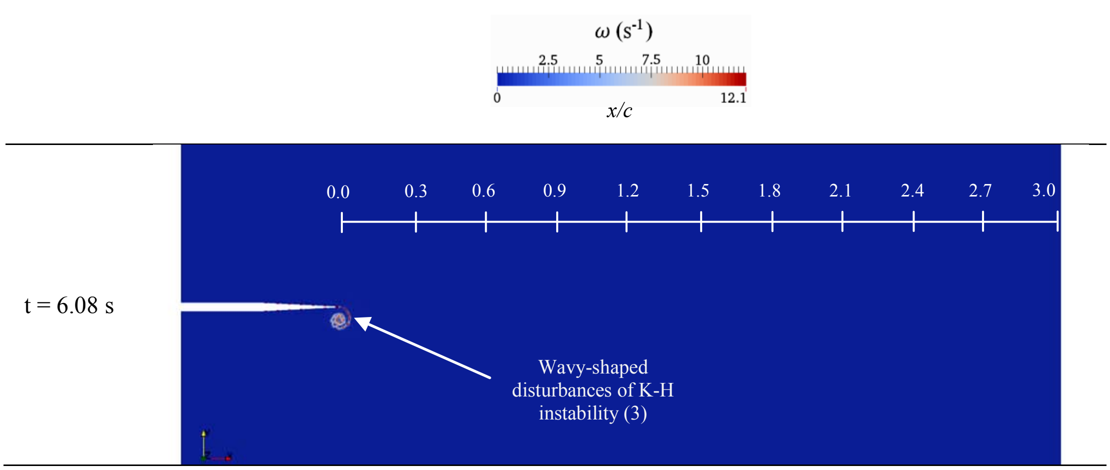

t = 19.79

t = 36.40

t = 52.89

t = 69.82

t = 87.54

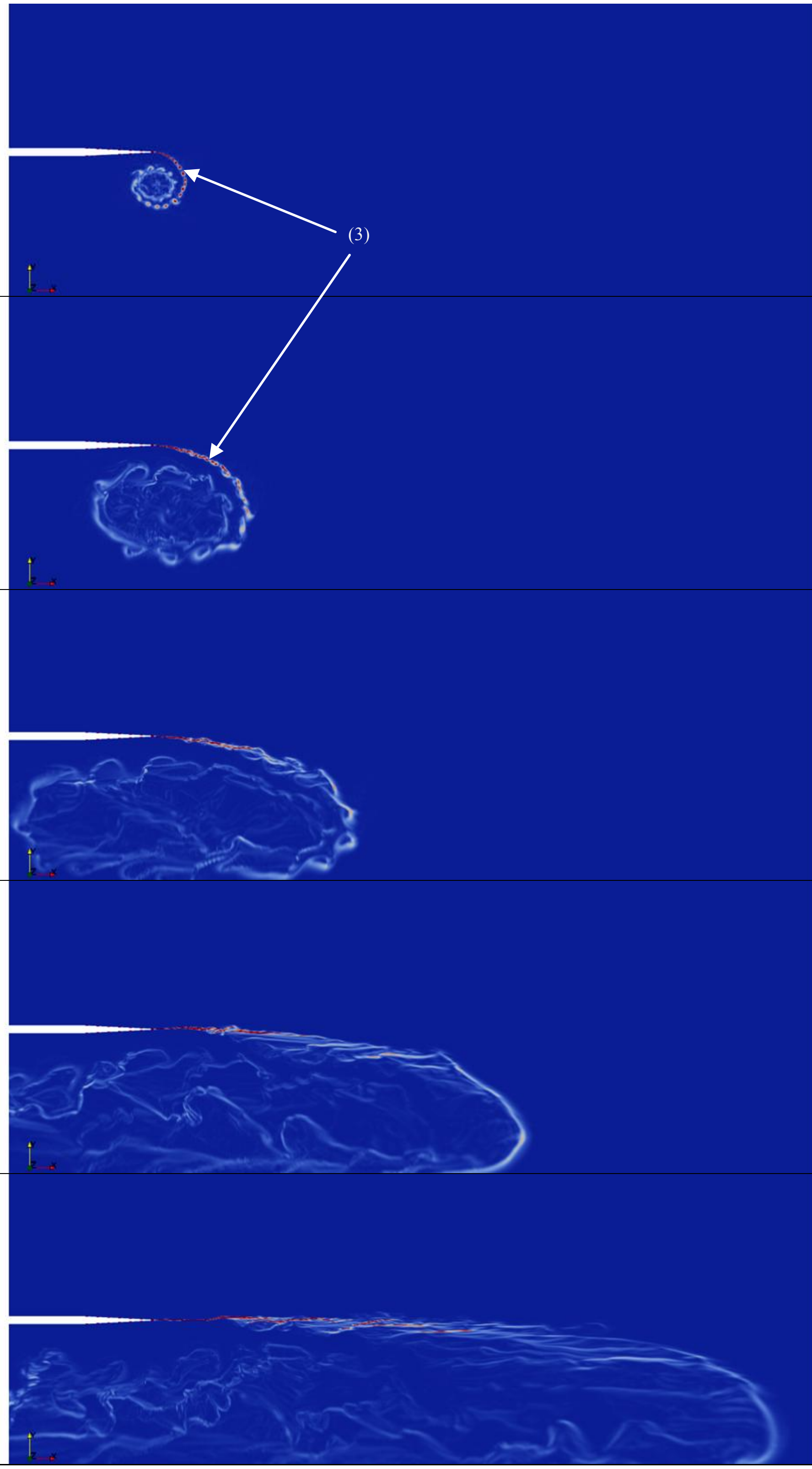

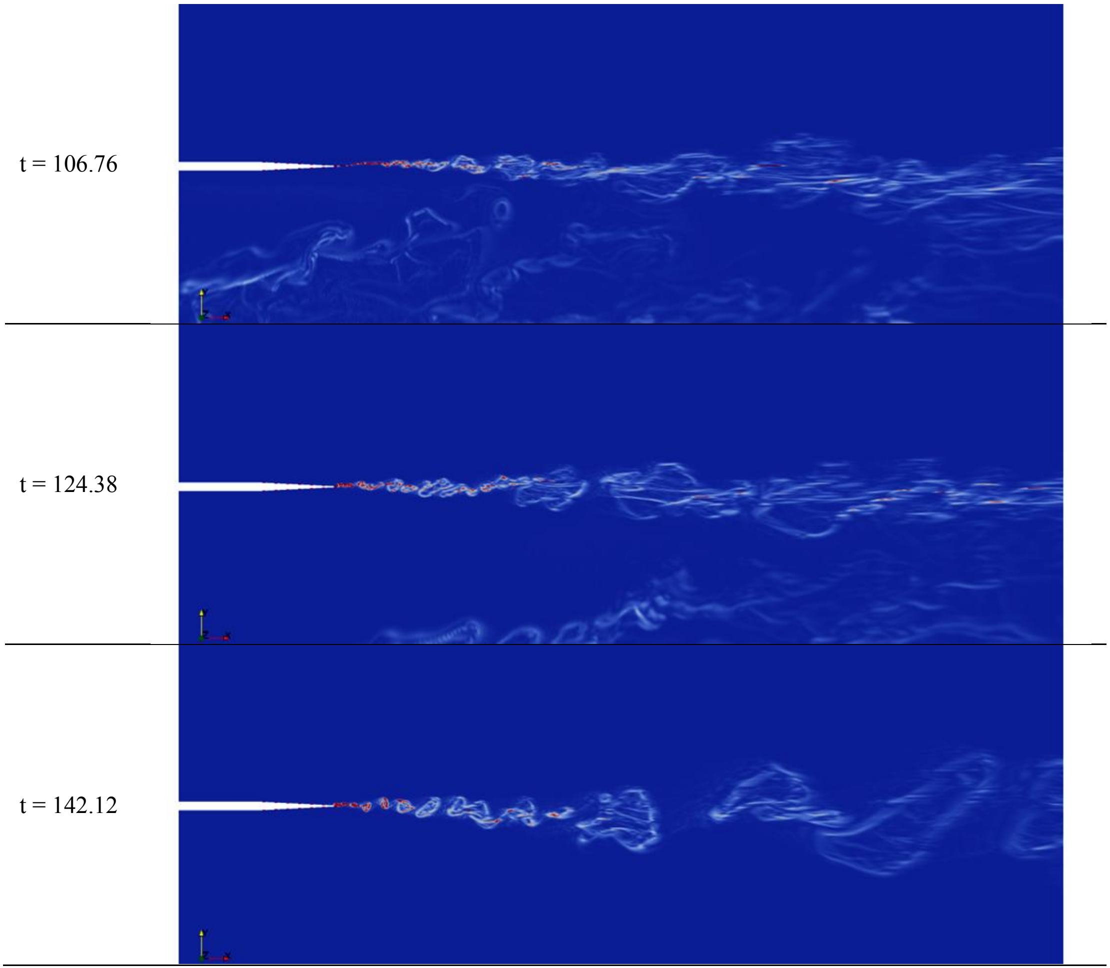

Fig. 58: Unsteady evolution of the cavitating mixing layer of LNG behind the splitter plate at Ca = 0.21: instantaneous contours of vorticity magnitude (1/s) at time instants of t = 6.08, 19.79, 36.40, 52.89, 69.82, 87.54, 106.76, 124.38, and 142.12 s.

Further expansion of the initially-incepted vapor cavities in the core of the mixing layer at $t >$ 69.82 s happens through a periodic process mainly comprised of 1) the development of re-entrant jet on the upper wall of the splitter plate (stage one); and 2) the progressive shedding process of the mixing layer (stage two). Within the stage one, an attached sheet cavity begins to appear on the plate upper side as a result of boundary layer separation, and grows until it reaches its maximum length (see for example Fig. 57 at t = 69.82-87.54 s). The entrained attached sheet cavity with convex rear shape then starts oscillating at its end, in upstream regions around the T.E., when it faces the highly-strained region with strong adverse pressure gradients. This eventually causes creation of an unsteady re-entrant jet on the plate which tends to irregularly break up the sheet cavity at its rear around the T.E. region (see for example Fig. 57-58 at t = 106.76 s). The unsteady re-entrant jet continually coincides with the attached sheet cavity interface, thus leading the sheet cavity to shed frequently at the T.E. and release vortex vapor pockets (Fig. 57-58 at t > 106.76 s) [168]. Such evolution occurs in the braid region of the mixing layer (x/c < 0.50) where streamwise vortices are concurrently stretched through the primary K-H instability and then expanded by secondary instability mechanisms onward [25,188]. The secondary instability mechanisms particularly supply the continuous pairing of counter-rotating vortices in the mixing layer, leading to production of larger coherent vortical structures within a few wavelengths downstream of the splitter plate [75, 189]. The vortical structures during this process grow quasi-linearly in the x-wise direction, as further explained in Section 9.4.

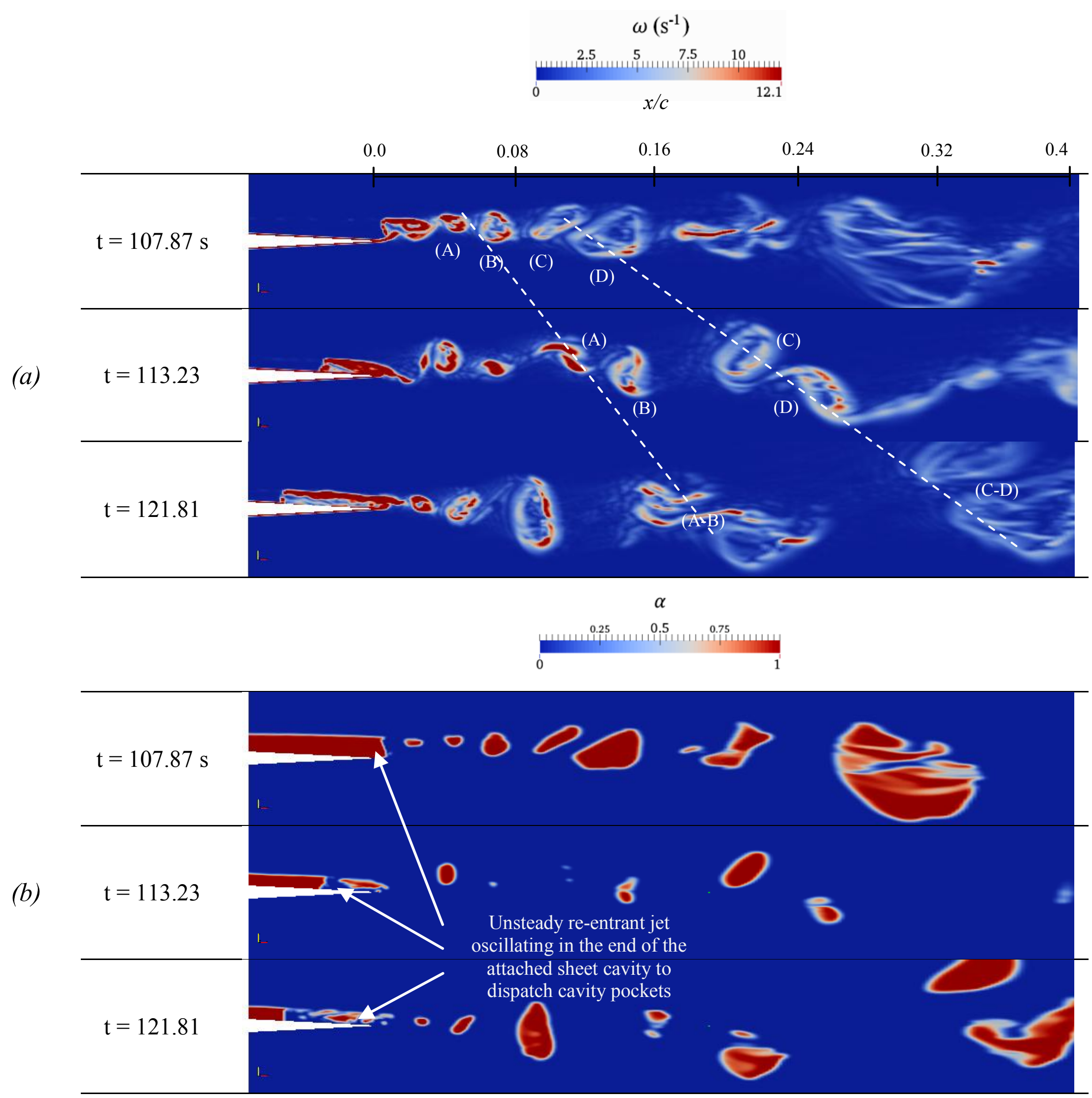

Fig. 59: Zoomed-in view (0.0 < x/c < 0.40 and -0.15 < y/c < 0.15) of the development of Kelvin-Helmholtz instabilities in the LNG cavitating mixing layer behind the splitter: instantaneous contours of (a) vorticity magnitude (1/s) and (b) vapor fraction at time instants of t = 107.87, 113.23, and 121.81 s. Note how the neighboring pairs of vortices roll around each other in the mixing layer core to form the vortex pairing phenomenon.

For better clarity, Fig. 59(a) displays a close-up view of the vortex pairing process near the T.E. Corresponding evolution of the vapor structures is also depicted in Fig. 59(b) showing how the cavity pockets are released from the oscillating re-entrant jet, and then turn into large cavities downstream. The pairing procedure of two sets of neighboring vortices (A)-(B) and (C)-(D) can be captured in Fig. 59(a). For example the primarily-separated vortices (C) and (D) in the second vortex set at $x/c \cong 0.11$ (t = 107.87 s) starts pairing at $x/c \cong 0.23$ (t = 113.23 s) until they merge at $x/c \cong 0.37$ (t = 121.81 s). The same procedure can be spotted in the case of the first neighboring vortices set (A) and (B), with the difference that the pairing occurs at smaller wave length relative to the splitter tip. During each pairing process, two neighboring vortices roll around each other and merge by linking the first vortex bottom right side to the top left side of the second one [190]. Such integration processes occur in the stretched region between two neighboring vortices, when the vortices diameters reach the vortex spacing, as reported in [97]. At situations like this, the vortices are large enough such that they cannot grow more without merging with the previous or following ones [75,185,191]. The newly-merged vortex then evolves with a shedding frequency half of the primary vortices' [190,192]. Vapor cavities nucleate and/or expand in the core of such coherent vortices as the local static pressure reduces due to locally high rotation rate [25,100]. The present observations in Fig. 57-58 are based on the observed coincidence of coherent vortices and vapor cavities. Note that the initiated pairing in the T.E. wake region is weakened further downstream where the grown-up vortices tend to gradually pair off (see also Fig. 58 at $t > 124.38$ s where fewer and fewer vortical structures are visible downstream) [135,193]. Typical viscous dissipation is the main reason for vortex decay [75,189].

The second stage of the cavitation development process occurs alongside the growth of secondary instabilities in the mixing layer, where the small upstream vapor pockets from the primary stage in the braid region eventually turn into large vapor clouds advecting downstream by the main liquid stream (Fig. 57-58 at $t > 106.76$ s). Such highly-unsteady vapor clouds expand in both streamwise and transverse directions inside the coherent vortices when the local static pressure is reduced below the saturation vapor pressure and/or, equivalently, the local temperature goes above the saturation temperature (Fig. 60) [25,100]. Improved cavity collapse/coalescence processes with stronger latent heat transfer in the cavity clouds, as well as enhanced roll-up in downstream regions of the mixing layer, are likely the main processes sustaining the clouds downstream [116,190,194]. The collapse of cavities particularly amplifies the local thermally-affected gradients of pressure and density (see also Section 9.6 for more discussion) in the flow, which consequently strengthen the local liquid-vapor exchange mechanisms [68,82,118]. Large magnitudes of vorticity in the liquid-vapor interfacial regions and vortex cores in Fig. 58 and Fig. 59(a) are indicative of this conclusion [75]. Note that the collapse of expanding cavity structures occurs downstream as the static pressure recovers. As further explained in Section 9.6, such collapse incidents are expected to cause localized pressure waves that irregularly break down the neighboring vapor spots, triggering their instability and collapse [116,172].

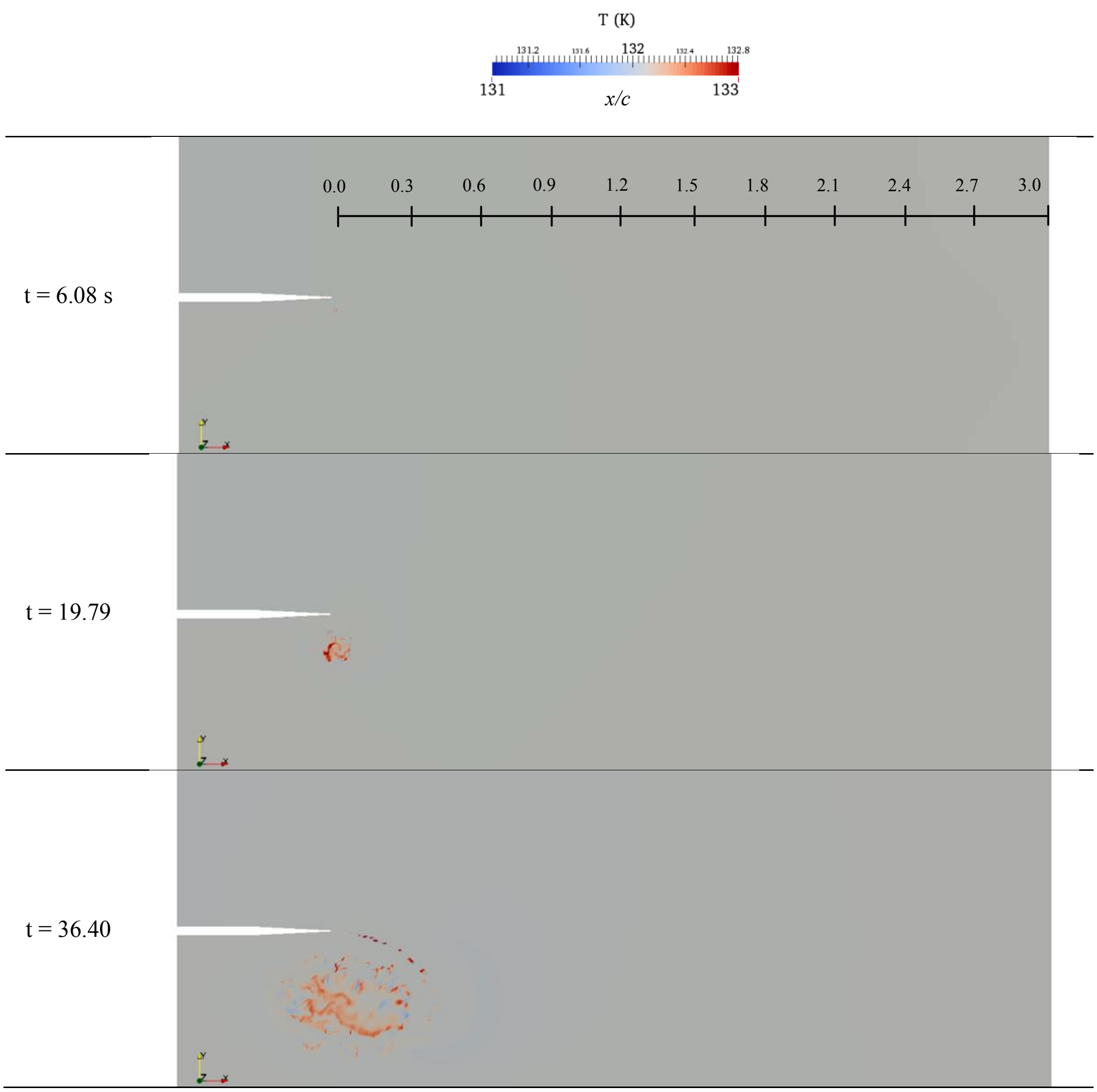

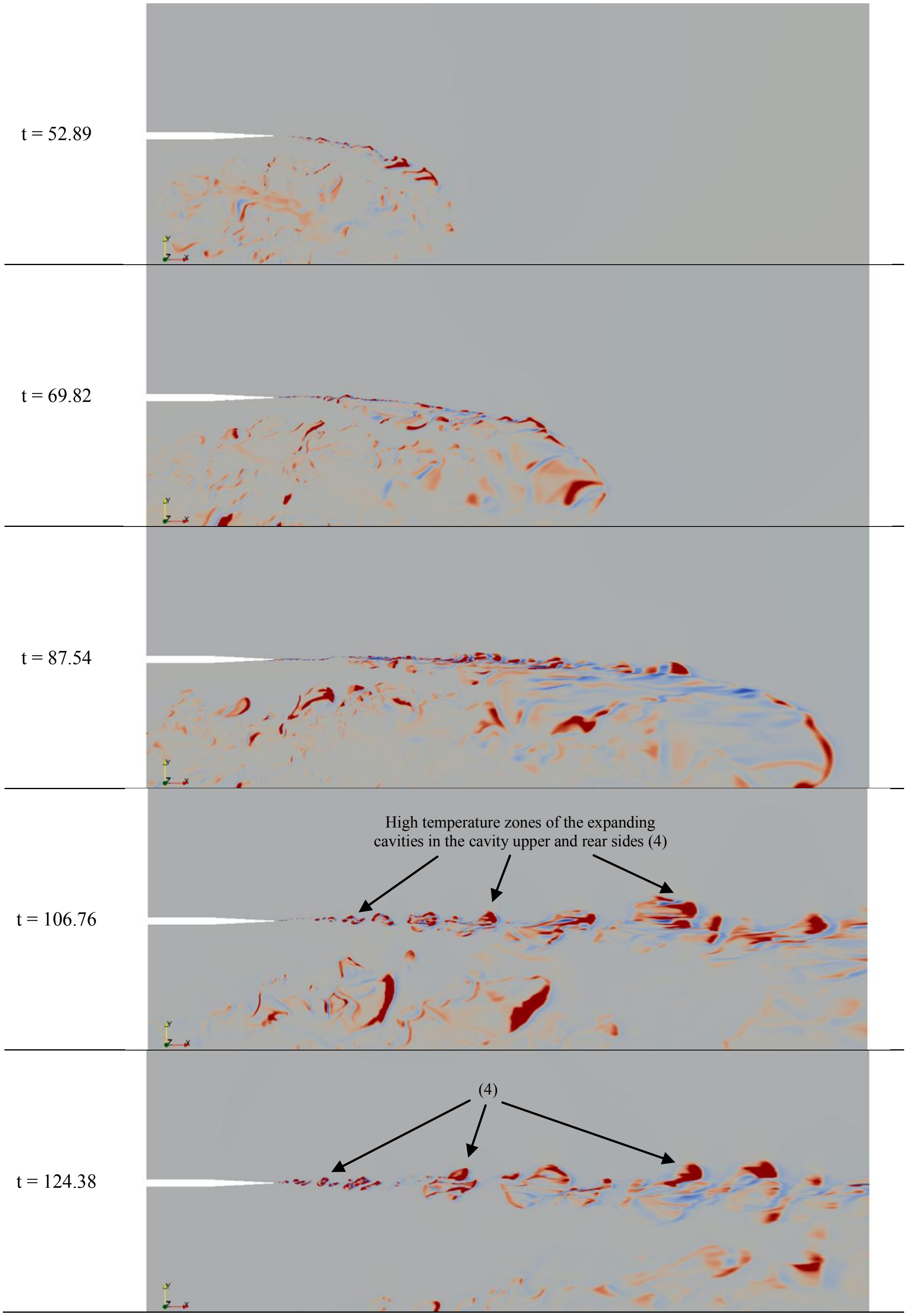
t = 52.89
t = 69.82
t = 87.54
t = 106.76
High temperature zones of the expanding cavities in the cavity upper and rear sides (4)
t = 124.38
(4)

t = 142.12

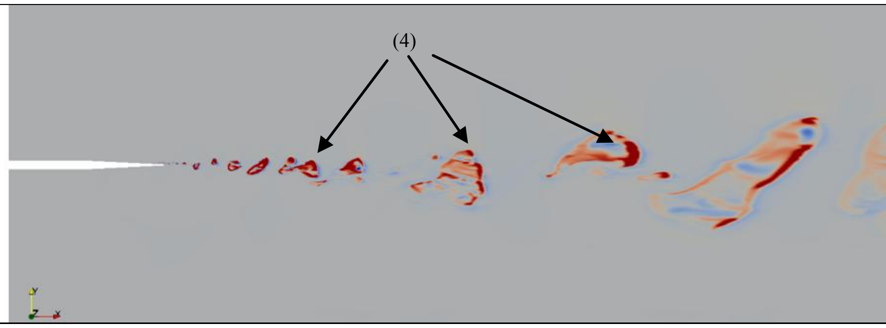

Fig. 60: Unsteady evolution of the cavitating mixing layer of LNG behind the splitter plate at Ca = 0.21: instantaneous contours of temperature (K) at time instants of t = 6.08, 19.79, 36.40, 52.89, 69.82, 87.54, 106.76, 124.38, and 142.12 s.

In addition to the mixing layer shedding mechanisms and the re-entrant jet oscillations, the cavitation development in the mixing layer evolves through latent heat exchange mechanisms between the neighboring vapor and liquid spots. This can be deduced from Fig. 60 showing the temporal evolution of the temperature field corresponding to the time instances in Fig. 57-58. It is observed that as the primary cavities are formed at the T.E. and turn into clouds downstream, because of the unsteady interactions of the re-entrant jet with the mixing layer roll-up process, their temperature varies through a combination of condensation and vaporization processes. For instance, larger temperature gradients within stronger latent heat transfers can be detected in the larger cavity cloud structures downstream as compared to the smaller detached cavities upstream (see for example Fig. 60 at $t > 106.76$ s). The high temperature zones of the expanding cavities, which predominantly occur in the cavity upper and rear sides due to the dominant gradient diffusion direction from the upper stream to the lower stream [75], indicate larger latent heat of vaporization transfer from the surrounding liquid into the cavity [21,188]. This process which simultaneously occurs with a temperature depression in the liquid is expected to assist in cavity expansion in the mixing layer by improving liquid-vapor interfacial mass transfers [37,65]. As a result of larger temperature depressions, vapor pressure in the surrounding liquid around the cavity is reduced more significantly, thus delaying the expansion of cavity compared to the regions with moderate temperature decrease [21,37,65]. Such evolution can also be seen, to a lesser extent, in the primary cavities that nucleate within the initial stages of cavitation development (see for example Fig. 60 at $t < 36.40$ s). Further discussion on the influence of thermodynamic parameters on the unsteady evolution of the present mixing layer is given in the comparative studies of Chapter 9.

8.3. Global Behavior of Vortex-Cavity Interactions

Vortex-cavity interactions are investigated by assessing the vorticity budgets in the vorticity transport Equation (30). Fig. 61-62 display the vorticity budgets for the present cavitating mixing layer of LNG operating at *Ca* = 0.21. Instantaneous vorticity strain-rate production budgets i.e. vortex stretching and tilting terms are depicted in Fig. 61, and the corresponding vorticity dilatation, baroclinic torque, and vorticity diffusion distributions are shown in Fig. 62. The vorticity contours are taken at a selected time instant of t = 151.22 s, and pertain to the cavitating region of $0.0 < x/c < 3.60$ and $-0.30 < y/c < 0.30$. Overall inspection of the results indicates that the vorticity is primarily produced within the liquid-vapor interface regions and central regions of cloud vapor structures.

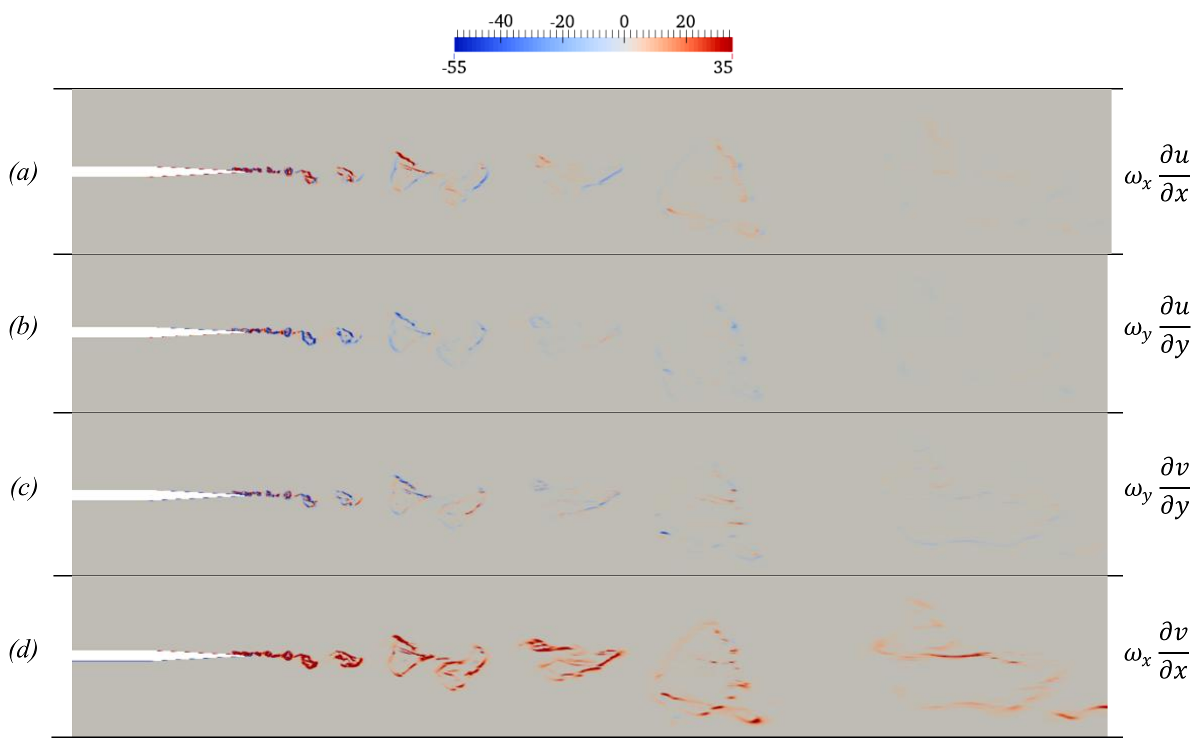

Fig. 61: Distribution of vorticity strain-rate production budget $((\boldsymbol{\omega} \cdot \nabla)\boldsymbol{u})$ components for the cavitating mixing layer of LNG at Ca = 0.21: vorticity stretching (a) and tilting (b) in streamwise direction; vorticity stretching (c) and tilting (d) in transverse direction at t = 151.22 s. Region of observation is 0.0 < x/c < 3.60 and -0.30 < y/c < 0.30. Units are in 1/s^2.

As indicated in the vorticity strain-rate production distributions (Fig. 61), the vortex stretching and tilting, which are affected by the velocity gradient, are dominant at the interface, rear, and the center of the cloud cavities in downstream regions [133,183]. These distributions seem to appear with larger magnitudes and be more uniform around the cavity structures that lie close to the trailing edge. Improved vorticity stretching in the streamwise direction (Fig. 61(a)) compared with the transverse component (Fig. 61(b)) is detected in the cavities near the T.E., which suggests that streamwise velocity gradients are dominant over transverse gradients in reorienting the shear-layer vorticity in the braid region. Significant reduction of the streamwise stretching and tilting (Fig. 61(a) and (b)), and transverse stretching (Fig. 61(c)) are observed in the cavity structures downstream. This reduction is smaller in the transverse tilting component (Fig. 61(d)), indicating it has a large contribution to the overall vorticity production downstream of the mixing layer. The excess of streamwise vorticity stretching is accompanied by a moderate reduction in the corresponding tilting distribution. The vorticity tilting in the transverse direction, however, seems to be more off-balance with the corresponding stretching term, suggesting more tendency of the vortex structures to tilt in the y-wise direction. The excess in vortex stretching leads the fluid particles to increase their angular speed and improve the vorticity production [169,171]. The opposite analogy can be deduced for the tilting term: the excess of vortex tilting causes the fluid particles to decrease their angular speed, thus reducing the vorticity production.

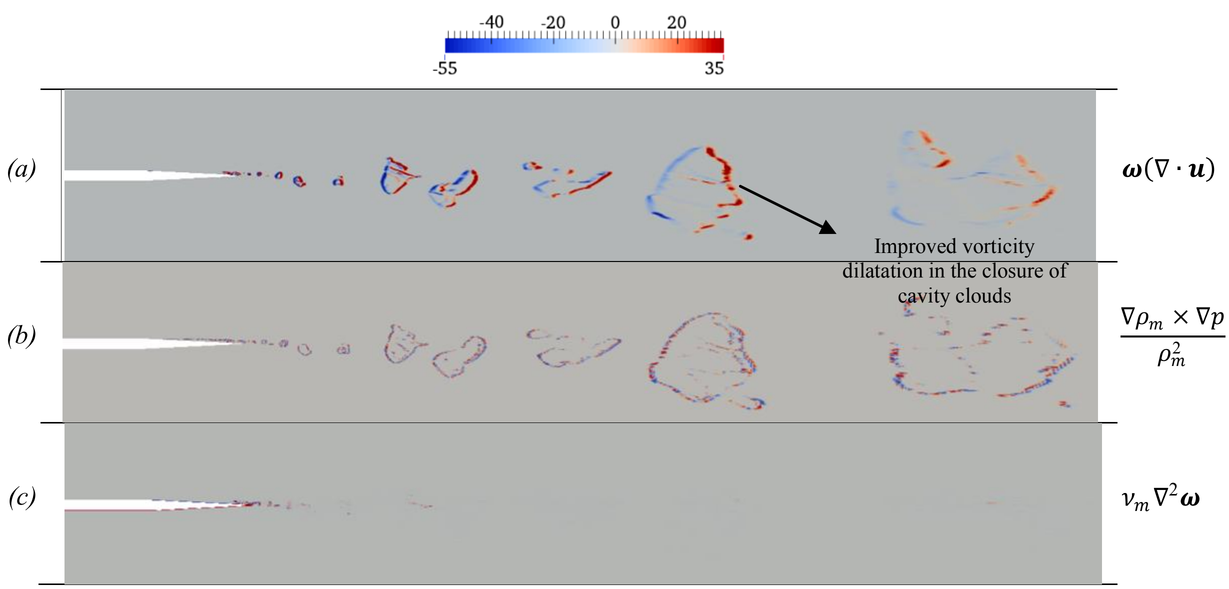

Fig. 62: Distribution of vorticity budgets for the cavitating mixing layer of LNG at Ca = 0.21: (a) vorticity dilatation; (b) baroclinic torque; and (c) vorticity diffusion at t = 151.22 s. Region of observation is 0.0 < x/c < 3.60 and -0.30 < y/c < 0.30. Units are in 1/s^2.

The dilatation term (Fig. 62(a)) and the baroclinic torque (Fig. 62(b)) seem to have the largest impact on the vorticity production, as compared to the vorticity strain-rate production budgets in Fig. 61. The vorticity diffusion term (Fig. 62(c)) is found to be negligible compared to the other terms. This is in line with the observations of Ji et al. [119] and Long et al. [127] suggesting that the shedding and collapse/coalescences of vapor clouds are largely associated with the vortex baroclinicity and dilatation. The dilatation term in Fig. 62 seems to appear with larger magnitudes in the regions with larger levels of vapor-liquid mass transfer, e.g. closure regions of vortex cavity structures with wider interface area [127,164]. The baroclinic term though is primarily concentrated along the liquid-vapor interfacial regions where the non-alignment of pressure and density gradients co-exists [100,116]. Large compressibility effects causing significant misalignment of the density and pressure gradients in these regions likely sustain cavitation by intensifying the baroclinic vorticity production [168]. Despite having smaller magnitudes against the dilatation term, the baroclinic term acts more actively in the interfacial regions which suggests it is more sensitive to vapor collapse and inception incidents [127]. The significance of active baroclinicity in both of upstream and downstream vapor structures can be further detected against the other vorticity budgets i.e. vortex stretching and tilting terms in Fig. 61 where the vorticity is essentially seen to decay longitudinally. This is mainly correlated to the thermally-affected pressure and density variations during cavitation processes, leading to more perturbation (vorticity) in shear layer and interfacial areas, as further discussed in Section 9.2.

From the vortex dilatation distribution in Fig. 62(a) it is also possible to distinguish the compression and expansion process of vortex regions [127]: according to the dilatation term $\left(\boldsymbol{\omega}(\nabla \cdot \boldsymbol{u})\right)$, vorticity is improved if the flow inside a vortex region is compressed, and is reduced if it undergoes expansion (see also Fig. 58 that shows smaller vorticity magnitudes as the vapor spots further expand downstream). Such behavior is based on the proportionality of vortex dilatation to velocity divergence, and thus mass transfer rate (see Equation (31)), which further confirms the large influence of compressibility on the vorticity distribution. A prominent example for this is the propagation of pressure waves through a cavity structure which increases the condensation rate in the cavity, so giving a rise to the velocity divergence and the vorticity dilatation [116,132]. Note that in a cavitating flow, the pressure waves are predominantly propagated by the collapse of downstream vapor spots, and tend to irregularly break down upstream cavities, as reported in [100,116,126]. This mechanism particularly leads to further development of vortical structures (including the re-entrant jets) and stronger cavity-vortex interactions through triggering local instabilities, as further illustrated in Sections 9.2-9.7.

The presented investigation on the baseline mixing layer simulation in this chapter is extended in the next chapter to evaluate the effects of operating conditions on the growth patterns of LNG cavitating spots and their detailed interaction mechanisms with instability characteristics.

9. Numerical Simulations of 2D Cavitating Mixing Layer of LNG at Different Cavitation Numbers

This chapter investigates the effects of operating conditions on the unsteady behavior of the 2D LNG cavitation mixing layer behind the flat plate splitter introduced in Chapter 8. Other than exploring the temporal evolution of LNG cavitating patterns, particular attention is given to characterizing the phase-change and shedding mechanisms inside the mixing layer: vortex-cavity instability characteristics at the given cavitation conditions are accurately evaluated to illustrate the shedding behavior of sheet and cloud cavitating spots under thermodynamic effects as well as their interactions with unsteady vortical structures.

To investigate the effects of operating conditions on the evolution of LNG cavitating mixing layer behind the splitter plate, the baseline test case with Ca = 0.21, as presented in Section 8.1, is further simulated here for cavitation numbers of Ca = 0.65 and 2.20, using the same numerical setup. A counterpart test to the flow at Ca = 0.65 is additionally simulated with the energy equation being switched off to better assess the influence of thermal parameters on the LNG phase-change behavior -- the simulated test resembles a thermo-insensitive version of the cavitating flow at Ca = 0.65 and is identified by Ca = 0.65i in the manuscript. Global behavior of the LNG cavitation mixing layer at the given operating conditions is addressed first in Section 9.1. Cavity-vortex interactions and instability mechanisms are then detailed in Sections 9.2-9.7.

9.1. Global Behavior of the Cavitation Flow

Fig. 63-64 respectively show the temporal evolutions of vapor fraction and vorticity magnitude fields for the 2D LNG cavitating mixing layer at the cavitation numbers of Ca = 0.21 and 0.65. The evolutions are depicted at time instants of t = 36.40, 87.54, and 142.12 s, in the mixing region of $0.0 < x/c < 3.0$ and $-0.45 < y/c < 0.45$. Note that the flow contours at Ca = 0.65i qualitatively behave in the same way as the Ca = 0.65 test so they are not shown here (detailed discussion on the comparisons of Ca = 0.65 and Ca = 0.65i tests is given in Sections 9.2-9.7). In Fig. 63-64, the cavitation flow development at Ca = 0.65 is observed to follow the same procedure as in the Ca = 0.21 test illustrated in Section 8.2: the primary deceleration of the mixing layer upper stream towards the lower stream develops an unsteady wavy-shaped K-H instability around the T.E. where the fluid sheet at the mixing layer interface behind the splitter rolls up at its tail to promote a primary vortex in the lower stream.

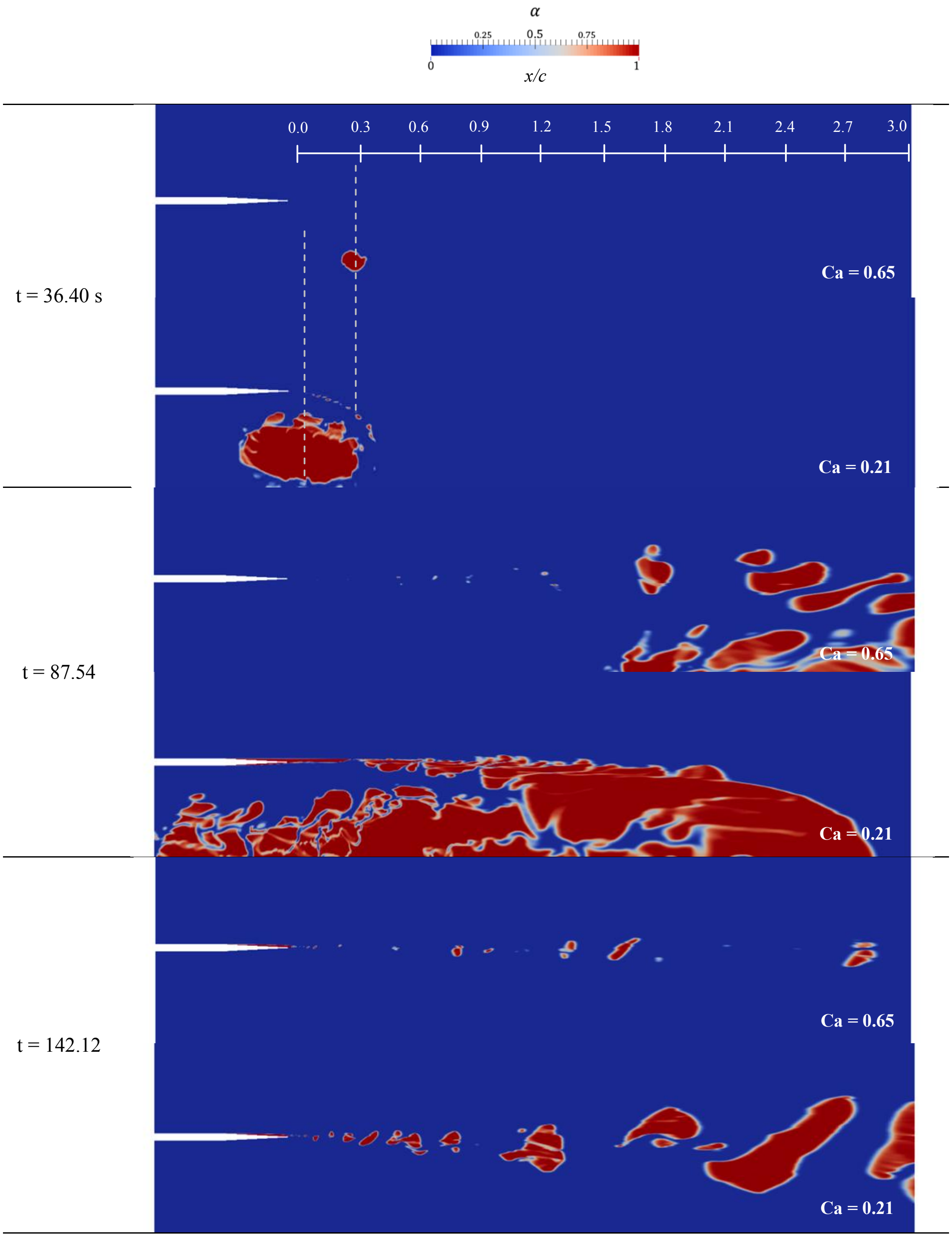

Fig. 63: Time evolution of the LNG cavitating mixing layer at cavitation numbers of Ca = 0.65 and 0.21: instantaneous contours of vapor fraction at time instants of t = 36.40, 87.54 and 142.12 s, in the mixing region of 0.0 < x/c < 3.0 and -0.45 < y/c < 0.45.

The static pressure drop in the primary vortex core below the local saturation vapor pressure triggers the onset of cavitation to appear in the form of an incipient vapor cavity (Fig. 63-64 at t = 36.40 s). As the incipient vapor convects downstream to leave the domain, the K-H instabilities are developed in the highly-strained braid region at the core of the mixing layer behind the splitter ($x/c < 0.50$) to create the primary vortical structures i.e. eddies (Fig. 64 at t = 87.54 s) [25,189]. Further expansion of the K-H instabilities with time advances secondary instability in the mixing layer (see Section 8.2 for more discussion), which is the main cause for pairing of vortical structures, and thus formation of larger coherent vortices further downstream (Fig. 64 at t = 142.12 s).

As the vortical structures are stretched and paired with neighboring vortices amid the secondary mixing layer instability development, their local angular velocity is raised, leading to formation of low-pressure vortex core(s). Depending on the operating conditions, pressure inside the generated vortex structures might drop down the local saturation vapor pressure where the liquid start evaporating [89,185,187]. More successive formation and collapse of cavity spots at the smaller cavitation number is deduced from the contours of Fig. 63-64 at t = 87.54-142.12 s, suggesting the presence of stronger local vaporization and condensation processes, including inception and collapse incidents, with larger temperature, density, and pressure gradients at improved cavitation conditions. As detailed in Section 9.6, this is likely due to the presence of larger recirculating zones in the mixing layer at smaller Ca = 0.21 that create stronger local instabilities through amplifying local vortex shedding events in smaller time periods [92,193].

The progress of shedding mechanisms in Fig. 63-64 at t = 87.54-142.12 s is concurrent to development of an unstable re-entrant flow in the closure region of the attached sheet cavity on the splitter upper wall, which is formed as a result of transient separation of the wall boundary layer (due to development of local adverse pressure gradients) coinciding with the highly-strained region at the splitter trailing edge [157] (see also Section 8.2 for more discussion). Continuous interactions of the sheet cavity with the unstable re-entrant jet around the T.E. lead the sheet cavity to frequently break off at its rear, releasing small vortex vapor pockets that convect downstream within the shedding vortices. The cavitating pockets are then triggered through the mixing layer instability mechanisms to form the unsteady large cavitation clouds successively shedding downstream.

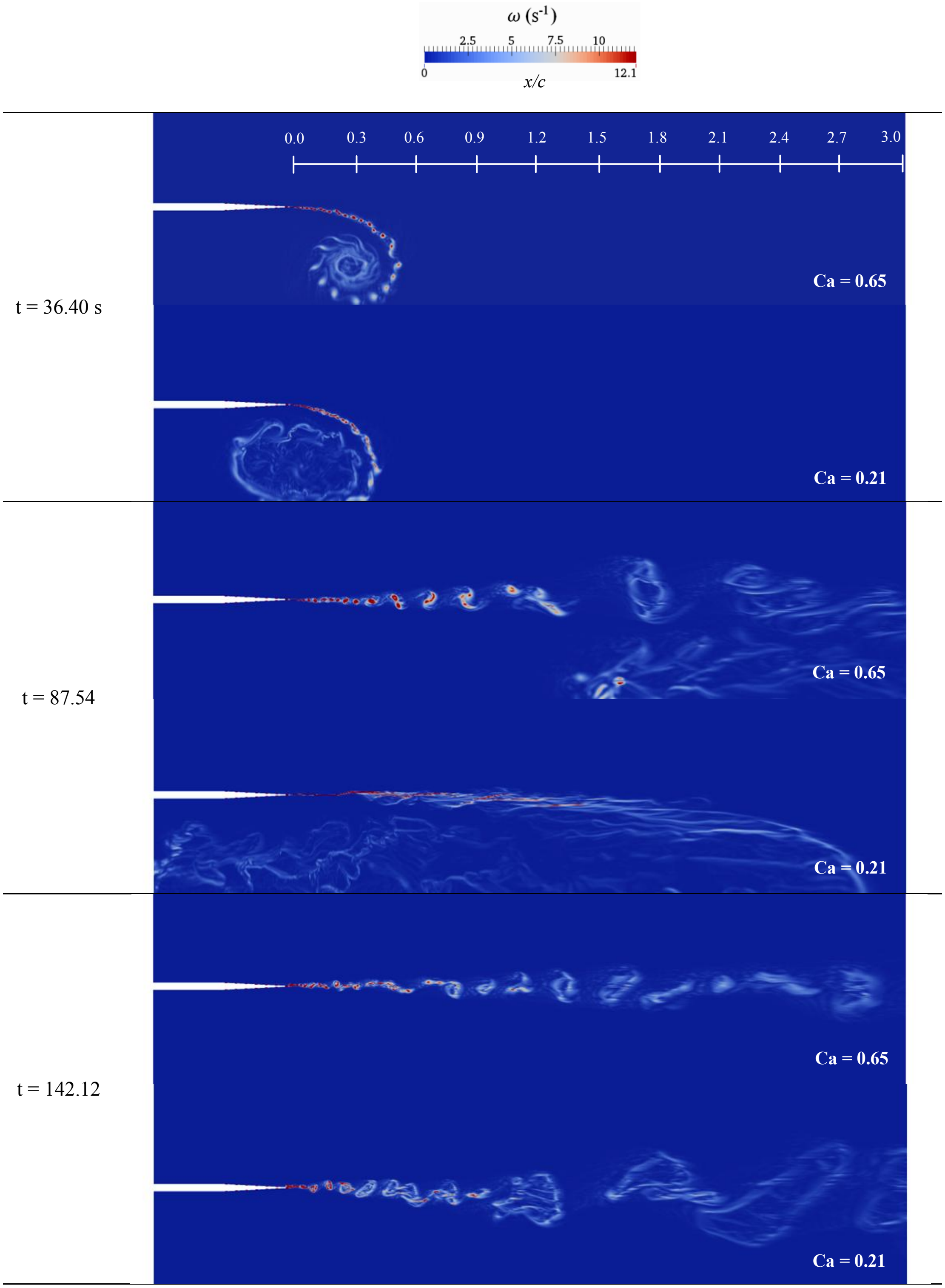

Fig. 64: Time evolution of the LNG cavitating mixing layer at cavitation numbers of Ca = 0.65 and 0.21: instantaneous contours of vorticity magnitude (1/s) at time instants of t = 36.40, 87.54 and 142.12 s, in the mixing region of 0.0 < x/c < 3.0 and -0.45 < y/c < 0.45.

As reported in [25,42,96], such cavities are primarily generated within the low-pressure cores of the paired K-H vortices where the mean velocity shear is maximized through the vortex distortion, i.e. stretching and tilting, processes. The excess of shear creates additional transverse pressure gradients inside the mixing layer so that cavitating spots smoothly develop from the mixing layer core to its boundaries. As discussed in Section 8.3, vorticity dilatation and baroclinicity are the major contributors for the progress of cavities into large cavitation clouds, due to the compressible characteristics of the flow.

The cavitation development procedure seen in Fig. 63-64 occurs similarly in both of the Ca = 0.21 and 0.65 tests with the main difference being on the level of cavitation; larger cavitating spots with improved vaporization-condensation processes within stronger recirculating zones are formed at the smaller Ca = 0.21. The formation of cavity structures in the Ca = 0.21 case also seems to be moderately slower than the Ca = 0.65 test (compare for example the primary vortex cavity location in $0.0 < x/c < 0.30$ in Fig. 63 at t = 36.40 s). Such differences mainly pertain to how the counterpart eddies pair, despite the fact that both Ca = 0.21 and 0.65 tests depict the same overall development of vortical structures. As detailed in Section 9.6, the amplified shear layer instability in Ca = 0.21 causes faster pairing of the counter-rotating vortices in smaller time periods within a few wavelengths past the splitter plate, leading to earlier formation of larger vortices compared to the Ca = 0.65 test (see Fig. 64 at t = 142.12 s) [25,92]. This conclusion can be also understood from the vapor fraction contours in Fig. 63 at for example t = 142.12 s showing that at the lower cavitation number the succession of cavity growth and collapse is increased as compared to the larger cavitation number test with longer breakup/growth periods.

In other words, the inhibited pairing processes that can lead to cavity inception/development at Ca = 0.65 causes the vortex structures to convect more easily, resulting in a faster convection of cavity spots downstream compared to the Ca = 0.21 test. Such behavior further suggests the effects of inertia in destabilizing cavity structures through easing the vortex breakup processes in the mixing layer. At smaller Ca = 0.21, the strengthened low-pressure core regions in the shedding vortex structures enhance the local temperature-dependent density and velocity gradients, which consequently increase the tendency to phase change through promoted local instabilities [24,35]. The presence of an initial sheet vapor cavity that quickly becomes unstable to shed longer and stronger cavity pockets additionally improves such behavior [116,154]. This is not the case at Ca = 0.65 where a slow small sheet cavity on the splitter wall does not provide the necessary conditions for frequent succession of large cavity clouds. The current observations are consistent with the established conclusion that the reduction of cavitation number in cavitating flows causes faster breakup and penetration of vapor spots into liquid phase, thus enhancing local vaporization processes [74,81].

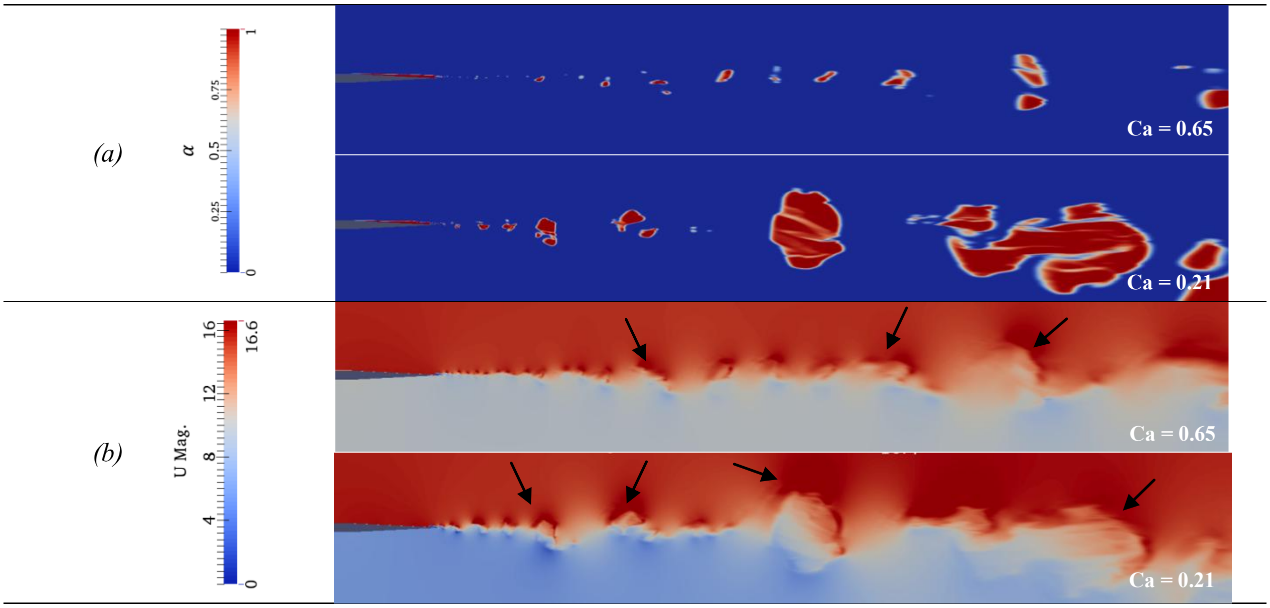

Fig. 65: Comparison of the LNG cavitating mixing layer at cavitation numbers of Ca = 0.65 and 0.21: instantaneous contours of (a) vapor fraction and (b) velocity magnitude (mm/s) at time instant of t = 126.21 s. Note the arrowed local flow accelerations as a result of unsteady development of vapor spots.

It is noteworthy that the mixing layer secondary instability is mainly originated from non-uniform acceleration of the primarily-shed structures through the non-uniform velocity field, as reported in [75,185]. The non-uniformity is improved with the presence of unsteady vapor spots developing inside the mixing layer, by means of altering the momentum exchange between the cavity and vortex structures [100,194]. This can be illustrated in Fig. 65 comparing the instantaneous vapor fraction and velocity magnitude contours of the present cavitating mixing layers at Ca = 0.21and 0.65, at time instant of t = 126.21 s. Local flow accelerations following the formation of vapor spots inside the vortex structures are illustrated with black arrows. These accelerations lead to temporal local density reduction, thus giving rise to increased velocity to conserve mass. This behavior is more pronounced at the smaller cavitation number owing to the formation of bigger and stronger cavity spots causing larger derivatives of density with respect to time [115,125].

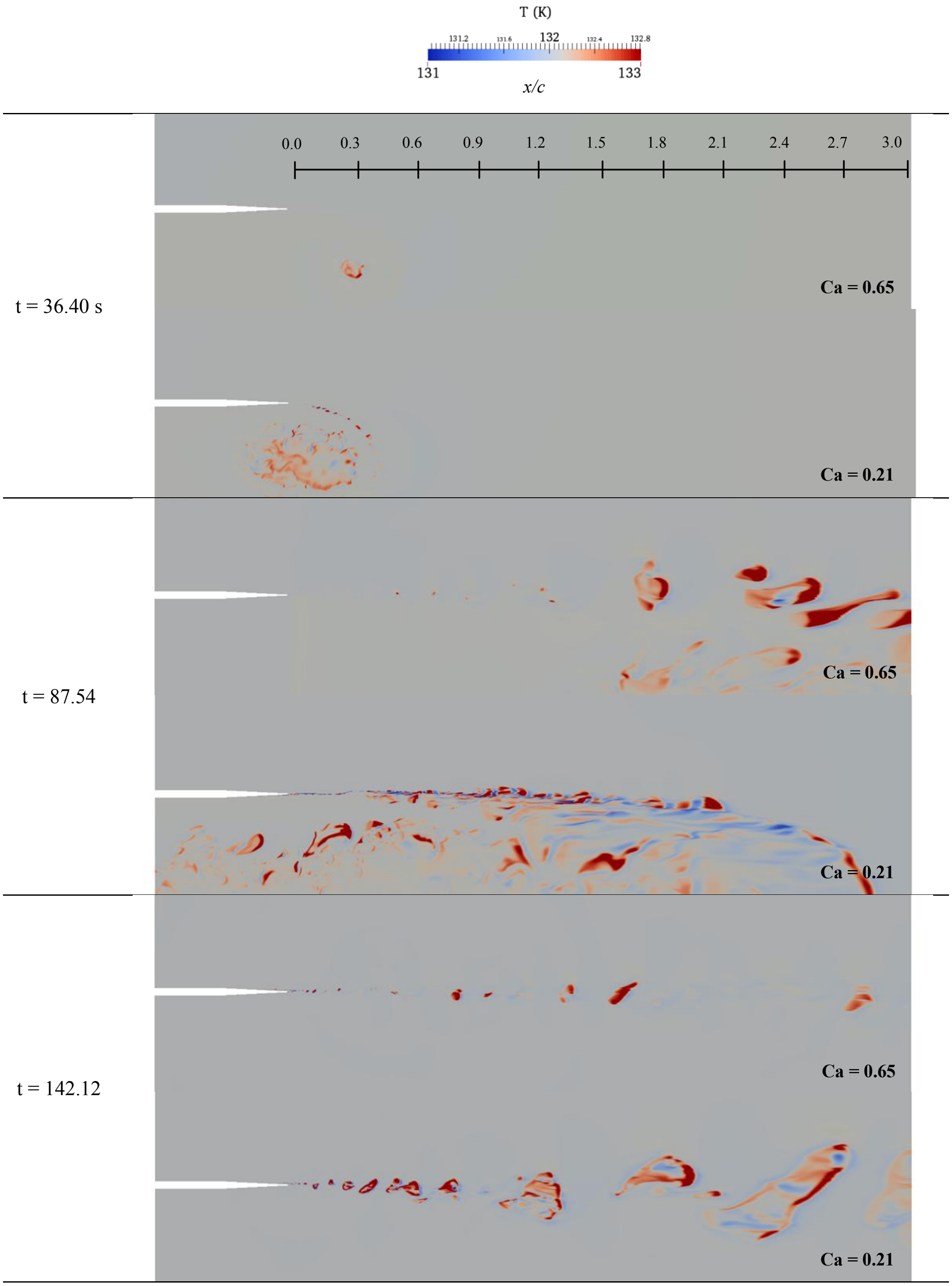

Fig. 66: Time evolution of the LNG cavitating mixing layer at cavitation numbers of Ca = 0.65 and 0.21: instantaneous contours of temperature (K) at time instants of t = 36.40, 87.54 and 142.12 s, in the mixing region of 0.0 < x/c < 3.0 and -0.45 < y/c < 0.45.

Other than the mixing layer shedding mechanisms, the expansion of cavity spots in Fig. 63, and so the overall cavitation level in the mixing layer, is affected by the vaporization latent heat transfers between the cavities and their surrounding liquid [21,37,159]. This can be deduced from the corresponding evolution of the temperature field in Fig. 66. A slight temperature variation of ±2 K is seen in the evolution of cavitating spots in both of the Ca = 0.21 and 0.65 tests, with high temperature gradients along the liquid-vapor interfaces and within the upper and frontal sides of the cavities [21,188]. Since the vortex-cavity interactions occur simultaneously with temperature-induced phase change incidents, the observed variation significantly alters the evolution of the cavities by imposing strong thermally-affected gradients which can substantially reshape the cavity structures. For instance, the temperature decrease around a cavity due to the exchange of latent heat during vaporization causes the cavity to further expand. However, as a result of the temperature depression, saturated vapor pressure in the surrounding liquid around the cavity is reduced and delays the progression of the cavity, particularly compared with cavitation processes without temperature change and/or with smaller temperature variations [21,37,65] (see also Sections 9.5-9.6 for more discussion). Such behavior is suppressed at larger cavitation number Ca = 0.65, as shown in Fig. 66 at t = 142.12 s, where weaker and smaller cavity structures are formed as a result of weakened instability and heat exchange mechanisms. The previously-observed delay in the cavity progress at Ca = 0.21 in Fig. 63 compared to Ca = 0.65 further pertains to this reason, caused by longer phase change processes with improved thermodynamic effects in larger cavitating spots in the former case. Note that the variation of thermally-induced gradients, and so instability, in the present cavitating mixing layers are estimated to be additionally influenced by the collapse of vapor spots especially in downstream regions, as denoted by [39,116,127]. Upon a collapse process, pressure waves propagate within the cavity structures, causing sudden changes in the local pressure, temperature, and volume fractions, as detailed in Section 9.6 [70,81]. More successive inception and collapse of the cavities at Ca = 0.21 adds more unsteadiness to the flow and thus to the local temperature field (Fig. 66 at t = 87.54-142.12 s), leading the cavities to be more strongly affected by temperature fluctuations, besides the other sources of unsteadiness i.e. variations of density and pressure [51,64].

Fig. 67-68 compare the corresponding temporal evolutions of the vorticity magnitude and temperature fields in the Ca = 2.20 test to the given contours of the Ca = 0.21 test in Fig. 64 and 66. Note that at the cavitation number of Ca = 2.20 cavitation does not occur in the mixing layer because static pressure does not drop below the saturation vapor pressure, so the flow resembles a single-phase behavior with no vapor evolution (vapor fraction field not shown).

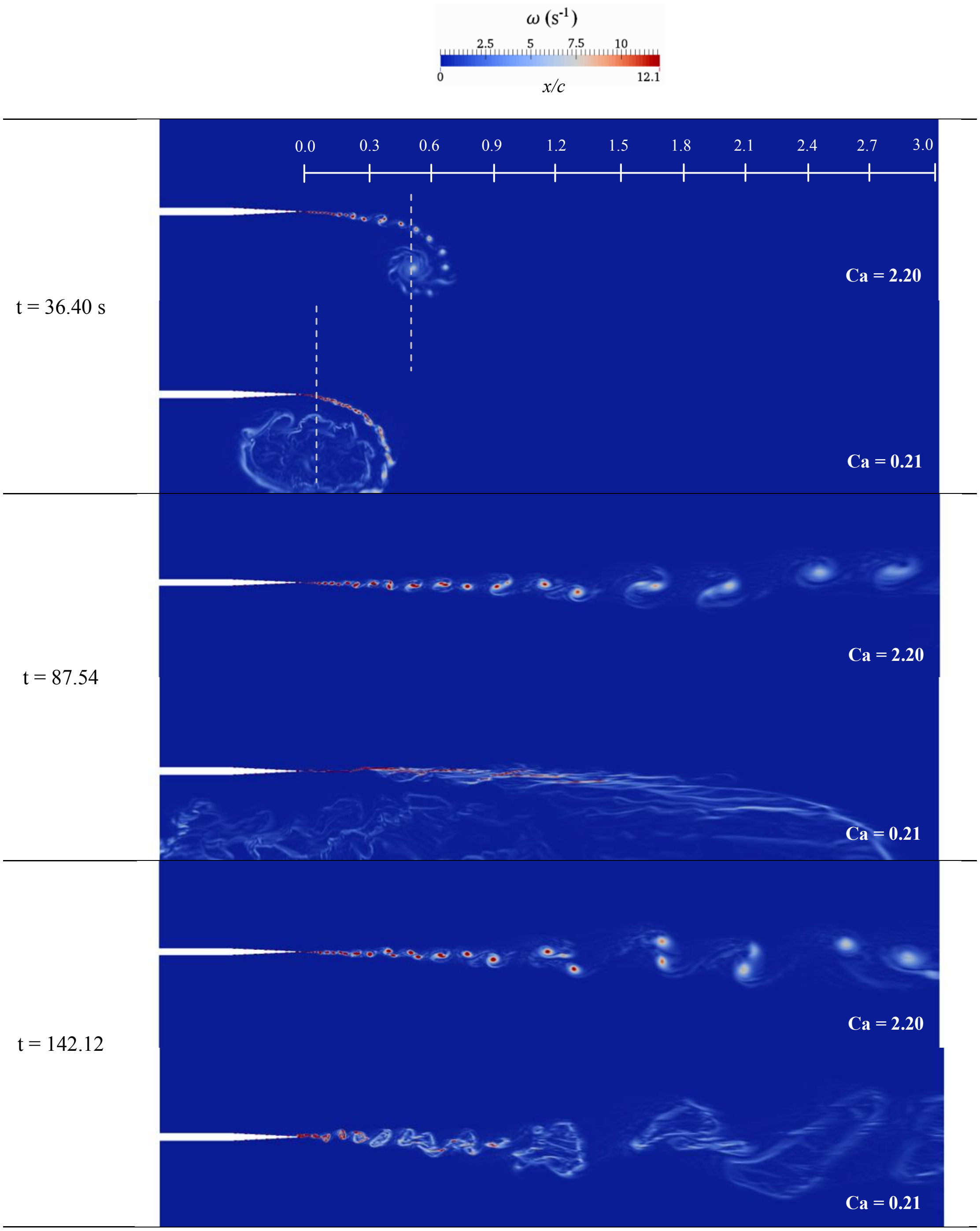

Fig. 67: Time evolution of the LNG cavitating mixing layer at cavitation numbers of Ca = 2.20 and 0.21: instantaneous contours of vorticity magnitude (1/s) at time instants of t = 36.40, 87.54 and 142.12 s, in the mixing region of 0.0 < x/c < 3.0 and -0.45 < y/c < 0.45.

In the vorticity contours of Fig. 67, both the non-cavitating and cavitating tests show the same overall shedding procedure, though a larger vortex development area is indicated in the latter case; the mixing layer shedding begins with a vortex roll-up right after the T.E. and continues through a follow-on pairing process, as detailed in Section 8.2. This is in agreement with Aeschlimann et al. [96] experimental work reporting that the vortex pairing phenomenon in cavitating and non-cavitating mixing layers of water is initiated when neighboring pairs of vortices roll around each other. In the non-cavitation test, the pairing process is further observed to proceed faster downstream (compare for example the primary vortex locations in Fig. 67 at t = 36.40 s), which consequently results in faster breakdown of the initial vortex structures into small-scale vortices [25,195,196]. In the cavitating case, however, the vortex structures are distorted additionally by the cavity spots, making the vortex development procedure longer than the non-cavitating test. The vapor cavities in such interactions typically tend to distort and break down the vortical structures into smaller eddies and thus improve the instability, while being diffused from the vortices cores into the mixing layer inter-eddy spaces, as reported in [96,125]. The improved instability is mainly caused by the development of larger gradients of density, pressure, and temperature particularly in the cavitating vortex cores and interfacial liquid-vapor regions, as can be spotted from the high-vorticity intermittent zones in Fig. 67 at t = 142.12 s; in the non-cavitation test, the high-vorticity regions are observed only in the vortex cores (see also Sections 9.2 and 9.6 for more discussion). Besides the mixing layer shedding mechanisms, the larger flow gradients at Ca = 0.21 are substantially altered by the presence of strong temperature variations within the cavitation spots, as can be deduced from Fig. 68. In the non-cavitating test, small temperature gradients are consistent with the decreased level of vorticity variations due to the absence of phase change. Note also in Fig. 67 that the evolution of cavities in the cavitation test seems to lead the vortical structures to become more coherent than those at the non-cavitation condition where the increased pressure levels in the vortices are likely the main reason for the loss of coherence [135]. The vortex structures in both of the present tests are weakened longitudinally as they convect downstream, which is mainly due to the dominance of viscous dissipation typically observed in free shear flows [75,125]. Further discussions on the LNG cavitation mixing layer instability and cavity-vortex interactions at the simulated operating conditions are given in the Sections 9.2-9.7.

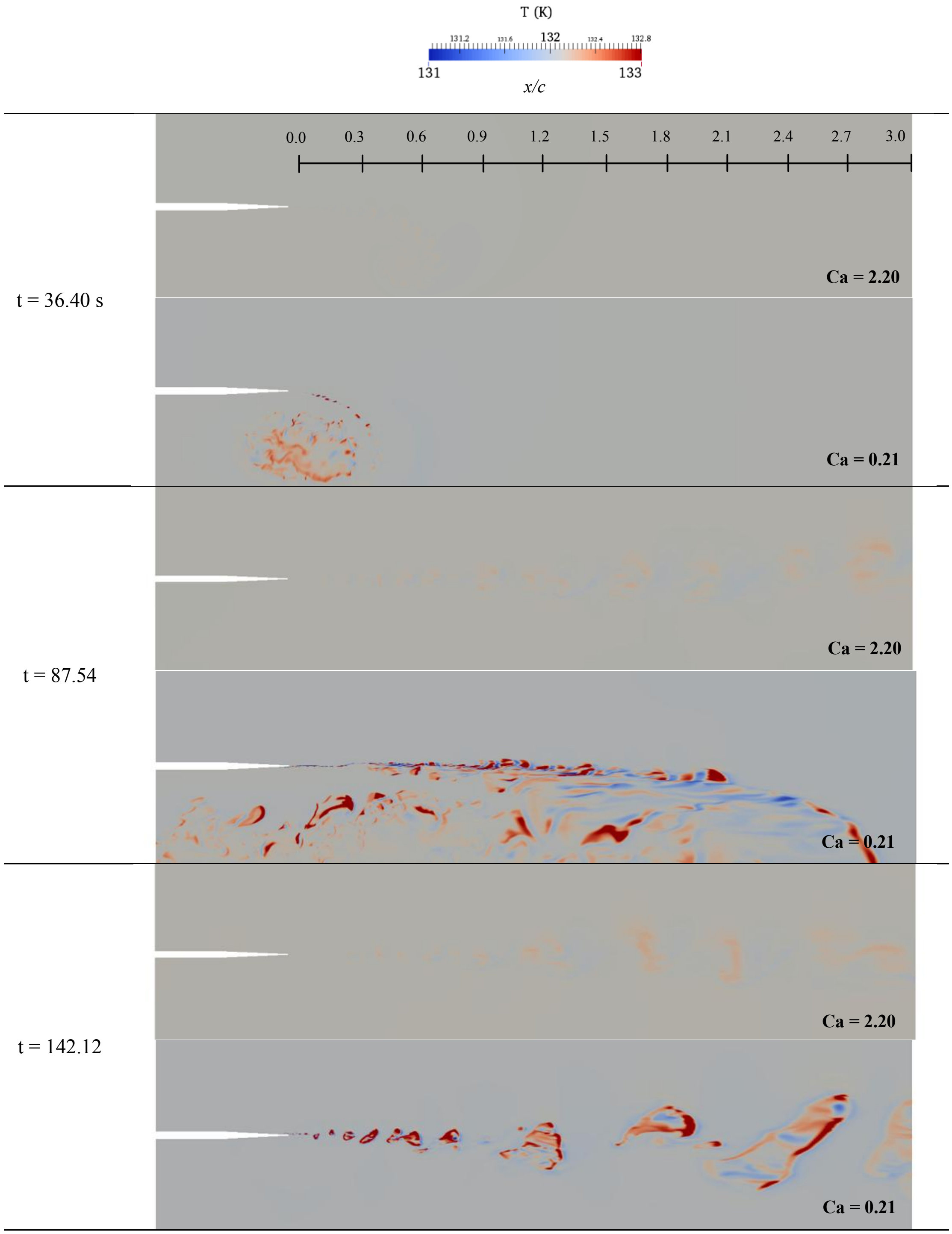

Fig. 68: Time evolution of the LNG cavitating mixing layer at cavitation numbers of Ca = 2.20 and 0.21: instantaneous contours of temperature (K) at time instants of t = 36.40, 87.54 and 142.12 s, in the mixing region of 0.0 < x/c < 3.0 and -0.45 < y/c < 0.45.

9.2. Vortex-Cavity Interaction Mechanisms

To further examine the effects of cavitation condition on the behavior of LNG cavitating mixing layer, Fig. 70 compares the instantaneous evolutions of streamwise and transverse vortex stretching and tilting terms along a horizontal reference line placed in the center of the mixing layer (y/c = 0.0) between x/c = 0.10 and 2.50. Fig. 69 presents the locations where data is analyzed in the subsequent figures. Corresponding evolutions of the vorticity dilatation and baroclinic torque along with the vorticity magnitude and vapor fraction fields are provided in Fig. 71. Viscous diffusion is found to be negligible compared to other terms so is not shown in the figures. Results pertain to the simulated operating conditions of Ca = 2.20, 0.65, 0.65i, and 0.21, and are taken at the time instant of t = 600.0 s when the flow has evolved around two flow-through times after reaching statistically steady state at $t \cong 300.0$ s. Overall examination of the results indicate that the vortex stretching (Fig. 70(a) and (c)) and tilting (Fig. 70(b) and (d)) in the cavitation tests are increased with the decrease of cavitation number and hit their largest values at the smallest Ca = 0.21 [125]. The increase is more visible in the upstream regions close to the splitter trailing edge (see $0.0 < x/c < 1.0$ in Fig. 70(a)-(d)) than the downstream where larger expansion of vapor spots reduces the overall density and velocity fields. Such increasing trend with the decrease of Ca is also observed in the vorticity dilatation (Fig. 71(a)) and baroclinic torque (Fig. 71(b)) terms, especially compared with the largest Ca = 2.20 where the mixing layer behaves as a single-phase flow and shows quite negligible vorticity dilatation and baroclinicity [125,174]. Increased vortex dilatation and baroclinicity at smaller Ca seem to be more extended in the streamwise direction (see for example $x/c > 1.50$ in Fig. 71(a)-(b)) compared to the corresponding vortex stretching and tilting variations in Fig. 70, indicating larger effects of these two terms in altering downstream vortex evolution, as similarly observed in the vorticity contours of Section 8.3. In the non-cavitation test with Ca = 2.20, significant vortex stretching and tilting are detected which makes the corresponding vorticity magnitude (see Fig. 71(c)) become comparable against the cavitation tests.

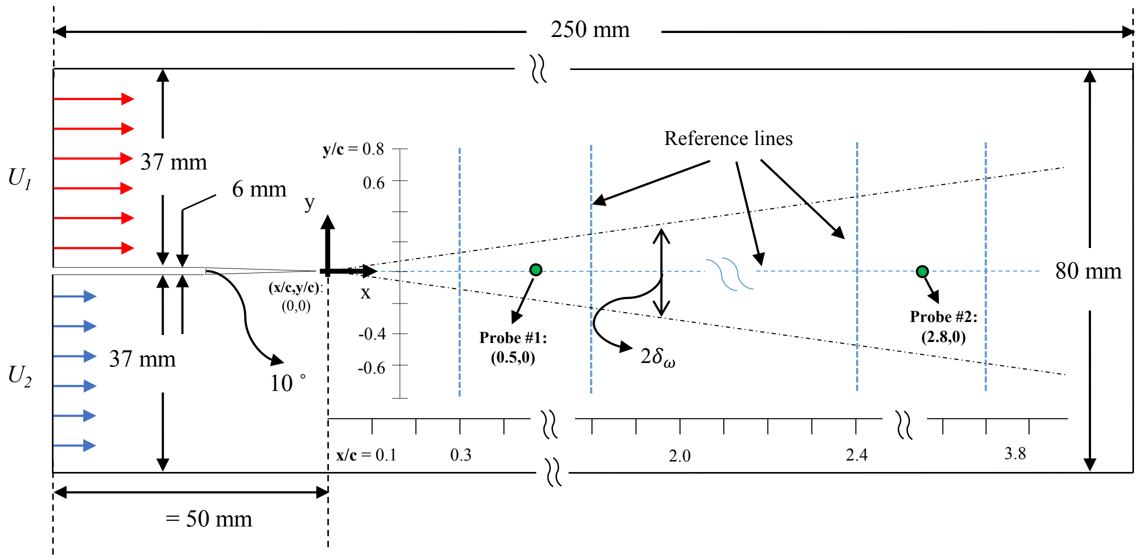

Fig. 69: Schematic location of the horizontal reference line, equally-spaced transverse reference lines, and reference probing stations, in the LNG cavitating mixing layer. Note that the transverse reference lines and the probing stations are employed in Sections 9.3-9.7.

(a)

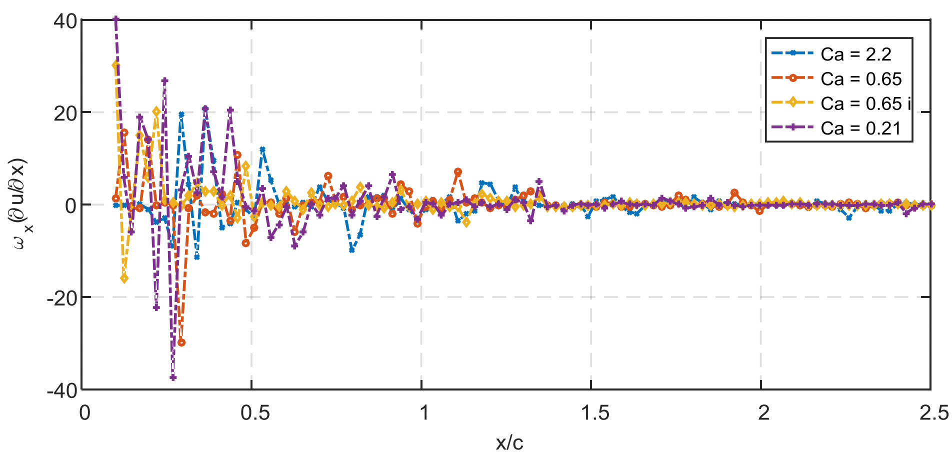

(b)

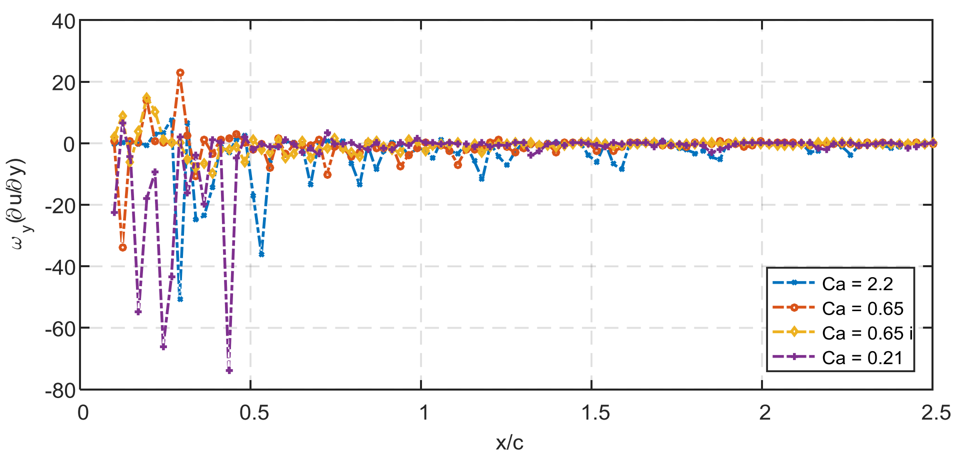

(c)

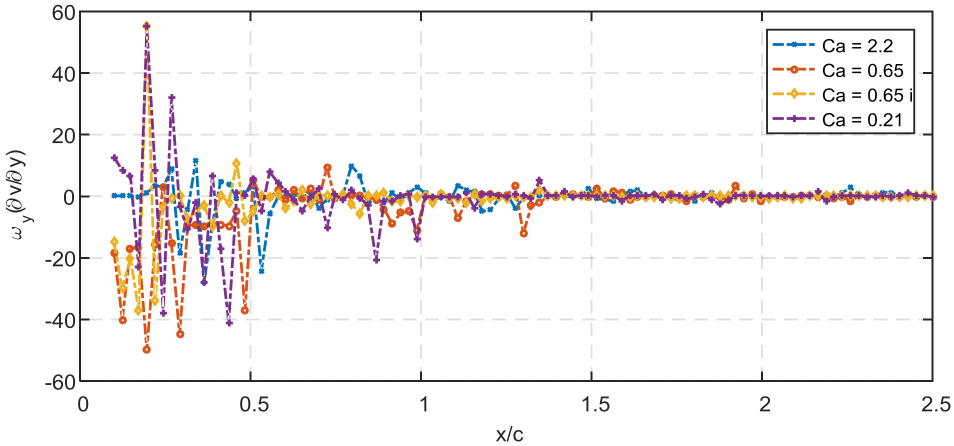

(d)

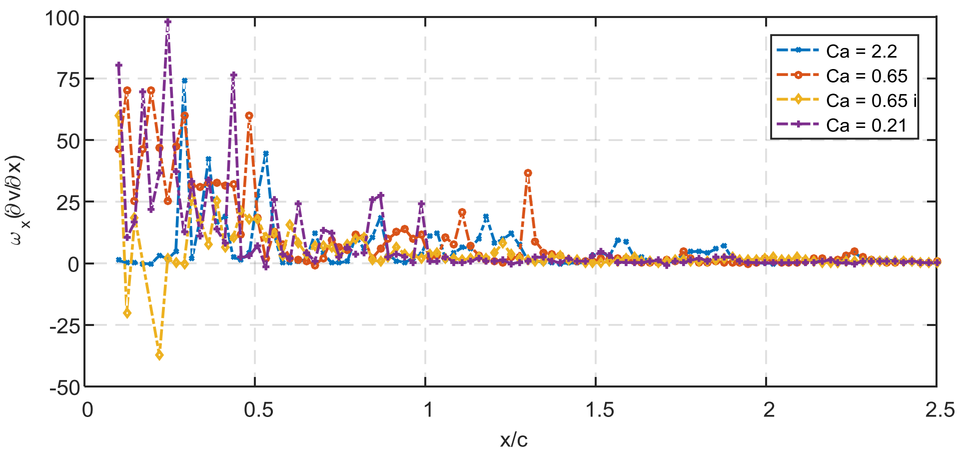

Fig. 70: Distributions of vorticity budgets along the horizontal reference line at t = 600.0 s for the cavitating mixing layer of LNG at Ca = 2.20, 0.65, 0.65i, and 0.21: streamwise vorticity stretching (a) and tilting (b); transverse vorticity stretching (c) and tilting (d). Units are in $1/s^2$.

In Fig. 70, improved upstream vorticity stretching and tilting with the reduction of *Ca*, in the cavitation tests from *Ca* = 0.65 to 0.21, is mainly due to the formation of larger cavity spots at smaller *Ca* which cause more distinctive distortion of the braid region close to the splitter T.E. as vapor structures expand [189]. The vorticity stretching and tilting are also observed to be larger in the transverse direction than those in the streamwise direction, highlighting the significance of transverse gradients in altering the cavity-vortex interactions in the present flows. As for the thermal influence, comparison of the thermo-insensitive *Ca* = 0.65i and the corresponding thermo-sensitive *Ca* = 0.65 tests indicate that the thermodynamic effects change the vortex-cavity patterns through increasing the longitudinal and transverse vortex stretching and tilting, especially in the upstream regions in x/c < 1.50. The observed patterns are found to be in accordance with the overall instability behavior of the mixing layer discussed in Section 9.6; the amplification rate of initial disturbances increases when cavitation number decreases [118,164].

The significant vorticity stretching in the non-cavitating case at Ca = 2.05 is in line with Dittakavi et al. [174] work stating that vortex stretching is reduced if cavitation occurs. This reduction seems to be quite evident in comparison of the Ca = 0.65i and Ca = 2.20 tests in Fig. 70(a) and (c) (see for example $x/c > 0.50$ region). Such behavior can be also detected in the vorticity tilting; it is more pronounced in the non-cavitation test as compared to the cavitation tests (see $x/c > 1.20$ region in Fig. 70(b) and (d)). This is likely attributed to the presence of vapor in the cores of vortical structures, decoupling the rate of vortex straining from the rotation rate, thus modifying the vortex stretching process. In the cavitating vortices, increase of the vortex stretching decreases the fluid vortex lines inertia and increases the vortex mixing, leading the fluid particles to rotate at larger angular speeds and so improve the local vorticity production [69,169]. Larger stretching in the cavitating vortices on the other hand results in more production of core vapor with little change of vortex diameter. Under such condition, the angular velocity of K-H vortices does not increase significantly as opposed to the non-cavitating vortices, as denoted in [89,97]. At larger cavitation numbers, conservation of momentum leads the vortex stretching to further decrease the rotation rate of cavitating vortical structures, resulting in the pressure at their cores to increase [92,174].

(a)

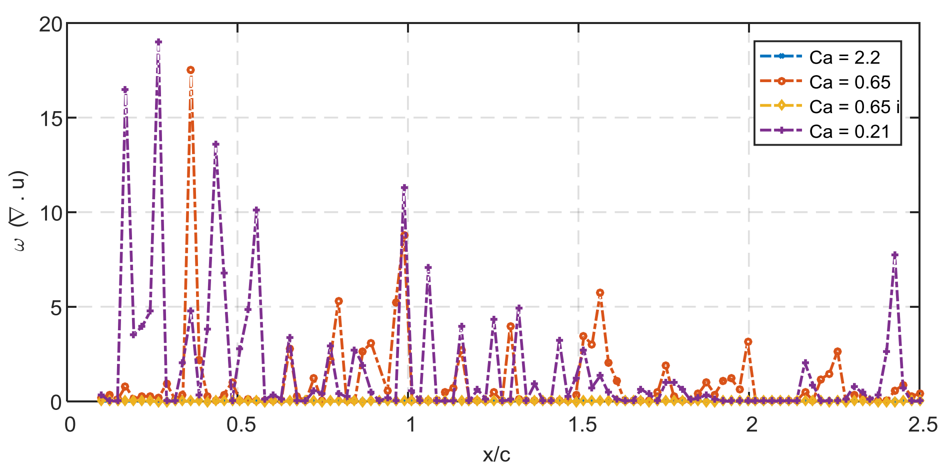

(b)

(c)

(d)

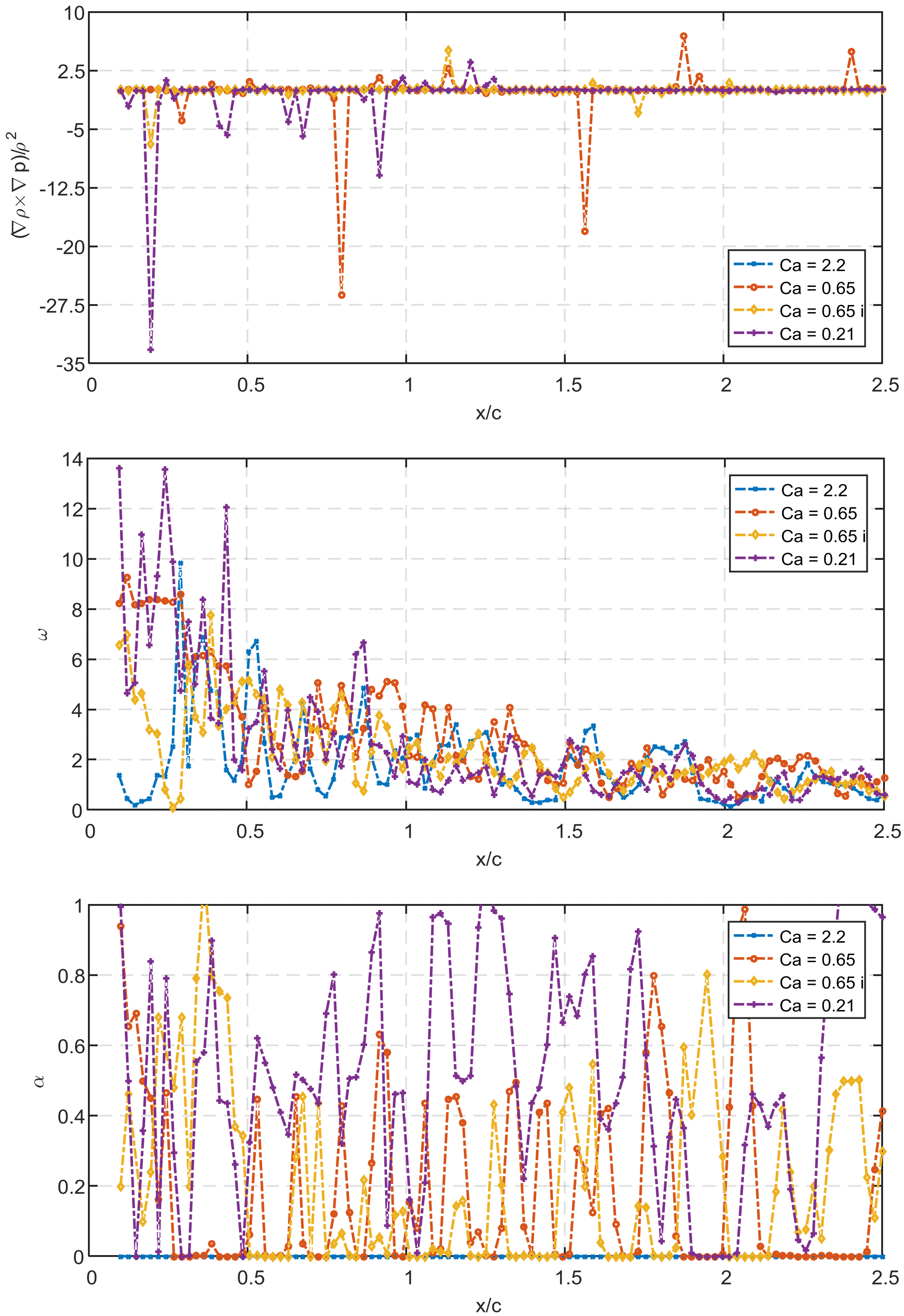

Fig. 71: Distributions of vorticity budgets along the horizontal reference line at t = 600.0 s for the cavitating mixing layer of LNG at Ca = 2.20, 0.65, 0.65i, and 0.21: (a) vorticity dilatation magnitude (1/s^2); (b) baroclinic torque (1/s^2); (c) vorticity magnitude (1/s); and (d) vapor fraction.

From the resulting distributions of vorticity dilatation (Fig. 71(a)), baroclinic torque (Fig. 71(b)), and vapor fraction (Fig. 71(d)), it can be suggested in the cavitation tests that the vorticity dilatation term is predominant in maintaining overall vorticity in the cavity structures, whereas the baroclinic term is likely the main reason for the presence of vorticity gradients within the interfacial areas of collapsing and/or incepting vortex cavity structures [127]. This observation is based on the resulting vorticity dilatation and baroclinicity contours in Fig. 62 and the given discussion on compressibility effects. Reduced baroclinicity in downstream regions of the *Ca* = 0.21 test compared to *Ca* = 0.65 (see $x/c > 1.75$ region in Fig. 71(b)) is estimated to be due to the delay in collapse/inception process of cavity spots which are longer lasting compared to those at larger cavitation numbers. In the non-cavitating case at *Ca* = 2.20 where no vapor-liquid interfacial mass transfer exists, vorticity variation is majorly associated with the vortex stretching and tilting, as seen in Fig. 70 [119,133].

It is notable in Fig. 71(a) and (b) that the non-zero values of vortex dilatation and baroclinic torque in the cavitation tests are likely caused by the mixing layer compressibility triggering the reproduction of cavitating structures through intensifying the local vorticity [119]. For instance, with the formation of vapor spots at *Ca* = 0.65, the presence of larger temperature-dependent density and pressure variations improves not only the local misalignments of density and pressure gradients but also the liquid-vapor interfacial mass flux compared to the non-cavitation test, so that the overall vorticity production in the flow is enhanced [174]. The improved density gradients, with larger variations of temperature, and the resulting enhanced interfacial mass flux at smaller cavitation numbers can be seen respectively in Fig. 72(a)-(c). Further note in 71(a) and (b) that at the smallest *Ca* = 0.21, the vortex baroclinicity and dilatation terms show more of a fluctuating behavior compared to the larger cavitation numbers (see for example $0.0 < x/c < 1.50$ region in the figures). As discussed in Section 9.6, this behavior is due to more frequent cavity collapse and/or inception events at smaller time periods causing stronger variations in flow properties and thus improved local instabilities (see also Fig. 71(d) that shows larger variations of the vapor fraction field at the smallest *Ca* = 0.21).

(a)

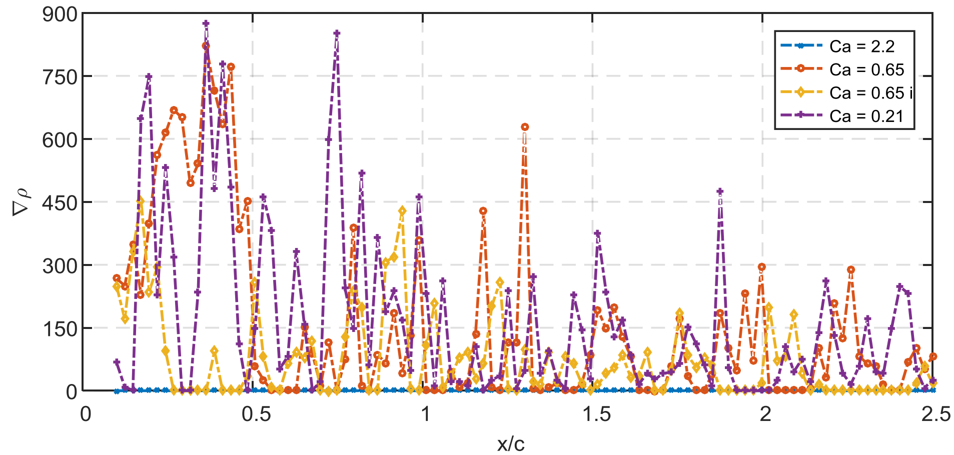

Ca = 2.2
Ca = 0.65
Ca = 0.65 i
Ca = 0.21
$\nabla\rho$
900
750
600
450
300
150
0
0
0.5
1
1.5
2
2.5
x/c

(b)

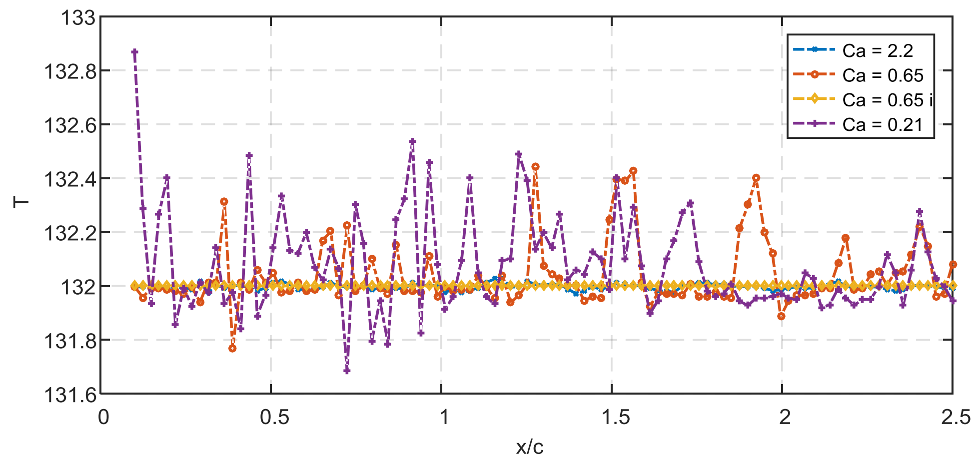

Ca = 2.2
Ca = 0.65
Ca = 0.65 i
Ca = 0.21
T
133
132.8
132.6
132.4
132.2
132
131.8
131.6
0
0.5
1
1.5
2
2.5
x/c

(c)

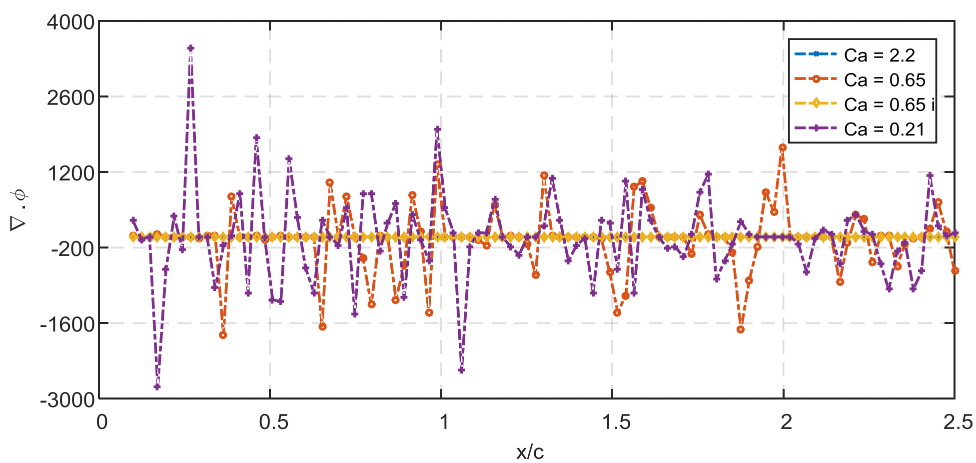

Ca = 2.2
Ca = 0.65
Ca = 0.65 i
Ca = 0.21
$\nabla.\phi$
4000
2600
1200
-200
-1600
-3000
0
0.5
1
1.5
2
2.5
x/c

(d)

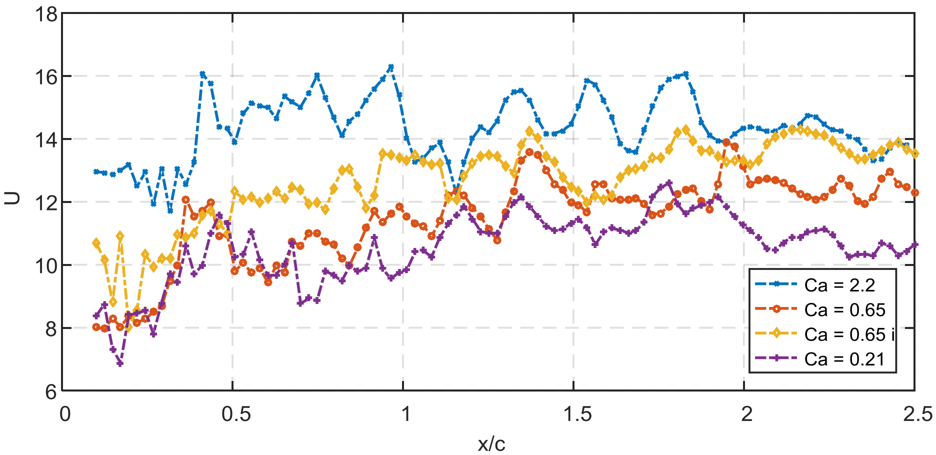

Fig. 72: Distributions of flow parameters along the horizontal reference line at t = 600.0 s for the cavitating mixing layer of LNG at Ca = 2.20, 0.65, 0.65i, and 0.21: (a) density gradient magnitude (kg/m^4); (b) temperature (K); (c) mass flux (g/s); and (d) velocity magnitude (mm/s).

The observed increasing behavior of the vorticity dilatation and baroclinic torque at smaller cavitation numbers in Fig. 71 is mainly due to the increase of liquid-vapor interfacial mass transfers along with the improved cavity production as *Ca* is reduced, which significantly trigger the thermal effects and flow gradients, as denoted in [115,127,168]. At the smallest *Ca* = 0.21 test, however, it is seen that despite the presence of more frequent vaporization and condensation processes with larger levels of local unsteadiness - which cause more frequent vorticity oscillations along the reference line - the magnitude of overall vorticity, especially in downstream regions (see $x/c > 0.75$ region in Fig. 71(c)), experiences a decrease as compared to the larger cavitation numbers. This is likely because of the increased momentum loss at the smallest *Ca* where larger vapor structures in the domain decrease the overall mixture velocity (see Fig. 72(d)). Conversely, absence of the vapor structures in the single-phase case at the highest *Ca* = 2.20 leads to larger magnitudes of velocity, and thus considerable vorticity generation even compared to the highly unsteady cavitation conditions. The large magnitudes of vorticity in the single-phase flow are caused by the dominant role of inertia, compared to thermal parameters, in driving the mixing layer instability mechanisms [25,186,190]. These observations suggest the significant effects of cavitation number in altering the cavity-vortex interaction mechanisms in free shear layers of LNG since the vorticity budgets are strongly modulated under different cavitation number conditions.

Another important point in Fig. 71 is the influence of thermal conditions on improving the vorticity dilatation and baroclinic torque, as can be detected by comparing the results of *Ca* =

0.65 and Ca = 0.65i tests. This improvement can be explained by Fig. 72(a)-(c) indicating that the presence of thermodynamic effects in the thermo-sensitive test causes larger thermally-induced density gradients with improved interfacial mass transfer processes, leading to enhanced local instabilities. The corresponding reduced velocity magnitudes at Ca = 0.65 in Fig. 72(d) compared to the thermo-insensitive Ca = 0.65i test is probably attributed to the so-called "thermodynamics delaying effect" that makes the local vaporizations intensified despite decelerating the mixing layer overall convection [21,44,68]. This conclusion is consistent with the previously-reported results that the presence of thermodynamic effects in cryogenic cavitation flows tend to amplify instability of vortical structures through enhancing the baroclinic and dilatation terms, leading to more vapor production (see also Sections 9.5-9.6 for more discussion) [21]. Further note that the thermal effects at Ca = 0.65, and Ca = 0.21, are observed to act more dominantly in downstream regions (see for example Fig. 71(a), (b), and (d); and Fig. 72(b)-(c) at $x/c > 1.50$). In upstream regions close to the T.E., cavitation shedding mechanisms are dominated by the vortex dynamics (inertia), while thermal effects are considered a secondary factor in modulating instability [70,125].

9.3. Longitudinal Velocity Profiles

To further address the global behavior of the LNG mixing layer under the simulated operating conditions, Fig. 73 shows the spatial evolution of dimensionless time-averaged velocity (u^*) profiles inside the mixing layer at cavitation numbers of Ca = 2.20, 0.65, 0.65i, and 0.21. The profiles are collected along eight transverse line stations (each in $-0.80 < y/c < 0.80$) equally distributed at x/c = 0.30, 0.60, 0.90, 1.20, 1.50, 1.80, 2.10, and 2.40 in the streamwise direction, as schematically shown in Fig. 69, and non-dimensionalized using $u^* = (u - u_2)/\Delta u$ relation, with $\Delta u = u_1 - u_2$, for ease of analysis [25,186]. Time-averaging is conducted when the simulated flows reach statistically steady state ($t \cong 300.0$ s), and taken over 320 equally-spaced time steps within about three flow-through times of cyclic progress.

Prominently in the profiles of Fig. 73 is the mean velocity gradient between the high- and low-speed streams. This is the main cause for development of instability in the mixing layer core and gradual formation of shedding process. In the upstream stations close to the T.E., where the flow is under the local effects of the splitter wake, the profiles at all the cavitation numbers show a double-peak behavior (see for example the velocity overshoots in Fig. 73(a)). The overshoots are due to the momentum loss in the splitter wake (decrease of mixture velocity) which is balanced by velocity increase at the edges of the mixing area, as reported in [25,185,195]. In further downstream regions, the double-peak evolution is gradually eliminated, so resulting in a smoothed-out, well-known S-shape velocity profile typically seen in fully-developed mixing layers [186,194,197]. The regional spotty (jagged) behavior of the profiles (see for example Fig. 73(d)) is likely attributed to the presence of intermittent regions formed at the interface of 1) mixing and non-mixing (outer layers), and 2) cavitation and non-cavitation zones [25,75]. The present velocity distributions are consistent with the result of Wang et al. [135] indicating that the influence of cavitation extent on velocity gradients tend to decrease with streamwise distance in cavitating shear layers, as a result of smaller pressure fluctuations upstream as opposed to larger pressure gradients within larger cavitating structures downstream. This is more investigated in the instability analysis of the present mixing layers in Sections 9.5-9.7.

(a)

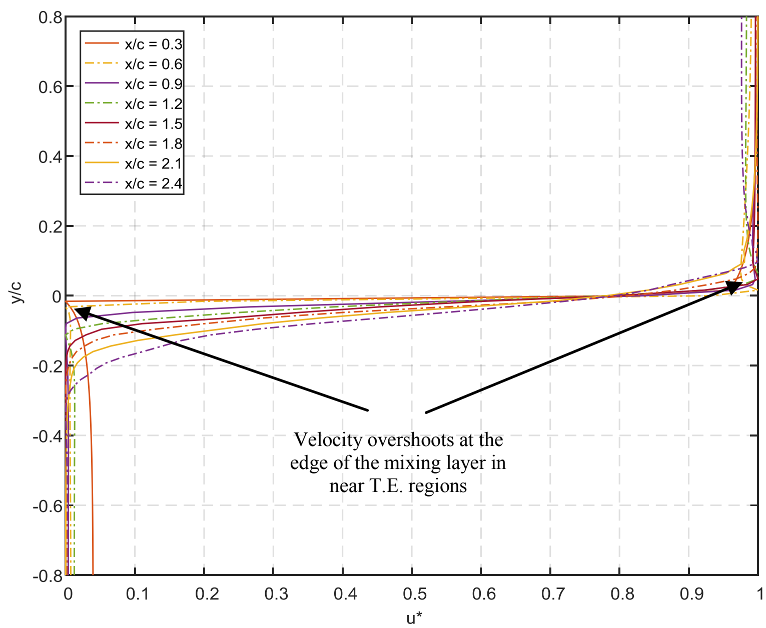

(b)

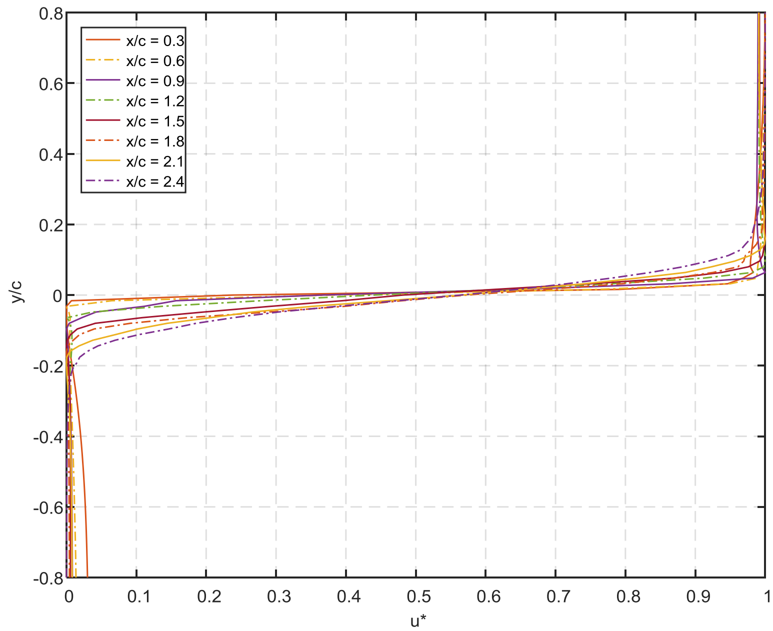
x/c = 0.3
x/c = 0.6
x/c = 0.9
x/c = 1.2
x/c = 1.5
x/c = 1.8
x/c = 2.1
x/c = 2.4
y/c
u*

(c)

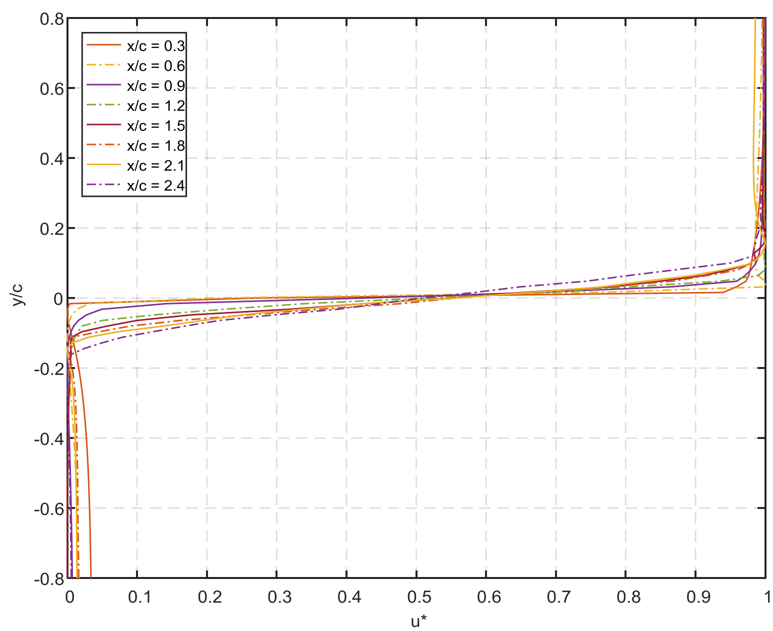
x/c = 0.3
x/c = 0.6
x/c = 0.9
x/c = 1.2
x/c = 1.5
x/c = 1.8
x/c = 2.1
x/c = 2.4
y/c
u*

(d)

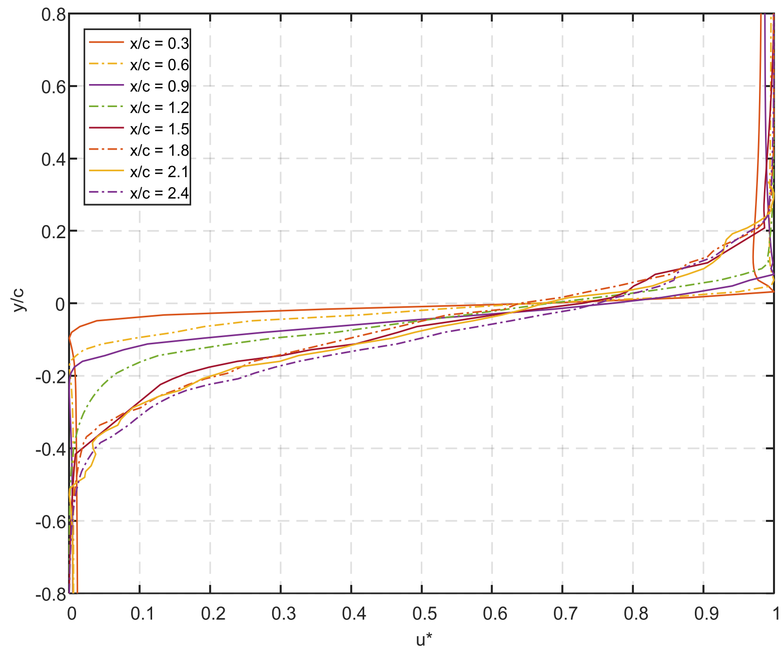

Fig. 73: Distributions of dimensionless velocity profiles (u^*) along the transverse reference line stations of x/c = 0.30, 0.60, 0.90, 1.20, 1.50, 1.80, 2.10, and 2.40 for the cavitating mixing layer of LNG at Ca = 2.20 (a), 0.65 (b), 0.65i (c), and 0.21 (d).

The S-shaped velocity profiles at all the *Ca* numbers in Fig. 73 reach a self-similarity state far downstream the splitter away from the wake [25,75,190]. The self-similarity is achieved when the velocity profiles after a certain downstream location do not change with space and time such that the global structure of the mixing layer becomes insensitive to inflow conditions (the so-called "self-similarity solution") [75,186]. In other words, the S-shaped and asymptotic behaviors of the velocity profiles, formed respectively inside and outside the mixing region, become invariant of streamwise location. Self-similarity in the present cavitation mixing layers is estimated through careful examination of the velocity profiles inside the mixing area: it occurs at *x/c* ≅ 2.54, 2.18, 2.12, and 1.79, respectively, for *Ca* = 2.20, 0.65, 0.65i, and 0.21. The commonly-approached self-similarity state at *x/c* > 1.75 in all the given tests suggests the presence of a "developing region" prior to *x/c* = 1.75 where the flow is majorly governed by the splitter wake and so the boundary layers on its sides [25,75,183].

Influence of the wake behind the splitter is proven to be stronger in non-cavitating mixing layers than cavitating ones, in agreement with [25,96,190]. This is visible in Fig. 73 showing that the overshoots at the edges of the mixing layer tend to stay longer in the absence of cavitation (Fig. 73(a)), causing the asymptotic behavior of the velocities in the outer layers and so the self-similarity (compare the profiles at *x/c* = 2.40 in the figure) to occur later compared to the cavitation tests in Fig. 73(b)-(d) [186,197]. In other words, the wake region behind the splitter in cavitating flows is filled in more quickly than the single-phase flow. These evolutions are likely due to the formation of vapor spots which improve the convective deceleration and viscous diffusion in the mixing layer, so leading the flow to increase in local instabilities and thus in overall level of mixing [96,198]. Higher level of mixing at smaller cavitation numbers causes the wake region to fill in faster, thus accelerating the occurrence of self-similarity [25,75,186]. In the non-cavitating test, the excess of pressure gradient and momentum at the core of the mixing layer, which are majorly imposed to the regions close to the splitter, leads the velocity profiles to need more time to recover [75,186,197]. Further on the thermal effects, comparison of the profiles at *Ca* = 0.65 and 0.65i suggests that the thermodynamic influence tends to moderately accelerate the occurrence of self-similarity, though making a very slight change on the global behavior of the velocities. This is attributed to the improving effects of thermal parameters in stronger production of vapor spots in the mixing layer, that are not present in the thermo-insensitive case, as further discussed in Sections 9.5-9.6. Note that the large mixing zone close to the outlet in the current tests is found to have negligible effect on the self-preserving behavior of the downstream velocity profiles. This is similarly reported in a number of previous investigations e.g. [25,190].

9.4. Mixing Layer Growth Rate

To represent the main characteristics of K-H instabilities at the interface of the simulated mixing layers, corresponding vorticity and momentum thicknesses at the given transverse reference stations of Fig. 69 is depicted in Fig. 74-75 for the cavitation conditions of *Ca* = 2.20, 0.65, 0.65i, and 0.21. The vorticity (δ_w) and momentum (θ) thicknesses, which identify the mixing layer growth rate along the *x*-axis, are respectively obtained by employing the following equations [25,75,135]

$$\delta_w = \Delta\rho u / (\tfrac{\partial \rho u}{\partial y})_{max} \tag{36}$$

$$\theta = \int_{-y}^{y} \frac{\rho u}{\rho_\infty u_\infty}\left(1 - \left(\frac{u}{u_\infty}\right)\right) dy \tag{37}$$

where $\Delta\rho u = \rho_1 u_1$ - $\rho_2 u_2$, with the subscripts ‘1’ and ‘2’ denoting the high- and low-velocity streams, respectively. Subscript ‘∞’ stands for free stream conditions. δ_w and θ are calculated using time-averaged quantities extracted after the simulated flows reach statistically steady state. Time averaging is taken over 320 consecutive time steps within time duration of Δt = 300.0-700.0 s.

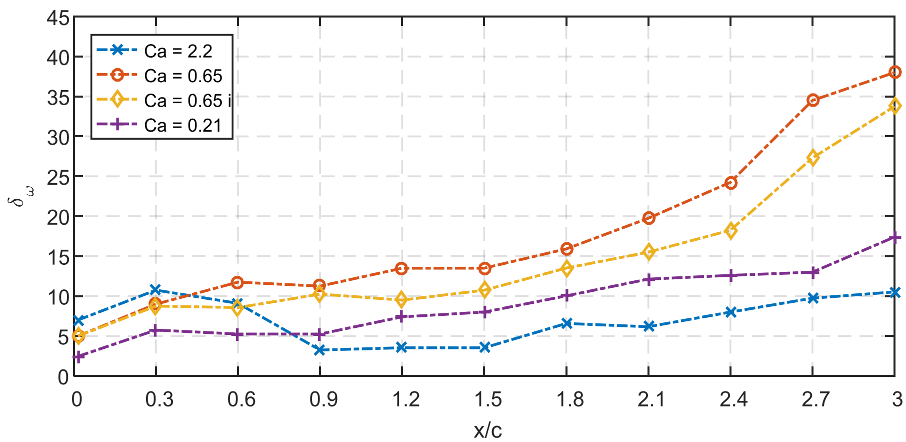

Fig. 74: Streamwise distributions of vorticity thickness δ_w(mm) along the transverse reference line stations for the cavitating mixing layer of LNG at Ca = 2.20, 0.65, 0.65i, and 0.21. Data are collected for the transverse span of -0.80 < y/c < 0.80.

The resulting vorticity thickness variations in Fig. 74 indicate a quasi-linear growth of the mixing area in the self-similarity region ($x/c > 1.75$) at all the given cavitation conditions, which is consistent with the previously-reported results in Section 9.3. This behavior is roughly detected in the splitter wake area as a result of large influence of the wake leading to non-preserved velocity profiles (see Fig. 73) and improved vorticity (see Fig. 70 and 71) [25,96]. The quasi-linear increasing behavior of the vorticity thickness is estimated to be mainly due to the gradual decrease of strain rate ($^{\partial u}/_{\partial y}$) and/or gradients of density ($\nabla\rho$) with streamwise distance [194,197], as can be also deduced from Fig. 73 and 72(a), respectively. Absence of such behavior in the upstream wake region further confirms the presence of large strain rates causing formation of highly-fluctuating small eddies (see also Fig. 64 and 67) [75].

The δ_w quasi-linear evolution in Fig. 74 further suggests that the spatial development of the mixing region is not significantly affected by cavitation such that the growth rate of the mixing layer (and thus the K-H instabilities) remains almost in the same order regardless of the operating condition. Nevertheless, the vorticity thickness is seen to increase when Ca is reduced from 2.20 to 0.65. This is primarily due to the formation of vapor spots bringing more instability (because of the improved shear and strain rate originated from vapor-liquid interfaces) into the flow, so leading to wider vortex sizes (see also the comparative vorticity contours in Fig. 64 and 67) [25,190]. Besides, as denoted in Section 9.3, the non-cavitation flow at Ca = 2.20 produces a stronger wake behind the splitter which leads the mixing layer to become weaker to grow as compared to the tests at smaller Ca; the non-cavitating wake needs longer time and so larger longitudinal distance to wash out of the domain.

More reduction of Ca from 0.65 to 0.21 seems however to oppose the observed increasing trend on δ_w when cavitation number drops from 2.20 to 0.65 -- δ_w decreases at Ca = 0.21 compared to Ca = 0.65. The reduction of vorticity thickness at the smallest Ca is likely caused by highly-unsteady large cavity spots in the domain through which the vapor content drastically reduces the overall mean density, velocity, and thus the overall flow rate in the mixture (see also Fig. 71(d) and 72(d)). This is in direct relation with compressibility effects in the flow (the so-called "net effects of compressibility", as described by Aeschlimann et al. in [25]) where improved speed of sound due to larger volume of vapor structures relaxes the net growth rate of the cavitating mixing layer [25,199]. Such behavior is normally expected to happen at very low cavitation numbers, e.g. Ca = 0.21 here, as reported in [89,92]. It is interesting to recall that although the presence of cavitation largely increases at the smallest Ca, the vorticity thickness remains in the same range as those at larger Ca, while keeping a quasi-linear longitudinal evolution. This observation particularly indicates the preservation of self-similarity even at much decreased cavitation numbers, so suggesting a globally similar spatial development mechanism of the present mixing layer eddies under cavitating and non-cavitating conditions [135].

Evaluation of the vorticity thickness for the thermo-insensitive Ca = 0.65i and thermo-sensitive Ca = 0.65 tests indicates larger values in the latter case. This is mainly attributed to the thermodynamic effects which tend to improve thermally-induced flow gradients in the thermo-sensitive Ca = 0.65 test through strengthening local liquid to vapor density ratios, and so the instability mechanisms (see also Fig. 71(a)-(b) and Fig. 72) [81,95,193]. Smoother process of vapor penetration into the liquid medium causing more vapor production in the domain is a prominent consequence of such influences, as further discussed in Sections 9.5-9.6 [25,74].

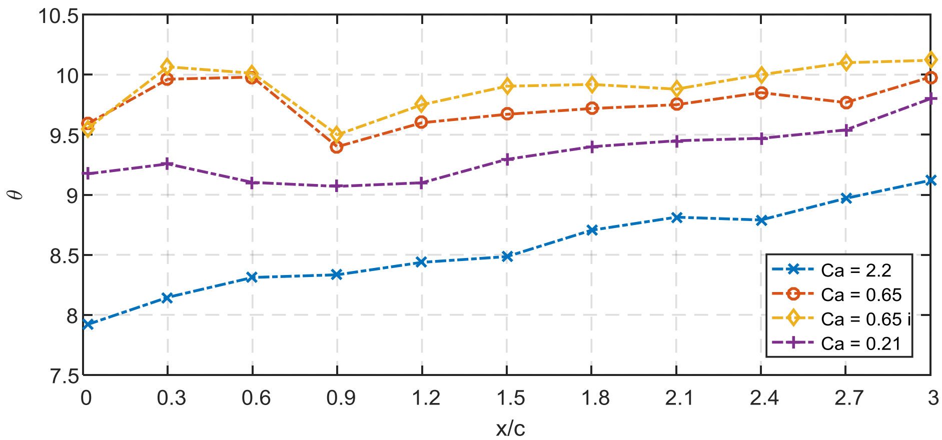

Fig. 75: Streamwise distributions of momentum thickness θ (mm) along the transverse reference line stations for the cavitating mixing layer of LNG at Ca = 2.20, 0.65, 0.65i, and 0.21. Data are collected for the transverse span of -0.80 < y/c < 0.80.

Development of the momentum thickness for the simulated tests is depicted in Fig. 75. Irrespective of cavitation content, it is seen that θ increases quasi linearly in the streamwise direction in the self-preservation zone, as similarly resulted in the vorticity thickness distributions in Fig. 74. This trend is not seen in the developing wake region especially at $x/c <$ 1.10 [96,190,197]. The fact that the momentum thickness increases with lowering *Ca* from 2.20 to 0.65 pertains to the production of vapor spots with low densities in the mixing layer which suppress the momentum exchange in liquid phase, so causing an overall increased momentum deficit. This behavior however seems to be reversed for *Ca* = 0.21, where dominant large unstable cavitating clouds with large thermally-affected density gradients cause more instability through inducing more momentum exchange between vapor and liquid regions [39,127]. Improved instability is due to enhanced succession of vapor collapse/coalescences incidents in the mixing layer, discussed further in Section 9.6. On the thermal effects, comparison of the *Ca* = 0.65 and 0.65i results suggests that the inclusion of thermal parameters slightly lowers the momentum thickness and thus the momentum deficit by increasing the momentum exchange via improving gradients of pressure and density [44,200]. Note that the observed quasi linear behaviors of the vorticity and momentum thicknesses in the self-similarity state is in accordance with Milane [201] and Wiecek and Mehta [198] who found that self-preservation of a mixing layer is guaranteed if the mean velocity profiles exhibit similarity, and linear growth of characteristic thicknesses, e.g. momentum thickness, is achieved. These conditions are satisfied in the present mixing layers, as seen in the velocity profiles of Fig. 73 and vorticity thicknesses of Fig. 74-75.

9.5. Cavitation Growth Rate

In order to quantify the vapor evolution inside the mixing region, time-averaged distributions of the vapor fraction field along the transverse line stations at x/c = 0.80, 1.70, and 2.80 are depicted in Fig. 76 for the simulated cavitation conditions of Ca = 0.21, 0.65, 0.65i, and 2.20. Collected vapor fractions are averaged over 320 equally-spaced time steps in t = 300.0-700.0 s when the flow is at statistically steady state. The profiles indicate that the vapor production is decreased in the streamwise direction, regardless of the cavitation content, while showing a somewhat symmetrical repartition around the centerline [25,89]. The predicted deflection off the centerline seems to improve at the smallest cavitation number (see for example the Ca = 0.21 test in Fig. 76(d)), which is probably resulted from larger momentum exchange from the mixing layer upper stream to the lower stream decelerating the cavitating structures progress towards the low-speed side. The longitudinal reducing behavior of the void fractions can be more clearly illustrated in Fig. 77 that depicts the maximum of time-averaged vapor fraction field ($\alpha_{t\text{-}max}$) at the transverse stations; it decreases gradually in the x-wise direction for all the simulated cavitation conditions.

(a)

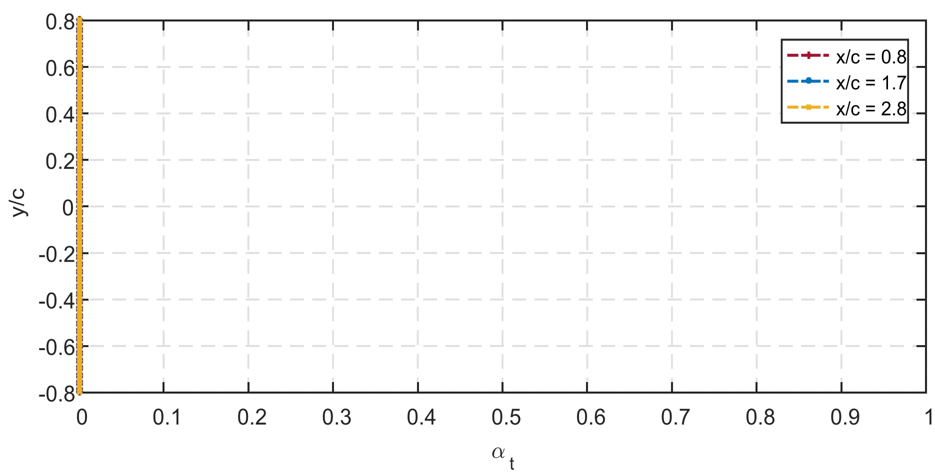

(b)

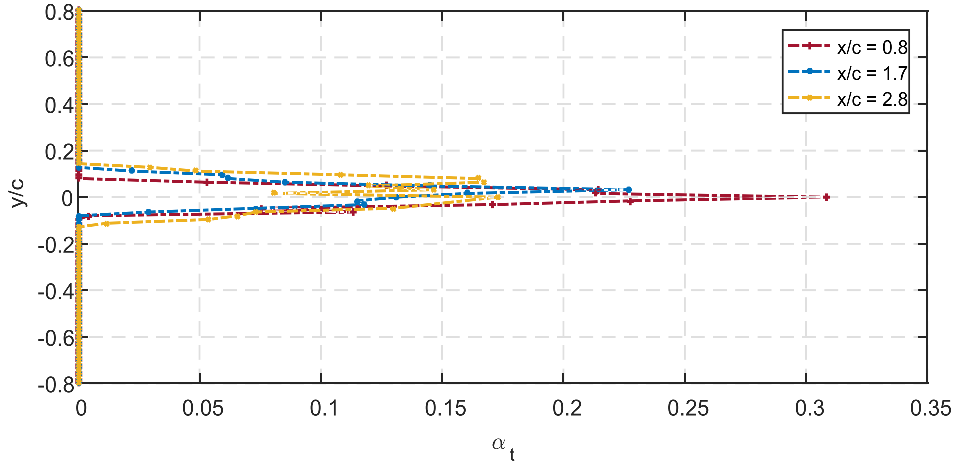

(c)

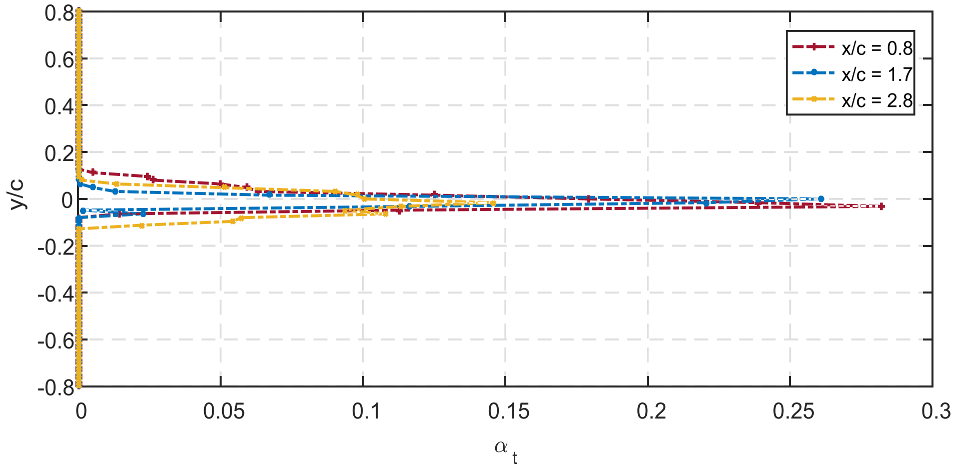

(d)

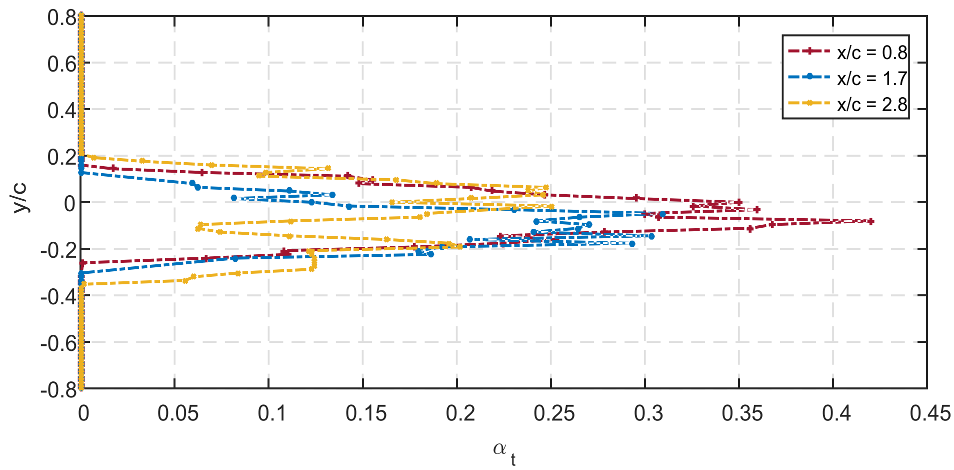

Fig. 76: Distributions of time-averaged vapor fraction along the transverse reference line stations of x/c = 0.80, 1.70, and 2.80 for the cavitating mixing layer of LNG at Ca = 2.20 (a), 0.65 (b), 0.65i (c), and 0.21 (d). Note the mixing layer at Ca = 2.20 (a) is non-cavitating so α = 0.0.

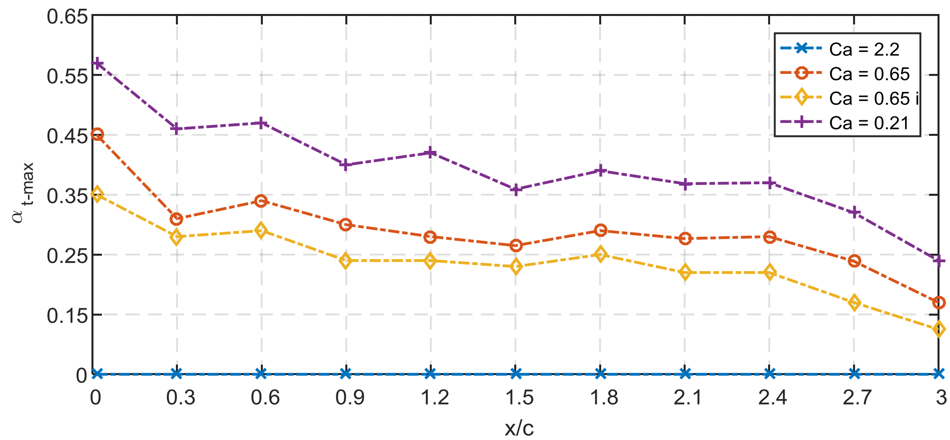

Fig. 77: Streamwise distributions of maximum time-averaged vapor fraction ($\alpha_{t\text{-}max}$) along the transverse reference line stations for the cavitating mixing layer of LNG at Ca = 2.20, 0.65, 0.65i, and 0.21. Data are collected for the transverse span of -0.80 < y/c < 0.80.

Another important observation in Fig. 76 is the increased width of the vapor-filled zone in further downstream stations (see for example the -0.40 < *y/c* < 0.20 region in Fig. 76(d) with vapor fractions of $\alpha_t < 10.0\%$), that is consistent with the vapor fraction contours of Fig. 63. This behavior is improved with the involvement of thermal parameters (compare the *Ca* = 0.65 and 0.65i tests for example in the -0.20 < *y/c* < 0.20 region of Fig. 76(b) and (c) with vapor fractions of $\alpha_t < 15.0\%$) and/or by reducing the cavitation number (compare the *Ca* = 0.65 and 0.21 tests for example in the -0.40 < *y/c* < 0.20 region of Fig. 76(b) and (d) with vapor fractions of $\alpha_t < 15.0\%$). The main reason for such streamwise expansions is likely the transport of vapor structures through diffusion processes moving them from the K-H vortices towards the mixing layer borders. These procedures together with the longitudinal increase of mixing layer vorticity thickness (see Fig. 74) develop the vapor-affected zone, as denoted in [25,190]. Reduction of cavitation number and improved thermal effects are suggested to be the main factors triggering the diffusion processes, and so the vapor production in the mixing region, through amplifying cavity-vortex interactions and shear layer instabilities.

An interesting part of the above-noted analysis is a contradiction between the qualitative and quantitative results [190]: on one hand in Fig. 63, contours of the vapor faction field visually show the development of cavity structures in the *x*-wise direction (i.e. increase of the vapor-affected zone in the streamwise direction); on the other hand, Fig. 77 indicates that the maximum of the time-averaged vapor fraction field along the transverse stations is reduced in the streamwise direction. This contradicting behavior can be addressed by analyzing the vapor quantity dynamics in the mixing layer through calculating equivalent vapor volume, $\alpha_V = \int_{y_1}^{y_2} \overline{\alpha(x,y)}\, dy$ ($\bar{\alpha}$ is the mean vapor fraction field in the entire simulation time), which is interpreted as "equivalent pure vapor thickness", a relative parameter to the previously-introduced vorticity and momentum thicknesses in Section 9.4 [190]. Fig. 78 displays the streamwise evolution of the equivalent pure vapor thickness along the given transverse stations of Fig. 77 for the present mixing layers at *Ca* = 2.20, 0.65, 0.65i, and 0.21.

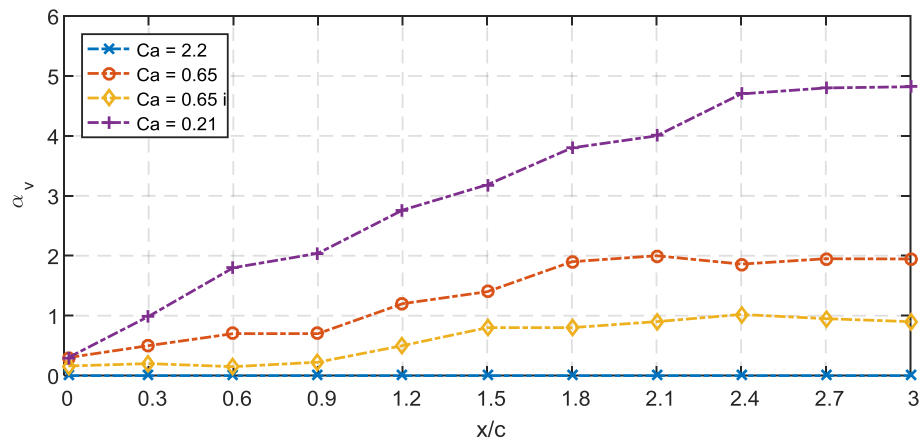

Fig. 78: Streamwise distributions of equivalent pure vapor thickness α_V (mm) along the transverse reference line stations for the cavitating mixing layer of LNG at Ca = 2.20, 0.65, 0.65i, and 0.21. Data are collected for the transverse span of -0.80 < y/c < 0.80.

As seen, the highest vapor thickness rate is predicted at the lowest *Ca* = 0.21 with an increasing trend up to *x/c* ≅ 2.40, and a following plateau with constant α_V ≅ 4.90 mm. As *Ca* is increased to 0.65, smaller vapor production in the mixing layer compared to the *Ca* = 0.21 case causes smaller vapor thickness, though still showing the same parabolic behavior as in the *Ca* = 0.21 test; the vapor thickness reaches the plateau at *x/c* ≅ 1.80 and continues with constant α_V ≅ 2.0 mm onward. As for the thermodynamic effects, it is observed that the vapor thickness is reduced in the thermo-insensitive *Ca* = 0.65i test compared to the counterpart *Ca* = 0.65 test, while the overall trend is almost kept the same; the plateau at *Ca* = 0.65i is reached earlier at *x/c* ≅ 1.50 with α_V ≅ 1.0 mm. The predicted quasi-linear behavior of the equivalent vapor thickness in all the simulated tests is relevant to Aeschlimann et al. [96] work reporting that the expansion of vapor spots in mixing layers follows a linear trend irrespective of the level of cavitation.

The resulting vapor fraction variations along the transverse stations in Fig. 76 can be further evaluated to accord with the distributions of velocity profiles and velocity fluctuations displayed, respectively, in Fig. 73 and 87 (see Section 9.7 for discussions on velocity fluctuations): particularly in the case of velocity fluctuations, the maximum values are spotted around the centerline of the mixing layer (y/c = 0.0) where the velocity exhibits its maximum gradient and not its maximum value [96,135]. This is consistent with the results of Aeschlimann et al. [25] reporting that velocity gradients and velocity fluctuations are maximized in the center region of cavitation mixing layers where the maximum of vapor fraction is also attained. Such evolutions in the present tests can be better illustrated in Fig. 79 comparing the distributions of vapor fraction, vorticity magnitude, strain rate (i.e. lateral velocity gradient, $\partial u/\partial y$), and temperature for the given cavitation conditions, along the transverse station of x/c = 2.85 at t = 600.0 s. It can be deduced that the liquid-vapor diffusion processes (see for example the vapor fraction in the Ca = 0.21 test at y/c = -0.19 in Fig. 79(a)) within the high-vorticity regions (see the corresponding vorticity magnitude in the Ca = 0.21 test at y/c = -0.19 in Fig. 79(b)) are mainly attributed to the local peaks in the shear field (see the corresponding strain rate in the Ca = 0.21 test at y/c = -0.19 in Fig. 79(c)). The predicted local peaks in the strain rate profiles can be particularly treated as local amplification source of vorticity, eventually leading to inception and/or development of vapor cavities in the flow. This conclusion is in agreement with the observations of [25,97,190] stating that highly sheared regions in cavitating flows can be considered as triggering points for larger variations of density and liquid-vapor interfacial mass flux. The observed behaviors in Fig. 79 are additionally affected by temperature variations in the mixing layer such that the larger local thermal gradients at stronger cavitation conditions, e.g. Ca = 0.21 (see for example the temperature distribution in the Ca = 0.21 test at y/c = -0.19 in Fig. 79(d)), strengthens the liquid-vapor interfacial processes by improving local density gradients, and so the shear rates (see also Section 9.2) [21,100].

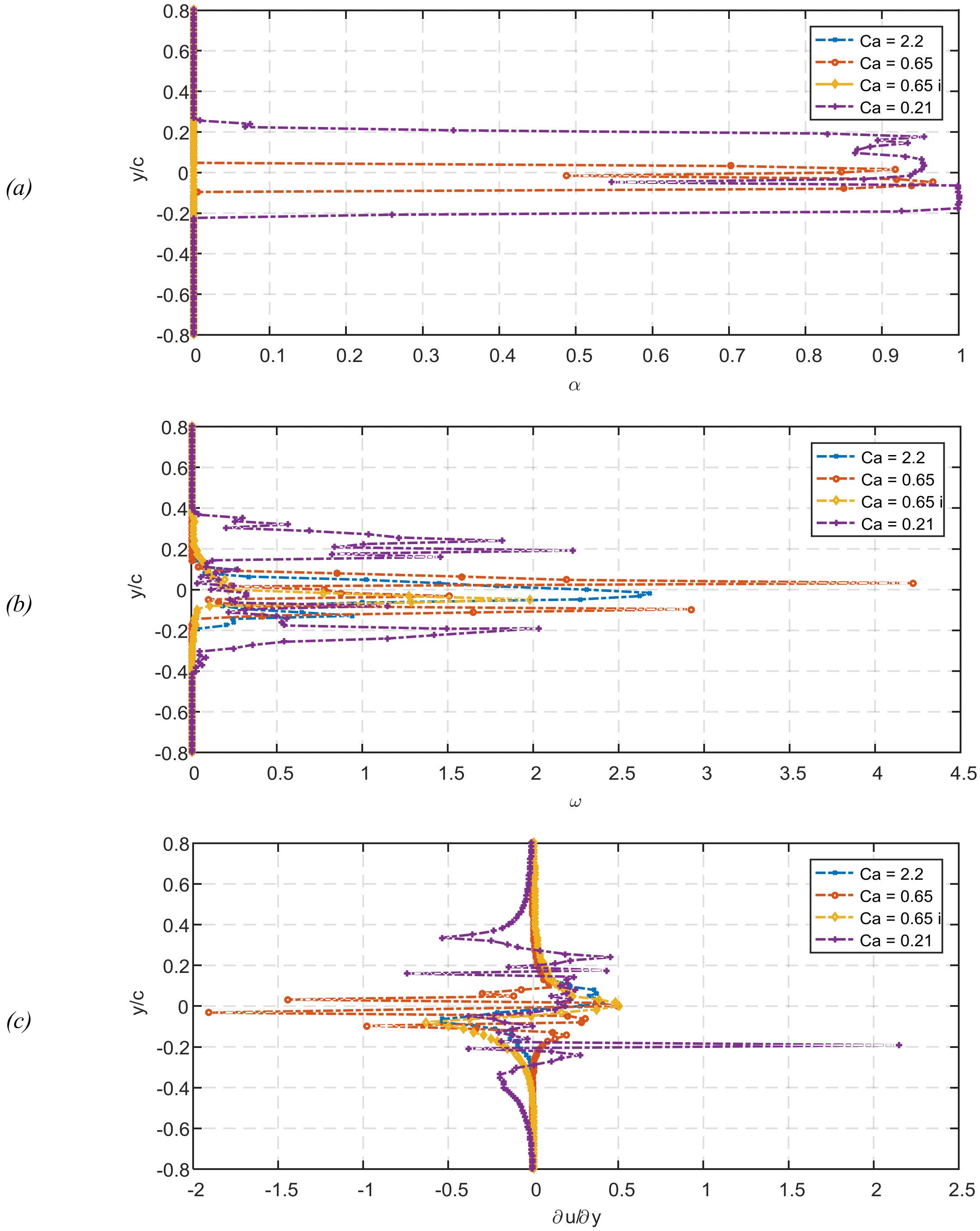
(a)
(b)
(c)
Ca = 2.2
Ca = 0.65
Ca = 0.65 i
Ca = 0.21
y/c
α
ω
∂u/∂y

(d)

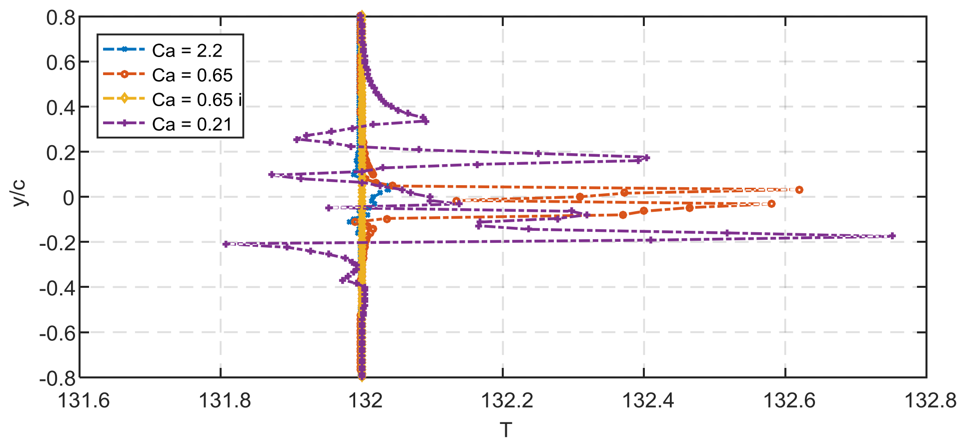

Fig. 79: Distributions of time-averaged flow parameters along the transverse reference line station of x/c = 2.85 for the LNG cavitating mixing layer at Ca = 2.20, 0.65, 0.65i, and 0.21: (a) vapor fraction; (b) vorticity magnitude (1/s); (c) strain rate (1/s); and (d) temperature (K).

By reducing the cavitation number from *Ca* = 2.20 to 0.21 in Fig. 79 it is also observed that the vapor production inside the mixing layer is enhanced due to improved vaporization processes with larger flow gradients. For example in the variations of transverse velocity gradient in Fig. 79(c), $\partial u/\partial y$ seems to become stronger with more intermittency as *Ca* is reduced and/or thermodynamic parameters are involved (compare the *Ca* = 0.65 and 0.65i conditions). There are however some regions on the $\partial u/\partial y$ profiles which seem not to follow this conclusion -- see for example the -0.10 < *y/c* < 0.10 region in Fig. 79 where larger vorticity, strain rate, and temperature are observed at larger *Ca* = 0.65 compared to *Ca* = 0.21, despite the larger vapor production at *Ca* = 0.21. As reported by Ito et al. [202], this behavior is likely due to reduced momentum at small to medium-scale vortical structures with embedded cavities, which are not stimulated enough to have the dominant roll-up frequency. This ultimately causes a counter-gradient diffusion of momentum in such vortices, balancing the overall excess in flow gradients.

9.6. Transition Characteristics of Shear Layer Instabilities

9.6.1. Time History of the Probed Flow Fields

To further investigate the local cavity-vortex interactions in the present cavitating mixing layers, Fig. 80 depicts the temporal evolutions of temperature, relative pressure (= p - p_{sat}), vapor fraction, and velocity magnitude at the probed station of (*x/c*,*y/c*) = (0.50,0.0) over the time interval of *t* = 100.0-300.0 s. The cavitation conditions of *Ca* = 2.20, 0.65, 0.65i, and 0.21 are compared in the figure. Overall inspection of the data indicates periodic behavior of the flow fields is observed in all the simulated tests. The periodicity is consistent with the transient nature of the LNG cavitating mixing layer qualitatively predicted in Section 9.1, suggesting that the resulting field variations are closely related to local unsteady characteristics of the flow. At the largest *Ca* = 2.20, the temperature variation (Fig. 80(a)) appears to have a periodic fluctuating behavior but with a very small amplitude, while the lower cavitation numbers experience strong temperature, and thus saturation pressure (Fig. 80(b)), fluctuations. This is because the given probe at *Ca* = 2.20 is exposed to a single liquid phase flow of LNG, so no vapor fraction field fluctuation (Fig. 80(c)), and thus no exchanges of latent heat of vaporization, are present. Due to the absence of vapor spots larger velocity magnitudes are present at *Ca* = 2.20 in comparison with the cavitating tests (Fig. 80(d)). The amplitude of velocity fluctuations at Ca = 2.20 seems to be lower though, which is probably owing to suppressed instability of the mixing layer due to the absence of vapor structures with phase change processes [57,92,101].

(a)

(b)

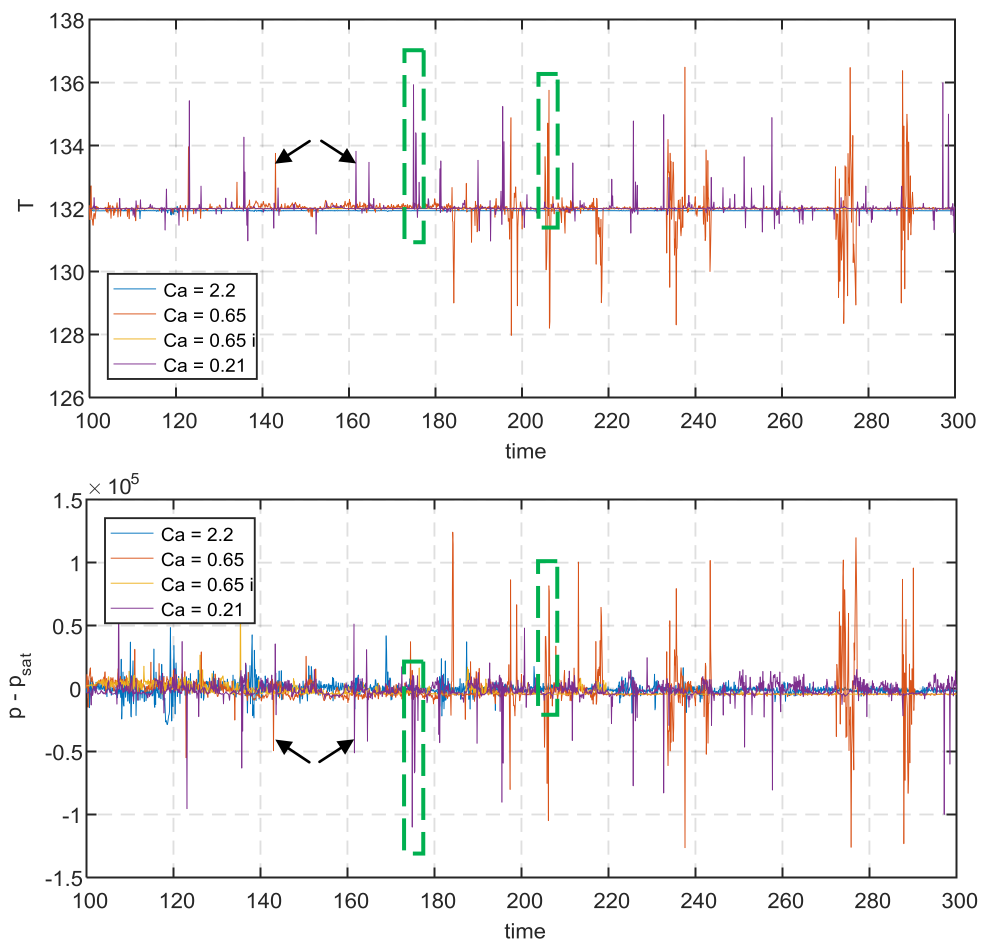

(c)

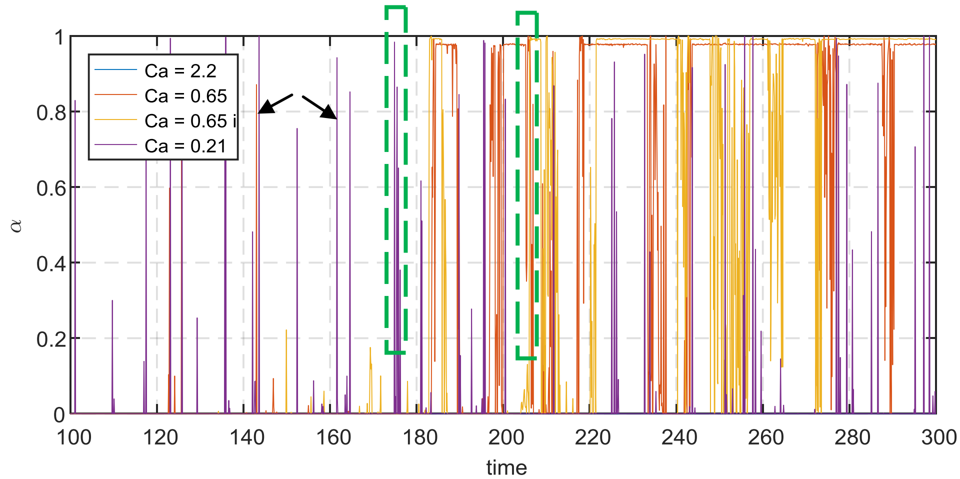

(d)

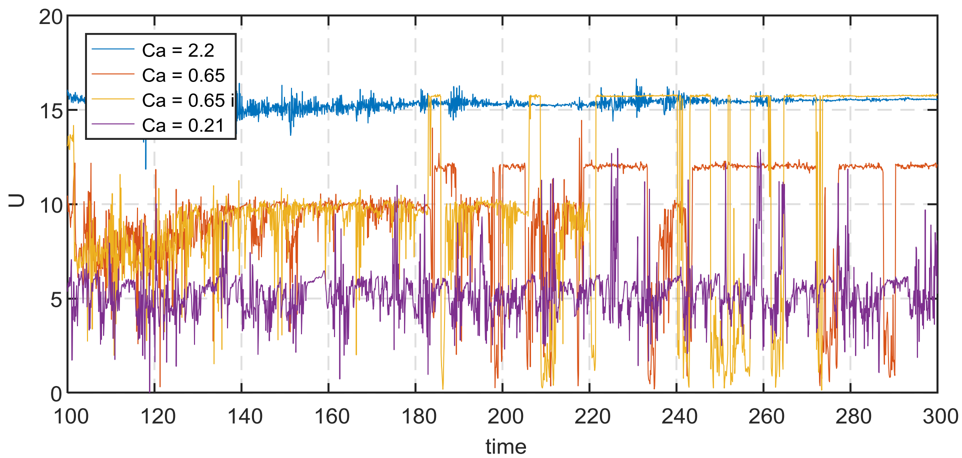

Fig. 80: Time histories of flow parameters at the probe location (x/c,y/c) = (0.50,0.0) in the cavitating mixing layer of LNG at cavitation numbers of Ca = 2.20, 0.65, 0.65i and 0.21: (a) temperature (K); (b) relative pressure (Pa); (c) vapor fraction; and (d) velocity magnitude (mm/s).

With the decrease of cavitation number to $Ca = 0.65$, primary irregular inception and breakup of small vapor cavities within the time interval of $t < 180.0$ s eventually turn into periodic formation of longer lasting and stronger vapor structures (see Fig. 80(c) at $t > 180.0$ s). The presence of such cavities is observed to cause intermittent fluctuations in the flow fields, so creating larger amplitudes in shorter time periods as compared to the $Ca = 2.20$ test (e.g. see temperature and vapor pressure fluctuations in Fig. 80(a)-(b)). Smaller velocity magnitudes are however observed as a result of decelerating effects of vapor spots (Fig. 80(d)). The behavior of vapor fraction at $Ca = 0.65$ in Fig. 80(c) also suggests the formation of somewhat alternating liquid and two-phase structures in the mixing layer, in which cavity inception and collapse incidents occur through clear-cut transitions. Thus the void fraction field signals appear in a quasi-rectangular shape (see Fig. 80(c) at $t > 200.0$ s) [96,135,190]. Longer clear-cut transition indicates longer residence time of cavities, causing less succession of cavity collapse/inception incidents. These evolutions are in accordance with the predicted contours in Fig. 64 and 67 that show how the vapor pockets are initiated through highly unstable upstream roll-up mechanisms around the T.E. that grow into larger cavity clouds downstream through convection of vortical structures [135].

In the case of thermo-insensitive cavitating mixing layer at *Ca* = 0.65i, it is observed that the overall behavior of the vapor fraction fluctuations (Fig. 80(c)) is almost similar to the thermo-sensitive case (*Ca* = 0.65), with the difference that the presence of additional temperature-based gradients in the latter case causes the temperature and relative pressure magnitudes to rise up significantly (see $t > 180.0$ s in Fig. 80(a)-(b)), leading to earlier nucleation of the primary cavity; nucleation at *Ca* = 0.65 starts at $t \cong 125.0$ s, whereas $t \cong 150.0$ s at *Ca* = 0.65i. As a result, the vapor fraction distribution shows more fluctuations in the given time period in the thermo-sensitive case [17,135,203]. This is consistent with the previously-reported increase in the equivalent pure vapor thickness (see Fig. 78) when thermal parameters are involved in the cavitation process. The presence of strengthened vapor products at *Ca* = 0.65 also causes an overall decrease in the mixing layer velocity magnitude, as indicated in Fig. 80(d), and further confirms the significance of "thermodynamic delay effects" in cryogenic cavitation [100,116].

The aforementioned observations in the *Ca* = 0.65 test are improved as the cavitation number is reduced to 0.21, in a way that highly unstable stronger vapor clouds with greater variations of temperature and relative pressure fluctuations (albeit with smaller amplitudes compared to the *Ca* = 0.65 test) evolve within higher frequencies (Fig. 80(a)-(b)), indicating an enhanced shedding mechanism at the smaller *Ca* = 0.21 (see also Sections 9.1 and 9.6.2 for more discussion). The occasional increase of amplitudes in the *Ca* = 0.65 test compared to the *Ca* = 0.21 test is estimated to be due to 1) more frequent vaporization and condensation processes in shorter time periods (Fig. 80(c)), and 2) improved dampening effects of larger vapor spots, at the smaller cavitation number. This is consistent with the contours of Section 9.1 where stronger and more connected vapor structures at *Ca* = 0.21 cover most of the mixing region with continuous periodic fluctuations of the vapor fraction field. Such evolution causes the corresponding vapor fraction signal in Fig. 80(c) to have smaller, more frequent cavity bursts with no clear-cut transition, as differed from the quasi-rectangular behavior seen in the *Ca* = 0.65 test [190]. Note that the more frequent vapor spots at *Ca* = 0.21 reduces the overall mixture velocity magnitudes in the flow (Fig. 80(d)), though showing more intense fluctuating behavior compared to larger cavitation numbers. As detailed in Section 9.6.2, this behavior is indicative of stronger phase change processes at smaller *Ca* where larger periodically-oscillating cavity clouds with amplified temperature-dependent gradients of density and pressure improve local instabilities through triggering vortex shedding mechanisms in the mixing layer [133,188]. This is also in line with Kikuta et al. [204] work concluding that the influence of thermal parameters on cavitation becomes stronger with larger scale cavities.

Further on the time histories of relative pressure in Fig. 80(b), a higher rate of change of vapor pressure due to larger temperature fluctuations at Ca = 0.21 (Fig. 80(a)) causes a stronger variation of local cavitation number, so suggesting a stronger involvement of thermal effects. This is not at all seen in the Ca = 2.20 case with single-phase behavior, as a result of much smaller temperature fluctuations compared to the cavitation tests. Such behavior highlights the significant influence of vapor spots on improving the thermally-induced gradients of density and pressure, and thus the overall instability in the present flows. This conclusion is in agreement with Okabayashi et al. [97] work stating that since single-phase mixing layers do not experience significant temperature gradients due to phase change, static pressure fluctuations are larger as compared to cavitating mixing layers where the pressure fluctuations are offset by thermally-driven changes in the vapor pressure in cavitating regions.

It is also notable in Fig. 80 that the presence of sudden steep gradients in the evolution of cavitation tests is likely attributed to the propagation of strong pressure waves during phase change processes [203]. Especially, the collapse and breakup process of vapor cavity structures, in particular of those large vapor clouds downstream, is estimated to be accompanied by subsequent vapor fraction "discontinuity propagations" which are resulted from an uneven distribution of bubbly shockwaves (see for example the pressure and temperature spikes in Fig. 80(a)-(b)) passing through upstream cavity structures [100,116]. As explained in [135], within a discontinuity propagation, composed of a pre- and a post-discontinuity regions, pressure peaks are generated at the shockwave front and cause the corresponding vapor fraction field to experience drastic changes (see for example the dashed green boxes in Fig. 80(c) where sharp decrease in void fraction distribution is induced by shockwave front) -- the pre-discontinuity area is almost pure vapor and the post discontinuity area consists of vapor-liquid mixture with relatively lower vapor fractions. Such drastic variations can be spotted equivalently in the corresponding field distributions, as indicated in for example Fig. 80(a)-(b) for pressure and temperature – e.g. the pressure pre- and post of a shock wave have a jump, with higher pressure post of the shock wave. Note that the propagation of discontinuity in a cavity structure leads the overall morphology of the cavity, e.g. cavity size and interface shape, to change gradually, while the local vapor fraction gradients inside the cavity experience large reduction through local breakdowns; the cavity dimensions change rapidly when it totally collapses. This can be deduced by visually inspecting the flow contours in Fig. 57-60 against the temporal distributions in Fig. 80, and is similarly reported in [135,203].

From the higher frequency contents of the given fluctuations in Fig. 80 one can further distinguish the “global” and “local” cavity collapse incidents in the present mixing layers, as introduced by Reisman et al. [205]. The local events correspond to the collapse of small-scale vapor spots propagating shock waves in the flow; they are identified by random distributions of small-magnitude pressure/temperature spikes (see the examples of local events in Fig. 80(a)-(c), indicated by black arrows). The global events are related to the coherent collapse of large-scale vapor clouds producing large-magnitude over-pressures in the domain (see the examples of global events in the dashed green boxes in Fig. 80(a)-(c)). Decreasing the cavitation number in the present tests is observed to promote the occurrence of these events by accelerating phase change processes imposing large gradients.

9.6.2. Spectral Analysis of the Probed Flow Fields

The operating conditions effects on the instability behavior of LNG cavitation mixing layer can be further illustrated by the fast Fourier transform (FFT) analysis. Fig. 81 shows the frequency characteristics of the mixing layer shedding found from conducting FFT of the vorticity magnitude time histories at the probed station of $(x/c,y/c) = (0.50,0.0)$, for the cavitation numbers of $Ca = 2.20$, 0.65, 0.65i, and 0.21. The FFT calculation follows the same procedure as described in Section 6.1.4.2, and is performed for about three flow-through times of progress after reaching statistically steady state. Primary inspection of the resulting distributions shows that the amplitude of noise increases as cavitation number decreases. The larger magnitudes of spectra in the cavitation tests in Fig. 81(b)-(d) mainly correspond to the presence of cavity-vortex interactions with improved unsteadiness, as opposed to the non-cavitation test at $Ca = 2.20$ (Fig. 81(a)) where the single phase flow is only affected by the shear layer vortex interactions. The noise improvements are also triggered by thermally-influenced flow gradients generated through phase change processes, as can be deduced from the comparison of Ca = 0.65 and 0.65i tests in Fig. 81(b)-(c) (see also Fig. 80). The suppressed spectra at the largest Ca = 2.20 further indicates the mixing layer incapability in smoothly transitioning from the wake to the self-similarity state. This is consistent with the results of Section 9.3 declaring that in the non-cavitation operating condition, transition of the strengthened wake to the self-similarity zone downstream is delayed compared to the cavitating conditions [25,190].

(a)

(b)

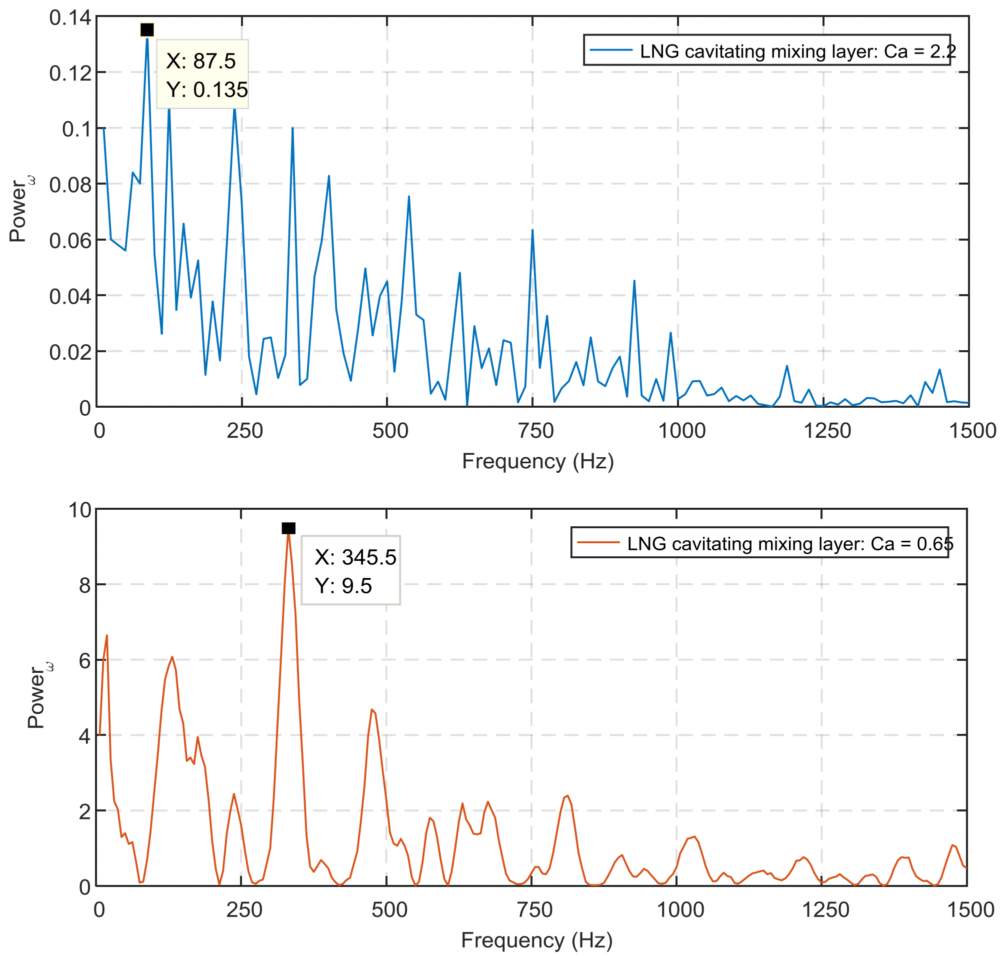

(c)

(d)

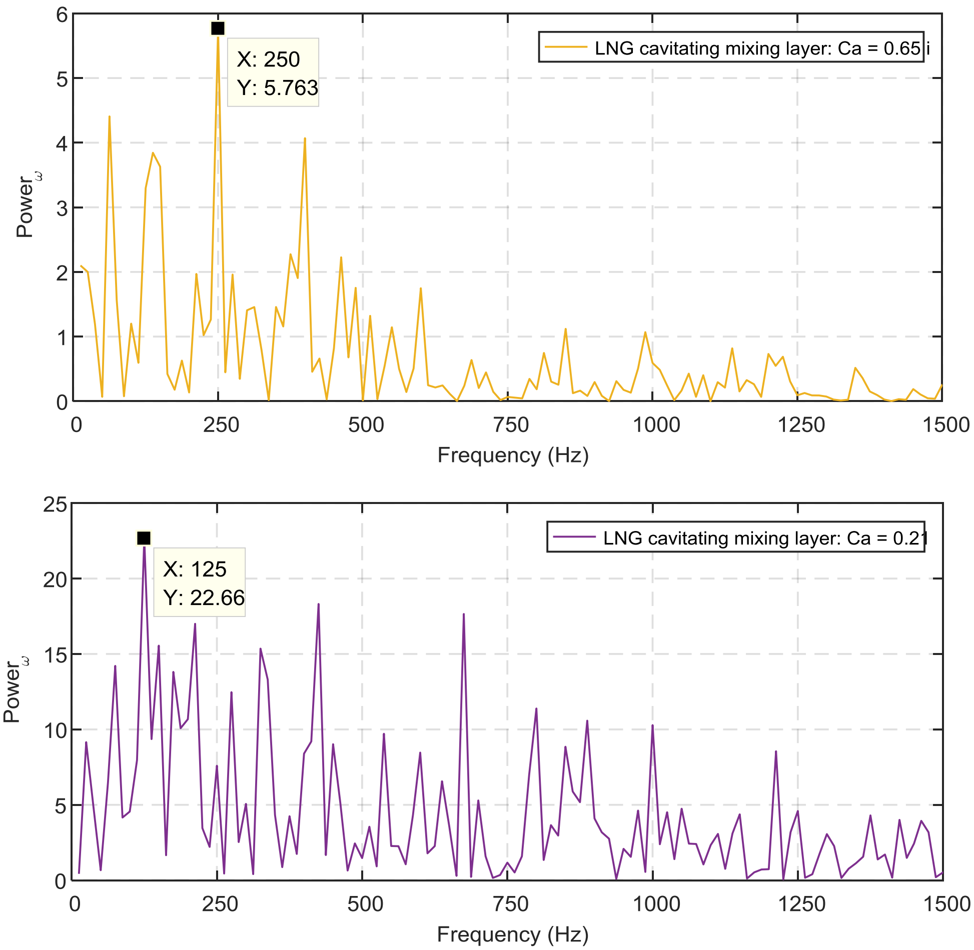

Fig. 81: Spectrogram of vorticity magnitude at the probe location (x/c,y/c) = (0.50,0.0) for the cavitating mixing layer of LNG at Ca = 2.20 (a), 0.65 (b), 0.65i (c), and 0.21 (d).

Characteristic frequencies in Fig. 81 are detected in a rather small frequency range for all the given tests. These frequencies, which pertain to the most energetic contributions from the vorticity magnitude traces, are indicative of the dominant shedding frequency of the K-H vortices affected by vapor spots [135]. At the non-cavitation condition (Fig. 81(a)), spectra is purely from the vortex shedding and has a spectral peak at the shedding frequency of f = 87.50 Hz. As the vortex structures grow and reach their available vortex spacing, they start merging with neighboring vortices to form a new vortex with half the shedding frequency, causing the second peak in the spectrum. The lower level peaks are typically the harmonic(s) of the main oscillation in such cases, as denoted in [43,135,164]. For Ca = 0.65 (Fig. 81(b)), however, the dominant noise is generated by breakdown and collapse of the alternating cavitation spots and the peak is observed at f = 345.50 Hz that is about triple of the vortex shedding frequency at $f \cong$ 126.0 Hz. The observed lower frequency peak at $f \cong$ 10.0 Hz likely pertains to the "low frequency behavior of the elongated vortex cavities", as reported in [126]. This spectral evolution can be similarly detected at *Ca* = 0.65i (Fig. 81(c)) and 0.21 (Fig. 81(d)), with dominant frequencies at *f* = 250.0 and 125.0 Hz, respectively. The dominant frequency at *Ca* = 0.21 is particularly estimated to reflect the instability from both of the vortex shedding and the alternating cavitation spots. The smaller secondary peaks after the dominant peak probably correspond to smaller cavities shed within a cycle at higher frequencies, which are strengthened at the smaller *Ca* = 0.21 [206]. The corresponding time histories of vorticity magnitudes in Fig. 82 also indicate the predicted characteristic frequencies. These observations suggest that the spectra characteristics under the cavitation conditions are made not only by the alternate collapse of the cavitating spots but also by the low frequency behavior of the elongated vortex cavities, which are both amplified as the cavitation number is reduced. Note that the breakdown and collapse of cavitating spots with vortex shedding are also likely affected by the low frequency behavior of the elongated cavities, so making the noise spectrum even more broadened against the non-cavitation condition [126,160]. At larger frequencies beyond 900.0 Hz, the resulting spectra show a relaxed behavior in all the given tests, with low amplitude oscillations for which spectral coherency becomes very low [116,190]. This behavior is less apparent as cavitation number decreases to *Ca* = 0.21, as a result of improved vaporization and condensation processes.

In characterization of the dominant peaks in the cavitation tests in Fig. 81 it should be recalled that the longer phase change processes at larger cavitation numbers are accompanied by increased convection velocity of the vortical structures (see also Fig. 80(d)). This particularly implies that only some vortices can be identified from the presence of vapor in the mixing layer [25,190], which is also understandable from the vorticity and vapor fraction contours in Fig. 63-64. Thus, noting that the cavitation does not necessarily occur at the same time in every vortex, it can be stated that the creation of peak in spectra is likely originated from those vortices carrying an adequate amount of vapor, while there are still other vortices in the flow which are not filled with vapor [96,190,207]. This likelihood is improved at the smaller cavitation number of *Ca* = 0.21 where larger production of vapor spots with stronger collapse/coalescence incidents amplify the cavity-vortex interactions, and thus the power spectrum [59,96]. The improved vorticity as a result of stronger cavity collapse/inceptions at *Ca* = 0.21 can be consistently seen in Fig. 82(d).

(a)

(b)

(c)

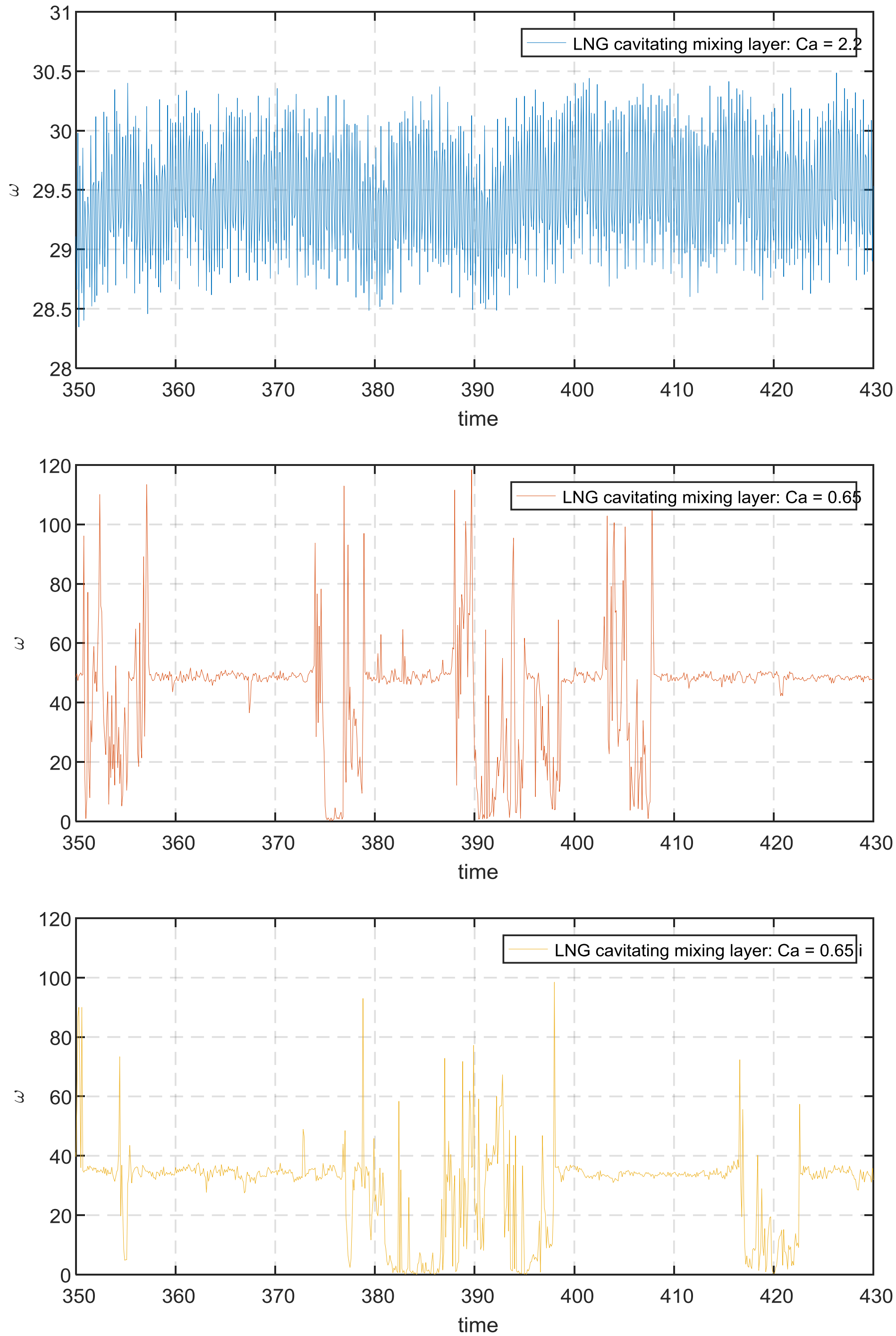
LNG cavitating mixing layer: Ca = 2.2
LNG cavitating mixing layer: Ca = 0.65
LNG cavitating mixing layer: Ca = 0.65i
ω
time

(d)

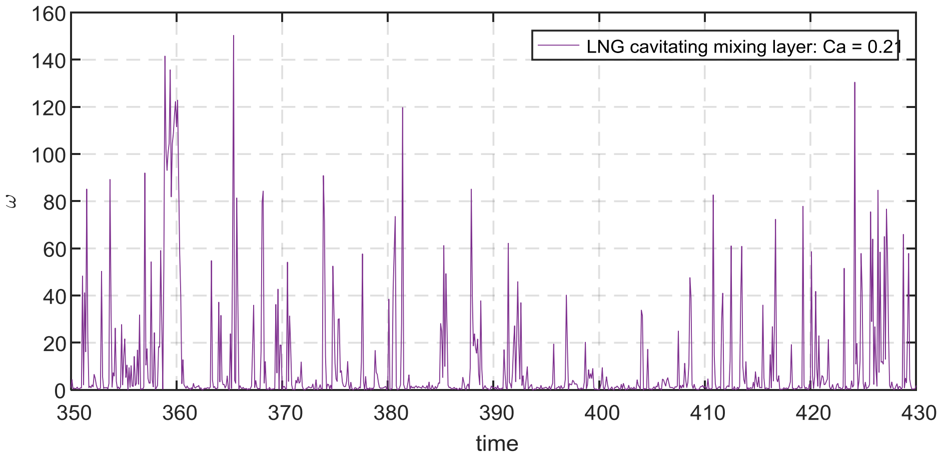

Fig. 82: Time history of vorticity magnitude (1/s) at the probe location (x/c,y/c) = (0.50,0.0) in the cavitating mixing layer of LNG at Ca = 2.20 (a), 0.65 (b), 0.65i (c), and 0.21 (d).

Variation of *St* number (= fc/U_∞ where f, c, and U_∞ respectively are the dominant shedding frequency, the splitter plate length, and the free stream velocity) corresponding to the spectra in Fig. 81 is shown in Table VII for the simulated operating conditions. Resulting numbers lay in the global range of *St*, i.e. 0.20 to 2.10, reported in reference mixing layer studies e.g. [190,194,208]. The table indicates that the decrease of *Ca* from 2.20 to 0.65 results in larger *St* number. Smaller shedding frequency and *St* number at *Ca* = 2.20 suggest an earlier occurrence of shedding process, in smaller frequency range $f < 400.0$ Hz, compared to *Ca* = 0.65. This behavior pertains to the probe location that is placed in the upstream splitter wake region: in the non-cavitation test larger wake causes stronger effects on the flow instability such that the vortex structures near the splitter evolve more quickly at smaller frequencies and under larger influence of inertia. With the decrease of *Ca* to 0.65, the vapor structures suppress the mixture velocity, compared to the non-cavitation test (see also Fig. 80(d)), thus leading to slower evolution of the vortical structures. Note that the influence of wake on the instability behavior at *Ca* = 0.65 is still estimated to be significant, despite the presence of vapor spots which typically tend to improve unsteadiness by reducing *St* number compared to non-cavitating conditions [25,96,190]. This interesting improvement of *St* at *Ca* = 0.65 against the non-cavitation test is similarly reported in Saito and Sato [160] work on a vortex cavity shedding flow behind a 2D cylinder. They concluded that at low enough cavitation numbers, dominant shedding frequency increases with cavity development in wake regions. As for the thermal effects, the absence of thermodynamic parameters in the *Ca* = 0.65i test is seen to reduce the shedding frequency and *St* number against the counterpart thermo-sensitive test at *Ca* = 0.65. This suggests the predominant role of inertia and vortex evolutions compared to the thermodynamic effects in governing the upstream instability mechanisms in these flows [39,92,97].

Cavitation Number (Ca)	Dominant Shedding Frequency (Hz)	Strouhal Number (St)
2.20	87.5	0.473
0.65	345.5	1.417
0.65i	250	0.933
0.21	125	1.141

Table VII: Comparison of St numbers for the cavitating mixing layer of LNG at Ca = 2.20, 0.65, 0.65i, and 0.21. Data correspond to the vorticity magnitude time history probed at (x/c,y/c) = (0.50,0.0).

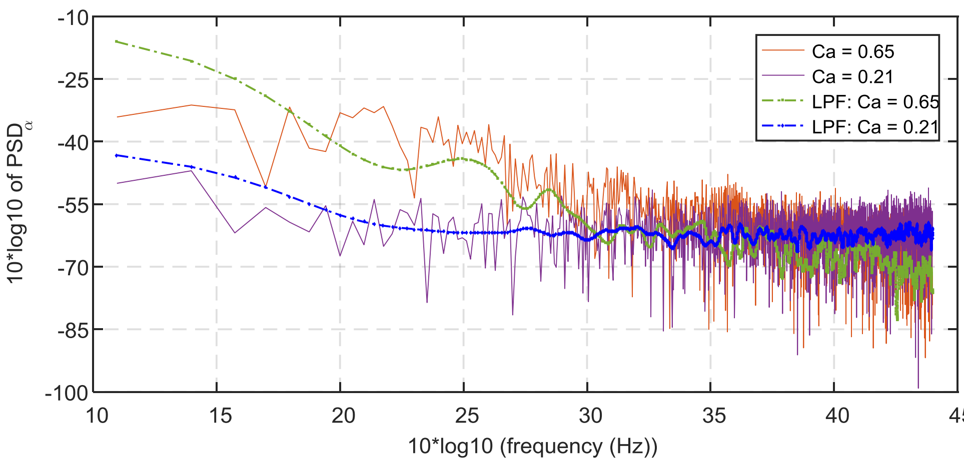

Fig. 83: Log-scale plot of vapor fraction spectra at the probe location (x/c,y/c) = (0.50,0.0) for the cavitating mixing layer of LNG at Ca = 0.65 and 0.21. LPF stands for low-pass filtered data.

Further reduction of cavitation number from *Ca* = 0.65 to 0.21 in Table VII decreases the shedding frequency and *St* number, which is indicative of suppressed effects of the splitter wake on the mixing layer instability at *Ca* = 0.21. As illustrated in Section 9.3, this behavior is mainly caused by contraction of the wake behind the splitter at the smaller cavitation number, which consequently improves the tendency of the flow to faster reach its self-similarity state. Other than the stronger collapse and coalescence processes at *Ca* = 0.21, which significantly increase the local instabilities due to stronger propagation of pressure shock waves [116], the improved local temperature gradients (see also Fig. 72(b) and Fig. 80(a)) are expected to depress *St* by triggering the shedding process of cavity structures, particularly by enhancing the high-frequency oscillations [120]. This is illustrated in Fig. 83 comparing the log-scale power spectrum density (PSD) distributions of the vapor fraction time histories at *Ca* = 0.21 and 0.65. Note that the decrease of *St* at *Ca* = 0.21 is not however large enough to greatly change the overall behavior of the upstream instability under cavitation conditions against the non-cavitation condition -- *St* number at *Ca* = 2.20 is still smaller than those of the *Ca* = 0.65 and 0.21 tests.

The predicted instability behaviors in Fig. 81-83 pertain to the upstream regions of the LNG cavitation mixing layer that is under large effects of the splitter wake. To better understand the instability in the entire mixing area, the same frequency analysis is performed for a downstream probed station at (*x/c,y/c*) = (2.80,0.0). The selected point is located inside the mixing layer self-similar area far away from the splitter so that the cavity-vortex interactions can be addressed in the absence of wake effects. Fig. 84 shows the frequency spectra of time histories of the vorticity magnitude at (*x/c,y/c*) = (2.80,0.0) for the present mixing layers at *Ca* = 2.20, 0.65, 0.65i, and 0.21. Variation of the corresponding *St* numbers is given in Table VIII. Resulting shedding frequencies and *St* numbers show an opposite trend compared to the observed variations upstream of the flow in Fig. 81 and Table VII; downstream characteristic frequency and *St* number are decreased as *Ca* is reduced from 2.20 to 0.21. Smaller shedding frequencies, and *St* number at smaller cavitation numbers indicate the earlier occurrence of shedding process and instability as larger unsteady vapor clouds are more successively generated in the domain. Production of such vapor spots particularly strengthens the local disturbances as well as the overall friction (shear) between liquid and vapor through faster cavity breakup/inception incidents compared to larger cavitation numbers (see also Fig. 80) [157,193]. This behavior is mainly caused by faster suppression of the wake region (see Section 9.3) past the splitter at smaller *Ca* which promotes the distorted vortical structures to become more coherent with larger spatial gradients of velocity [97].

Conversely, increase of *Ca* seems to dampen out the instabilities downstream of the mixing layer, hence leading to the formation of smaller-scale vortex structures shed at larger characteristic frequencies [81]. For instance at *Ca* = 0.65, the presence of slender vapor cavities interacting with smaller vortex structures through suppressed roll-up mechanisms, compared to *Ca* = 0.21 (see also contours of Fig. 63-65), causes an unlimited interaction between the vortical structures and the cavities interfacial regions (due to the dominance of vortices against the vapor spots), eventually disallowing the production of highly unstable large cavity clouds seen at *Ca* = 0.21 [157]. The current predictions in Fig. 84 and Table VIII are in agreement with Aeschlimann et al. [96] results stating that in cavitation mixing layers, presence of vapor structures provokes sufficient irregularities to enhance periodic pairing across the mixing layer. In Table VIII, reduction of *St* number at smaller *Ca* suggests an improvement in the pairing process of vortical structures. It is recalled that the observed behaviors in Fig. 84 and Table VIII may change drastically depending on the variation of inertia, vortex-cavity interaction patterns, and the evolution of thermally-influenced parameters in the mixing layer [97,135,183]. This was clearly seen in the upstream behavior of instabilities in Fig. 81 and Table VII -- the dominant influence of inertia in a strong wake dramatically reduced the *St* number at the non-cavitation (Ca = 2.20) condition of the flow.

(a)

(b)

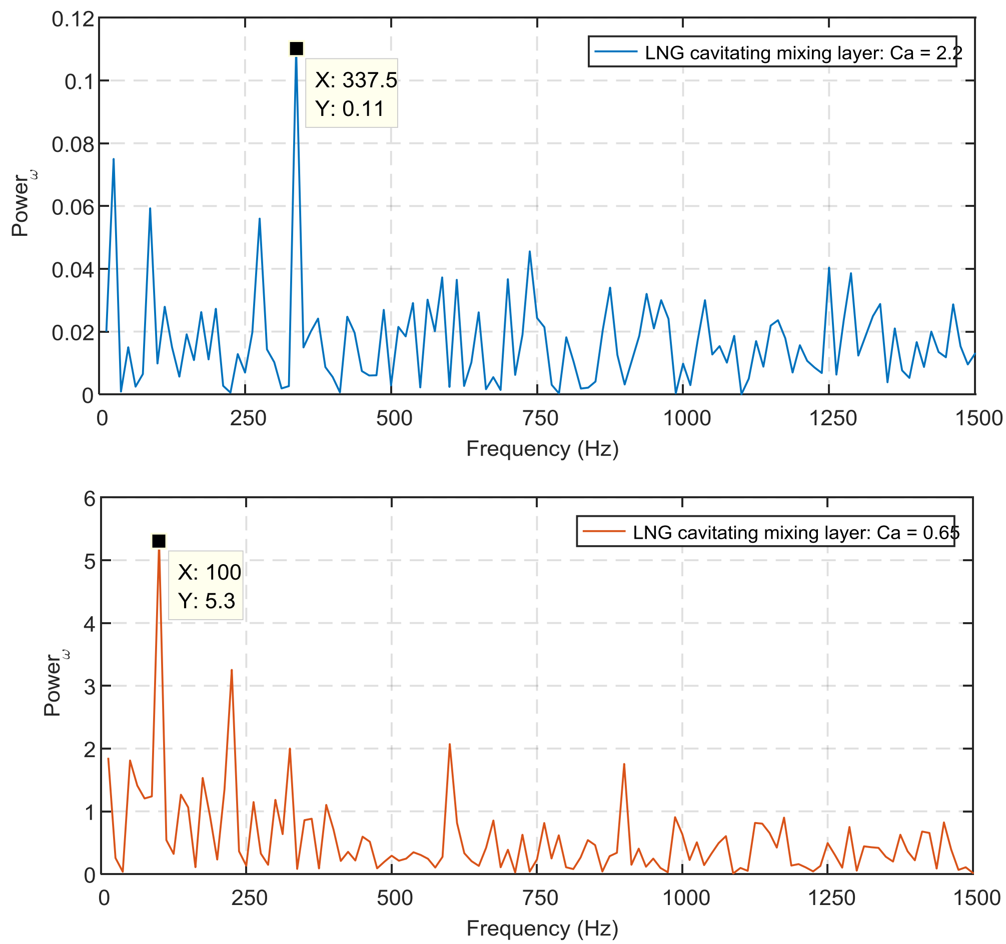

(c)

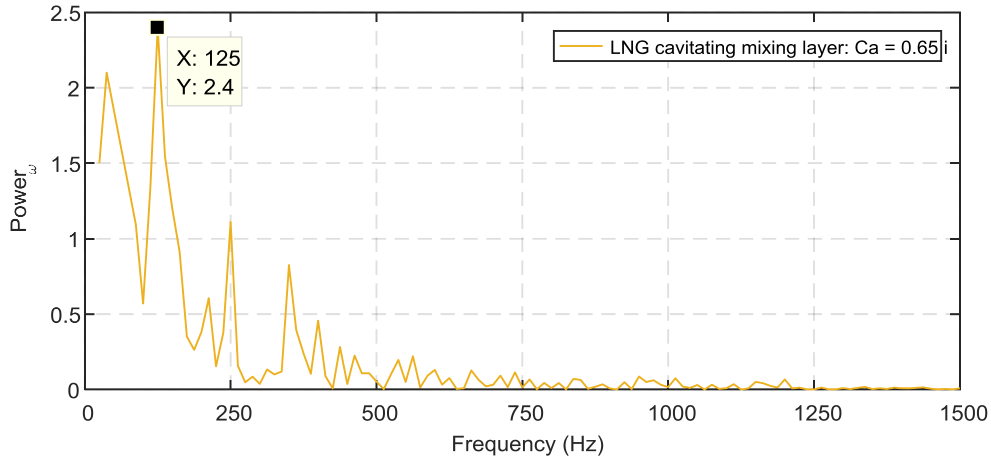

(d)

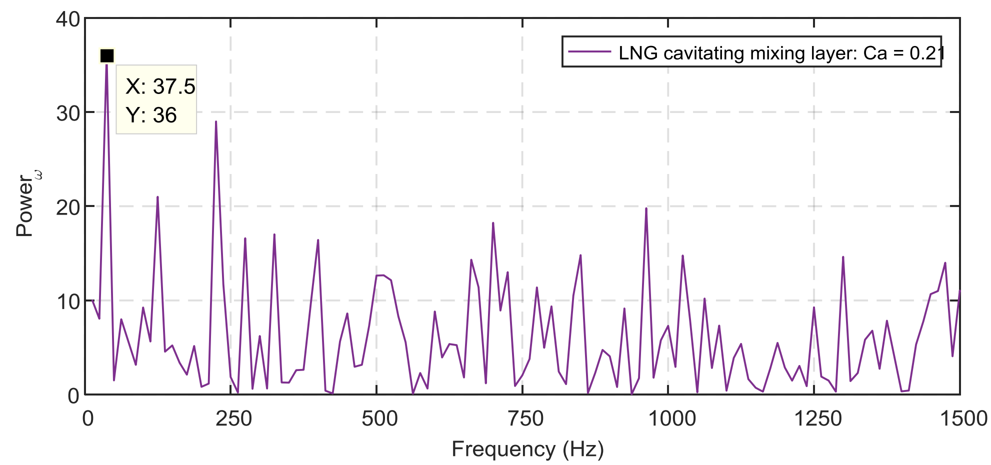

Fig. 84: Spectrogram of vorticity magnitude at the downstream probe location (x/c,y/c) = (2.80,0.0) for the cavitating mixing layer of LNG at Ca = 2.20 (a), 0.65 (b), 0.65i (c), and 0.21 (d).

Cavitation Number (Ca)	Dominant Shedding Frequency (Hz)	Strouhal Number (St)
2.20	337.5	1.114
0.65	100	0.471
0.65i	125	0.483
0.21	37.5	0.312

Table VIII: Comparison of St numbers for the cavitating mixing layer of LNG at Ca = 2.20, 0.65, 0.65i, and 0.21. Data correspond to the vorticity magnitude time history probed at the downstream location (x/c,y/c) = (2.80,0.0).

As for the thermodynamic effects, smaller *St* at the lower *Ca* = 0.21 suggests the improved influence of thermal parameters against inertia in governing the mixing layer instability mechanisms in downstream regions [25,127]. This dominance mainly occurs due to improved thermally-induced gradients of density and pressure within highly unstable vaporization and condensation processes at *Ca* = 0.21 [90,91]. The same behavior is also observed in comparing the *Ca* = 0.65 and 0.65i tests; *St* for the thermo-sensitive at *Ca* = 0.65 case is smaller against the counterpart thermo-insensitive case at *Ca* = 0.65i. These evolutions confirm the important role of thermal involvement in triggering instability in downstream regions of the present mixing layers, and further remark that the thermal effects tend to decrease *St* number. The log-scale PSD distribution of vapor fraction field at the given downstream probe, depicted in Fig. 85, also supports the current results -- the improved thermodynamic effects within larger unstable cavitating clouds at smaller cavitation number enhances the mixing layer downstream instability.

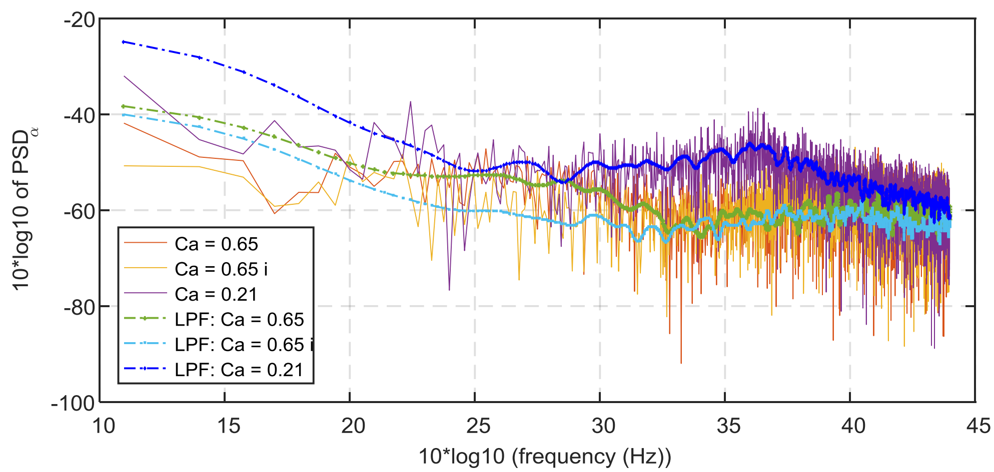

Fig. 85: Log-scale plot of vapor fraction spectra at the downstream probe location (x/c,y/c) = (2.80,0.0) for the cavitating mixing layer of LNG at Ca = 0.65, Ca = 0.65i, and 0.21. LPF stands for low-pass filtered data.

In any case, it should be recalled that the influence of thermal parameters on the behavior of cavitation clouds largely depend on the dominance of these parameters against the shear flow instabilities caused by inertia i.e. vortex and/or re-entrant jet [100,127,157]. For example, as shown in Table VII, *St* number at *Ca* = 0.65 is larger compared to *Ca* = 0.65i, implying that the effects of thermal parameters in upstream regions of the mixing layer are substantially weakened relative to the inertia [93,116]. This is opposite the downstream behavior observed in Table VIII. Note also that the present thermal behaviors are additionally under the influence of propagated pressure waves induced by the collapse of cavity clouds. An indicative example of this is the formation of smaller cavity clouds in upstream of the thermo-insensitive *Ca* = 0.65i case which make the pressure waves become less intense with smaller pressure amplitudes (see Fig. 80(a)-(b) in Section 9.6.1), so leading to a further drop in the characteristic frequency and *St* number compared to the thermo-sensitive counterpart at *Ca* = 0.65.

By and large, the present spectral results suggest that the unsteadiness in cavitating free shear layers of LNG is caused not only by the temporal behavior of cavity-vortex mechanisms but also through their interactions with thermal parameters [135]. In this context, and in agreement with Aeschlimann et al. [96] work, it can be stated that the cavitation process of LNG in a mixing layer can be considered as somewhat a "tracer" of the vortex pairing process [96,197]. This is supported by two reasons: 1) cavitation is mainly associated with vapor inception and collapse incidents that are closely correlated to the periodic and highly intermittent pressure and density variations under thermal conditions; and 2) vortex pairing processes specifically alter the pressure and temperature variations within the vortex cores, which consequently change the density and so the vapor fraction variations [135,193]. This concluding statement however does not disregard the strong double-sided interactions of cavity clouds and vortical structures under thermodynamic conditions. As discussed, depending on the spatial development state of the mixing layer (i.e. wake-influenced or self-similar) the complexity of such interactions can change noticeably.

9.6.3. Transition Characteristics and Net Vapor Production

The observed instability behavior of the LNG cavitation mixing layer in Section 9.6.2 can be particularly relevant to understanding the net vapor production in the mixing region at the given cavitation conditions. This can be illustrated in Fig. 86(a) showing the temporal evolution of spatially-averaged volume fraction field (α_{mean}) in the simulated mixing layers at Ca = 2.20, 0.65, 0.65i, and 2.20, over about three flow-through times of progress. The figure compares α_{mean} for the mixing area of 235 mm long and 70 mm high, as indicated in Fig. 86(b). Spatial averaging of the vapor fractions is conducted by use of the mean vapor fraction formula, α_{mean} = $\frac{\iint_{x,y_1}^{x,y_2} \alpha_i dA_i}{\iint_{x,y_1}^{x,y_2} dA_i}$, given in Section 6.1.4.1. Overall, it is seen that the mean vapor production shows a fluctuating trend regardless of the cavitation condition (note the absence of vapor production in the non-cavitation test at Ca = 2.20), but with larger magnitudes at smaller Ca. This is a typical result of the improved gradients at the smaller cavitation numbers, created within stronger shedding mechanisms and thus led to larger unsteady cavitation clouds. The fluctuation of α_{mean} around a constant value at each test is indicative of periodic shedding process, and further confirms the solution has reached a statistically steady state.

(a)

(b)

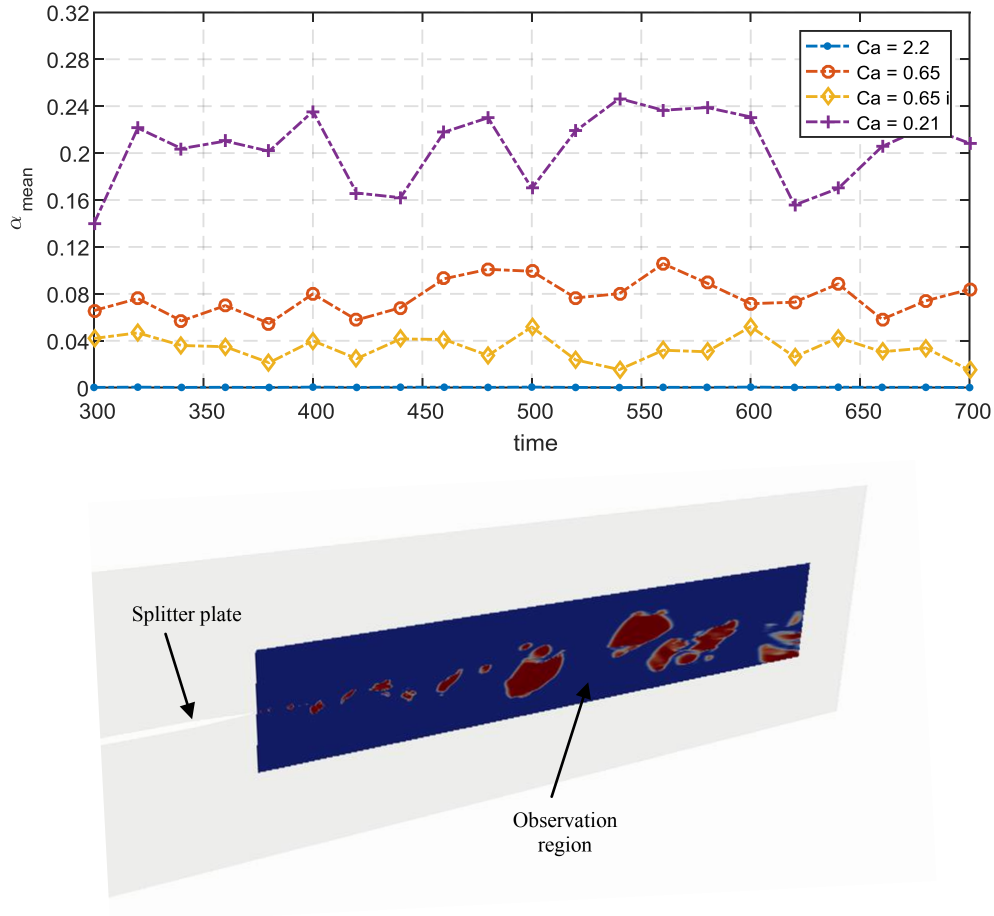

Fig. 86: Temporal distribution of spatially-averaged vapor fraction field (α_{mean}) for the LNG cavitating mixing layer at cavitation numbers of Ca = 2.20, 0.65, 0.65i, and 2.05 (a). α_{mean} is found for the mixing region of 0.0 < x/c < 3.60 and -0.45 < y/c < 0.45 (b).

More on the thermodynamic effects in Fig. 86(a), the net vapor production at *Ca* = 0.65 is larger compared with the counterpart thermo-insensitive case at *Ca* = 0.65i, indicating greater size of the shed off cavity clouds in the former case. This difference between the cavity fields is primarily attributed to the presence of thermal parameters triggering the shear flow instability (see also Sections 9.2-9.6 for more details). In addition, the smaller liquid to vapor density ratios in the thermo-sensitive case requires more liquid content to be vaporized (so more vaporization occurs and causes stronger cloud structures) in the mixing layer to make it fully developed and reach its equilibrium state [73,100]. In this process, unlike the thermo-insensitive case, the incoming liquid flow in the thermo-sensitive test can easily pierce into the vapor cavities due to heat exchange within the interfacial regions, as reported in [100,127], so improving the instability of vapor spots, and thus local vaporization events, by imposing larger density gradients [17,53,116]. The present behavior is consistent with the results of Section 9.6

concluding that the suppressed instability in the thermo-insensitive test *Ca* = 0.65i compared to the counterpart thermo-sensitive case directly pertains to the absence of thermal effects inhibiting cavitation-induced pressure oscillations in the mixing layer.

The observed improvements of net vapor production under thermodynamic effects in Fig. 86(a) further suggests that although saturation pressure decrease due to temperature drop during cavitation process might depress "global" vaporization rate of LNG due to thermodynamic delaying effects [70,100], the produced "local" temperature variations tend to intensify local vaporization processes inside the cavities by amplifying local density gradients (see also Fig. 72(a)) and thus local liquid-vapor interfacial flow rates (see also Fig. 72(c)). This is relevant to Long et al. [127] results stating that cavitating regions in cryogenic fluids appear as "mushy" structures with stronger local entrainment rates compared to isothermal cavitation fields under similar conditions. It is recalled that the predicted mean vapor production variations are always affected by the mixing layer behavior at vapor collapse/inception incidents. For instance, the formation of smaller cavity spots in the thermo-insensitive case *Ca* = 0.65i leads the propagated pressure waves, induced by collapse of vapor clouds, to become suppressed and appear with smaller pressure amplitudes (see the temporal pressure and temperature variations in Fig. 80(a)-(c)), eventually leading to smaller gradients in the flow as compared to the *Ca* = 0.65 test. These gradients are clearly improved with the decrease of cavitation number to 0.21, as a result of larger vapor productions.

9.7. Velocity Fluctuation Profiles

To further demonstrate the effects of cavitation number on the LNG cavitating mixing layer unsteady characteristics, Fig. 87 compares the variations of dimensionless mean-square velocity fluctuations along two transverse reference line stations of *x/c* = 0.40 (upstream) and 3.20 (downstream) (see Fig. 69), for the operating conditions of *Ca* = 2.20, 0.65, 0.65i, and 0.21. The streamwise ($\overline{u'u'}$), transverse ($\overline{v'v'}$), and shear ($\overline{u'v'}$) velocity fluctuations are evaluated in the figure for about three flow-through times of progress after reaching statistically steady state. The profiles are non-dimensionalized with the local mean velocity at each station. As seen, the upstream (Fig. 87(a)-(c)) and downstream (Fig. 87(d)-(f)) profiles overall share the well-known "top-hat" variations with non-uniform large magnitudes inside and smaller magnitudes outside (outer layers) the mixing layer [75,185,196]. Note that the transverse mixing length, to determine the inside and outside bounds of the mixing layer, can be determined based on the transverse velocity profiles -- for the present stations in Fig. 87, it is found to be 0.25c, 0.21c, 0.19c, and 0.17c at the upstream, and 0.82c, 0.54c, 0.46c, and 0.34c at the downstream stations, respectively, for the cavitation numbers of Ca = 0.21, 0.65, 0.65i, 2.20. The largest magnitudes of fluctuations in Fig. 87 are observed in the core of the mixing layer, regardless of the cavitation content and thermodynamic parameters, indicating the accumulation of vorticity and strain rate in the core [193]. Also, in line with typical features of mixing layers (see e.g. [185,196-198]), the streamwise fluctuations indicate larger amplitudes than the transverse and lateral components. As reported by Aeschlimann et al. [25] and Gopalan et al. [183], the excess of longitudinal fluctuations is mainly due to complex combination of coupled vaporization and condensation processes where the two-phase mixture structures are imploded and expanded in a periodic fashion. This specially includes the collapse of vapor spots which results in propagation of shock-induced pressure waves triggering local instabilities by improving velocity fluctuations (see also Section 9.6) [116,126].

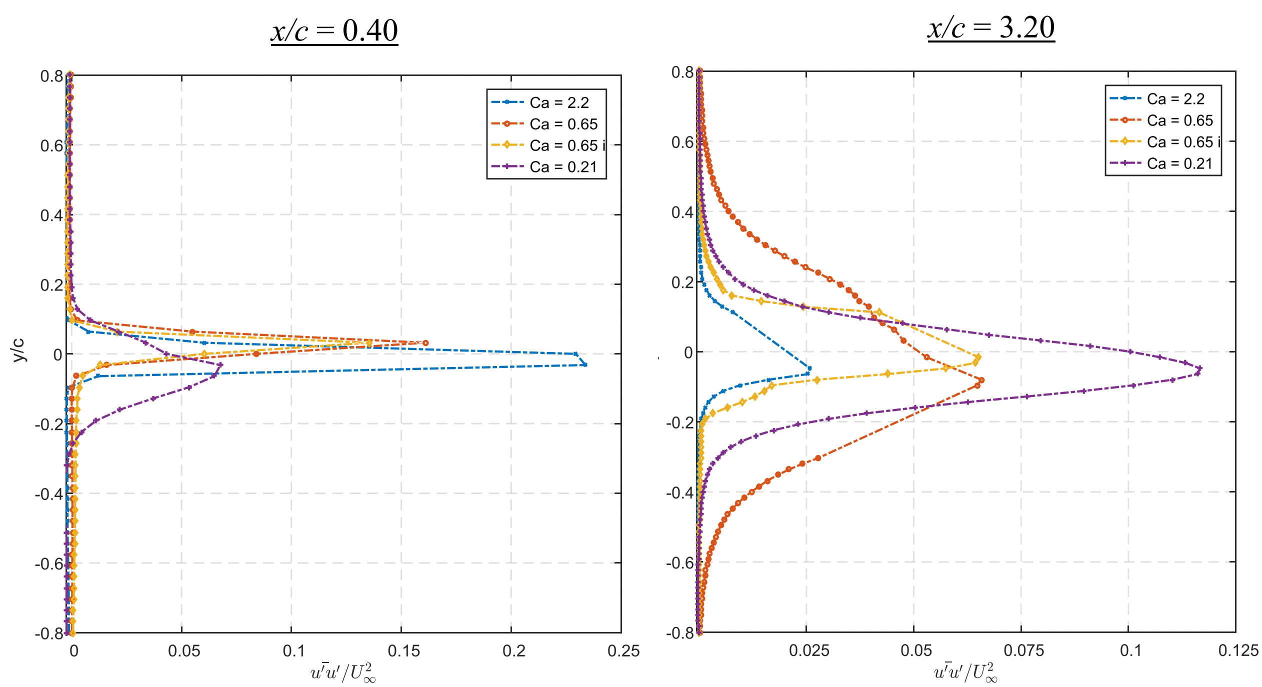

(a) *(d)*

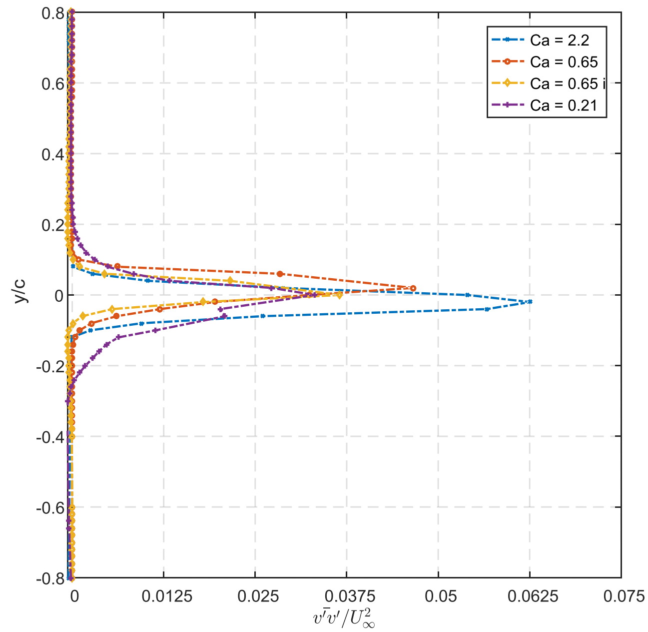

(b)

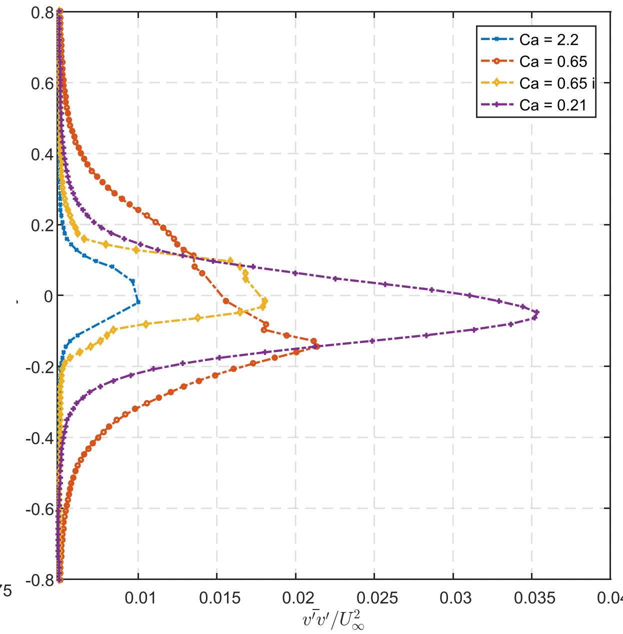

(e)

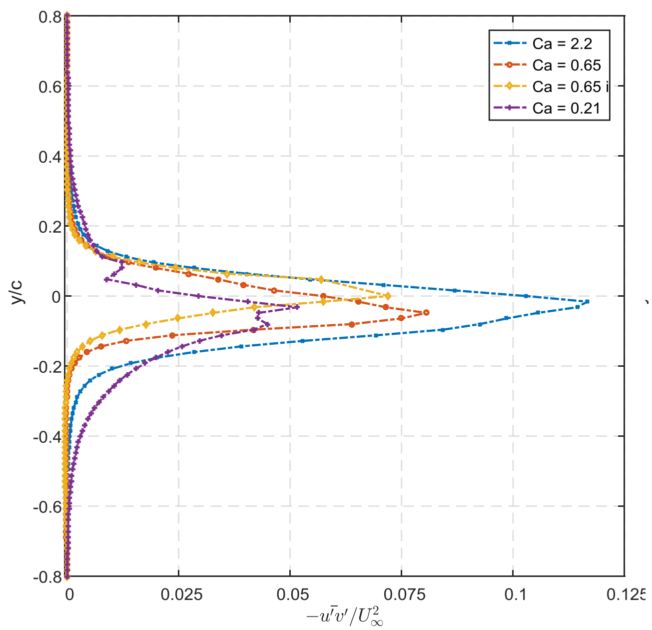

(c)

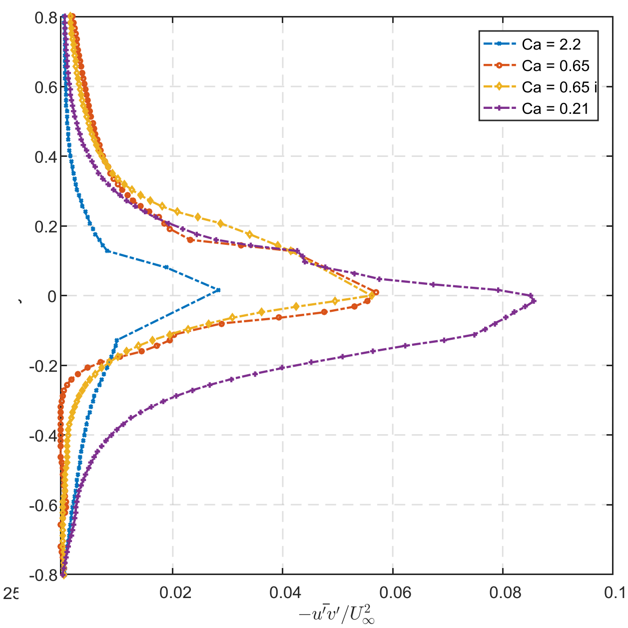

(f)

Fig. 87: Profiles of dimensionless mean-square velocity fluctuations along the transverse reference line stations of x/c = 0.40 and 3.20 for the LNG cavitating mixing layer at Ca = 2.20, 0.65, 0.65i, and 0.21: (a,d) streamwise normal; (b,e) transverse normal; and (c,f) lateral shear components. Data are collected for the transverse span of -0.80 < y/c < 0.80.

The significance of normal velocity fluctuations compared to the transverse fluctuations in Fig. 87 is indicative of non-isotropic turbulence/anisotropy ($u' > v'$) in all the simulated tests, which seems to be amplified by further development of vapor structures at smaller *Ca* [75,96].

The anisotropy is especially found inside the mixing layer, where the cavity-vortex dynamics are more likely generated through time-dependent streamwise and transverse velocity interactions [25]. A major increase of anisotropy is observed in the upstream station (Fig. 87(a)-(c)) as the cavitation number increases from 0.21 to 2.20, i.e. due to large influence of the splitter wake. This trend is however reversed when the mixing layer reaches its self-similar state downstream (Fig. 87(d)-(f)), where the shear fluctuation increases with decrease in Ca. These observations suggest a strong dependence of turbulence diffusion ($\propto \overline{u'v'}$) on the trade-off between inertia, cavitation, and thermal effects in the present mixing layers. Note that the non-zero values of $\overline{u'v'}$ outside the mixing layers (see for example $0.50 < y/c < 0.80$ in Fig. 87(f)), that can be also spotted in the normal components, are likely attributed to the presence of intermittent superlayers in the interface of the mixing and non-mixing zones. The intermittent superlayers typically tend to amplify velocity fluctuations [75,189,209]. The local reductions of $\overline{u'v'}$ with reduction of Ca in the core (see for example $-0.20 < y/c < 0.20$ in Fig. 87(f)) and outside of the mixing layer (see for example $-0.30 < y/c < -0.80$ in Fig. 87(c) and 87(f)), which is also detected in the normal streamwise and transverse profiles (see for example $0.30 < y/c < 0.80$ in Fig. 87(d) and 87(e)), likely pertain to angular velocity of non-cavitating streamwise vortices which tends to increase with the decrease of cavitation number, as similarly observed by Okabayashi et al. [97]. Related to this, in downstream of the test at $Ca = 0.65$ (see for example $-0.20 < y/c < -0.80$ in Fig. 87(d) and 87(e)), the enhanced influence of thermal parameters against liquid-vapor interfacial shear/inertia seems to be the main cause for regional improvements in the normal fluctuations outside the mixing layer, as compared to the other tests. The suppressed fluctuations at the smallest $Ca = 0.21$ in these regions suggest that the intensified cavitation at $Ca = 0.21$ necessarily enhances the velocity fluctuations inside the mixing layer (see for example $-0.20 < y/c < 0.20$ in Fig. 87(d) and 87(e)), rather than outside, through amplifying interfacial gradients.

The observed reverse behavior of the shear velocity fluctuations in the upstream and downstream of the mixing layer in Fig. 87 can be similarly detected in the streamwise and transverse normal components. In the upstream wake station, cavitation reduces the velocity fluctuations (see Fig. 87(a)-(b)), with larger reductions at smaller Ca. The reduction is however smaller in the transverse component $\overline{v'v'}$. The largest fluctuations are observed in the non-cavitation test at $Ca = 2.20$ and the smallest at Ca = 0.21. The decrease in fluctuation amplitude with cavitation number is likely due to depression of K-H rollers in the braid region close to the

T.E. in the cavitation tests as a result of inception and expansion of vapor cavities [89] -- the presence of cavities in the low-pressure cores of vortical structures suppress the vortical structures modulations, so reducing the velocity fluctuations [25,75,96]. As explained by Okabayashi et al. [97], pressure variations around the vapor pressure in the cavitating spots, which cause the pressure fluctuations to become smaller than that of single-phase flow, also suppress upstream K-H rollers. This particularly causes the energy redistribution from $\overline{u'u'}$ to $\overline{v'v'}$ through pressure fluctuations to diminish, as reported in [96,207]. The current observations are consistent with Okabayashi et al. [97] results stating that the reduction of normal velocity fluctuations in cavitation flows is the main reason for decrease of shear velocity fluctuations, as indicated in Fig. 87(c).

The reduced fluctuations in the cavitating tests compared to the non-cavitating flow in the upstream station in Fig. 87(a)-(c) are further estimated to be due to weakened correlation between streamwise and transverse velocities as a result of vapor cavity production [89]. This conclusion can be better explained by Belahadji et al. [92] analogy: in a non-cavitating flow, since vortex stretching in streamwise direction causes the vortex rotation rate to increase, streamwise velocity fluctuations are coupled to transverse fluctuations. However, in a cavitating flow, the presence of vapor in the core of vortical structures modifies the vortex stretching mechanisms by decoupling the vortex rotation and strain rate. Since the core of a cavitating vortex is able to maintain a constant pressure, i.e. saturation pressure (unlike the non-cavitating case where the increase of rotation rate causes the pressure in the vortex core to reduce), the streamwise stretching only results in generation of more vapor in the core with a little change in the core diameter and rotation rate. The predicted behaviors are consistent with Iyer and Ceccio [89] and Laberteaux and Ceccio [90] studies remarking that reduction of mean density in braid region of cavitating shear layers may suggest an overall reduction in shear velocity fluctuations, particularly at extremely cavitating conditions.

Contrary to the upstream behavior, in the downstream self-similarity zone inside the mixing layer, larger velocity fluctuations (see Fig. 87(d)-(f)) are detected with the increase of vapor content, which are likely due to strengthened vortex variations and larger thermally-induced density gradients as a result of stronger and/or more frequent collapse-coalescence of vapor spots (see also Fig. 71-72) [25,97]. These improvements of turbulence characteristics at smaller *Ca* are estimated to directly impact the K-H instabilities, as discussed in Section 9.6, such that the formation of larger density gradients from more successive vaporizations and condensations of fluid particles further distort the main roll-up process through imposing stronger anisotropy and shear strain rate [25]. This is in accordance with the results of Pentelow [210] stating that triggering local instabilities in shedding process of free shear flows produces additional velocity fluctuations within vortical structures. Other than reducing Ca, the predicted velocity fluctuations in Fig. 87(d)-(f) are improved with the presence of thermodynamic effects, as can be detected in comparing the Ca = 0.65 and 0.65i tests -- the improvement seems to be more significant in the transverse $\overline{v'v'}$ fluctuations (compare the peaks), and less evident in the shear component $\overline{u'v'}$. Such influence was observed to be smaller in the upstream station (Fig. 87(a)-(c)) because of the wake dominance.

The larger velocity fluctuations at smaller Ca in the downstream station in Fig. 87(d)-(f) can be further explained by the fact that the expansion of vapor inside vortical structures makes them weakened in a way that their angular velocity - and so the overall flow vorticity - are suppressed, as reported in [187]. This causes the vortices to diminish their interaction with vapor spots, eventually leading them to be more significantly affected by local phase change processes as compared to non-cavitation situations. For instance, at the smallest Ca = 0.21 such behavior results in the strongest interactions between cavity and vortex structures, making the predicted velocity fluctuations (see Fig. 87(d)-(f)) significantly greater than the other tests [97]. This conclusion is relevant to Iyer and Ceccio [193] work stating that increase in velocity fluctuations suggests an increase in local vorticity and strain rate. Qualitative comparison of the velocity fluctuations in Fig. 87(d)-(f) with the vorticity magnitude and strain rate variations in Fig. 71(c) and 79(b)-(c) also confirms this observation in downstream regions of the present mixing layers.

It is also worth-noting that the predicted upstream and downstream velocity fluctuations in Fig. 87(a)-(c) and Fig. 87(d)-(f) show an asymmetric behavior with an apparent bias toward the mixing layer low-speed side, in all the simulated operating conditions. This is likely attributed to: 1) the faster velocity field in the upper side of the mixing layer, causing the upper stream to be decelerated towards the lower stream; and 2) the dominant momentum transfer within large-scale eddies in their normal gradient diffusion direction, i.e. from the upper side to the lower side of the mixing layer -- eddies with downward motion increase streamwise velocity fluctuations, assuming a positive shear strain ($\partial u/\partial y > 0.0$), and vice versa, as explained in [75,186]. The asymmetry can also pertain to the previous observations in Sections 9.5-9.6 pointing out that the transverse gradients of mean velocity across the mixing layer are enhanced by the presence of wake and/or the vapor spots. So, since the transverse gradient is regarded as a turbulence production parameter, larger upper to lower side momentum transfer in any case leads to larger velocity fluctuations with the preferred low-speed side deflection [194,207]. For example, at the smallest cavitation number Ca = 0.21 in Fig. 87(a)-(f), more amplification of pressure gradients as a result of improved temperature-dependent density gradients through stronger vapor collapse and coalescence processes brings a stronger asymmetry in the mixing layer, especially in downstream regions, as compared to the larger cavitation numbers.

10. Numerical Simulation of 3D Cavitating Mixing Layer of LNG

This chapter investigates the compressible laminar to transitional cavitating mixing layer of LNG behind a 3D planar configuration of the baseline reference test described in Section 8.1. The global behavior of the 3D LNG cavitating structures in the mixing layer at selected time instants is studied to reveal the temporal evolution of cavitating patterns in the first cavitation cycle, including unsteady vapor nucleation, attached sheet cavitation, and cloud cavitation development. Instability and cavity-vortex interaction mechanisms are also qualitatively assessed with the ultimate goal of identifying three-dimensionality influence in modulating vapor and vortex structures in the mixing layer.

10.1. Numerical Setup

The 3D laminar to transitional cavitating mixing layer of LNG behind the splitter is built by extruding the 2D domain of Section 8.1 (see Fig. 56) in the spanwise direction for a span length of Δz = 2.40 mm. The 3D simulation is then performed by using the same operating condition and setup as described in Section 8.1, except that the maximum acoustic Courant number is reduced to 1.0 to improve the numerical stability, and 480 numbers of processors are used to speed up the computation. A periodic boundary condition is used on the side patches of the extruded geometry. To accurately resolve the 3D eddy structures in the flow, similar to the method described in Section 7.1, the grid in spanwise direction is carefully examined for a thermo-insensitive counterpart test of the 3D cavitating mixing layer of LNG at the cavitation condition of Ca = 0.21, using three spanwise node numbers of 34, 62, and 88. Corresponding numerical tests with the three generated mesh configurations are performed for a single flow-through time of progress to find the maximum values of pressure created in the flow for each mesh. The spatially-averaged vapor fractions (α_{mean}) are also compared at the last recorded time step of t = 185.0 s to evaluate the net vapor production in the domain. As seen in Table IX, the results of the medium and fine resolution grids collapse well, hence, the grid with the medium resolution, comprised of 39,187,000 cells, is selected to optimize the computational costs. It is noted that the selection of 62 nodes for the spanwise length of 2.40 mm ensures the proper capture of Kolmogorov length scale in the present 3D flow [75,181,182], given the operating Reynolds number of Re = 60,981.41, as indicated by Dittakavi et al. [174]. The selected spanwise length with uniform distribution of nodes also results in $\Delta z^{+} \cong 1.48$, satisfying the 3D grid spacing criterion to a reasonable extent [75,174]. The current mesh setup is based on the reported grid configuration in Okabayashi et al. [97] work where spatial node grading ratio of $\Delta z^{+} \cong 1.59\Delta y^{+}$ is used for turbulent simulations of 3D cavitating mixing layer of water.

Number of Nodes in Spanwise Direction	Maximum Pressure (Pa)	Spatially-Averaged Vapor Fraction
34	560648	0.2674
62	628515	0.2353
88	628503	0.2345

Table IX: 3D LNG cavitating mixing layer mesh convergence study: comparison of flow parameters, i.e. maximum pressure and net vapor production (α_{mean}), for different spanwise grid resolutions in the 3D domain. Data correspond to approximately one flow-through time of progress.

10.2. 3D Evolution of Cavity-Vortex Structures in the Cavitation Flow

Temporal behavior of the 3D cavitation mixing layer of LNG during the first flow-through time of progress is shown in Fig. 88-89 for the mixing region of $0.0 < x/c < 2.50$ and $-0.25 < y/c < 0.25$. Fig. 88 displays the evolution of iso-contours of vapor fraction field for vapor structures with α = 0.85, at time instants of t = 10.25, 28.12, 43.86, 62.51, 81.15, 98.59, 116.14, 136.92, 153.07, and 175.63 s. Fig. 89 depicts the corresponding evolution of the iso-contours of Q-criterion with Q = 240.0 s^{-2} superimposed with the iso-contours of vapor fraction field with α = 0.95. Overall assessment of the contours indicate that the cavitating flow is initially formed as a combination of spanwise thin and large vapor tubes distributed unevenly in the mixing layer lower stream within highly-rotating vortices close to the T.E. With time, the mixing layer periodic roll-up process dominates the flow and gradually guides the deflected primary vapor tubes into the mixing layer core. The centerline tubes then become distorted as they move downstream, due to interactions with neighboring cavity and/or vortex structures. This process is concurrent to developing an unstable attached sheet cavitation flow on the splitter upper surface, which successively dispatch unsteady vapor pockets upstream. The small vapor pockets gradually turn into large cavity clouds downstream as the mixing layer shedding continues. The non-uniform evolution of the observed cavity-vortex structures in streamwise and spanwise directions is indicative of three-dimensionality that significantly alters the cavitation development behavior compared to the 2D flow resulted in Section 8.2. This is mainly due to the additional crosswise gradients in the 3D test [75,164], leading the sheet and cloud vapor structures to often appear with rounded closure surfaces, and be comprised of complex U-shaped vapor structures tightly interacting with surrounding coherent hairpin vortices [97,116].

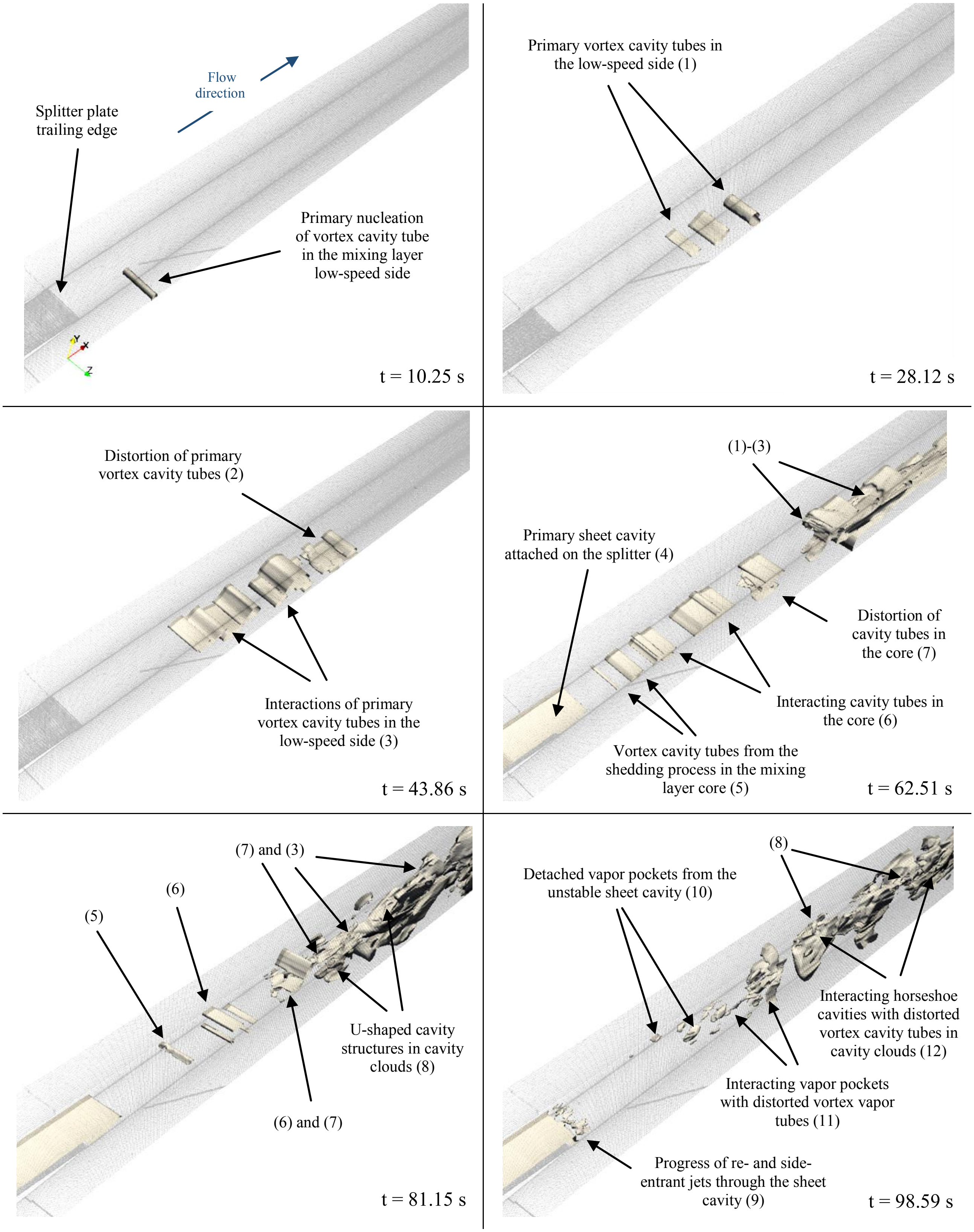

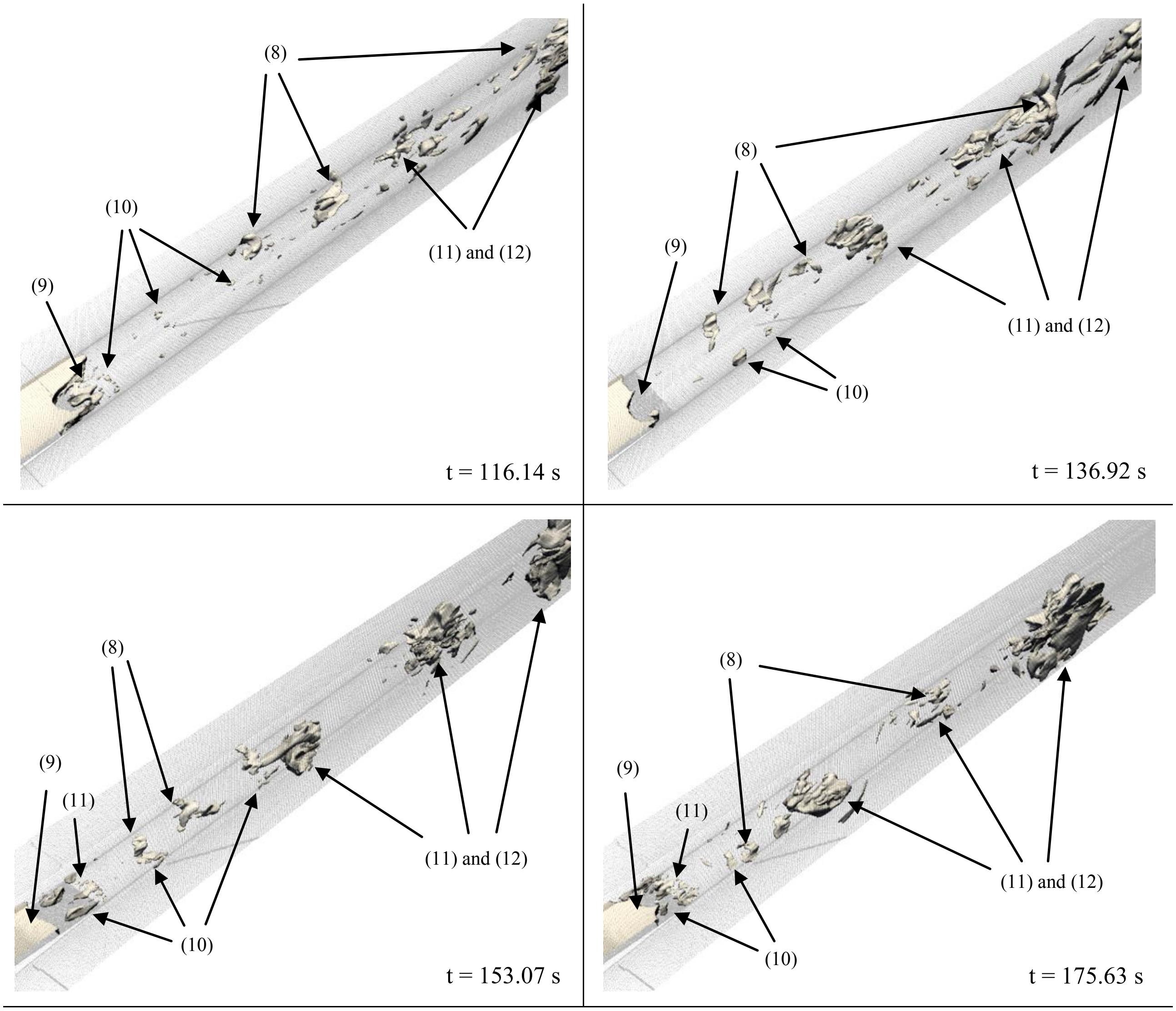
(8)
(10)
(9)
(11) and (12)
t = 116.14 s
(8)
(9)
(11) and (12)
(10)
t = 136.92 s
(8)
(9)
(11)
(10)
(11) and (12)
t = 153.07 s
(8)
(9)
(11)
(10)
(11) and (12)
t = 175.63 s

(a)

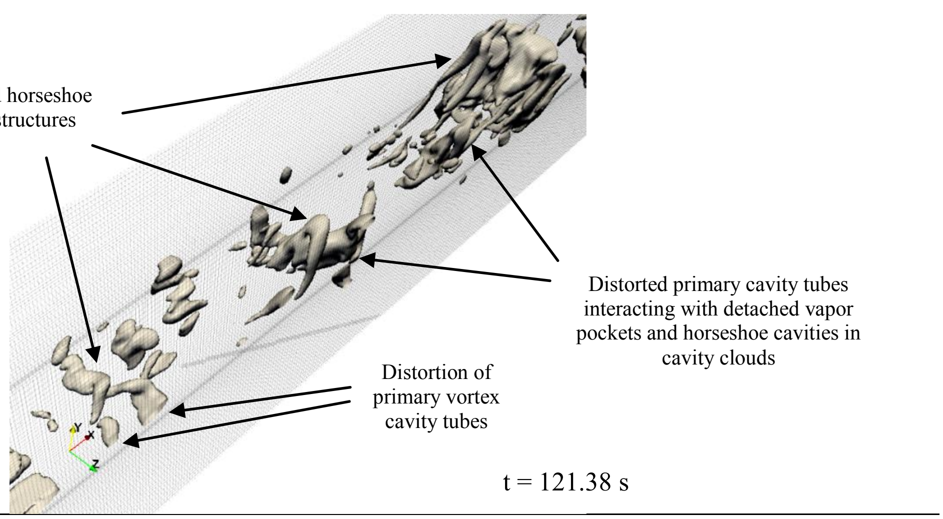
U-shaped horseshoe
cavity structures
Distorted primary cavity tubes
interacting with detached vapor
pockets and horseshoe cavities in
cavity clouds
Distortion of
primary vortex
cavity tubes
t = 121.38 s

(b)

Fig. 88: Time evolution of the 3D cavitating mixing layer of LNG in the mixing region of 0.0 < x/c < 2.50 and -0.25 < y/c < 0.25: instantaneous iso-surface contours of vapor fraction with α = 0.85 at time instants of t = 10.25, 28.12, 43.86, 62.51, 81.15, 98.59, 116.14, 136.92, 153.07 and 175.63 s (a). Note the zoomed-in contour in the region of 0.05 < x/c < 0.21 at t = 121.38 s (b) to better clarify the U-shaped cavity interactions.

The cavitation development in Fig. 88 is closely related to how the unsteady vortical structures evolve in the mixing layer roll-up process. As depicted in Fig. 89, faster separation of the flow on the upper side of the splitter combined with the high-vorticity region at the T.E. lead to roll-up of the sheet of the fluid behind the splitter primarily in the low-speed stream (Fig. 89(a) at t = 10.25-28.12 s), that is followed by the formation of trailing edge vortex tubes through the wavy-shape K-H instabilities in the mixing layer core (see also Section 8.2 for more discussion) [75]. Gradual progression of the primary infinitesimal K-H instabilities at the mixing layer braid region in the core then causes the neighboring pairs of counter-rotating vortices (K-H rollers) to stretch and roll around each other, and eventually amalgamate into larger vortex pairs i.e. eddies (Fig. 89(a) at t = 43.86-62.51 s) [189,197]. This is the dominant mode of vortex interactions in the mixing layer that continues by secondary K-H instability mechanisms onward (Fig. 89(a) at t > 62.51 s) [75,189]. The secondary mechanisms provide continuous pairing of the counter-rotating vortices within a few wavelengths downstream of the splitter plate, leading to the formation of larger coherent vortical structures with twice the primary streamwise period (see also Fig. 59) [25,188,190].

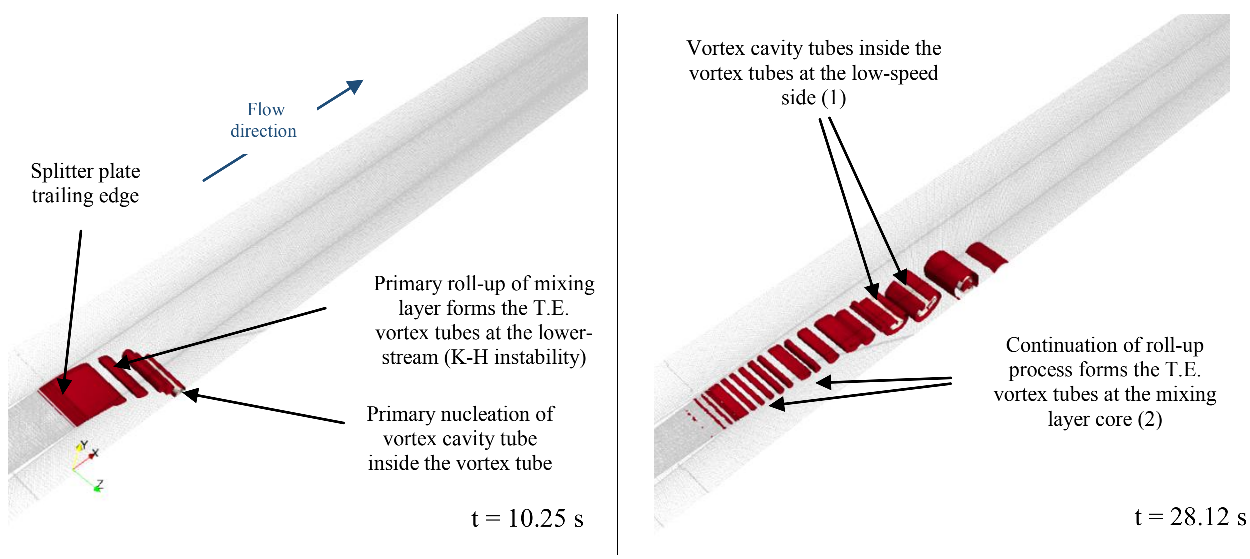

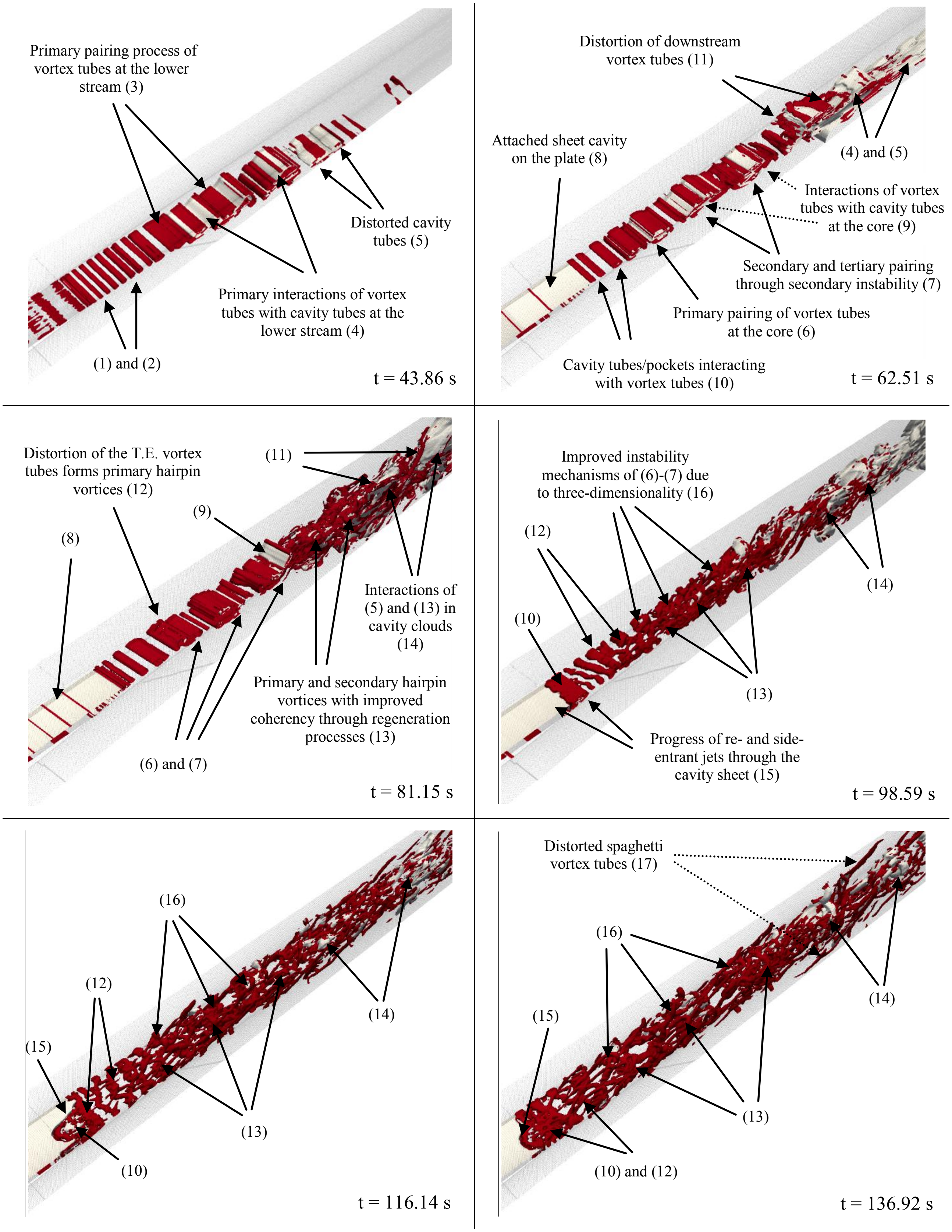
Primary pairing process of vortex tubes at the lower stream (3)
Distorted cavity tubes (5)
Primary interactions of vortex tubes with cavity tubes at the lower stream (4)
(1) and (2)
t = 43.86 s
Distortion of downstream vortex tubes (11)
Attached sheet cavity on the plate (8)
(4) and (5)
Interactions of vortex tubes with cavity tubes at the core (9)
Secondary and tertiary pairing through secondary instability (7)
Primary pairing of vortex tubes at the core (6)
Cavity tubes/pockets interacting with vortex tubes (10)
t = 62.51 s
Distortion of the T.E. vortex tubes forms primary hairpin vortices (12)
(11)
(9)
(8)
Interactions of (5) and (13) in cavity clouds (14)
Primary and secondary hairpin vortices with improved coherency through regeneration processes (13)
(6) and (7)
t = 81.15 s
Improved instability mechanisms of (6)-(7) due to three-dimensionality (16)
(12)
(10)
(14)
(13)
Progress of re- and side-entrant jets through the cavity sheet (15)
t = 98.59 s
(16)
(12)
(15)
(14)
(13)
(10)
t = 116.14 s
Distorted spaghetti vortex tubes (17)
(16)
(15)
(14)
(13)
(10) and (12)
t = 136.92 s

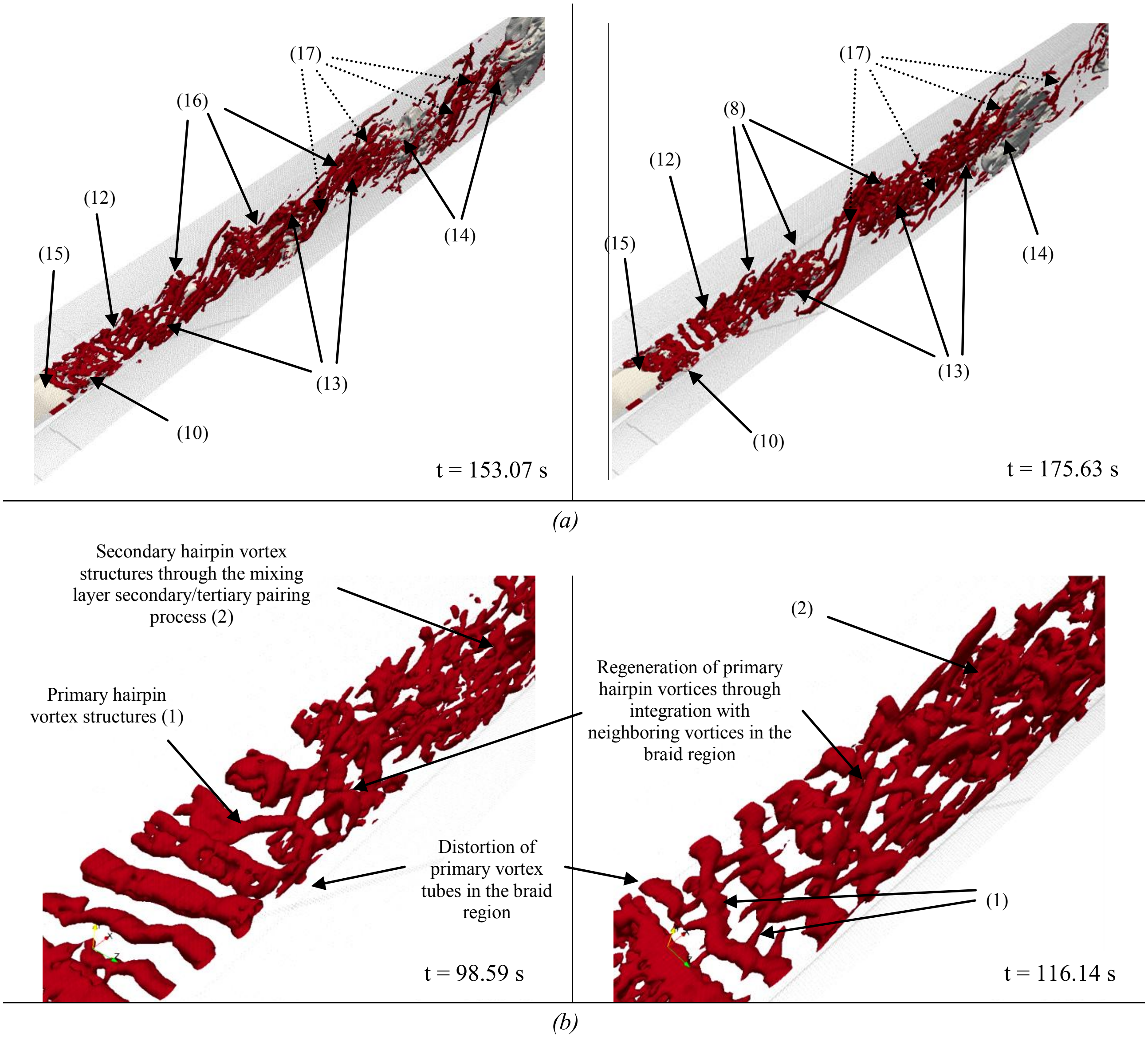

Fig. 89: Time evolution of the 3D cavitating mixing layer of LNG in the mixing region of 0.0 < x/c < 2.50 and -0.25 < y/c < 0.25: instantaneous iso-surface contours of Q-criterion with Q = 240.0 s^{-2} superimposed with iso-surface contours of vapor fraction with α = 0.95 at time instants of t = 10.25, 28.12, 43.86, 62.51, 81.15, 98.59, 116.14, 136.92, 153.07, and 175.63 s (a). Iso-surfaces of Q-criterion are colored in black red. Note the zoomed-in contours of Q in the region of 0.07 < x/c < 0.17 at t = 98.59 and 116.14 s (b) to better clarify the coherent hairpin vortices.

As the longitudinal vortex tubes in upstream regions are stretched and expanded through the instability mechanisms, conservation of momentum leads the angular velocity of the vortices to rise up, hence causing their core pressure to decrease [90,97,207]. Provided that the static pressure drops below the local saturation vapor pressure, cavity nucleation begins such that primarily long and thin vapor tubes are generated inside the streamwise vortices low-pressure cores. Fig. 88(a) at *t* = 10.25 s shows a primary nucleated vapor cavity from a primary low-pressure vortex core (see Fig. 89(a) at t = 10.25 s), which is enlarged with time and followed by consecutive formation of larger cavity tubes through the progression of mixing layer roll-up (Fig. 88(a) and 89(a) at t = 28.12-62.51 s) and the latent heat exchange mechanisms (see Section 10.3 for more discussion) [21,89,187]. Note that the deflection of the initiative cavities toward the lower stream is due to initial deceleration of the mixing layer high-speed side towards the low-speed side. As the mixing layer deflection is removed with time, follow-on cavities are successively nucleated around the mixing layer centerline (Fig. 88(a) at $t > 43.86$ s).

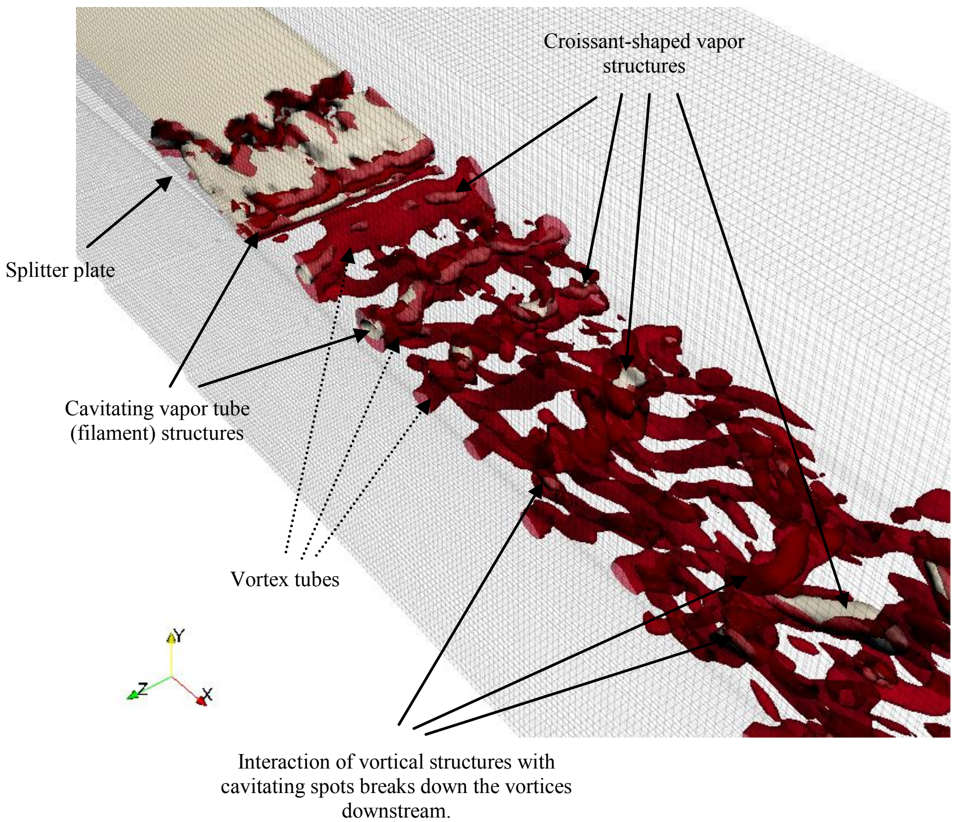

Fig. 90: 3D cavitating mixing layer of LNG downstream of the splitter plate: zoomed-in view of superimposed iso-surface contours of vapor fraction and Q-criterion (colored in red) in the mixing region of 0.0 < x/c < 0.13 at time instant of t = 104.51 s.

When the secondary and tertiary vortex pairing occurs, the vapor cavities grow into unsteady cavitation clouds (Fig. 88(a) and 89(a) at $t > 62.51$ s). This is estimated to be primarily due to interactions of the distorted longitudinal vortical structures upstream with neighboring rolling vortices, i.e. K-H rollers, through the mixing layer instability mechanisms, which improves the formation of low-pressure regions within adjacent rollers [96,207]. As seen in Fig. 90, the cavities at this stage typically appear in the form of slender vapor tubes (filaments) and/or “croissant-shaped” vapor spots inside the low-pressure cores of vortices [170,183,193]. The presence of such unstable cavities leads the primary vortex structures to experience major distortions and breakdown, so depressing the promotion to large vortex tubes downstream, as denoted in [125]. The resulting contour in Fig. 90 is in agreement with experimental observations of Katz and O’Hern [95] on cavitation onset and growth in a shear layer of water downstream of an upright sharp-edged plate: inception of cavity primarily occurs through vortex stretching in between of large-scale spanwise vortices in the shear layer, as a result of decreased vortex core diameter and pressure. Note also in the figure that the incepted cavities do not necessarily fill the original viscous cores, as similarly described in Briançon-Marjollet and Merle [211] work on an airfoil tip-vortex cavitation flow. When a vortex tube fills with vapor tube, diameter of the vapor tube eventually becomes smaller down to several times the size of the original core, which is principally due to vapor diffusion into the vortex core, as reported in [95,193].

In the meantime of the mixing layer pairing process, an unstable sheet cavitation flow also starts developing on the upper surface of the splitter, which successively dispatches small vapor pockets from its rear around the T.E. (Fig. 88(a) at $t > 98.59$ s). The dispatched vapor pockets tend to gradually turn into expanding unsteady cavity clouds as convecting downstream by the main stream, primarily through integrations with the previously-distorted cavity tubes [89,119]. Strong interactions of the distorted vapor tubes with the dispatched vapor pockets through the mixing layer shedding mechanisms can be widely seen at this stage (e.g. Fig. 88(a) at $t > 98.59$ s). Upon approaching the end of cavitation cycle (Fig. 88(a) at $t > 136.92$ s), the tightly-interacting cavity spots eventually appear in a regular way and are separated by condensation events corresponding to the “inter-eddy” space of the generated vortical structures (Fig. 89(a) at $t > 136.92$ s) [91]. The described periodic cavitation cycle in Fig. 88 maintains by the permanent shedding of vortex structures, three-dimensionality, and frequent collapse of the vapor cloud with propagated pressure waves (see also Section 9.6 for more discussion) [23,116,132]. The generated cavities in a cycle are additionally sustained by mass transfers from their surrounding liquid zones through latent heat of vaporization exchange mechanisms at liquid-vapor interfaces, as further explained in Section 10.3 [17]. A major consequence of these transfers is more entrainment and penetration of the vapor spots into the regions where the static pressure is higher than the vapor pressure and/or, equivalently, the static temperature is smaller than the saturation temperature [70]. This clearly causes more distortion of the cavities, as detected in, for example, Fig. 88(a) at $t > 98.59$ s (see also Fig. 93-96 in Section 10.3 at $t > 112.34$ s).

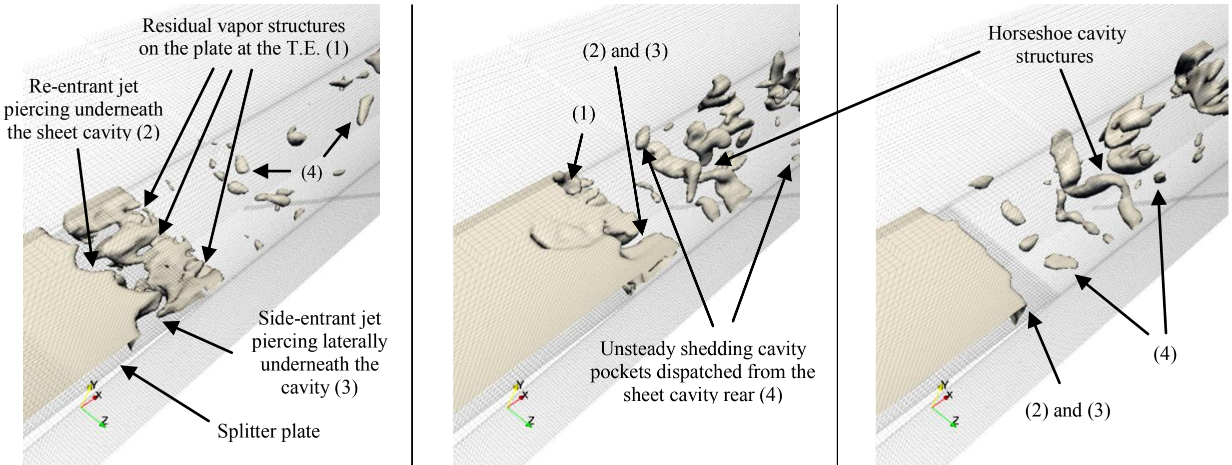

t = 89.57 s | t = 121.38 s | t = 143.76 s

Fig. 91: Temporal evolution of the 3D attached sheet cavity on the splitter plate in the 3D cavitating mixing layer of LNG: zoomed-in view of the iso-surface contours of vapor fraction with $\alpha = 0.85$ at time instants of t = 89.57, 121.38 and 143.76 s. Note the re- and side-entrant jets cutting the sheet cavity through, respectively, upstream reverse and lateral side motions on the splitter beneath the cavity.

The unsteady cavitation development process on the splitter plate in Fig. 88 can be further observed to be composed of three main stages: (1) growth of an attached sheet cavity; (2) development of re- and side-entrant jets; and (3) shedding of cavity pockets from the sheet rear close to the T.E. These three mechanisms occur continuously during each process and can be identified as follows: within the initial stages of development (see Fig. 88(a) at t = 62.51-81.15 s), an attached sheet cavity begins to appear on the plate upper surface as a result of boundary layer separation, and grows longitudinally until it reaches its maximum length. The entrained attached sheet cavity with convex rear shape then rolls up at its end around the T.E. as it faces the highly-sheared region with strong adverse pressure gradients at the interface of the mixing layer upper and lower streams. This eventually causes non-uniform creation of re- and side-entrant jets on the plate which tend to irregularly break up the sheet cavity, respectively, at its rear and lateral sides around T.E., so promoting the formation of small vapor pockets (Fig. 88(a) at $t > 98.59$) that are successively shed off downstream (see also Fig. 91 showing a zoomed-in view of the unsteady sheet cavity evolution on the splitter) [100,127,168]. As reported in [101,120], the shedding of such cavitating pockets are additionally triggered by the presence of residual vapor layers on the splitter surface which are left over from the prior sheet cavities development processes, as can be spotted in Fig. 91 at t = 89.57 and 121.38 s. Collapse of the vapor spots with propagation of pressure waves is anticipated to further promote the unsteady cavitation flow on the plate, primarily by enhancing the instability of entrant jets through frequent breakdown and contraction of the sheet cavity at its rear, as discussed in [116,126,132].

A major difference in the 3D cavitation flow in Fig. 88 against the counterpart 2D case in Section 8.2 is the presence of three-dimensionality causing frequent formation of the 3D U-shaped vapor structures in the shedding process of cavitating clouds (see for example Fig. 88(a) at $t > 81.15$ s). These so-called horseshoe vapor structures are typically generated when the tails of the distorted sheet cavities around the T.E. and/or the cavity tubes inside the mixing layer eventually curl into a somewhat rounded shape (see also the zoomed-in view of horseshoe vapor structures in Fig. 88(b)) [97]. Such process primarily occurs due to the progression of radially-diverging re- and side-entrant jets on the plate (see also Fig. 91) which impose large flow gradients in the streamwise and crosswise directions, so promoting the interactions of recirculating regions with shedding cavity clouds right from the T.E. [134,160,168]. The unsteady nature of the mixing layer, which is essentially composed of the periodic shedding mechanisms under three-dimensionality effects, then guarantees sustainable production of the horseshoe vapor spots in the domain, as can be deduced from Fig. 88(a) and 89(a) at $t > 98.59$ s. Frequent local cryogenic phase change processes, in particular the cavity collapse incidents with propagation of pressure waves and the latent heat transfers in liquid-vapor interfacial regions, are further anticipated to trigger the reproduction of horseshoe vapors mainly by improving local instabilities in the flow (see also Sections 9.6 and 10.3 for more discussion). The horseshoe vapor structures interact continuously with the vortical structures in the mixing layer and expand longitudinally until they collapse downstream [25,97].

Moreover in Fig. 89, the presence of well-known coherent hairpin vortical structures tightly interacting with the U-shaped vapor structures is a prominent observation. This is another indication of three-dimensionality which makes the present 3D flow behavior even more distinct from the 2D case in Section 8.2. The hairpin vortices are mainly created as a result of spanwise evolution of the streamwise vortical structures being in transition state in the primary and/or secondary instability mechanisms [75,185,197], which was not present in the 2D case. As detected in Fig. 89(a) at $t = 81.15$-98.59 s, such evolution is mainly initiated from distortion (e.g. stretching and tilting) of the primary spanwise vortex tubes, e.g. K-H rollers, in the braid region close to the T.E. during the initiative stages of mixing layer development (see also the zoomed-in view of coherent hairpin vortical structures in Fig. 89(b)) [185,191]. The primary spanwise rollers are stretched longitudinally through unsteady expansions of the braid region, leading to frequent formation of the primary hairpin vortices as a result of developing crosswise shear fields [198,209].

Further progression of the upstream vortex structures near the T.E. is followed by the production of secondary hairpin vortical structures that are created mainly due to distortion of the primary hairpin vortices in the beginning of the occurrence of the mixing layer pairing process (see Fig. 89(a) at, for example, t = 98.59 and 116.14 s; and Fig. 89(b)) [195]. The primary hairpins through these distortions normally tend to be amalgamated to neighboring hairpins and/or K-H rollers [185,189]. For instance, in Fig. 89(b), it can be detected that stretching of a primary spanwise roller leads its neighboring counter-rotating hairpin vortex pairs to gradually spread and connect the remaining spanwise rollers, thus forming larger slender hairpins downstream, as similarly reported in [189,196]. The periodic mixing layer instability mechanisms seem to be the major cause for maintaining the reproduction of secondary hairpin vortices in the domain, probably through providing strong variations of shear stress and strain fields [184,186,198]. Such variations are estimated to be additionally strengthened by the presence of three-dimensionality as a result of differences in streamwise velocity of vortex structures, as discussed in [212]. Note that the contours of Fig. 89(a) at $t > 116.14$ s indicate the dominance of coherent hairpin vortices in the later stages of mixing layer development; this is typical in free shear layers and extensively reported in literature (see e.g. [75,97,185,186]).

From Fig. 89, it can be also suggested that the presence of vapor cavities affects the evolution of vortices downstream in a way that the secondary hairpin structures in liquid-vapor mixture regions are amplified through frequent integrations with neighboring vapor spots in unstable large cavitating clouds (see Fig. 89(a) at $t > 98.59$ s) [25,97,100]. The vapor spots in such processes are estimated to enhance the spatial variation of mean velocity gradients by improving overall skewness of the vorticity field (see also Fig. 90), eventually improving the reproduction of secondary vortices in the flow [16,199]. Smaller eddies in these improvements also tend to be rearranged to further help growing large hairpin structures surround the initial vortices, as reported in [185,194]. In agreement with [96,97,135], it is observed in Fig. 89(a) at $t > 136.92$ s that the tight interactions of the vapor spots with the secondary vortices in cavitating clouds may characteristically lead to formation of distorted vortex tubes like "spaghetti" evolving unsteadily in the domain. Further reduction of pressure in such stretched vortices through the mixing layer instability mechanisms helps improve the formation of coherent vapor spots in the cavitating clouds. The current observations are consistent with the conclusion of Sections 9.6 and 10.3 suggesting that the presence of vapor structures, and so cavitation, in the present LNG mixing layers enhance the reproduction of coherent vortical structures by amplifying local disturbances. These amplifications exist because of unsteady phase change processes such as the collapse of vapor structures and/or the liquid-vapor latent heat exchange mechanisms [116,127]. Note that the vortical structures in Fig. 89 also tend to decay with time as they convect downstream through the mixing layer core, which is estimated to be mainly due to typical viscous dissipation in free shear layers [75,184]. This is in line with single phase mixing layer observations in [185,189] commonly stating that spanwise rollers exhibit their strongest effects in near-wake zones upstream of a mixing layer, by gradually aligning vortices in mainstream direction. Their contribution is then decreased further downstream as streamwise and spanwise vortices are governed by viscous dissipation (see also the 2D test vorticity contours in Fig. 58) [198]. Nevertheless, the significant thermally-influenced gradients in liquid-vapor mixture regions of the current mixing layer are estimated to at least partially compensate the viscous loss by improving reproduction of the vapor spots, and so the local instabilities, within the coherent vortical structures. This occurs more likely when the primary and secondary hairpin structures are highly distorted in the streamwise and lateral directions, as a result of large interactions with expanding vapor spots [96,189,190].

10.3. Cross-Sectional Evolution of Cavitating Structures

To further illustrate the physical mechanisms governing the dynamics of cloud structures in the 3D LNG cavitation mixing layer, Fig. 93-96 depict the temporal evolution of vapor fraction, temperature, and velocity magnitude fields during the first flow-through time of progress at time instants of t = 8.67, 24.34, 41.85, 59.43, 78.21, 96.75, 112.34, 129.35, 147.71 and 165.49 s. The flow contours are respectively shown for the selected cross-sectional spanwise reference plane of z/c = 0.0 (Fig. 93); transverse reference plane of y/c = 0.0 (Fig. 94); and streamwise reference planes of x/c = 0.50 (Fig. 95) and 3.30 (Fig. 96), as schematically displayed in Fig. 92. Spatial growth of the 3D mixing layer through a periodic shedding evolution is the prominent observation in Fig. 93-96.

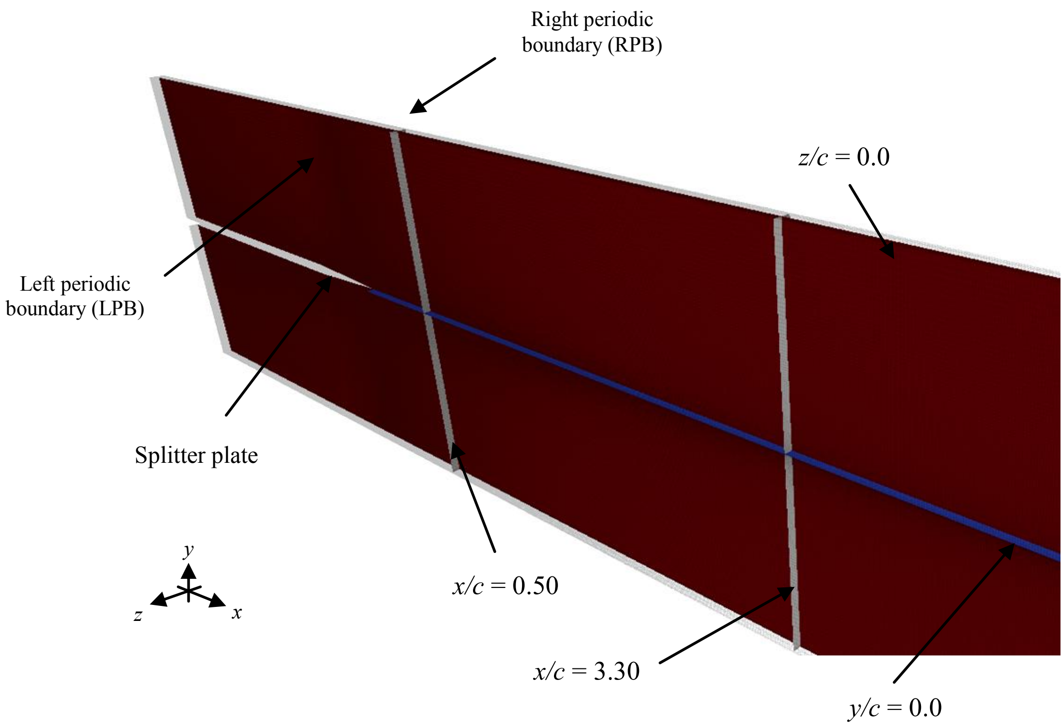

Fig. 92: Schematic of the selected 2D cross-sectional reference planes in the 3D LNG cavitating mixing layer domain: spanwise z/c = 0.0; transverse y/c = 0.0; and streamwise x/c = 0.50 and 3.30 planes are shown. Corresponding flow contours are respectively depicted in Fig. 93-96. Note the right (RPB) and left (LPB) periodic side boundaries of the domain.

In an overall similar development procedure to the 2D case discussed in Section 8.2, the unsteady 3D cavitation flow behind the splitter appears with wavy-shape K-H instabilities, primarily as a result of faster advection of the mixing layer upper stream than the lower one (see Fig. 93(c) and 94(c) at t = 8.67-59.43 s) [25,75,186]. Faster separation of the flow on the upper side of the splitter, i.e. due to larger adverse pressure gradients compared to the lower side, combined with the high-vorticity region around the T.E. lead the near-wall vorticity to roll up the sheet of the fluid behind the splitter into discrete vortical structures through the K-H instability (see also the evolution of primary vortices in Fig. 89(a) at t = 10.25-43.86 s). The generated infinitesimal disturbances during this shedding process then develop to promote larger vortical structures downstream, while the initiated mixing layer at the T.E. periodically breaks down with time (see for example Fig. 93(c) and 94(c) at t = 78.21-129.35 s). After this transitional stage, the mixing layer becomes intermittent in a laminar to transitional regime with permanent periodic shedding of the vortices (t > 147.71 s) [75]. The absence of streamwise streaks in the velocity contours of Fig. 94-96, which are typical in fully-developed turbulent mixing layers, confirms the operating regime of the present mixing layer [75,185,186]. Spanwise evolution of the K-H instabilities in Fig. 94-96 is indicative of three-dimensionality [75,198] that complies with the contours of Section 10.2.

When the longitudinal T.E. vortical structures are stretched and/or paired with neighboring vortices in the upstream braid region their angular velocities is increased, so causing their core pressures to drop. Cavity nucleation is started at such instants, provided that the pressure drop goes below the local vapor pressure. For example Fig. 93(a)-(c) at t = 8.67 s shows a primary nucleated cavity from a primary low-pressure vortex core in the beginning of the mixing layer development (see also Fig. 88(a) at t = 10.25 s where the primary cavity appears in the form of a slender vapor tube) [89,187]. As time proceeds, the primary cavity expands through the progressive mixing layer roll-up process and the vaporization latent heat transfer from the liquid surrounds it (see for example Fig. 93(a)-(c) at t = 24.34-59.43 s; and Fig. 89(a) at t = 28.12-43.86 s). Note that the initial deceleration of the mixing layer upper stream toward the lower stream deflects the primary cavity nucleation and expansion to occur in the low-speed side of the mixing layer (see for example Fig. 93(a)-(c) at t = 8.67-41.85 s). The cavity, which is of an incipient type, is however washed out gradually with time (see for example Fig. 93(a)-(c) and 95(a)-(c) at t = 59.43-96.75 s; and Fig. 96(a)-(c) at t = 96.75-129.35 s) before the first cavitation cycle ends (Fig. 93-96 at $t > 147.71$ s). Gradual elimination of the deflected mainstream during this process brings the follow-on cavities nucleation after the T.E. to the mixing layer centerline (see for example Fig. 93(a)-(c), 94(a)-(c), and 95(a)-(c) at t = 59.43-112.34 s).

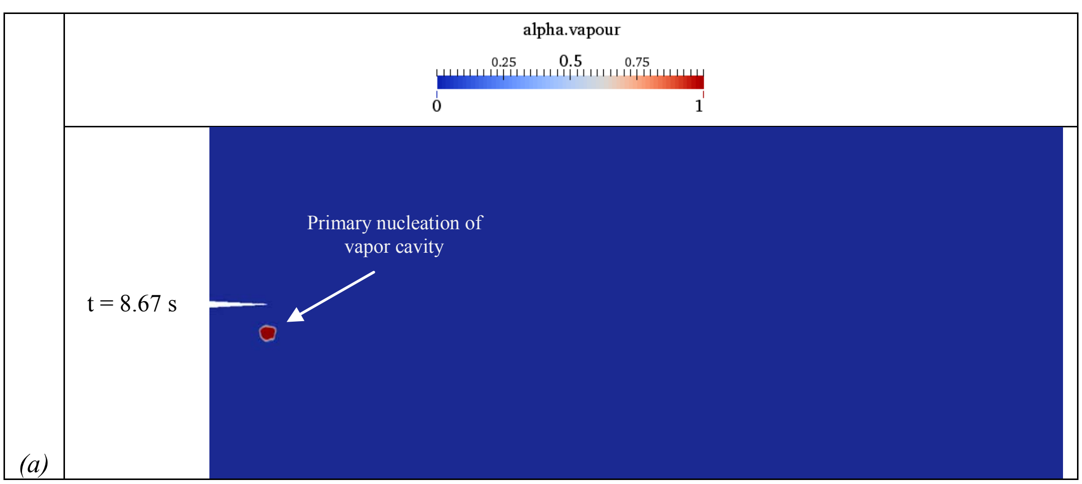

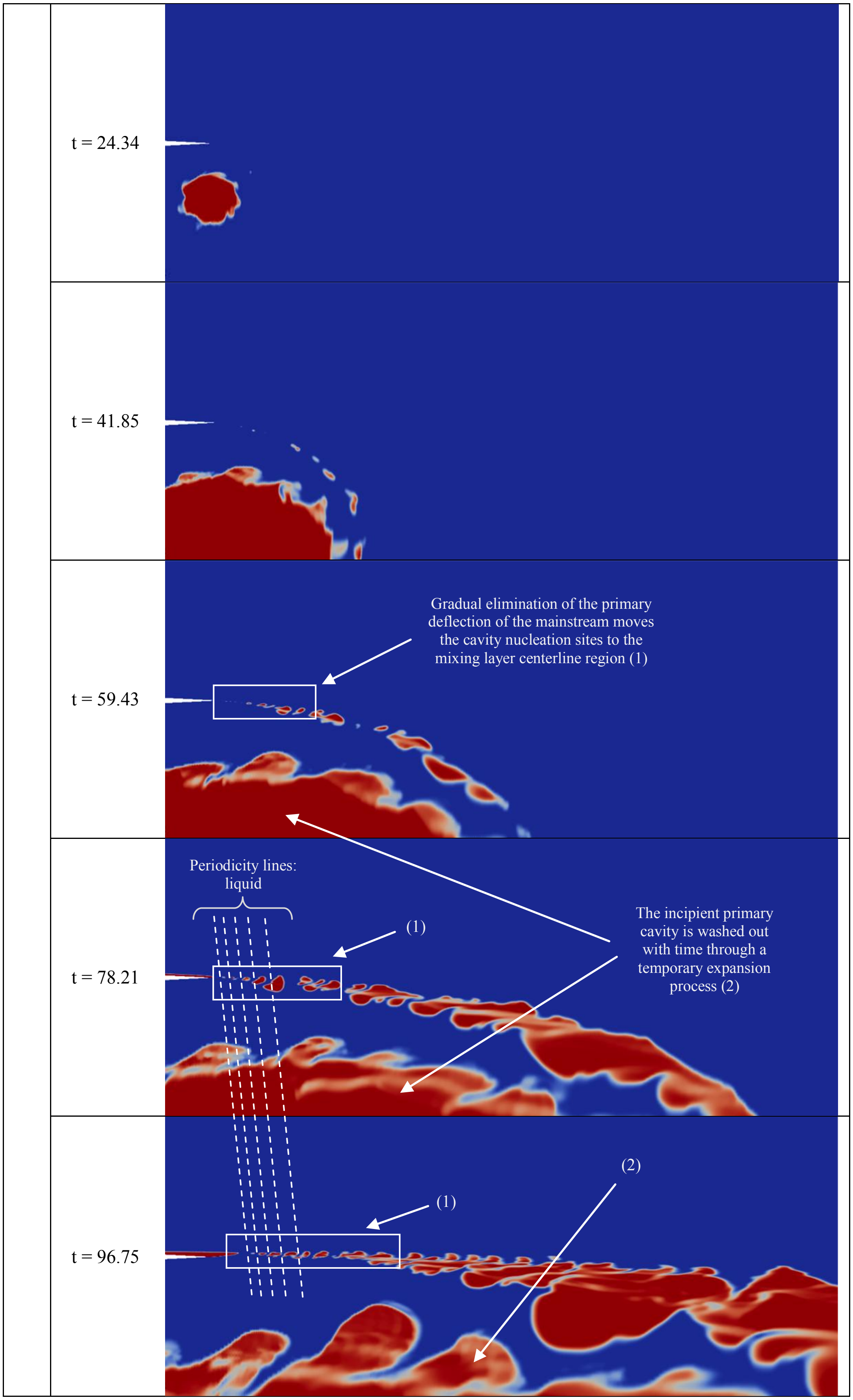
t = 24.34
t = 41.85
t = 59.43
Gradual elimination of the primary deflection of the mainstream moves the cavity nucleation sites to the mixing layer centerline region (1)
t = 78.21
Periodicity lines: liquid
(1)
The incipient primary cavity is washed out with time through a temporary expansion process (2)
t = 96.75
(2)
(1)

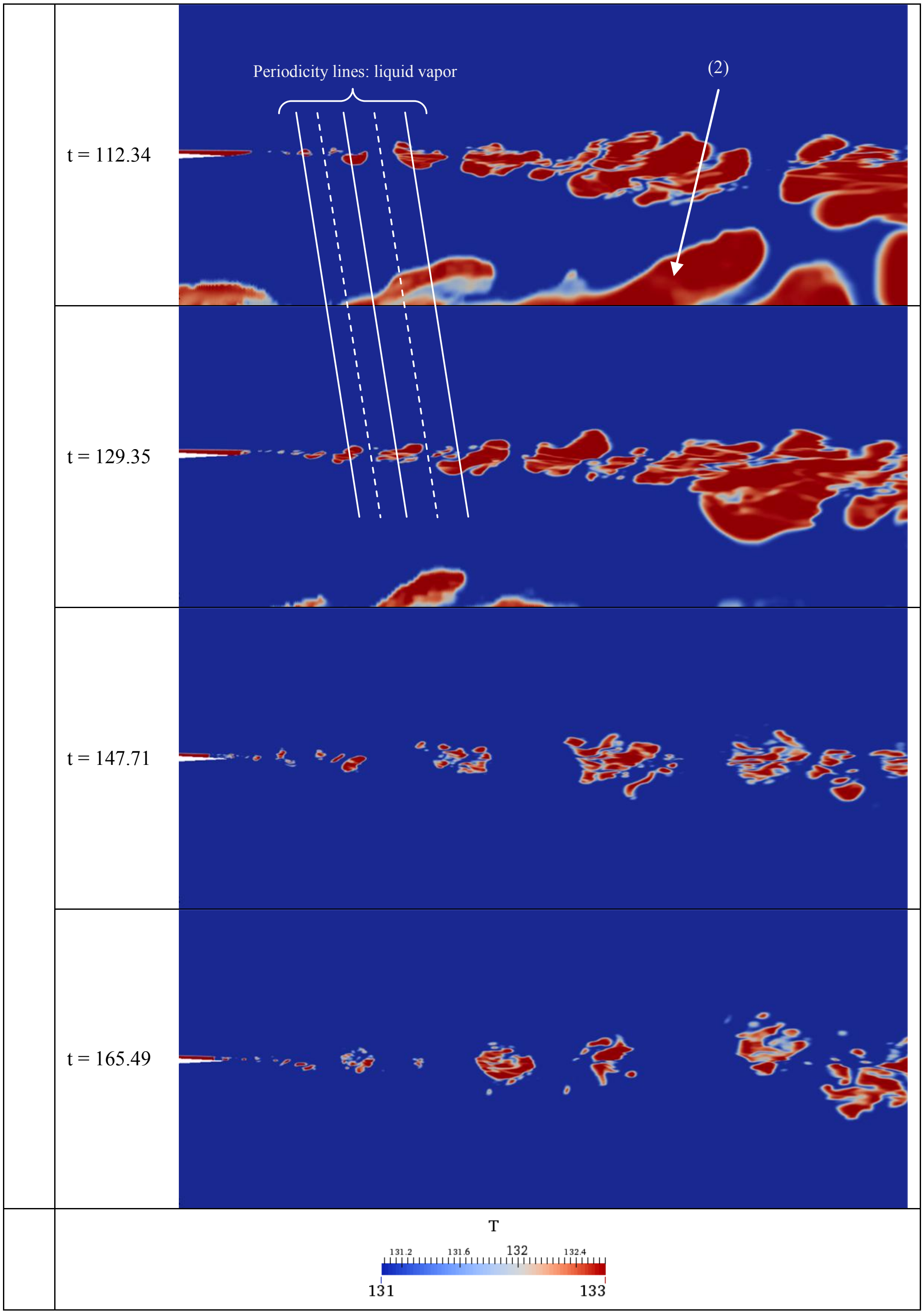

t = 112.34
Periodicity lines: liquid vapor
(2)
t = 129.35
t = 147.71
t = 165.49
T
131.2
131.6
132
132.4
131
133

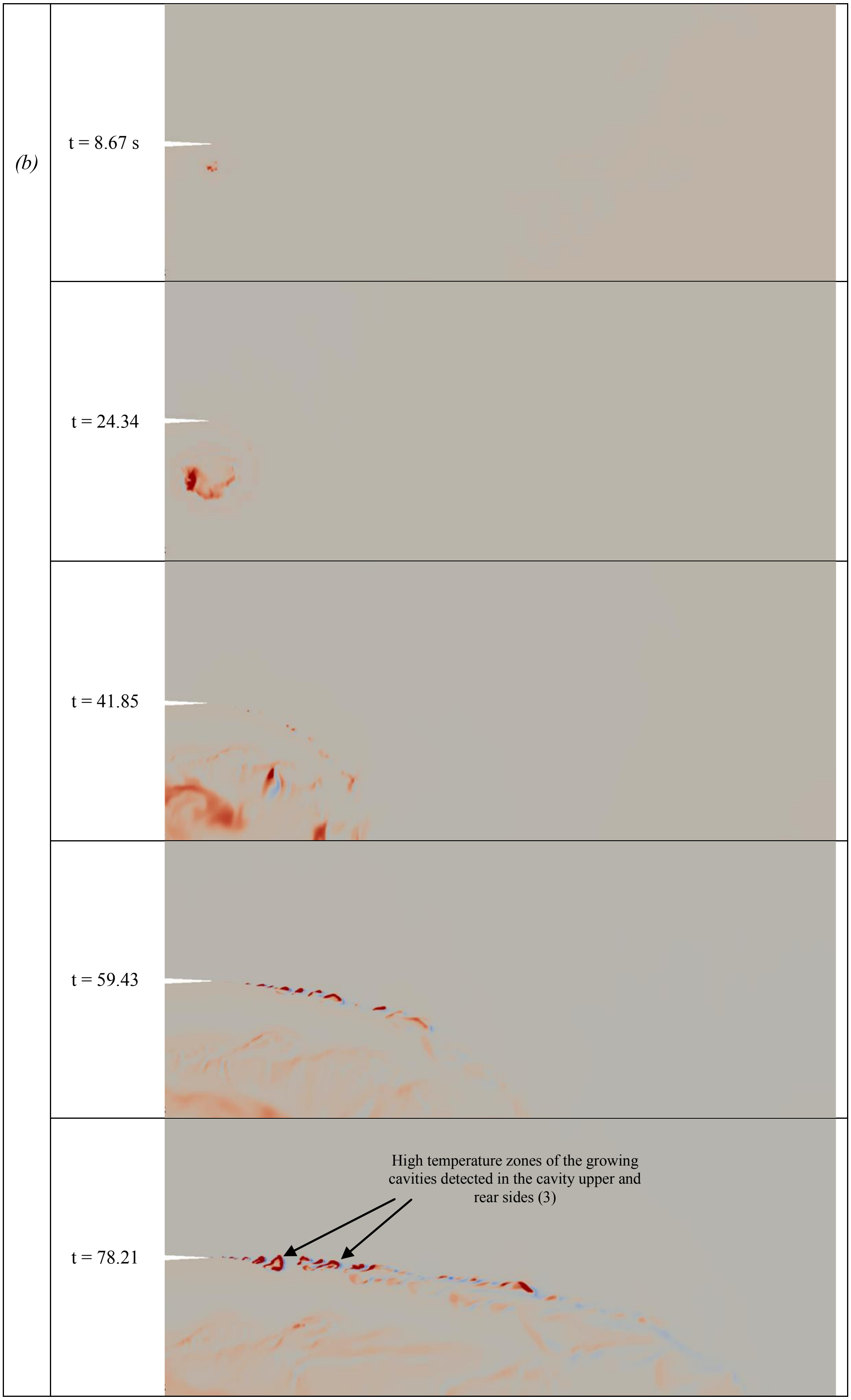
(b)
t = 8.67 s
t = 24.34
t = 41.85
t = 59.43
t = 78.21
High temperature zones of the growing cavities detected in the cavity upper and rear sides (3)

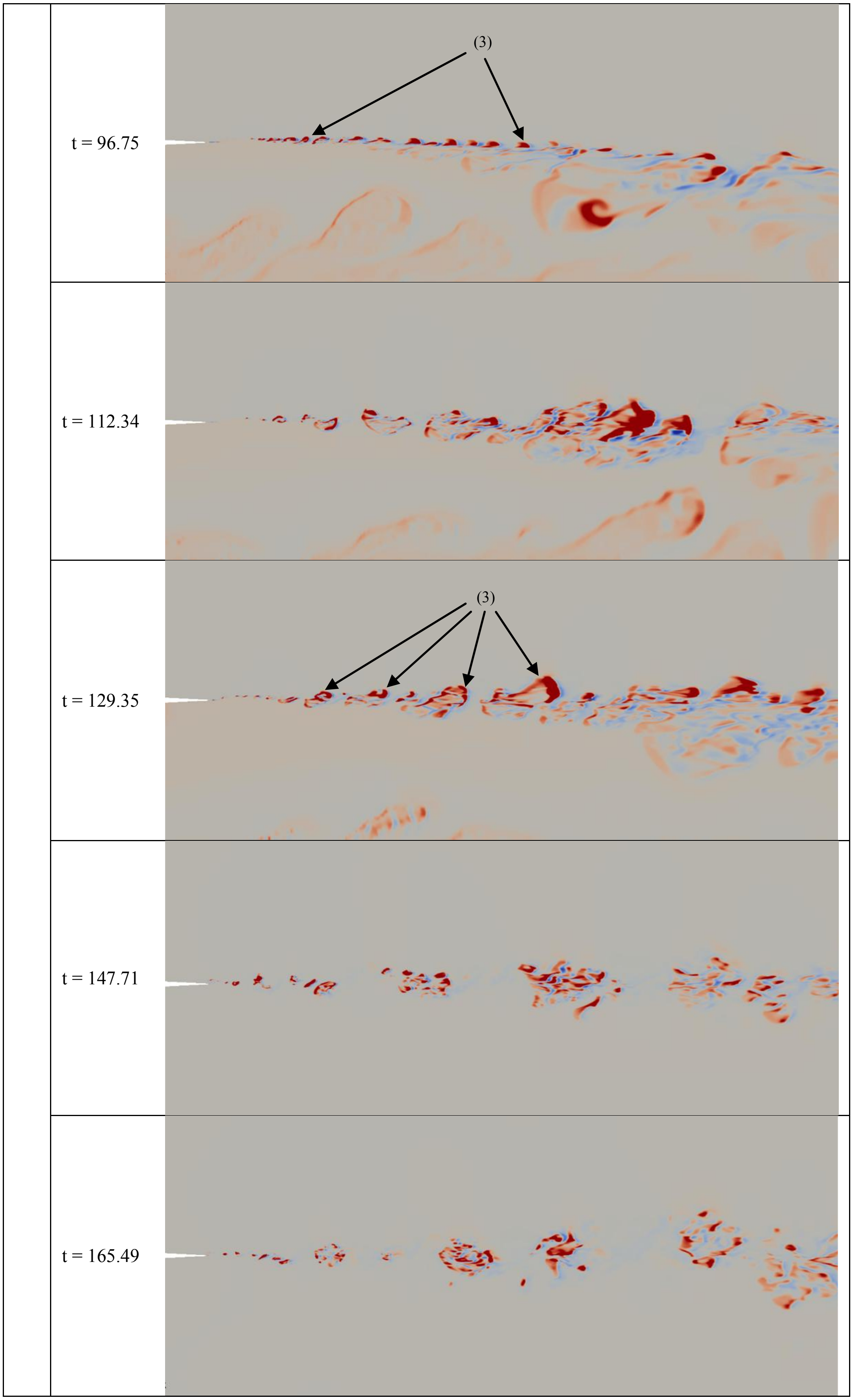
(3)
t = 96.75
t = 112.34
(3)
t = 129.35
t = 147.71
t = 165.49

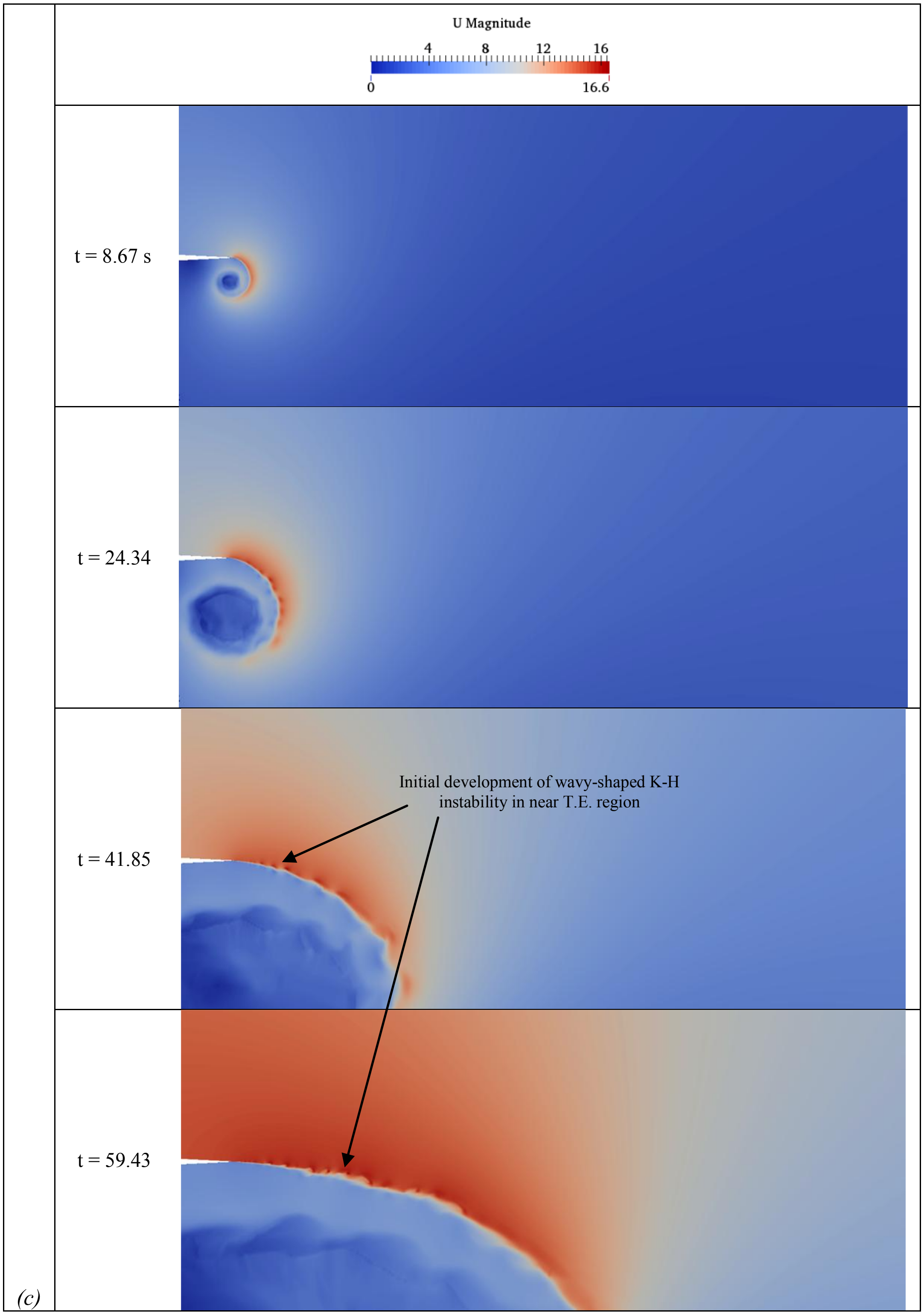
U Magnitude
0
4
8
12
16
16.6
t = 8.67 s
t = 24.34
t = 41.85
Initial development of wavy-shaped K-H instability in near T.E. region
t = 59.43
(c)

t = 78.21

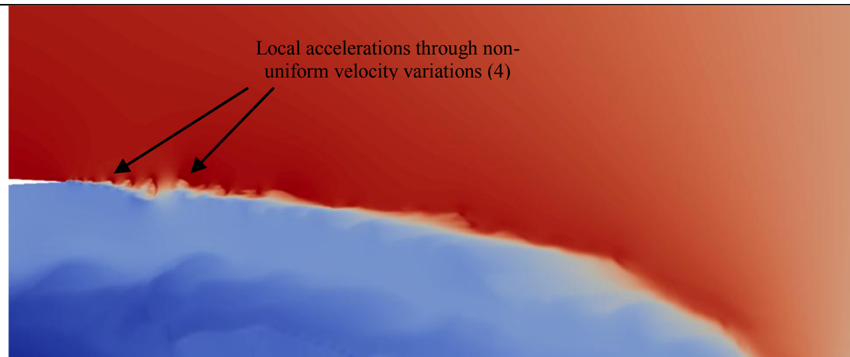

t = 96.75

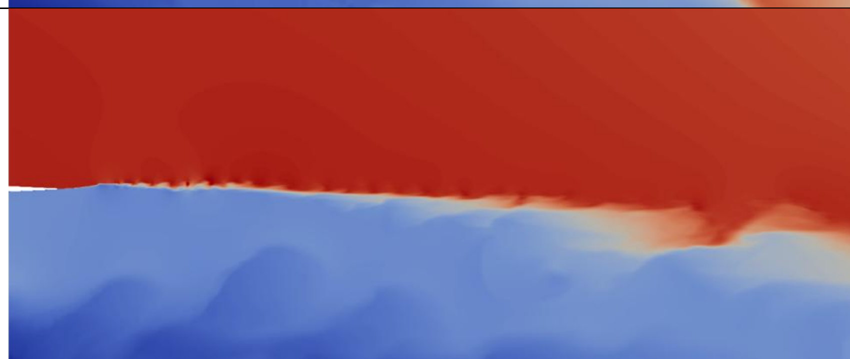

t = 112.34

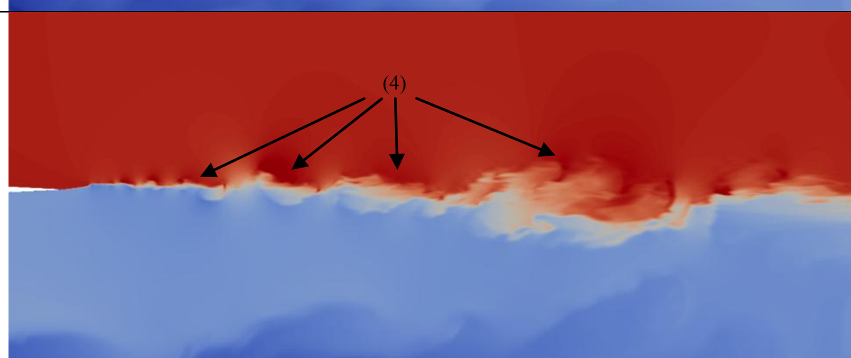

t = 129.35

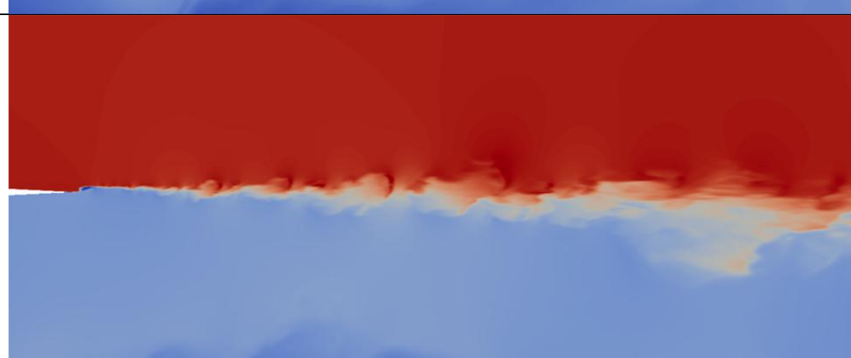

t = 147.71

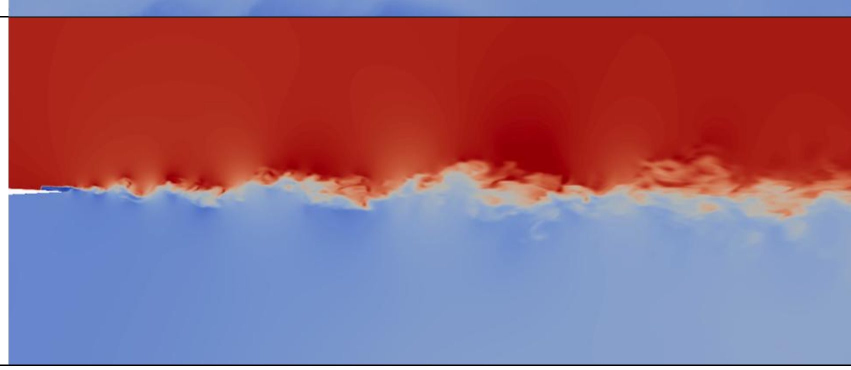

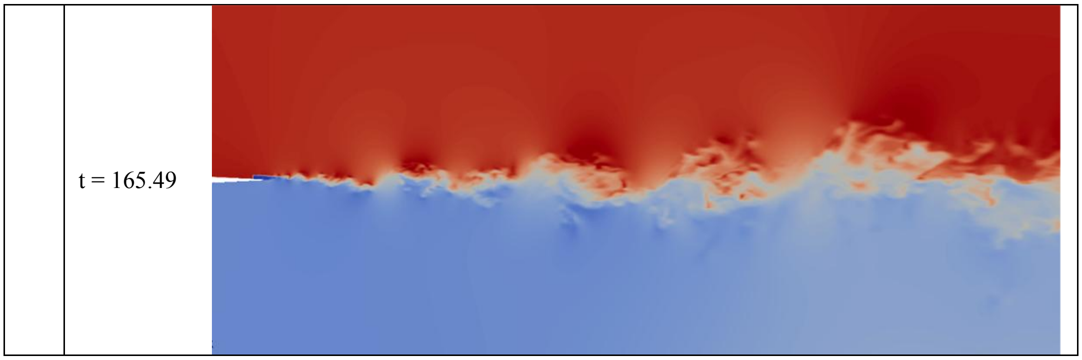

Fig. 93: Temporal evolution of the 3D cavitating mixing layer of LNG on the spanwise reference plane of z/c = 0.0: distributions of (a) vapor fraction; (b) temperature (K); and (c) velocity magnitude (mm/s) at time instants of t = 8.67, 24.34, 41.85, 59.43, 78.21, 96.75, 112.34, 129.35, 147.71 and 165.49 s. Note that the zoomed-in region of observation is 0.0 < x/c < 2.60 and -0.50 < y/c < 0.50 for better resolution.

The cavity evolution in Fig. 93-96 at $t < 59.43$ s is followed by a periodic process pertaining to the consecutive formation of unsteady shedding cavitating spots. This process is composed of two main stages: in stage one, continuous collision of the re- and side-entrant jets on the upper side of the splitter with the attached sheet cavity interface (see Fig. 88(a) at $t > 98.59$ s; and Fig. 91) leads the sheet cavity to shed off frequently at the T.E. and dispatch small vapor pockets successively (see for example Fig. 93(a)-(c), 94(a)-(c), and 95(a)-(c) at t = 78.21-112.34 s) [168]. This is initiated in the braid region of the mixing layer where the streamwise vortices are stretched through the primary K-H instability mechanism close to T.E., and then followed by the secondary instability mechanisms onward [25,188]. The secondary instability mechanisms essentially provide the continuous pairing of counter-rotating vortices within a few wavelengths downstream of the splitter, so leading to formation of larger-scale coherent vortical structures with twice the initial streamwise period (see also Sections 8.2 and 10.2 for more description) [188,190]. Vapor cavities typically nucleate in the core of these coherent vortices when the local static pressure is reduced sufficiently as a result of large rotation rates [25,97,100]. This follows the previous observations in Fig. 89(a) on how the coherent vortices and vapor cavities coincide (see also Fig. 59); the cavity spots appear periodically and are separated by condensation events corresponding to the inter-eddy space of the generated vortical structures (see for example Fig. 93(a)-(c) and 94(a)-(c) at t = 78.21-129.35 s) [96]. Note that, besides the mixing layer roll-up procedure, shedding of the re- and side-entrant jets on the splitter, and three-dimensionality, the instability mechanisms are likely excited by frequent accelerations of the shedding vortical structures through non-uniform velocity variations in the mixture regions [75,185,199]. These local accelerations (see the examples of local accelerations in Fig. 93(c) and 94(c) at t = 78.21

and 112.34 s; and Fig. 95(c) at t = 129.35-165.49 s), which are mainly resulted from unsteady evolution of the vapor spots within the vortex structures, particularly lead to local reductions of density, so enhancing the spatial derivatives of velocity to fulfill the conservation of mass [125,172].

With the occurrence of secondary instability mechanisms, the vapor cavities also grow into unsteady cavitating clouds. This introduces the second stage of cavitation development periodic process, where the small upstream vapor pockets eventually turn into large vapor clouds advecting downstream by the main liquid stream (Fig. 93-96 at $t > 112.34$ s). The cavity clouds are expanded in streamwise and lateral directions such that the recirculating areas beneath and/or inside them are non-uniformly filled with liquid-vapor mixture regions (see for example Fig. 93(a)-(c), 95(a)-(c), and 96(a)-(c) at $t > 129.35$ s) [89].

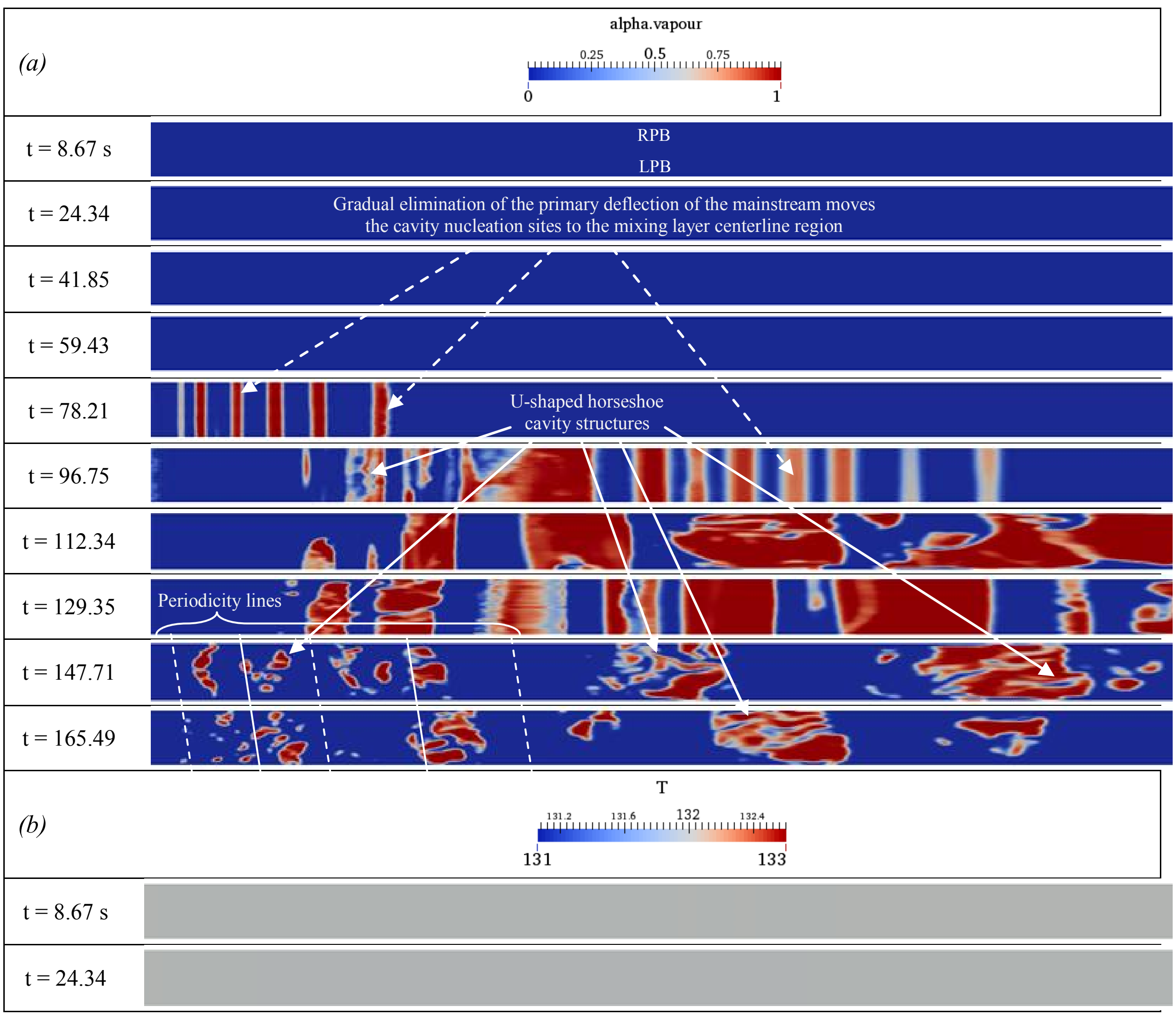

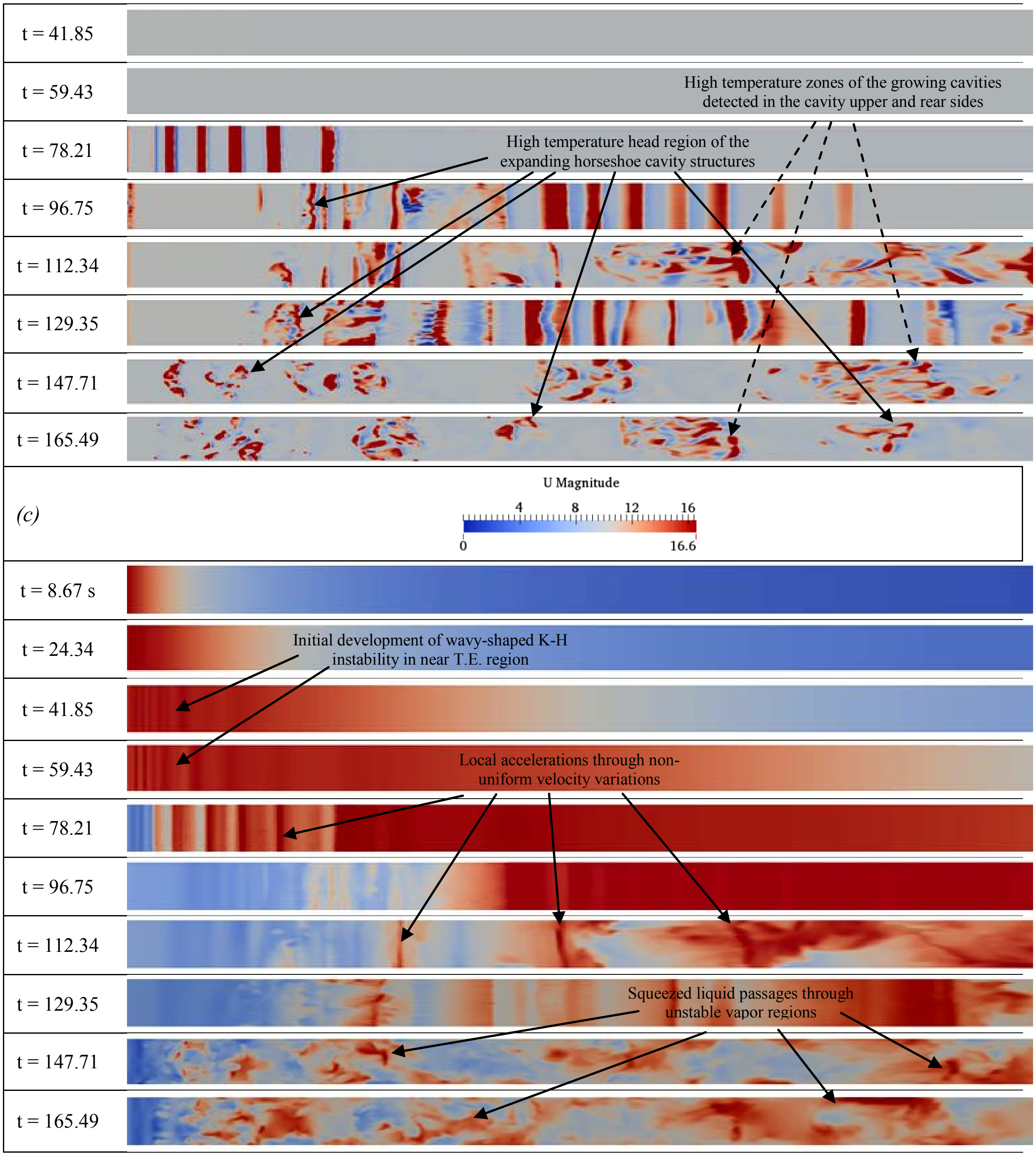

Fig. 94: Temporal evolution of the 3D cavitating mixing layer of LNG on the transverse reference plane of y/c = 0.0: distributions of (a) vapor fraction; (b) temperature (K); and (c) velocity magnitude (mm/s) at time instants of t = 8.67, 24.34, 41.85, 59.43, 78.21, 96.75, 112.34, 129.35, 147.71 and 165.49 s. Note that the zoomed-in region of observation in the streamwise direction is 0.0 < x/c < 2.0 for better resolution.

The amplified instability downstream of the mixing layer along with strong collapse/coalescence of the cavity clouds, imposing large local thermally-affected gradients through three-dimensionality (this is further discussed in Fig. 98 by comparing the probed upstream and downstream PSD levels), are the main reasons promoting these evolutions [116,190,194]. The enhanced “mushiness” of the vapor spots at the final stages of flow development (see for example Fig. 93(a) and 94(a) at t > 147.71 s) is also estimated to be due to such improvements, which particularly strengthen the local liquid-vapor exchange mechanisms through further interactions of cavities with coherent vortical structures [68,82,118]. Note that the collapse of expanding cavities occurs as they become exposed to high-pressure flow passages through the low pressure wake and recirculation zones [100]. The collapse process downstream, in particular, is estimated to cause strong propagation of pressure waves that constrain the development of upstream cavities -- i.e. through irregular breakdowns of cavity volume -- so causing larger production of small vapor pockets, as discussed in [116,172].

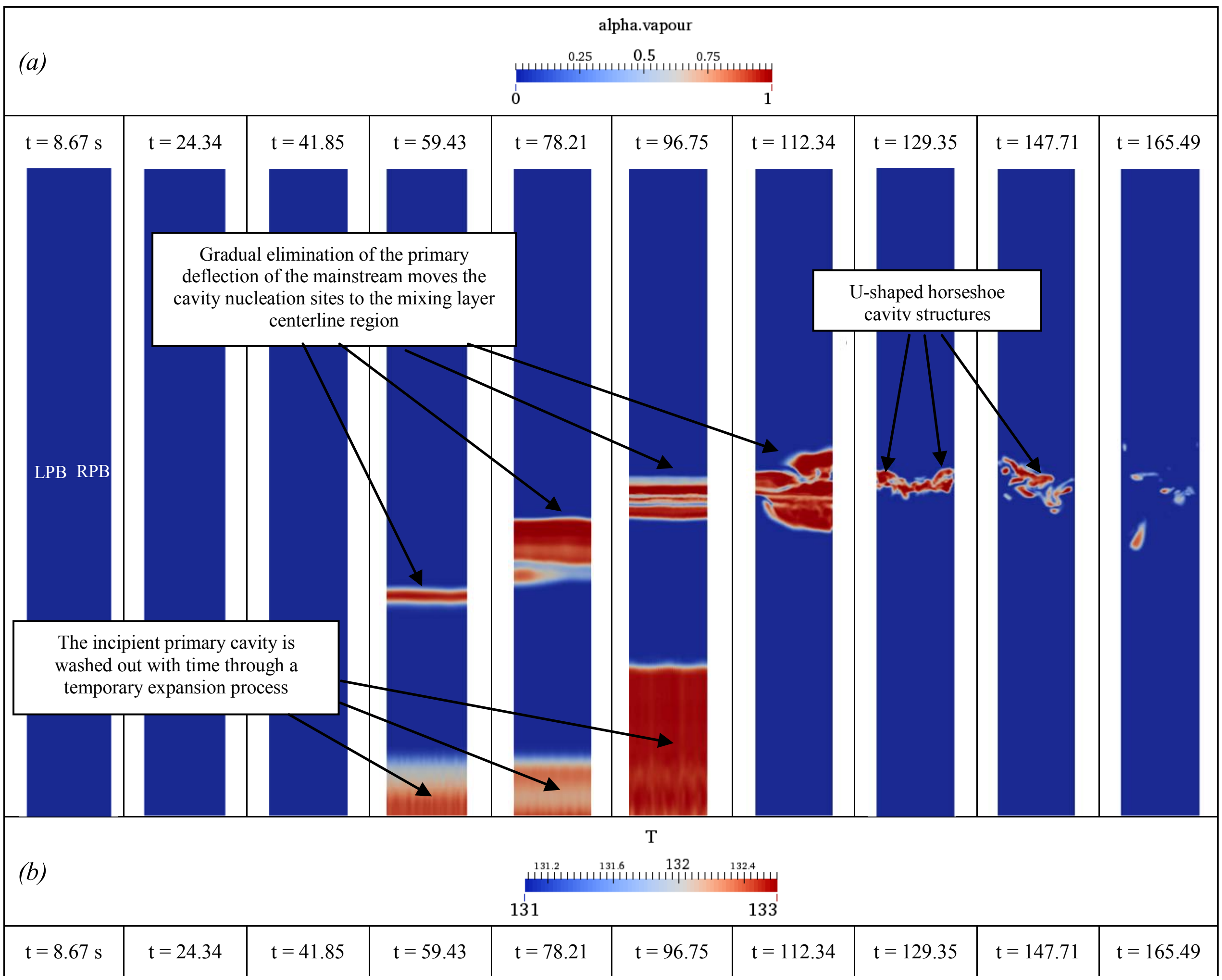

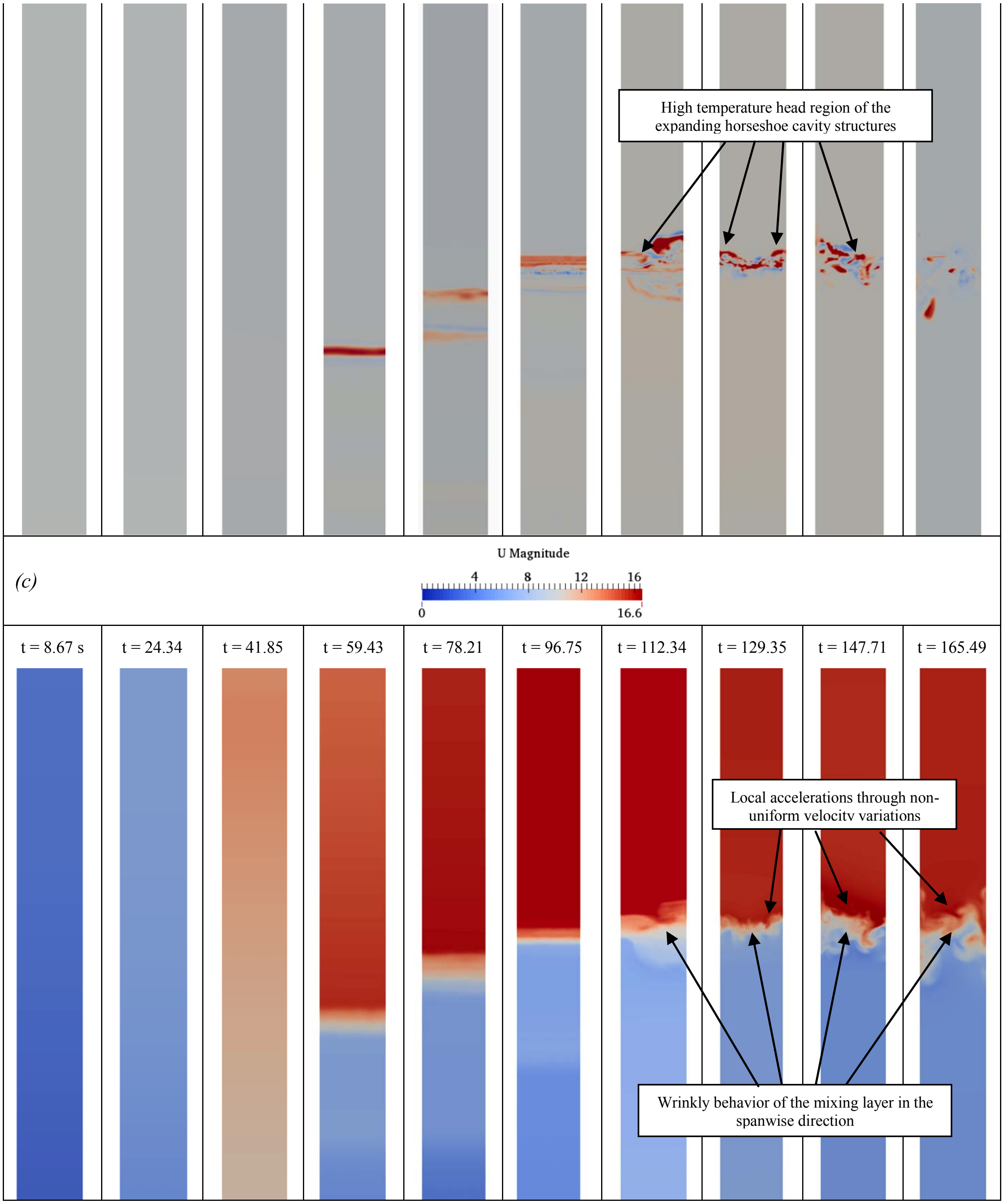

Fig. 95: Temporal evolution of the 3D cavitating mixing layer of LNG on the streamwise reference plane of x/c = 0.50: distributions of (a) vapor fraction; (b) temperature (K); and (c) velocity magnitude (mm/s) at time instants of t = 8.67, 24.34, 41.85, 59.43, 78.21, 96.75, 112.34, 129.35, 147.71 and 165.49 s. Note that the zoomed-in region of observation in the transverse direction is -0.60 < y/c < 0.60 for better resolution.

The vaporization and/or condensation of the vapor cavities in either of the aforementioned stages, is further accompanied by the latent heat of vaporization exchange to and from the surrounding liquid around the cavities. As seen in Fig. 93(b), 94(b), 95(b), and 96(b), the temperature of cavitating regions alters in the range of ± 2 K, and larger temperature gradients indicative of stronger latent heat transfers occur in the larger cavity clouds downstream as compared to the smaller detached cavities upstream (see Fig. 93(b), 94(b), 95(b), and 96(b) at $t > 112.34$ s). The high temperature zones of the growing cavity clouds, mostly detected in the cavity upper and rear sides (see for example Fig. 93(b) at t = 78.21-129.35 s; and Fig. 94(b) at t = 112.34-165.49 s), suggest larger latent heat of vaporization is absorbed from the surrounding liquid in these regions [188,209]. This causes temperature depression in the liquid, which aids expansion of the cavities inside the mixing layer by amplifying local vaporization incidents [21,37,65]. From the given temperature distributions, the previously-noted influences of three-dimensionality in changing the cavitation patterns can be also confirmed. As discussed in Fig. 89, distortion of the longitudinal vortical structures in the crosswise direction leads to production of additional crosswise gradients under thermal effects, so improving the overall vortex-cavity interactions inside the mixing layer, as against the 2D test [185]. This significance can be clearly indicated in the present crosswise temperature, and velocity, variations in Fig. 94(b,c) and 96(b,c) at, for example, t = 112.34-165.49 s.

The periodic re-growth of the cavities in the mixing layer downstream is simultaneous with alternate breakdown of the neighboring and/or upstream vapor spots, as can be deduced from Fig. 93(a)-(c) and 94(a)-(c) at $t > 112.34$ s; and Fig. 88(a) at $t > 116.14$ [25,190]. In this process, additional unsteadiness imposed by the local vapor collapse/inception incidents, besides the cavity-vortex instability mechanisms under spanwise non-uniformity, seem to result in significant "self-induced motions" in the flow [190,202]. This is because the collapse incidents are typically accompanied by random propagation of shock-induced pressure waves which tend to modify pressure and vorticity fields through strong thermally-affected density gradients (see also Section 9.6) [43,90,92]. And, the cavity-vortex instability mechanisms mainly involve distortion of the coherent vortex structures through unsteady interactions with highly unstable cavitating spots (see also Fig. 89-90) [25,185]. The self-induced motions are indicative of local shear variations, and basically lead the local liquid passages through the vapor regions to frequently become squeezed and expanded with time, as reported in [185,202]. For instance, the high-velocity zones indicated in Fig. 94(c) at t = 147.71-165.49 s illustrate the liquid phase contraction behavior through which individual liquid passages are accelerated by the unsteady vapor spots, so behaving like a jet. The observed local irregularities in the resulting evolutions in Fig. 93-96 (see for example Fig. 94 and 96 at t > 112.34 s), particularly in downstream regions, are estimated to be due to these motions, which accord with the non-uniform local interactions of the cavity-vortex structures described in Fig. 89-90 [191,209].

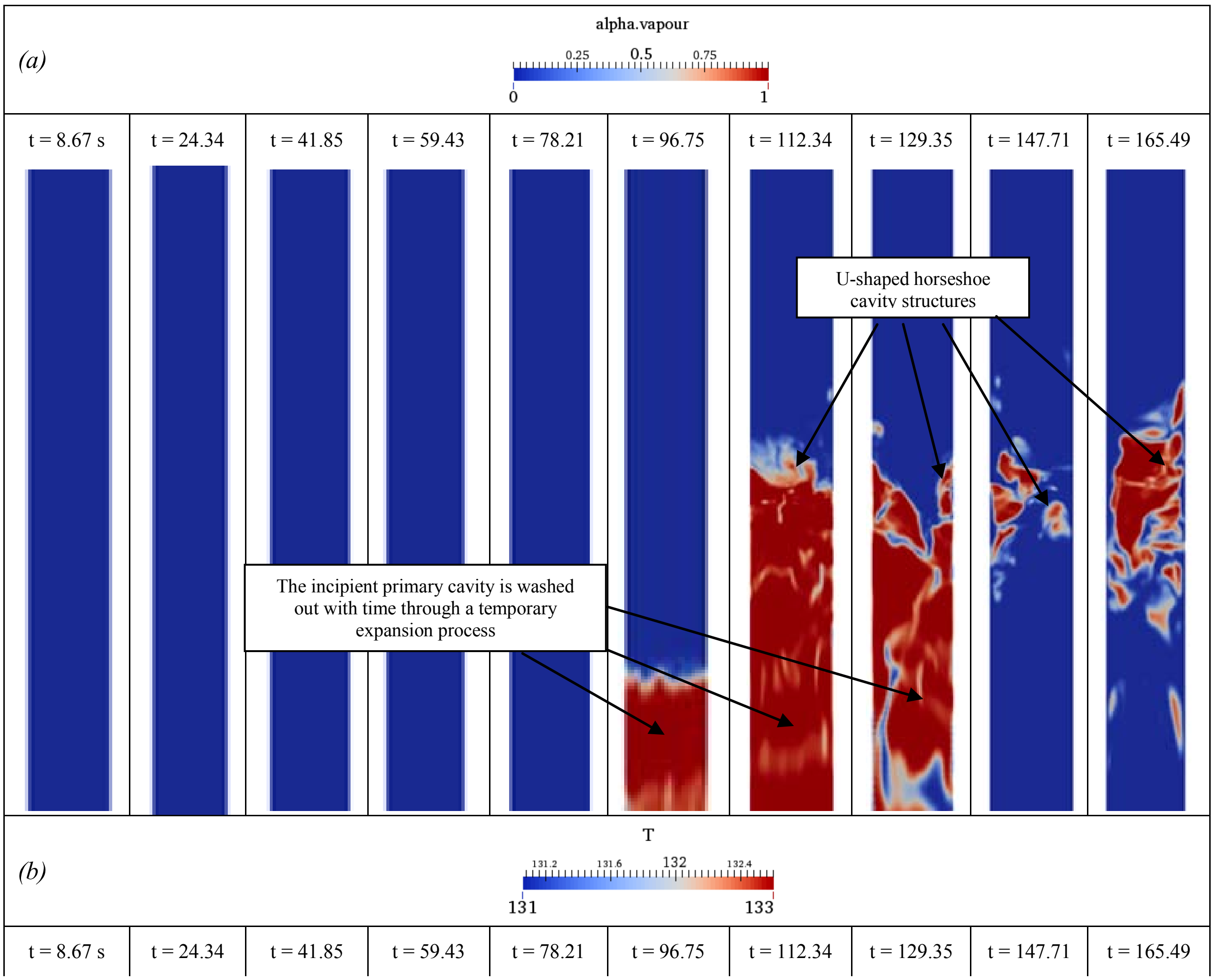

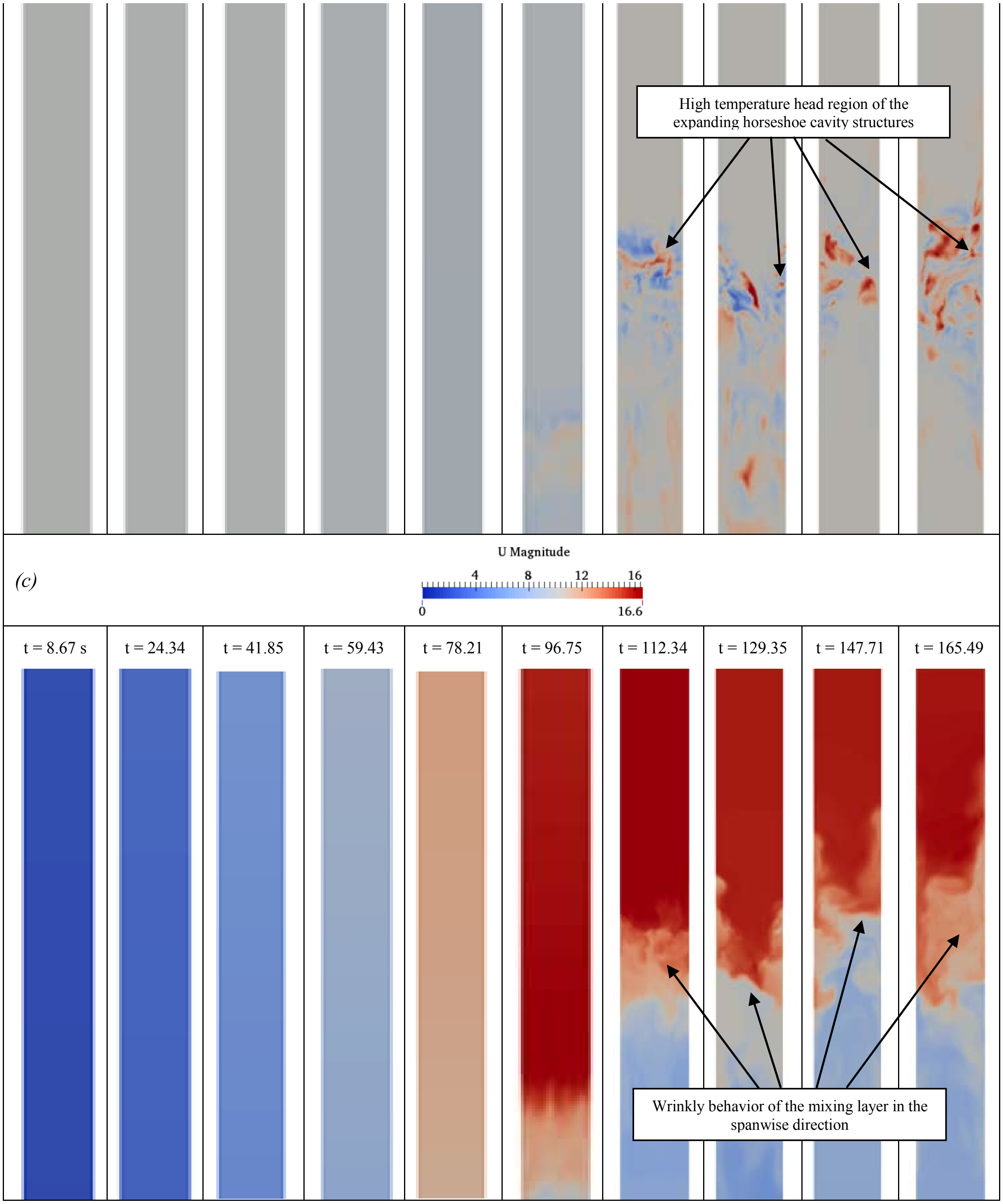

Fig. 96: Temporal evolution of the 3D cavitating mixing layer of LNG on the streamwise reference plane of x/c = 3.30: distributions of (a) vapor fraction; (b) temperature (K); and (c) velocity magnitude (mm/s) at time instants of t = 8.67, 24.34, 41.85, 59.43, 78.21, 96.75, 112.34, 129.35, 147.71 and 165.49 s. Note that the zoomed-in region of observation in the transverse direction is -0.60 < y/c < 0.60 for better resolution.

In the predicted vapor fraction contours of Fig. 93-96, it can be also seen that the tails of the attached sheet and/or the cloud cavities on the splitter and/or inside the mixing layer often curl into a somewhat rounded shape to form the U-shaped horseshoe vapor structures (see the examples of horseshoe vapor structures in Fig. 94(a), 95(a), and 96(a) at $t > 96.75$ s) [97]. As previously indicated in the iso-contours of Fig. 89(a), the horseshoe cavities interact continuously with the coherent vortical structures and expand longitudinally until they collapse downstream. The unsteady nature of the mixing layer, which is essentially composed of periodic shedding mechanisms of coherent vortices under three-dimensionality effects, is the main reason for promoting such vapor structures (see also Fig. 88). The unstable attached sheet cavitation on the splitter with shedding entrant jet structures (see also Fig. 91) is further estimated to trigger the recreation of U-shaped cavities around T.E., as denoted in [116,135,174]. The frequent cavity collapse/inception processes typically leading to large pressure and density gradients in the mixing layer cause major distortions in the horseshoe cavities likely by breaking them into smaller vapor spots [116,127].

Note that the presence of three-dimensionality in the development process of U-shaped vapor spots can be better detected in Fig. 94(a), 95(a), and 96(a) at time instants of t = 147.71 and 165.49 s when the coherent horseshoe cavities are more frequently formed, likely due to improved crosswise shear gradients [75,100], amid the shedding of developed cavitating clouds near the end of cavitation cycle (see also the 3D iso-contours of Fig. 88(a)-89(a) showing how the coherent U-shaped cavity and vortical structures are strongly interacted through the mixing layer instability mechanisms). The generated U-shaped vapor spots also seem to appear with increased temperature in their heads as they grow downstream (see for example Fig. 94(b), 95(b), and 96(b) at $t > 96.75$ s). This suggests larger exchange of latent heat of vaporization from the surrounding liquid regions into a horseshoe cavity through its head, and further confirms the important role of latent heat transfer mechanisms in modulating phase-change behavior of the interacting cavity-vortex structures in the present mixing layer.

The wavy-like behavior of the velocity field in Fig. 93(c) at $t > 112.34$ s (see also Fig. 95(c) and 96(c) at $t > 112.34$ s) also implies that the mixing layer is initially accelerated in near T.E. regions through the upstream disturbance waves, and then expanded non-uniformly downstream while approaching its self-preservation state. Such a behavior is primarily associated with the high convective acceleration of the unsteady wake behind the splitter that is gradually entrained downstream within the mixing layer shedding process [75,186]. As reported in [17,53,190], frequent inception and collapse of the vapor spots through sweeping motions of the streamwise and spanwise vortical structures are the other reasons setting off this behavior by enhancing flow gradients. These enhancements are estimated to be more substantial in downstream regions of the mixing layer, likely due to improved influence of the three-dimensionality on local cavity-vortex interactions, as will be further discussed in Fig. 98. Nevertheless, because of the natural viscous dissipation in the streamwise direction, the vortical structures also tend to decay while they expand downstream, despite being continuously integrated with the highly-unsteady cavitating clouds [75,97,190]. This is based on the earlier observations on the longitudinal behavior of the vortical structures in Fig. 58 and 89 indicating that the initiated vortex pairing processes near the T.E. are weakened downstream where the grown-up vortical structures start pairing off as the self-similarity state is reached [89,135]. Larger spatial variation of the velocity field in downstream regions in Fig. 93(c), 94(c), 95(c), and 96(c) at $t > 112.34$ s is also indicative of this conclusion. The current observations are relevant to the experimental findings of Wiecek and Mehta [198] stating that distortion of vortices in crosswise direction in 3D mixing layers typically appear in the form of sinusoidal "wrinkles", due to non-uniform momentum transfer within unsteady coherent vortical structures [189]. This wrinkly behavior can be clearly spotted in the velocity evolutions of Fig. 95(c) and 96(c) at $t > 112.34$ s.

Further comparison of the temporal evolution of the 3D mixing layer in Fig. 93-96 against the counterpart 2D case in Section 8.1 qualitatively reveals that the flow variations in the 3D case are significantly improved due to the presence of three-dimensionality, as it imposes additional gradients in the crosswise direction which tend to alter the overall shedding characteristics of the mixing layer (see also Section 10.2) [75]. To better illustrate these characteristics, Fig. 97 plots the temporal evolutions of vapor fraction and relative pressure ($= p - p_{sat}$) in the 2D and 3D tests at a downstream probing station of ($x/c,y/c$) = (2.30,0.0) over the time interval of t = 100.0-200.0 s. Noticing mutual shedding patterns in both flows, an increase in the rate of fluctuations (i.e. higher-frequency oscillations with smaller amplitudes) in the 3D case as compared to the 2D case can be deduced from the plots (this is further discussed in the corresponding power spectra in Fig. 98). This improvement suggests faster inception and collapse of the vapor spots in the 3D case, which are estimated to more strongly change the morphology of cavitating structures in the mixing layer [125]. Such behavior seems to be also relevant to Arndt et al. [93] results stating that the cavity inception and collapse mechanisms in cavitating shear flows are mainly associated with vortex pairing processes -- enhanced variations of flow parameters in the present 3D mixing layer suggest improved pairing processes as against the 2D counterpart. Stronger thermodynamic involvements in the 3D case are also conjectured to be another reason for the behavior of signals in Fig. 97, as it accords with the experimental findings of [114,122] remarking that increase of thermal effects causes an effective increase of shedding frequency (see also Fig. 98).

(a)

(b)

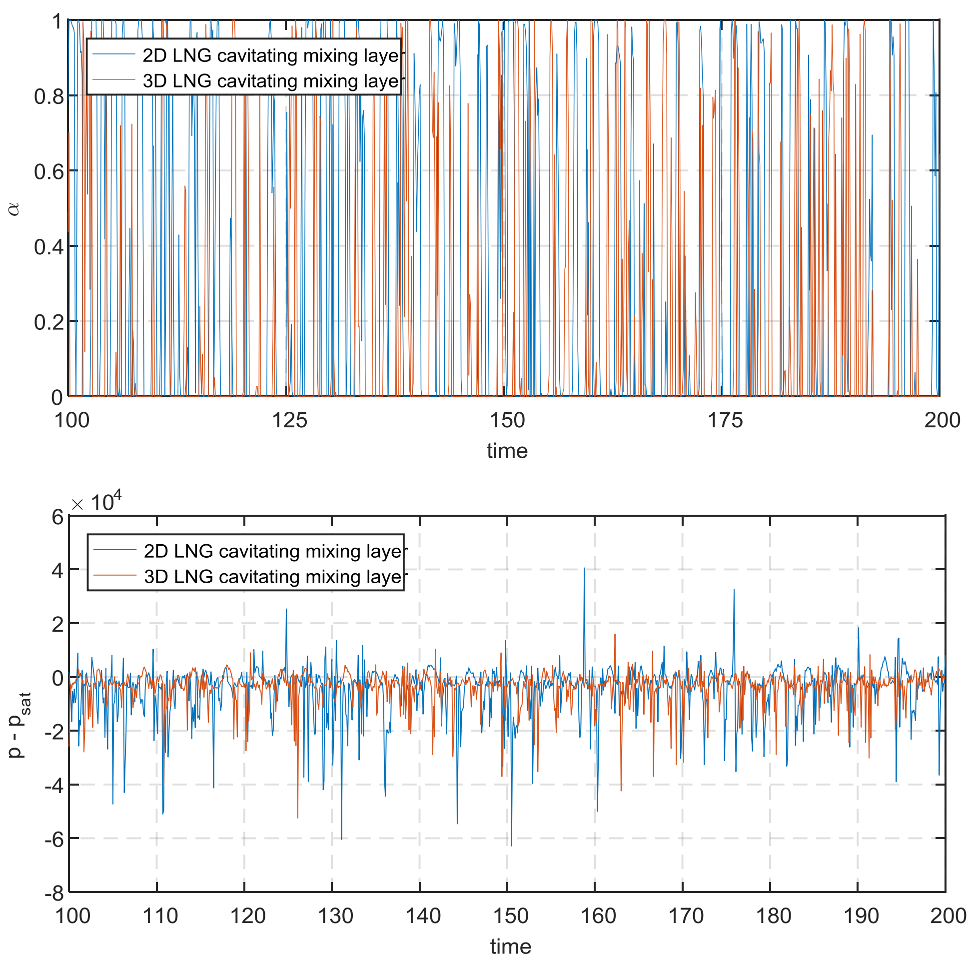

Fig. 97: Time histories of (a) vapor fraction and (b) relative pressure (Pa) at the probe location (x/c,y/c) = (2.30,0.0) for the 2D and 3D cavitating mixing layers of LNG.

From the predicted time signals in Fig. 97 it can be further stated that the local "cavity volume accelerations" are of the main causes for cavitation-induced pressure fluctuations in the mixing layer, as denoted in [127]. The sharp variations of pressure corresponding to these volume accelerations are likely due to remarkable local reductions of speed of sound in liquid-vapor mixture regions [135,213]. This is mainly associated with the collapse of vapor spots in larger scale cavitating clouds, resulting in propagation of discontinuity shock waves at high magnitudes through liquid-vapor interfacial regions, as previously indicated in Section 9.6.1 [43,116]. Such processes not only reduce the overall mixture sound speed but also cause strong momentum transfer within the cavities, as explained in [116,126]. Note that the randomly distributed smaller pressure spikes in Fig. 97(b) are either caused by the pinch-off of vortex cavities or the collapse of small-scale vapor spots; whereas the larger over-pressure pulses are created through shock wave emissions during coherent collapse of large-scale cavity clouds (see also Section 9.6.1 for more discussion) [127,135].

Moreover in Fig. 97(b), the magnitude of pressure spikes seems to be suppressed as three-dimensionality becomes involved in the mixing layer evolution. This behavior, which is primarily due to the addition of crosswise span (larger wave propagation domain decreases the level of wave intensity [75,100]) in the 3D test, mainly pertains to the improved instability as a result of three-dimensionality: suppressed pressure spikes are balanced by strengthened local disturbances in the flow through improving shear between liquid and vapor regions, resulting in faster cavity breakup/inception incidents compared to the 2D test. This is likely because of the enhanced roll-up mechanisms in the 3D case which promote the vortical structures to be more coherent with larger spatial gradients, and shed off more frequently within smaller time periods. The absence of three-dimensionality in the 2D case dampens out these instabilities, leading to the formation of weaker vortex structures [81].

This conclusion can be further demonstrated in Fig. 98(a) which compares the corresponding log-scale power spectrum density (PSD) distributions of vapor fraction in the 2D and 3D flows at the probed station of Fig. 97; larger spectra are observed in the 3D case especially in most part of the high frequency domain. Improved PSD in the 3D test is particularly indicative of higher coherence level in most of the energetic eddies in the flow, as denoted in [96]. It also suggests the presence of larger temperature-based gradients, and thus amplified thermodynamic effects, which typically tend to trigger the instability of cavitating spots by improving density and vapor fraction variations [21,43,120]. Nevertheless, the described effects of three-dimensionality seem to be suppressed in the upstream regions, as indicated in Fig. 98(b) for an upstream probing station at $(x/c,y/c)$ = (0.30,0.0) -- the vapor fraction spectrum specially in the low frequency range is larger in the 2D test. These different behaviors suggest stronger influence of three-dimensionality in the mixing layer self-preservation states which typically occur far downstream away from the splitter. Enhanced fluctuations of the vapor fraction (Fig. 98(c)) and relative pressure (Fig. 98(d)) at the downstream probe, as against the upstream probe, in the 3D case further confirm this conclusion.

(a)

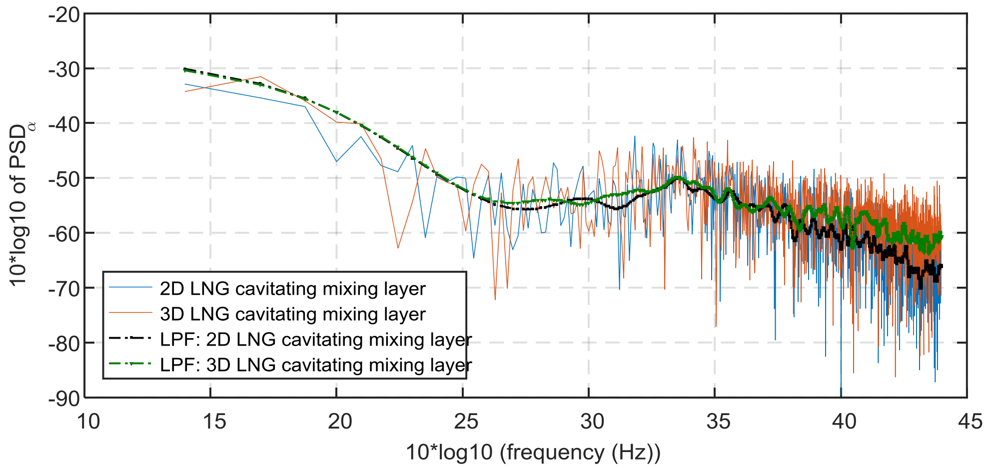

(b)

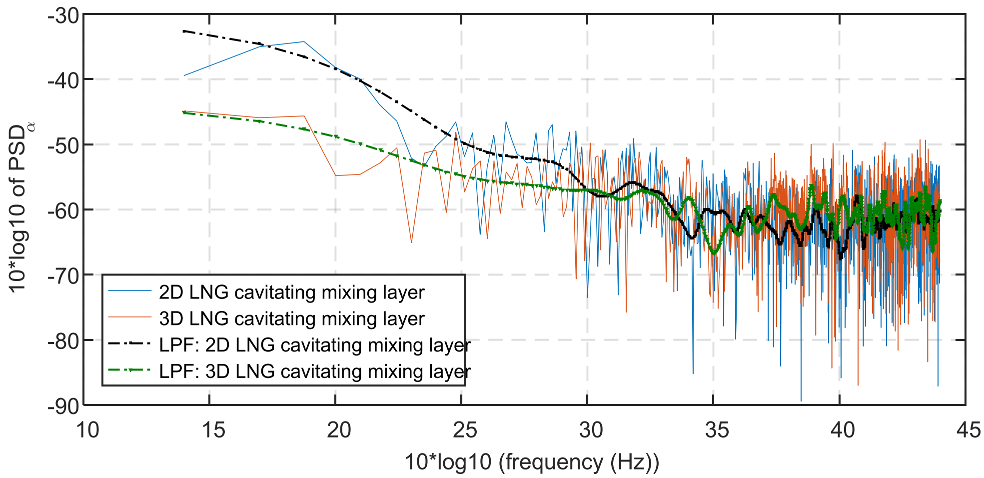

(c)

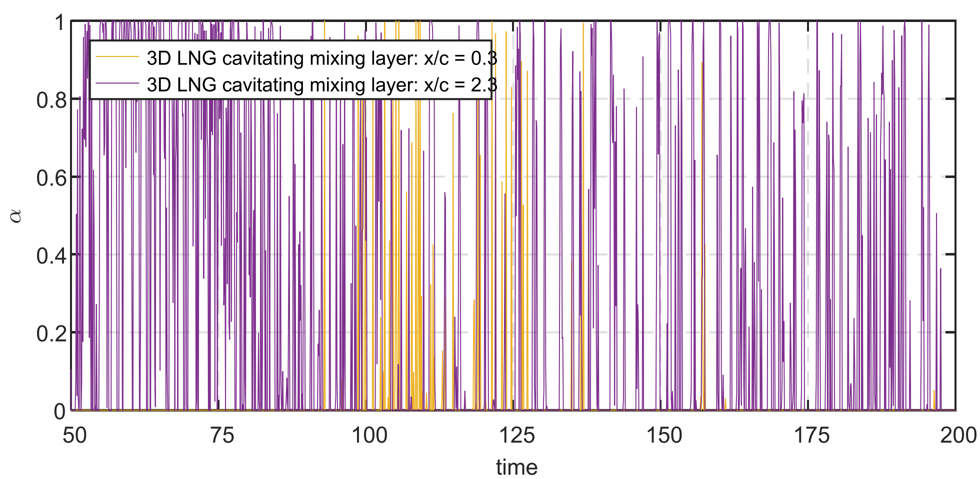

(d)

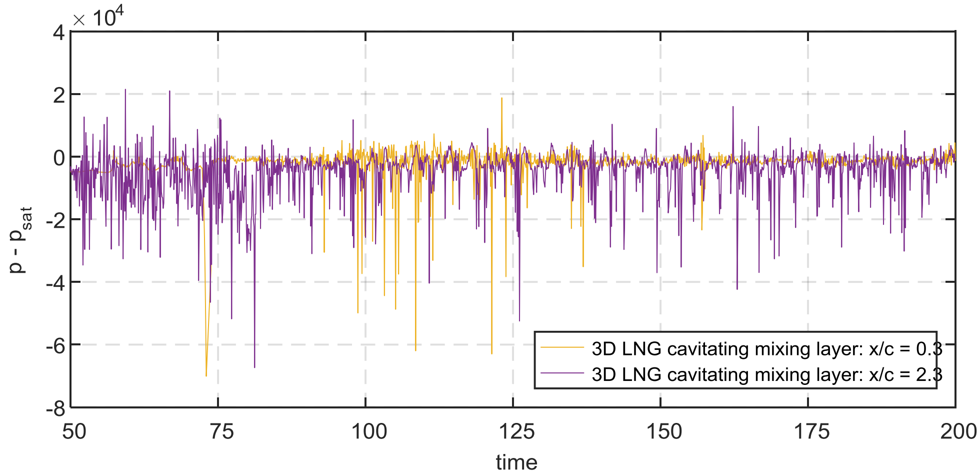

Fig. 98: Log-scale plot of vapor fraction spectra at the probing stations of (x/c,y/c) = (2.30,0.0) (a) and (x/c,y/c) = (0.30,0.0) (b) for the 2D and 3D cavitating mixing layers of LNG. LPF stands for low-pass filtered data. Time histories of vapor fraction and relative pressure (Pa) at the upstream and downstream probes in the 3D case are respectively shown in (c) and (d).

11. Summary, Contributions, and Recommendations

This chapter summarizes the key research contributions of the previous chapters to illustrate how they combine to address the overall research objectives of the present thesis. This chapter also recommends a list of potential avenues for future research.

11.1. Summary of Investigations

In the present thesis, a computational fluid dynamics solver for modeling cavitation in cryogenic fluids is developed and validated to gain insight into the dynamics of thermally-influenced cavitating flows of liquefied natural gas (LNG) in LNG-based turbomachinery. The cryogenic cavitation model is developed in the CFD package OpenFOAM based on modifications to an isothermal cavitation library. The developed solver employs the homogenous equilibrium mixture (HEM) approach to compute the multiphase solution in a density-based Eulerian framework, with a barotropic equation of state based on the Wallis compressibility model. Thermal effects pertinent to cryogenic fluids are captured through an enthalpy-based energy equation that is sequentially solved along with cryogenic forms of the mass and momentum equations. To accurately capture thermophysical properties of the cryogenic fluids, dynamic viscosity and specific heat values are obtained from customized Sutherland and JANAF thermophysical libraries that are extended via the NIST property database to account for both temperature and pressure variations at cryogenic temperatures. In addition, the saturation vapor pressure is made dependent on temperature by using the Clausius-Clapeyron equation to capture latent heat transfer during phase-change. An extended merged PISO-SIMPLE algorithm is also used to iteratively couple the resulting temperature field to the pressure, velocity, and vapor fraction fields. These modifications ensure that thermally-induced variations of the density field are captured properly to resolve the baroclinic nature of the vorticity production in the cryogenic cavitation flow. The developed solver is validated against liquid nitrogen flows in a circular orifice and a converging-diverging Laval nozzle, achieving good agreement with experimental measurements. The resulting fluid properties of a simulated LNG cavitation flow inside the Laval nozzle are also verified with a good accuracy against the NIST property database.

The detailed physics of the LNG phase change phenomena is investigated by employing the developed solver for simulating two fundamental case studies: 1) cavitating flow of LNG inside the Laval nozzle; and 2) cavitating mixing layer of LNG behind a flat plate splitter. The conducted studies address the detailed dynamics of LNG cavitation, respectively, in wall-bounded and free shear layers of LNG, hence collecting a refined database for identifying cavity-vortex interactions in complex LNG-based machinery. A summary of the findings in studies (1) and (2) is given in the following Sections 11.1.1-11.1.2.

11.1.1. Numerical Simulations of Cavitating Flow of LNG inside the Laval Nozzle

The developed cavitation solver is employed for simulating 2D and 3D cavitating flows of LNG inside the Laval nozzle, to investigate the cavity-vortex interactions and instability behaviors, with the main goal of finding correlative mechanisms governing the evolution of vapor structures and shear layers under thermodynamic effects. The 2D in-nozzle LNG cavitation flow is studied for a range of operating conditions including three different cavitation numbers, i.e. Ca = 0.82, 1.41, and 2.05, and four different diffusion angles of the nozzle, i.e. DA = 1°, 2.5°, 7.5° and 15°. The cavitation flow at Ca = 1.41 is further simulated with the liquid-vapor interfacial tension forces activated in the modeling. The 3D in-nozzle LNG cavitating is built by a spanwise extrusion of the 2D domain, and simulated based on the 2D case at Ca = 1.41. A summary of the observations is reviewed as follows.

11.1.1.1. 2D In-nozzle Cavitating Flow of LNG at Different Operating Conditions

- **Effects of Cavitation Number**

The cavitating flows at the simulated cavitation numbers are found to follow the same development patterns. At Ca = 0.82 and 1.41, the improved wall boundary layer at the surface discontinuity between the throat and diverging section of the nozzle develops the local wall shear stress, causing accumulation of vorticity. As the local vorticity grows, the static pressure continues to drop until it dips below the saturation pressure, so the cavity nucleation begins. This process does not occur in the non-cavitation test at Ca = 2.05, and so no vapor is generated. The continuous interaction between the developing wall boundary layer and vorticity in the near-wall regions triggers the low-pressure vapor nuclei to expand into the attached vapor cavity. The attached cavity appears primarily as a sheet, and gradually detaches from the wall at its end to promote vapor clouds with oscillating vapor-liquid interfaces. Detachment of the cavity is due to the presence of re-entrant liquid jets that impinge on the wall, with approximately the same velocity as the main liquid stream, and "dissect" the attached sheet cavity to generate unsteady regions of reversed flow. The detached vapor spots from the sheet are shed continuously, while their shedding is mainly governed by the re-entrant jets. Continued growth of the attached sheet cavity reveals two major observations. First, the attached cavity lengthens in its streamwise extent, and that a stable cavity behaving like a wake cavity is formed upstream of the flow. Second, the separated vapor cavities from the sheet grow progressively unsteady downstream.

The resulting temperature in all the tests is found to vary insignificantly, but effectively, in the small range of ± 1.7 K. As the vapor spots nucleate and grow, the latent heat of vaporization is absorbed from the surrounding liquid by the expanding cavities; thus, the liquid temperature surrounding the vapor cavity is reduced. The local reduction in temperature however lowers the saturation pressure, so slowing down the cavity expansion. Opposite behavior is also observed for the condensation of vapor spots. The preponderance of high-temperature regions in most of the vapor spots suggests that the temperature variation is mostly associated with heat transfer into vapor, causing delayed condensation of vapor to liquid. The delay of vapor condensation improves the mean net vapor production in the domain.

Despite showing the same development patterns, different progression level of cavitation is observed at the simulated cavitation numbers. At Ca = 2.05, cavitation does not occur in the nozzle, so the flow depicts a single-phase behavior with small temperature variations. With the formation of cavity structures at Ca = 1.41, the cavitating flow is altered through variations of the temperature-dependent vapor pressure in mixture regions. Larger cavitating regions with improved vaporization processes in stronger recirculating zones are formed earlier at the smallest Ca = 0.82. This highlights the dominant effects of inertia; at larger Ca, suppressed small-scale sheet cavities are formed on the wall due to the presence of weaker adverse pressure gradients. Reducing Ca improves these gradients and leads the sheet to quickly become unstable and shed larger cavity clouds over smaller time periods. Stronger vorticity variations at Ca = 0.82 implies the improved unsteadiness in the re-entrant jets and recirculating zones.

On the behavior of cavitation flow in the near-wall regions, it is observed that the wall shear stress increases as Ca decreases and more vapor is generated. This is because of the weaker adverse pressure gradients, and so the suppressed disturbances, at the wall at larger Ca. The disturbances are found to be minimal at Ca = 2.05 where the presence of large favorable pressure gradients resists the formation of a re-entrant jet. At *Ca* = 1.41, increase of the velocity gradients due to the strengthened separation process results in larger vorticity magnitudes at the wall as against the *Ca* = 2.05 case. These improvements become more substantial at *Ca* = 0.82.

On the cavity-vortex interactions in the simulated tests, it is noted that at the cavitating conditions the vorticity dilatation and baroclinic torque have the largest impact on the overall vorticity distribution, contrary to the vorticity diffusion with negligible effects. With the decrease of *Ca,* spatially more concentrated baroclinic torque occurs in the cavitating spots, due to the greater compressibility effects. The dilatation term is found to rise up at smaller *Ca*. This is explained by a compressibility criterion indicating that the velocity divergence increases with decrease in *Ca*. The streamwise stretching and transverse tilting are also found to increase at smaller *Ca*, as opposed to the streamwise tilting and transverse stretching. This suggests vortex structures are preferentially elongated in the streamwise direction. It is highlighted that all the vorticity budgets contribute to some extent to enhancing the vorticity production in the simulated flows. In the non-cavitating condition, with the absence of cavity, the vorticity production is mainly dependent on the vortex stretching and tilting.

Temporal behaviors of the probed signals indicate that the decrease in *Ca* improves the signals oscillation frequencies. At *Ca* = 0.82, the pressure and temperature oscillations appear with larger magnitudes and larger spikes, and occur more successively because of more vapor collapse and coalescence incidents. These oscillations are suppressed at larger *Ca*. The oscillations spikes are found to be due to the collapse of vapor spots -- the propagated pressure waves as a result of collapse processes break down the cavities into smaller segments, so causing sudden changes in the flow fields. Such strong variations are completely suppressed in the non-cavitating case at *Ca* = 2.05 and only sinusoidal pulsations are detected.

Instability analysis of the simulated flows shows that *St* number is reduced with the decrease of *Ca*, due to the formation of larger vapor structures further delaying the shedding of vortex structures. The delay pertains to the reduction of mixture velocity as a result of production of vapor -- it is improved when *Ca* is reduced and larger cavities are generated more successively at smaller time intervals. The maximum amplification rate frequency at *Ca* = 1.41 is found to be due to the low frequency behavior of the elongated vortex cavities, whereas in the *Ca* = 0.82 case is caused by the alternate collapse/inception of the cavity structures. At the non-cavitation case with *Ca* = 2.05, the characteristic frequencies represent the shear layer instability and sub-harmonics due to the adverse pressure gradients. The instability at *Ca* = 2.05 is also concluded to be due to pulsation of the shear layer without vortex shedding, unlike the cavitating cases where the instability is due to the vortex and cavitation shedding with cavity collapse processes. The resulting spectra further suggest that with the improvement of thermal effects at smaller *Ca*, there is more depression in the *St* number. The stronger thermal effects imply the presence of larger local temperature gradients, making the vaporization more strengthened locally inside the cavities despite delaying their expansion.

The mean-square velocity fluctuations are found to decrease by increasing *Ca,* with the maximum drop at the non-cavitation condition with *Ca* = 2.05. In the cavitating tests, streamwise fluctuations show their peaks in the liquid zone, whereas the transverse and shear fluctuations show their peaks in the vapor and/or interfacial regions away from the walls. This is because of the: 1) faster velocity in the liquid regions; and 2) dominant momentum, mass, and heat transfers in the favorable gradient direction i.e. from liquid to vapor. These evolutions are improved as *Ca* declines, causing more entrainment of the liquid phase. The increase of shear fluctuations with the reduction of *Ca* is attributed to the presence of stronger cavities in the vortex structures, which affects the process of vortex stretching by decoupling the vortex strain and rotation rate, weakening the relationship between streamwise and transverse fluctuations.

- **Effects of Nozzle Diffusion Angle**

The overall behavior of the LNG cavitation flows at the simulated diffusion angles is found to follow the same patterns, and the differences mainly pertain to how the attached sheet cavity on the nozzle lower wall are impacted by the re-entrant jets, and so how the cloud cavity structures are shed from the sheet. At *DA* = 1º, the sheet cavity does not show a periodic behavior, and appears as a slender, quasi-stable vapor region that is progressed steady without generating unsteady cavity cloud. This is due to the absence of separation/recirculation zones in most of the development process to develop a re-entrant jet. In the final stages of the development, however, a small separation region at the lower wall, along with the flow exposure to the buffer zone are found to form a weak re-entrant jet far downstream near the outlet. By contrast, at *DA* =15º, it is seen that the sheet cavity experiences an early breakdown, through faster progression of unstable re-entrant jets on the wall, causing successive shedding of the unsteady cavitating clouds. This is due to an earlier separation of the flow and immediate formation of the recirculating zones past the throat which quickly destabilize the sheet. These processes are degraded as *DA* decreases.

A slight temperature variation of ±2 K is predicted at all the simulated *DA*, with the prominent observation that the local temperature drops around the vapor areas delays the growth of the vapor regions, and vice versa. The preponderance of high-temperature vapor regions implies that the latent heat transfer is more into the cavity, leading to delayed condensation of vapor into liquid. Larger temperature gradients are detected at larger *DA*, which is linked to the presence of stronger phase change mechanisms within larger recirculating zones and interfacial regions. This is found to be consistent with the distributions of vorticity showing larger values along the liquid-vapor interfacial regions, as well as in the shear layers of recirculating zones.

On the dynamics of the simulated cavitating flows along the nozzle lower wall, it is seen that the vapor fraction and shear stress decrease as *DA* increases, due to the faster and more frequent detachment of the vapor spots from the wall at larger *DA*. This is different from the flow behavior away from the wall where larger *DA* leads the liquid phase to experience more local accelerations within larger recirculating zones, so providing larger low-pressure areas for the formation of cavities. The increase of the wall shear stress at smaller *DA* is also found to be due to the improved local accelerations of the liquid at the wall due to the presence of vapor spots. These local accelerations contribute to raising spatial derivatives of velocity, and so the vorticity.

As for the vorticity budgets, it is observed that the vorticity dilatation and baroclinic terms are improved as the diffusion angle increases to *DA* = 7.5º. At *DA* = 15º, these terms are decreased compared to the smaller angles. The baroclinicity is found to be spatially more concentrated in the liquid-vapor interfacial regions, and show smaller magnitudes than the dilatation term, while acting with more sensitivity to the vapor collapse/inception incidents. The vorticity stretching and tilting terms are observed to increase as *DA* increases up to 7.5º, and then decrease at *DA* = 15º. The improvement of vorticity stretching and tilting with *DA* up to 7.5º is due to the strengthened liquid-vapor interfacial mass transfers and the improved vapor production at larger *DA*. At *DA* = 15º, in spite of more frequent phase-change processes with larger levels of unsteadiness, the overall vorticity is suppressed as against the smaller *DA*. This is likely due to the excess of vapor and its dampening influence on velocity oscillations.

On the temporal behavior of the probed signals, it is observed that the frequency of the oscillations improves as *DA* increases. At smaller *DA*, the signals show moderate fluctuations with larger magnitudes. This implies the occurrence of cavity growth and decay processes in longer periods of time through more relaxed shedding processes. Conversely, at larger *DA*, stronger oscillations appear with reduced amplitudes and within smaller time periods. This suggests more periodicity in shedding. The relative pressure signals further note that the stronger temperature fluctuations at larger *DA* lead the cavities to be formed more slowly due to improved condensation processes. This is based on monitoring the temporal behavior of mean vapor production in the nozzle. With the increase of *DA* up to 7.5º larger mean values are observed up to a certain time, after which the trend is reversed through an inflection point, such that smaller values are seen at larger *DA*. The inflection point presents the time instant when the thermally-influenced gradients substantially improve the flow instability by promoting the cavity inception-collapse processes. These processes are largely accelerated at *DA* = 15º where more succession of the phase change incidents induce larger gradients into the flow. At smaller *DA*, the absence of such gradients causes the dominance of vaporization against the condensation.

As for the instability analysis, smaller *St* numbers are found at larger diffusion angles up to *DA* = 7.5º, which highlights the earlier occurrence of shedding process and instability as *DA* increases. The *St* behavior also suggests the dominance of inertia in governing the instability as against the thermal effects at larger *DA*; the dominance relaxes as *DA* decreases. At *DA* = 15º, the *St* number experiences a little increase, as opposed to the decreasing trend in the smaller *DA* tests. Although the suppression of thermal effects against the inertia is significant at *DA* = 15º, the presence of stronger local temperature-based gradients enhances the instability at larger frequencies. The maximum characteristic frequency at *DA* = 7.5º is found to be due to the low-frequency behavior of the elongated vortex cavities, whereas at *DA* = 15º is related to the alternate collapse/inception of the cavity structures with over-pressures. At *DA* = 1º and 2.5º, the maximum amplification rate frequencies represent the shear layer vortex instability.

As for the mean-square velocity fluctuations, it is indicated that they tend to increase at the upstream station as *DA* increases. The same behavior is spotted at the downstream station except for *DA* = 15º where the streamwise normal and shear fluctuations are decreased compared to the smaller angles. This is likely due to the presence of larger downstream vapor spots with stronger vortex-cavity interactions at *DA* = 15º. At the upstream station, the increased fluctuations at larger *DA* indicate the presence of unsteady re-entrant jets which tend to strengthen the vapor-liquid interactions by improving local gradients. In the streamwise direction from the first to the second station, the velocity fluctuations are observed to decrease in the *DA* = 1º, 2.5º, and 7.5º tests. This is similarly detected at *DA* = 15º with the difference that the transverse fluctuations increase. The longitudinal improvement of the transverse fluctuations indicates the presence of larger recirculating zones, and so stronger shedding mechanisms downstream. It further suggests that the vortices experience significant tilting and stretching in the transverse direction due to the increased transverse velocity gradients.

- **Effects of Interfacial Tension Forces**

To address the effects of interfacial tension forces (ITF) on the cavitation flow of LNG in the nozzle, the developed cryogenic cavitation solver is extended to accommodate a surface tension force term into the modeling framework. To do so, the surface tension source term is incorporated into the momentum equation in a volumetric form, and updated iteratively through the PIMPLE loop. A generic interface property library which enables the solver to capture the vapor-liquid interface properties is also coupled to the incorporated surface tension term and customized based on the NIST property database and accounts for both temperature and pressure variations. The presence of interfacial tension forces in the in-nozzle LNG cavitation flow is found to suppress the breakup of cavities as compared to the case without ITF, especially by decaying the progress of re-entrant jets. This shows the interfacial forces tendency to cause more local stability in the flow by resisting the progress of re-entrant jets through enhancing the local vaporization processes, relaxing the local growth of large-scale interface disturbances. In the case of probed time histories, smaller vorticity magnitudes and suppressed fluctuations of the relative pressure are detected in the ITF case. As for the spectra, smaller power levels, especially in the larger frequency range, are indicated in the ITF test. These observations further suggest the degraded effects of pressure waves on destabilizing the flow when ITF exists. Nevertheless, the interfacial tension forces are found to slightly improve the net vapor production in the nozzle, which implies the pre-dominance of temperature-dependent inertia and convective forces in governing the vaporization processes, as against the ITF with secondary importance.

11.1.1.2. 3D In-nozzle Cavitating Flow of LNG

The overall development behavior of the 3D flow is found to be similar to the 2D case, with the difference that the cavitating structures evolve non-uniformly in the streamwise and lateral directions -- the spanwise evolution of the cavitation flow indicates the presence of three-dimensionality. The primary cavity inception is formed on the lower wall of the nozzle due to a flow separation that develops a shear layer through a primary recirculation zone. The shear layer is then promoted and eventually turns into elongated and inclined vortical structures downstream. Local static pressure drop below the local saturation pressure in the core of the generated vortices results in nucleation and growth of the cavities. The unsteady cavitation transition from the partially-attached sheet cavity near the throat into the highly unstable cavity clouds downstream is made through the progression of re- and side -entrant jets that release small cavity pockets from the sheet. The detached shedding cavity pockets evolve unevenly to gradually turn into unstable cavity clouds downstream. The presence of side-entrant jets is another indication of three-dimensionality that develops spanwise gradients in the flow.

Other than the shear layer development process, the cavity structures are found to change by the latent heat exchange mechanisms. For instance, the higher temperature gradients spotted in the cavity clouds indicate larger latent heat of vaporization is absorbed from their surrounding liquid. Small temperature gradients are seen in the sheet cavity residuals on the lower wall. These temperature gradients however impose significant variations on the density and pressure fields, so altering the local behavior of the vorticity and thus the cavitation.

The other indication of three-dimensionality is found to be the production of horseshoe U-shaped vapor structures tightly interacting with the coherent hairpin vortices. These interactions are majorly seen downstream away from the throat. The U-shaped vapor structures are primarily created by breakdown of the attached sheet cavity into detached vapor pockets due to the development of re- and side -entrant jets, and then their complex interactions with the vortical structures under significant spanwise gradients. They are also found to appear with slightly increased temperature in their heads when convecting downstream. The improved cavity-vortex interactions in larger recirculating zones downstream of the nozzle are suggested to be the main reason for the reproduction of U-shaped vapor structures. These interactions are accompanied by the collapse processes which break down the cavities into smaller vapor spots by propagating pressure waves. This benefits the coherent vortex structures to become even more irregularly enlarged and distorted, and so more destabilized despite the longitudinal dissipation.

Other than the primary shedding mechanism through the development of entrant jets within the recirculation zones, a secondary shedding mechanism is found in the periodic evolution of the cavitating spots in the nozzle. The secondary mechanism originates from the unstable sheet cavities residuals left on the wall, along with the scattered liquid spots in the vaporized regions. In particular, the cavity residuals on the wall are found to alternately accumulate the vortices in lateral sides of the domain in the spanwise direction. This strengthens the entrant jets penetration into the flow by enhancing the spanwise gradients, so improving the flow resistance to form a fully vaporized region. The presence of secondary mechanism is also realized from the spanwise periodicity of the large clusters of vapor spots passing across the side boundaries of the domain. These observations are attributed to the effects of three-dimensionality, and highlight the improved instability in the 3D case as against the 2D case. The improved instability is further noted from the amplified power spectra of the probed signals in the 3D case.

11.1.2. Numerical Simulations of Cavitating Mixing Layer of LNG behind the Splitter

The developed solver is further applied for simulating 2D and 3D cavitating mixing layers of LNG behind a splitter plate, to gain insight towards the evolution of cavitation-vortex patterns, instability behaviors, and their correlations with thermal effects in free (un-bounded) shear flows of LNG. The 2D LNG cavitating mixing layer is studied for three different cavitation numbers, i.e. Ca = 2.20, 0.65, and 0.21 covering a range of non-cavitating to highly cavitating operating conditions. An additional test with the energy equation being switched off (Ca = 0.65i) is also conducted to specifically evaluate the effects of thermal parameters. The 3D LNG cavitating mixing layer is built by a spanwise extrusion of the 2D domain, and simulated based on the 2D case at Ca = 0.21. Analysis of the results in the cavitating mixing layer tests is performed using the same framework as in the nozzle tests. A summary of the findings is given as follows.

11.1.2.1. 2D Cavitating Mixing Layer of LNG at Different Cavitation Numbers

The cavitation development process at the simulated cavitating conditions, i.e. Ca = 0.21, 0.65, and 0.65i is found to be based on the periodic evolution of vortical structures in the mixing layer. The vortices evolution in the non-cavitating condition (Ca = 2.20) helps better explain how the cavities are generated within the expansion of vortices in the mixing layer. Faster convection of the high-speed side of the mixing layer at the trailing edge of the splitter plate (T.E.) rolls up the high-vorticity shear layer on the splitter upper wall to form a primary vortex region in the low-speed side of the mixing layer which expands unsteady downstream in the primary stages of the development process. A primary K-H instability mechanism is then gradually created in the mixing layer core to develop primary vortices in the vicinity of the T.E. The generated primary vortices expand downstream from the upstream braid region through pairing with neighboring vortices to initiate the mixing layer shedding. The secondary instability mechanisms further downstream then guarantee the primary shedding, by facilitating continuous pairing of the vortical structures. The pairing of vortices occurs when they become large enough such that they cannot grow more without merging with their neighboring ones. The initiated pairing upstream close to the T.E. is weakened further downstream due to typical viscous dissipation.

When the vortical structures are expanded and/or stretched between two neighboring rolling vortices (K-H rollers) their angular velocities are increased so causing the core pressure to drop. If the pressure drop falls below the vapor pressure, cavity nucleates. This describes the main cavitation development mechanism in the simulated mixing layers, which is found to initially form an incipient cavity in the mixing layer lower side, and then followed by the successive formation of unsteady cavities in the mixing layer core. Other than the main cavitation mechanism, an attached sheet cavity is created on the splitter plate upper side that frequently sheds off detached, small cavity pockets around the T.E. The small upstream cavities gradually turn into highly unstable vapor clouds downstream while maintaining a regular shedding.

In comparing the cavitating tests, larger cavities with strengthened phase change processes in stronger sheared zones are seen at $Ca = 0.21$ as against $Ca = 0.65$. The convection of vortices at $Ca = 0.21$ is however slower because of the larger vapor production. These differences mainly pertain to how the counterpart vortices are paired in the mixing layer. At $Ca = 0.21$, the amplified shear layer instability causes an earlier pairing/destruction of the counter-rotating vortices in smaller time periods as against $Ca = 0.65$. This further increases the number of cavity growth/collapse successions as against $Ca = 0.65$. In other words, the inhibited pairing processes, that can lead to a cavity inception/development, at $Ca = 0.65$ leads the vortices to convect more easily compared to $Ca = 0.21$. These observations highlight the dominant effects of inertia.

In addition to the vortex shedding mechanisms, the cavities are sustained by exchanging mass with the liquid regions surrounding them, through the interfacial latent heat transfer mechanisms. In particular, the high-temperature vapor areas indicate the latent heat of vaporization into the cavities, causing more vapor expansion. A slight temperature variation of ± 2 K is seen in the evolution of cavitating spots in both of the *Ca* = 0.21 and 0.65 tests, with significant gradients along the liquid-vapor interfaces and in the front/upper side of the cavities. These gradients are reduced at *Ca* = 0.65 where weaker and smaller cavities present due to suppressed instability and heat exchange mechanisms. The noted delay in the convection of cavities at *Ca* = 0.21 further pertains to such improvements in thermodynamic effects that occur through longer phase change processes within larger cavitating zones.

Comparing the non-cavitating case *Ca* = 2.20 with the cavitating case *Ca* = 0.21 shows that both of the flows emerge the same overall shedding patterns, though a larger vortex development area is formed in the cavitating case. In the non-cavitating test, the pairing process is found to convect faster downstream, causing faster breakdown of the primary vortices. In the cavitating case, however, the vortex structures are distorted additionally by the cavity spots, lengthening the vortex development procedure. The cavities in these interactions break down the vortices and thus improve the instability as compared to the non-cavitating test. The improved instability is due to the development of larger gradients, and seen particularly in the cavitating vortex cores and interfacial liquid-vapor regions, unlike the non-cavitating test where occurs only in the vortex cores. These gradients are improved by the presence of strong temperature variations in the cavitating spots. Much smaller temperature variations are seen in the non-cavitating test.

As for the vorticity budgets, the vorticity stretching and tilting in the cavitating tests are found to increase with the decrease of *Ca*. Improved vorticity stretching and tilting with decrease in *Ca* is due to the formation of larger cavity spots causing more distortion of the vortices. Larger stretching and tilting are also seen in the transverse direction than the streamwise direction, which implies the significance of transverse gradients in altering the cavity-vortex interactions. Comparison of the *Ca* = 0.65i and *Ca* = 0.65 tests shows that the thermodynamic effects increase the streamwise and transverse vortex stretching and tilting, especially in the upstream regions. The vortex stretching and tilting in the non-cavitation test are found to be significant as against the cavitating tests. This is linked to the presence of vapor in the cores of the vortical structures, decoupling the rate of vortex-stretching from the rotation rate. Larger stretching in cavitating vortices improves production of core vapor and not the vortex angular velocity, as opposed to the non-cavitation condition.

The dilatation and baroclinic terms are also enhanced with the decrease of *Ca*. It is noted that the larger temperature-dependent density variations at smaller *Ca*, i.e. a result of more frequent formation of the vapor spots, improve not only the local misalignments of density and pressure gradients but the liquid-vapor interfacial mass fluxes. Comparing the *Ca* = 0.65 and *Ca* = 0.65i tests shows that the thermodynamic effects improve density gradients and interfacial mass transfer processes, so enhancing local instabilities. The reduced velocity magnitudes at *Ca* = 0.65 against *Ca* = 0.65i is also attributed to the thermodynamics effects which intensify the local vaporization events despite decelerating the overall convection. This behavior is likewise detected in the *Ca* = 0.21 case where the overall vorticity is decreased compared to the larger *Ca*, despite more frequent phase change processes with larger levels of local disturbances. This is due to the increase in momentum loss because of more vapor production.

The well-known S-shaped velocity in the mixing region is captured at all the simulated tests, as a result of velocity gradient between the high- and low-speed streams. In the upstream wake region, velocity profiles appear with a double-peak behavior with overshoots at the borders of the mixing layer. The overshoots are due to the momentum deficit in the wake balanced by increasing velocity at the edges of the mixing area; they are dampened far downstream the T.E. where the mixing layer reaches its self-similarity state. This process is found to be accelerated at smaller *Ca*, where larger cavities with improved thermal effects relax the velocity at the core of the mixing layer, thus speeding up the occurrence of self-similarity. Other than reducing *Ca*, the thermal influence is found to accelerate the occurrence of self-similarity. The resulting profiles further indicate that the influence of the splitter wake is stronger in the non-cavitating test at *Ca* = 2.20, causing the self-similarity to occur later than the cavitating tests.

Spatial growth rates of the simulated mixing layers are evaluated in terms of the vortex and cavity development patterns. The following observations are attained:

1) Quasi-linear behavior of the vorticity thickness in the self-preservation region, with an increasing trend in the streamwise direction, at all the simulated *Ca*. Larger vorticity thicknesses are seen in the cavitating tests than the non-cavitating test. However, at the *Ca* =

0.21 smaller vorticity thickness is seen compared to *Ca* = 0.65. Larger vorticity thickness is also detected at *Ca* = 0.65 than *Ca* = 0.65i.

2) Quasi-linear behavior of the momentum thickness in the self-preservation region, with an increasing trend in the streamwise direction, at all the simulated *Ca*. Increased momentum thickness at smaller *Ca* is noted to be due to the presence of cavities suppressing the momentum transport. The reversed behavior at the smallest *Ca* = 0.21 pertains to the dominance of vapor clouds with large thermally-affected density gradients. Larger momentum thickness is indicated at *Ca* = 0.65 compared to *Ca* = 0.65i.

3) Quasi-linear behavior of the equivalent vapor thickness in the streamwise direction, with larger values at smaller *Ca*. The amplified vaporization processes with stronger thermodynamic effects at smaller *Ca* are suggested to be the main reasons for improving the vapor thickness. The absence of thermodynamic effects at *Ca* = 0.65i is found to reduce the equivalent vapor thickness as against the thermo-sensitive case *Ca* = 0.65.

The probed signals indicate periodic oscillations at all the simulated *Ca*. At *Ca* = 2.20, smaller amplitudes in the temperature signal are observed, though showing comparable relative pressure values as against the cavitating tests. This is because the mixing layer at *Ca* = 2.20 is a single liquid phase flow, and no vapor fraction fluctuation is present. Larger velocity magnitudes are however seen at *Ca* = 2.20 than the cavitating tests. At *Ca* = 0.65, inception and breakup of the cavities cause intermittency in the signals such that larger amplitude oscillations occur in shorter time periods as compared to *Ca* = 2.20. The velocity magnitudes however reduce due to the production of vapor. The cavity inception /collapse incidents at *Ca* = 0.65 appear through clear-cut transitions, leading the vapor fraction signal to show a quasi-rectangular shape. Longer clear-cut transition indicates longer residence time of cavities. The same behavior is seen at *Ca* = 0.65i with the difference that the presence of additional temperature-based gradients at *Ca* = 0.65 improve the temperature and relative pressure. Stronger vapor spots at *Ca* = 0.65 are also found to decrease the mixture velocity as against *Ca* = 0.65i, highlighting the “thermodynamic delaying effects”. At *Ca* = 0.21, smaller amplitude fluctuations in larger frequencies are indicated compared to the larger *Ca*. This is due to the enhanced shedding mechanisms at *Ca* = 0.21, and clarifies 1) the presence of more frequent phase-change processes in shorter time intervals, and 2) improved dampening effects of the larger cavities, reducing the mixture velocity; the vapor fraction signal at *Ca* = 0.21 shows smaller, more frequent cavity bursts with no clear-cut transition. The higher rates of change of vapor pressure at *Ca* = 0.21 also suggest stronger involvement of the thermal effects. The sudden, steep gradients in the cavitating tests signals are linked to the propagation of pressure waves during phase change processes. These are identified by spotting the "discontinuity propagation" events, and categorizing the "global" and "local" cavity collapse incidents in the vapor fraction signals. Decreasing *Ca* promotes the successive occurrence of these events/incidents by accelerating the phase change processes.

Different instability behaviors are indicated at the upstream and downstream probing stations. At the upstream probe, *St* number increases in the cavitating tests as compared to the non-cavitating test. This is due to the presence of cavity-vortex interactions in the cavitating tests which improve unsteadiness significantly, contrary to the non-cavitation test where the instability only originates from the shear layer vortex interactions. Smaller *St* number at the non-cavitation test however indicates the earlier occurrence of shedding process and instability, i.e. likely related to the stronger effects of the splitter wake upstream. Decreasing *Ca* from 0.65 to 0.21 is found to reduce the *St* number and indicates a delay in the mixing layer shedding process. This suggests that the vortices become slower as the vapor content increases in the upstream. The absence of thermal effects at *Ca* = 0.65i is also seen to reduce the *St* number at the upstream probe, suggesting the predominance of inertia against thermodynamic parameters in governing instability. At the downstream probe, the mixing layer self-similarity alongside the improved cavity coalescence/collapse incidents alter the upstream behavior by inducing more instability at smaller *Ca*. Reduction of the *St* number at smaller *Ca* suggests an improvement in pairing of the downstream vortices. The *St* number decrease is also seen in the downstream of the *Ca* = 0.65 case as against the *Ca* = 0.65i case, indicating the improved influence of the thermal parameters against inertia in modulating the downstream cavity-vortex interactions. The characteristic frequency in the non-cavitation test is found to be purely from the vortex shedding, with lower-amplitude secondary peaks as the sub-harmonic of the main oscillation. At *Ca* = 0.65, the characteristic frequency is related to the breakdown and collapse of the alternating cavities, while the secondary peaks are due to the vortex shedding frequency and/or the low frequency behavior of the elongated vortex cavities. Similar spectral characteristics to *Ca* = 0.65 are indicated in the *Ca* = 0.65i and 0.21 cases, but with the dominant peaks at smaller frequencies.

As for the mean-square velocity fluctuations, the well-known top-hat profiles are mutually captured at both of the upstream and downstream stations, at all the simulated *Ca*. The largest fluctuations occur in the core of the mixing layer, regardless of the cavitation content, indicating the accumulation of vorticity and strain rate in the core. The streamwise fluctuations show larger magnitudes than the lateral ones. The streamwise fluctuations significance against the transverse components indicates the presence of turbulence anisotropy, and suggests a strong dependence of turbulence diffusion on the trade-off between inertia, cavitation, and thermal effects. The upstream and downstream fluctuations also mutually show an asymmetric behavior with an apparent bias towards the mixing layer lower stream, at all the *Ca*. On the distinctions between the upstream and downstream velocity fluctuations, it is noted that at the upstream station, cavitation reduces the fluctuations as *Ca* decreases. This is linked to the degraded modulation of the vortical structures by frequent inception and expansion of vapor spots, decoupling the vortex rotation and strain rate. The suppressed pressure variations around the saturated vapor pressure in the cavitating zones are also suggested to trigger the upstream behavior. By contrast, at the downstream station, larger velocity fluctuations are resulted at smaller *Ca*. This is attributed to the presence of strengthened vortical structures and larger thermally-induced density gradients, as well as more vulnerability of the vortices to interactions with cavities. The same downstream behavior is seen in comparing the *Ca* = 0.65 and 0.65i tests, with larger transverse fluctuations at *Ca* = 0.65. The enhancement is smaller at the upstream station because of the stronger effects of wake. A significant decrease in anisotropy at larger *Ca* is further suggested at the downstream station, because of the occurrence of self-similarity and increase of the shear fluctuations with the decrease of *Ca*. This trend is reversed at the upstream station.

11.1.2.2. 3D Cavitating Mixing Layer of LNG

The resulting 3D cavitating mixing layer is found to evolve in the same way as the periodic evolution noted in the 2D case, with the main difference that the cavity-vortex interactions are altered by three-dimensionality. The 3D cavitation flow is initially formed as spanwise slender vapor tubes distributed unevenly in the mixing layer lower side within the rotating vortex tubes close to the T.E. The lower side deflection is due to the faster convection of the upper stream, which guides the sheets of fluid behind the splitter to roll up primarily in the lower stream. The generated vortex tubes in this process promote nucleation of cavity tubes in their cores, if the local pressure drops below the local vapor pressure. The primary roll-up process continues in the mixing layer core, with the regular formation of the vortex tubes through a primary K-H instability mechanism. The primary instability forms a gradual progression of wavy infinitesimal instabilities in the braid region, causing the neighboring pairs of counter-rotating vortices (K-H rollers) to stretch and roll around each other to amalgamate into larger vortices (primary pairing process). The evolution of the primary cavities is thus continued in the braid region through the primary instability, when the vortices are stretched enough to lower the pressure below the vapor pressure. This completes the first stage of the cavitation development process.

With time, the primary instability mechanism is followed by the secondary K-H instability mechanisms further downstream, which ensure continuous pairing of the shedding counter-rotating vortices in the domain. As the secondary pairing processes occur through the secondary instability mechanisms, the shedding vapor cavities also grow into unsteady cavitation clouds. This is the second stage of the cavitation development process where the small upstream vapor pockets turn into large vapor clouds downstream. The generated cavities at this stage mainly appear in the form of slender vapor "filaments" and/or "croissant-shaped" vapor spots, and are found to be dependent on complex distortions of the longitudinal vortical structures in the crosswise direction. Other than the vortex instability mechanisms, the local latent heat exchange mechanisms are noted to affect the expansion/condensation of the cavities. For instance, the high-temperature zones in the upper and/or rear sides of the expanding cavities indicate exchange of the latent heat of vaporization into the cavity from its surrounding liquid.

In the meantime of the mixing layer pairing processes, a sheet cavitation flow is also observed to develop unsteady on the splitter upper surface. The sheet cavity development is made of three stages; in stage (1), an attached, thin sheet cavity begins to appear on the plate upper surface as a result of boundary layer separation, and then grows longitudinally until it reaches its maximum length; in stage (2), the entrained attached sheet cavity with convex rear shape rolls up at its end around the T.E. and leads to non-uniform creation of the unstable re- and side-entrant jets on the plate; in stage (3), the entrant jets irregularly break down the sheet at its rear and lateral sides, dispatching small vapor pockets successively. The entrant jets are additionally noted to be destabilized by the residual vapor layers on the splitter which are left over from the prior sheet cavities development processes and/or the cavity collapse incidents. Strong interactions of the distorted vapor tubes with the dispatched vapor pockets are widely observed within the mixing layer shedding mechanisms.

Three-dimensionality is further found to often curl the tails of the sheet and/or the cloud cavities on the splitter and/or inside the mixing layer into rounded shapes and form the U-shaped horseshoe cavities. The horseshoe vapors interact continuously and tightly with the well-known coherent hairpin vortical structures and expand longitudinally until they collapse downstream. The unsteady periodic shedding process of the coherent vortices under crosswise gradients is noted to be the main reason for promoting the horseshoe vapor spots. The horseshoe vapors also appear with increased temperature in their heads as growing downstream. This suggests larger exchange of latent heat of vaporization into a horseshoe cavity through its head.

As against the horseshoe cavities, the coherent hairpin vortical structures are indicated to be substantially dominant in the mixing layer, and created as a result of spanwise evolution of the streamwise vortices within the instability mechanisms. The hairpin vortices evolution is initiated from the primary spanwise vortex tubes, e.g. the K-H rollers, in the braid region close to the T.E.; the primary spanwise rollers are stretched longitudinally through unsteady expansion of the braid region and eventually form the primary hairpin vortices by developing unsteady crosswise shear fields. Further progression of the upstream vortices is found to cause production of the secondary hairpin vortices downstream, through distortion of the primary hairpin vortices within the mixing layer pairing processes. The primary vortices through these distortions particularly amalgamate into the neighboring hairpins and/or the K-H rollers. The presence of vapor spots is also anticipated to affect the evolution of the secondary hairpin vortices especially in the mixture regions of the downstream cavitating clouds -- they are suggested to enhance the spatial variation of the mean velocity gradients by improving the skewness of the vorticity field, triggering the reproduction of the secondary vortices. This is based on spotting the highly-distorted “spaghetti” vortex tubes amid the tight interactions of the cavity spots with the secondary vortices in the large cavitating clouds downstream.

Further on the comparison of the 3D and 2D mixing layers, the power spectra of the probed signals shows larger values in the 3D case, suggesting that the enhanced pairing mechanisms in the 3D flow promotes the vortical structures to be stronger, with larger spatial gradients, and shed at smaller time sequences. The amplified spectra in the 3D case is detected in most of the high frequency range, which indicates higher coherence level in most of the energetic eddies, as against the 2D case. Despite the improved instability, the pressure spikes are suppressed in the 3D case. This means more contribution of energy to strengthening the local disturbances, causing faster cavity collapse/inception incidents through enhancing the shear between the liquid and vapor spots. The improved PSD in the 3D case also suggests the presence of larger temperature-based gradients, and thus amplified thermodynamic effects.

11.2. Contributions of Research

A numerical CFD solver is developed and validated in the present research project to facilitate simulation and analysis of the cryogenic cavitation flows of LNG in LNG-based turbomachinery. The developed model is employed for simulating different scenarios of two fundamental case studies; 1) cavitating flow of LNG inside the Laval nozzle, and 2) cavitating mixing layer of LNG behind the flat splitter plate, with the aim of gaining insights towards LNG cavitation mechanisms and their correlations with shear layer instabilities and thermal parameters. The major contributing observations from the simulations results are highlighted as follows:

1) In-nozzle cavitating flow of LNG:

- Detachment of vapor cavities from the attached sheet cavity through roll-up of the re-entrant jet, and promotion to highly unsteady cavity clouds in the recirculating zones.
- Quasi-unsteady behavior of the cavitation: combination of steady upstream pure vapor region and unsteady downstream cavity clouds.
- Stronger impacts of temperature variations, including stronger cavity collapse/ coalescences in larger recirculating zones, on larger cavities at larger diffusion angles.
- Local stabilizing effects of the interfacial tension forces on cavities.

2) Cavitating mixing layer of LNG:

- Nucleation of vapor cavities at the center of the coherent vortices, and their gradual turn into large cavity clouds through vortex pairing processes (K-H instability mechanisms).
- Correlation of the growth of the unsteady cavity spots to the growing coherent vortical structures following the shear layer roll-up.
- Stronger effects of inertia in the upstream regions -- e.g. wake and braid -- in governing the cavitation mechanisms, as opposed to the suppressed effects of thermodynamic parameters.
- Stronger and longer lasting effects of splitter wake at larger cavitation numbers.

Other than the above-noted observations, some important findings are mutually captured in both of the investigations (1) and (2). A summary of these findings is listed in the following:

- Slower cavitation inception and development at larger cavitation numbers.
- More successive vaporization and collapse of cavities at smaller cavitation numbers due to amplified flow unsteadiness; vapor cavities are more strongly affected by temperature variations.
- Larger effects of temperature-based baroclinic torque and vorticity dilatation on cavity-vortex interactions, as compared to the other vorticity production budgets.
- Presence of temperature-induced flow gradients: triggering effects of thermal parameters on instability.
- Significant sensitivity of local instability characteristics to the operating conditions: distinct and unpredictable upstream and downstream vortex-cavity interactions.
- Triggering effects of cavitation on instability, as compared to non-cavitation conditions.
- Large influence of compressibility, in particular cavity collapse/inception mechanisms, on cavitating patterns and instability behaviors.
- Significant effects of temperature variations due to latent heat transfer and local saturation pressures on the vaporization and condensation mechanisms; stronger thermodynamic delays at smaller cavitation numbers cause longer vaporization processes, and thus larger vapor production.
- Triggering effects of three-dimensionality on instability, phase-change mechanisms, and thermodynamic characteristics by imposing secondary crosswise flow gradients.
- Formation of the horseshoe cavity structures alongside the coherent hairpin vortices.

11.3. Recommendations for Future Work

Even though the present research proposed an accurate numerical framework and collected a refined database on the detailed physics of basic LNG cavitating flows, there are still multiple avenues for future investigations that can be considered to address the current research limitations, and thus extend the range of applicability of the findings. These investigations can potentially target 1) application of the developed solver for simulating complex flow configurations, and 2) enhancement of the accuracy of the developed solver by incorporating more accurate numerical approaches and/or extended cavitation models. The following address the limitations of the present research and suggest potential future investigations:

- **Implement High Order Formulations of Saturation Pressure and/or Latent Heat Dependency on Temperature**

The saturation pressure dependency on temperature in the developed model, i.e. Equation (12), is based on the Clausius-Clapeyron Equation (11) and works for a primary assumption that the initial state of the operating flow is isothermal. This assumption is mainly employed to make an initiative explicit correlation between the existing reference isothermal solver in OpenFOAM, called `cavitatingFoam`, and the developed solver, `cryogenicCavitatingFoam`; and though, is iteratively resolved by the modified PIMPLE loop to ensure proper capture of latent heat and saturation pressure variations during simulation as the flow undergoes cryogenic cavitation. Although this approach has shown reliable and reasonably accurate results for the selected applications in this research, its accuracy and range of applicability can be extended by deriving higher order formulations for saturation pressure (or latent heat) -- e.g. implicit evaluation of the Clausius-Clapeyron equation using Taylor series or polynomial/higher order distributions of p_{sat}/L as function of temperature, without assuming the noted initial isothermal state. Implementation of these formulations in the developed solver and compare the findings against the present data are considered as future work.

- **Perform Numerical Simulations of Turbulent Cavitating Flows of LNG**

As indicated in Chapter 1, cavitating flows in LNG-based turbomachinery may operate in fully-turbulent regimes, depending on the design operating condition. The presence of turbulence is mainly due to the high levels of unsteadiness generated by unstable cavitating spots in addition to the strong shear layer instabilities, leading the dynamics of vortex-cavity structures to involve complex interactions. These interactions that correlate the turbulent flow shear characteristics to cavitating structures are not sufficiently understood in LNG-based applications, so highlighting the need for more fundamental studies on turbulent cavitating flows of LNG. As an initiative suggestion to this end, the basic LNG cavitating flows in this research can be built on to operate in transitional to fully-turbulent regimes to provide introductory understanding of the LNG turbulence-cavitation correlative mechanisms. This is preliminarily addressed by the authors as a first step towards future direct numerical simulations (DNS) of fully turbulent cavitating flows of LNG. The preliminary results are reviewed in Appendix C.

- **Reevaluate the Validation Studies Using Turbulence Modeling Frameworks**

The validation studies in Chapter 4 are conducted for 2D configurations of the reference experimental data, in transitional to laminar operating flow regimes, and without the use of turbulence modeling. Despite capturing reasonably good match between the simulations results from the developed solver and the experimental measurements, it is recommended that the validation studies are reevaluated by employing turbulence modeling approaches, e.g. LES, for real life 3D configurations of the reference experiments, so that the influences of three-dimensionality and turbulence in reducing the observed mismatch between the CFD findings and experimental data can be identified.

- **Implement Modules for TEM-Based Two-Phase Cavitation Models**

The developed solver in this research works based on a homogenous mixture modeling framework that assumes vapor regions to be clusters of bubbles with no slip velocity between the vapor and liquid phases. This assumption, in spite of its advantages, causes the solver not to be able to capture and track the phase change behavior of a single bubble(s) -- an example of this is expansion of a single bubble with specific diameter on a heated wall in a liquid domain. This limitation, on the other hand, has been addressed in the so-called transport equation-based models (TEM) such as those of Kunz, Zwart, and Schnerr-Sauer, which have become recently more popular in simulations of cavitating flows, as indicated in Chapter 3. Though yielding some levels of uncertainty, the implementation of user-defined coefficients in the TEM models, which includes initial distributions/dimensions of simulating bubble(s), is the key factor for their applicability in many industrial applications. It is suggested that these models are incorporated as a new module into the present homogenous mixture modeling framework to resolve the described limitation. Comparison of the HEM- and TEM-based simulations of complex cavitating flows of LNG and evaluation of the findings against experimental data can be considered as an interesting avenue for future work.

- **Couple an Adaptive Mesh Refinement Library**

A major challenge in simulating the complex cavitating flows of LNG with the developed solver is the computational cost, which may require a significant number of processors and computing time to accurately solve the governing equations for highly-resolved spatial grids. Although this issue is typical in numerical modeling of cavitating flows, it may become critical when it comes to simulating complex large-scale turbomachinery, direct numerical simulations, and simulations with moving boundaries. Although one way to work around this problem is to use the LES approach, which is common in cavitation research to date, a more efficient way is to incorporate an adaptive mesh refinement library that is able to dynamically refine the coarse background mesh based on the behavior of the flow in shear layers, e.g. more refinement in near-wall regions and/or interfacial regions, while preserving the original background mesh topology. The mesh refinement adaptivity based on user-defined gradients of flow fields is conventionally utilized in single-phase flow modeling where a specific range for e.g. velocity gradient is set to refine the mesh successively by factors of 2, 4, 8 cells and so on.

- **Implement Modern Formulations of Equation of States**

Phase-change modeling through modern formulations of equations of states (EoS) has recently been in focus of a number of research works, to more precisely capture the state properties of cavitating fluids. Among these equations, complex formulation of convex stiffened gas EoS for the pure phases; Tait EoS for the liquid phase; two-phase and sinusoidal barotropic EoS for the mixture phase, have shown improvements in the accuracy of cavitation modeling frameworks. An interesting future research is to implement these EoS in the current solver and reassess the precision of calculations in terms of capturing phase properties especially in the liquid-vapor interfacial regions and/or cavity collapse areas.

Bibliography

[1] T. Düren, L. Sarkisov, O. Yaghi, R. Snurr, *Design of New Materials for Methane Storage*, Langmuir 20, 2004, pp. 2683-2639.

[2] Envocare Ltd., Liquefied Petroleum Gas (LPG), *Liquefied Natural Gas (LNG) and Compressed Natural Gas (CNG)*, Envocare Ltd., 2013.

[3] D. Levinson, M. Corbett, M. Hashami, *Operating Costs for Trucks*, University of Minnesota, Minneapolis, Minnesota, USA, 2006.

[4] V. Lamaris, D. Hountalas, *A General Purpose Diagnostic Technique for Marine Diesel Engines-Application on the Main Propulsion and Auxiliary Diesel Units of a Marine Vessel*, Energy Conversion and Management 51, 2010, pp. 740-753.

[5] B. Yoon, J. Shin, S. Lee, *Technology Assessment Model for Sustainable Development of LNG Terminals*, Journal of Cleaner Production 172, 2018, pp. 927-937.

[6] A. Arteconi, F. Polonara, *LNG as Vehicle Fuel and the Problem of Supply: The Italian Case Study*, Energy Policy 62, 2013, pp. 503-512.

[7] J. Yu, H. Hillamo, V. Vuorinen, et al., *Experimental Investigation of Characteristics of Transient Low Pressure Wall-Impinging Gas Jet*, IOP Publishing: 13th European Turbulence Conference (ETC13) & Journal of Physics: Conference Series 318, 2011.

[8] V. Vuorinen, J. Yu, S. Tirunagari, et al., *Large Eddy Simulation of Highly Under-Expanded Transient Gas Jets*, Physics of Fluids, 2013, Vol 25, pp. 016101-0161022.

[9] M. Abdi, E. Jassim, M. Haghighi, et al., *Applications of CFD in Natural Gas Processing and Transportation, in: Computational Fluid Dynamics*, Hyoung Woo (editor), INTECH, 2010.

[10] A. Hamzehloo, P. Aleiferis, *Large Eddy Simulation of Highly Turbulent Under-Expanded Hydrogen and Methane Jets for Gaseous-Fuelled Internal Combustion Engines*, International Journal of Hydrogen Energy 39, 2014, pp. 21275-21296.

[11] T. Gohil, A. Saha, K. Muralidhar, *Direct Numerical Simulation of Free and Forced Square Jets*, International Journal of Heat and Fluid Flow 52, 2015, pp. 169-184.

[12] Y. Yang, C. Wen, S. Wang, et al., *Effect of Inlet and Outlet Flow Conditions on Natural Gas Parameters in Supersonic Separation Process*, PLoS ONE 9, 2014, e110313.

[13] R. Arina, *Numerical Simulation of Near-Critical Fluids*, Applied Numerical Mathematics 51, 2004, pp. 409-426.

[14] J. Yu, V. Vuorinen, O. Kaario, et al., *Visualization and Analysis of the Characteristics of Transitional Under-Expanded Jets*, International Journal of Heat and Fluid Flow 44, 2013, pp. 140-154.

[15] V. Vuorinen, A. Wehrfritz, C. Duwig, et al., *Large Eddy Simulation on the Effect of Injection Pressure and Density on Fuel Jet Mixing in Gas Engines*, Fuel 130, 2014, pp. 241-250.

[16] Y. Tsuchiya, C. Horikoshi, T. Sato, *On the Spread of Rectangular Jets*, Experiments in Fluids 4, 1986, pp. 197-204.

[17] J. Zhu, D. Zhao, L. Xu, et al., Interactions of Vortices, *Thermal Effects and Cavitation in Liquid Hydrogen Cavitating Flows*, International Journal of Hydrogen Energy 41, 2016, pp. 614-631.

[18] S. Sklavounos, F. Rigas, *Simulation of Coyote Series Trials-Part I: CFD Estimation of Non-Isothermal LNG Releases and Comparison with Box-Model Predictions*, Chemical Engineering Science 61, 2006, pp. 1434-1443.

[19] W. Ikealumba, H. Wu, *Some Recent Advances in Liquefied Natural Gas (LNG) Production, Spill, Dispersion, and Safety*, Energy Fuels 28, 2014, pp. 3556-3586.

[20] E. Tahmasebi, P. Albertelli, T. Lucchini, et al., *CFD and Experimental Analysis of the Coolant Flow in Cryogenic Milling*, International Journal of Machine Tools and Manufacture 140, 2019, pp. 20-33.

[21] S. Rahbarimanesh, J. Brinkerhoff, J. Huang, *Development and Validation of a Homogeneous Flow Model for Simulating Cavitation in Cryogenic Fluids*, Applied Mathematical Modeling 56, 2018, pp. 584-611.

[22] OpenCFD, OpenFOAM User's Guide, URL: https://www.openfoam.com/documentation/user-guide/. (Retrieved Sep. 2015).

[23] X. Zhang, L. Qiu, Y. Gao, et al., *Computational Fluid Dynamic Study on Cavitation in Liquid Nitrogen*, Cryogenics 48, 2008, pp. 432-438.

[24] T. Nagashima, N. Tani, *Cryogenic Cavitating Flow in 2D Laval Nozzle*, Department of Aeronautics and Astronautics, University of Tokyo, Japan, Journal of Thermal Science 2, 2003, pp. 157-161.

[25] V. Aeschlimann, S. Barre, H. Djeridi, *Velocity Field Analysis in an Experimental Cavitating Mixing Layer*, Physics of Fluids 23, 2011, 055105.

[26] G. Wang, I. Senocak, W. Shyy, et al., *Dynamics of Attached Turbulent Cavitating Flows*, Progress in Aerospace Sciences 37, 2001, pp. 551-581.

[27] E. Rood, *Review-Mechanisms of Cavitation Inception*, Journal of Fluids Engineering 113, 1991, pp. 163-175.

[28] E. Sergent, *Vers une Méthodologie de Couplage entre la Simulation des Grandes Echelles et les Modèles Statistiques*, PhD Dissertation, L'Ecole Centrale de Lyon, 2002.

[29] F. Mathey, D. Cokljat, J. Bertoglio, et al., *Assessment of the Vortex Method for Large Eddy Simulation Inlet Conditions*, Progress in Computational Fluid Dynamics 6, 2006, pp. 58-67.

[30] J. Leroux, O. Coutier, J. Astolfi, *A Joint Experimental and Numerical Study of Mechanisms Associated to Instability of Partial Cavitation on Two-Dimensional Hydrofoil*, Physics of Fluids 5, 2005, pp. 52-101.

[31] S. Barre, J. Rolland, G. Boitel, et al., *Experiments and Modeling of Cavitating Flows in Venturi: Attached Sheet Cavitation*, European Journal of Mechanics - B/Fluids 28, 2009, pp. 444-464.

[32] J. Hord, *Cavitation in Liquid Cryogens II – Hydrofoil*, NASA Report, NASA CR – 2156, 1973a.

[33] J. Hord, *Cavitation in Liquid Cryogens III* – Ogives, NASA Report, NASA CR – 2242, 1973b.

[34] R. Simoneau, R. Hendricks, *Two-Phase Choked Flow of Cryogenic Fluids in Converging-Diverging Nozzles*, NASA Report TP-1484, 1979.

[35] J. Franc, E. Janson, P. Morel, et al., *Visualizations of Leading Edge Cavitation in an Inducer at Different Temperatures,* in: Proceedings of the 4th International Symposium on Cavitation (CAV2001), B7.002, 2001.

[36] I. Yuka, O. Naoya, Y. Yoshiki, et al., *Numerical Investigation of Thermodynamic Effects on Unsteady Cavitation in Cascade*, in: S. L. Ceccio, J. Katz, G. Chahine, eds., in: Proceedings of the 7th International Symposium on Cavitation (CAV2009), Ann Arbor, USA, 2009.

[37] K. Niiyama, S. Hasegawa, S. Tsuda, et al., *Thermodynamic Effects on Cryogenic Cavitating Flow in an Orifice*, in: Proceedings of the 7th International Symposium on Cavitation (CAV2009), Ann Arbor, Michigan, USA, 2009.

[38] A. Stepanoff, *Cavitation Properties of Liquids*, Journal of Engineering for Gas Turbines and Power 80, 1964, pp. 195-200.

[39] Y. Yoshida, K. Kikuta, S. Hasegawa, et al., *Thermodynamic Effects on a Cavitating Inducer in Liquid Nitrogen*, Journal of Fluids Engineering 129, 2007, pp. 273-278.

[40] M. Billet, D. Weir, *The Effect of Gas Diffusion on the Flow Coefficient for a Ventilated Cavity*, ASME Journal of Fluids Engineering 97, 1975, pp. 501-506.

[41] F. Larrarte, A. Pauchet, P. Bousquet, et al., *On Morphology of Natural and Ventilated Cavities*, in: Proceedings of ASME Symposium on 30th Cavitation and Multiphase Flow, FED-210, 1995, pp. 31-38.

[42] Y. Utturkar, J. Wu, G. Wang, et al., *Recent Progress in Modeling of Cryogenic Cavitation for Liquid Rocket Propulsion*, Progress in Aerospace Sciences 41, 2005, pp. 558-608.

[43] Z. Jiakai, X. Huangjun, F. Kesong, et al., *Unsteady Cavitation Characteristics of Liquid Nitrogen Flows through Venturi Tube*, International Journal of Heat and Mass Transfer 112, 2017, pp. 544-552.

[44] T. Sun, X. Ma, Y. Wei, et al., *Computational Modeling of Cavitating Flows in Liquid Nitrogen by an Extended Transport-Based Cavitation Model*, Science China 2 (Technological Sciences), 2015, pp. 337-346.

[45] I. Senocak, W. Shyy, *A Pressure-Based Method for Turbulent Cavitating Flow Computations*, Journal of Computational Physics 176, pp. 2002, pp. 363-383.

[46] I. Senocak, W. Shyy, *Interfacial Dynamics-Based Modeling of Turbulent Cavitating Flows, Part-1: Model Development and Steady-State Computations*, International Journal for Numerical Methods in Fluids 44, 2004, pp. 975-995.

[47] I. Senocak, W. Shyy, *Interfacial Dynamics-Based Modeling of Turbulent Cavitating Flows, Part-2: Time-Dependant Computations*, International Journal for Numerical Methods in Fluids 44, 2004, pp. 997-1016.

[48] J. Brackbill, D. Kothe, C. Zemach, *A Continuum Method for Modeling Surface Tension*, Journal of Computational Physics 100, 1992, pp. 335-354.

[49] M. Deshpande, J. Feng, C. Merkle, *Numerical Modeling of the Thermodynamic Effects of Cavitation*, Journal of Fluids Engineering 119, 1997, pp. 420-427.

[50] A. Kubota, H. Kato, H. Yamaguchi, *A New Modeling of Cavitating Flows: A Numerical Study of Unsteady Cavitation on Hydrofoil Section*, Journal of Fluid Mechanics 240, 1992, pp. 59-96.

[51] Y. Delannoy, J. Kueny, *Cavity Flow Predictions Based on the Euler Equations*, in: ASME Cavitation and Multi-Phase Flow Forum 109, 1990, pp. 153-158.

[52] B. Bicer, A. Tanaka, T. Fukuda, et al., *Numerical Simulation of Cavitation Phenomena in Diesel Injector Nozzles*, in: 16th Annual Conference ILASS-ASIA, Nagasaki, Japan, 2013, pp. 58-65.

[53] O. Coutier-Delgosha, J. Reboud, Y. Delannoy, *Numerical Simulation of the Unsteady Behavior of Cavitating*, International Journal for Numerical Methods in Fluids 42, 2003, pp. 527-548.

[54] R. Kunz, D. Boger, D. Stinebring, et al., *A Preconditioned Navier-Stokes Method for Two-Phase Flows with Application to Cavitation Prediction*, Computers & Fluids 29, 2000, pp. 849-875.

[55] P. Zwart, A. Gerber, T. Belamri, *A Two-Phase Flow Model for Predicting Cavitation Dynamics*, in: 5th International Conference on Multiphase Flow, Yokohama, Japan, 2004.

[56] G. Schnerr, J. Sauer, *Physical and Numerical Modeling of Unsteady Cavitation Dynamics*, in: Proceedings of the 4th International Conference on Multiphase Flow (ICMF), New Orleans, USA, 2001.

[57] G. Wang, M. Ostoja-Starzewski, *Large Eddy Simulation of a Sheet/Cloud Cavitation on a NACA0015 Hydrofoil*, Applied Mathematical Modeling 31, 2007, pp. 417-447.

[58] V. Hidalgo, X. Luo, X. Escaler, et al., *Numerical Investigation of Unsteady Cavitation Around a NACA66 Hydrofoil Using OpenFOAM*, in: 27th IAHR Symposium on Hydraulic Machinery and Systems (IAHR) & IOP Conference Series: Earth and Environmental Science, 2014.

[59] A. Singhal, M. Athavale, H. Li, et al., *Mathematical Basis and Validation of the Full Cavitation Model*, Journal of Fluids Engineering 124, 2002, pp. 617-624.

[60] X. Zhang, J. Zhu, L. Qiu, et al., *Calculation and Verification of Dynamical Cavitation Model for Quasi-Steady Cavitating Flow*, International Journal of Heat and Mass Transfer 86, 2015, pp. 294-301.

[61] P. Cooper, *Analysis of Single and Two-Phase Flows in Turbopump Inducers*, Journal of Engineering for Power 89, 1967, pp. 577-588.

[62] A. Prosperetti, *The Thermal Behavior of Oscillating Gas Bubbles*, Journal of Fluid Mechanics 222, 1991, pp. 587-616.

[63] C. Brennen, *The Dynamic Balances of Dissolved Air and Heat in Natural Cavity Flows*, Journal of Fluid Mechanics 37, 1969, pp. 115-127.

[64] A. Hosangadi, V. Ahuja, *Numerical Study of Cavitation in Cryogenic Fluids*, Journal of Fluids Engineering 127, 2005, pp. 267-281.

[65] X. Zhang, Z. Wu, S. Xiang, et al., *Modeling Cavitation Flow of Cryogenic Fluids with Thermodynamic Phase-Change Theory*, Chinese Science Bulletin 4-5 (Engineering Thermophysics) , 2013, pp. 567-574.

[66] P. Van, *Liquid-Vapor Phase Change Phenomena: An Introduction to the Thermophysics of Vaporization and Condensation Processes in Heat Transfer Equipment*, Washington: Hemisphere Publishing Corporation, 1992.

[67] X. Cao, X. Zhang, L. Qiu, et al., *Validation of Full Cavitation Model in Cryogenic Fluids*, Chinese Science Bulletin 10, 2009, pp. 1633-1640.

[68] Y. Utturkar, *Computational Modeling of Thermodynamic Effects in Cryogenic Cavitation*, PhD Dissertation, University of Florida, 2005.

[69] J. Wu, Y. Utturkar, I. Senocak, et al., *Impact of Turbulence and Compressibility Modeling on Three-Dimensional Cavitating Flow Computations*, in: 33rd AIAA Fluid Dynamics Conference and Exhibit (AIAA 2003-4264), Florida, 2003.

[70] C. Tseng, W. Shyy, *Modeling for Isothermal and Cryogenic Cavitation*, International Journal of Heat and Mass Transfer 53, 2010, pp. 513-525.

[71] T. Ohrn, D. Senser, A. Legebvre, *Geometrical Effects on Spray Cone Angle for Plain-Orifice Atomizers*, Atomization Spray 01, 1991, pp. 253-268.

[72] A. Minato, T. Tanaka, T. Nishimura, *Investigation of Premixed Lean Diesel Combustion with Ultra High Pressure Injection*, in: SAE Paper 2005-01-0914, 2005.

[73] Y. Park, J. Hwang, C. Bae, et al., *Effects of Diesel Fuel Temperature on Fuel Flow and Spray Characteristics*, Fuel 162, 2015, pp. 1-7.

[74] Z. Sun, G. Li, C. Chen, et al., *Numerical Investigation on Effects of Nozzle's Geometric Parameters on the Flow and the Cavitation Characteristics within Injector's Nozzle for a High-Pressure Common-Rail DI Diesel Engine*, Energy Conversion and Management 89, 2015, pp. 843-861.

[75] F. White, *Viscous Fluid Flow*, 3rd edition, New Delhi: McGraw Hill Education, 2006.

[76] S. Som, S. Aggarwal, E. El-Hannouny, et al., *Investigation of Nozzle Flow and Cavitation Characteristics in a Diesel Injector*, Journal of Engineering for Gas Turbines and Power 132, 2010, 042802.

[77] S. Som, A. Ramirez, D. Longman, et al., *Effect of Nozzle Orifice Geometry on Spray, Combustion, and Emission Characteristics under Diesel Engine Conditions*, Fuel 90, 2011, pp. 1267-1276.

[78] R. Payri, F. Salvador, J. Gimeno, et al., *Study of Cavitation Phenomena Based on a Technique for Visualizing Bubbles in a Liquid Pressurized Chamber*, International Journal of Heat and Fluid Flow 30, 2009, pp. 768-777.

[79] R. Payri, F. Salvador, J. Gimeno, et al., *Study of Cavitation Phenomenon Using Different Fuels in a Transparent Nozzle by Hydraulic Characterization and Visualization*, Experimental Thermal and Fluid Science 44, 2013, pp. 235-244.

[80] Y. Ito, K. Seto, T. Nagasaki, *Periodical Shedding of Cloud Cavitation From a Single Hydrofoil in High-Speed Cryogenic Channel Flow*, Journal of Thermal Science 18, 2009, pp. 58-64.

[81] F. Yan, Y. Du, L. Wang, et al., *Effects of Injection Pressure on Cavitation and Spray in Marine Diesel Engine*, International Journal of Spray and Combustion Dynamics 9, 2017, pp. 186-198.

[82] X. Wang, W. Su, *Using Double Fluid Model Study Cavitation Flow in High Pressure Nozzle*, Chinese Science Bulletin 53, 2008, pp. 1864-1870.

[83] R. Reitz, *Modeling Atomization Processes in High-Pressure Vaporizing Sprays*, Atomization Spray 3, 1987, pp. 309-337.

[84] P. O'Rourke, *Collective Drop Effects on Vaporizing Liquid Sprays*, PhD Dissertation, University of Princeton, 1981.

[85] L. Zhao, X. He, L. Zheng, et al., *Spray Characteristics of Biodiesel under High Injection Pressure*, Transactions from the Chinese Society of Agricultural Engineering 43, 2012, pp. 6-10.

[86] J. Zhang, Q. Du, Y. Yang, et al., *Study on Cavitating Flow in Different Types of Diesel Nozzle Orifice*, Transactions CSICE 02, 2010, pp. 133-140.

[87] S. Hohmann, U. Renz, *Numerical Simulations of Fuel Spray at High Ambient Pressure: the Influence of Real Gas Effects and Gas solubility on Droplet Vaporization*, Heat and Mass Transfer 46, 2003, pp. 3017-3028.

[88] H. Huang, Y. An, W. Su, et al., *Investigation on the Influence of Injection Pressure and Nozzle Diameter Spray of Blended Fuel in Diesel Engine*, Transactions CSICE 31, 2013, pp. 200-207.

[89] C. Iyer, S. Ceccio, *The Influence of Developed Cavitation on the Flow of a Turbulent Shear Layer*, Physics of Fluids 14, 2002, pp. 3414-3431.

[90] K. Laberteaux, S. Ceccio, *Flow in the Closure Region of Closed Partial Attached Cavitation*, 3rd International Symposium on Cavitation, Grenoble, France, 1998.

[91] K. Laberteaux, S. Ceccio, V. Mastrocola, et al., *High Speed Digital Imaging of Cavitating Vortices*, Experiments in Fluids 24, 1998, pp. 489-498.

[92] B. Belahadji, J. Franc, J. Michel, *Cavitation in the Rotational Structures of a Turbulent Wake*, Journal of Fluid Mechanics 287, 1995, pp. 383-403.

[93] R. Arndt, C. Song, M. Kjeldsen, et al., *Instability of Partial Cavitation: A Numerical/Experimental Approach*, Proceedings of 23rd Symposium on Naval Hydrodynamics, Val deReuil, France, 2000.

[94] J. Lasheras, J. Cho, T. Maxworthy, *On the Origin and Evolution of Streamwise Vortical Structures in a Plane, Free Shear Layer*, Journal of Fluid Mechanics 172, 1986, pp. 231-258.

[95] J. Katz, T. O'Hern, *Cavitation in Large Scale Shear Flow*, Journal of Fluids Engineering 108, 1986, pp. 373-376.

[96] V. Aeschlimann, S. Prothin, S. Barre, et al., *High Speed Visualizations of the Cavitating Vortices of 2D Mixing Layer*, European Journal of Mechanics B/Fluids 31, 2012, pp. 171-180.

[97] K. Okabayashi, T. Kajishima, T. Ohta, *DNS and LES of Cavitating Turbulent Flow*, 6th International Symposium on Turbulence and Shear Flow Phenomena, Seoul, Korea, 2009.

[98] K. Okita, T. Kajishima, *Three-Dimensional Computation of Unsteady Cavitating Flow in a Cascade,* Proceedings of the 9th International Symposium on Transport Phenomena and Dynamic of Rotating Machinery, No FD-ABS-076, 2002.

[99] Y. Chen, S. Heister, *Two-Phase Modeling of Cavitated Flows*, Computers & Fluids 24, 1995, pp. 799-809.

[100] J. Franc, J. Michel, *Fundamentals of Cavitation*, in: Fluid Mechanics and Its Applications Series 76, Grenoble Sciences: Kluwer Academic Publishers, 2005.

[101] H. Yu, L. Goldsworthy, P. Brandner, et al., *Development of a Compressible Multiphase Cavitation Approach for Diesel Spray Modeling*, Applied Mathematical Modeling 45, 2017, pp. 705-727.

[102] E. De Villiers, A. Gosman, H. Weller, *Large Eddy Simulation of Primary Diesel Spray Atomization*, SAE Transactions 113, 2004, pp. 193-206.

[103] T. Michael, J. Yang, F. Stern, *A Sharp Interface Approach for Cavitation Modeling Using Volume-of-Fluid and Ghost-Fluid Methods*, Journal of Hydrodynamics 26, 2017, pp. 917-925.

[104] M. De Giorgi, A. Ficarella, D. Fontanarosa, *Implementation and Validation of an Extended Schnerr-Sauer Cavitation Model for Non-Isothermal Flows in OpenFOAM*, Energy Procedia 126, 2017, pp. 58-65.

[105] H. Liu, C. Cai, X. Xi, et al., *A Novel Model for the Bubble Growth in the Cavitation Region of an Injector Nozzle*, International Journal of Heat and Mass Transfer 119, 2018, pp. 128-138.

[106] J. Riznic, G. Kojasoy, N. Zuber, *On the Spherically Symmetric Phase Change Problem*, International Journal of Fluid Mechanics Research 26, 1999, pp. 110-145.

[107] L. Scriven, *On the Dynamics of Phase Growth*, Chemical Engineering Science 10, 1959, pp. 1-13.

[108] D. Chang, C. Lee, *Development of a Simplified Bubble Growth Model for Flash Boiling Sprays in Direct Injection Spark Ignition Engines*, Proceedings of the Combustion Institute 30, 2005, pp. 2737-2744.

[109] M. Lü, Z. Ning, K. Yan, et al., *Instability and Breakup of Cavitation Bubbles within Diesel Drops*, Chinese Journal of Chemical Engineering 23, 2015, pp. 262-267.

[110] Y. Zeng, C. Lee, *An Atomization Model for Flash Boiling Sprays*, Combustion Science and Technology 169, 2001, pp. 45-67.

[111] G. Falcucci, E. Jannelli, S. Ubertini, et al., *Direct Numerical Evidence of Stress-Induced Cavitation*, Journal of Fluid Mechanics 728, 2013, pp. 362-375.

[112] W. Lee, R. Reitz, *Simulation of Transient Cavitation Processes in Diesel Injectors Using Kiva with a Homogeneous Equilibrium Model*, in: Proceedings of the International Multidimensional Engine Modeling User's Group Meeting, Detroit, 2009.

[113] J. Gustavsson, K. Denning, C. Segal, *Hydrofoil Cavitation under Strong Thermodynamic Effect*, Journal of Fluids Engineering 130, 2008, 091303.

[114] S. Kelly, C. Segal, *Experiments in Thermo-Sensitive Cavitation of a Cryogenic Rocket Propellant*, PhD Dissertaion, University of Florida, Gainesville, USA, 2012.

[115] K. Mani, A. Cervone, J. Hickey, *Turbulence Modeling of Cavitating Flows in Liquid Rocket Turbopumps*, Journal of Fluids Engineering 139, 2017, 011301.

[116] Z. Jiakai, W. Shunhao, Q. Limin, et al., *Frequency Characteristics of Liquid Hydrogen Cavitating Flow over a NACA0015 Hydrofoil*, Cryogenics 90, 2018, pp. 7-19.

[117] D. Joseph, *Cavitation and the State of Stress in a Flowing Liquid*, Journal of Fluid Mechanics 366, 1998, pp. 367-378.

[118] B. Ji, X. Luo, Y. Wu, et al., *Partially-Averaged Navier-Stokes Method with Modified k-ε Model for Cavitating Flow around a Marine Propeller in a Non-Uniform Wake*, International Journal of Heat and Mass Transfer 55, 2012b, pp. 6582-6588.

[119] B. Ji, Y. Long, X. Long, et al., *Large Eddy Simulation of Turbulent Attached Cavitating Flow with Special Emphasis on Large Scale Structures of the Hydrofoil Wake and Turbulence-Cavitation Interactions*, Journal of Hydrodynamics 29, 2017, pp. 27-39.

[120] T. Sun, Z. Zong, L. Zou, et al., *Numerical Investigation of Unsteady Sheet/Cloud Cavitation over a Hydrofoil in Thermo-Sensitive Fluid*, Journal of Hydrodynamics 29, 2017, pp. 987-999.

[121] S. Girimaji, *Partially-Averaged Navier-Stokes Model for Turbulence: A Reynolds-Averaged Navier-Stokes to Direct Numerical Simulation Bridging Method*, Journal of Applied Mechanics 73, 2006, pp. 413-421.

[122] S. Kelly, C. Segal, J. Peugeot, *Simulation of Cryogenics Cavitation*, AIAA Journal 49, 2011, pp. 2502-2510.

[123] J. Billard, P. Galivel, D. Fruman, *Effect of Preturbulence on the Cavitating Bubble Inception, Noise and Morphology in a Venturi*, ASME FED 176, 1993, pp. 31-38.

[124] T. Baur, J. Ngeter, *Measurements in the Shear-Layer Behind a Surface-Mounted Obstacle for the Determination of Coherent Structures*, 9th International Symposium on Applications of Laser Techniques to Fluid Mechanics, Lisbon, Portugal, 1998.

[125] T. Xing, Z. Li, S. Frankel, *Numerical Simulation of Vortex Cavitation in a Three-Dimensional Submerged Transitional Jet*, Journal of Fluids Engineering 127, 2005, pp. 714-725.

[126] J. Seo, Y. Moon, B.Shin, *Prediction of Cavitating Flow Noise by Direct Numerical Simulation*, Journal of Computational Physics 227, 2008, pp. 6511-6531.

[127] X. Long, Q. Liu, B. Ji, et al., *Numerical Investigation of Two Typical Cavitation Shedding Dynamics Flow in Liquid Hydrogen with Thermodynamic Effects*, International Journal of Heat and Mass Transfer 109, 2017, pp. 879-893.

[128] M. Dreyer, J. Decaix, C. Münch-Alligné, et al., *Mind the Gap: A New Insight into the Tip Leakage Vortex Using Stereo-PIV*, Experiments in Fluids 55, 2014, pp. 1-13.

[129] X. Peng, B. Ji, Y. Cao, et al., *Combined Experimental Observation and Numerical Simulation of the Cloud Cavitation with U-Type Flow Structures on Hydrofoils*, International Journal of Multiphase Flow 79, 2016, pp. 10-22.

[130] S. Barre, J. Rolland, G. Boitel, et al., *Experiments and Modeling of Cavitating Flows in Venturi: Attached Sheet Cavitation*, European Journal of Mechanics - B/Fluids 28, 2009, pp. 444-464.

[131] X. Yu, C. Huang, T. Du, et al., *Study of Characteristics of Cloud Cavity around Axisymmetric Projectile by Large Eddy Simulation*, Journal of Fluids Engineering 136, 2014, 051303.

[132] M. Pendar, E. Roohi, *Investigation of Cavitation around 3D Hemispherical Head-Form Body and Conical Cavitators Using Different Turbulence and Cavitation Models*, Ocean Engineering 112, 2016, pp. 287-306.

[133] B. Ji, X. Luo, R. Arndt, Y. Wu, *Numerical Simulation of Three Dimensional Cavitation Shedding Dynamics with Special Emphasis on Cavitation-Vortex Interaction*, Ocean Engineering 87, 2014, pp. 64-77.

[134] E. Foeth, T. van Terwisga, C. van Doorne, *On the Collapse Structure of an Attached Cavity on a Three-Dimensional Hydrofoil*, Journal of Fluids Engineering 130, 2008, 071303.

[135] C. Wang, B. Huang, G. Wang, et al., *Unsteady Pressure Fluctuation Characteristics in the Process of Breakup and Shedding of Sheet/Cloud Cavitation*, International Journal of Heat and Mass Transfer 114, 2017, pp. 769-785.

[136] M. Dular, R. Bachert, B. Stoffel, et al., *Experimental Evaluation of Numerical Simulation of Cavitating Flow around Hydrofoil*, European Journal of Mechanics B/Fluids 24, 2005, pp. 522-538.

[137] OpenCFD, OpenFOAM User's Guide, URL: https://github.com/OpenFOAM/OpenFOAM-dev/tree/master/applications/solvers/multiphase/cavitatingFoam, and http://www.opencfd.co.uk/. (Retrieved Sep. 2015).

[138] OpenCFD, OpenFOAM User's Guide, URL: http://cfd.direct/openfoam/user-guide/standard-libraries/, and https://github.com/OpenFOAM/OpenFOAM-2.2.x/blob/master/src/thermophysicalModels/basic/psiThermo/hePsiThermo.C. (Retrieved Oct. 2015).

[139] G. Wallis, *One-Dimensional Two-Phase Flow*, New York: McGraw-Hill, 1969.

[140] F. Kärrholm, H. Weller, N. Nordin, *Modeling Injector Flow Including Cavitation Effects for Diesel Applications*, in: ASME Fluids Engineering Conference, 2007, pp. 465-474.

[141] D. Schmidt, C. Rutland, M. Corradini, et al., *Cavitation in Two-Dimensional Asymmetric Nozzles*, SAE Technical Paper, 1999, 1999-01-0518.

[142] OpenCFD, OpenFOAM User's Guide, URL: http://cfd.direct/openfoam/energy-equation/. (Retrieved Nov. 2015).

[143] E. Lemmon, M. McLinden, D. Friend, *Thermophysical Properties of Fluid Systems*, in: NIST Chemistry WebBook, NIST Standard Reference Database Number 69: P. Linstrom and W. Mallard, National Institute of Standards and Technology, Gaithersburg MD, 20899, URL: https://webbook.nist.gov/cgi/cbook.cgi?ID=74-82-8. (Retrieved Aug. 2015).

[144] R. Weast, CRC Handbook of Chemistry and Physics, Chemical Rubber Company (CRC), 65th edition, CRC Press, Florida, USA, 1984, URL: http://www.lmnoeng.com/Flow/GasViscosity.php. (Retrieved Sep. 2015).

[145] R. Prydz, R. Goodwin, *Experimental Melting and Vapor Pressures of Methane*, Journal of Chemical Thermodynamics 1, 4, 1972, pp. 127-133.

[146] OpenCFD, OpenFOAM User's Guide, URL: https://github.com/OpenFOAM/OpenFOAM-dev/blob/master/src/thermophysicalModels/basic/, and http://caefn.com/author/fumiya. (Retrieved May 2016).

[147] OpenCFD, OpenFOAM User's Guide, URL: http://cfd.direct/openfoam/user-guide/fvsolution/. (Retrieved Nov. 2016).

[148] H. Aguerre, S. Damián, J. Gimenez, et al., *Modeling of Compressible Fluid Problems with OpenFOAM Using Dynamic Mesh Technology*, Mecánica Computational 32, 2013, pp. 995-1011.

[149] S. Patankar, *Numerical Heat Transfer and Fluid Flow*, CRC Press, 1980.

[150] J. Ferziger, M. Peric, *Computational Methods for Fluid Dynamics*, Springer, 2002.

[151] T. Behrens, *OpenFOAM's Basic Solvers for Linear Systems of Equations*, CFD Course Report, Chalmers University of Technology, Sweden, 2009.

[152] S. Rahbarimanesh, J. Brinkerhoff, *Numerical Simulation of Cavitating Flow of Liquefied Natural Gas (LNG) in a Converging-Diverging Nozzle*, Canadian Society for Mechanical Engineering International Congress (CSME2016) and 24th Annual Conference of the CFD Society of Canada (CFDSC2016), Kelowna, Canada, 2016.

[153] C. Sarraf, Y. Bouziad, H. Djeridi, et al., *Effect of Cavitation on the Structure of the Boundary Layer in the Wake of a Partial Cavity*, in: Proceedings of the 6th International Symposium on Cavitation CAV2006, Wageningen, Netherlands, 2006.

[154] M. Callenaere, J. Franc, J. Michel, *Influence of Cavity Thickness and Pressure Gradient on the Unsteady Behavior of Partial Cavities*, in: Proceedings of the 3rd International Symposium on Cavitation, Grenoble, France, 1998.

[155] S. Ganz, E. Gutierrez, *Cavitation: Causes, Effects, Mitigation and Application*, Project Report, Rensselaer Polytechnic Institute, Hartford, Connecticut, 2012.

[156] J. Franc, J. Michel, *Attached Cavitation and the Boundary Layer: Experimental Investigation and Numerical Treatment*, Journal of Fluid Mechanics 154, 1985, pp. 63-90.

[157] M. Callenaere, J. Franc, J. Michel, et al., *The Cavitation Instability Induced by the Development of a Re-Entrant Jet*, Journal of Fluid Mechanics 444, 2001, pp. 223-256.

[158] S. Rahbarimanesh, J. Brinkerhoff, *Diffusion Angle Effects on Cavitating Flow of Liquefied Natural Gas (LNG) inside a Laval Nozzle*, Proceedings of the 26th Canadian Congress of Applied Mechanics (CANCAM 2017), Victoria, Canada, 2017.

[159] S. Rahbarimanesh, J. Brinkerhoff, *A Numerical Study on Cavitating Flow of LNG inside a Laval Nozzle: Effects of Cavitation Number and Nozzle Expansion Angle*, Proceedings of the 16th European Turbulence Conference (ETC16), Stockholm, Sweden, 2017.

[160] Y. Saito, K. Sato, *Cavitation Bubble Collapse and Impact in the Wake of a Circular Cylinder*, Proceedings of the 5th International Symposium on Cavitation (CAV2003), Japan, 2003.

[161] S. Rahbarimanesh, J. Brinkerhoff, *Effects of Interfacial Tension Forces on Cavitating Flow of Liquefied Natural Gas (LNG) in a Laval Nozzle*, 26th Annual Conference of the CFD Society of Canada (CFDSC2018), Winnipeg, Canada, 2018.

[162] Y. Shah, A. Pandit, V. Moholkar, *Cavitation Reaction Engineering*, Springer, 1999.

[163] G. Kuvshinov, *Effect of Surface Tension on the Collapse of a Cavitation Bubble*, Journal of Engineering Physics and Thermophysics 60, 1991, pp. 34-37.

[164] J. Zhu, H. Xie, K. Feng, et al., *Unsteady Cavitation Characteristics of Liquid Nitrogen Flows through Venturi Tube*, International Journal of Heat and Mass Transfer 112, 2017, pp. 544-552.

[165] K. Laberteaux, S. Ceccio, *Partial Cavity Flows, Part 2: Cavities Forming on Test Objects with Spanwise Variation*, Journal of Fluid Mechanics 431, 2001b, pp. 43-63.

[166] M. Dular, R. Bachert, C. Schaad, et al., *Investigation of a Re-Entrant Jet Reflection at an Inclined Cavity Closure Line*, European Journal of Mechanics - B/Fluids 26, 2007, pp. 688-705.

[167] J. Hunt, A. Wray, P. Moin, *Eddies, Streams, and Convergence Zones in Turbulent Flows*, in: Proceedings of the 1988 Summer Program In its Studying Turbulence Using Numerical Simulation Databases 2 (N89-24538, pp. 18-34), Center for Turbulence Research, 1988.

[168] B. Ji, X. Luo, Y. Wu, et al., *Numerical Analysis of Unsteady Cavitating Turbulent Flow and Shedding Horse-Shoe Vortex Structure around a Twisted Hydrofoil*, International Journal of Multiphase Flow 51, 2013, pp. 33-43.

[169] J. Wu, H. Ma, M. Zhou, *Vorticity and Vortex Dynamics*, Springer, Berlin, 2006.

[170] T. Xing, S. Frankel, *Effect of Cavitation on Vortex Dynamics in a Submerged Laminar Jet*, AIAA Journal 40, 2002, pp. 2266-2276.

[171] P. Kundu, I. Cohen, *Fluid Mechanics*, 3rd edition, Elsevier Academic Press, 2004.

[172] G. Schnerr, I. Sezal, S. Schmidt, *Numerical Investigation of Three-Dimensional Cloud Cavitation with Special Emphasis on Collapse Induced Shock Dynamics*, Physics of Fluids 20, 2008, 040703.

[173] R. Bensow, G. Bark, *Implicit LES Predictions of the Cavitating Flow on a Propeller*, Journal of Fluids Engineering 132, 2010, 041302.

[174] N. Dittakavi, A. Chunekar, S. Frankel, *Large Eddy Simulation of Turbulent-Cavitation Interactions in a Venturi Nozzle*, Journal of Fluids Engineering 132, 2010, pp. 121301-121311.

[175] Y. Kawanami, H. Kato, H. Yamaguchi, et al., *Mechanism and Control of Cloud Cavitation*, Journal of Fluids Engineering 119, 1997, pp. 788-794.

[176] H. Liu, C. Cai, X. Xi, et al., *A Novel Model for the Bubble Growth in the Cavitation Region of an Injector Nozzle*, International Journal of Heat and Mass Transfer 119, 2018, pp. 128-138.

[177] M. Lü, Z. Ning, K. Yan, et al., *Instability and Breakup of Cavitation Bubbles within Diesel Drops*, Chinese Journal of Chemical Engineering 23, 2015, pp. 262-267.

[178] Y. Shah, A. Pandit, V. Moholkar, *Cavitation Reaction Engineering*, Springer, 1999.

[179] H. Yu, L. Goldsworthy, P. Brandner, et al., *Development of a Compressible Multiphase Cavitation Approach for Diesel Spray Modeling*, Applied Mathematical Modeling 45, 2017, pp. 705-727.

[180] G. Kuvshinov, *Effect of Surface Tension on the Collapse of a Cavitation Bubble*, Journal of Engineering Physics and Thermophysics 60, 1991, pp. 34-37.

[181] S. Tavoularis, *Theory of Turbulence (lecture notes)*, University of Ottawa, Canada, 2012.

[182] J. Kim, P. Moin, R. Moser, *Turbulence Statistics in Fully Developed Channel Flow at Low Reynolds Number*, Journal of Fluid Mechanics 177, 1987, pp. 133-166.

[183] S. Gopalan, J. Katz, O. Knio, *The Flow Structure in the Near Field of Jets and Its Effects on Cavitation Inception*, Journal of Fluid Mechanics 398, 1999, pp. 1-43.

[184] J. Brinkerhoff, M. Yaras, *Numerical Investigation of the Generation and Growth of Coherent Flow Structures in a Triggered Turbulent Spot*, Journal of Fluid Mechanics 759, 2014, pp. 257-294.

[185] J. Bell, R. Mehta, *Development of a Two-Stream Mixing Layer with Tripped and Untripped Boundary Layers*, AIAA Journal 28, 1990, pp. 2034-2042.

[186] S. Rahbarimanesh, *Numerical Simulations of Laminar and Turbulent Mixing Layers behind a Thin Airfoil*, Master's Thesis, University of Ottawa, Faculty of Engineering, 2015.

[187] T. Kajishima, T. Ohta, H. Sakai, et al., *Influence of Cavitation on Turbulent Separated Flow*, Proceedings of the 5th International Symposium on Turbulence and Shear Flow Phenomena (TSFP5), 2007.

[188] S. Rahbarimanesh, J. Brinkerhoff, *A Numerical Study on the Effects of Cavitation Number on Cavitating Mixing Layer of Liquefied Natural Gas (LNG) behind a Flat Plate Splitter*, ASME series: Proceedings of the 10th International Cavitation Symposium (CAV2018), 2018, ASME Press.

[189] R. Leboeuf, R. Mehta, *Vortical Structure Morphology in the Initial Region of a Forced Mixing Layer: Rollup and Pairing,* Journal of Fluid Mechanics 315, 1996, pp. 175-221.

[190] V. Aeschlimann, S. Barre, S. Legoupil, *X-Ray Attenuation Measurements in a Cavitating Mixing Layer for Instantaneous Two-Dimensional Void Ratio Determination*, Physics of Fluids 23, 2011, 055101.

[191] R. Metcalfe, S. Orszag, M. Brachet, et al., *Secondary Instability of a Temporally Growing Mixing Layer*, Journal of Fluid Mechanics 184, 1987, pp. 207-243.

[192] S. Rahbarimanesh, J. Brinkerhoff, *Numerical Investigation of a Cavitating Mixing Layer of Liquefied Natural Gas (LNG) behind a Flat Plate Splitter*, Proceedings of the 70th Annual Meeting of the APS Division of Fluid Dynamics (APS-DFD), Denver, United States, 2017.

[193] C. Iyer, S. Ceccio, *The Influence of Developed Cavitation on the Flow of a Turbulent Shear Layer*, Physics of Fluids 14, 2002, pp. 3414-3431.

[194] V. Roig, C. Suzanne, L. Masbernat, *Experimental Investigation of a Turbulent Bubbly Mixing Layer*, International Journal of Multiphase Flow 24, 1998, pp. 35-54.

[195] C. Tung, *Initial Streamwise Vorticity Formation in a Two-Stream Mixing Layer*, PhD Dissertation, Department of Mechanical Engineering, University of Houston, 1992.

[196] R. Mehta, *Effect of Velocity Ratio on Plane Mixing Layer Development: Influence of Splitter Plate Wake*, Experiments in Fluids 10, 1991, pp. 194-204.

[197] J. Bell, R. Mehta, *Measurements of the Streamwise Vortical Structures in a Plane Mixing Layer*, Journal of Fluid Mechanics 239, 1992, pp. 213-248.

[198] K. Wiecek, R. Mehta, *Effects of Velocity Ratio on Mixing Layer Three-Dimensionality*, Experimental Thermal and Fluid Science 16, 1998, pp. 165-176.

[199] J. Buell, N. Mansour, *Asymmetric Effects in Three-Dimensional Spatially Developing Mixing Layers*, Proceedings of the 7th Symposium on Turbulent Shear Flows, Stanford University, 1989.

[200] Y. Wang, C. Brennen, *Numerical Computation of Shock Waves in Spherical Cloud of Cavitation Bubbles*, ASME Journal of Fluid Engineering 121, 1999, pp. 872-880.

[201] R. Milane, *Large Eddy Simulation (2D) Using Diffusion-Velocity Method and Vortex-in-Cell*, International Journal for Numerical Methods in Fluids 44, 2004, pp. 837-860.

[202] Y. Ito, K. Nagata, Y. Sakai, et al., *Momentum and Mass Transfer in Developing Liquid Shear Mixing Layers*, Journal of Experimental Thermal and Fluid Science 51, 2013, pp. 28-36.

[203] H. Ganesh, S. Mäkiharju, S. Ceccio, *Bubbly Shock Propagation as a Mechanism for Sheet-to-Cloud Transition of Partial Cavities*, Journal of Fluid Mechanics 802, 2016, pp. 37-78.

[204] K. Kikuta, Y. Yoshida, M. Watanabe, et al., *Thermodynamic Effect on Cavitation Performances and Cavitation Instabilities in an Inducer*, Journal of Fluids Engineering 130, 2008, 111302.

[205] G. Reisman, Y. Wang, C. Brennen, *Observations of Shock Waves in Cloud Cavitation*, Journal of Fluid Mechanics 355, 1998, pp. 255-283.

[206] A. Gnanaskandan, K. Mahesh, *Large Eddy Simulation of the Transition from Sheet to Cloud Cavitation over a Wedge*, International Journal of Multiphase Flow 83, 2016, pp. 86-102.

[207] R. Arndt, *Cavitation in Vortical Flows*, Annual Review of Fluid Mechanics 34, 2002, pp. 143-175.

[208] M. Johnson, *On the Flow Structure within a Turbulent Spot*, International Journal of Heat and Fluid Flow 22, 2001, pp. 409-416.

[209] L. Bernal, A. Roshko, *Streamwise Vortex Structure in Plane Mixing Layers*, Journal of Fluid Mechanics 170, 1986, pp. 499-525.

[210] S. Pentelow, *Wing-Tip Vortex Structure and Wandering*, Master's Thesis, University of Ottawa, Faculty of Engineering, 2014.

[211] L. Briançon-Marjollet, L. Merle, *Inception, Development and Noise of a Tip Vortex Cavitation*, 21st Symposium on Naval Hydrodynamics, Norway, 1996.

[212] A. Schröder, R. Geisler, G. Elsinga, et al., *Investigation of a Turbulent Spot and a Tripped Turbulent Boundary Layer Flow Using Time-Resolved Tomographic PIV*, Experiments in Fluids 44, 2008, pp. 305-316.

[213] A. Prosperetti, *The Speed of Sound in a Gas-Vapor Bubbly Liquid*, Interface Focus 5, 2015, 20150024.

[214] N. Jarrin, *Synthetic Inflow Boundary Conditions for the Numerical Simulation of Turbulence*, PhD Dissertation, University of Manchester, Faculty of Engineering and Physical Sciences, 2008.

[215] M. Klein, A. Sadiki, J. Janicka, *A Digital Filter Based Generation of Inflow Data for Spatially Developing Direct Numerical or Large-Eddy Simulations*, Journal of Computational Physics 186, 2003, pp. 652-665.

[216] L. di Mare, M. Klein, W. Jones, et al., *Synthetic Turbulence Inflow Conditions for Large-Eddy Simulation*, Physics of Fluids 18, 2006, 025107.

[217] A. Smirnov, S. Shi, I. Celik, *Random Flow Generation Technique for Large-Eddy Simulations and Particle-Dynamics Modeling*, Journal of Fluids Engineering 123, 2001, pp. 359-371.

[218] N. Sandham, Y. Yao, A. Lawal, *Large-Eddy Simulation of Transonic Turbulent Flow over a Bump*, International Journal of Heat and Fluid Flow 24, 2003, pp. 584-595.

[219] L. Davidson, *Using Isotropic Synthetic Fluctuations as Inlet Boundary Conditions for Unsteady Simulations*, Advances and Applications in Fluid Mechanics 1, 2007a, pp. 1-35.

[220] A. Aly, H. Gol-Zaroudi, *Atmospheric Boundary Layer Simulation in a New Open-Jet Facility at LSU: CFD and Experimental Investigations*, Measurement 110, 2017, pp. 121-133.

[221] Johns Hopkins Turbulence Databases, URL: http://turbulence.pha.jhu.edu/Channel_Flow.aspx. (Retrieved Dec. 2018).

Appendices

Appendix A: Derivation of Conservation Equations in the Cryogenic Cavitation Solver

The governing equations are found by incorporating the saturation pressure relationship from the Clausius-Clapeyron Equation (12) into the conservation equations for an isothermal cavitating flow [52,137]. As a result of this substitution, the governing equations include source terms for the time-varying mass, momentum, and the latent heat transfer that occurs between phases during vaporization and condensation processes.

The mixture density of isothermal fluid is found from the continuity equation,

$$\frac{\partial \rho_m^*}{\partial t} + \nabla \cdot (\rho_m^* \boldsymbol{u}^*) = 0\,, \tag{38}$$

by using Kärrholm's theory which introduces an iterative mixture's equilibrium equation of state for the isothermal mixture density:

$$\rho_m^* = (1-\alpha^*)\rho_l^{0^*} + (\alpha^*\psi_v^* + (1-\alpha^*)\psi_l^*)\, p_{sat}^* + \psi_m^*(p^* - p_{sat}^*) \tag{39}$$

where the superscript '*' stands for isothermal fluid. Employing the linear compressibility function,

$$\psi_m^* = \alpha^*\psi_v^* + (1-\alpha^*)\psi_l^*\,, \tag{40}$$

results in

$$\rho_m^* = (1-\alpha^*)\rho_l^{0^*} + \psi_m^* p^* \tag{41}$$

where

$$\rho_l^{0^*} = \rho_{l,sat}{}^* - \psi_l^*\, p_{sat}^*\,. \tag{42}$$

Thus,

$$\rho_m^* = (1-\alpha^*)\left(\rho_{l,sat}{}^* - \psi_l^*\, p_{sat}^*\right) + \psi_m^* p^* \tag{43}$$

which represents the Kärrholm's mixture equilibrium equation of state for an isothermal fluid. Equations (42)-(43) in the case of cryogenic fluids are rewritten as follows

$$\rho_l^0 = \rho_{l,sat} - \psi_l\, p_{sat} \tag{44}$$

and

$$\rho_m = (1-\alpha)\left(\rho_{l,sat} - \psi_l\, p_{sat}\right) + \psi_m p \tag{45}$$

which indicate the initial liquid phase and mixture densities of a cryogenic mixture, respectively. Saturation pressure in cryogenic fluids is not a constant value. Hence, incorporating the saturation pressure Equation (12) in (45) results in an equation of state for cryogenic fluids:

$$\rho_m = (1-\alpha)\left[\rho_{l,sat} - \psi_l\left(\frac{\Delta T \rho_v L}{T_\infty}\right) - \psi_l\, p_{sat}^*\right] + \psi_m p\,. \tag{46}$$

Assuming $\psi_m = \psi_m^*$, $\psi_l = \psi_l^*$, $\alpha = \alpha^*$, $\rho_{l,sat} = {\rho_{l,sat}}^*$, $p = p^*$, and $\boldsymbol{u} = \boldsymbol{u}^*$ for initialization procedure, equations (45) and (46) are correlated by Equation (47):

$$\rho_m = \rho_m^* - (1-\alpha)\,\frac{\psi_l\,\Delta T \rho_v L}{T_\infty} \tag{47}$$

which compares the Kärrholm's mixture density for cryogenic and isothermal fluids.

Governing equations in the present cryogenic cavitation model can be derived by using the cryogenic-isothermal mixture density correlation presented in Equation (47). By doing so, and employing a comparative notation, differences between governing equations of cryogenic and isothermal cavitating flows are declared as follows:

- Cryogenic continuity equation: continuity equation for a cryogenic cavitating flow is:

$$\frac{\partial \rho_m}{\partial t} + \nabla\cdot(\rho_m \boldsymbol{u}) = 0 \tag{48}$$

where ρ_m can be substituted from Equation (47); thus, giving

$$\frac{\partial \rho_m^*}{\partial t} + \nabla\cdot(\rho_m^* \boldsymbol{u}) = \frac{\partial}{\partial t}\left(\frac{(1-\alpha)\,\psi_l\,\Delta T \rho_v L}{T_\infty}\right) + \nabla\cdot\left(\frac{(1-\alpha)\,\psi_l\,\Delta T \rho_v L}{T_\infty}\,\boldsymbol{u}\right), \tag{49}$$

which could be rewritten as

$$\frac{\partial \rho_m}{\partial t} + \nabla\cdot(\rho_m \boldsymbol{u}) = \frac{\partial}{\partial t}\left(\frac{(1-\alpha)\,\psi_l\,\Delta T \rho_v L}{T_\infty}\right) + \nabla\cdot\left(\frac{(1-\alpha)\,\psi_l\,\Delta T \rho_v L}{T_\infty}\,\boldsymbol{u}\right) \tag{50}$$

using the assumption $\rho_m = \rho_m^*$ for initialization. Equation (50) represents the continuity equation in the proposed cryogenic cavitation model. As shown, this equation is distinguished from its isothermal counterpart by having two source terms on RHS. These two terms illustrate the mass and latent heat transfer correlation during phase change process.

- Cryogenic pressure equation: pressure field in the cryogenic fluid is iteratively computed from the pressure equation:

$$\frac{\partial(\psi_m\, p)}{\partial t} - (\rho_l^0 + (\psi_l - \psi_v)\, p_{sat})\frac{\partial \alpha}{\partial t} - p_{sat}\frac{\partial \psi_m}{\partial t} + \nabla\cdot(\rho_m \boldsymbol{u}) = 0\,. \tag{51}$$

Employing the initial liquid density (44) and the saturation pressure (12) equations into (51) results in

$$\frac{\partial(\psi_m\, p)}{\partial t} - \left(\rho_l^{0^*} - \frac{\psi_l\, \Delta T \rho_v L}{T_\infty} + (\psi_l - \psi_v)\,\frac{\Delta T \rho_v L}{T_\infty} + (\psi_l - \psi_v)\, p_{sat}^*\right)\frac{\partial \alpha}{\partial t}$$
$$- \left(\frac{\Delta T \rho_v L}{T_\infty}\right)\frac{\partial \psi_m}{\partial t} - p_{sat}^*\,\frac{\partial \psi_m}{\partial t} + \nabla\cdot(\rho_m \boldsymbol{u}) = 0 \tag{52}$$

where $\rho_l^{0^*} = {\rho_{l,sat}}^* - \psi_l^*\, p_{sat}^*$ by assuming $\psi_l = \psi_l^*$ and $\rho_{l,sat} = {\rho_{l,sat}}^*$ for initialization. Thus, substituting ρ_m from Equation (47) in (52) results in

$$\frac{\partial(\psi_m\, p)}{\partial t} - \left(\rho_l^{0^*} - \frac{\psi_l\, \Delta T \rho_v L}{T_\infty} + (\psi_l - \psi_v)\frac{\Delta T \rho_v L}{T_\infty} + (\psi_l - \psi_v)\, p_{sat}^*\right)\frac{\partial \alpha}{\partial t} - \left(\frac{\Delta T \rho_v L}{T_\infty}\right)\frac{\partial \psi_m}{\partial t}$$
$$- p_{sat}^*\,\frac{\partial \psi_m}{\partial t} + \nabla\cdot(\rho_m^* \boldsymbol{u}) - \nabla\cdot\left((1-\alpha)\frac{\psi_l\, \Delta T \rho_v L}{T_\infty}\boldsymbol{u}\right) = 0 \tag{53}$$

which is rearranged as

$$\frac{\partial(\psi_m\, p)}{\partial t} - (\rho_l^0 + (\psi_l - \psi_v)\, p_{sat}^*)\,\frac{\partial \alpha}{\partial t} - p_{sat}^*\,\frac{\partial \psi_m}{\partial t} + \nabla\cdot(\rho_m \boldsymbol{u})$$
$$= -\,\psi_v\,(\frac{\Delta T \rho_v L}{T_\infty})\,\frac{\partial \alpha}{\partial t} + (\frac{\Delta T \rho_v L}{T_\infty})\,\frac{\partial \psi_m}{\partial t} + \nabla\cdot\left((1-\alpha)\frac{\psi_l\, \Delta T \rho_v L}{T_\infty}\,\boldsymbol{u}\right) \tag{54}$$

by assuming $\rho_m = \rho_m^*$ and $\rho_l^0 = \rho_l^{0^*}$ for initialization. Equation (54) shows the cryogenic pressure equation, differentiated from the isothermal counterpart by having three additional source terms on RHS.

- Cryogenic momentum equation: velocity field for a cryogenic cavitating flow is found from the momentum equation,

$$\frac{\partial(\rho_m\, \boldsymbol{u})}{\partial t} + \nabla\cdot(\rho_m\, \boldsymbol{u}\boldsymbol{u}) = -\,\nabla p + \nabla\cdot[\,\mu_m\,(\nabla\boldsymbol{u} + (\nabla\boldsymbol{u})^T)] \tag{55}$$

where μ_m is calculated from the Sutherland model described in Section 3.2.3. Using the cryogenic mixture's density Equation (47) in (55) gives

$$\frac{\partial}{\partial t}\left(\left(\rho_m^* - (1-\alpha)\,\frac{\psi_l\, \Delta T \rho_v L}{T_\infty}\right)\boldsymbol{u}\right) + \nabla\cdot\left(\left(\rho_m^* - (1-\alpha)\,\frac{\psi_l\, \Delta T \rho_v L}{T_\infty}\right)\boldsymbol{u}\boldsymbol{u}\right)$$
$$= -\,\nabla p + \nabla\cdot[\,\mu_m(\nabla\boldsymbol{u} + (\nabla\boldsymbol{u})^T)]\,, \tag{56}$$

resulting in

$$\frac{\partial(\rho_m\, \boldsymbol{u})}{\partial t} + \nabla\cdot(\rho_m\, \boldsymbol{u}\boldsymbol{u}) = -\,\nabla p + \nabla\cdot[\,\mu_m(\nabla\boldsymbol{u} + (\nabla\boldsymbol{u})^T)]$$
$$+\frac{\partial}{\partial t}\left((1-\alpha)\,\frac{\psi_l\, \Delta T \rho_v L}{T_\infty}\,\boldsymbol{u}\right) + \nabla\cdot\left((1-\alpha)\,\frac{\psi_l\, \Delta T \rho_v L}{T_\infty}\,\boldsymbol{u}\boldsymbol{u}\right) \tag{57}$$

with the assumption $\rho_m = \rho_m^*$ for initialization. Equation (57) shows that the cryogenic momentum equation has two additional source terms on RHS describing the latent heat-momentum correlation during phase change.

- <u>Cryogenic energy equation:</u> In cryogenic cavitation, the energy equation with no additional heat source term is given by

$$\frac{\partial \rho_m h}{\partial t} + \nabla \cdot (\rho_m \boldsymbol{u} h) + \frac{\partial \rho_m K}{\partial t} + \nabla \cdot (\rho_m \boldsymbol{u} K) - \frac{\partial p}{\partial t} = -\nabla \cdot \boldsymbol{q} + \nabla \cdot (\boldsymbol{\tau} \cdot \boldsymbol{u}) + \rho_m \, \boldsymbol{g} \cdot \boldsymbol{u} \ . \tag{58}$$

Similar to the previous conservation equations, substitution of ρ_m from Equation (47) in (58), with neglecting the gravity term for the present work, yields

$$\begin{aligned} &\frac{\partial \rho_m h}{\partial t} + \nabla \cdot (\rho_m \boldsymbol{u} h) + \frac{\partial \rho_m K}{\partial t} + \nabla \cdot (\rho_m \boldsymbol{u} K) - \frac{\partial p}{\partial t} = -\nabla \cdot \boldsymbol{q} + \nabla \cdot (\boldsymbol{\tau} \cdot \boldsymbol{u}) \\ &+ \frac{\partial}{\partial t}\left((1-\alpha)\frac{\psi_l \, \Delta T \rho_v L}{T_\infty}(K+h)\right) + \nabla \cdot \left((1-\alpha)\,\frac{\psi_l \, \Delta T \rho_v L}{T_\infty}(K+h)\,\boldsymbol{u}\right) \end{aligned} \tag{59}$$

using the assumption $\rho_m = \rho_m^*$ for initialization. Equation (59) represents the energy conservation equation for a cryogenic cavitating flow, in which two additional source terms on RHS demonstrates the latent heat transfer mechanisms during phase change processes. The LHS of Equation (59) includes five different terms derived in terms of the cryogenic mixture density, pressure, and velocity, which are iteratively found from the cryogenic continuity (50), pressure (54), and momentum (57) equations and updated through the modified PIMPLE loop discussed in Section 3.2.5.

Appendix B: 2D Mesh Convergence Studies

a) Mesh Convergence Study for the Laval Nozzle Simulations

The optimum number of cells for the numerical simulations of LNG and LN_2 cavitating flows inside the Laval nozzle was determined by using mesh convergence analysis. In this case, three numerical tests were performed by using the developed solver for three different grids with 1,113,100, 721,600, and 478,200 non-uniform hexahedral elements. As shown in Fig. 99, the resulting streamwise pressure distribution on the nozzle upper wall (see Section 4.1 for details) for the grids with 1,113,100 and 721,600 cells reveals much the same trend compared to the distribution resulted from the coarsest grid. To reduce the computational costs, the Laval nozzle simulations are conducted with the grid of 721,600 elements.

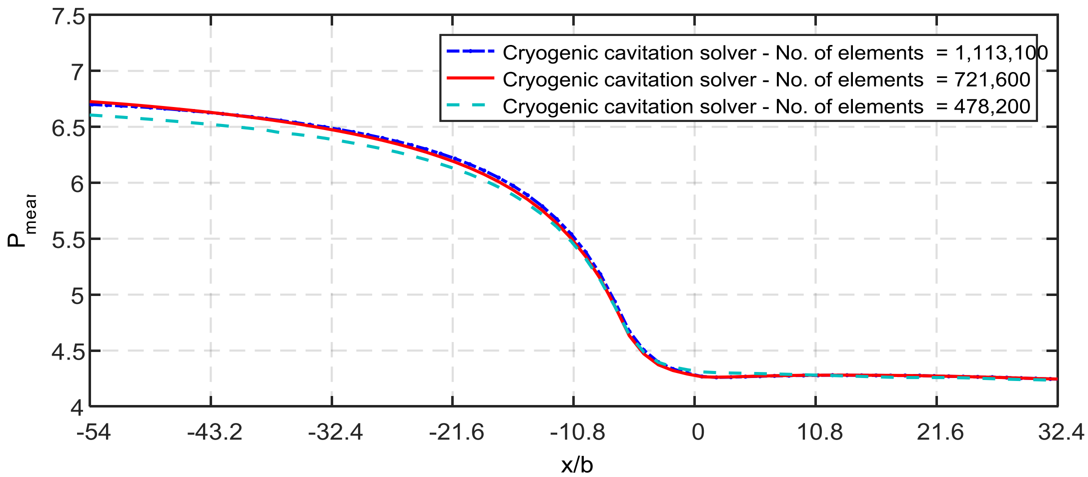

Fig. 99: Mesh convergence study for the Laval nozzle simulations; comparison of the mean pressure (bar) distribution in the cavitating LNG flow along the upper wall of the nozzle for the grids with 1,113,100, 721,600, and 478,200 elements.

b) Mesh Convergence Study for the Orifice Simulations

In the case of cavitating flow of LN_2 inside the orifice a similar mesh convergence study to the nozzle case was conducted by employing three structured grids with 915,700, 580,500, and 345,200 non-uniform elements. For the selected grids, streamwise variation of the B-factor along the four streamwise stations (see Section 4.2 for details) placed after the orifice is shown in Fig. 100. As indicated, the best match between the numerical results and experimental data are detected for the grids with 580,500 and 915,700 elements. The grid with 580,500 elements is selected for the orifice simulations.

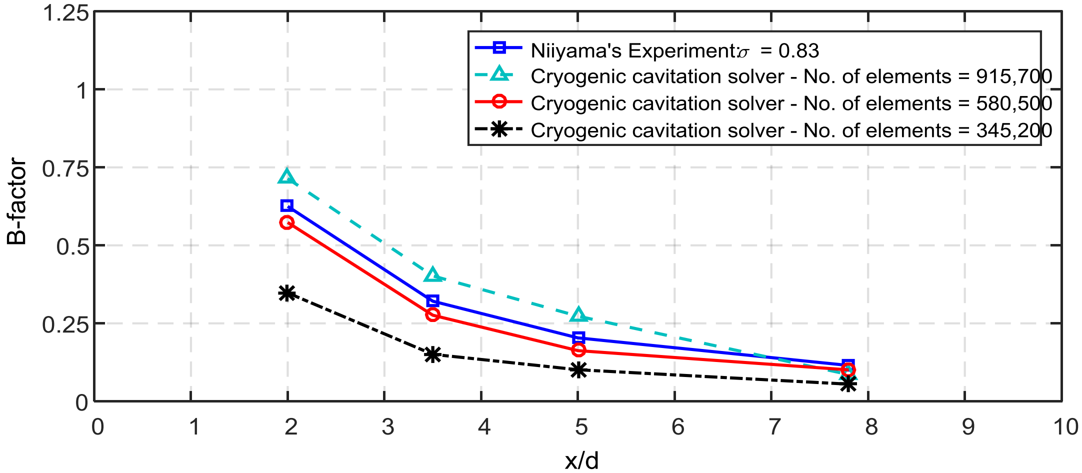

Fig. 100: Mesh convergence study for the orifice simulations; comparison of the B-factor at four streamwise stations in the cavitating flow of LN_2 for the grids with 915,700, 580,500, and 345,200 elements.

c) Mesh Convergence Study for the Mixing Layer Simulations

In the case of cavitating mixing layer of LNG behind the splitter plate, the same mesh convergence study as in the nozzle and orifice cases in (a) and (b) was conducted by using four structured grids with 645,681, 525,700, 435,140, and 265,620 non-uniform elements. For the selected grids, Fig. 101 depicts the streamwise evolution of the vorticity thickness at the transverse line stations downstream of the splitter plate (see Section 9.4 for details). As seen, the resulting vorticity thicknesses for the grids with 525,700 and 645,681 elements collapse well, so the grid with 525,700 elements is selected for the mixing layer simulations.

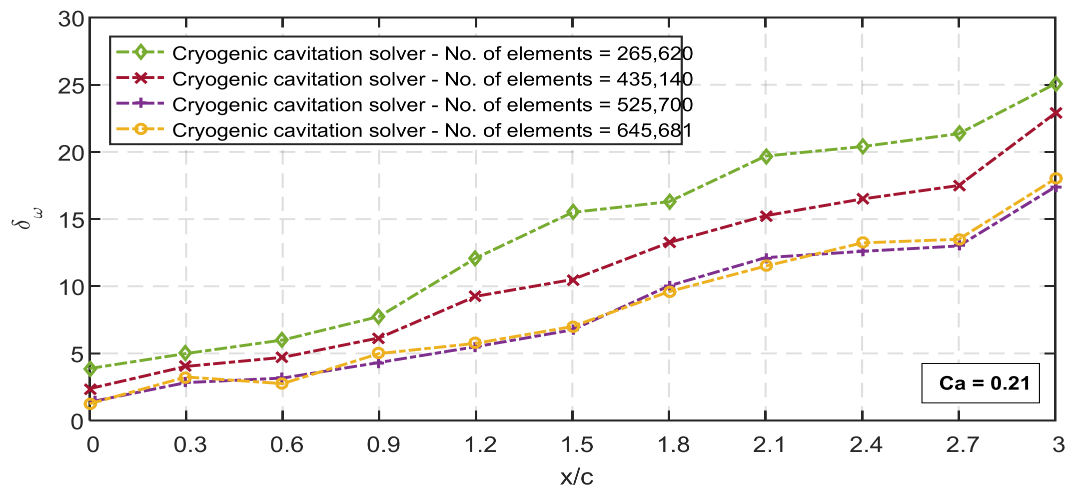

Fig. 101: Mesh convergence study for the mixing layer simulations; comparison of the vorticity thickness (mm) at the transverse reference line stations in the cavitating mixing layer of LNG for the grids with 645,681, 525,700, 435,140, and 265,620 elements.

Appendix C: Preliminary Investigations of the Turbulent Cavitating Flows of LNG

a) Turbulent Cavitating Flow of LNG inside the Laval Nozzle

The turbulent LNG cavitation flow inside the Laval nozzle is built by imposing an upstream source of perturbation in the previously-investigated transitional flow in Chapter 5.1. To create the upstream perturbation, the Iyer and Ceccio [193] work is employed, and a transverse upward jet with the diameter of $d = 0.1b$ is placed on the lower wall of the throat at the location with the largest streamwise velocity (i.e. $x/b \cong -12.0$) to maximize the perturbation influence. The simulation is performed 2D, with the same setup and operating condition as described in Section 4.5. The upward jet velocity is set to $v_{jet}/U_{throat} = 0.20$. Fig. 102 shows the behaviors of LNG vapor phase fraction and temperature fields in the nozzle at time instants t = 0.54, 0.72 and 0.81 s. As seen, the presence of upstream disturbance triggers the in-nozzle flow to promote an earlier cavitation process, as compared to the transitional case without the upstream turbulence (see also Fig. 14). The small-scale vortex and cavity structures generated through the jet injection process (these cavities are incepted in the low-pressure cores of the eddies formed immediately downstream of the jet (see Fig. 103)), cause the flow on the lower wall of the nozzle to become destabilized quickly, so leading to an early formation of a transient to turbulent regime in the separated shear layer.

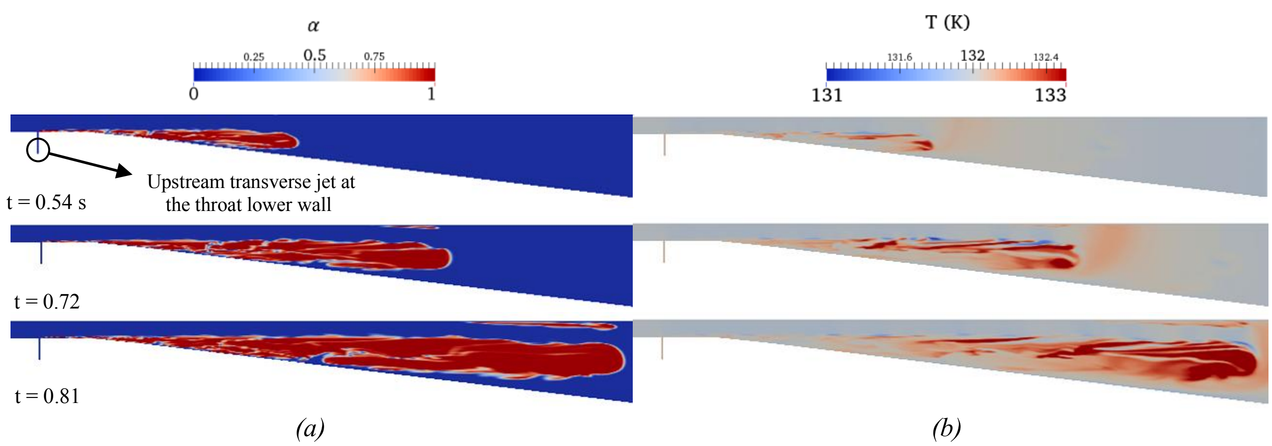

Fig. 102: Temporal evolution of the cavitating flow of LNG inside the nozzle with the throat transverse jet: (a) vapor phase fraction and (b) temperature (K).

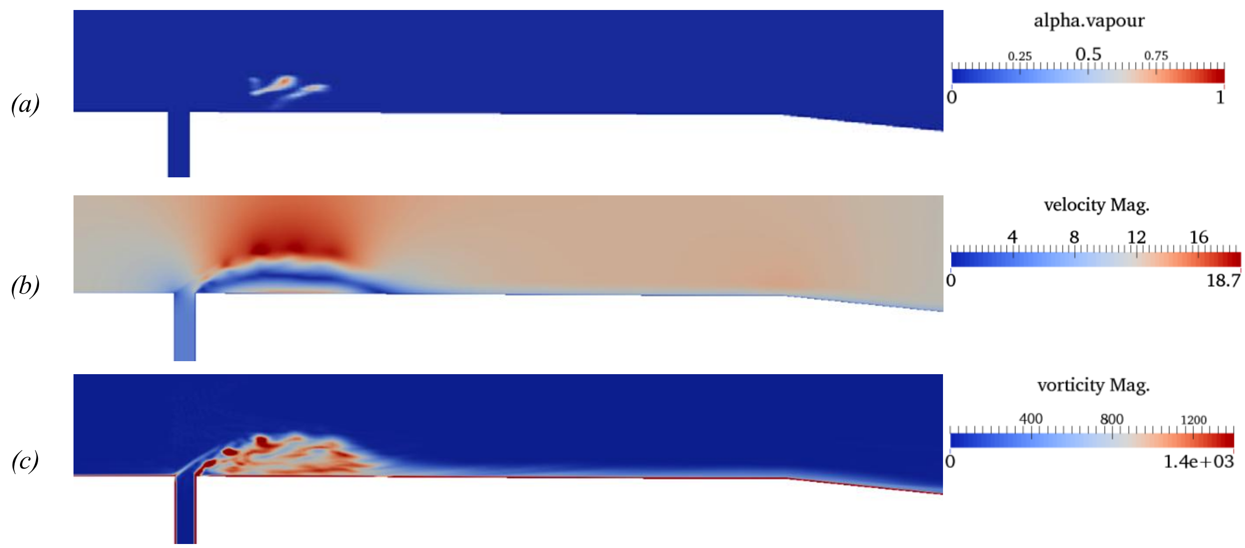

Fig. 103: Close-up view of the LNG cavity inception in the vortex structures formed in the recirculation region past the jet: (a) vapor phase fraction, (b) velocity magnitude (cm/s), and (c) vorticity magnitude (1/s) at t = 0.19 s.

Further downstream, the unstable shear flow past the jet merges with the separated shear layer at the intersection of the throat and the diverging part, to form the highly unsteady turbulent cavitating clouds. The unsteady cavitating clouds evolve throughout the whole diverging section of the nozzle such that no steady fully-vaporized region -- which was observed in the transitional case (see Fig. 14) -- is spotted even in the latest stages of the development process. This implies the significant influence of the correlations between the shear flow separation behavior and the occurrence of transition to turbulence, on the dynamics of cavity generation mechanisms [125]. This conclusion is reported in literature (see for example [85,87,100,183]) to be also valid for the cavitating flows without separation, where the intense upstream fluctuations are the only cause for triggering cavitation. An indicative example of this is Gopalan et al. [183] who observed the cavitation occurrence in the cores of vortex rings generated through a tripped boundary layer of a submerged water jet -- in absence of the tripped boundary layer cavitation is found in the cores of streamwise vortex tubes. It can be thus stated that although cavitation in the present in-nozzle LNG flow is largely associated with inertia due to the local dynamic and static pressure gradients with temperature-dependent density variations, the viscous effects including the variations of vorticity -- in particular because of the upstream turbulence -- substantially modify the cavitation patterns. Future investigations of the present work will focus on evaluating the local instability behaviors at distinct probing stations to characterize the effects of upstream perturbation on local cavity-vortex interactions. Performing parametric studies for different configurations of the jet, as well as conducing 3D simulations of the present test in an extruded nozzle with a full-span upstream jet are also suggested as future work.

b) Turbulent Cavitating Mixing Layer of LNG

To the best of our knowledge and based on the conducted literature survey in Chapter 2, despite the significant number of investigations on turbulent cavitating flows, an efficient method that is able to accurately capture the transitional to turbulent cavitating structures in cryogenic flows has not yet been reported. This is mainly due to the presence of complicated thermo-sensitive phase-change processes, compressibility effects, and vortex-cavity interactions at very small spatio-temporal scales in these flows, as well as to the simplifying assumptions, e.g. over-prediction of the turbulent viscosity of small-scale structures, in the currently-available numerical models. Although capability of these models in precisely resolving cavity and vortex structures has recently improved in a few DNS studies (see for example [111,125]), their limited applications to the isothermal cavitation in simple geometries, yet with inherently iterative, time consuming, and expensive computations still highlight the need for much more effort in developing more efficient numerical frameworks for properly capturing the complex thermo-sensitive cavity-vortex interaction mechanisms in turbulent cryogenic cavitating flows.

Since the application of direct numerical simulations is limited in turbulence modeling of cavitation flows, using the large eddy simulation (LES) approach with an incorporated alternate turbulent inflow generator, which is able to precisely assimilate the desired fully-developed turbulent conditions, can significantly reduce the computational costs while providing a high-level accuracy comparable to DNS [214]. In this context, the commonly-used random turbulent inflow generators (i.e. a simplified turbulent inlet velocity composed of random fluctuations added to a specified mean velocity profile) are not capable of properly resolving all the scales in transitional to turbulent structures due to the following reasons [28,29]:

1) The inlet velocity fluctuations are created randomly, so causing the lack of spatial and temporal correlations between computing fields and physical meaning of characteristic eddies.

2) The energy spectrum in small- and large -scale eddies is distributed improperly, so leading the turbulence to become dissipated quickly due to energy overload in small-scale eddies.

Nevertheless, some of the above-noted defects in generating a proper turbulent inflow have been addressed in more recently developed models, including: digital filtering procedures of Klein et al. [215] and di Mare et al. [216] which remedy the lack of large-scale dominance in the inflow data by randomly generating 3D fields for each velocity component; spectral methods of Smirnov et al. [217] and Sandham et al. [218] which use a decomposition procedure of the inflow signal into Fourier modes; and combined framework of Davidson [219] which generates an inlet condition for LES/DNS simulations using both of the Fourier decomposition and digital filtering methods. In the present study, the synthetic turbulent inflow generator based on the vortex method of Mathey et al. [29] is adopted to address the use of spatio-temporally varying turbulent inflow conditions in accurately modeling of 3D turbulent cavitating flows of LNG. A review of the development procedure and a test case showing the functionality of the developed inflow generator is given as follows.

1. Methodology

The synthetic turbulent inflow of Sergent [28] and Mathey et al. [29] is implemented as a boundary condition library in OpenFOAM. The boundary condition is composed of randomly generated transverse fluctuations (which vary with space and time based on the variations of computing vorticity field), developed via a vortex method (VM), and a prescribed mean velocity profile. Assuming an initial vorticity field $\boldsymbol{\omega}$ across an inlet patch cells centers (normal to the streamwise direction) of a computational domain, the local amount of vorticity carried by a vortex point i at a randomly moving position $\boldsymbol{x} = (x, y)$ on the patch (the reference point (0,0) is located at the patch center) at time t is given by

$$\boldsymbol{\omega_i}(\boldsymbol{x}, t) = \sum_{i=1}^{N} \Gamma(\boldsymbol{x_i}, t)\, \eta(|\boldsymbol{x} - \boldsymbol{x_i}|, t) \tag{60}$$

where N is the number of random vortex points on the patch convected in the flow while carrying the information of the vorticity field; and, Γ and η are, respectively, circulation and spatial distribution of the vortex point i. In Equation (60), the circulation $\Gamma(\boldsymbol{x_i}, t)$ represents the intensity of generated fluctuations, and is adjusted locally to approximate the velocity fluctuations in terms of the level of turbulent kinetic energy k as follows

$$\Gamma(\boldsymbol{x_i}, t) \approx 4\sqrt{\frac{\pi A k(\boldsymbol{x_i}, t)}{3N(2ln(3) - 3ln(2))}} \tag{61}$$

where A is the inlet patch area and k is approximated by

$$k(\boldsymbol{x_i}, t) = \frac{3}{2}(u(\boldsymbol{x_i}, t)I) \tag{62}$$

in which u is the streamwise velocity at $\boldsymbol{x_i}$ and I is the turbulence intensity given by

$$I = \frac{1}{log(\frac{y}{y_0})} \tag{63}$$

where y_0 is a reference average boundary layer thickness at which the power law matches to the logarithmic law [220]. The vortex spatial distribution η in Equation (60) is

$$\eta(\boldsymbol{x}, t) = \frac{1}{\pi\xi^2}\left(2e^{-\frac{|\boldsymbol{x}|^2}{2\xi^2}} - 1\right)e^{-\frac{|\boldsymbol{x}|^2}{2\xi^2}} \tag{64}$$

in which the parameter ξ is characteristic turbulent mixing length [28,29]. Note that ξ is bounded by the local grid size, Δ, such that $\xi \geq \Delta$ to control the vortex size and ensure that the vortices belong to the resolved scale. By substituting Equation (60) in the Biot-Savart law to correlate the vorticity to velocity, the tangential velocity field $\boldsymbol{r}(\boldsymbol{x}, t)$ yields

$$\boldsymbol{r}(\boldsymbol{x}, t) = \frac{1}{2\pi}\sum_{i=1}^{N}\Gamma(\boldsymbol{x_i}, t)\frac{(\boldsymbol{x_i} - \boldsymbol{x}) \times \boldsymbol{n}}{|\boldsymbol{x} - \boldsymbol{x_i}|^2}\left(1 - e^{\frac{|\boldsymbol{x}-\boldsymbol{x_i}|^2}{2\xi^2}}\right)e^{\frac{|\boldsymbol{x}-\boldsymbol{x_i}|^2}{2\xi^2}} \tag{65}$$

where the vector $\boldsymbol{n}$ is the unit vector in the streamwise direction. Equation (65) describes the local tangential velocity fluctuations at the randomly moving position $\boldsymbol{x} = (x, y)$ on the inlet patch, which change through variations of the neighboring vortex points randomly distributed at vortex positions $\boldsymbol{x_i}$ = (x_i , y_i). The fluctuating velocity component found from Equation (65) is then added to a prescribed mean inlet velocity to form the synthetic turbulent inflow.

2. Validation Test Simulation

To examine the functionality of the developed turbulent inflow boundary condition, a validation test simulation is set up based on the turbulent channel flow DNS dataset of JHTDB [221]. The validation test is proposed to reproduce a fully turbulent flow of water in a 3D rectangular channel geometry with dimensions of 20.0×2.54×2.0 m^3, which operates with initial free stream mean velocity of U = 1.0 m/s (Re = 4000.0) and initial wall boundary thickness of δ = 0.0005 m. To generate the turbulent inflow on the inlet patch of the channel, the turbulent 1/7th power law velocity profile of Prandtl [75], given by

$$\frac{\bar{u}}{U} = (\frac{y}{\delta})^{1/7} , \tag{66}$$

is incorporated into the boundary condition library as the initial mean velocity profile. The Prandtl's profile is selected because it accurately describes the mean velocity behavior in fully developed turbulent boundary layer flow over a flat plate [75]. For the given JHTDB operating setup, the mean velocity thus yields $\bar{u}$ = 2.54 $y^{0.15}$, assuming $y_0 = \delta$ = 0.0005 m. As a first step towards validating the developed boundary condition, the initiative behavior of the vortex points on the inlet patch of the simulated channel is evaluated using N = 10 number of random vortex points. Fig. 104 shows the preliminary results of the vortex points evolution at time instants of t = 0.20 and 0.80 s on the inlet patch. As observed, the generated vortex points evolve in time and space, leading the tangential velocity fluctuations to correspondingly behave spatio-temporally. Continuous correlation of the generated fluctuations in the inlet patch, which are transmitted along with the mean velocity field downstream, with the computing vorticity field over time, ensures permanent turbulence reproduction in the simulated eddies. Future investigation of the current work is to utilize the developed turbulent inflow, with an effective number of vortex points (N), in a LES framework to accurately reproduce the JHTDB data. The present approach supplies the necessary building blocks towards future direct numerical simulations of turbulent cavitating flows of LNG.

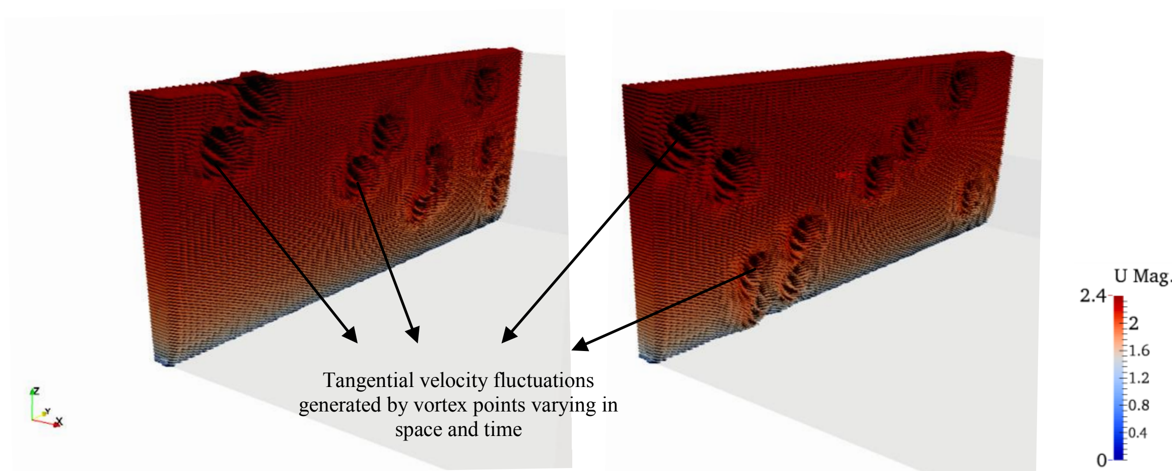

Fig. 104: Turbulent inflow generator with N = 10: temporal distribution of velocity vectors (m/s) across the inlet patch of the 3D channel flow at t = 0.20 and 0.80 s.